Rare earth ion doped antimony-based chalcogenide fibres for biologically relevant wavelengths in the mid-IR.



Richard Crane, BSc. MSc.

Supervisors: Angela B. Seddon, Sendy Phang, Trevor M. Benson

Thesis submitted to the University of Nottingham for the degree of Doctor of Philosophy.

July 2022

Abstract

The wide mid-IR transmission window and rare earth dopant solubility of chalcogenide glasses have identified them as a potentially novel medium to facilitate mid-IR (Mid-IR) fibre lasing. These glasses, with their comparatively low phonon energy matrices, are capable of transmitting and accommodating radiative transitions at wavelengths not accessible by other doped fibre systems such as ZBLAN (ZrF_4-BaF_2-LaF_3-AlF_3-NaF) or indium fluoride (InF_3-ZnF_2-SrF_2-BaF_2). Reported instances of mid-IR fibre lasing are few, with extrinsic oxygen and hydrogen impurities increasing fibre losses and potentially conferring a high phonon energy local environment to the active rare earth ions, reducing the probability of mid-IR radiative transitions. Therefore, the work here aims to develop high purity, devitrification resistant, optically active antimony-based chalcogenide fibres.

Initial work focused on the development of a Ge-Sb-Se-Ga glass composition that was suitable for rare earth ion doping. This was to be a lower phonon energy alternative to the more commonly reported Ge-As-Se-Ga doped glasses. A 1000 ppmw Sm^{3+} $Ge_{20}Sb_{10}Se_{65}Ga_5$ at. % preform documented in the literature was replicated, but extensive crystallisation resulted from the processing methods used. A second composition, $Ge_{19.4}Sb_{9.7}Se_{67.9}Ga_3$ at. %, was designed and demonstrated resistance to devitrification during fibre drawing up to doping concentrations of 1000 ppmw. A 1000 ppmw Sm^{3+} doped $Ge_{19.4}Sb_{9.7}Se_{67.9}Ga_3$ at. % fibre exhibited lowest losses of 2.15 dB/m at 6.04 µm wavelength with photoluminescence measured between 3.25-4.25 µm, and 6-9 µm wavelengths when pumped at 1.3 µm, and 1.47 µm, respectively. A 500 ppmw Dy^{3+} doped $Ge_{19.4}Sb_{9.7}Se_{67.9}Ga_3$ at. % fibre exhibited lowest losses of 3.2 dB/m at 6.63 µm.

With the aim to achieve fibre lasing, a small core, step-index fibre is required. Therefore, the next step was to design an accompanying cladding glass for the $Ge_{19.4}Sb_{9.7}Se_{67.9}Ga_3$ at. % host glass composition. A straight substitution of 2.9 at. % selenium for sulfur ($Ge_{19.4}Sb_{9.7}Se_{65}Ga_3S_{2.9}$ at. %) was trialled, but excessive devitrification prevented this composition from being drawn. A series of glasses with compositions $Ge_{19.4}Sb_{9.7}Ga_{1\text{-}2}Se_{67.9\text{-}(Ga+S)}S_{1\text{-}3}$ at. %, and a standalone

$Ge_{21}Sb_{10}Se_{69}$ at. % composition were produced with the target of T_g (glass transition temperature) being ± 10 °C of the T_g of the core glass, $Ge_{19.4}Sb_{9.7}Se_{67.9}Ga_3$ at. % (T_g 232 °C). Mid-IR variable angle spectroscopic ellipsometry (VASE) was used to measure refractive index values of these glasses finding values between 2.5218-2.5615 at 2.8 µm and 2.5264-2.5565 at 4.3 µm, wavelengths chosen based on the Dy^{3+} radiative emissions. An ellipsometry model comprised of one pole (Sellmeier) oscillator centred in the electronic absorption edge, a second pole oscillator centred in the vibrational fundamental absorption bands, and a Gaussian oscillator around the fundamental absorption of Se-Se homobonds (~33 µm) was found to consistently provide a good fit to the measured ellipsometry data. An assumed (lower refractive index) oxide surface layer was also incorporated into the model using a surface roughness feature. This added a layer between 5.52 – 14.45 nm thick that assumed air(void)-glass was in a 50:50 ratio. $Ge_{21}Sb_{10}Se_{69}$ at. % was proved to match the T_g criteria (T_g 227 °C) and had a refractive index to provide a suitable numerical aperture (NA) at Dy^{3+} photoluminescent wavelengths (0.3438 at 2.8 µm, 0.3638 at 4.3 µm).

A 500 ppmw Dy^{3+} doped $Ge_{19.4}Sb_{9.7}Se_{67.9}Ga_3$ at. % core glass was successfully fibre drawn to a small core, step-index fibre with a $Ge_{21}Sb_{10}Se_{69}$ at. % cladding. This novel antimony-based cladding glass was also successfully fibre drawn to a small core fibre with a 500 ppmw Ce^{3+} doped $Ge_{15}As_{21}Se_{63}Ga_1$ at. % core glass. This Ce^{3+} small core fibre was optically pumped at 4.15 µm (NA: 0.4704) to excite the Ce^{3+}: $^2F_{7/2} \rightarrow {}^2F_{5/2}$ radiative transition. Three laser peaks at 5.12 µm (NA: 0.4757), 5.17 µm (NA: 0.4759), and 5.28 (NA: 0.4764) were observed. This is the first recording of mid-IR fibre CW (continuous wave) lasing in a chalcogenide glass fibre host.

An open vacuum distillation method for purification of anhydrous, powdered $DyCl_3$ in silica glass tubing housing was trialled. After 0.5 hours heat treatment above 850 °C, $DyCl_3$ had distilled into a large translucent crystalline form and a fine colourless powder form. A $Ge_{15}As_{21}Se_{63}Ga_1$ at. % host glass was distilled with 1000 ppmw $TeCl_4$ (hydrogen getter) and 700 ppmw aluminium (oxygen getter). This was then sectioned into two batches with one doped with 250 ppmw of the distilled translucent $DyCl_3$ crystals and the second batched with 500 ppmw dysprosium foil that had undergone a mechanical surface exfoliation. The resulting

fibres measured their lowest loss of 4.86 dB/m at 6.085 µm ($DyCl_3$) and 2.07 dB/m at 6.13 µm (Dy foil), respectively.

A moth eye patterning at the chalcogenide glass surface designed to be antireflective in the infrared, aimed to increase incident pump power into rare earth ion doped fibres. A silicon mould was fabricated *via* electron beam lithography (EBL) and dry plasma etching the features into the silicon wafer (negative mould). Initial attempts to transfer the pattern into bulk chalcogenide glass samples proved unsuccessful and so focus was switched to fibre pressings. A manually controlled hot-pressing rig, with real time force sensing feedback, was designed and produced moderate pattern transfer with poor replicability due to its strong dependence on the operator. To circumvent this, an automatic feedback-loop based rig was designed which controlled the process, based on pre-selected parameters to reduce inter-pressing variability.

Not only did this Project lead to the realisation of the first CW chalcogenide mid-IR fibre laser operating beyond 5µm, this was the first glass fibre laser worldwide to operate beyond 4 µm wavelength. In addition, substantial progress to the continuing development of these fibres was made with the development of rare earth ion doped, antimony-based step-index fibres, potentially allowing future lasing at biologically relevant wavelengths for new precision cutting or welding in laser medical surgery.

Publications

Fang Y, Furniss D, Jayasuriya D, Parnell H, **Crane R**, Tang ZQ, Barney E, Canedy CL, Kim CS, Kim M, Merritt CD, Bewley WW, Vurgaftman I, Meyer JR, Seddon AB, *et al.* Determining small refractive index contrast in chalcogenide-glass pairs at mid-IR wavelengths. *Optical Materials Express* 2019;**9**:2022. https://doi.org/10.1364/OME.9.002022.

Crane R, Seddon A, Sojka L, Furniss D, Nunes J, Barney E, Farries M, Benson T, Sujecki S. Experimental photoluminescence and lifetimes at wavelengths including beyond 7 microns in Sm^3+-doped selenide-chalcogenide glass fibers. *Optics Express* 2020;**28**:12373–84. https://doi.org/10.1364/oe.383033.

Nunes JJ, **Crane RW**, Mabwa D, Furniss D, Farries M, Benson TM, Seddon AB. Internal examination of mid-IR chalcogenide glass optical fiber preforms and fiber using near-infrared imaging [Invited]. *Optical Materials Express* 2021;**11**:1353. https://doi.org/10.1364/ome.415518.

Mabwa D, Gajjar K, Furniss D, Schiemer R, **Crane R**, Fallaize C, Martin-Hirsch PL, Martin FL, Kypraios T, Seddon AB, Phang S. Mid-IR spectral classification of endometrial cancer compared to benign controls in serum or plasma samples. *Analyst* 2021. https://doi.org/10.1039/d1an00833a.

Nunes J, Sojka L, **Crane R**, Furniss D, Mabwa D, Xiao B, Benson T, Farries M, Kalfagiannis N, Barney E, Phang S, Seddon A, Sujecki S, Tang Z. Room temperature mid-IR fiber lasing beyond 5 μm in chalcogenide glass small-core fiber. *Optics Letters* 2021;**46**:3504–7. https://doi.org/10.1364/ol.430891.

Seddon AB, Sojka L, Shen M, Tang ZQ, Furniss D, Barney E, Sakr H, Jayasuriya D, Parnell H, Butterworth J, **Crane RW**, Nunes JJ, Mabwa DP, Farries M, Phang S, *et al.* Breaking through the wavelength barrier: The state-of-play on rare-earth ion, mid-IR fiber lasers for the 4–10 μm wavelength region. *Mid-IR Fiber Photonics*. Elsevier; 2022. p. 401–502. https://doi.org/10.1016/b978-0-12-818017-4.00012-4

Nunes JJ, **Crane RW**, Tang Z, Sójka Ł, Kalfagiannis N, Furniss D, Farries M. C, Benson T. M, Sujecki S, & Seddon AB. (2022). *Mid-IR photoluminescence in Ce^{3+} doped selenide-chalcogenide glass and fiber*. Accepted by Optical Materials, in press.

Acknowledgments

First I would like to thank Professor Angela Seddon, Professor Trevor Benson, and Dr Sendy Phang for their exceptional support and supervision. I knew I could always count on their guidance through the many endeavours undertaken over the course of this degree.

I would also like to thank Dr David Furniss, Dr Mark Farries, and Dr Zhuqoi Tang. Their guidance and teachings in the labs has changed the way I approach research questions and it was always fruitful to bounce ideas around with them in the lab.

To my PhD colleagues: Joel Nunes, Dr David Mabwa, and Boyu Xiao. You always made the days go quicker either through joking around or creating further discussion on the work we were carrying out, leading to new experiment designs.

Lastly, I would like to thank my incredibly supportive family and friends. They were there to celebrate the good days, and also there to take the edge off of the bad days. Having them to lean on gave me great peace of mind when the going got a bit tough.

Knowing I had such great network around me that wanted me to succeed was a massive motivation for me, and I cannot be thankful enough for those involved.

Glossary list

Chemicals	
Al	Aluminium
As	Arsenic
$DyCl_3$	Dysprosium (III) chloride
Ga	Gallium
Ge	Germanium
H	Hydrogen
HCl	Hydrochloric acid
HF	Hydrofluoric acid
O	Oxygen
S	Sulfur
Sb	Antimony
Se	Selenium
Te	Tellurium
$TeCl_4$	Tellurium (IV) chloride
Techniques	
BSE	Back scatter electron (detector)
DSC	Differential scanning calorimetry
EDX	Energy dispersive X-ray analysis
EBL	Electron beam lithography
EMT	Effective medium theory
FDTD	Finite-difference time-domain
FEG	Field emission gun
FEM	Finite element method
FTIR	Fourier transform infrared spectroscopy
RCWA	Rigorous couple wave analysis
SE	Secondary electron (detector)s
SEM	Scanning electron microscopy
VASE	Variable angle spectroscopic ellipsometry
XRD	X-ray diffractometry

Abbreviations	
AR	Antireflective
At. %	Atomic %
BB	Broadband
Ca.	Circa “approximately”
Ce^{3+}	Cerium ion
CW	Continuous wave
dB/m	Decibels per meter
DTGS	Deuterated triglycine sulfate
Dy^{3+}	Dysprosium ion
Et al.	Et alia “and others”
FBG	Fibre Bragg grating
g	Gramme
GUI	Graphical user interface
Ho^{3+}	Holmium ion
I.e.	Id est “that is”
InF_3	Indium fluoride
InSb	Indium antimonide
ID/OD	Internal diameter / outer diameter
IR	Infrared
ISO	International Organisation for Standards
KBr	Potassium bromide
LTS	Linear translation stage
n	Refractive index
NA	Numerical aperture
MCT	Mercury cadmium telluride
mg	Milligram
MPa	Megapascal
ms	Millisecond
mW	Milliwatt
Pa·s	Pascal second
Pr^{3+}	Praseodymium ion

Abbreviations	
QCL	Quantum cascade laser
RE(E)	Rare earth (element)
RI (also, “n”)	Refractive index
SIF	Step-index fibre
Sm^{3+}	Samarium ion
Tb^{3+}	Terbium ion
T_f	Fictive temperature
T_g	Glass transition temperature
WAT	Weak absorption tail
ΔE	Transition energy change
ΔG	Gibbs free energy change
µm	Micrometre
µs	Microsecond
µW	Microwatt

Contents

Abstract 2
Publications 5
Acknowledgments 7
Glossary list 8
1. Introduction 18
2. Literature review 22
2.1 Fibre lasers – an overview 22
2.1.1 Operation of a fibre laser 22
2.1.2 The mid-infrared, and considerations for mid-IR fibre lasing 25
2.2 Chalcogenide glasses 28
2.2.1 Chalcogenide glass systems 28
2.2.2 Glass formation 30
2.2.3 Devitrification 32
2.2.4 Propagation of crystal structure 36
2.3 Mid-IR emissions and lasing of rare earth ions in chalcogenide glasses 37
2.3.1 Rare earth ions and their incorporation into chalcogenide glass 37
2.3.2 Rare earth ion doped chalcogenide glass systems 39
2.3.3 Optical loss in chalcogenide glass 47
2.3.3.1 Intrinsic loss mechanisms 47
2.3.3.2 Extrinsic loss mechanisms 49
2.4 Surgical uses for a mid-IR fibre laser 51
2.4.1 Absorption in the mid-IR 52
2.4.2 Tissue ablation and considerations 53
2.4.3 Non-ablative thermal effects on tissue 56
3. Methodology 60
3.1 Chemicals used: source, purity, and form 60
3.2 Selenide-based chalcogenide glass synthesis 63
3.2.1 Pre-purification of silica melt ampoule 63
3.2.2 Chalcogenide glass precursor materials – pre-purification and batching 65
3.2.2.1 Pre-purification of Se elemental precursor 68
3.2.2.2 Pre-purification of S elemental precursor 71
3.2.2.3 Pre-purification of As elemental precursor 72
3.2.2.4 Pre-purification of Sb elemental precursor 73

3.2.2.5 Pre-purification of Ga elemental precursor.....74
3.2.3 Batching, sealing, and securing ampoule 74
3.2.4 Chalcogenide glass melting.....76
3.2.5 Distillation 78
3.2.6 Quenching and annealing 84
3.2.7 Addition of rare earth elements and re-melting.....84
3.2.8 Extrusion.....85
3.2.9 Fibre drawing.....87
3.3 Chalcogenide glass and glass fibre characterisation.....91
3.3.1 Differential scanning calorimetry.....91
3.3.2 X-ray powder diffraction (XRD).....92
3.3.3 Scanning electron microscopy (SEM).....93
3.3.4 Energy dispersive X-ray spectroscopy (EDX) 95
3.3.5 Ellipsometry 96
3.3.6 Optical fibre loss measurement of chalcogenide fibre 98
3.3.7 Fourier transform infrared spectroscopy (FtIR) of bulk glass.....101
4. Development of a novel antimony-based chalcogenide glass host composition with Sm^{3+} and Dy^{3+} doping.....102
4.1 Development of a novel antimony-based host glass composition 102
4.1.1 Introduction to previous work 102
4.1.2 Initial work 105
4.1.2.1 Development of $Ge_{19.4}Sb_{9.7}Se_{67.9}Ga_3$ at. % (M235RC) as a host glass system. 110
4.2 Samarium foil doped $Ge_{19.4}Sb_{9.7}Se_{67.9}Ga_3$ at. % bulk glass (M227RERC) and fibre (F099RERC).....115
4.2.1 FtIR analysis of bulk glass: 1000 ppm Sm-doped $Ge_{19.4}Sb_{9.7}Se_{67.9}Ga_3$ at. % (M227RERC). 115
4.2.2 Fibre loss of 1000 ppm Sm^{3+} doped $Ge_{19.4}Sb_{9.7}Se_{67.9}Ga_3$ at. % fibre (F099RERC).....119
4.2.3 1000 ppmw Sm^{3+} doped $Ge_{19.4}Sb_{9.7}Se_{67.9}Ga_3$ at. % fibre photoluminescence and photoluminescent lifetimes (F099RERC).....120
4.2.3.1 Photoluminescence of 1000 ppmw Sm^{3+} doped $Ge_{19.4}Sb_{9.7}Se_{67.9}Ga_3$ at. % unstructured fibre.....121
4.2.3.2 PL lifetime measurements of 1000 ppmw Sm^{3+} doped $Ge_{19.4}Sb_{9.7}Se_{67.9}Ga_3$ at. % unstructured fibre 125
4.3 Dy^{3+} $Ge_{19.4}Sb_{9.7}Se_{67.9}Ga_3$ at. % unstructured fibre (F104RERC) 129

4.3.1 FtIR analysis of 500 ppmw Dy^{3+} doped bulk $Ge_{19.4}Sb_{9.7}Se_{67.9}Ga_3$ at. % glass. 130

4.3.2 Fibre drawing and fibre loss of 500 ppmw Dy^{3+} doped $Ge_{19.4}Sb_{9.7}Se_{67.9}Ga_3$ at. % unstructured fibre (F104RERC) 132

4.4 Summary of chapter 4. 134

5. Development of antimony-based selenide chalcogenide cladding to clad antimony-based selenide rare earth ion doped core glass, aiming to make small-core fibre. 137

5.1 Requirements of cladding glass to be developed for core glass: rare earth ion doped $Ge_{19.4}Sb_{9.7}Se_{67.9}Ga_3$ at. % 138

5.1.1 Composition tailoring of the cladding glass for T_g matching to core glass $Ge_{19.4}Sb_{9.7}Se_{67.9}Ga_3$ at. % 139

5.1.2 Substitution of 3 at.% selenium with 3 at. % sulfur in the $Ge_{19.4}Sb_{9.7}Se_{67.9}Ga_3$ at. % core glass composition, to form a lower refractive index cladding glass with the composition: $Ge_{19.4}Sb_{9.7}Se_{65}Ga_3S_{2.9}$ at. % 144

5.1.2.1 Philosophy of Composition design and glass melting of $Ge_{19.4}Sb_{9.7}Se_{65}Ga_3S_{2.9}$ at. % (M237RC) 144

5.1.2.2 DSC for T_g of $Ge_{19.4}Sb_{9.7}Se_{65}Ga_3S_{2.9}$ at. % (M237RC) 145

5.1.3.2 Extrusion of outer cladding tube: cladding glass: $Ge_{19.4}Sb_{9.7}Se_{65}Ga_3S_{2.9}$ at. % (M237RC) (to clad cane of core glass: $Ge_{19.4}Sb_{9.7}Se_{67.9}Ga_3$ at. % + 500 ppmw Dy foil (M240RERC)) 146

5.1.3.3 Drawing of fibre from cane-in-tube (*i.e.* cane of core glass: $Ge_{19.4}Sb_{9.7}Se_{67.9}Ga_3$ at. % + 500 ppmw Dy foil (F104RERC, M240RERC) in tube of cladding glass: $Ge_{19.4}Sb_{9.7}Se_{65}Ga_3S_{2.9}$ at. % (M237RC) 147

5.2 Series (i) and Series (ii) of exploratory cladding glass compositions: Alterations to sulphur, selenium, germanium, and gallium content of $Ge_{19.4}Sb_{9.7}Se_{67.9}Ga_3$ at. % in designing a drawable cladding glass 150

5.2.1 Series (i) of exploratory cladding glasses: M262RC, M263RC, M264RC 151

5.2.1.1 Philosophy of design of compositions for Series (i) 151

5.2.1.2 Fabrication of Series (i) exploratory cladding glasses 152

5.2.1.3 T_g and refractive index (RI) values of Series (i) glasses M262-M264RC 153

5.2.2 Series (ii) of exploratory cladding glasses: M265RC, M266RC, M267RC 156

5.2.2.1 Philosophy of design of compositions for Series (ii) 156

5.2.2.2 Fabrication of Series (ii) exploratory cladding glasses 158

5.2.2.3 T_g and refractive index (RI) values of Series (ii) glasses (M265-M267RC) 160

5.2.3 Summary of effects of varying S, Se, Ga, and Ge at. % content in the exploratory cladding glass series on T_g and RI, and how these dictates cladding glass choices for the core glass composition $Ge_{19.4}Sb_{9.7}Se_{67.9}Ga_3$ at. %. 166

5.2.3.1 Summary of effects of compositional changes on T_g.....166

5.2.3.2 Summary of effects of compositional changes on RI 166

5.3 Mid-IR ellipsometry to calculate refractive index values in chalcogenide bulk samples of potential cladding glasses (Table 5.1) to match core glass (*e.g.*, M240RERC ($Ge_{19.4}Sb_{9.7}Se_{67.9}Ga_3$ at. % + 500 ppmw Dy foil).....167

5.3.1 Introduction 167

5.3.2 Methodology of refractive index measurements and sample preparation.168

5.3.3 Transmittance measurements of bulk glass samples for use in refractive index ellipsometry models.....169

5.3.4 Development of a GenOsc® Layer based model for refractive index determination.....173

5.3.4.1 Multiple Gaussian oscillator model 175

5.3.4.2 Three oscillator model (2 Pole, 1 Gaussian).....175

5.4 M266RC ($Ge_{19.4}Sb_{9.7}Se_{65.9}Ga_3S_2$ at. %) and M267RC ($Ge_{21}Sb_{10}Se_{69}$ at. %) as potential cladding glasses for small core, rare earth ion doped chalcogenide glass fibres whose core glass composition is similar to $Ge_{19.4}Sb_{9.7}Se_{67.9}Ga_3$ at. % 179

5.5 Summary of chapter 5 184

6. Fabrication and characterisation of antimony-based, arsenic core /antimony cladding hybrid, and high purity arsenic-based, small-core, step index fibres resulting in: (i) 500 ppmw doped Dy^{3+} Sb fibre, (ii) 500 ppmw doped Ce^{3+} fibre, which exhibited the first recorded continuous wave chalcogenide fibre lasing beyond 5 μm wavelength, (iii) 500 ppmw doped Dy^{3+} As fibre, and (iv) 250 ppmw doped $DyCl_3$ fibre.....187

6.1 Antimony based; dysprosium (III) doped small core step-index fibre (500 ppmw Dy foil $Ge_{19.4}Sb_{9.7}Se_{67.9}Ga_3$ at. % / $Ge_{21}Sb_{10}Se_{69}$ at. %) 189

6.1.1 SEM EDX characterisation of F129RERC ($Ge_{19.4}Sb_{9.7}Se_{67.9}Ga_3$ at. % + 500 ppmw Dy foil core / $Ge_{21}Sb_{10}Se_{69}$ at. % cladding) small core, antimony-based step-index fibre. 191

6.2 Mid-IR fibre lasing in a 500 ppmw cerium (III) doped arsenic-based core glass (F109REZQT(RCJN), $Ge_{15}As_{21}Se_{63}Ga_1$ at. % + 500 ppmw Ce^{3+} doped) and antimony-based cladding glass (M287RC, $Ge_{21}Sb_{10}Se_{69}$ at. %, E093RC) drawn to a small-core, step index fibre (F130RERC) in a laser cavity.....196

6.2.1 SEM EDX characterisation of F130RERC ($Ge_{15}As_{21}Se_{63}Ga_1$ at. % + 500 ppmw Ce^{3+} doped core / $Ge_{21}Sb_{10}Se_{69}$ at. % cladding).....198

6.2.2 Calculating numerical aperture using mid-IR ellipsometry models of the glasses comprising F130RERC ($Ge_{15}As_{21}Se_{63}Ga_1$ at. % + 500 ppmw Ce^{3+} doped core (M259REZQT) / $Ge_{21}Sb_{10}Se_{69}$ at. % cladding (M287RC)) 201

6.2.3 Mid-IR FtIR, photoluminescence, photoluminescence lifetimes, and fibre loss in unstructured F109REZQT(RCJN) ($Ge_{15}As_{21}Se_{63}Ga_1$ at. % + 500 ppmw Ce^{3+}) and fibre lasing in small core step-index fibre F130RERC ($Ge_{15}As_{21}Se_{63}Ga_1$ at. % + 500 ppmw Ce^{3+} doped core/ $Ge_{21}Sb_{10}Se_{69}$ at. % (M287RC) cladding) 205

6.2.3.1 FtIR characterisation of as-annealed, bulk M259REZQT ($Ge_{15}As_{21}Se_{63}Ga_1$ at. % + 500 ppmw Ce^{3+}).....206

6.2.3.2 Fibre optical loss, photoluminescence (PL), and PL lifetime of unstructured fibre F109REZQT(RCJN) ($Ge_{15}As_{21}Se_{63}Ga_1$ at. % + 500 ppmw Ce^{3+}) 207

6.2.3.3 Mid-IR fibre lasing at 5.13, 5.17, and 5.28 µm in small-core step-index fibre: F130RERC ($Ge_{15}As_{21}Se_{63}Ga_1$ at. % + 500 ppmw Ce^{3+} doped core / $Ge_{21}Sb_{10}Se_{69}$ at. % cladding).....210

6.3 Fabrication of Dy^{3+} doped $Ge_{15}As_{21}Se_{63}Ga_1$ at. % glass preform *via* distillation of core glass material and its doping with Dy foil and $DyCl_3$ following a novel, all silica glass vessel-based distillation method for anhydrous $DyCl_3$. 217

6.3.1 Distillation of $Ge_{15}As_{21}Se_{63}Ga_1$ at. % host glass (M283REC, D047RERC) 218

6.3.2 Closed vacuum distillation of anhydrous dysprosium (III) chloride (D043RC) 219

6.3.3 Open vacuum distillation of anhydrous dysprosium (III) chloride (D044RC) 222

6.4 Fabrication and characterisation of 500 ppmw Dy foil (M285RERC) and 250 ppmw distilled $DyCl_3$ (M286RERC) doped $Ge_{15}As_{21}Se_{63}Ga_1$ at. % unstructured (F125RERC, F126RERC, respectively) and step-index fibres (F127RERC, F128RERC, respectively) with the cladding glass $Ge_{16.5}As_{16}Se_{61.5}Ga_1S_3$ (M284RC, E092RC).....233

6.4.1 Fibre loss of unstructured, distilled, dysprosium doped fibres (F125RERC ($Ge_{15}As_{21}Se_{63}Ga_1$ at. % + 500 ppmw Dy foil) and F126RERC ($Ge_{15}As_{21}Se_{63}Ga_1$ at. % + 250 ppmw open-distilled $DyCl_3$)).....235

6.4.2 Fibre drawing and SEM characterisation of distilled small-core step-index fibres: F127RERC ($Ge_{15}As_{21}Se_{63}Ga_1$ at. % + 500 ppmw Dy foil core / $Ge_{16.5}As_{16}Se_{61.5}Ga_3S_3$ at. % cladding) and F128RERC ($Ge_{15}As_{21}Se_{63}Ga_1$ at. % + 250 ppmw distilled $DyCl_3$ core / $Ge_{16.5}As_{16}Se_{61.5}Ga_3S_3$ at. % cladding).....239

6.4.3 Absorption measurements of M285RERC ($Ge_{15}As_{21}Se_{63}Ga_1$ at. % + 500 ppmw Dy foil) and photoluminescence, and PL lifetime measurements of unstructured F125RERC ($Ge_{15}As_{21}Se_{63}Ga_1$ at. % + 500 ppmw Dy foil).....242

6.4.3.1 FtiR absorption measurement of bulk M285RERC ($Ge_{15}As_{21}Se_{63}Ga_1$ at. % + 500 ppmw Dy foil).....242

6.4.3.2 Photoluminescence (PL) and PL lifetimes of fibre samples of unstructured F125RERC ($Ge_{15}As_{21}Se_{63}Ga_1$ at. % + 500 ppmw Dy foil)243

6.4.3.3 Photoluminescence (PL) and PL lifetimes of powdered samples of unstructured F125RERC ($Ge_{15}As_{21}Se_{63}Ga_1$ at. % + 500 ppmw Dy foil)249

6.5 Summary of chapter 6 254

7. Antireflective moth eye nanoimprinting on chalcogenide bulk glasses fibre end faces.....256

7.1 Antireflective patterning for 1.5 µm and bulk sample embossing. 260

7.1.1 FDTD modelling for 1.55 µm anti-reflectance on $Ge_{10}Sb_{20}Se_{70}$ at. % bulk glass 261

7.1.1.1 Diameter over pitch optimisation for conical geometries.....262

7.1.1.2 Height and pitch optimisation for conical, cylindrical, and paraboloid geometries.....263

7.1.2 Fabrication process of produced silicon mould "1550NM". 266

7.1.3 Hot pressing of moth eye patterns onto $Ge_{20}Sb_{10}Se_{70}$ at. % (M182HAP) bulk samples. 266

7.1.4 1.55 µm reflectometry of pressed bulk glass $Ge_{20}Sb_{10}Se_{70}$ at. % (M182HAP) samples. 270

7.1.5 SEM imaging of hot-pressed bulk samples $Ge_{20}Sb_{10}Se_{70}$ at. % (M182HAP) 274

7.2 Imprinting of anti-reflective moth eye structures onto unstructured $Ge_{19.4}Sb_{9.7}Se_{67.9}Ga_3$ at. % (F101RC) fibre end faces. 278

7.2.1 Design of a hot-pressing rig for chalcogenide fibres. 278

7.2.2 Manually controlled hot-pressing of $Ge_{19.4}Sb_{9.7}Se_{67.9}Ga_3$ at. % (F101RC) fibres. 281

7.2.3 SEM and light microscopy imaging of imprinted fibre samples. 285

7.3 An automated, feedback loop controlled stage for optimised imprinting onto chalcogenide fibre faces. 291

7.3.1 Incorporation and automated control of the linear translation stage to the imprinting rig. 292

7.3.2 Effects of varying pressing parameters of the automated, feedback loop-controlled fibre hot-pressing rig as seen through microscope characterisation of pressed $Ge_{15}As_{22}Se_{63}$ at. % (F124CODF) unstructured fibres. 296

7.4 Summary of Chapter 7 301

8. Conclusions and future work.....304

8.1 Conclusions 304

8.1.1 Chapter 4 - Development of a novel antimony-based chalcogenide glass host composition with Sm^{3+} and Dy^{3+} doping.....304

8.1.2 Chapter 5 - Development of antimony-based selenide chalcogenide cladding glass for rare earth ion doped, small-core fibre.....305

8.1.3 Chapter 6 - Fabrication and characterisation of antimony-based, arsenic core /antimony cladding hybrid, and high purity arsenic-based step index fibres resulting in the first recorded chalcogenide fibre lasing. 308

8.1.4 Chapter 7 - Antireflective moth eye nanoimprinting on chalcogenide fibre faces. 309

8.2 Overall conclusions of the work.....311

8.3 Future work 312

8.3.1 Further investigations of doped core glasses. 312

8.3.2 Further investigations of cladding glasses. 315

8.3.3 Further improvements to moth eye antireflection nanoimprinting. 316

9. References 317

Appendix 1 – Redesigned distillation rig. 339

1. Introduction

The mid-IR (mid-IR) wavelength range (3-50 μm) [1], and the fundamental vibrational absorption fingerprint region it encompasses, has the potential to be utilised across a variety of different industries requiring the detection of specific covalently bonded molecules. This includes, but is not limited to, environmental monitoring (air pollution [2], water quality, greenhouse gases), quality control (agriculture, pharmaceuticals, manufacturing), security (illicit drugs, explosives), and healthcare (tissue analysis, breath analysis, tissue imaging)[3–7]. Mid-IR light absorption of water and proteins (Amide I and II) bands also opens up mid-IR light sources as potential candidates to replace conventional surgical lasers [6,8,9]. Various commercially available mid-IR light sources such as quantum cascade lasers, doped bulk solid state lasers, optical parametric oscillators, and gas lasers sporadically cover various wavelengths over the 3-25 μm range[10,11], yet these sources do not lend themselves to the practical environment of the "field" use cases listed above.

Chalcogenide glasses, that is, glasses, usually partly, comprised of either sulfur (S), selenium (Se), or tellurium (Te) can be tailored to transmit near and mid-IR light over the 1-20 μm wavelength range[12]. These chalcogenide fibres can also be designed as active light sources through the doping of rare earth ions into the glass matrix that exhibit mid-IR radiative transitions. Rare earth ion doped chalcogenide fibre lasers could then provide access to the mid-IR region with the combined inherent benefits of fibre lasers such as robustness, low maintenance, high beam quality, high gain efficiency, and potentially high power output alongside the chemical stability of the chalcogenide glasses [13,14]. This potentially opens exploitation of the mid-IR in environments not accessible with the current generation of mid-IR sources.

Work presented in this thesis in collaboration with colleagues from the Mid-IR Photonics group, University of Nottingham, UK, has produced the first reported instance of continuous wave mid-IR fibre lasing in a Ce^{3+} doped, small core chalcogenide fibre [15]. The recorded lasing emission peaking at 5.13 μm represents a single radiative transition of Ce^{3+}: $^2F_{7/2} \rightarrow {}^2F_{5/2}$. Mid-IR bulk lasing had been reported in Tb^{3+} and Pr^{3+} doped chalcogenide glasses [16,17] and fibre lasing in Tb^{3+} producing up to 35 mW power with a slope efficiency of 5.3 % [18] has also been reported.

Mid-IR photoluminescence has been recorded in chalcogenide glasses doped with Ce^{3+}, Tb^{3+}, Dy^{3+}, Pr^{3+}, Sm^{3+}, and Nd^{3+} [19–25]. To realise lasing at the wavelengths accessible through these rare earth ions and to access additional lasing wavelengths in Ce^{3+} and Tb^{3+}, further research needs to be conducted into the chalcogenide glass matrices. Designing doped host glasses around their intrinsic material properties to have sufficient transparency at the dopant ion pumping wavelength, as well as at the target emission wavelength is a crucial criterion to meet. The use of lower phonon energy element analogues, such as substituting arsenic by the heavier antimony, can provide a lower phonon energy local environment for the rare earth ions and thus provide a higher probability of radiatively transitioning mid-IR emissions. With a suitable doped host core glass designed, a corresponding cladding glass to form a step-index fibre also needs to be designed if laser action is to be achieved. Extrinsic loss mechanisms also need to be considered during the fibre fabrication process. The composition must have sufficient devitrification resistance to be able to be drawn to optical fibre. The formation of crystalline structures in the glass introduces scattering losses detrimental to fibre performance. Oxygen and hydrogen-based extrinsic impurity absorptions incorporated into a glass fibre can blot out large swathes of the mid-IR fingerprint region from being accessed as specific wavelengths of light are strongly absorbed. To minimise these effects, the continuous improvement of precursor purification methods to reduce unwanted impurities is desired.

The overall aim of this Project was to develop new rare earth ion doped chalcogenide glass compositions capable of facilitating mid-IR fibre lasing, with the intention to develop a laser light source emitting at biologically relevant (protein absorption) wavelengths such as 6.1 or 6.45 μm [8,26]. High chemical purity, antimony-based rare earth doped chalcogenide host glass compositions were designed and characterised as lower phonon energy, cytocompatible alternatives to arsenic-based chalcogenide fibres [27]. A suitable antimony-based cladding glass to accompany this host glass was also designed to produce a doped small core, step-index fibre. Further development of precursor purification process was attempted with the hope to decrease the effects of extrinsic loss mechanisms on the fibre. The application of biomimetic, anti-reflecting, moth eye surface features to these fibre

end faces was also investigated. To achieve these goals the following objectives are presented:

- Develop and characterise (optical, thermal, chemical) properties of prospective antimony-based host glass compositions.
- Develop and characterise (optical, thermal, chemical) properties of corresponding cladding glass compositions.
- Fabricate a rare earth doped, small core, step-index fibre using the above-mentioned glasses.
- Development of a suitable purification method for target rare earth dopants.
- Design of a suitable biomimetic antireflecting "moth eye" pattern and suitable apparatus to hot emboss the design into a chalcogenide fibre face.

Following this introductory chapter (Chapter 1), this thesis continues with a review of current literature on chalcogenide glasses (Chapter 2). This review details the nature and fabrication of chalcogenide glass fibres (and the challenges involved), explains the mechanisms of rare earth ion doping and current reports of mid-IR emissions in chalcogenide glasses, and finishes with a review of the effects of mid-IR light on biological tissue as a potential use case for chalcogenide fibres. The following chapter describes the various experimental procedures used throughout the project (Chapter 3). The first experimental results chapter (Chapter 4) further elaborates on results on Sm^{3+} doping published by the author in Crane *et al.* [19]. It details the development of a low optical loss antimony-based host glass fibre that was first successfully doped with samarium, with an additional fibre then being successfully doped with dysprosium. The proceeding chapter (Chapter 5) describes the development of a suitable cladding glass for the novel doped host glass fabricated in Chapter 4. The thermal and optical characterisation of a series of potential cladding glasses was conducted and a suitable model to fit ellipsometric data was produced. The investigative work on new fibre compositions is bookended with the follow up chapter (Chapter 6). The fabrication and characterisation of various small-core step-index fibres incorporating the glasses designed in Chapters 4 and 5 is presented. This includes collaborative work with PhD colleague Joel Nunes (Mid-IR Photonics group, University of Nottingham,

UK) in which mid-IR CW fibre lasing was achieved [15]. A novel method of purification of a potential dopant, $DyCl_3$, is also explained. The final chapter (Chapter 7) focuses on the design of a biomimetic, antireflective, moth eye pattern with the intention to hot imprint this pattern to a chalcogenide fibre surface. Various hot-pressing rigs were designed and tested, and work was conducted to find optimal force, temperature, and time parameters for pattern replication.

2. Literature review

This literature review will begin with an overview of fibre lasers and the principles behind their operation. Section 2.2 will focus on chalcogenide-based glasses and their relevance to this project. Section 2.3 explores the role of rare earth ions in pursuit of mid-IR fibre lasing. Previous work on Dy^{3+} doped selenide glasses carried out by Mid-IR photonics group, University of Nottingham, UK is outlined in Section 2.4. The potential for mid-IR fibre lasers to be used in a surgical setting is detailed in Section 2.5. Potential avenues to investigate to realise a mid-IR surgical laser, operating beyond 4 µm wavelength are summarised in Section 2.6. Aims and objectives of the Project are summarised in Section 2.7.

2.1 Fibre lasers – an overview

This Section begins with a brief introduction to the mechanisms by which a fibre laser operates (2.1.1). It then introduces some of challenges encountered when trying to create a mid-IR fibre laser and the status of mid-IR fibre lasing (2.1.2). The concepts introduced in this Section will be elaborated on later in Sections 2.2 and 2.3.

2.1.1 Operation of a fibre laser

"Laser" is an acronym standing for "Light Amplification by Stimulated Emission of Radiation"[28]. Stimulated emission, theorised by Einstein back in 1917 [29], is one of three transitions possible when a photon excites an atom or ion into a higher energy level. When a photon is absorbed by an ion, an electron can be excited from its ground state to a higher energy state if the photon energy is equal to the energy difference, or transition energy, (ΔE) between the two electron energy levels (Figure 2.1a). Photon energy is denoted as hν according to Planck's relation (Equation 2.1) [30].

$$E = h\nu \qquad \text{Equation 2.1}$$

E = Photon energy h = Planck's constant ν = photon frequency

Stimulated emission occurs when an incident photon of energy of frequency ν interacts with an excited electron, in which hν is equal to ΔE. The electron will drop to the lower energy state and emit this energy as a second photon with the same energy, phase, polarisation, and mode as the incident photon (Figure 2.1c). Spontaneous emission (Figure 2.1b) occurs when no incident photon interacts with an electron in an excited state. A single photon is emitted 'spontaneously' from the excited state in a seemingly random phase and direction with an energy equal to ΔE. Non-radiative decay is a process in which the electron returns to a lower energy level through the emission of phonons. Phonons are quasiparticles of (generally) much smaller energy compared to photons. The release of the energy occurs *via* quantised vibrational absorptions related to the lattice chemical bond vibrations in a material. This is a concerted process with multiple phonons potentially being released per electron. As the energy of these phonons is dependent on the lattice structure of the material, the probability of non-radiative decay occurring can be tailored by changing the host composition of the fibre.

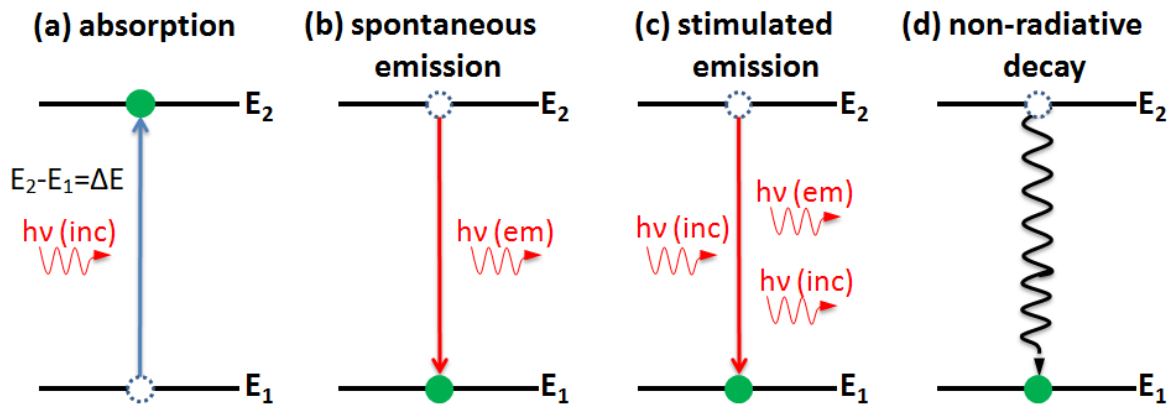


Figure 2.1 (a) The process of absorption of an incident photon to increase the energy level of an electron. (b) Spontaneous emission of a photon. (c) Stimulated emission leading to the effective doubling of the incident photon. (d) Non-radiative decay via phonon emission (heat). Image taken from [31]*. (Note: inc denotes an incoming photon, em denotes an emitted photon).*

A fibre laser is a laser in which an optical fibre is the active gain medium [32,33]. Gain in fibres is commonly achieved through doping with rare earth ions [15,34–36]. The gain medium is usually placed in a resonator (or laser cavity). A Fabry-Pérot resonator is commonly used for fibre lasers. These consist of two high reflectivity dielectric mirrors being butt-coupled to each end of the fibre [15,33,37]. Alternatively, fibre Bragg gratings (FBGs) can be integrated within the fibre. FBGs are made by

introducing variations in refractive index in sections of a fibre core tailored to reflect specific wavelengths of light. Figure 2.2 shows a schematic of an active rare earth ion doped fibre which has been spliced with undoped fibre containing FBGs on both ends [33]. These resonators act as mirrors to reflect the light in the optical system back and forth through the active fibre multiple times, increasing the power of the emitted light at the output. Alternatively, the FBGs can be written directly into the doped fibre. Photomasks or interference effects are used to vary the intensity of incident light of a wavelength the target fibre is photosensitive to[38–43]. This causes atomic scale movement, with bonds breaking and reforming, which leads to local regions of a fibre have their refractive index periodically changed [38–43]. By increasing the intensity of the light, more drastic changes to refractive index are measured [40].



Figure 2.2 Figure 1 Schematic of a fibre laser utilising fibre Bragg gratings to create the resonator cavity (2).

To maintain a high beam quality, rare earth ion doped fibre lasers or amplifiers are commonly designed around single mode (or fundamental mode) operation. These fibres consist of a core glass and cladding glass that have a slight refractive index (RI, or, "n" in equation 2.2) difference between the two compositions with the core glass RI being higher than the cladding glass. This results in a step-index fibre (SIF) with a numerical aperture (NA) which defines the angle of light acceptance in the core. For a step-index fibre, single mode propagation of light is dependent on the V number of the fibre. This V number needs to be < 2.405 to accommodate a single mode. This V number is dependent on wavelength of light, size of the fibre core, and NA[44,45]. The equation is given in Equation 2.2 [45].

$$V = \frac{2\pi}{\lambda} aNA = \frac{2\pi}{\lambda} a\sqrt{n_{core}^2 - n_{cladding^2}} \qquad \text{Equation 2.2}$$

V = V number λ = wavelength a = core radius

NA = numerical aperture n = refractive index

As the core size of a prospective fibre can alter this V number, and thus change the mechanics of light propagation through a fibre, it is important that this parameter of core diameter is tightly controlled during fibre fabrication. In most cases, rare earth doped ion fibres lasers have a small core size in comparison to their cladding but whether they are monomodal in action also depends on the core refractive index in comparison to the cladding.

2.1.2 The mid-infrared, and considerations for mid-IR fibre lasing

The mid-infrared (mid-IR) light wavelength range spans 3-50 μm as per the standard *BS ISO 20473:2007 Optics and photonics. Spectral bands*[1]. This wavelength range encompasses what is known as the molecular 'fingerprint region', loosely defined between 6-15 μm, which houses many fundamental vibrational absorption bands of covalently bonded molecules (some examples seen in Figure 2.3)[46]. These absorptions are 2-3 orders of magnitude stronger and up to 10^5 x stronger than the overtone and combination absorptions present in the near-infrared[47]. This enhanced absorption intensity (cross section) allows the mid-IR wavelength specific identification of individual molecules and molecular types. This has a wide range of potential applications over a variety of industries from environmental monitoring (air pollution [2], water quality), quality control (agriculture, pharmaceuticals, manufacturing), security (illicit drugs, explosives), and healthcare (tissue analysis, breath analysis, surgical lasers, tissue imaging)[3–7].

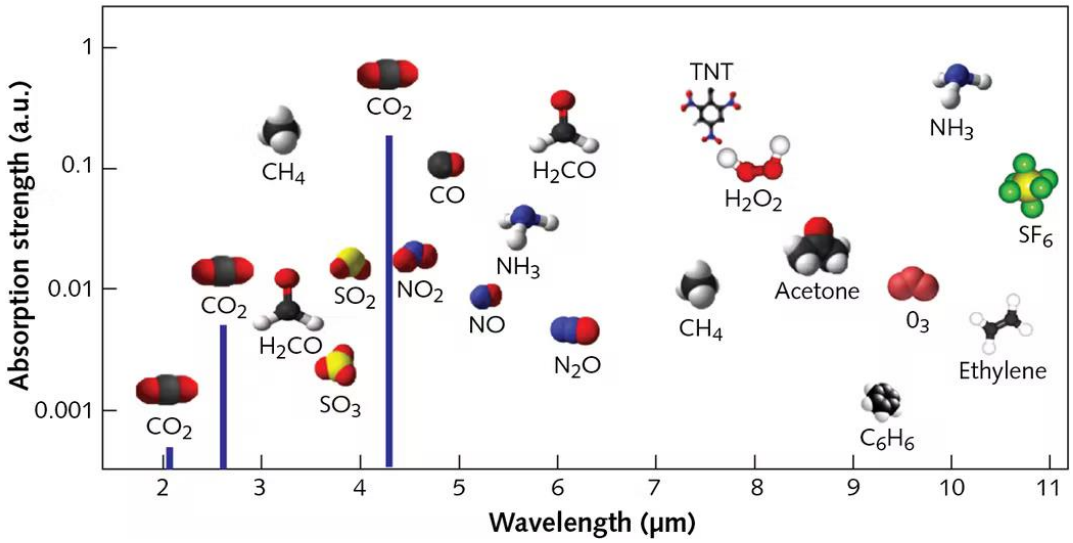


Figure 2.3 Diagram showing examples of various covalently bonded molecules that have vibrational absorptions in the mid-IR fingerprint region. This is not an exhaustive list of molecules [46].

To realise mid-IR lasing, special considerations need to be made regarding the properties of the glass fibres. The fibres must be transparent at both the pump wavelength(s) being fed into the fibre as well as the emission wavelengths of the rare earth ion dopants. For example, the Ho^{3+}: $^5I_5 \rightarrow ^5I_6$ radiative transition that was demonstrated to lase in an indium fluoride (InF_3) based fibre required a glass that was transparent in the near-infrared to allow optical pumping at 888 nm, while also having sufficiently low losses and high transmittance in the mid-IR at the Ho^{3+} lasing emission wavelength of 3.92 μm [48]. To achieve these mid-IR radiative transitions, low phonon energy glass compositions should be used to avoid non-radiative transitions (See figure 2.1(d)) [49]. Closer spaced energy levels increase the probability of the transitions decaying non-radiatively through multiphonon relaxation. This likelihood of non-radiative decay is decreased with low phonon energy compositions as more phonons will have to be emitted at once to lower the energy level of an excited electron. The doping concentration of rare earth elements (more usually elemental dopants used in doping chalcogenide glasses) and ions, and their solubility in the host glass composition, also need to be considered.

While RE ion doped fibres have inherently high gain efficiency, high doping concentrations will further increase the gain. However, if doping concentrations are too high, then the physical space between the ions can become small enough for

excitation energy to move between the ions causing the probability of energy transfer to exceed that for emission and the energy eventually dissipates. This is referred to as concentration quenching and leads to lower lifetimes [33]. An increase in rare earth ion dopant concentration has also been documented to reduce devitrification (crystallisation) resistance in chalcogenides glasses and form rare earth-oxide based crystals (Section 2.2) [50–53]. Devitrification resistance is another important consideration as a potential glass composition must remain amorphous during the fibre drawing process. Extensive crystallisation occurring during fibre drawing can lead to the production of brittle fibres, with various surface defects that prevent stable drawing of the fibre or can break and end the drawing process prematurely [54]. It is also possible for small, crystalline, scattering centres to form during the fibre fabrication process, which may not adversely affect the mechanical properties of the fibres, but may cause wavelength specific scattering losses. In chalcogenide fibres, these ~1 µm and < 1 µm, Mie and Rayleigh, respectively, scattering centres can cause high losses in the near-infrared region between 1-3 µm [50,55].

Fibre lasing in rare earth ion doped chalcogenide glasses (Section 2.2), the subject of this Project, has now been recorded thrice[15,56]. The longest wavelength fibre laser reported to date is 5.38 µm lasing in a 1050 ppmw Tb^{3+} doped step-index fibre with a $Ga_{3.2}Ge_{24.9}As_{15.3}Se_{56.6}$ atomic weight % (at. %) core glass and a $Ge_{18}As_{22}S_{60}$ at. % cladding [56]. The resulting fibre had a 420 µm outer diameter (including a 20 µm fluoroplastic coating) and a core diameter of 18 µm. With an input power of 2W continuous wave (CW) at 1.98 µm, average output powers at 5.38 µm were predicted to be < 10 µW (Shiryaev *et al.*[56]). The highest power output reported, at 36 mW at 5.25 µm wavelength, was from a $2*10^{19}$ cm^{-1} Tb^{3+} doped step-index fibre with a $Ge_{20}Sb_{10}Se_{65}Ga_5$ at. % core and a $Ge_{12}As_{20}Sb_5S_{63}$ at. % cladding (Denker *et al.*[18]). The core diameter measured 19 µm, with the outer diameter given as 270 µm, including a Fluoroplast-42 polymer coating of unspecified thickness. Lasing was achieved in fibres 10-105 cm in length. Optimal results were recorded with a fibre length of 41 cm being pumped at 1.98 µm, achieving a slope efficiency of 5.3 % [18]. The report of chalcogenide mid-IR fibre lasing from the Mid-IR photonics group, University of Nottingham, UK, was at 5.13 µm, 5.17 µm, and 5.28 µm in a 500 ppmw Ce^{3+} doped step-index fibre with a $Ge_{15}As_{21}Se_{63}Ga_1$ at. % core glass and

a $Ge_{21}Sb_{10}Se_{69}$ at. % cladding. The fibre was uncoated with polymer, of outer diameter of 190 µm and a core size of 9 µm. With an input power of 616 mW at 4.15 µm, average output power was < 100 µW (Section 6.2) [15]. Preceding these three studies, chalcogenide fibre lasing had only been realised in the near-infrared at 1080 nm [57]; a Ga-La-S-O glass fibre host, *i.e., an* oxysulfide fibre in which the phonon energy was too high to achieve MIR fibre lasing.

2.2 Chalcogenide glasses

2.2.1 Chalcogenide glass systems

Glass may be defined as an X-ray amorphous material which exhibits a glass transition temperature (T_g); a change in temperature above or below this T_g rapidly alters derivative thermodynamic properties such as heat capacity and thermal expansion [58]. "Host glass" or "core glass" refers to a composition which could potentially be used as the medium to support homogeneously dispersed, optically active rare earth ions. The term "cladding glass" is used in this work to describe a second, commonly undoped glass composition with a lower refractive index than an associated host glass. This aims to provides a stepped refractive index profile in a fibre between the optically active host glass and the cladding glass.

Glasses that have garnered interest as host media for fibre lasers are shown in figure 2.4 [12]. The chalcogenides, i.e., multi-component sulfide, selenide, and telluride glasses have transmission cut offs at longer wavelengths than other host glass systems studied due to their lower intrinsic phonon energy. From these spectra, it can be noted that these glasses are the only robust host glass system capable of transmittance at 10.6 µm, a wavelength commonly used in surgical procedures [59,60], as chloride glasses are hygroscopic [61]. It is to be noted that the apparent drastic decrease in background transmission across the chalcogenide glasses compared to silica and fluoride glasses as seen in Figure 2.4 is an artefact of the measurement used and subsequent data handling to determine transmission, and not due to the properties of the glass itself. This is because the chalcogenide glasses have a high refractive index, leading to a large amount of light (up to 20 %, Section 7.1) being reflected due to Fresnel reflection, which is not accounted for in Figure 2.4.

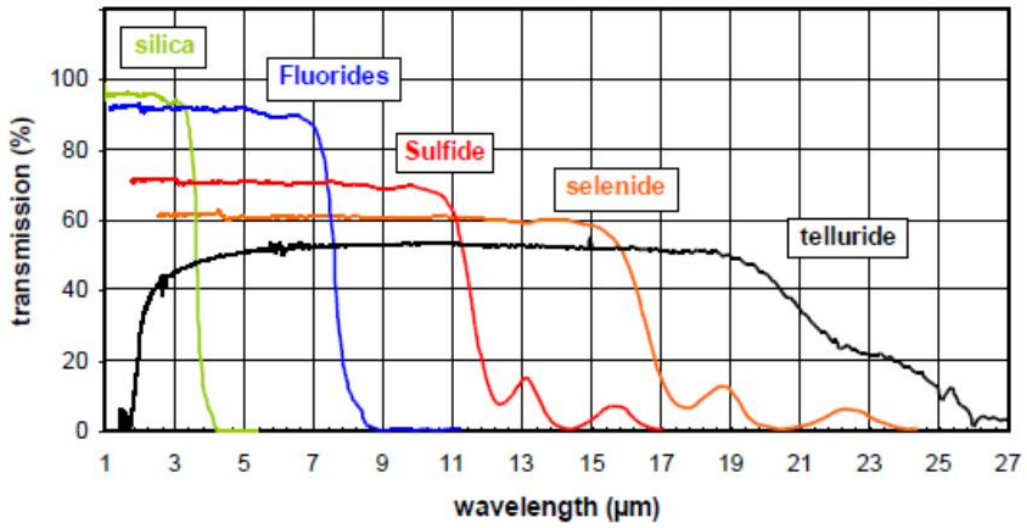


Figure 2.4 Light transmission spectra of various host glasses; note that the increasing low background transmission of all the glasses with mass of anion is due to the increasing refractive index of the glass and can be offset to 100% transmission by means of AR (antireflection) coatings on incident and exit fibre faces [12].

Chalcogenide glasses are based on the Group 16 (of the Periodic Table) anions: sulfur, selenium, and tellurium. These glasses also contain other p-block elements such as Ge, As, Sb, In, and Ga that act as network formers by covalently bonding the chalcogenides and subsequently altering the glass properties, such as making the glasses more robust and raising T_g [35,62,63]. The bicomponent arsenic-selenide (As_2Se_3) can be considered as one of the simpler chalcogenide glass compositions. The short-range order of As_2Se_3 resembles an almost polymeric 2-D structure, and the glass can be considered as a series of strata held together by van der Waals forces [54,62,64]. The addition of tetravalent components such as germanium or gallium act as crosslinkers for these layers of As-Se [62,65,66]. All these chalcogens (S, Se, Te) and other network forming elements (Ge, As, Sb, Ga) have a heavy atomic mass and form bonds of weak bond strengths leading to the creation of a network bearing low phonon energy, thus mediating mid-IR radiative emissions [32,67]. Phonon energy values of the chalcogenide glasses measured range from 350-425 cm^{-1} in sulfide glasses[68], 250-300 cm^{-1} in selenide [69], and 150-200 cm^{-1} in tellurides [70]. These values will vary depending on the atomic composition of the rest of the network. For example, substituting arsenic by the larger atomic mass of antimony will put the phonon energy on the lower end of the range. The relatively

high refractive index values of chalcogenide glasses (compared to silica glasses) are due to their higher densities and their strong polarisability [62].

2.2.2 Glass formation

A glass composition can be designed around the perfect optical properties but if this composition fails to form a glassy product, it cannot be considered for use as a fibre laser; this is because it remains extremely difficult to form single crystal fibres, and polycrystalline fibres are scattering. While Section 3.2 outlines a process for creating a selenide-based glass, the science behind the formation of glass is presented here. An understanding of this process is needed to be able to efficiently 'troubleshoot' a composition in the event unwanted effects are observed during glass characterisation.

Glass can be considered a state of matter structurally like a liquid state in which the kinetic energy of the system is insufficient for atoms to move *i.e.*, translate. This fixes the atoms into a disordered arrangement with no atomic periodicity or long-range order [71,72]. Figure 2.5 shows an illustrated 'cartoon' comparison between a glassy and crystalline state.

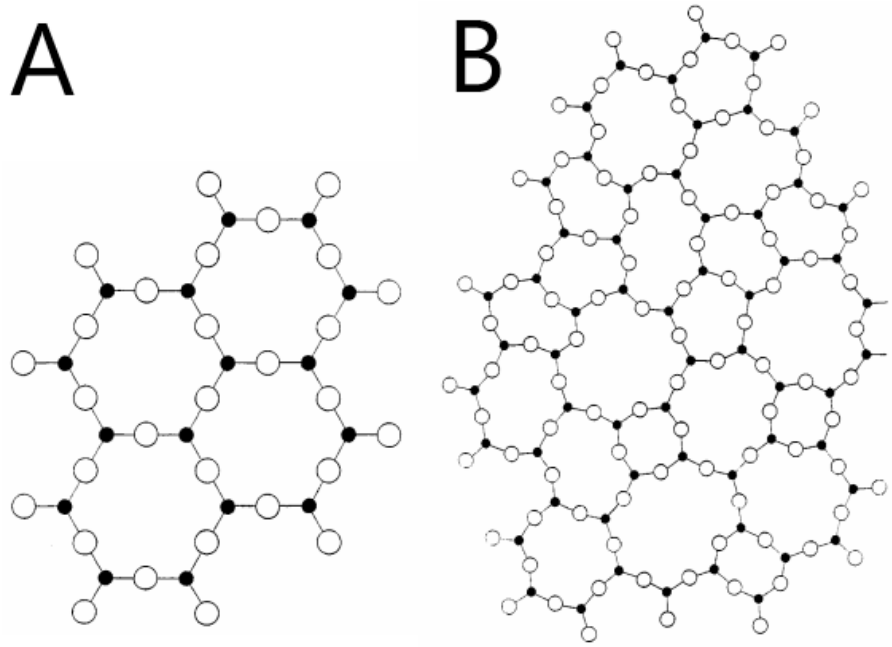


Figure 2.5 Diagram comparing the proposed 2-D atomic structure of an undefined material in (A) crystalline form and (B) glass form [73].

Enthalpy-temperature (or volume-temperature) diagrams (Figure 2.6) explain the glass forming process in which a liquid is supercooled below its thermodynamic liquidus to a solid whilst avoiding devitrification.

With reference to Figure 2.6, consider a liquid which crystallises on cooling as follows. Enthalpy in the melt will slowly decrease as the liquid (A) is cooled to the liquidus point (B) and the glass melt will begin to contract. From B-E there is a sharp drop in enthalpy (latent heat of freezing) and change in volume. This is the product of a slow cooling process which has allowed nuclei (more in Section 2.2.3) to develop and initiate crystallisation in the material. It is to be noted that often the liquid super cools a little below the true freezing temperature as the formation of nuclei and crystal growth are kinetic processes, taking time to occur. As the temperature drops, as the system is cooled further, the further enthalpy decreases are dependent on the heat capacity of the crystal (F) [71]. On the other hand, following on Figure 2.6, if the melt is subject to a rapid decrease in temperature, there is no effect at the liquidus and the liquid smoothly drops in enthalpy through and below the liquidus. The melt below the liquidus is termed a supercooled liquid. If the melt is subject to a further rapid decrease in temperature, a small decrease in enthalpy is seen as the melt enters its glass transition temperature (T_g).

T_g can be defined as the range in which a glass has a viscosity of $10^{12.5}$ Pa·s [74]. Once in this range, it is thermodynamically favourable to crystallise but kinetically energetically unfavourable for crystallisation to occur as the atoms cannot overcome potential energy barriers for movement towards a more ordered state. If a glass is below its onset T_g, the material is considered to be a solid with no flow properties, and essentially of infinite viscosity.

If a melt is subject to a slightly faster cool rate, the glass will have a higher enthalpy (B-C) while a glass that was subjected to a slower cool rate will have a lower enthalpy (and volume) as the melt had more time for conformational changes to take place and the structure to relax(B-D). The fictive temperature (T_f) is obtained by reheating the glass and it theoretically could be used as a measure of the glass structure [75]. Extrapolating the glass lines (C/D) and the supercooled liquid line (B) until they intersect will yield the T_f. In unaged glasses or glasses which have had

their T_f calculated from a point deep in the glassy state, the T_f can be referred to as the limited fictive temperature (T_f'). This T_f' can be considered to be equal to T_g [76,77].

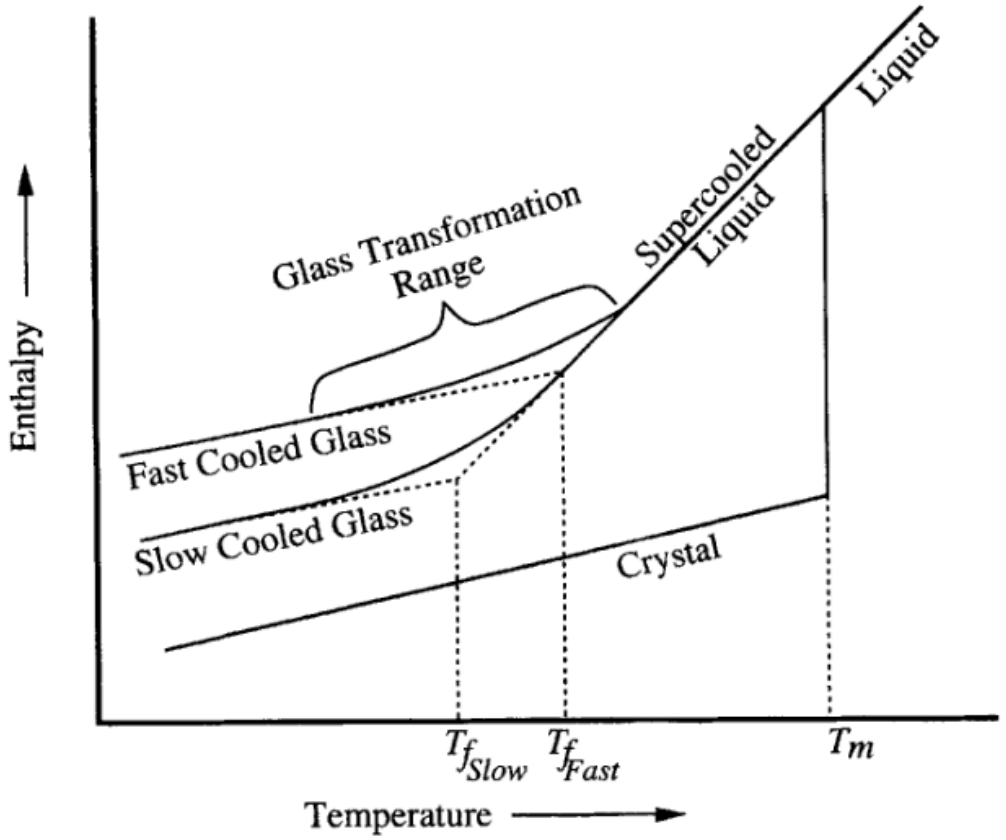


Figure 2.6 Enthalpy-temperature diagram describing the change in enthalpy (and the volume) of a glass melt as a function of temperature. Taken from [71].

2.2.3 Devitrification

Thermodynamics dictates that a system will move towards its lowest energy state. In the case of glass, the kinetics of the system has taken precedence over thermodynamics and prevented a stable crystalline solid from forming. The disordered glass with its higher internal energy will readily shift to an unwanted crystalline state if heated above its T_g. Crystallisation is a process dictated by two steps; nucleation followed by crystal growth.

Nucleation can occur via homogenous or heterogenous mechanisms. Volmer described nuclei as "an entity that already belongs to the new phase but is in unstable equilibrium with respect to the supersaturated parent phase" [78]. Homogenous nucleation establishes a crystal phase purely through fluctuations of density and kinetic energy which leads to continuous precipitation and dissolution of embryos [72,79]. In this context, an embryo is defined as a structure with longer range atomic order than the surrounding environment [72]. When these embryos exceed a critical diameter, they can become stable nuclei. This critical diameter is determined by two competing factors. The energy reduction per unit volume, due to the ordered structure having lower Gibbs free energy (ΔGv), and the energy cost associated with the formation of an interface between the embryo and the liquid (γ). The misfit strain energy cost per unit volume from the structural change must also be considered (ΔG_s) [80]. The Gibbs free energy change can be calculated using equation 2.3 [79].

$$\Delta G = -\frac{4}{3}\pi r^3 \Delta G_v + 4\pi r^2 \gamma + \Delta G_s \qquad \text{Equation 2.3}$$

ΔG = Gibbs free energy change r = radius of embryo

γ = surface stress value (interfacial energy required for the formation of the new nucleus surface)

ΔG_v = free energy change per unit produced when nucleus is formed (due to the increase in density at the structural transition leading to energy reduction)

ΔG_s = elastic distortion energy

A negative ΔG value indicates that the interfacial energy and the strain energy are smaller than the volume energy. These embryos, now referred to as critical nuclei, will be above the critical diameter needed and the nucleus will grow in size. Figure 2.7 demonstrates this graphically [79]. Critical diameter, d^*, can be calculated using equation 2.4 [80]. The energy barrier for nucleation, ΔG^*, which controls nucleation rate can be calculated using equation 2.5 [80]. A positive ΔG value will arise if the

interfacial energy is greater than the energy released during small scale ordering, this indicates the embryos are subcritical and will dissolve back into a liquid phase.

$$d^* = \frac{4\gamma}{\Delta G_v - \Delta G_s} \qquad \text{Equation 2.4}$$

d^* = critical diameter γ = surface stress value

ΔG_v = free energy change per unit produced when nucleus is formed

ΔG_s = elastic distortion energy

$$\Delta G^* = \frac{16\pi\gamma^3}{3(\Delta G_v - \Delta G_s)^3} \qquad \text{Equation 2.5}$$

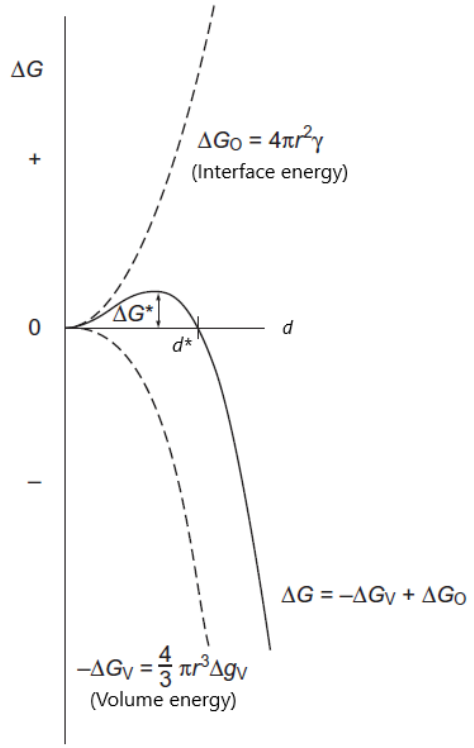


Figure 2.7 Change in Gibbs free energy as a function of nucleus diameter. ΔG - energy barrier for nucleation, d* -critical diameter of nucleus formation. Particles with d < d* have a +ΔG, a particle with d >d* have a -ΔG and so these nuclei have a probability to grow into a crystalline structure. Adapted from* [79].

Heterogeneous nucleation is a product of the (unwanted) inclusion of foreign substrates which lower this ΔG* barrier. These small inclusions, such as a piece of silica from a melt ampoule wall, can act as nucleation sites to initiate devitrification which then propagates. The extent to which the energy barrier for nucleation is lowered (ΔG^*_h) is dependent on the contact angle of the nascent nuclei on the catalyst's surface. That is, the better contact an embryo has with the foreign substrate, the increased probability it will develop to a nucleus above the critical diameter. This can be expressed with Equation 2.6 [79]. Contact angles sub-180° will preferentially form heterogeneous nuclei of critical diameter [79].

$$\Delta G_h^* = \Delta G * f(\theta) \qquad \text{Equation 2.6}$$

With

$$f = (\theta)\frac{(2+cos\theta)(1-cos\theta)^2}{4} \qquad \text{Equation 2.7}$$

ΔG_h^* = Critical Gibbs free energy in heterogenous nucleation

θ = contact angle

The rate of nucleation (Equation 2.8) is expressed as the number of nuclei per unit volume formed per unit time [71]. The thermodynamic (W*) and kinetic (ΔG_D) energy barriers are considered. The absolute temperature (T), Boltzmann constant (k) and a final constant (A) are also accounted for.

$$I = A \exp\frac{-(W^* + \Delta G_D)}{kT} \qquad \text{Equation 2.8}$$

W^* = thermodynamic energy barrier ΔG_D = Kinetic energy barrier

A = A constant k = Boltzmann constant T = Temperature (K)

2.2.4 Propagation of crystal structure

Figure 2.8 describes how rates of nucleation and crystal growth change over the temperature region a glass melt is subjected to [72,81]. The metastable zone between T_M and T_1 may transiently house subcritical homogenous nuclei and remains vulnerable to heterogenous nucleation if any foreign particulate is above the critical diameter. As temperatures decrease below T_1, so does the critical diameter for nuclei and subsequently, the rate of homogenous nucleation increases (reaching a maximum rate at T_N). Further decreases in temperature, sub T_2, increase the viscosity of the glass melt and the low kinetic energy in the environment prevents crystal growth and further nucleation. The hatched section indicates a temperature region in which both nucleation and crystal growth are likely to occur (homogenously and heterogeneously). Ideally during glass formation, the melt will be rapidly cooled through this region.

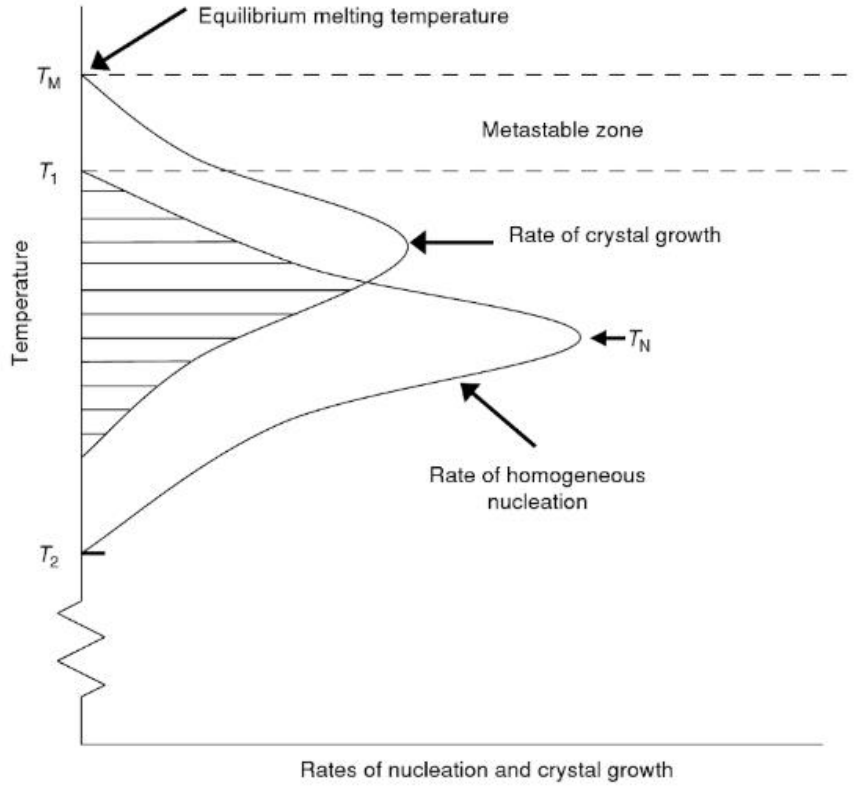


Figure 2.8 Effect of changing temperature on the rates of nucleation and crystal growth [72]. Above T_1 nucleation is transient due to the low viscosity and high energy in the melted material. As temperature decreases between T_1 and T_2 the probability of homogenous nucleation and crystal growth increases until temperature (as a function of energy in the system) is decreased to the point that the atoms can no longer rearrange.

2.3 Mid-IR emissions and lasing of rare earth ions in chalcogenide glasses

A suitable active host glass system also needs to be able to accommodate the optically active rare earth ions. Section 2.3.1 provides a background to these ions and the steps taken to aid their inclusion into a chalcogenide glass. Section 2.3.2 details various glass systems which have been investigated in recent years and section 2.3.3 explains various loss mechanisms which can disrupt transmission of pump and emitted light through the glass.

2.3.1 Rare earth ions and their incorporation into chalcogenide glass

Rare earth elements refer to the 15 lanthanide elements with atomic numbers 57 to 71, as well as yttrium and scandium. These elements can be doped into chalcogenide glasses where they are assumed to reside as a trivalent ion (with a potential for bi- and tetra- valency, depending on the element [62,82]) namely, RE ions, also known as lanthanide ions. These RE ions then behave as optically active impurity centres which potentially exhibit luminescence in the mid-IR when appropriately excited. In glasses, these radiative transitions provide a larger bandwidth than if incorporated into a crystal structure. This is due to inhomogeneous broadening in which the ions are subject to differing local environments, a characteristic of a glassy structure [63]. Lanthanide ions are comprised of a xenon core, an unfilled 4*f* shell, and filled 5*s*, 5*p*, and 6*s* shells (Figure 2.9). The electrons in the inner unfilled 4*f* shell are responsible for the optical properties exhibited by the elements (*f-f* transitions) while the surrounding 5*s* and 5*p* shells provide a degree of protection from the effects of the ligand field, the electric field produced by the host glass [63,83]. As stated above, once incorporated into a chalcogenide glass, these ions are usually trivalent even if initially added elementally as valence zero. Exceptions included in this work are cerium (Section 6.2), which can also exhibit tetravalency, and samarium (Section 4.2) which can also exhibit bivalency [62,82,84].

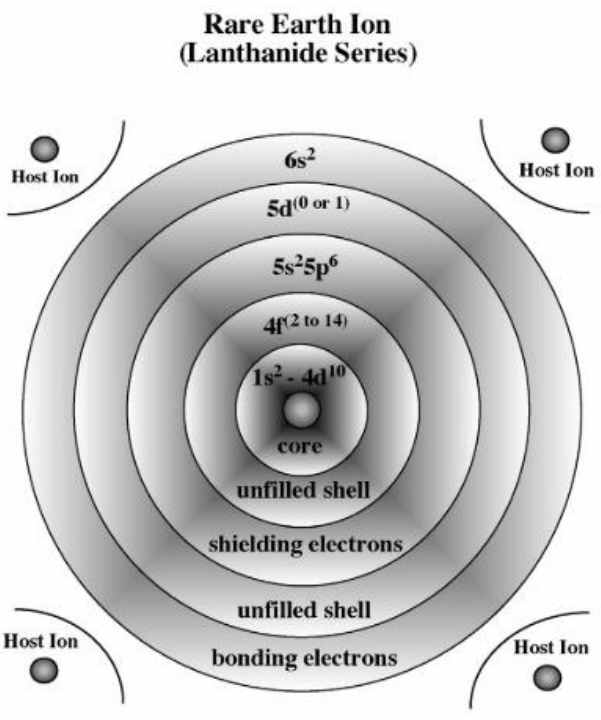


Figure 2.9 Simplified structure of the shells of a rare earth ion from [63]*. 4f shell weakly affected by the surrounding host ions. This provides narrow spectral lines with large cross sections. Strucure applicable to La, Ce, Pr, Nd, Pr, Sm, Eu, Gd, Tb, Dy, Ho, Er, Tm, Yb.*

Multiple considerations need to be made during the fabrication stage when introducing rare earth elements into a chalcogenide glass system. Dysprosium has been shown to corrode silica glass ampoules during chalcogenide glass melting [52]. Silica glass ampoules are commonly used to house the chalcogenide glass melt during melting of the glasses. Evidence for the formation of Dy_2O_3 and Si-O-Dy complexes which are detrimental to transmission of light across the near and mid-IR spectrum has been presented [37,50,52]. To minimise the effects of corrosion on the silica, an initial melt stage can be carried out to homogenise the undoped chalcogenide glass and a second re-melt using lower temperatures and shorter melting times can then be carried out once the RE dopant has been added, to minimise contact time between the silica glass of the housing and the rare earth elements. These dopants have poor solubility in chalcogenide glasses which potentially leads to clustering of the RE ions – it is not clear whether this is partially a phase separation effect or a result of crystallisation. These clusters can sequester photoluminescence through concentration quenching [85]. The addition of elements such as gallium and indium increase the solubility of the REE by forming $[RE^{3+}]$-Se-[Ga/In(III)] complexes [86]. The addition of gallium has been shown to increase

the intensity of photoluminescence emitted in Pr^{3+} doped GeAsS bulk glass by a factor of ten when gallium was added in a ratio of ≥10:1 Ga:REE [87]; it is not clear whether the absence of Ga led to a decrease in photoluminescence through the formation of praseodymium based crystals or through liquid/liquid immiscibility forcing the rare earth ions into closer proximity in a separated phase and hence causing the ions to be too close to one another manifesting in a shortening of the excited state lifetimes. A similar phenomenon has been observed in erbium (III) doped silica glasses in which aluminium oxide was added to increase solubility [88].

2.3.2 Rare earth ion doped chalcogenide glass systems

Multicomponent chalcogenide glass systems have been extensively researched in pursuit of a suitable host for mid-IR fibre lasing. Table 2.1 contains glass compositions and doping concentrations studied by various international research groups since 2012 (date chosen arbitrarily to dovetail the PhD thesis work reported by Dr Zhuoqi Tang, previously of the Mid-IR Photonics Group, University of Nottingham, UK). In Table 2.1, glasses have been grouped based on their constituent chalcogenide element. Table 2.2 contains the details of chalcogenide glass compositions that have exhibited mid-IR lasing.

Sulfides and selenides have seen the most active research in recent years, this is likely a result of the generally large glass forming temperature regions, based on composition regions, that these glasses exhibit. The lower phonon energy telluride glasses have relatively poor devitrification resistance which can prevent both efficient fibre drawing and luminescence [89]. Selenide-telluride glasses have been created to incorporate tellurium into the system while retaining adequate glass forming capability.

Arsenic (As) and its lower phonon energy analogue, antimony (Sb), are frequently substituted for each other and in some cases, may be both included into a glass system. Radiative transitions quenched by multiphonon relaxation in arsenic containing glasses have been observed when As is substituted for the heavier Sb [25,90]. The As for Sb substitution provides a potentially lower phonon energy glass system without having to accommodate the poor devitrification resistance of tellurium-based glasses.

Germanium is included in most of the chalcogenide glasses systems studied over this time. Some research groups have attempted to drop germanium from their systems and compensate for this by increasing gallium and chalcogen concentration [91] as germanium and gallium both form tetrahedral complexes in the glass system and have a similar mass [62,66,91,92]. However, the oxidation states of these two are different as Ga forms Ga(III) and Ge: Ge(IV), meaning that Ga(III) can have a unsatisfied valency bond, may be charged and is more likely to complex the La(III) ions. The inclusion of germanium to an As-Se composition would be expected to increase T_g and decrease refractive index (Section 5.2) because of the increased overall mean coordination number [93].

Gallium and indium (same group of the periodic table), important for RE ion solubilisation, can be substituted for each other. Indium containing glasses have demonstrated superior photoluminescent properties but are more prone to devitrification at doping concentrations ≥ 1000 ppmw [86,94]. Indium, like gallium, also incorporates itself through tetrahedral complexes yet with (III) oxidation state [94].

Table 2.1 Collation of mid-IR emissions recorded from rare earth ion doped chalcogenide glasses from 2012 to date (dovetails similar table in PhD thesis of ZQ Tang[31].

Note: Mid-IR emissions measured in rare earth ion doped chalcogenide glass studies conducted 2012-2022. Glass compositions in parentheses indicate (core/cladding) glass composition for step-index fibres (SIF). Modelled data indicates stimulated emission was predicted by authors referenced.

Host glass	Rare earth ion	Rare earth ion concentration	Pump wavelength / (μm)	Emission wavelength / (μm)	Form	Year	Ref.
Sulfide							
GaGeSbS	Ho^{3+}	5 wt%	-	2.9, 3.9, 4.8	Bulk	2012	[96] Kadono

Table 2.1 continued.

Host glass	Rare earth ion	Rare earth ion concentration	Pump wavelength / (μm)	Emission wavelength / (μm)	Form	Year	Ref.
GaGeSbS	Dy^{3+}	0.1 wt%	0.92	4.35	Fibre	2013	[92] Nazabal
GaGeSbS	Pr^{3+}	500 ppmw	2	4.80	Fibre	2013	
GaSbS	Dy^{3+}	0.05, 0.1, 0.2, 0.3, 0.4, 0.6 wt%	1.32	2.95, 4.40	Bulk	2015	[97] Tang
GaGeSbS	Dy^{3+}	-	0.92	2.9, 4.4	Bulk, Fibre	2015	[2] Nazabal
GaGeSbS	Er^{3+}	1000 ppmw	0.982	4.2-4.8	Fibre	2015	[98] Nazabal
		1000, 5000			Bulk		
GaGeSbS	Dy^{3+}	1000 ppmw	0.916	4.4	Fibre	2016	[99]Nazabal
		5000 ppmw					
GaGeSbS	Dy^{3+}	1200 ppmw	0.918	4.4	Fibre	2016	[100] Nazabal
GaGeSbS	Pr^{3+}	500, 1000 ppmw	1.49, 2.0	3.5-5.5	Bulk, Fibre	2016	[101] Nazabal
GaSbS	Tm^{3+}	0.5 wt%	0.808	3.8	Bulk	2016	[102] Tang
GaSbAsS	Dy^{3+}	0.8 wt%	1.32	2.95, 4.4	Bulk	2017	[103] Tang

Table 2.1 continued.

Host glass	Rare earth ion	Rare earth ion concentration	Pump wavelength / (μm)	Emission wavelength / (μm)	Form	Year	Ref.
(GaSbAsS/ GaSbAsS)	Dy^{3+}	0.05 wt%	1.32	2.95, 4.4	SIF	2017	[103] Tang
GaGeSbS	Pr^{3+}	1000 ppmw	0.920	2.2-5.5	Fibre	2018	[104] Nazabal
	Dy^{3+}	200, 500, 1000 ppmw	1.55				
GaGeSbS	Nd^{3+}	200, 500, 1000 ppmw	0.815	4.2-5.6	Fibre	2018	[21] Nazabal
GaAsS	Er^{3+}	0.4-4 wt%	0.808	4.3-5.4	Bulk	2018	[90] Nazabal
GeGaSbS	Dy^{3+}	-	1.32, 1.7	4.3	Model	2018	[105] Peng
GeS	Pr^{3+}	1400 ppmw	1.975	2.0-2.8, 3.5-5.8	Bulk	2019	[106]Churbanov
GeAsS		700 ppmw					
(GaGeSbS/ GaGeSbS/ GaGeSbS)	Dy^{3+}	0.1-1 wt %	1.707	2.975 4.258	Fibre	2020	[107]Guo
Selenide							
GeAsGaSe	Pr^{3+}	500-1500 ppmw	2.04	4.60 3.20	Model	2012	[95] Seddon
	Dy^{3+}	1000-2000 ppmw	1.71	4.89 3.70			

Table 2.1 continued.

Host glass	Rare earth ion	Rare earth ion concentration	Pump wavelength / (μm)	Emission wavelength / (μm)	Form	Year	Ref.
GeAsGaSe	Tb^{3+}	500-1500 ppmw	2.95	7.5 5.1	Model	2012	[95] Seddon
GaGeSbSe	Pr^{3+}	500 ppmw	2.0	3.5-5.5	Fibre	2013	[92] Nazabal
	Dy^{3+}		0.92	4.35			
GeAsGaSe	Pr^{3+}	500 ppmw	1.55, 1.94	3.5-5.5	Fibre	2014	[108] Seddon
(GeAsInSe/ GeAsInSe)	Pr^{3+}	498 ppmw	1.55	3.5-6.0	SIF	2014	[109] Seddon
(GeAsGaSe/ GeAsGaSe)	Pr^{3+}	493 ppmw	1.55	3.5-6.0	SIF		
GeAsGaSe	Pr^{3+}	493 ppmw	1.55	3.5-6.0	Bulk	2014	[86] Seddon
		994 ppmw	1.55	3.5-6.0	Bulk		
GeAsInSe		527 ppmw	1.55	3.5-6.0	Bulk		
		1027 ppmw	1.55	3.5-6.0	Bulk		
(GeAsGaSe/ GeAsGaSeS) (10 μm core / 230 μm OD)	Pr^{3+}	500 ppmw	1.55	3.5-6.0	SIF	2015	[110] Seddon
GeAsGaSe		500 ppmw			Fibre		

Table 2.1 continued.

Host glass	Rare earth ion	Rare earth ion concentration	Pump wavelength / (μm)	Emission wavelength / (μm)	Form	Year	Ref.
GeAsGaSe	Tb^{3+}	500 ppmw	2.013	4.90	Fibre	2015	[111] Seddon
		1000 ppmw		4.60	Bulk		
GeGaSbSe	Pr^{3+}	1300, 2000, 2600 ppmw	1.98	3.5-5.5	Bulk	2016	[22] Churbanov
(GeAsInSe/ GeAsInSeS) (20 μm core/ 230 μm OD)	Pr^{3+}	500 ppmw	1.55	3.5-6.0	SIF	2017	[94] Seddon
GeAsGaSe	Tb^{3+}	500, 1000, 1500 ppmw	2.013	4.3-6.0	Bulk	2017	[23] Seddon
		500 ppmw			Fibre		
(GaGeAsSe/ GaGeAsSe) (36 μm core/ 330 μm OD)	Pr^{3+}	1300 ppmw	1.97	3.5-5.5	SIF	2017	[112] Churbanov
(GaGeAsSe/ GeAsS) (16 μm core/ 320 μm OD)		1300 ppmw					
(GeAsSeInI/ GeAsS) (80 μm core/ 220 μm OD)		2000 ppmw					

Table 2.1 continued.

Host glass	Rare earth ion	Rare earth ion concentration	Pump wavelength / (μm)	Emission wavelength / (μm)	Form	Year	Ref.
GaGeSbSe	Sm^{3+}	500,1000 ppmw	1.45 2.05	6.5-8.5	Fibre	2018	[113] Nazabal
GaGeSbSe	Tb^{3+}	500, 1000 ppmw	2.05	2.8-3.4 4.0-6.0 7.0-9.0	Fibre	2018	[90] Nazabal
GaGeAsSe	Pr^{3+}	1300 ppmw	1.56	2.1-3.2 3.5-6	Bulk	2019	[20]Churbanov
GaGeSbSe	Dy^{3+}	1000 ppmw	0.92, 1.12, 1.32	4.3, 5.4, 7.3	Fibre	2020	[25]Nazabal
GaGeSbSe	Sm^{3+}	1000 ppmw	1.3, 1.47	2.7, 3.7, 7.3	Fibre	2020	[19]Seddon
GaGeSbSe	Ce^{3+} Dy^{3+}	5×10^{19} cm^{-1} 3.1×10^{19} cm^{-1}	1.3, 1.7, 2.9	3.5 – 6, 2.9, 4.3	Fibre	2021	[114] Churbanov
GaGeSbSe	Sm^{3+}	700	1.1, 1.5	1.2-1.3, 1.4-1.6, 1.75-2, 2.2-3, 3.5-4.2	Fibre	2022	[115]Shiryaev
Selenide/Telluride							
GaAsSeTe	Pr^{3+}	1000 ppmw	2.00	3.9-5.5	Fibre	2015	[116] Nazabal
GaGeSbSeTe	Tb^{3+}	1000 ppmw	2.05	2.8-3.4 4.3-6.0	Fibre	2018	[89] Nazabal

Table 2.1 continued.

Host glass	Rare earth ion	Rare earth ion concentration	Pump wavelength / (μm)	Emission wavelength / (μm)	Form	Year	Ref.
Chalcohalide							
GeGaSAgI	Dy^{3+} Tm^{3+}	0.2-0.8 wt% 0.5 wt%	0.808	2.9 4.3	Bulk	2013	[117] Peng
GeGaSCdI	Pr^{3+}	0.2 wt%	2.01	4.25-4.90	Bulk	2014	[118] Peng
GeGaSPbCsI	Dy^{3+}	0.2 wt%	0.808	-	Bulk	2014	[119] Peng
	Dy^{3+} Tm^{3+}	0.2 wt% 0.5 wt%	0.808	2.93 4.32			
GeAsSeInI	Pr^{3+}	1300 ppmw	1.98	3.5-6.0	Fibre	2016	[120]Churbanov
GeGaSCdI	Dy^{3+}	0.2 – 3 wt%	1.32	2.95, 3.59, 4.16, 4.45	Bulk	2017	[121] Peng
GeSbSeInI	Pr^{3+}	1300 ppmw	1.98	3.5-6.0	Bulk	2017	[122]Churbanov
GeSbSI	Dy^{3+}	0.1 wt%	1.32	2.9, 4.32	Bulk	2017	[123] Peng
GeSbSeGaI	Pr^{3+}	0.1-1.5 wt%	1.55	3.0-5.5	Bulk	2018	[124] Dai

Table 2.2 Mid-IR lasing reported in chalcogenide glass systems.

Glass compositions in parentheses indicates (core/cladding) glass composition for step-index fibres (SIF).

Host glass	Rare earth ion	Rare earth ion concentration	Pump wavelength / (μm)	Lasing wavelength / (μm)	Form	Year	Ref.
(GaGeAsSe/ GeAsS)	Tb^{3+}	1050	1.98	5.38	SIF	2021	[56]Shiryaev
GaGeSbSe	Ce^{3+}	3 x 10^{19} cm^{-1}	4.1	5.2	Bulk	2021	[125]Velmuzhov
(GeAsSeGa/ GeSbSe)	Ce^{3+}	500 ppmw	4.15	5.14, 5.17, 5.28	SIF	2021	[15]Seddon
(GeSbSeGa/ GeAsSbS)	Tb^{3+}	2 ×10^{19} cm^{-3}	1.98	5.25	SIF	2022	[18]Denker

2.3.3 Optical loss in chalcogenide glass

2.3.3.1 Intrinsic loss mechanisms

Dielectric materials such as chalcogenide glasses have their optical transmission windows intrinsically dictated through three intrinsic mechanisms. The Urbach edge refers to electronic absorption at short wavelengths, multiphonon absorption dominates longer wavelengths, and Rayleigh scattering occurs at these middling wavelengths [126]. A fourth mechanism, seen in amorphous semiconductors such as arsenic selenides, is the weak absorption tail (WAT). This mechanism also occurs in this central wavelength region and is much more pronounced than Rayleigh scattering in these materials [126].

The electronic absorption edge (Urbach edge) is a product of optical bandgap, which is realised by the electronic configuration and positioning of the atoms in the material. In chalcogenide glasses, the short-range local order is retained but long-range order will be absent. This places the electronic edge in a similar wavelength range that would be observed in a crystal of a similar composition, but this range will extend to longer wavelengths into a more gradual absorption edge [127,128]. The

WAT is subject to the medium range order of the glass and the localised energy states in the bandgap. The absorption tail is thought to be a product of atoms being 'frozen' into a glassy, disordered structure without forming the correct amount of bonds their valence dictates. This causes coordination defects in the glass, and these "dangling bonds" can cause variations of the bandgaps, which can overlap throughout the material [62]. These dangling bonds can be considered free radicals so: ≡Ge-Se• which opens the potential for these bonds to "mop up" extrinsic hydride impurities [129]. It can also then be inferred that the WAT is altered by the thermal history and purity of the glass [130].

Rayleigh scattering, more commonly attributed to an extrinsic loss mechanism, can also originate intrinsically from density and composition fluctuations present in the glass; it can be expressed using equation 2.9 [30].

$$\alpha_R = \frac{8\pi^3 n^8 p^2 \beta k T_f}{3\lambda^4} \qquad \text{Equation 2.9}$$

α_R = Rayleigh scattering n = refractive index p = photoelastic coefficient

β = isothermal compressibility at T_f T_f = Fictive temperature

k = Boltzmann constant λ = wavelength

The multiphonon edge of a glassy, inorganic compound is the long wavelength 'cut off edge' at which the material transmission of mid-infrared light is first affected by the overtone and combination bands due to the fundamental absorption bands of the glass matrix vibrational absorption itself. This edge is dependent on the vibrational resonances of the atomic network which alters depending on the atomic weight and bond strength [126]. Chalcogenide glasses, with their large atomic masses and weaker bonds, do not reach this vibrational resonance until the longer wavelengths (lower frequencies) compared to ZBLAN or silica glasses. Figure 2.10 demonstrates the theoretical minimal loss in an arsenic sulfide fibre through these intrinsic mechanisms.

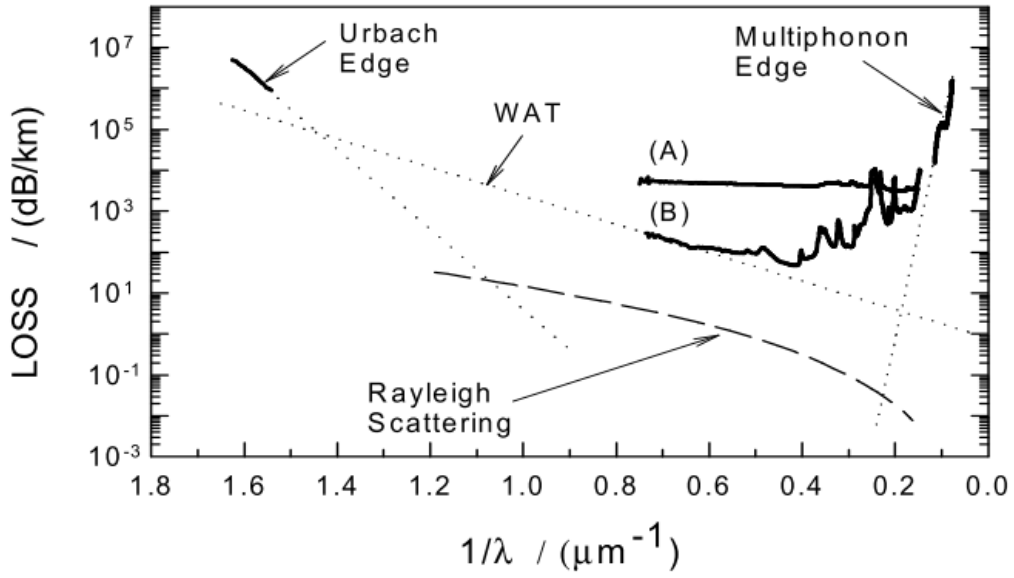


Figure 2.10 Theoretical minimal intrinsic loss in an arsenic sulfide fibre. (A) represents a poor-quality glass (B) represent a higher quality glass exhibiting lower intrinsic losses [131].

2.3.3.2 Extrinsic loss mechanisms

The mid-IR spectrum encompasses vibrational absorption bands of which the wavelength absorbed depends on the bonding between atoms. In chalcogenide glasses, oxides, hydroxides, hydrides, and molecular water present in the glass act as impurity absorptions and increase the loss of the fibre at the characteristic wavelength that particular bond absorbs at e.g., 4.55 μm for Se-H or 6.1-6.4 μm for H_2O (See Table 2.3) [92,131,132]. This can prevent or limit applications for the fibres at these specific wavelengths if optical losses are too great. Oxide-based impurities have also been identified as participants in the formation of crystal structures inside chalcogenide glasses [133]. Ideally, these impurities would be excluded from a glass system. Various purification techniques such as high temperature baking or distilling with getters are employed to minimise the oxygen and hydrogen impurity content of chalcogenide glasses and/or their precursor elements (Section 3.2.2, 3.2.5). However, even with extensive purification, some of these groups, particularly -Se-H, can still be observed on a fibre loss spectrum [134], moreover the extinction coefficient shows that only 1 ppm of -Se-H impurity causes 1 dB/m loss centred at 4.55 μm [64] (also see Table 2.3[132]) and the band is broad again due to

inhomogeneous broadening. Table 2.3 shows various impurity compounds observed in chalcogenide glasses and their corresponding extinction coefficients (a measure how much light is absorbed at that wavelength) [132]. Table 2.3 was assembled by Yadav *et al.* from reported experimental absorption data published in the literature. Figure 2.11 displays common impurity absorptions as well as displaying additional intrinsic and extrinsic loss mechanisms [7].

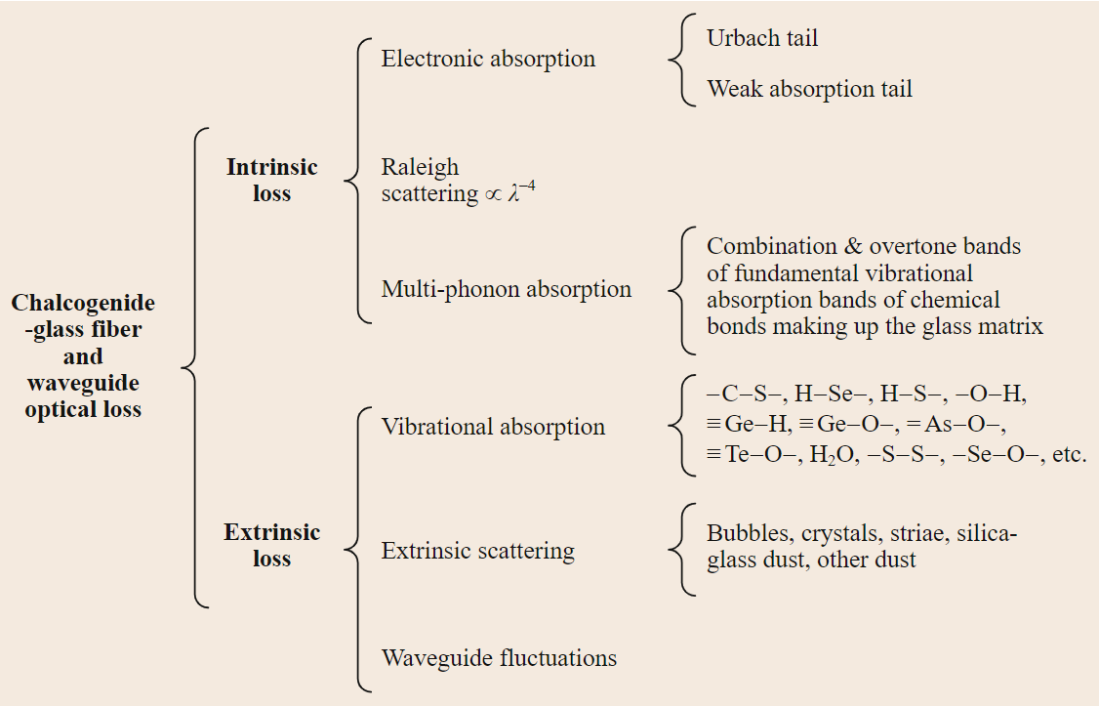


Figure 2.11 Various optical loss mechanisms encountered in chalcogenide glass fibres. Loss mechanisms are further categorised as either intrinsic (loss introduced through the inherent properties of the material) or extrinsic (loss introduced through externally originating changes to the glass. Taken from [7].

Other loss mechanisms involve the scattering of light due to crystallisation, phase separation, bubbles, and unwanted inclusions such as silica glass dust and nanoparticles (Figure 2.11) [62,135,136]. Rayleigh scattering occurs when the scattering centre is smaller than the wavelength of light it interacts with. Two theories are used to describe scattering when the wavelength is similar in size to the incoming wavelength: 1) Rayleigh-Gans theory is used for non-spherical, inhomogeneous scattering centres 2) Mie scattering is used when scattering centres

are spherical and homogenous [137]. Wavelength-independent scattering results from the scattering centre being much larger than the incoming wavelength of light [126].

Table 2.3 Impurities commonly observed in chalcogenide glasses, their corresponding absorption wavelengths, and extinction coefficients. Taken from [132]

Impurity compound or functional group leading to absorption	Position of the maximum of the absorption band (μm)	Extinction Coefficient ($dBm^{-1}ppm^{-1}$)
OH^-	2.92	5.0
Se-H	4.55	1.0
As-H	5.02	-
H_2O	6.3	34
H_2Se/-Se-H	3.5	-
	4.1	-
	7.8	-
SeO_2	7.96	-
	8.7	-
Se-O	10.6	0.38
Si-O	9.2/9.5/10.0/10.4	-
Arsenic Oxides		
Glassy As_2O_3	7.5	0.09
	7.9	0.26
Glassy As_2O_3, claudetite	8.9	0.35
As_4O_6	9.5	1.03
As-O-H	10.8	-
As_4O_6	12.7	43.0
Glassy As_2O_3, claudetite	15.4	14.78

2.4 Surgical uses for a mid-IR fibre laser

Therapeutic applications for mid-IR light work on the basis of vibrational absorption of radiation by biological molecules (Section 2.5.1). This absorption translates to thermal effects such as ablation or coagulation of tissue (Section 2.5.2-2.5.3).

2.4.1 Absorption in the mid-IR

Biological molecules present in various tissues are comprised of bonds which exhibit strong vibrational absorptions in the mid-IR spectral region. Photon energy absorbed by these bonds is converted to vibrational (heat) energy, causing these bonds to stretch or bend at greater amplitude whilst retaining their characteristic frequency. These molecules can be referred to as chromophores. While the mid-IR covers an entire fingerprint region (usually meaning 3-15 microns), water and protein are of main interest regarding mid-IR fibre lasers as they are the principal chromophores in soft tissue. Absorptions in proteins is split into two distinct bands. The amide-I band covering 5.88-6.25 µm involves the vibration of C=O peptide bonds and the amide-II band covering 6.25-6.66 µm is related to C-N stretching and N-H bending [8]. Water, the main component of tissue, has absorption bands at 2.94 µm involving the symmetrical stretching of the molecule and deformation vibrations when radiation is absorbed at 6.1 µm as well as vibrations at 9.3 and 10.6 µm. The effects of these absorptions are shown in Figure 2.12.

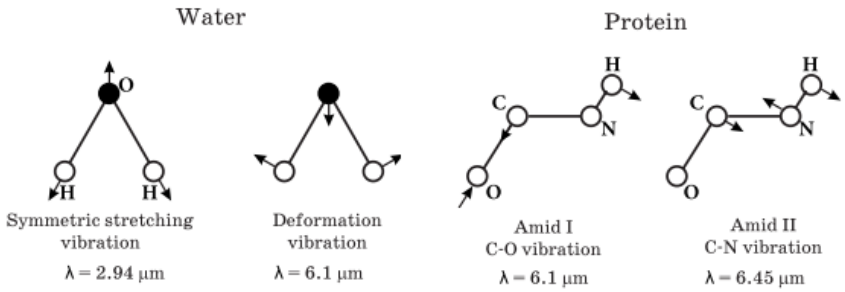


Figure 2.12 Schematic diagram of water and protein molecules and their corresponding IR absorbance wavelength [8].

CO_2 lasers emitting at a water absorption band, 10.6 µm, are the current 'gold standard' for soft tissue ablation [60,138,139]. CO_2 lasers tuned to 9.3 µm have seen success in dental applications due to an absorption band for hydroxyapatite occurring there; hydroxyapatite is the mineral component of teeth and bones [140]. Due to the lack of success in lasing at sufficient powers in the mid-IR region outside of CO_2 lasers, little research has been carried out on the effects of differing wavelengths in the 3-10 µm region. The overlapping water and amide-I absorption bands at 6.1 µm have drawn the attention of various groups in recent years. The absorption of proteins is twice the absorption of water at this wavelength (that is,

the extinction coefficient is double that of water and so for each single moiety the absorption is double) which provides improved ablation of tissues while minimising collateral thermal damage [6,8,9]. At 6.45 µm, the absorption by the most abundant protein in the human body, collagen (a structural protein), in the amide-II band is six times that of water at the expense of the water absorption band being weaker by a factor of around 3.5 when compared to 6.1 µm [9]. It has been theorised that 6.45 µm lasers would be superior for surgical use as the increase in temperature provided by the H_2O absorption would be accompanied by a decrease in the mechanical integrity of the tissue due to the amide-II absorption providing destruction of proteins, resulting in a less "explosive" vaporisation [26]. However, research has found that lasers emitting at 6.1 µm still provide superior ablation with less concomitant damage as the ablation threshold is lower [141]. Other research has found that different tissue types have differing wavelengths at which collateral damage is minimised during surgical lasing treatment [8]. Serebryakov *et al.* lists optimal wavelengths at 6.45 µm, brain tissue; 6.0 µm corneal tissue; and 6.0-6.45 µm, 7.2-7.2 µm, and 7.6-7.8 µm for skin [8].

Potential rare earth ion mid-IR emissions covering these surgically relevant absorptions are as follows (taken from [142]):

- Pr^{3+}: $^3F_3 \rightarrow {}^3H_6$ (4.9-8.3 µm)
- Nd^{3+}: $^4I_{15/2} \rightarrow {}^4I_{13/2}$ (3.8-6.5 µm)
- Sm^{3+}: $^6F_{1/2+3/2} + {}^6H_{15/2} \rightarrow {}^6H_{13/2}$ (5.7-8.7 µm)
- Dy^{3+}: $^6F_{11/2} \rightarrow {}^6H_{11/2}$ (5.4-6.2 µm)

2.4.2 Tissue ablation and considerations

For use as precision surgical instruments, mid-IR lasing needs to be able to provide enough thermal energy at wavelengths centred on these target absorption bands for ablation to occur. The increasing vibrations when stimulated leads to an increase of temperature in the tissue. The heat generated either by the direct absorption of intra- and inter- cellular water content or by absorption of other molecules such as proteins creates pressurised steam vacuoles which leads to the vaporisation of tissue once the critical temperature of the chromophores is reached [143]. Table 2.4 outlines

the effects of rising temperature on tissue structures. Sub physiological temperatures (~37 °C), tissue damage is repaired. With increasing temperatures, more extensive tissue damage is observed, with ablation occurring above 300 °C. Working with mid-IR lasers in any setting thus poses an inherent risk of tissue damage, the International Standard for the Safety of Laser Products, IEC 60825-1, has defined a maximal permissive exposure (MPE) of skin to IR radiation at different wavelengths (Table 2.5) [144]. The shorter the exposure time, the higher the permitted irradiance ($W \cdot m^{-2}$) on skin, with irradiance also being wavelength specific.

Table 2.4 Comparison of changing thermal, optical and mechanical properties of tissue as a function of temperature.[143]

	Effects on tissue		
Temp [°C]	Thermal	Optical	Mechanical
< 37	Reversible damage, only	–	–
40–45	enzyme induction edema, membrane alteration (cell death)	–	–
60–65	Protein denaturing, coagulation, necrosis	Whitening, light scattering	Incipiant weakening
70–85	Collagen denaturing, membrane damage, incipient necrosis	Opacification	Waterless tissue desiccation
90–100	Desiccation		Shrinkage, drying
> 150	Carbonization	Blackening increased absorption	Strong mechanical damage
300 >	Vaporization	fumes	Ablation

Table 2.5 MPE of skin to IR laser radiation [144]

Wave-length λ nm \ Exposure time *t* s	<10^{-9}	10^{-9} to 10^{-7}	10^{-7} to 10^{-3}	10^{-3} to 10	10 to 10^{3}	10^{3} to 3×10^{4}
1 400 to 1 500	10^{12} W·m^{-2}	10^{3} J·m^{-2}		5 600 $t^{0,25}$ J·m^{-2}	1 000 W·m^{-2}	
1 500 to 1 800	10^{13} W·m^{-2}	10^{4} J·m^{-2}				
1 800 to 2 600	10^{12} W·m^{-2}	10^{3} J·m^{-2}		5 600 $t^{0,25}$ J·m^{-2}		
2 600 to 10^{6}	10^{11} W·m^{-2}	100 J·m^{-2}		5 600 $t^{0,25}$ J·m^{-2}		

There is only limited evidence about effects for exposures of less than 10^{-9} s. The MPEs for these exposure times have been derived by maintaining the irradiance applying at 10^{-9} s.

For exposed skin areas greater than 0,1 m^2, the MPE is reduced to 100 W·m^{-2}.
Between 0,01 m^2 and 0,1 m^2, the MPE varies inversely proportional to the irradiated skin area.

An ideal laser for laser surgery would deliver the appropriate amount of energy to the target location with as little non-essential energy as possible, as this can lead to thermal stresses in the surrounding tissue. Therefore, certain intricacies need to be considered when designing a surgical laser. For example, subjecting tissue to radiation suitable to ablate will alter the surrounding local environment depending on the beam profile. This potentially leads to coagulation, desiccation, or carbonisation of the surrounding tissue [143].

Coagulation of surrounding tissue can be advantageous as it will reduce bleeding at the surgical site around the ablated tissue. Depending on factors such as exposure time, tissues reaching temperatures <42 °C are likely to avoid any coagulation necrosis due to the activation of heat shock proteins [145,146].

To minimise these effects, surgical lasers would ideally be tailored to their target tissues; three considerations need to be made [140]. Wavelengths providing strong absorptions of the radiation in the tissue will minimise scattering and keep radiation local to the target area with higher absorptions decreasing the penetration depth of the laser. Pulse energy, or fluency, needs to deliver enough energy to heat tissue above the ablation threshold. Pulse duration should be designed around the thermal relaxation time of the tissue, the time it takes a heated section of tissue to dissipate 67 % of the peak incident heat [147,148]. Generally, the collateral damage to tissue can be said to be inversely proportional to the absorption of the wavelength used. Even the stronger absorption bands such as H_2O at 2.94 µm which provides effective ablation with penetration depths of around 1 µm can still diffuse heat to surrounding tissue causing damage. Compared to lasers at 2.94 µm, 6.45 µm lasers have shown reduced thermal damage depths to surrounding tissues by a factor two despite having a higher penetration depth. Figure 2.13 compares a corneal sample irradiated at 6.45 µm, which had a collateral damage zone of 40 µm, and 2.94 µm, which had a collateral damage zone of 150 µm [8].

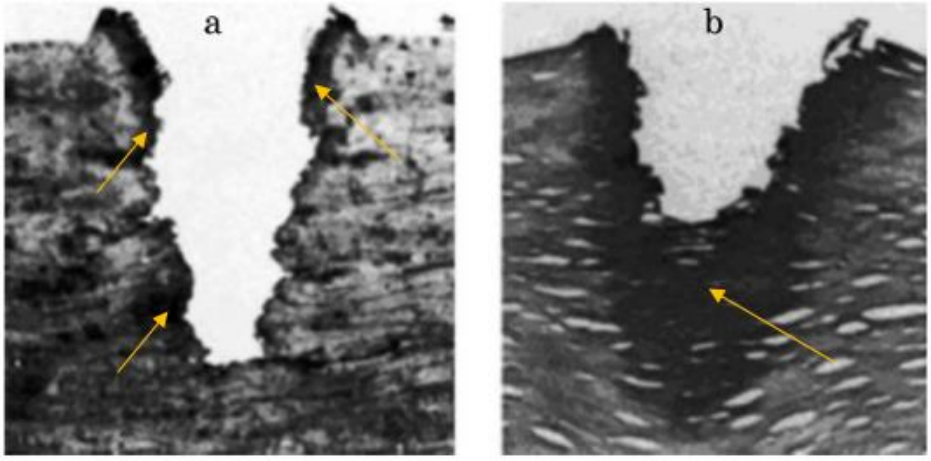


Figure 2.13 Free electron laser emitting at (a) 6.45 µm and (b) 2.94 µm pulsed 10 times onto corneal tissue. Darker areas (see arrows) are indicative of thermal damage [8]. *No scale bar available but average corneal thickness between 500-600 µm.*

2.4.3 Non-ablative thermal effects on tissue

Therapeutic effects provided by a laser extend beyond simply ablating tissue. Haemostasis through coagulation of blood can be achieved through the tissue surrounding an ablation site as the increase in temperature causes blood vessels to contract and seal shut [149]. This is particularly important for neurosurgery in which the tissues have many blood vessels with a rich blood supply. Laser welding of tissues has been proposed as an alternative to sutures for connecting soft tissues together. It operates on the principal that heating a tissue will disrupt bonds between constituent components in the extracellular matrix which induces the formation of new interactions and cross-bonding when the tissue returns to its native temperature [150,151]. Figure 2.14 demonstrates the effects of laser welding temperatures on collagen, the most abundant protein in the extracellular matrix. The process of denaturation begins with proteoglycan bridges breaking between the fibrils, disrupting their previously organised structure [152]. Further temperature increases lead to the breakdown of intramolecular hydrogen bonds in individual fibrils, and further breakdown of intermolecular covalent bonds between fibrils[152].

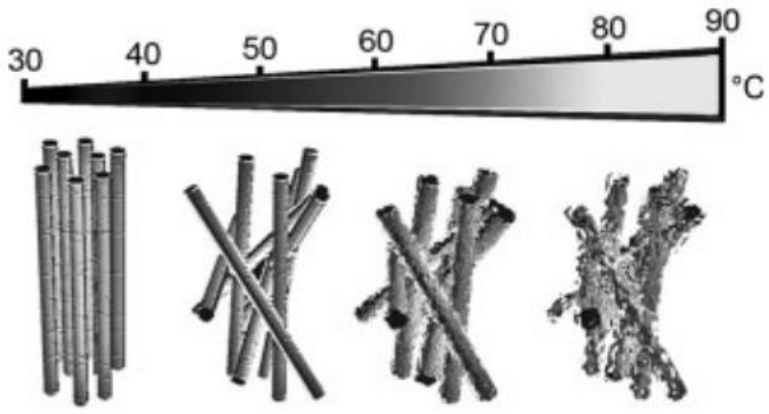


Figure 2.14 Thermal effects on collagen fibres from physiological to laser welding temperatures. Damage progresses from intermolecular bonding failure to intramolecular failure followed by further breakdown between fibrils. Taken from [152]. *Fibril diameter varies from 10nm to 250 nm, lengths highly variable from µm to mm scale* [153].

Mechanisms of laser welding can further be defined based on the temperature dependent extent to which the tissue is deformed. "Soft" laser welding, occurring between 50-65 °C, is proposed to be the product of the rearrangement of glycosaminoglycans that interconnect these collagen fibrils[152]. Breaking these bonds under heat leaves them free to bond with other broken glycosaminoglycan chains once the laser power is removed[152,154]. This type of welding has shown particular success in ophthalmic surgery, specifically in keratoplasty, in which it is vital that cells and extracellular components retain their native shape and orientation for the cornea to remain transparent[154]. Through the addition of absorptive chromophores, sections of transplanted donor corneas have been successfully soft welded to a recipient's own tissue [154].

"Moderate" laser welding occurs at temperatures > 60 °C. At these temperatures, the intramolecular bonding begins to break down, leading to the unravelling of the triple helix structure of collagen fibrils (see the increased diameter of the fibrils in Figure 2.13). These fibres begin to "interdigitate" amongst themselves, and this new structure is frozen in upon cooling of the tissue [152,154,155].

"Hard" laser welding occurs at temperatures >70 °C and is a product of full tissue homogenisation (hyalinosis)[152]. The increased temperature leads to further denaturation of the extracellular collagen proteins which interlink to a further extent

than described with "moderate laser welding"[152]. The higher temperatures also lead to the destruction of local cellular membranes, causing the release of the protein rich intracellular matrix[152]. These additional proteins, such as albumin, from inside damage cells photocoagulate act as a solder or an "endogenous glue" [152]. The use of the externally added proteins such as albumin and fibrinogen, as "solder" to aid laser welding by sterically linking collagen has been shown to improve prognosis [156–158]. The use of this solder is to mimic the more destructive effects of "hard" laser welding, without the need to induce that extent of damage to the native tissue [156–158]. Work incorporating "plasmonic polypeptide nanocomposite solder" has been used to laser weld intestinal ruptures, with the resulting solder weld having twice the ultimate tensile strength of a tissue weld sans solder (0.2 MPa compared to 0.1 MPa)[159]. Laser welding has so far demonstrated a high failure rate (the weld fails to hold the seal) and still carries the risk of collateral thermal damage [160]. This has hindered its adoption in the surgical field.

With current generation of mid-IR fibre laser sources having low power outputs but potentially high absorption coefficients for biological tissues, the exploitation of non-ablative thermal effects may be more suitable application for these sources. The current record power output for a chalcogenide fibre laser is 36 mW at 5.25 µm from a Tb^{3+} doped fibre[18]. Successful tissue welding has been reported with powers as low as 100 mW at 1.98 µm and an irradiance of 34.6 $W \cdot m^{-2}$ with its efficacy attributed to water vibrational absorptions [161]. However, it is unlikely that the fibre reported in Denker *et al.*[18] would see use as a surgical laser, even if power outputs were increased. This is because the efficacy of a laser for either ablation or welding of tissue is dependent on fluence and wavelength of the laser, as well as the properties of the target tissue [152,155]. To reiterate, the mechanisms of ablation or welding are thermal effects, thus, a laser that is strongly absorbed by tissue will require lower fluency than a laser at a wavelength at which tissue is transparent. The 5.25 µm wavelength laser is not absorbed by any biomolecule that is abundant in tissue.

While it is difficult to determine exactly what power outputs are needed at specific wavelengths to achieve ablation or tissue welding, mathematical models have been developed to describe how the laser energy is converted to heat energy in tissue[152,162] Equation 2.10, the bio-heat equation, is one (non-wavelength specific)

example used to model temperature profiles on different tissues to calculate optimum laser parameters [152].

$$\varrho C \frac{\partial T}{\partial t} - \nabla(k\nabla T) = \varrho_b C_b \omega_b (T_b - T) + Q_{met} + Q_{ext} \qquad \text{Equation 2.10}$$

ϱ = Density of tissue (kg m^{-3}) ϱ_b = Density of blood (kg m^{-3})

C = Specific heat capacity of tissue (J kg^{-1} K^{-1})

k = thermal conductivity of tissue (W m^{-1} K^{-1})

C_b = Specific heat capacity of blood (J kg^{-1} K^{-1})

ω_b = blood perfusion rate (which acts to dissipate heat from a tissue) (s^{-1})

T_b = arterial blood temperature (also acts to dissipate heat) (K)

Q_{met} = metabolic heat source (body temperature) (W m^{-3})

Q_{ext} = external heat source (laser absorption, scattering) (W m^{-3})

The equation primarily describes the physiological conditions of the target tissue, with Q_{ext} being the only parameter pertaining to the laser. It is key to note that the laser is referred to as a "heat source" and that this equation does not directly account for wavelength specificity and corresponding vibrational absorptions. With the laser sources at 2.94 µm and 6.45 µm (Figure 2.13 [8]), strong absorption by water (and protein) would correspond to a greater increase in tissue temperature as the energy is transferred to the tissue more efficiently[8]. The aforementioned 100 mW 1.98 µm laser source successfully used in tissue welding was close to a water absorption band and thus heat energy transfer was also efficient [161]. However, the 5.25 µm wavelength of the Tb^{3+} chalcogenide fibre reported by Denker *et al.* is not absorbed by any prominent biomolecule. As a poorly absorbing laser, with comparatively low power output, the 36 mW 5.25 µm Tb^{3+} doped chalcogenide fibre laser is unlikely to compete with currently available surgical laser sources as it would provide minimal heating to biological tissue. For rare earth ion doped, chalcogenide mid-IR fibre lasers to compete with existing surgical lasers, further work to achieve emissions at biologically relevant wavelengths (e.g., between 6-6.5 µm) at higher output powers is needed.

3. Methodology

This Chapter details the experimental procedures carried out. Section 3.1 lists all chemicals used in this work and their source and purity. Section 3.2 briefly describes the general chalcogenide glass making process as well as the extrusion and fibre-drawing processes. Section 3.3 presents the experimental characterisation techniques used for material characterisation and optical characterisation of the synthesised glasses and glass fibre.

3.1 Chemicals used: source, purity, and form

Table 3.1 lists the various chemicals used to create the chalcogenide glass for this project. It lists the precursors, the getters used for distillation, and the various dopants used. Table 3.2 lists all other chemicals used during the project.

Table 3.1 Source and purity of chalcogenide glass constituent elements, getters, and rare earth dopants

Chemical	**Source**	**Purity (%)**	**Form**
Glass precursors			
Antimony	Materion	9.9999	1-4 mm pieces
Arsenic	Furukawa	9.9999995	1-4 mm pieces
Gallium	Alfa Aesar	9.999999	Ingot
Germanium	Materion	9.9999	3-6 mm pieces
Selenium	Materion	9.9999	<3 mm shot
Sulphur	Materion	9.99999	4-8 mm pieces
Distillation getters			
Aluminium	Alfa Aesar	9.99999	Wire
Tellurium (IV)Chloride	Alfa Aesar	99.9	Powder
Rare earth dopants			
Cerium	Alfa Aesar	99.9 (REO)	0.25 mm thick foil
Dysprosium	Alfa Aesar	99.9 (REO)	0.25 mm thick foil
Samarium	Alfa Aesar	99.9 (REO)	0.25 mm thick foil
Dysprosium (III) chloride	Alfa Aesar	99.98 (REO)	Ultra-dry powder

Table 3.2 Source and purity of additional chemicals used during this project.

Chemical	**Source**	**Purity**	**Use case**
Acetone	Sigma-Aldrich	99.8+ %	General cleaning
Isopropanol	Fisher chemicals	HPLC (99.9+ %)	General cleaning
Propylamine	Fluka Analytical	>99.0%	Etching
Deionised water	Tap water purified through a Centra system (Elga LabWater)	-	General cleaning
5% v/v Hydrochloric acid	VWR	-	Cleaning
40% Hydrofluoric acid	Rockwood Electronic Materials	Isoclean grade	Etching
Galinstan	Alfa Aesar	99.99%	Mode cladding stripper
Polishing oil	Buehler		Cutting and polishing
10 µm SiC powder	Buehler		Grinding samples
1, 3, 6 µm diamond paste	Buehler		Polishing samples
Nitrogen	BOC	99.998%	Glovebox purge gas
5% Hydrogen/ Nitrogen	BOC	Standard	Regeneration of glovebox
Liquid nitrogen	BOC		Cold traps, detectors
Oxygen	BOC	Standard	Oxy-propane torch
Propane	Calor gas	Standard	Oxy-propane torch
Argon	BOC	99.998%	DSC purge gas

3.2 Selenide-based chalcogenide glass synthesis

To create a high purity chalcogenide glass fibre capable of lasing, precautions were taken to minimise the inclusion of any material not intended to be present in the glass composition. The cleaning and dehydrating of the ampoules are discussed in sections 3.2.1. Section 3.2.2 elaborates on the heat-treatment processes employed for As, Sb, Se, and S, as well as the physical refining of Ga. Further precautions were then taken as the materials were batched and melted, as explained in sections 3.2.3 – 3.2.4; 3.2.6. The glass quenching and annealing processes are discussed in 3.2.5, that were used to complete the bulk glass fabrication.

3.2.1 Pre-purification of silica melt ampoule

Throughout the Project, silica glassware (< 1 ppm OH) produced by Multilab Ltd, UK, was used as the vessel in which constituent elements were melted. Where this differs, it is highlighted, because for some silica glass shapes the Supplier could only deliver 5 ppm OH glass purity.

For preliminary work on new cladding chalcogenide glass compositions, 10/14 mm ID / OD (internal diameter / outer diameter), 300 mm (length) silica glass, tube ampoules were used. For rare earth ion doped chalcogenide glass compositions, 10/14 mm ID/OD, of 400 mm length silica glass, tube ampoules were used because the process involved a remelt and so a longer ampoule was required for batching-on of the dopants. For chalcogenide cladding glasses that were to be extruded, a tube ampoule with a 10/14 mm neck with a 26.5/30 mm, 100 mm length melting chamber was used for chalcogenide glass melting to produce directly, on chalcogenide glass-quenching, the correctly shaped chalcogenide glass boule for directly placing in the extruder. The glassware used during distillation is described in Section 3.2.5.

The first steps taken to optimise the quality of chalcogenide glasses involved the treatment of the low hydroxide content (< 1 ppm OH) silica ampoules. The ampoule was first checked visually for any surface defects which could have potentially led to failure during the melt process. It was then checked under a cross-polariser to scrutinise for stress birefringence; residual strain would have rendered the ampoule unsuitable for heating at high temperature during the

chalcogenide glass melting. The ampoule was then cleaned with acetone (Sigma-Aldrich, 99.95%, see Table 3.1), by sluicing out three times, followed by isopropanol (Fisher scientific, HPLC grade), *ditto,* then deionised water, *ditto*. The ampoule was then held vertically and filled with 40% by volume hydrofluoric acid ($HF_{aq.}$ Rockwood electronic materials, Isoclean grade) held at ambient temperature for 5 minutes. The HF_{aq} was used to etch the interior of the ampoule by reacting with silicon dioxide, as follows:

$$SiO_{2\,(s)} + 4HF_{(aq)} \rightarrow SiF_{4(g)}\uparrow + 2H_2O_{(l)} \qquad \text{Equation 3.1}$$

In that way, congruent etching of the silica glass surface would take place and blunting of any defects such as surface abrasion which may lead to crack initiation, growth, and subsequent ampoule failure during use.

The silica glass ampoule was then taken to the Clean-Room FabLab (Class- 10,000) where it was air-baked in a vertical resistance furnace (TF105/4.5/1ZF, Instron, lined with alumina tubing) to remove any carbonaceous deposits present. A silica glass circular plate was used to cover the open end of the furnace to aid insulation and prevent any particulate from entering the ampoule. Table 3.3 details the heating schedule of this air-bake. Following the air-bake, the ampoule was attached to a vacuum system (Pfeiffer Ltd, Mode:Duo 2) using a closely fitting Saunders' diaphragm valve (Edwards, SP16K) and pressure was taken to 10^{-4} Pa. The ampoule was again insulated with a silica glass plate and was subjected to the same heating schedule seen in Table 3.3, but this time under the stated vacuum. This combined heat-treatment aimed to reduce any hydroxide (chemically bound water) and physically hydrogen-bonded water groups (-OH and -HOH, respectively) both at the silica glass surface and diffusion out of the silica glassware. Following the vacuum bake, the ampoule was kept under vacuum by means of the closely fitting valve and then transferred into a glove box (MBraun 150B-G, $\leq$1 ppm H_2O and $\leq$1 ppm O_2) with a nitrogenous atmosphere (BOC, 99.998%) ready for the chalcogenide glass batching into the silica glass ampoule. This same procedure was conducted for every ampoule used for heat treating individual elements (exception of arsenic, due to instead cleaning with HCl and no glass melting is conducted in the purification ampoule, see Section 3.2.2) and ampoules used to melt chalcogenide glasses.

Table 3.3 Heating schedule for air and vacuum-baking of silica glass ampoule containment for the chalcogenide precursors during chalcogenide glass melting.

Step	Step from ambient to 70 °C
1	Ramp to 1000 °C @ 200 °C/ hour
2	Dwell 6 hours at 1000 °C
3	Ramp to 70 °C @ 200 °C/ hour

3.2.2 Chalcogenide glass precursor materials – pre-purification and batching

The computer program 'Batch' (in-house, written by Dr David Furniss) was used to calculate the desired total mass of the glass melt and the desired relative atomic mass percentages to determine how much of each precursor material was to be added to the final melt ampoule. In the initial stages of the fabrication process, the programme was used to give an approximation of how much of each elemental precursor was needed. This allowed an appropriate excess amount of each material to be purified (accounting for material loss) in small quantities as and when needed. All batching was conducted in the same nitrogen atmosphere glove box (MBraun 150B-G) alluded to in section 3.2.1. Table 3.4 contains the heating schedules each element was subject to and phenomena in the ampoules. Table 3.5 notes physical properties of the respective elements pertinent to heat treatment. The following subsections (i-iv) are devoted to individual elements. Equation 3.2, the Antoine equation [163,164], is used with the Antoine coefficients (calculated from measured vapour pressure data[164]) in Table 3.5 to calculate vapour pressure of precursor elements and potential contaminants (oxides, hydrides) over the temperature range states (TMIN and TMAX). It can therefore be used to calculate what temperatures are needed during heat-treatment to remove these contaminants.

Table 3.4 Heat treatment schedule for element pre-purification prior to chalcogenide glass melting.

(i) Antimony (Sb)		
Step	Programme	Observations
1	Ramp to 500 °C @ 250 °C/ Hour	-
2	Ramp to 570 °C @ 100 °C/ Hour	-
3	Dwell at 570 °C 3 hours	Accumulation of white Sb-O and silver Sb outside of hot zone.
4	Ramp to 30 °C @ 300 ° C/ Hour. End.	-
(ii) Arsenic (As)		
Step	Programme	Observations
1	Ramp to 210 °C @ 200 °C/ Hour	-
2	Ramp to 260 °C @ 200 °C / Hour	-
3	Dwell at 260 °C for 0.5 hours	-
4	Ramp to 310 °C @ 100 °C/ Hour	-
5	Dwell at 310 °C for 1.5 hours	Accumulation of white As-O and silver As outside of hot zone.
6	Ramp to 30 °C @ 300 °C / Hour. End.	-

Table 3.4 continued.

(iii) Selenium (Se)		
Step	Programme	Observations
1	Ramp to 210 °C @ 200 °C / Hour	-
2	Ramp to 260 °C @ 100 °C / Hour	-
3	Dwell at 260 °C for 1-2 hours	Accumulation of red-black Se outside of hot zone.
4	Flame* Se accumulate back to hot zone	-
5(a) – for 10/14 mm	Ramp to 30 °C @ 300 °C/ Hour	-
5(b) – for 26.5/30 mm	Ramp to 320 °C @ 200 °C/ Hour. End.	-
(iv) Sulfur (S)		
Step	Programme	Observations
1	RT to 140 °C @ 200 °C/h	-
2	Dwell 0.5 hour	Accumulation of yellow S outside of hot zone.
3	Flame* S accumulate back to hot zone	-
4	Dwell 5 mins	-
5	Flame, furnace off	-

* An oxypropane flame set to a mild heat was used to gently heat the distilled S back to a liquid. At this point the liquid S was observed to fall back down into the hot zone of the furnace.

Table 3.5 Physical properties of heat-treated precursors and their contaminants [163,165].

	°C at 1 atm		Antoine constant			Temperature (°C)		kPa
	M.P.	B.P.	A	B	C	TMIN	TMAX	V.P at H.T.T
Sb	630.6	1587	5.88125	4984.6752	74.32	343.85	1587	0.002
Sb_2O_3	656	1425	4.06652	1464.9462	-189.49	400	1550	0.22
As	616*		10.60233	6313.8843	216.09	280	601	0.005
As_2O_3	312.2	465	4.99289	1001.4246	6.99	133.70	467.15	9.091
Se	220	684.8	7.05403	3441.9628	139.77	227	685	0.004
SeO_2	340	350	18.01392	11598.1403	451.41	115	335	6.851
S	115.2	444.6	7.86630	3464.9835	250.34	102	444	0.013
SO_2	-72	-10	7.33311	1013.4609	237.65	-75.48	157.60	5948.5783

M.P. – Melting point B.P- Boiling point TMIN & TMAX – range in which Antoine constant can be used.

V.P. at H.T.T – Vapour pressure at heat treat temperature *Arsenic sublimes at 616 °C

$$log_{10}\, p = A - \frac{B}{C+T} \qquad \text{Equation 3.2}$$

p = Vapour pressure T = temperature (°C) A, B, C = element constants

3.2.2.1 Pre-purification of Se elemental precursor

As Se melts (220 °C M.P. at atmospheric pressure) during its purification (270 °C at 10^{-3} Pa) it was more convenient to retain heat treated selenium in the ampoule, add the additional glass forming components, and complete the melt in the same ampoule. The ampoule was subject to the cleaning and dehydration steps detailed in section 3.2.1. At these temperatures, volatile selenium oxide (SeO) with a vapour pressure of 6.851 kPa at 270 °C is expected to dissociate from Se (vapour pressure 0.004 kPa at 270 °C) leading to its removal.

Prior to batching, the as-received Se (≈ 19-20 g for a ≈30 g melt) (see Table 3.1) was transferred between three weighing boats (Fisherbrand™ Polystyrene, 85 mL) to physically remove any small pieces of debris or dust which may have adhered to the side of the ampoule outside of the hot zone of the furnace or remained adhered onto the weigh boat, therefore being included in the final weighed mass, but not being included into the final glass melt. All the Se to be weighed was transferred to the first boat and agitated through a gentle shaking, this was then poured into the second boat. This was then repeated to the third boat. Residual dust and small particles remaining on the first two boats (assumedly through static interactions) was disposed of. Typically, around 0.1-0.3 g of the ~20 g Se mass was lost during purification, so the batching 'error' was arranged to be + 0.3 g at this stage.

An 'O' ring was added to the top of the ampoule in preparation for the ampoule to be connected to the vacuum *via* a Saunders' valve. The ampoule was then placed onto a weighing balance (Sartorious, model BP221S) inside the nitrogen glovebox (MBraun, 150 B-G). To minimise the interference of static build up on the ampoule (due to low humidity in the glovebox) tending to cause false readings, an air ioniser (MBraun, Static eliminator) was slowly manually waved close to and around the ampoule. Additionally, metal tweezers (stainless steel) were drawn along the exterior of the ampoule to dissipate any static electricity before a reading of the ampoule mass was taken.

The Se shot was then poured into the ampoule directly from the weighing boat. A clean silica glass tube (MultiLab < 1ppm OH, 7/9 mm ID/OD, 180 mm length for 300 mm 10/14 ampoules or 280 mm for 400 mm 10/14) was fitted with an "O" ring (ID 7 mm, RS, Nitrile) approx. 5 mm from one end and slotted into the top of the silica glass ampoule. The purpose of this inserted tube was to collect, on its inside, the bulk of the volatile SeO released during the heat treatment. This approach avoided any residuals (Se or SeO) depositing on the interior of the ampoule which was therefore cleaner: an important consideration as the final melt was carried out in this same ampoule.

The silica glass ampoule was then fitted with a Saunders' valve, which was closed off, ready to be taken out of the glove box. The ampoule was fixed to a vacuum system (HiCube Eco, Pfeiffer) housed in a fume cupboard and equipped with

roughing diaphragm vacuum pump (MVP 015, Pfeiffer) and turbo pump (HiPace 80, Pfeiffer). Liquid nitrogen was then added to the cold trap situated between the Se-containing ampoule and the start of the vacuum system connected to the vacuum pump. This cold trap prevented any particulates from the ampoule getting into the pump. The vacuum system was then switched from the roughing pump to the diffusion pump which reached around 10^{-4} Pa. A tube resistance furnace (in-house, ID 28 or 38 mm) fitted to a stand was vertically raised to cover the ampoule and the top of the furnace was insulated with furnace wool (Superwool, Morgan Thermal Ceramics). Table 3.4 details two commonly used heating schedules used to purify selenium. One for smaller batches in a 10/14 mm ampoule, and the second at a higher temperature for larger batches in a 26.5/30 mm ampoule.

As selenium comprised the bulk of the glasses studied (*i.e.*, usually > 65 at. %), it was often the case that the pre-heat-treated raw material *i.e.*, the as-received Se shot extended beyond the 60 mm hot zone of the tube furnace when a 10/14 ampoule was used. To accommodate for this, the furnace was moved between three positions during the 260 °C dwell, while the ampoule remained static to ensure uniform heat treatment of the Se containing section of the ampoule. This furnace movement was likely of minimal consequence as radiant heat kept the majority portion of the ampoule in the furnace above the Se melting point (220 °C) and the batched Se would melt down to a liquid often around 60 mm in height, thus fitting in the hot zone. Upon completion of the heat treatment, when the ampoule and contents had returned to ambient temperature, the Saunders' valve on top of the ampoule was closed, to isolate the ampoule from the vacuum system. The exterior of the ampoule was cleaned with isopropanol (wiped with a wetted paper towel, followed by rinsing straight from the squirt bottle to remove any tissue paper residue), to remove any residual ceramic fibres originating from the insulating furnace blanket, and the ampoule containing the purified Se was returned to the glove box. The valve was removed as was the smaller silica glass tube.

The ampoule containing the purified selenium was then treated again with the ionizer and tweezers to remove static and was re-weighed. The final weight of the purified selenium was then calculated using the initial weight of the clean silica ampoule and the final weight of the ampoule containing the purified selenium. This accounted for any loss of material, be it Se adhered to the silica inner tube or SeO,

which occurred during heat treatment. Pre-purified chalcogenide glass constituents were then weighed and batched on immediately following Se purification to begin the melting process the same day to avoid re-oxidation of Se which could act as a getter even in the reduced oxygen atmosphere of the glovebox and undo the work of purification.

3.2.2.2 Pre-purification of S elemental precursor

For glasses containing S, the sulfur purification ampoule was instead designated as the melt ampoule. Sulfur was included at 1-3 at. % and only ever as part of cladding glass intended for a small core fibre to lower its refractive index. A static minimising weighing procedure identical to that done with Se was carried out pre- and post-heat treatment (detailed in Table 3.4) to calculate the true weight of purified sulfur. Table 3.5 details the vapour pressure for S and SO_2 at 140 °C. During this procedure, the as-received S (Table 3.1) melted (M.P 115 °C), releasing gaseous SO_2, SO_3, H_2S, and H_2O from the liquid. At 10^{-4} Pa, the S began to distil to the cooler sections of the ampoule outside the hot zone of the furnace. The furnace was thus temporarily lowered, and the oxy-propane flame employed to gently heat the deposit, thereby dropping it back to the base of the ampoule and into the furnace hot zone. The selenium for incorporation in sulfur-containing glasses was purified in a cleaned, etched, and dehydrated (Section 3.2.1) 26.5/30 mm ampoules (Table 3.4, section iii, step 5b) and then removed from the furnace at 320 °C. Commonly around 50-70 g of Se would be purified in such an ampoule. The ampoule was then angled roughly 30 ° and held to cool to room temperature. The reasoning for this was three-fold. Firstly, it allowed a faster cooling of the material. Secondly, it aimed to minimise the risk of ampoule failure. If the Se solidifies in a large cylinder shape (taking the form of the 26.5 ID of the ampoule) and contracts, it can leave a small gap between the Se and the wall of the silica ampoule. There is a possibility that a small piece of another precursor such as As, Sb, or Ge could fall into this gap during batching, which is then pressed into the ampoule wall as the material expands during heating, potentially leading to ampoule failure. Thirdly, this cooled to a solid mass of selenium which was easily extractable for batching to the melting ampoule.

3.2.2.3 Pre-purification of As elemental precursor

The as-received arsenic was purified in a 19/25 mm ID/OD, length 300 mm ampoule dedicated for As heat treatment. It was cleaned with hydrochloric acid(*aq.*), acetone, isopropanol, and deionised water (see Table 3.2 for source and purities). At this stage, the accuracy of the amount weighed was not important so long as more than required was purified but no more than 30 g of arsenic was to be purified at any one time. The arsenic was swapped between three weigh boats (Fisherbrand™ Polystyrene, 85 mL) to aid in the removal of any fine particulates, as described in Section 3.2.2.1. This aimed to physically remove any small pieces of debris or dust which may have adhered to the side of the ampoule outside of the hot zone of the furnace. Residual dust and small particles remaining on the first two boats (assumedly through static interactions) were disposed of. The remaining bulk As pieces were then batched into the purification ampoule. A valve was attached to the ampoule and was subjected to the same evacuation process as detailed in Section 3.2.2.1. Table 3.4 details the heat treatment schedule for the purification process. Table 3.5 highlights the difference in vapour pressure between As (0.005 kPa) and As_2O_3 (9.091 kPa) at 310 °C. Gaseous As_2O_3 and small amounts of sublimed As deposit on the cooler sections of the ampoule and form white and grey deposits, respectively. Following heat treatment, the Saunders' valve was closed, and the ampoule was disconnected from the pump system (with the contents still at 10^{-4} Pa). The ampoule exterior was cleaned with isopropanol (wiped with a wetted paper towel, followed by rinsing straight from the squirt bottle to remove any tissue paper residue) to remove any furnace blanket debris and returned into the glove box. Ideally this process was carried out the day preceding the Se purification and glass melting to avoid re-oxidation of the arsenic. Due to arsenic oxide contaminant being present on the interior of the ampoule, the purified arsenic was then transferred into removal plastic cap covered silicate bottles (unknown supplier, acquired from School of Chemistry stores, University of Nottingham) that had previously been cleaned then dried under vacuum. The As was then stored in the glove box ready for batching.

3.2.2.4 Pre-purification of Sb elemental precursor

As-received antimony (See Table 3.1) heat treatment was performed in 10/14 mm, 300 mm ampoules subject to a similar procedure to that described in Section 3.2.2.1. The ampoule was fitted with a 7/9 mm (ID/OD), 180 mm long silica tube (also explained in section 3.2.2.1). At this stage, accuracy of batching was not a concern but generally an excess of 5 g more than the required amount was purified. The long duration (*ca.* six hours) of this heat treatment process meant in some cases it was desirable to heat treat more than double the required batch to save time for future glass melts. Although usually carried out the day before the Se purification and glass melting, heat treated antimony was stored for up to two weeks, after which, a repeat heat treatment would be preferable due to possibility of re-oxidation. As conducted in the purification of the other materials, the antimony was transferred between three weighing boats to remove any small debris (as described in Section 3.2.2.3). The antimony was then batched into the ampoule and a valve was attached. Following a similar method to that in Section 3.2.2.1 the ampoule was put under high vacuum and subjected to the heating schedule detailed in Table 3.4. The comparatively small (to the other elements in Table 3.5) difference in vapour pressures between Sb_2O_3 (0.22 kPa) and Sb (0.002 kPa) at 570 °C warranted a comparatively longer heat treatment of 3 hours at the target temperature to ensure adequate dissociation of the oxide. Powder deposits (colourless to dark grey) assumed to be Sb and Sb_2O_3 accumulated on the interior of the ampoule at the mouth of the furnace, with bright silver deposits assumed to be Sb accumulating below the powder. Post-heat-treatment, the Saunders' valve was closed, and the ampoule was disconnected from the pump (with the contents still at 10^{-3} Pa). The ampoule exterior was cleaned with isopropanol (wiped with a wetted paper towel, followed by rinsing straight from the squirt bottle to remove any tissue paper residue) to remove any furnace blanket debris and returned into the glove box. Similar to the As purification, residuals assumed to be Sb_2O_3 were potentially caught on the interior of the ampoule. For this reason, the Sb was removed from the ampoule and stored in plastic cap covered silicate bottles (unknown supplier, acquired from School of Chemistry stores, University of Nottingham) that had previously been cleaned then dried under vacuum.

3.2.2.5 Pre-purification of Ga elemental precursor

The low melt point of gallium (29.77 °C, at normal pressure [166]) was exploited to allow precise (±1 mg) batching of small liquid droplets. Initially sourced as ingots (see Table 1), the solid, as-received, gallium was transferred to a polyethylene bottle (30 mL, Sigma Aldrich) stored in the glovebox and placed onto a heating element (created in house by Dr Furniss). When gallium was to be batched, a heating element (made in-house) was powered until the gallium was in liquid form (*i.e.* > M.P. and ~ 30 °C). A low-density polyethylene (LDPE) transfer pipette (Fisher) was used to extract an aliquot from the bulk of the molten Ga which was then placed on an antistatic weighing boat (Fisherbrand™ Polystyrene, 85mL). A visually observed surface film, assumed to be gallium oxide β-Ga_2O_3 appeared to accumulate at the gallium during storage [167]. This assumption was based on multiple deductions. It was deemed unlikely to be a product of contamination from our chosen storage method as polyethene and other plastics have been shown to be unreactive to gallium even when stored under extreme temperature [168] and is commonly sold in polyethene packaging. It was also deemed unlikely to be a product of another elemental impurity because of the high metallic purity (7n5) of the as-received ingot, but Ga_2O_3 being a common intermediate used during the purification of Ga[169]. It is possible that these oxide impurities were incorporated and 'frozen into' the gallium ingot during manufacturing then emerge at the surface of the material over time at temperatures above melting. Ga_2O_3 was assumed to be present in β form as it is the only stable crystal structure[167]. To minimise any β-Ga_2O_3 inclusions in the chalcogenide glass melt, a fresh LDPE transfer pipette was then used to remove a second aliquot from the centre of the extracted liquid Ga mass. This was repeated until the transferred liquid gallium had a brilliant, shiny surface quality free from any surface film observed on the bulk. The liquid gallium was then weighed and directly deposited to the melt ampoule *via* a stainless-steel spoon.

3.2.3 Batching, sealing, and securing ampoule

With the precursors purified, it was important to batch accurately the material into the melt ampoule and seal said ampoule under vacuum in a timely manner. This was done to minimise any potential re-oxidation of the elements. The ampoule was

then wrapped with Nickel-Chromium wire (0.64 ⌀, The Crazy Wire Company) to secure the ampoule in a fixed position during melting and facilitate easy removal of the melt ampoule from the furnace.

Pre-purified Sb, As, Se (in melts containing S), Ga, and un-treated Ge were weighed out to 4 decimal places on the balance (Sartorious, model BP221S) housed in the glovebox. Batched weights were ±1 mg of the values calculated with the 'batch' programme meaning ±0.0003% of the total weight for a 30 g chalcogenide melt. Anti-static weighing boats and deionising (see sub-section 3.2.2.1) the local environment improved accuracy of weighing. The Ge, in piece form, occasionally needed to be broken into smaller pieces with stainless steel tweezers (Blunt S/S, Taab laboratories) to achieve ±1 mg from the calculated mass. Precursors were dropped directly from the weighing boats into the purified silica glass ampoule in which the chalcogenide glass melting was to be carried out. The ampoule containing the precursors was fitted with the Saunders' valve, removed from the glove box, and was connected to the vacuum system (same pump system described in 3.2.2.1) which brought the pressure inside the ampoule to 10^{-4} Pa as measured using an APG100-XM and AIM-X vacuum gauge (Both Edwards) and displayed on an active digital controller (Edwards).

An oxygen-propane torch (Gas detailed in Table 3.2) was used to seal the ampoule roughly 80 mm below the valve fittings. The silica ampoule would be taken above its T_g (≈ 1200 °C) to allow sealing. This procedure would take a maximum of two minutes, ensuring the precursor material below and the O ring fitting above the seal were subjected to minimal heat and minimising the thermodynamically favourable silica breakdown > 900 °C at atmospheric pressure (Equation 3.3)[170]:

$$SiO_2 \rightarrow SiO + ½\ O_2 \qquad \text{Equation 3.3}$$

Once sealed, the base of the ampoule containing the batched elemental precursors was slowly pulled away from the vacuum system with the torch still focused on the recently sealed section. The sealed end of the ampoule was slowly moved away from the hot zone of the torch (blue flame) to the cooler parts of the flame (orange flame). This action of gradually withdrawing the sealed end helped to provide an annealing of the silica glass in effect to minimise any stresses which may have been introduced.

The melt ampoule can be subjected to temperatures up to 900 °C during the melting of antimony-based glasses and was extracted from the melting furnace at temperatures as high as 700 °C. To remove the ampoule from the melt furnace, a nickel-chromium wire was wrapped around the ampoule to act as a handle. The wire was crossed over the ampoule around 10 mm above where the predicted glass melt will be sitting Figure 3.1). The wire was then twisted over itself multiple times before being lifted vertically where it was then wrapped around again. This was repeated until the top of the ampoule is reached and then any excess is twisted together to act as a handle. A firm pull assessed whether the wire was tight enough on the ampoule to keep is secure.

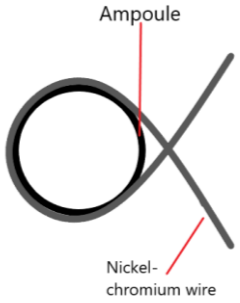


Figure 3.1 Schematic diagram of method used to create a handle on the melt ampoule to allow removal from the furnace at 700 °C.

3.2.4 Chalcogenide glass melting

Following on from Section 3.2.3, with the purified chalcogenide glass precursors sealed in the melt ampoule and fastened with wire, the next stage was to place the ampoule in the furnace and set an appropriate heating schedule (Table 3.6) specific to the melt composition.

The ampoule is suspended in the hot zone of a tube furnace (Instron TF105/4.5/1ZF, ID 86 mm with Eurotherm 2408 controller) housed on a mobile frame which could be programmed to rock. The furnace initially lies horizontally and slowly heats above the materials liquidus point and then mechanically rocks the ampoule to promote mixing of the materials. Towards the end of the melting programme, the furnace will be adjusted to sit vertically and continue rocking. This aims to agitate any bubbles present in the melt to migrate to the top. The final stages involve the temperature dropping and the ampoule remaining in a static

vertical position to allow the glass to settle. Table 3.6 contains melting schedules for both an arsenic containing glass and an antimony containing glass. Glass preforms melted in this project were assigned a code beginning with the letter "M" followed by an identification number and the initials of the maker. If a melt included a rare earth ion dopant, "RE" was included before the makers initials. For example, M240RERC (500 ppmw Dy^{3+} doped $Ge_{19.4}Sb_{9.7}Se_{67.9}Ga_3$ at. %).

Table 3.6 Furnace heating schedule for (i) Arsenic containing melts and (ii) Antimony containing melts

(i) Arsenic		
Melting schedule	**Re-melt schedule**	**Note**
Ramp to 450 °C @ 40 °C/h	Ramp to 450 °C @ 40 °C/h	30° to the ground
450 °C to 850 °C @ 40 °C/h	450 °C to 850 °C @ 40 °C/h	Rocking
Dwell @ 850 °C for 12 h	Dwell @ 850 °C for 2 h	Rocking
Dwell 850 °C for 1 h	Dwell 850 °C for 1 h	Vertical Rocking
850 °C to 700 °C @ 50 °C/h	850 °C to 700 °C @ 50 °C/h	Vertical
Dwell 1 hour @ 700 °C	Dwell 1 hour @ 700 °C	Vertical
(ii) Antimony		
Melting schedule	**Re-melt schedule**	**Note**
Ramp to 450 °C @ 40 °C/h	Ramp to 450 °C @ 40 °C/h	30° to the ground
Dwell 2 hours	Dwell 2 hours	Stationary
Ramp to 900 @ 450 °C/h	Ramp to 900 @ 450 °C/h	Rocking
Dwell 900 °C for 12 h	Dwell 900 °C for 2 h	Rocking
Dwell 900 °C for 1 h	Dwell 900 °C for 1 h	Vertical rocking
Ramp to 700 °C @ 50 °C/h	Ramp to 700 °C @ 50 °C/h	Vertical stationary
Dwell 1 hour	Dwell 1 hour	Vertical stationary

3.2.5 Distillation

As discussed in Section 2.3.3, minimising the presence of oxygen, hydrogen, and carbon impurities is essential to producing low optical loss chalcogenide glass. To improve glass purity beyond what is achieved through the heat treatment methods described in Section 3.2.2, chalcogenide glass was distilled in the presence of getters.

Figure 3.2 (a) was the first iteration of the distillation rig used in this project. This design had proven successful with previous group members but there was potential to make improvements to the design. Figure 3.2 (b) shows the rig redesigned for this project (Appendix 1 for full size). The most notable changes are to the length of the collection chamber (Right side of figure, 26.5/30 mm chamber) and the offset of the 10/14 tubing feeding into the charge chamber (Left side of figure, 44/50 mm chamber). The additional length at the collection chamber allowed the introduction of a second heating coil leading to better thermal management and subsequently reducing blockage of the 160 mm 10/14 mm tubing, increasing yield. The offset of the 10/14 mm tubing in the charge chamber allows whole preforms, melted and annealed in 10/14 mm ampoules, to be slotted into the charge chamber, eliminating the need to break the chalcogenide into smaller pieces to batch. The change in collection chamber diameter from 29/32 mm to 26.5/30 mm was due to the manufacturer (Multilab) no longer fabricating the larger size.

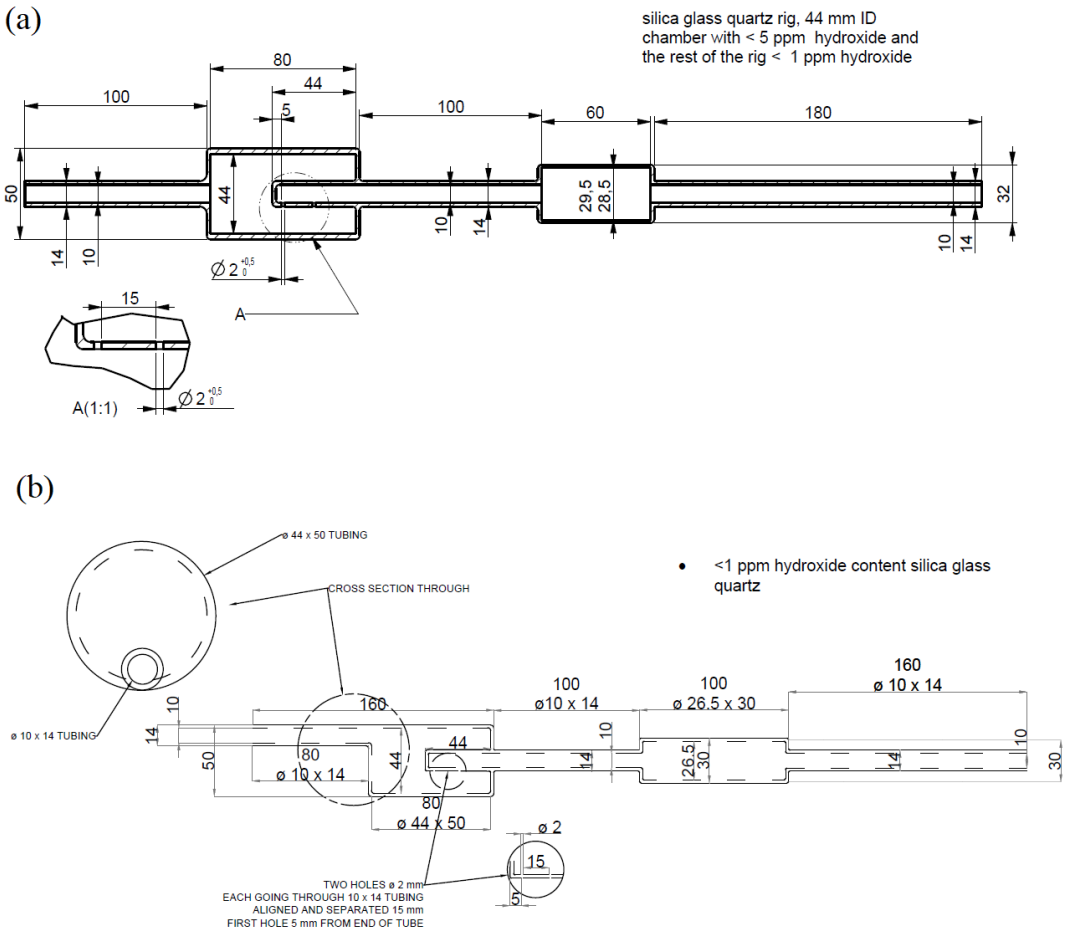


Figure 3.2 Schematic diagrams of both distillation rigs used throughout the project. (a) Initial design which produces a 29 mm chalcogenide boule. (b) Redesigned rig with a longer collection chamber and offset "batching tube". All dimensions are in mm. Appendix 1 for full size schematic.

Following the HF etching (as described in Section 3.2.1), an oxypropane torch was used to heat a silica cane above T_g to melt 5 mm silica spots, 5 mm apart from one another, along the length of the link tube and the distillate chamber. This prevents the heating wires (further explained below) from moving along the length of the rig, potentially causing an uneven temperature profile or a short circuit between power supplies.

The rigs were subject to the same clean-etch-air bake-vacuum bake procedure as detailed in 3.2.1 with slight modification to the method. Due to the length of the rig, the air bake procedure had to be conducted twice. The first time keeping the charge chamber in the hot zone, the second keeping the collection chamber in the

hot zone. The vacuum bake method was also altered. The distillation rig was fitted with an Edwards valve at the charge end and a stainless-steel end cap at the collection end. This rig was then removed from the class 10,000 cleanroom and attached to the HiCube vacuum system described in Section 3.2.2. The rig was inserted into a two-zone furnace (Instron, TF1798, tube ID 86 mm) with both extremities of the rig remaining outside of the furnace hot zone. The rig was suspended in the centre of the furnace tubing with clamps fitted to stands to prevent any scratching of the rig. As rubber O-rings were used to aid vacuum with the end caps and valve fittings, the vacuum bake was taken up to 800 °C as opposed to the 1000 °C used for the standard procedure.

In preparation for distillation, glass was prepared using the standard procedure (as detailed in Sections 3.2.2-3.2.4, 3.2.6) with the addition of 1000 ppm wt. $TeCl_4$ (Table 3.2) to the batched precursors before the ampoule was sealed off for melting. The reason being the $TeCl_4$, acting as the hydrogen getter, would have ample time at high temperatures to react and "capture" any hydrogen, forming HCl gas. Gallium was not added at this stage due to its inability to distil at the temperatures and pressures used. Due to the cost and complexity of the distillation process, it was common to produce a large mass of glass in a 26.5/30 mm ampoule. This ensured that the distillate could be divided, and multiple glasses could be produced from one distillation.

Following quenching and annealing of this glass, the ampoule was scored with a diamond saw and opened in the dry nitrogenous atmosphere of the glovebox (MBraun 150B-G with 99.998% dry nitrogen, See Table 3.2). A pestle and mortar were used to break down this boule into pieces that could pass through the 10/14 mm batching tube on the distillation rig. These pieces were then batched into the distillation rig alongside 700 ppm wt. Al wire, the oxygen getter. The valve fitting was then again attached to the 80 mm batching tube and the steel endcap was fitted to the 160 mm distillate collection tube. This was then connected to the HiCube vacuum system, and the batching tube was sealed off. The remnants of the batching tube were removed from the valve and the valve was returned to the glovebox alongside the distillation rig, now sealed at one end. The valve was fitted to the 160 mm 10/14 collection tube and removed from the glovebox.

The charge chamber was placed into a clamshell furnace (Carbolite, UK) with the rest of the distillation rig suspended horizontally with clamps. Five separate lengths nickel-chromium wire were then wrapped around the rig. Two lengths (denoted L1A and L1B) were wrapped around the tube linking the charge and collection chamber. The third length was wrapped into a coil (denoted Coil) and placed around the 100 mm link tube, butted to the end of the collection chamber. The intention of this was to ensure that increased heating could be provided to this region to avoid any potential blockages due to material condensing. The final two lengths (denoted D1 and D2) were each wrapped around one half of the collection chamber. The remainder of these lengths that were not around the rig were then insulated with ceramic fish spine beads and the ends were screwed into terminal blocks. These terminal blocks were fitted with rubber insulated wire end capped with banana plugs. These rubber insulated wires were then plugged into a benchtop power supply (72-10495, Tenma). Each of the five lengths of wire was given its own power supply to allow localised temperature changes across the length of the distillation rig by varying the voltage or current set in the power supply. Thermocouples were then wired in the centre of each of the five lengths with two additional thermocouples wired to each end of the charge chamber and attached to a computerised thermocouple logger (TC-08, PicoTech). A multi-metre was then used to check for any potential shorts between the wires. Five separate pieces of insulting fibre furnace blanket were then added to each section to allow temporary removal (for monitoring or rapid temperature reducing) of individual sections while minimising temperature change in neighbouring regions. The wired rig was then attached to the liquid nitrogen cooled HiCube vacuum system operating between $1x10^{-5}$ to $8x10^{-6}$ mbar ($1x10^{-3}$ to $8x10^{-4}$ Pa).

The distillation procedure began by bringing the charge chamber to 300 °C using the clam shell furnace and the rest of the distillation rig to 600 °C through heating of the wires. This aimed to provide a final bake out procedure of the rig and potentially any HCl present in the chalcogenide formed from the $TeCl_4$. It also allowed for calibration of the power supplies to determine which voltages and currents would provide certain temperatures with the wire used. This was left for 40 minutes. Following this, the entire rig was brought to 300 °C and kept stable for roughly six hours. This temperature reduction and dwell stage serves no purpose to

the distillation process but is designed to let the operator break up the work over a two-day period. Care must be taken to not let the liquid nitrogen cold traps run dry at this stage. After this dwell period, the furnace is increased to 500 °C and the distillate chamber is reduced to 250 °C. The aim of this is to get the chalcogenide above its T_L. The wires L1A, L1B, and Coil, are then heated to 500 °C with care taken to maintain the distillate chamber at 250 °C. This was then left to dwell for 1 hour. The L1A, L1B, and Coil were then heated to 600 °C and the furnace heated to 700 °C. The charge chamber was carefully monitored to determine when distillation was complete. Upon completion, L1A and L1B were dropped to 300 °C and the furnace was turned off. The distillate chamber was kept at 200 °C for 20 minutes to aid in the removal of any potential CSe_2. Following this the power supplies were turned off. The rig was then sealed either end of the distillate collection chamber and was ready to melt as described in section 3.2.5.

Table 3.7 Tabulated process for chalcogenide distillation.

Step	Action
1	Visual inspection of distillation rig. Acetone, isopropanol, deionised water rinsing.
2	HF_{aq} etching 40% 5 minutes. Distilled water rinse.
3	Silica dots to guide heating wire added.
4	Air bake (Clean room) x 2. First with charge chamber towards base of furnace, second with distillate/collection chamber down.
5	Vacuum bake in 2-zone furnace x 1.
6	Remove rig from furnace, clean exterior with isopropanol, return to glovebox.
7	Batch chalcogenide and Al getter.
8	Attach rig to vacuum system, seal off batching tube.
9	Return to glovebox to attach valve
10	Place charge chamber of rig in clam shell furnace, suspend rig with clamps.
11	Wrap NiCr wire around the separate, predesignated heating areas.
12	Add ceramic fish spine beads to insulate the tail ends of the wrapped wire.
13	Insulate thermocouples with ceramic tubing and secure to rig with wire.
14	Ensure the separate heating wires are not in contact with its neighbouring wire. Use multi-metre set to 200 Ω. Circuit should be open (displaying "1") when in contact with two different NiCr wires.
15	Connect NiCr wire to terminal/choc boxes fitted with rubber insulated wire.
16	Add insulating blanket to separate heating regions. Connect to vacuum system.
17	Begin bake out: Clam shell furnace to 300 °C, heating wires to 600 °C. Leave 40 minutes.
18	Heating wires to 300 °C, left overnight once stable.
19	Clam shell to 500 °C, L1A, L1B, Coil to 500 °C. D1, D2 to 250 °C. Dwell 1 hour
20	L1A, L1b to 600 °C. Furnace to 700 °C.
21	Check charge chamber periodically to observe distillation status. Once complete, L1A and L1B to 300 °C. Clamshell furnace turned off.
22	D1, D2, L1A, L1B to 200 °C. Dwell 20 minutes.
23	Power off heating wires. Remove wires and seal off the distillate for remelting.

3.2.6 Quenching and annealing

Critical to glass forming, the steps of quenching and annealing must be carried out immediately after the melting process. A suitable quenching scheme is vital to avoid devitrification. For these glasses, the process of quenching and annealing was broken into multiple stages. First the glass melt was removed from the melt furnace and held at room temperature for 0.5-2 minutes (time dependent on melt mass, larger melts needing longer time as the larger mass takes longer to cool). It was then transferred into a quenching furnace which has been set to the expected T_g of the melt, again the glass melt was held isothermally for 0.5-2 minutes, during which the melt was equilibrating to T_g. The ampoule was then slowly physically raised out of the quench furnace *via* the nichrome wire and was subjected to a sustained jet of nitrogen gas (see Table 3.2) which was focused on the top of the chalcogenide glass melt until the chalcogenide contracts away from the inner surface of the silica glass ampoule. The nitrogen gas jet was then used to slowly follow/chase the points where the melt had contracted away down the ampoule, until the bottom of the ampoule was reached. Immediately following this, the ampoule was transferred to a furnace preheated to the T_g. The furnace remained at T_g for around an hour before beginning a slow decrease to room temperature; in other words, the furnace was switched off and cooled naturally to room temperature (Newton's Law of Cooling) with the silica glass ampoule and its contents in thermal equilibrium inside the furnace. This aimed to reduce or remove residual stresses present in the chalcogenide glass.

3.2.7 Addition of rare earth elements and re-melting

Evidence has been put forward that rare earth elements, when subject to the melting schedules detailed in Table 3.6, can corrode the silica glass ampoule [52]. To minimise the extent of silica glass corrosion (and subsequent potential contamination of the glass), two consecutive melt processes were carried out. The first melting of the undoped host glass described in Table 3.6, aimed to create a homogenised host glass structure over a 12-hour period. This melt was quenched and annealed and was returned to the glovebox. The ampoule was then reopened, and the rare earth was batched. A re-melt of this host glass, now containing the batched rare earth, with a 2-hour step at the mixing temperature encouraged a high

degree of homogenisation of the rare earth to be achieved in the host glass at high temperatures, while minimising the contact time of rare earth with the silica melt ampoule.

3.2.8 Extrusion

As an overview, to fabricate structured, small-core, step index fibre, chalcogenide glass boules were extruded through a 3-legged spider die (stainless steel, made in-house) to form a small-bore jacket tube of cladding glass. A cane of rare earth doped core glass was then inserted into this jacket tube (rod-in-tube preform) to be drawn to structured fibre.

All extrusions were conducted with an extruder built in-house by Dr David Furniss, Mid-IR Photonics Group, University of Nottingham, UK. A schematic diagram of the extruder is shown in Figure 3.3(a). Extrusions were carried out vertically with the hydraulic cylinder at the top of the extruder, pushing the glass supercooled melt (at a temperature between T_g and the liquidus and at a viscosity of ~ $10^{7.5}$ Pa·s) down through the spider die. Figure 3.3(b) is a labelled photograph showing the components used.

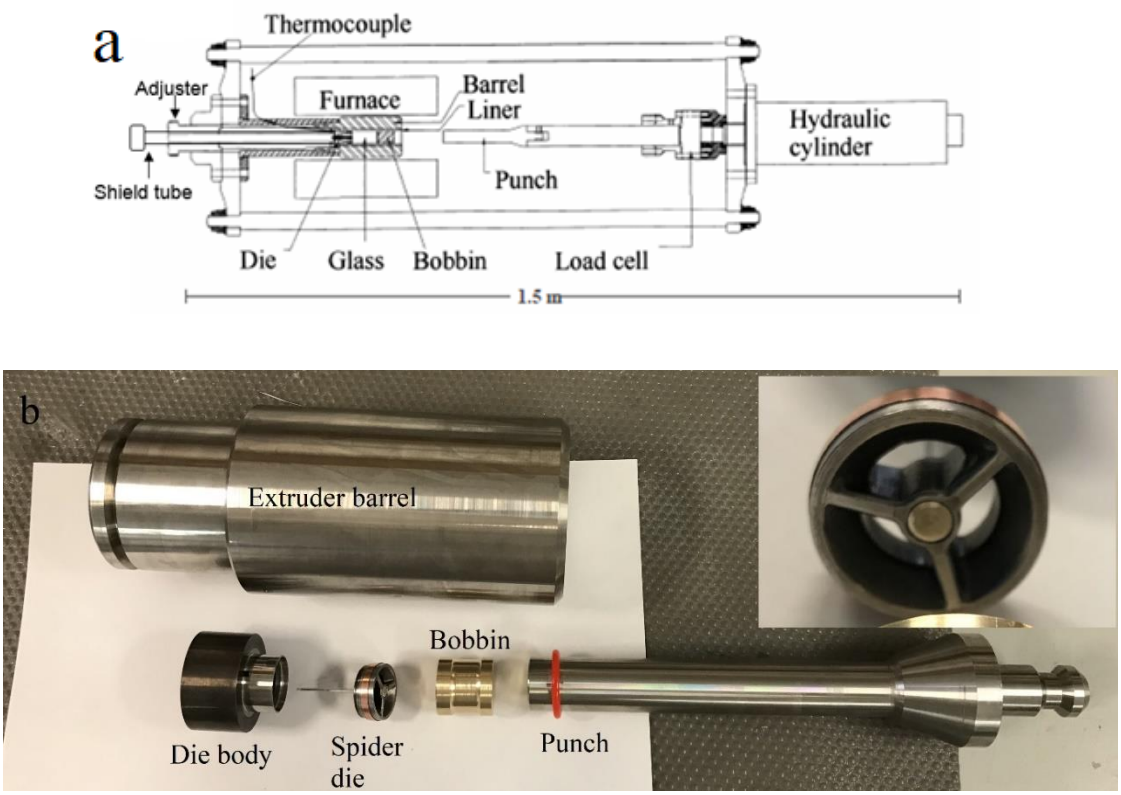


Figure 3.3 a) Schematic diagram of the extruder. Taken from [171]. *During operation, the extruder would be turned 90 ° with the hydraulic cylinder facing upwards. The spider die had 3 legs 120 ° from each other to facilitate an even tube formation. b) Extrusion components which were brought into the furnace. The three legs of the die can be seen in the inset. The glass boule would be placed between the die and bobbin.*

The glass boules' feed to be extruded were 26.5 mm diameter and between 30-40 mm in height. To aid an even extrusion across the die and even force distribution through the bobbin, the ends of the as-annealed boules were cut flat on a low-speed saw (Isomet saw, Buehler Ltd, LECO Instruments Ltd) fitted with a diamond saw blade. These ends were then cleaned of debris and oil with acetone followed by isopropanol (Table 3.2 for details). Optionally, the ends could be ground or polished to further improve surface contact, however, that was forgone for the extrusions carried out in this Project.

With the boule cut, the components (Figure 3.3b) were assembled in the extruder barrel and placed into the furnace. The furnace temperature, die temperature, bobbin position, and load, were monitored throughout the process with a data logger (TC-08, PicoTech). The system was purged with nitrogen gas (BOC) and

the furnace temperature was initially brought to around 70 °C above T_g. The load (starting with 100 kg, moving up to as high as 500 kg) was then applied (through the hydraulic piston pushing on the punch, which pushed on the bobbin) and monitored. Furnace temperature and load were occasionally readjusted until a suitable, stable extrusion rate (around 0.2 mm per minute) was achieved. Using Equation 3.3, assuming a boule with a diameter of 26.5 mm, being pressed at 500 kg (4903 N), a resulting pressure of 1887 kg/cm^2 is applied.

$$Pressure = \frac{Force}{Area} \qquad \text{Equation 3.3}$$

The chalcogenide supercooled melt would flow through the three feeds of the spider die and the streams would reconnect around the pin. This pin size therefore determined the ID of the tube. This reconnected stream would then flow down the graphite-lined interior of the die body (made in-house) which would guide the shape of the tube. The OD of the tube will be determined by the ID of the die body. For this Project, chalcogenide glass tubes were extruded with an OD of 10 mm and an ID of 1 mm, with lengths generally ranging between 100-200 mm. Upon completion, the extruded tube, die, and bobbin were lowered out of the hot zone of the furnace to allow for a basic annealing to take place.

Glass boules that were extruded in this project were assigned a code beginning with the letter "E" followed by an identification number and the initials of the maker. For example, E093RC ($Ge_{21}Sb_{10}Se_{69}$ at. %).

3.2.9 Fibre drawing

Unstructured chalcogenide fibre was drawn directly from as-annealed, rare-earth ion doped preforms (Figure 3.4 (c)). Depending on preform length, 10-20 m of fibre was drawn to allow for a fibre loss measurement (Section 3.3.6) and the remainder of the preform was drawn to a much thicker diameter (500 µm – 1000 µm) which was referred to as "cane".

A cane puller fitted to the fibre draw tower was used on these thicker diameters that couldn't be wound onto a drum. This cane can be seen in the centre of Figure 3.4 (a). This cane was inserted through the bore hole of an extruded jacket tube (Section 3.2.8) to form the rod-in-tube preform (Figure 3.4(b)) used to draw small core fibre.

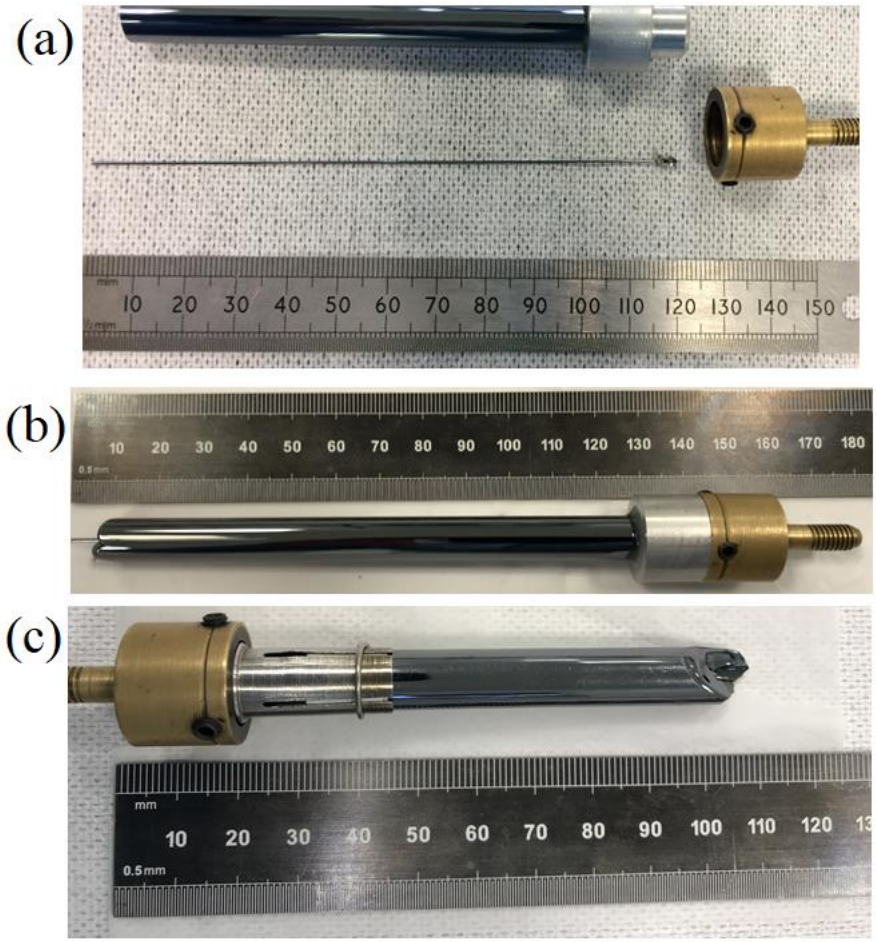


Figure 3.4 The two types of preform drawn in this Project. (a) The extruded jacket tube (top) and rare earth doped chalcogenide cane (bottom) before being assembled. (b) The jacket tube and cane assembled as a rod-in-tube preform. (c) As annealed preform to be drawn to unstructured fibre or cane.

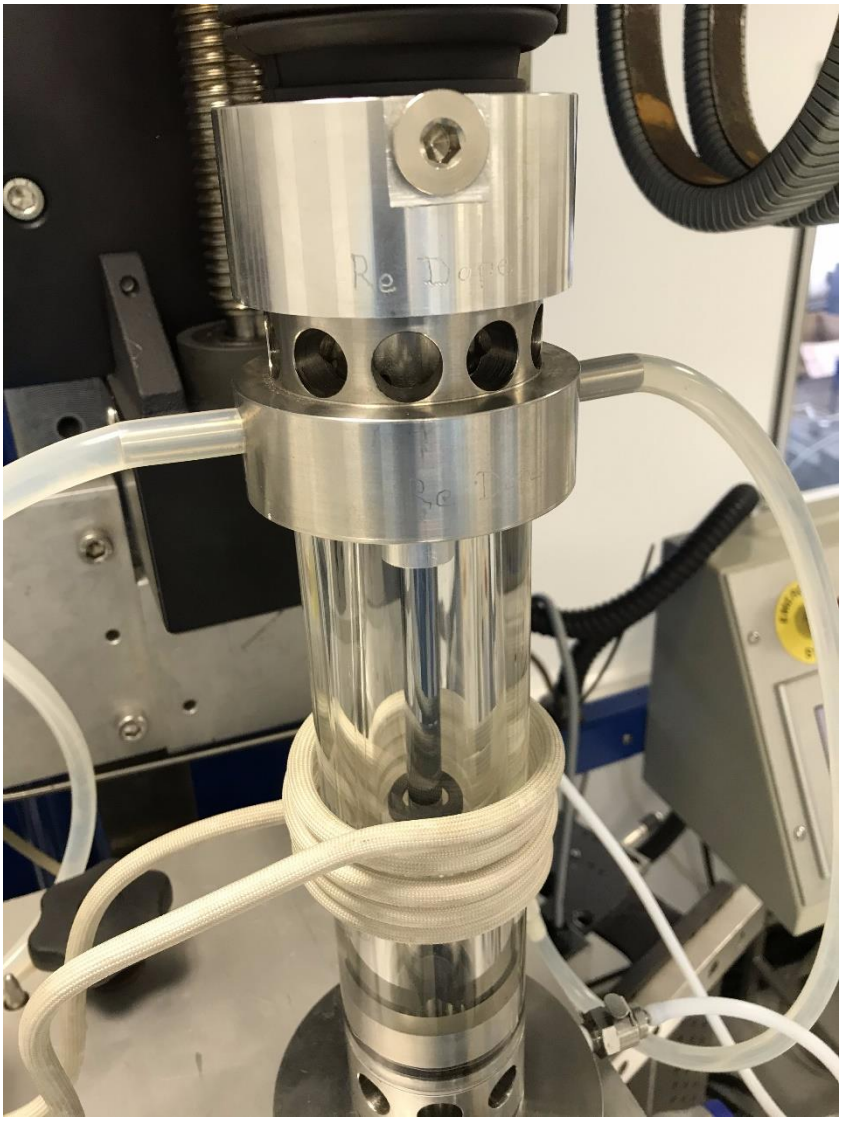


Figure 3.5 Rod-in-tube chalcogenide glass preform lowered into the graphite heating receptor, inside the double walled silica tube.

A modified Heathway tower located in a class 10,000 cleanroom was used to draw both types of preform. The chalcogenide preform holder was screwed vertically into an arm towards the top of the tower. This arm was then lowered into a double walled silica tube in which the cavity between the walls was flushed with water to provide cooling. The interior of the tube, containing the preform, was purged with freeze dried nitrogen gas. To begin the drawing process, a copper coil wrapped around the exterior of the silica tube was slowly fed increasing amounts of radiofrequency power. This radiofrequency was picked up by a graphite receptor (Figure 3.5) located in the interior of the tube. As power increased, the graphite receptor would increase in temperature and provide localised heating to the distal end of the preform. This heating method was difficult to characterise, as there was

no suitable procedure to measure the temperature of the heating element. During the fibre drawing, the input parameters on the radio frequency generator (Power and Demand) were used to quantify the working temperatures used. For example, a standard chalcogenide preform would begin to fibre draw at around 22 % Power, 32 % Demand.

A $Ge_{20}Sb_{10}Se_{70}$ at. % host glass was expected to reach fibre drawing viscosity at around 358 °C, so it was assumed that at these power and demand values, the temperature of the graphite receptor exceeded 358 °C. A small, sacrificial part of the preform (termed "gob" in the UK glass industry) would be lowered below the receptor and once the preform was heated to a viscosity above $10^{4.5}$ Pas, the gob would gently lower under gravity and begin the fibre drawing process. For rod-in-tube fibre drawing, a small vacuum would be applied to the preform. This aimed to encourage the collapse of the jacket tube over the rod core to improve the core/clad interface of the fibre.

The fibre was wound to a 1 m diameter drum (Expanded polystyrene (EPS), Columbus precision moulding). The speed at which the drum wound the fibre would affect the tension on the fibre, and its subsequent diameter. The speed of the drum rotation would be adjusted accordingly to achieve the target diameter, forming a control loop within the operation. Equation 3.4 was used to calculate the feed-out rotation rate needed to achieve a specific diameter with a fixed feed-in rate.

$$\left(\frac{Preform\ diameter}{Target\ fibre\ diameter}\right)^2 = x \qquad \text{Equation 3.4}$$

$$feed\ in\ (mm/min) * \left(\frac{x}{1000}\right) = feed\ out(m/min)$$

e.g. $$\left(\frac{9.898\ mm}{0.9\ mm}\right)^2 = 120.951$$

$$2 * 0.120 = 0.241\ (winder\ speed)$$

The above example would provide a 0.9 mm diameter cane from a preform with a diameter of 9.898 mm, using a 2 mm/min feed in speed. The division by 1000 to put the output to (m/min) was done to match the input parameter units on the winding mechanism controller.

Glass preforms melted in this project were assigned a code beginning with the letter "F" followed by an identification number and the initials of the maker. If a melt included a rare earth ion dopant, "RE" was included before the makers initials. For example, F104RERC (500 ppmw Dy^{3+}-doped $Ge_{19.4}Sb_{9.7}Se_{67.9}Ga_3$ at. %).

3.3 Chalcogenide glass and glass fibre characterisation

There are multiple avenues (thermal, optical, mechanical) to investigate once a new chalcogenide glass or chalcogenide glass fibre has been fabricated. This sub-section will cover the techniques which have been used to characterise rare earth doped glasses at this stage of the Project, which include: differential scanning calorimetry (Section 3.3.1), X-ray powder diffraction (Section 3.3.2), scanning electron microscopy (Section 3.3.3), energy dispersive x-ray spectroscopy (Section 3.3.4), ellipsometry (Section 3.3.5), optical fibre loss measurements (Section 3.3.6), and Fourier transform infrared spectroscopy (Section 3.3.7)

3.3.1 Differential scanning calorimetry

(i) Introduction

By measuring the difference in heat flow between a sample with a specified mass and a reference, Differential scanning calorimetry (DSC) demonstrates how a glasses heat capacity changes with temperature. Using this data, the glass transition temperature of the sample can be calculated by extrapolating the endothermic curve.

(ii) Sample preparation and equipment

The Perkin Elmer Pyris 1 DSC analyser maintains both sample and reference temperature across a programmed heating/cooling schedule and plots the energy input required. The analyser was calibrated with indium (M.P. 156.6 °C) and zinc

(M.P. 419.5 °C) to cover expected T_g ranges of chalcogenides. Baseline measurements using two empty pans were taken as the sample was prepared. The curved base of the chalcogenide rods, removed with a low-speed saw (Isomet saw, Buehler Ltd, LECO Instruments Ltd) fitted with a diamond saw blade, was crushed and ~20-30 mg was weighed and placed into a pan. Ensuring the sample was positioned to not pierce the upper lid, the two halves were cold welded with the chalcogenide inside. The samples were taken to approximately 50 °C above predicted T_g at 10 °C/ min before then being cooled back to 40 °C to standardise the effect of thermal history on the sample. This heating/cooling schedule was repeated three more times, for a total of four scans. This allowed an average of three extrapolated values to be found as T_g.

(iii) Data processing

The baseline measurement was automatically subtracted by the software (Pyris thermal analysis, Perkin Elmer). Data from the heating steps, displayed graphically as temperature vs endothermic heat flow, were isolated from the cooling and isothermal steps. Using an in-programme tool, the endothermic curve was extrapolated to determine the onset T_g of the sample for each of the heating steps and a mean average was calculated. The first scan was omitted due to the unknown thermal history of the sample.

3.3.2 X-ray powder diffraction (XRD)

(i) Introduction

X-rays are produced when a cathode tube produces high energy electrons which are beamed at a copper target. These X-rays are then passed through a monochromator, collimated, and shot onto the rotating sample stage. The diffracted X-rays are picked up by a detector which is also rotating. The rotation of both the sample and the detector allows a wide range of angles to be measured. The degree of the rotation of the detector is plotted vs the X-ray counts (or intensity) to determine the structure of the material. As the glass samples should be amorphous there should be no sharp peaks recorded on the XRD pattern as there are no crystals to diffract the incoming beam.

(ii) Sample preparation and equipment

Samples are prepared by grinding fibre or bulk sample into a fine powder with an agate pestle and mortar inside a fume hood. 30 – 50 ml of acetone or isopropanol (See Table 3.2) was added to the mortar to keep the sample cool and minimise any powder dispersion. The powder was gently tapped into the sample holder until it was densely packed. The sample powder was then gently pressed with a microscope slide to ensure flatness. A D8 advanced Da Vinci diffractometer was used in a Bragg-Brentano optical configuration with a Cu-Kα1 parallel beam. A 1D LynxEye XE-T detector was used to collect data. A coupled TwoTheta/Theta scan type in continuous PSD (position sensitive detector) fast scan mode with 2930 steps (one second dwell) between 10-70 ° 2Theta, in 0.02 ° increments was used with total scan times around one hour.

(iii) Data processing

Raw data was imported into DIFFRAC.EVA (Bruker) software. From here, background scattering was properly subtracted to aid in the identification of any peaks present. By using the search/match function, the peaks in the XRD data are compared to scans of 100,000 patterns present in the software's database. The search function can then be used accordingly to identify peaks based on positions and intensities. If the sample data shows the material to be amorphous, there is no need to run the search function.

3.3.3 Scanning electron microscopy (SEM)

(i) Introduction

SEM involves rastering high energy electrons across a sample to generate an electronic image. These high energy electrons are fired from an electron gun onto the sample which leads to the generation of secondary electrons (SE) as a product of ionisation and back scattered electrons (BSE) as gun electrons are reflected off the sample. A detector for SE produces an image providing information on the topography of the sample whereas a detector for BSE produces an image based on the atomic number of the constituent elements of the glass.

(ii) Sample preparation and equipment

Electrostatic charges can accumulate on the surface of the non-conductive chalcogenide glass leading to artefacts during imaging. To counter this, a rotary pumped carbon cord coater (Q150R ES, QuorumTech) was used to apply a 10 nm coating of carbon to the SEM samples. The microscope used to collect data shown in this report is a JEOL 6490LV fitted with a X-Max 80 Oxford Instruments EDX detector (Further details on EDX in Section on HRTEM). This is fitted with a tungsten wire filament as the electron source and can reach resolutions of 3 nm and magnifications up to 300,000. Two different methods of preparing glass fibres were used. To observe any surface defects on the fibres, small sections were cleaved and set on the aluminium sample holder with an adhesive carbon disc (leit tab). For investigations into the condition of the interior of the fibre, small lengths are cleaved and mounted vertically onto an aluminium block with double sided carbon tape. The fibres are then secured with a layer of aluminium tape, leaving only the cleaved ends exposed. This aluminium block is then adhered to the sample holder with a leit tab. Imaging this way can highlight defects such as holes using SE detectors. It can also be used to image core structures in core/clad structured fibre using BSE detectors. Photographs of both methods are shown in Figure 3.6.

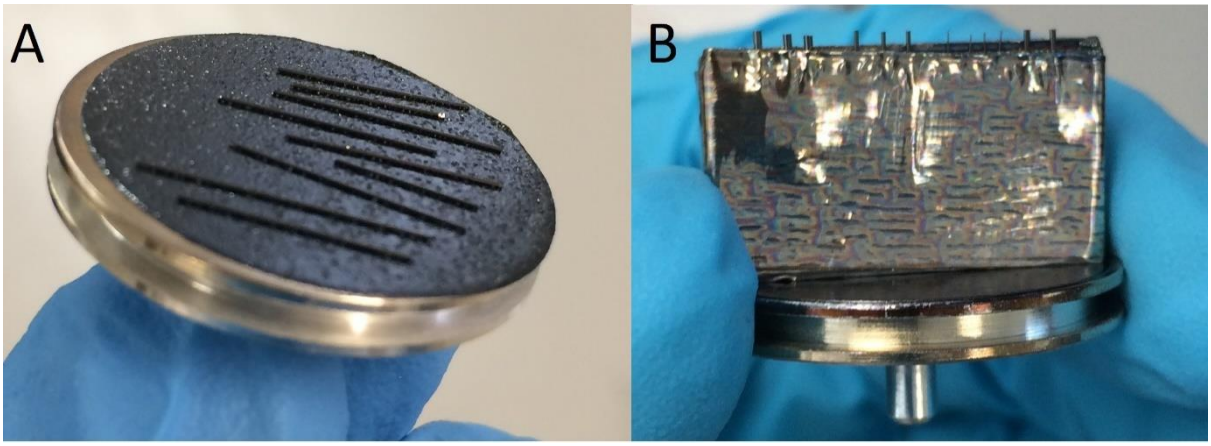


Figure 3.6 Chalcogenide fibres prepared for SEM. (A) shows the horizontally place fibre set up used to observe the surface the samples. (B) shows the vertically mounted samples for investigations into the internal structure of the fibres.

3.3.4 Energy dispersive X-ray spectroscopy (EDX)

(i) Introduction

EDX utilises the high energy electron sources used in SEM and TEM to create the X-rays allowing EDX to easily be conducted alongside one of these imaging techniques. Detection limits for EDX when conducted in a SEM are around 0.5 weight % meaning that rare earth dopants are unlikely to be observed. TEM resolution is better due to higher electron energies used and has detection limits which are around 0.1 weight %.

(ii) Sample preparation and equipment

As EDX is carried out in a SEM or TEM, the sample preparation is identical to that explained above (section 3.2.3). The X-Max 80 (Oxford instruments) fitted inside the JEOL 6490LV was used to detect X-rays.

(iii) Data processing

There were three common methods of collecting data. Point EDX focused on collecting data from a small, specific point (roughly 5 μm) and area EDX collected data from a specified, drawn region on the sample. EDX mapping was used for cross sections of step index fibres with < 2 at. % sulfur as these could not be imaged conventionally with BSE detectors. This allowed us to still get an idea of the geometry of the core. All data was collected through the programme INCA (Oxford instruments). This software used a numerical scale from 1-6 to indicate process times for the returned X-ray emissions from the sample. Larger numbers indicated longer processing times, and thus, higher accuracy of element identification. However, increasing these process times would also lead to longer "dead times" in which no data is being collected. An upper limit of 50 % dead time was generally used for the processing times used. If this limit was exceeded, the processing time was lowered. Values of 4-6 were used for Point EDX and 1-3 was used for elemental mapping. The elements to be detected by the software could be fixed by the operator or the software could be allowed to automatically identify the constituent elements based on the X-ray emission lines. INCA outputs a numerical value of the atomic percentages (at. %) of each element based on the intensity of the returned x-rays. Although these percentage values were generally accurate (within +/- 2 at. %), the overlapping of emission lines of Ge, As, Sb, Se, and Ga

makes it difficult to get a true measurement as there is potential for signal to be misinterpreted by the detector (see Figure 3.7). The graph of X-ray emission lines could be used as a qualitative identification of the elements present.

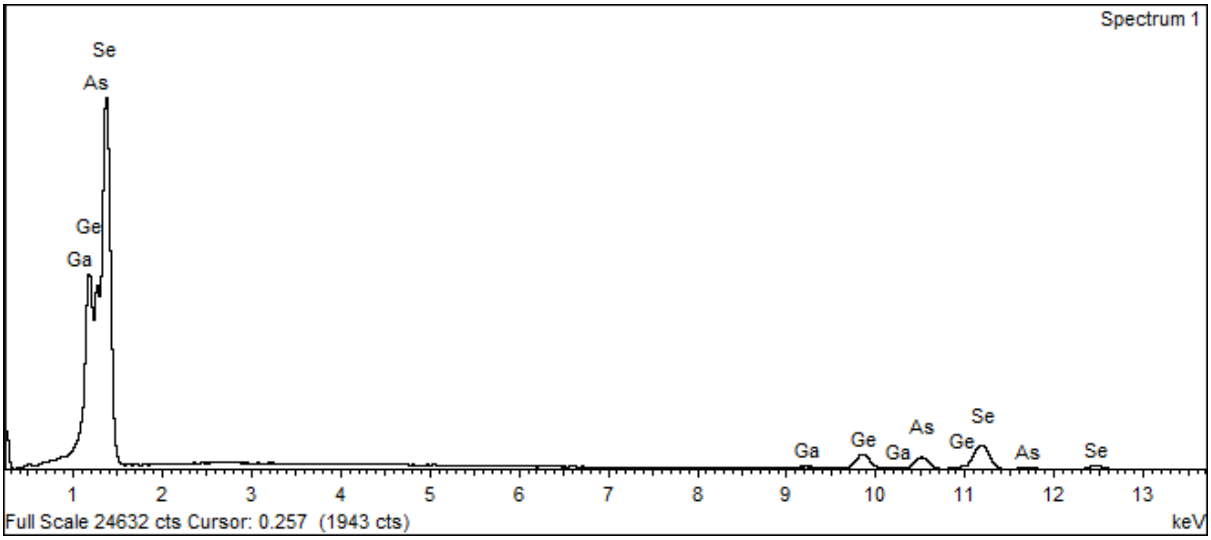


Figure 3.7 Spectrum showing the detected X-ray emissions from a GeAsSeGa glass fibre. Note the overlaps between 1 – 2 keV which can obscure proper element classification.

3.3.5 Ellipsometry

(i) Introduction

Ellipsometry is a non-destructive technique which measures changes in polarized light that have been reflected off a sample surface over a set wavelength range. These changes in polarization state are described in values of Psi (Ψ) and Delta (Δ). Ellipsometry cannot be used to directly measure refractive index of a material (its target use in this project). However, as the ratio of these values are related to the physical properties of the sample material, it is possible to calculate properties such as optical constants, film thickness, or doping concentration from these measured values. The optical constants of interest in the project were refractive index (n) across 2 – 20 µm. Using the reflectance data and known parameters, a model is created to describe the Psi and Delta values (See Section 5.2). The model can then be used to determine values such as n or extinction coefficient k across the wavelength range examined.

(ii) Sample preparation and equipment

3mm thick discs were cut from as-annealed 10 mm diameter chalcogenide rods on a low-speed saw (Isomet saw, Buehler Ltd, LECO Instruments Ltd) fitted with a diamond saw blade. A small amount of wax was melted onto the sample holder and the sample was placed into the wax. As the wax solidified, it provided suitable adherence to the sample holder for polishing. The sample holder was then assembled into the polishing jig (made in-house, University of Nottingham). These discs were ground with 1000 grit silicon carbide powder (Buehler) lubricated with polishing oil (Buehler). Discs were then polished to a 1 μm finish with diamond paste (Buehler). Samples were washed with acetone.

Hot pressing was performed between two aluminium plates fitted with induction heating coils. The top plate, affixed on a frame, remained static throughout the process. The base plate was connected to a pneumatic piston, facilitating vertical movement. Both plates housed a thermocouple which provided feedback to the PID temperature controller (Eurotherm 2408). Two tungsten carbide discs (800 mm diameter, flatness 0.08 μm, surface finish 0.009 μm) placed on the aluminium heating plates provided the interface in which the sample would be "sandwiched" between. Secondary thermocouples were fixed to the tungsten carbide surface with Kapton tape for a more accurate measurement of the temperatures the chalcogenide was subject to. A bell jar fitted over the frame and a vacuum intake below the base plate formed a chamber which was then evacuated with a rotary pump to (10^{-3} Pa). The aluminium plates were then heated to get the glass sample between 10-25 °C above T_g, at which point, the base plate was raised so the top tungsten carbide disc was in contact with the top aluminium plate. A load controller and transducer were then used to monitor and increase pressure between the plates allowing the softened glass to deform under load. A readout displaying the distance the base plate had traversed was monitored until the desired sample thickness was reached (1-1.5 mm).

An IR-VASE ellipsometer (Infrared – Variable Angle Spectroscopic Ellipsometry, Woollam, U.S.A) capable of covering a range from 1.5-40 μm was used for all ellipsometry work presented. The ellipsometer is housed at the iSMART facility at Nottingham Trent University, with experiments designed with the guidance of Dr

Nikolaos Kalfagiannis. An ultra-flat, hot-pressed sample would first undergo a transmittance measurement to aid in the modelling of the refractive index. For transmittance measurements, two cycles consisting of 10 scans at 8 cm^{-1} resolution were collected to obtain an averaged transmittance spectrum. One side of the 1 µm polished, hot-pressed sample was then roughened with the use of a Dremel tool fitted with a diamond point wheel bit (unspecified diamond particle size and finish quality). The reflectance ellipsometric measurements were then taken over a range of angles. For all glasses here subject to ellipsometry, 55 °, 65 °, and 75 ° angles were used, each angle was scanned for three cycles consisting of 20 scans each to allow for an averaging of the spectra. Measurements were collected at a resolution of 4 cm^{-1}. Background measurements were taken and subtracted from the results.

(iii) Data processing

Data is collected in the VASE software (Woollam) and is then exported to completeEASE (Woollam). A general oscillator layer (GenOsc®) was used as the basis for each model developed in this work. This allowed the inclusion of multiple oscillators (such as Sellmeier and Gaussian) to be additively placed into a single layer. These oscillators and their parameters (e.g. centre energy, broadening, amplitude) were iteratively changed manually until a reasonable fit between measured data and modelled were achieved. The programme then used a Levenberg Marquardt multivariate regression analysis to optimise these parameters to give a best fit. Chapter 5.3.4 details the models used in this work and how they were developed.

3.3.6 Optical fibre loss measurement of chalcogenide fibre

(i) Introduction

Fibre loss measurements were conducted as soon as possible after the fibre drawing process. A preliminary test using a 0.5 – 1 m length of fibre was conducted to give an initial insight into the quality of the fibre being tested. This measured intensity was then used to approximate the maximum length of fibre that could be used for the test proper, while still being detectable by the liquid nitrogen cooled InSb and MCT (mercury-cadmium-telluride) detectors (generally 3-4 m for undistilled, doped glass. 10 m for undoped, undistilled. 20 + m for undoped distilled). A

longer fibre sample was targeted as this provided a more accurate measurement, predominantly reflecting the quality of the glass system, cleave quality, and fibre geometry[134]. It was preferable to overestimate the starting fibre lengths, as cutbacks could be performed until signal is detected. This shorter fibre also facilitated an easy alignment procedure due to the high intensity of the transmitted light.

To measure loss through a section of fibre, a 'group-cleave' cut-back method was used [134]. This method involves making 2 groups (of 3+ cleaves) of fibre cleaves. The first group was cleaved, and measurements are taken from each cleave. A long section of fibre was then removed, and the second group of fibre cleaves are made. The input 'launch' cleave remained static throughout the process. This method allows the optical losses of a fibre to be recorded in a more reliable fashion as the effect of the fibre cleave on the loss measurement can be minimised.

The loss measurement was used as a metric of fibre quality. Lower optical losses (in dB/m) at expected impurity absorption wavelengths indicated lower levels of that specific impurity. Therefore, it could be used to validate the efficacy of host glass distillation work or novel purification methods. Low baseline losses indicate a high purity, stable, glass composition, free from devitrification and other scattering losses. High baseline losses could also be used as preliminary indicators of fibres that had partially devitrified or were otherwise improperly fabricated and could be investigated further.

(ii) Sample preparation and equipment

An FTIR spectrometer (Bruker IFS 66/S), Globar source, Mercury-Cadmium-Telluride (MCT) (Kolmar Technologies, V100-1B-7/190) detector, and an Indium-Antimonide (InSb) detector (InfraRed Associates, Inc. ID413), both liquid nitrogen cooled, covering wavelength ranges 2-11 µm, and 0.9 – 5,4 µm, respectively, were used for mid-IR fibre loss studies. For near-IR fibre loss measurements, a tungsten light source (Bruker), CaF_2 broadband beam splitter (Bruker), InGaAs (Indium Gallium Arsenide) detector (Bruker) (0.9 – 1.7 µm), and InSb detector (InfraRed Associates) were used.

A programmable fibre cleaver (LDC401, Vytran, U.S.A.) was used for the initial cleaves and a ruby tipped scribe (S90R, ThorLabs) was used to manually cleave

shorter samples the cleaver could not accommodate. The predominantly changed parameter in the fibre cleaver programme was applied fibre tension. Depending on composition, fibre quality (brittleness), and fibre diameter, applied tension was iteratively adjusted to achieve a cleave with a large mirror finish surface area. If a fibre face were damaged (fractured, angled), the fibre would be re-cleaved. A manual cleave was performed by gently scoring a fibre piece ~5-10 mm from the fibre tip. This tip was then pulled away by hand while maintaining as little lateral movement as possible, mimicking the action of the programmable cleaver. Cleave quality was judged *via* light microscopy.

The globar light source was directed out of the FTIR and into the "launch" fibre face with 2 off-axis parabolic mirrors. The test end of the fibre was placed in the fibre holder (already aligned during the preliminary test) which directed the transmitted light to one of the two detectors. Measurements were taken with a resolution of 8 cm^{-1} with scan times of 10-20 minutes. Scan times would be consistent across an entire fibre loss measurement. A scan would be carried out with each detector before the next cleave was made. As the fibre was cleaved back, the cleaved pieces were measured, and length was recorded as these values were needed to calculate the distance between the two cleaves.

(iii) Data processing

The best quality cleave from each group was determined by calculating the loss between each cleave, with the highest quality cleaves then used to calculate the final optical loss spectrum using equation 3.5.

$$Loss\ (dB/m) = -\left(\frac{10}{L}\right) Log_{10}\left(\frac{P_{out}}{P_{in}}\right) \quad \text{Equation 3.5}$$

L is the length between fibre cleaves, P_{out} is the intensity readout from a group 1 cleave, P_{in} is the intensity measurement from a group 2 cleave.

To create a single optical loss spectrum, the single best cleaves for both groups were calculated and used to plot the graph. This was calculated by calculating the fibre loss between all group 1 cleaves versus one fixed cleave in group 2. The lowest optical loss cleave was then designated as the cleave to be included in the spectrum. Fibre loss was then calculated with this best group 1 cleave versus all the group 2 cleaves. In this instance, the best quality cleave in group 2 would be shown

to have a higher output power and so would appear to demonstrate the highest losses.

3.3.7 Fourier transform infrared spectroscopy (FtIR) of bulk glass

(i) Introduction

FtIR spectroscopy was used to assess the transparency of glasses over a wavelength range from 1-12 μm allowing an identification of rare earth electronic absorption or impurity vibrational absorption bands. This was primarily carried out on novel compositions, such as $Ge_{19.4}Sb_{9.7}Se_{67.9}Ga_3$ at. %, to get data on the transmission window (section 4.1) or on compositions doped with rare earth elements previously untested by the Nottingham Mid-IR photonics group (section 4.2).

(ii) Sample preparation and equipment

Chalcogenide discs were prepared with a 1 μm finish on each side (as described in section 3.3.5) and placed in an FtIR spectrometer (Bruker IFS 66/S) housing a DTGS (deuterated triglycine sulfate, 0.8 – 27 μm, Bruker) detector for mid-IR measurements or InGaAs (0.9-1.7 μm, Bruker) for near-IR. For near-IR measurements, a tungsten light source was employed with a broadband beam splitter; for mid-IR, globar and KBr beam splitter (As seen with fibre loss measurements). The FTIR was vented with a dry air supply (Parker Filtration, FT-It purge gas generator, 75-52-12VDC) for 15-20 minutes preceding measurement to avoid the interference of CO_2 and H_2O. An initial baseline measurement with no sample present was taken before the sample run. The OPUS software (Bruker) would subtract this baseline from the measured data. The sample holders were aluminium plates each with various sized apertures in the centre. For this work, an aperture of 5 mm was used for each sample. The sample was placed on the holder, covering the aperture, allowing the probe light to pass through the sample and onto the detector. A Fourier transform was carried out by OPUS and the resulting data was exported.

(iii) Data analysis

The absorption data output by the FtIR was divided by the thickness of the disc sample, the optical pathlength (in mm), to give absorption coefficient (cm^{-1}), and plotted.

4. Development of a novel antimony-based chalcogenide glass host composition with Sm^{3+} and Dy^{3+} doping

With the identification of antimony-based chalcogenide fibres as providing potentially lower phonon energy host glass systems when compared to arsenic-based chalcogenide fibres, initial work set out to replicate published antimony-based compositions ($Ge_{20}Sb_{10}Se_{65}Ga_5$ at. %). Complications encountered during the fibre drawing process of these published compositions led to the development of a novel composition ($Ge_{19.4}Sb_{9.7}Se_{67.9}Ga_3$ at. %) which was more suitable to the fibre drawing set up used by the Mid-Infrared Photonics Group, University of Nottingham, UK. This fibre type was successfully doped individually with Sm^{3+} and Dy^{3+}. Section 4.1 details the issues encountered with the $Ge_{20}Sb_{10}Se_{65}Ga_5$ at. % composition (M226RERC) and the development of the $Ge_{19.4}Sb_{9.7}Se_{67.9}Ga_3$ at. % composition (M235RERC). Section 4.2 covers the optical characterisation (FtIR bulk glass absorption, fibre loss, and photoluminescence) of 1000 ppmw Sm^{3+} doped $Ge_{19.4}Sb_{9.7}Se_{67.9}Ga_3$ at. % bulk glass (M227RERC) and fibre (F099RERC). Section 4.3 covers the fabrication and characterisation of Dy^{3+} doped $Ge_{19.4}Sb_{9.7}Se_{67.9}Ga_3$ at. % bulk glass (M236RERC, M240RERC) and fibres (F102RERC, F104RERC). Finally, Section 4.4 summarises the findings in this chapter.

4.1 Development of a novel antimony-based host glass composition

4.1.1 Introduction to previous work

Previous work of the Mid-Infrared Photonics Group at Nottingham regarding rare earth ion doped chalcogenides had only focused on the development of arsenic-based glasses. Substituting arsenic (relative atomic mass: 74.92) with a heavier network forming analogue, antimony (relative atomic mass: 121.76), would theoretically lower the total phonon energy of the host glass system. This would increase the probability of radiative transitions of rare earth ions from excited states, potentially facilitating emissions at longer wavelengths than those seen in arsenic-based glasses. Evidence for this is seen in Tb^{3+} doped glasses in which a 3.1 µm emission was observed by Starecki *et al.* [90] in an antimony-based host glass,

Starecki *et al.* [90] then proposed this transition was non-radiatively depopulated in an arsenic-based host glass [23]. The longest wavelength photoluminescence observed in a rare earth doped arsenic-based fibre is a Pr^{3+} emission which extends out to 6 µm[86,94]. Antimony based glasses have reported emissions out to 8 µm in both Tb^{3+} and Sm^{3+} doped samples [19,90,113]. Antimony based chalcogenide fibres have also shown minimal cytotoxicity during extensive contact with cell culture[27]. With an aim to achieve mid-IR fibre lasing at 6.1 or 6.45 µm for surgical use [8,26], it is concluded that antimony-based fibres are indeed a prime candidate for producing a bioinert delivery system of surgically relevant wavelengths.

As mentioned in Section 2.3, Table 2.1, an antimony-based chalcogenide glass developed by the Laboratoire Verres et Céramiques group in Renne, $Ge_{20}Sb_{10}Se_{65}Ga_5$ at. %, was successfully doped with a range of rare earth ions (Dy^{3+} [25] , Tb^{3+} [89,90] , Sm^{3+} [113] and Pr^{3+} [92]) and could be drawn to low loss fibre. 1000 ppmw Dy^{3+} doped glasses of this composition measured lowest losses <1 dB/m between 6-7 µm [25] with the same group also producing a 1000 ppmw Tb^{3+} doped $Ge_{20}Sb_{10}Se_{65}Ga_5$ at. % fibre demonstrating baseline losses of around 2.5 dB/m [90].

Although difficult to draw direct comparisons between As and Sb glasses due to the differences in the overall host glass composition, there are notable disparities in documented photoluminescent lifetimes of rare earth ions doped into the glasses. A low loss 700 ppmw Sm^{3+} doped $Ga_{2.2}Ge_{26.5}As_{14.6}Se_{56.7}$ (0.5 dB/m at 5.7 µm) fibre measured the photoluminescence lifetime of the $^6H_{13/2} \rightarrow {}^6H_{9/2}$ transition at 60 µs[115]. Despite this being the lowest oxygen (<0.1 ppmw As-O, <0.1 ppmw Ge-O, 1 ppmw Si-O) and hydrogen (<0.005 ppmw Se-H) impurity containing rare earth ion doped chalcogenide glass made to date, this 60 µs lifetime is substantially shorter than that measured for the same Sm^{3+} $^6H_{13/2} \rightarrow {}^6H_{9/2}$ transition in an antimony-based host glass with lower purity. Thus, a 1000 ppmw Sm^{3+} doped $Ge_{19.4}Sb_{9.7}Se_{67.9}Ga_3$ at. % fibre (lowest loss 2.15 dB/m at 6.04 µm) exhibited a lifetime of 101 µs for the same $^6H_{13/2} \rightarrow {}^6H_{9/2}$ transition[19]. One potential explanation for the discrepancy is the composition of the arsenic-based fibre. It was claimed by Shiryaev *et al.*[115] that the arsenic-based composition was used for its high resistance to crystallisation and was evidenced by X-ray diffraction (XRD) analysis of the glass [172,173]. However, this XRD analysis was performed on undoped fibres of this composition. It is well documented that the introduction of rare earth elements into a chalcogenide host

increases probability of devitrification [50–52,55,133]. It therefore cannot be ruled out that the drastically shorter lifetime in the arsenic-based host glass was due to the formation of a crystalline inclusion formed from devitrification of the 700 ppmw Sm^{3+} doped $Ga_{2.2}Ge_{26.5}As_{14.6}Se_{56.7}$ fibre. Crystallites containing the RE ions would have meant that the RE-ions had precipitated out of the glass and would have been likely to reside in close proximity to one another. The short ion-to-ion distance could enable reabsorption of the PL emission and shortening of the lifetime; moreover, any rare earth ion crystallites that had been oxidised would have presented with high local phonon energy and hence again the RE-ion PL lifetime measured would have been shortened.

Conversely, a 500 ppmw Dy^{3+} doped $Ge_{15}As_{21}Se_{63}Ga_1$ fibre (F125RERC) measured a photoluminescent lifetime of 5.21 ms for the $^6H_{13/2} \rightarrow {}^6H_{15/2}$ radiative emission and a lifetime of 1.75 ms for the $^6H_{11/2} \rightarrow {}^6H_{13/2}$ transition (as reported in Section 6.4.3.3 of this work). These were slightly longer than lifetimes observed in a 1000 ppmw Dy^{3+} $Ge_{20}Sb_{10}Se_{65}Ga_5$ at. % host which measured in at 3.3 ms, and 1.46 ms, respectively[25]. It is also to be noted that this photoluminescence measurement was conducted in bulk Dy^{3+} doped $Ge_{20}Sb_{10}Se_{65}Ga_5$ at. % samples and it is known from Zhuoqi *et al.*[110] that Pr^{3+} doped GeAsGaSe small core fibre that fibre PL lifetimes are usually shorter that those of the bulk chalcogenide glass because the extra thermal processing of the glass matrix means that some of the RE-ion sites are no longer ideal. The resulting 1000 ppmw Dy^{3+} $Ge_{20}Sb_{10}Se_{65}Ga_5$ at. % antimony-based fibre demonstrated remarkably low losses (appearing to be <1 dB/m between 6-7 µm) which would have been expected to further increase the measured lifetimes[25]. Despite shorter lifetimes for both Dy^{3+}: $^6H_{13/2} \rightarrow {}^6H_{15/2}$ and Dy^{3+}: $^6H_{11/2} \rightarrow {}^6H_{13/2}$ in the antimony $Ge_{20}Sb_{10}Se_{65}Ga_5$ host, fibre samples of this composition from Starecki *et al.* [25] were used to measure the first recorded instance of 7.2 µm emissions from Dy^{3+} in chalcogenide glass fibres [25]. A radiative transition emitting a wavelength not yet measured from arsenic-based chalcogenide fibres. In both cases, it can importantly be concluded that these results are indicative that the total phonon energy of the chalcogenide host glass system, and hence PL lifetimes of doped rare earth ions, are more dependent on the entire chalcogenide host glass composition, and its tolerance to rare earth ion doping and resistance to

devitrification, as opposed to simply depending on varying a single network former such as switching As for Sb.

4.1.2 Initial work

The initial attempt to create a rare earth ion doped antimony-based, unstructured fibre during this Project involved replicating the chalcogenide glass composition ($Ge_{20}Sb_{10}Se_{65}Ga_5$ at. %) published by Laboratoire Verres et Céramiques group, Renne[25,90,113], and doping the glass with nominally 1000 ppmw samarium foil (see Table 3.1 for chemical form and purity). It should be noted that all chalcogenide compositions stated here, in Chapter 4, are nominal, as-batched compositions as it is known that small losses due to volatile constituents that leave the main melt and condense on the upper side of the melt containment will slightly affect the final chalcogenide composition. The precursors Sb and Se were purified (see section 3.2.2 for procedures), the glass was not distilled. 30 g total batch was weighed into a 10 mm/14 mm ID/OD (internal diameter/outside diameter) purified silica glass ampoule (see Section 3.2.1 for purification procedure) to make an unstructured, rod fibre optic preform of total length (including contraction cone) of *ca.* 90 mm. The heating schedule used to melt and anneal the glass rod preform is detailed in Table 3.6 (ii). The product appeared to the naked eye to be glassy and was annealed at 272 °C, *i.e.*, at the T_g stated in the literature for the composition [90]. The preform was given the melting code M226RERC.

An ~ 8 mg sample of the annealed glass product (M226RERC), taken from the opposite end relative to the contraction cone, was analysed by means of DSC (Differential Scanning Calorimetry, see Section 3.3.1 for methodology) and displayed a mean T_g of 282 ± °C.

The remainder of the as-annealed rod preform was then prepared for fibre drawing (see Section 3.2.9 for method). The fibre drawing temperature was unknown but previous work on similar compositions suggested a suitable fibre drawing viscosity ($10^{4.5}$ Pa·s) was around T_g + ~150°C [54]. Therefore, power to the graphite heating receptor was gradually increased and adjustments were made based on observed phenomena of the preform.

As standard fibre drawing temperatures was approached, a thin surface "skin" was observed on the heated preform (see Figure 4.1(a)). This skin tore as the initial gob at the start of the fibre-drawing process dropped but was observed to persist around the whole preform surface and along the preform length as soon as it was fed into the hot zone of the fibre drawing furnace – that is, into the graphite radio frequency receptor held inside the silica encasement (see Figure 3.5, Section 3.2.9 for the setup).

The resulting fibre was of exceedingly poor quality and of variable diameter. A target diameter of 230 µm was attempted but fluctuated +/- 30 µm with portions of the "foil like skin" causing larger, transient increases in fibre diameter up to around 400 µm (Figure 4.1b). Poor surface quality was observed along the length of the fibre drawn with portions of the skin of various sizes being present along the fibre surface conferring a "lumpy" look (Figure 4.1(1)). The ultimate fibre obtained would tend to fracture by shattering with any minor manipulation. The fibre drawing was then stopped and the preform was removed from the fibre tower. Around 2-3 m of this fibre was drawn from the 80 mm length preform, leaving the remaining preform with a length of 70 mm.

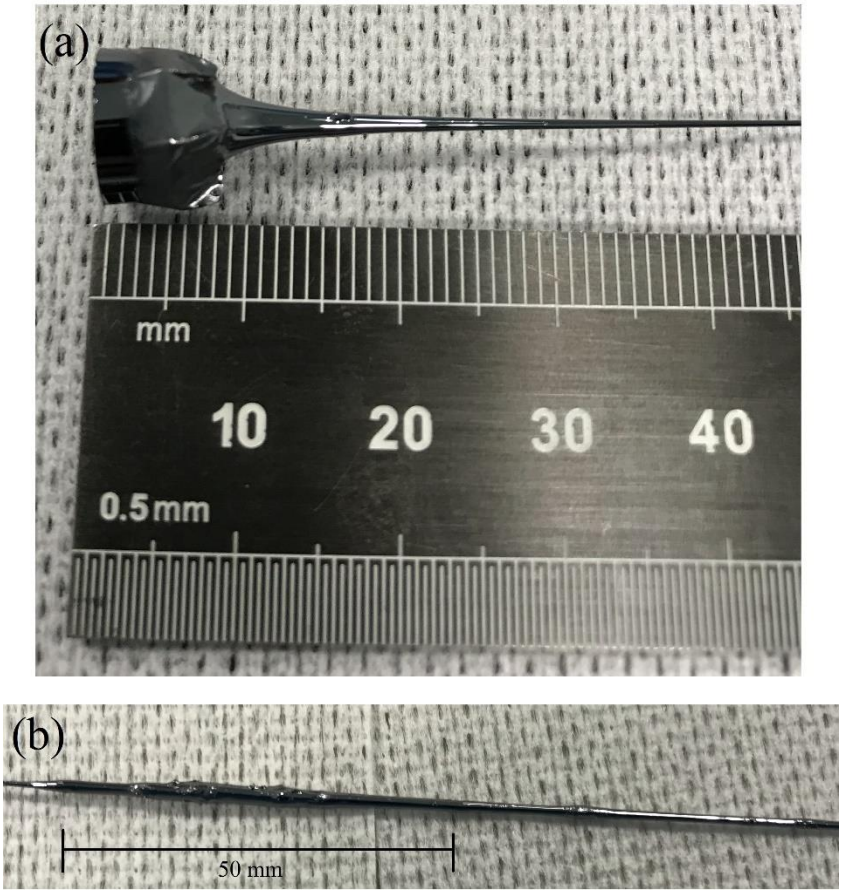


Figure 4.1 (a) The 1000 ppmw Sm^{3+} $Ge_{20}Sb_{10}Se_{65}Ga_5$ at. % preform gob (M226RERC) with "foil like" skin after being taken to fibre drawing temperature. (b) Misshaped 1000 ppmw Sm^{3+} $Ge_{20}Sb_{10}Se_{65}Ga_5$ at. % fibre that was removed from the tower during the fibre drawing process.

The remainder of the undrawn 1000 ppmw Sm^{3+} $Ge_{20}Sb_{10}Se_{65}Ga_5$ at. % preform that was removed from the fibre tower was immersed in room temperature propylamine for 135 hours and then washed thoroughly with acetone and then isopropanol (Table 3.1 for sources and purities) and dried under vacuum at around 0.5-1 mbar in a glovebox antechamber for 90 minutes. A visual inspection confirmed no liquids on the preform surface. As the tip of the preform had been subject to heating during the initial fibre drawing, this process aimed to etch away the surface layer of the preform, potentially removing the interfering surface skin at the preform tip, and the remaining length of the rod. Fibre drawing was attempted a second time, but the skin re-formed at roughly the same temperature. A similar, poor-quality fibre was also produced this second time, so it was decided to stop the fibre drawing process.

Previous work published by Dr Harriet Parnell (formerly Mid-IR Photonics Group, University of Nottingham, UK) documented a similar occurrence of this surface layer forming during the fibre drawing of a preform with a composition of $Ge_{25}Sb_{10}Se_{65}$ atomic % (at. %)[54]. X-ray Diffraction (XRD) analysis of this preform identified that monoclinic germanium diselenide: $GeSe_2$ was present in the foil-like skin which had formed on the fibre drawn sample but was absent in the as-annealed samples. It has been shown that high temperature monoclinic $GeSe_2$ can readily form from [$GeSe_4$], an integral tetrahedral, network-forming unit to these chalcogenide glass matrices [174–176]. This foil-like skin was not observed by Parnell *et al.* [54] on a preform composed of $Ge_{20}Sb_{10}Se_{70}$ at. % and it was proposed that an excess of germanium in ratio to the other elements (as in $Ge_{25}Sb_{10}Se_{65}$ at. %) conferred a poor resistance to devitrification. Gallium provides a similar, tetrahedral, coordination as germanium in these glass systems, is a metalloid like germanium from the 'p' block of the Periodic Table and has a similar mass and similar selenium bond length[91,92]. From this it can be predicted that a composition of $Ge_{20}Sb_{10}Se_{65}Ga_5$ at. % has [Ge+Ga] = 25 at. %, and so is structured similarly to the crystallised $Ge_{25}Sb_{10}Se_{65}$ at. % and would hence be considered to tend to crystallise in a similar fashion during fibre drawing.

It is possible that the lack of success with the replication of this fibre composition: $Ge_{20}Sb_{10}Se_{65}Ga_5$ at. %, is partially related to the purity of the host glass, which then may resultingly be contributing to devitrification. Articles published by the Rennes, France, group consistently reference back to a documented process involving distillation of chalcogenides with aluminium [177]. Aluminium would be introduced to getter oxide impurities present in the chalcogenide melt [177]. The chalcogenide was then distilled away from this solid aluminium oxide impurity product, further improving the purity of the melt. The replicative study described above which was conducted at Nottingham to make $Ge_{20}Sb_{10}Se_{65}Ga_5$ at. % fibre did not employ any distillation or gettering of the chalcogenides. Precursor materials were heat treated as described in Section 3.2.2 and melted to preform.

Despite the extensive purification steps conducted by the Rennes, France, group, their (generally under-reported) fibre losses remain relatively high. Their reported 500 ppmw Sm^{3+} doped $Ge_{20}Sb_{10}Se_{65}Ga_5$ at. % fibre was quoted to have "relatively high losses" with no publication of a loss spectrum but purported losses of 7-18

dB/m between 7-8 µm[113]. The same distilled composition of $Ge_{20}Sb_{10}Se_{65}Ga_5$ at. % doped with 500 ppmw Tb^{3+} was reported by the Renne group to have baseline losses of 2.5 dB/m between 6-8 µm [90]. This value of 2.5 dB/m is higher than the fibre loss measured from an alternative antimony-based composition ($Ge_{19.4}Sb_{9.7}Se_{67.9}Ga_3$, lowest loss of 2.15 dB/m at 6.04 µm) which was not subject to gettering or distillation and had double the dopant concentration (1000 ppmw) as reported by Crane *et al.* [19] .

The high fibre losses reported by Starecki *et al.* in 500 ppmw Tb^{3+} (2.5 dB/m at 6-8 µm) [90] and 500 ppmw Sm^{3+} (7-18 dB/m between 7-8 µm) [113] doped $Ge_{20}Sb_{10}Se_{65}Ga_5$ at. % may therefore be the product of devitrification of the fibre due to its high Ge + Ga content (25 at. %) as well as the remaining presence of oxide and hydride impurities. As the Rennes, France, group only reports on short lengths of fibre (from 100-170 mm [25,90,113]) being used for photoluminescence measurements, and make no mention of the lengths used for their fibre attenuation spectra, the current Author surmises that this group may not necessarily be producing longer lengths of stable fibre during fibre drawing, whereas the Mid-Infrared Photonics Group routinely produce 10s metres when fibre-drawing their most stable glass compositions. In this instance, the poor fibre drawing capabilities of $Ge_{20}Sb_{10}Se_{65}Ga_5$ at. % are not critical if suitable short lengths are drawn. It is to note, the Rennes, France, group appear to employ a similar fibre drawing method to that used by the Mid-Infrared Photonics group, University of Nottingham, UK with the added step of first polishing the preform[177].

More recent publications from the Rennes group (2020) have reported distillation following gettering with magnesium (Mg) and tellurium chloride ($TeCl_4$), active as oxygen, and hydrogen getters, respectively[25]. The resulting 1000 ppmw Dy^{3+} $Ge_{20}Sb_{10}Se_{65}Ga_5$ at. % fibre appears to have substantially lower fibre losses then previously reported by the Rennes group with <1 dB/m between 7-8 µm and a reported loss of 1.2 dB/m at 7.2 µm [25]. It can be speculated that the hydrogen gettering with $TeCl_4$ and oxygen gettering with Mg provided a higher purity chalcogenide glass which could then be drawn to a more amorphous fibre, while retaining the original ($Ge_{20}Sb_{10}Se_{65}Ga_5$ at. %) composition. Further evidence for the requirement for distillation of $Ge_{20}Sb_{10}Se_{65}Ga_5$ at. % to produce effective fibre has come from the work of Denker *et al* [18]. Following distillation of

$Ge_{20}Sb_{10}Se_{65}Ga_5$ at. % with oxygen and hydrogen getters[56], a fibre capable of 36 mW output lasing power at 5.25 µm was produced[18].

4.1.2.1 Development of $Ge_{19.4}Sb_{9.7}Se_{67.9}Ga_3$ at. % (M235RC) as a host glass system.

With the $Ge_{20}Sb_{10}Se_{65}Ga_5$ at. % selenide chalcogenide composition being deemed unsuitable and incompatible with the Nottingham fibre fabrication process without distillation, it was decided to design a new GeSbSeGa composition with a lower amount of gallium. High gallium compositions (>3 at %.) have been shown to be prone to crystallisation in GeAsSeGa host glass systems by forming Ge-modified face centric cubic (*fcc*) α-Ga_2Se_3, with rare earth oxides found to act as heterogenous nucleation sites for these crystals[51,133]. Therefore, with the aim to create a gallium containing GeSbSe composition which could be rare earth ion doped and drawn to fibre, reducing the gallium content was favoured over reducing the germanium content. As $Ge_{20}Sb_{10}Se_{70}$ at. % had demonstrated reasonable resistance to devitrification in Parnell *et.al* [54], it was decided to alter this composition to facilitate gallium. To accommodate 3 at %. Ga, Ge could have been reduced by 3 at. % but instead, 3 at. % Ge:Sb:Se were removed, in ratio to their original composition *i.e.* $(Ge_{20}Sb_{10}Se_{70})_{97}Ga_3$. That is, 70% of the 3 at. % (2.1%) was subtracted from the Se, 20 % of the 3 at. % taken from Ge (0.6%), and 10 % of the 3 at. % taken from Sb (0.3%), the resulting composition being $Ge_{19.4}Sb_{9.7}Se_{67.9}Ga_3$ at. %.

To assess the suitability of this new composition as a rare earth ion host glass, an undistilled, undoped preform of $Ge_{19.4}Sb_{9.7}Se_{67.9}Ga_3$ at. % was next batched and melted (M235RC). As this was a novel composition, a prediction had to be made regarding the T_g of the glass to allow for adequate annealing. Work from Shiryaev *et al.* has shown that an increase in 5 at. % Ga content slightly increases the T_g of arsenic-based host glasses ($Ge_{25}As_{15}Se_{60,}$ T_g 318 °C; $Ge_{25}As_{15}Se_{55}Ga_5$, T_g 333 °C) [172]. However, it was theorised that the addition of Ga in antimony-based glasses may have a larger effect on T_g ($Ge_{20}Sb_{10}Se_{70,}$ T_g 214 °C [54]; $Ge_{20}Sb_{10}Se_{65}Ga_5$ at. %, Tg 272 °C [90]). A counterpoint to this being that in Shiryaev *et al.*, the T_g of 318 °C

in $Ge_{25}As_{15}Se_{60}$ was already comparatively high to other selenide chalcogenide glasses, and thus the substitution of 5 at. % gallium in lieu of selenium may have had diminishing returns on T_g increase [172]. As mentioned above, Ga occupies an analogous structural niche to Ge ($GeSe_4$ and $GaSe_4$ are both tetrahedral network formers)[54,178]. A 5 at. % increase in Ge in lieu of Se was shown to increase the T_g of an antimony-based glass by 100 °C[54]. When comparing $Ge_{20}Sb_{10}Se_{70}$ at. % (T_g of 214 ± 2 °C)[54] to $Ge_{20}Sb_{10}Se_{65}Ga_5$ at. % (T_g of 282 ± 2 °C, measured from the 1000 ppmw Sm^{3+} $Ge_{20}Sb_{10}Se_{65}Ga_5$ at. % preform described in Section 4.1.2, data not published here), it was expected $Ge_{19.4}Sb_{9.7}Se_{67.9}Ga_3$ at. % would have a T_g at a midpoint between these two with the T_g increasing, with increasing content of the tetravalent network former. A provisional annealing temperature of 246 °C was used for this 30 g preform. This was estimated assuming temperature increased linearly with increasing Ga content, using $Ge_{20}Sb_{10}Se_{70}$ at. % and $Ge_{20}Sb_{10}Se_{65}Ga_5$ at. % as the only two available data point.

After annealing and cooling to ambient, a small section of the preform (M235RC, $Ge_{19.4}Sb_{9.7}Se_{67.9}Ga_3$ at. %), was removed from the base (away from the contraction cone because refractory impurities tend to accumulate there during the static hold vertically of the melt for refining (see Section 3.2.3) and prepared for DSC (Section 3.3.1). The sample was taken through 4 cycles of heating/cooling at 10 °C/min with the average of the final three cycles used to determine a T_g of 232 ± 1 °C (Figure 4.2). The reason for discounting the initial cycle was two-fold. First it was used as a determinant of the true T_g of the glass, second it served to reset the thermal history of the (likely improperly annealed) sample and provided a known thermal history. As the provisional annealing temperature was 14 °C above the measured T_g, it was proposed that the annealing had likely led to the relaxation of internal stresses while minimising the risk of crystallisation of the sample.

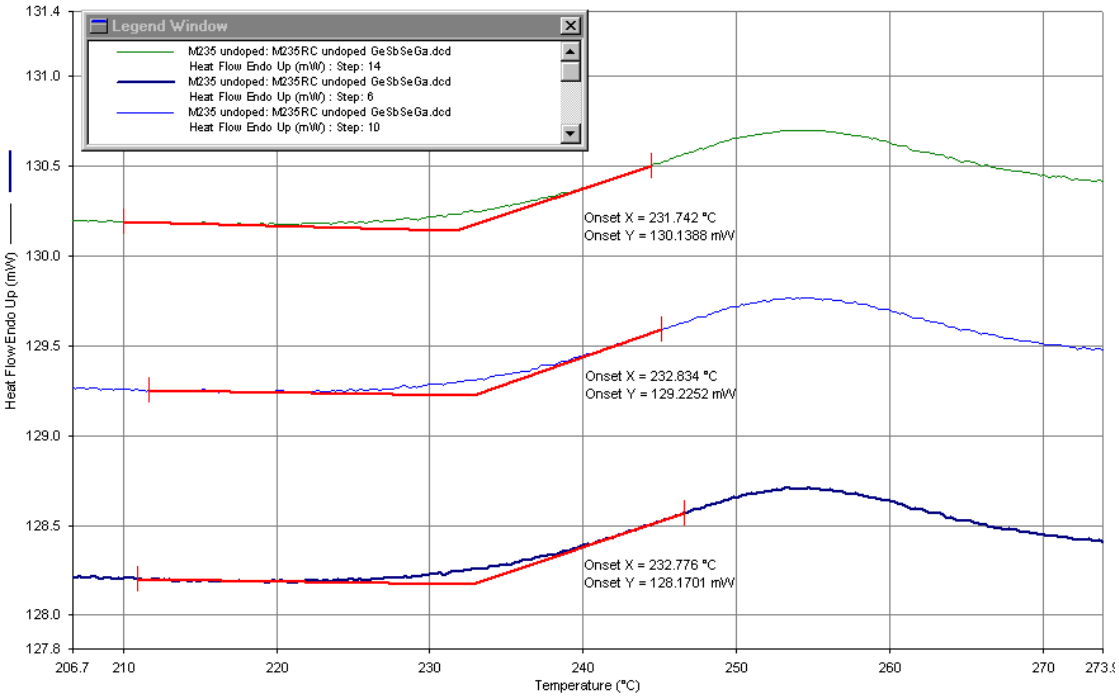


Figure 4.2 DSC cycles of an 8 mg sample of $Ge_{19.4}Sb_{9.7}Se_{67.9}Ga_3$ at. % (M235RERC) showing an average T_g onset of 232 °C +0.834/-0.258 °C. Cycle 1 measurement excluded, Cycle 2 in navy blue, Cycle 3 in blue, Cycle 4 in green. Sample was annealed at a provisional T_g of 246 °C due to no previous knowledge of T_g. Sample preparation and interpretation elaborated in section 3.3.1.

A disc was removed from the end of the $Ge_{19.4}Sb_{9.7}Se_{67.9}Ga_3$ at. % bulk preform and prepared for FtIR analysis, producing a disc with faces polished to a 1 µm finish of thickness, 2.662 mm (see section 3.3.7). Both near-IR and mid-IR measurements were taken after the FTIR equipment (Bruker IFS 66/S fitted with Parker Filtration, FT-It purge gas generator, 75-52-12VDC) had been purged for 10 minutes with a continuous flow of dry air (Section 3.3.7). Despite this purge process, from Figure 4.3, the interference of (predominantly, assumed) atmospheric water can be observed between 5.5 to around 7 µm. The reason it was thought to be adventitious water vapour vibrational absorption is that the rotational fine structure of the water molecules is visible on the spectrum and water molecules would tend to be hydrogen bonded if bonded into the glass itself and then would not have the rotational degree of freedom. Figure 4.3 shows the measured spectrum. The labelled bands at 3.0, 4.6, and 7.9 µm correspond to the impurity absorption bands O-H, Se-H, and Ge-O, respectively. The evidence of the fine rotationally structured

water band calls into question whether the purge equipment was in fact working satisfactorily.

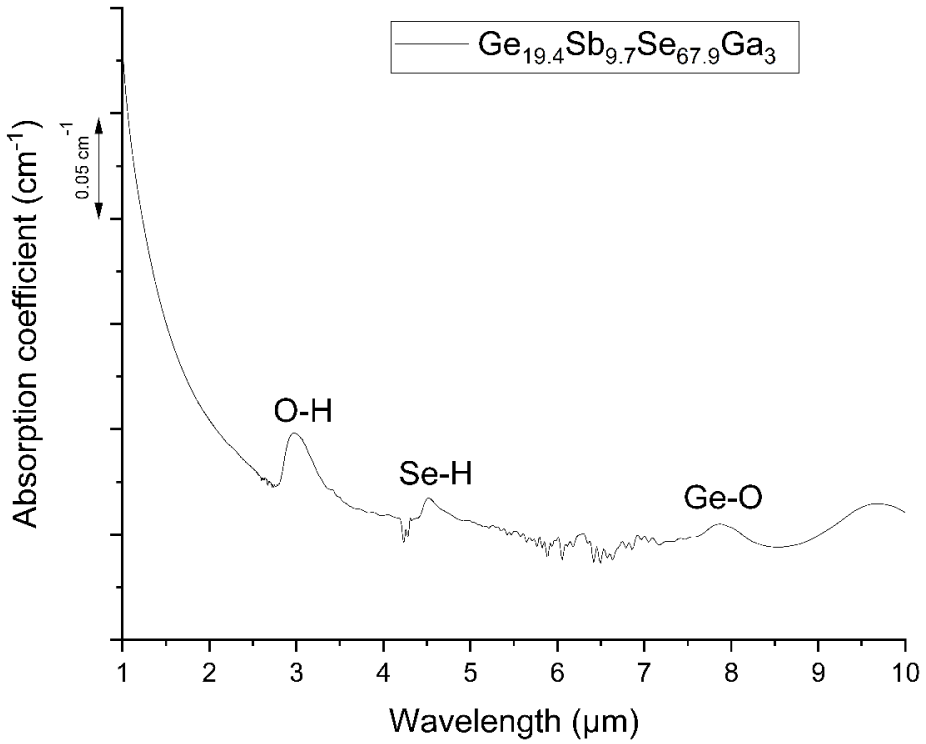


Figure 4.3 Absorption spectra of undoped M235RC $Ge_{19.4}Sb_{9.7}Se_{67.9}Ga_3$ at. % bulk sample with thickness of 2.662 mm. Labelled absorptions indicate impurity bands[19].

This $Ge_{19.4}Sb_{9.7}Se_{67.9}Ga_3$ at. %. (M235RC) rod preform was then etched in propylamine (Table 3.1 for sources and purity) for 120 hours at ambient temperature under dust-cover, then washed thoroughly with acetone and then isopropanol (Table 3.1 for sources and purities) and dried from the propanol under vacuum at around 0.5-1 mbar (50- 100 Pa) in a glovebox antechamber for at least 90 minutes to prepare for fibre drawing.

After mounting the as-annealed rod preform of $Ge_{19.4}Sb_{9.7}Se_{67.9}Ga_3$ at. % on the fibre tower, as the approximate fibre drawing temperature was approached and the gob formed, the surface of the preform remained smooth with minor blemishes. The resulting fibre (F100RC) was of stable diameter (230 μm ± 5 μm) over approximately 30 meters and had good handleability. A 7.5 m starting length of

fibre was used to measure the optical loss across the mid-IR spectral region (see section 3.3.6 for methodology). The fibre exhibited its lowest optical loss of 1.17 dB/m at 6.19 µm (Figure 4.4).

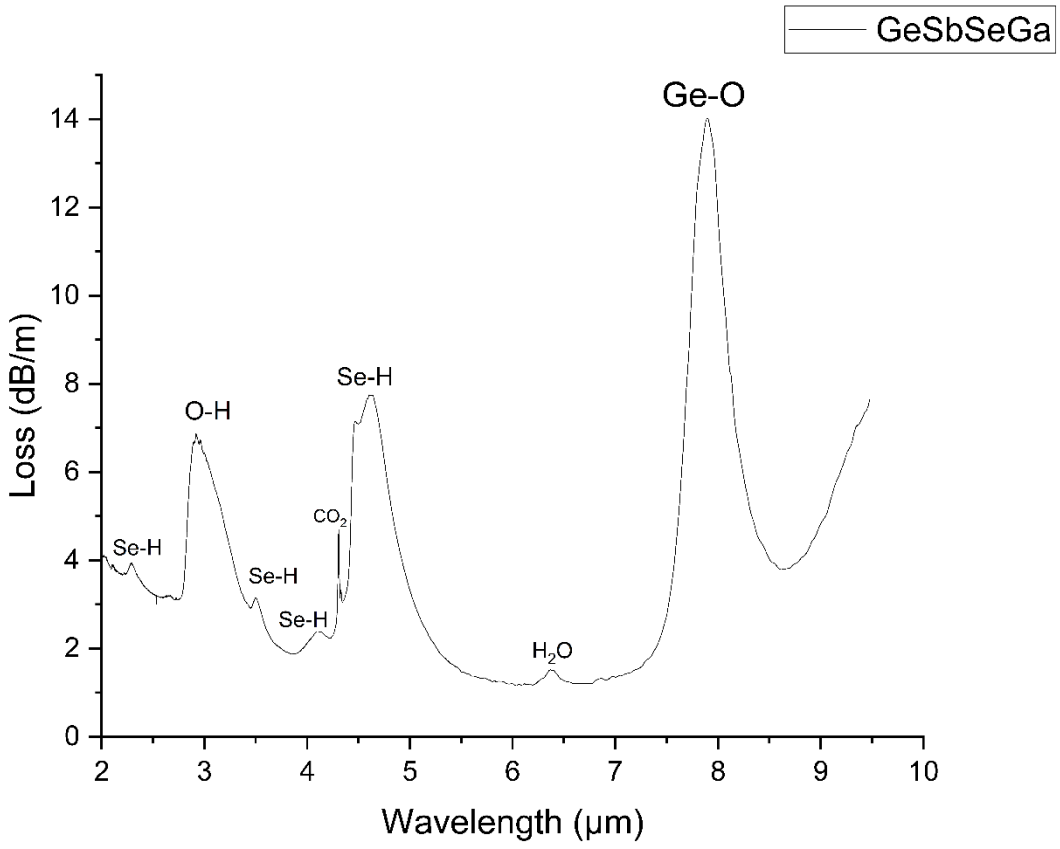


Figure 4.4 Optical loss spectrum of unstructured F100RC $Ge_{19.4}Sb_{9.7}Se_{67.9}Ga_3$ at. % fibre drawn from a propylamine-etched preform[19].

As in Figure 4.3, the labelled peaks are a product of various impurities (oxygen and hydrogen) present in the glass despite the heat treatment purifications of the precursor chemicals as detailed in Section 3.2.2. These impurities are anticipated to present themselves in chalcogenide fibre loss spectra unless more stringent purification methods such as distillation are used, which was not applied on this first trial melt of $Ge_{19.4}Sb_{9.7}Se_{67.9}Ga_3$ at. %. The CO_2 peak is believed to be a product of atmospheric absorption, due to the fibre loss rig being in open atmosphere at the launch and collection ends of the fibre. For an undistilled, gallium containing composition, the fibre displayed relatively low optical background losses (< 1.35 dB/m between 5.5-7 µm) across the spectrum measured

with lowest losses of 1.16 dB/m at 6.03 µm and so was deemed a suitable candidate for trial rare earth ion doping.

4.2 Samarium foil doped $Ge_{19.4}Sb_{9.7}Se_{67.9}Ga_3$ at. % bulk glass (M227RERC) and fibre (F099RERC)

A 30 g $Ge_{19.4}Sb_{9.7}Se_{67.9}Ga_3$ at. % unstructured rod preform was melted, doped with nominally 1000 ppmw Sm foil, as detailed in section 3.2. A disc sample was sawn (method in section 3.3.7) and removed for FtIR analysis (results presented in next section, 4.2.1), then the preform was etched for 65 hours in propylamine at ambient temperature under dust-cover, before being thoroughly washed with acetone and then isopropanol (Table 3.1 for sources and purities). Then dried under vacuum at around 0.5-1 mbar in a glovebox antechamber for 90 minutes to prepare for fibre drawing. The doped preform behaved identically to the undoped (section 4.1.2) with minimal foil-like skin formation during fibre drawing and a relatively stable fibre diameter throughout the process. Fibre was drawn (methodology in section 3.2.9) in 230 and 300 µm diameter. Larger diameter fibre, hereby referred to as "cane", was cane-drawn (methodology in section 3.2.9) to 400 and 1000 µm. Fibre loss measurements are presented in Section 4.2.2. Initial publication of the work detailed in this section is available in [19].

4.2.1 FtIR analysis of bulk glass: 1000 ppm Sm-doped $Ge_{19.4}Sb_{9.7}Se_{67.9}Ga_3$ at. % (M227RERC).

A disc cut from the 1000 ppm Sm^{3+} doped $Ge_{19.4}Sb_{9.7}Se_{67.9}Ga_3$ at. % preform (M227RERC) was polished to a 1 µm finish, with a 2.74 mm thickness, and both near-IR and mid-IR transmission measurements were taken using FtIR spectroscopy, as described in section 3.3.7. Figure 4.5 shows the absorption spectra of the bulk glass across: (a) 1-2.2 µm and (b) 2-10 µm wavelength range.

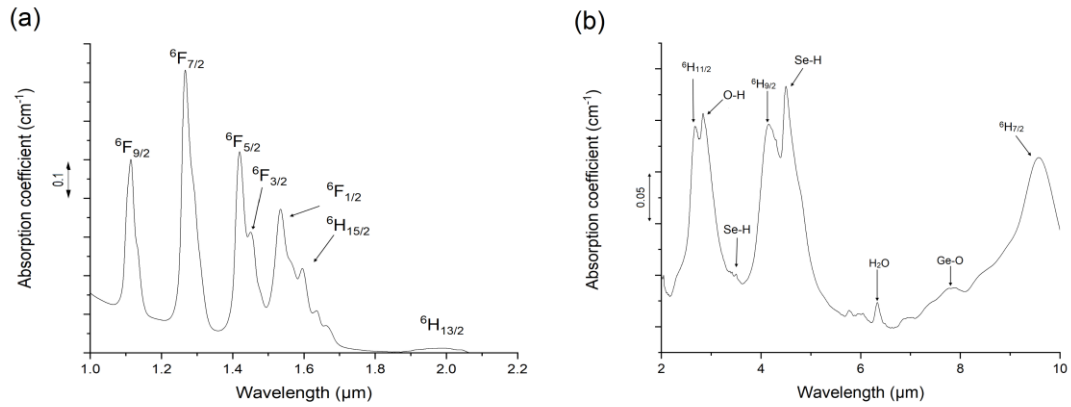


Figure 4.5 Absorption spectra of bulk 1000 ppmw Sm^{3+} doped $Ge_{19.4}Sb_{9.7}Se_{67.9}Ga_3$ at. % glass disc (M227RERC), polished to a 1 µm finish resulting in a 2.74 mm thickness spanning: (a) the near-IR and (b) the near-IR to mid-IR[19]. All electronic Sm^{3+} absorptions presented here (in the near and mid-IR) are from the $^6H_{5/2}$ ground state.

Figure 4.5 shows the results of the near-IR and mid-IR FtIR measurements on the disc sample of M227RERC, 1000 ppm Sm^{3+} doped $Ge_{19.4}Sb_{9.7}Se_{67.9}Ga_3$ at. %. From Figure 4.5, several Sm^{3+} electronic ground state absorptions are observed in the 1-2.2 µm region. An energy level diagram taken from Shaw *et al.* was used to aid in labelling the peaks[49]. An adapted energy level diagram is seen in Figure 4.6. Table 4.1 lists the observed wavelength positions and assignment of Sm^{3+} $^6H_{5/2}$ ground-state to excited state transitions; assignments were compared with those of other authors. Starecki *et al.* [113] for (500 or 1000 ppm, unstated) Sm^{3+} doped $Ga_5Ge_{20}Sb_{10}Se_{65}$ at. % bulk glass and Němec *et al.*[179] for $(Sm_2Se_3)0.5(Ge_{30}Ga_5Se_{65})99.5$ molar ratio, bulk glass[19]. Figure 4.5(b) shows extrinsic impurity vibrational absorption bands and Sm^{3+} electronic absorptions in the 2-10 µm wavelength range.

As seen in Figure 4.4, the absorption band centred around 3 µm was attributed to O-H impurity absorptions, therefore the 2.65 µm, strong, absorption band, missing in undoped glasses, was assigned as Sm^{3+}:$^6H_{5/2} \rightarrow ^6H_{11/2}$ (*cf.* 2700 nm expected, Table 4.1). Similarly, the strong band at 4.6 µm may be assigned as [H-Se-] extrinsic absorption; a much smaller Se-H band was also expected at 4.1 µm but was not observed (likely hidden under the observable absorption bands covering ~4-5.5 µm (Se-H impurity absorption and Sm^{3+} $^6H_{9/2}$ electronic)). Therefore, it is suggested that the Sm^{3+} transition: $^6H_{5/2} \rightarrow ^6H_{9/2}$ manifests in Fig. 4.6(b) as the small shoulder at 4.30 µm (*cf.* 4500 nm expected as taken from [179], Table 4.1) and that

the 4.1 μm [H-Se-] appears to have been artificially inflated in Fig. 4.5(b) in intensity due to its wavelength proximity to the large 4.30 μm Sm^{3+} band.

From Figures 4.5 (absorption spectrum) and 4.6 (energy level diagram), the absorption band at 9.58 μm was assigned to the Sm^{3+}: $^6H_{5/2} \rightarrow ^6H_{7/2}$ electronic absorption band (*cf.* 9600 nm expected [179]). Extrinsic vibrational absorption bands due to unwanted oxide contamination (=Sb-O, -Se-O, and ≡Ga-O) are to lie >10 μm wavelength [180], except [≡Ga-O] is reported to absorb also at 7.3 μm [179]. In Figure 4.5, extrinsic vibrational bands due to H-O-H, ≡Ge-O and ≡Ga-O are observed at 6.3 μm [181], 7.83 μm [182] and 7.25 μm [179], respectively.

Table 4.1. Wavelength positions and transition assignments of Sm^{3+} electronic absorption bands observed here (see Fig. 4.5)

For transitions from the ground state: $^6H_{5/2}$, up to excited states. Assignments are compared with those of: Starecki et al. [113] for (500 or 1000 ppm, unstated) Sm^{3+}-doped $Ga_5Ge_{20}Sb_{10}Se_{65}$ at. % bulk glass and Němec et al.[179] for Sm_2Se_3)0.5 ($Ge_{30}Ga_5Se_{65}$)99.5 molar ratio, bulk glass. Taken from Crane et. al [19].

Key: wk is weak, br is broad, sh is sharp, v is very.

Observed in this work. Peak wavelength / nm, for transition from $^6H_{5/2}$ to:	**Observed in [179]. Peak wavelength / nm, for transition from $^6H_{5/2}$ to:**	**Observed in [113]. Peak wavelength / nm, for transition from $^6H_{5/2}$ to:**
9580 (strong) $^6H_{7/2}$	9600 (expected, not measured).	Not measured.
4300 (strong) $^6H_{9/2}$	4500 (expected, not measured).	Not measured.
2650 (strong) $^6H_{11/2}$	2700 (expected, not measured).	Not measured.
2000 (wk, br) $^6H_{13/2}$ (tentative)	2000 (wk, br) Not identified	1970 (wk br) $^6H_{13/2}$
1670 (wk, br shoulder). See*	~1675 (wk, br shoulder). See*	1675 (wk br shoulder). $^6F_{1/2}$
1630 (wk, sh shoulder). See*	1630 (wk, sh shoulder). See*	1630 (wk, sh shoulder) Not identified.
1600 (wk, sh shoulder). See*	1600 (wk, sh shoulder). See*	1595 (wk, sh shoulder). $^6F_{3/2}$
1570 (v wk, br shoulder). See*.	1570 (v wk, br shoulder). See*	1570 (v wk, br shoulder). Not identified.
1530 (strong) (*authors suggest encompasses 1570, 1600, 1630, 1670) $^6F_{1/2}$ $^6F_{3/2}$ $^6H_{15/2}$	1528 (strong), (*authors imply covers 1570, 1600, 1630, 1675) $^6F_{1/2}$ $^6F_{3/2}$ $^6H_{15/2}$	1530 (strong) $^6H_{15/2}$
1440 (wk sh shoulder) Not identified.	1430 (wk sh shoulder) Not identified.	1450 (wk br shoulder) Not identified.
1420 (strong) $^6F_{5/2}$	1414 (strong) $^6F_{5/2}$	1425 (strong) $^6F_{5/2}$
1260 (strong) $^6F_{7/2}$	1262 (strong) $^6F_{7/2}$	1270 (strong) $^6F_{7/2}$
1110 (strong) $^6F_{9/2}$	1108 (strong) $^6F_{9/2}$	1120 (strong) $^6F_{9/2}$
Not measured.	966 $^6F_{11/2}$	Not measured.

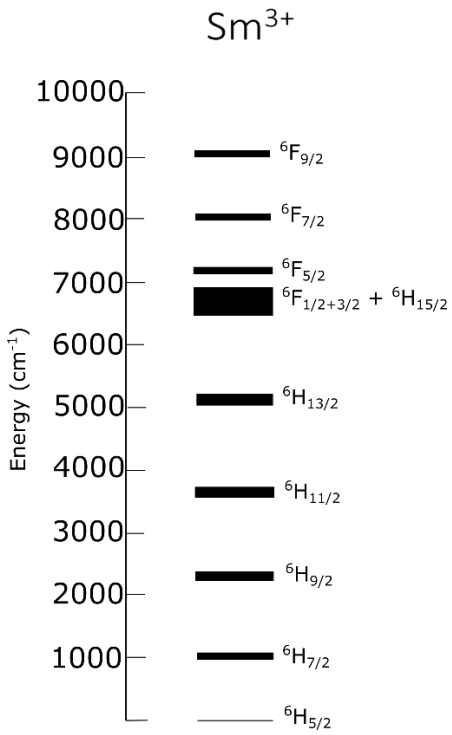


Figure 4.6 Sm^{3+} energy level diagram, redrawn from [49].First published in [19].

In Table 4.1, the observed absorptions from the 1000 ppmw Sm^{3+} doped $Ge_{19.4}Sb_{9.7}Se_{67.9}Ga_3$ at. % bulk glass (M227RERC) are compared with Sm^{3+} absorptions reported from other glass compositions in literature. Below 2 µm wavelength, absorption peaks between compositions appear to largely agree with each other with ~5-10 nm variation between peaks. The absorptions identified beyond 2 µm in Figure 4.5 were not reported in literature but are in close agreement with predictions made by Němec *et al.* [179].

4.2.2 Fibre loss of 1000 ppm Sm^{3+} doped $Ge_{19.4}Sb_{9.7}Se_{67.9}Ga_3$ at. % fibre (F099RERC)

Figure 4.7 shows the mid-IR optical loss for the Sm^{3+} doped $Ge_{19.4}Sb_{9.7}Se_{67.9}Ga_3$ at. % unstructured fibre (F099RERC). The 4-5 µm region has been omitted due to strong, overlapping absorptions (impurity vibrational Se-H and electronic $^6H_{9/2}$ from Sm^{3+}, Table 4.1, Figure 4.7). The measurement was initiated with 3.3 m of fibre, which was cut back to a final length of 295 mm, with over 2000 mm being removed for the "2 group cutback method" [134]. The starting length of the fibre was determined by using a separate test piece of the same fibre (300 mm) and

measuring the intensity of the transmitted light. This measured intensity was then used to approximate the maximum length of fibre that could be used, while still being detectable by the liquid nitrogen cooled InSb and MCT detectors. A longer fibre sample was targeted as this provided a more accurate measurement, predominantly reflecting the quality of the glass system and fibre geometry[134]. It was preferable to overestimate the starting fibre lengths, as cutbacks could be performed until signal is detected. The full procedure is detailed in Section 3.3.9. From Figure 4.7, the lowest loss of this fibre was 2.15 dB/m at 6.04 µm.

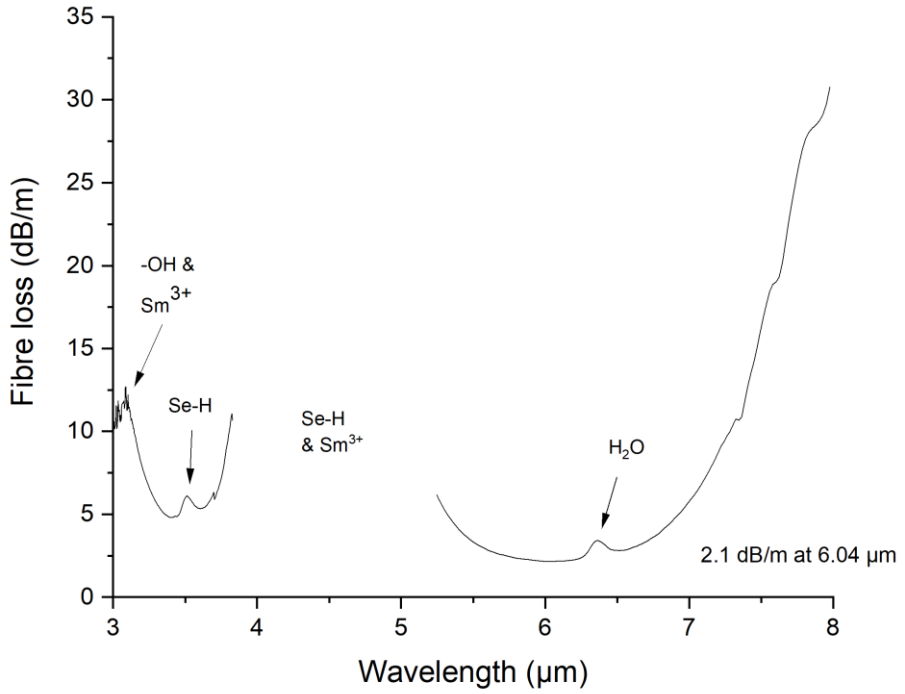


Figure 4.7 Mid-IR optical loss of 1000 ppmw Sm^{3+}-doped $Ge_{19.4}Sb_{9.7}Se_{67.9}Ga_3$ at. % glass fibre in the 3-8 µm range. 4-5 µm region omitted due to dominating vibrational (Se-H) and electronic (Sm^{3+}) absorptions[19].

4.2.3 1000 ppmw Sm^{3+} doped $Ge_{19.4}Sb_{9.7}Se_{67.9}Ga_3$ at. % fibre photoluminescence and photoluminescent lifetimes (F099RERC)

400 µm diameter, 75 mm length cane samples of 1000 ppmw Sm^{3+} doped $Ge_{19.4}Sb_{9.7}Se_{67.9}Ga_3$ at. % (F099RERC) were supplied by the current Author to Dr Łukasz Sójka of the Telecommunications and Teleinformatics Department, Wroclaw University of Technology, Poland who carried out both the photoluminescence (PL) and PL lifetime measurements on the fibre. The following

sections 4.2.3.1. and 4.2.3.2 summarise the PL, and PL lifetime, results of Dr Sójka, respectively, and the interpretation of these results.

4.2.3.1 Photoluminescence of 1000 ppmw Sm^{3+} doped $Ge_{19.4}Sb_{9.7}Se_{67.9}Ga_3$ at. % unstructured fibre

The following study and results were of the 1000 ppmw Sm^{3+} doped $Ge_{19.4}Sb_{9.7}Se_{67.9}Ga_3$ at. % unstructured fibre (F099RERC). Sm^{3+} ions doped in the selenide-chalcogenide glass fibre host were excited by either a 1470 nm laser diode (SemiNex: 4PN-127) or 1300 nm laser diode (SemiNex: 4PN-116). These pumped into the $^6F_{7/2}$ and $^6F_{5/2}$ energy levels, respectively.

The pump laser beams were chopped to reduced thermal background noise from the sample, optical elements, and other laboratory equipment. For example, the remaining pump power exiting the fibre-end, opposite to that pumped, tended to heat up a long-pass filter, down- circuit (Figure 4.8) and thereby produced thermal background noise. Chopping the pump laser beam meant not only that the absolute heat load of the sample was reduced, but also that blackbody radiation from the sample, optical components, etc. were not acting as noise at the detector as they were not modulated by the chopper. Thus, the pump beam was electronically chopped by means of a function generator (GW INSTEK GFG-3015) of low frequency, ~20 Hz; the chopping period of 50 ms was chosen to be long compared to the Sm^{3+} MIR PL lifetimes (~100 µs, see Section 4.2.3.2). The resulting PL emission, from the fibre end opposite to that pumped (Figure 4.8), was focused through a pair of Ge aspheric lenses (Edmund Optics: code 89-607, AR (anti-reflection coated) for 3-12 µm wavelength range), each of NA (numerical aperture): 1, and focal length: 12.7 mm. Lenses of short focal length/high NA were best suited for efficient collection of the fibre PL (photoluminescence), and selected to match the high refractive index (n) of the unstructured chalcogenide glass fibre (e.g. n ~2.55 at 3-10 µm, for undoped $Ge_{20}Sb_{10}Se_{70}$ at. % [183]) and high fibre NA (>1). The Ge lens pair also acted as a 2 µm long-pass filter, thus any residual pump signal exiting the fibre-end was eliminated before reaching the next long-pass filter and monochromator further along the optical circuit (Figure 4.8). The PL exiting the fibre, resulting from excitation with the 1300 or 1470nm laser diode, was first directed through the Ge lens pair, then passed through a long-pass filter of cut-on

wavelength 3 µm (Spectrogon: 71M09339) into a monochromator (MSH-150, Quantum Lot (focal length: 150 mm), calibrated by Bentham in 2018) operating with a 4000 nm blazed, 150 line/ mm grating and onto the detector. Detection of the signal was achieved with a thermoelectric cooled (200 K) MCT (mercury cadmium telluride) detector (Vigo System: PVI-4TE-8), operating in the spectral range: 3 µm to 9 µm. Additionally, the thermoelectric cooled (200 K) MCT (Vigo System: PVI-4TE-5) was used operating in the spectral range: 2 µm to 6.0 µm.

For long wavelength emission experiments (centred on 7.25 µm), the PL exiting the fibre, resulting from excitation with the 1300 or 1470 nm laser diode, was directed through the Ge lens pair, then passed through a long-pass filter of cut-on wavelength 6.15 µm (Spectrogon: 71M09001) then into the same monochromator as above, but operating with a 9000 nm blazed, 100 line/ mm grating, and then onto the same MCT detectors as above. All measured spectra were corrected for system response.

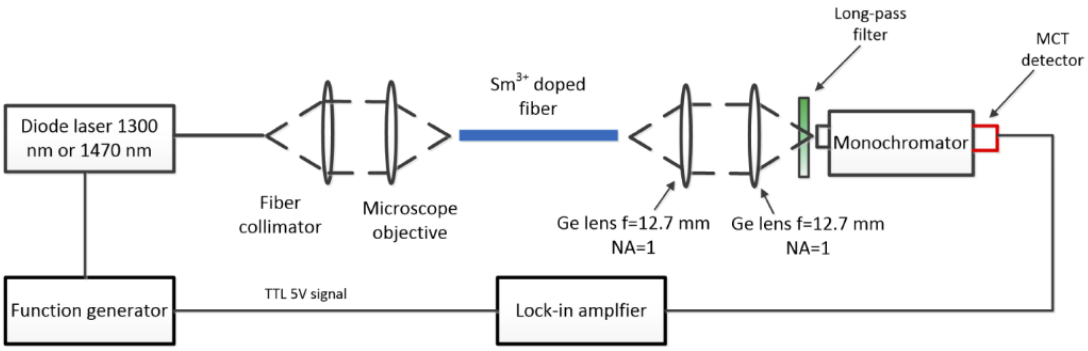


Figure 4.8 Fibre-end-collection set-up for measurement of PL intensity at ca. 2.7, 3.7 and 7.3 µm wavelengths from the 1000 ppmw Sm^{3+}doped $Ge_{19.4}Sb_{9.7}Se_{67.9}Ga_3$ at. % unstructured glass fibre (F099RERC) of 75 mm length and 415 ±3 µm diameter[19].

End-pumping at 1470 nm / 300 mW or 1300 nm / 350 mW of 75 mm of unstructured 1000 ppmw Sm^{3+} doped $Ge_{19.4}Sb_{9.7}Se_{67.9}Ga_3$ at. % fibre (F099RERC), of 415 ±3 µm diameter, was investigated for PL at nominally 3.75 µm (expected due to $^6H_{13/2} \rightarrow {}^6H_{9/2}$ transition) from the fibre-end opposite that end-pumped with cut-on filter at 3000 nm. This $^6H_{13/2} \rightarrow {}^6H_{9/2}$ transition was reported to have a relatively high branching ratio of ~ 0.33 from Judd-Ofelt modelling [113], providing a stronger PL signal and thus was simpler to detect than PL >7 µm expected for $^6H_{13/2} \rightarrow {}^6H_{11/2}$. The initially low intensity PL signal, centred at 3.75 µm, was improved

with optimal optical alignment of the optical circuit. Measurement parameters were: MCT detector (Vigo, PVI-4TE-8 (3 µm-9 µm); lock-in amplifier: sensitivity 30 mV, time-constant 300 ms; monochromator software: time averaging: 3 s.

Figure 4.9a shows the normalised emission spectra in the 3.25-4.5 µm wavelength range when pumped with 350mW at 1300 nm, or 300mW at 1470 nm. The slight decrease in intensity at around 4.25 µm was attributed to inadvertent atmospheric CO_2 absorption from the open beam path in the optical circuit. From Figure 4.9, the spectral shape and central wavelength (3.75 µm) are in good agreement with the results of Starecki *et al.* (1000 ppmw Sm^{3+} doped $Ge_{20}Sb_{10}Se_{65}Ga_5$) [113].

PL at nominally 7.25 µm (end-pumping at 1470 nm / 300 mW or 1300 nm / 350 mW)) 75 mm long of unstructured 1000 ppmw Sm^{3+}-doped $Ge_{19.4}Sb_{9.7}Se_{67.9}Ga_3$ at. % fibre of 415 ±3 µm diameter was investigated (expected due to the $^6H_{13/2} \rightarrow {}^6H_{11/2}$ transition) exiting from the fibre-end opposite to that end-pumped (Fig. 1) with a cut-on filter at 6150 nm. This $^6H_{13/2} \rightarrow {}^6H_{11/2}$ transition was reported to have a relatively low branching ratio of ~ 0.08 from Judd-Ofelt modelling[113] and was more difficult to detect than the ~3.75 µm wavelength emission.

From Figure 4.9b, PL centred at 7.25 µm, also had spectral shape and central wavelength in good agreement with results by Starecki *et al.* (1000 ppmw Sm^{3+} doped $Ge_{20}Sb_{10}Se_{65}Ga_5$) in [113]. The 6150 nm cut-on filter caused an abrupt PL onset at ~ 6230 nm (see Figure 4.9b).

From the observed PL band shape (Figure 4.9b), the 6–9 µm emission band appeared to be mainly associated with the $^6H_{13/2} \rightarrow {}^6H_{11/2}$ transition, expected at 7.18 µm[113]. However, it's suggested that emission from $^6H_{11/2} \rightarrow {}^6H_{9/2}$, expected at 7.77 µm, with the same branching ratio of 0.08 as the larger gap transition: $^6H_{13/2} \rightarrow {}^6H_{11/2}$, is likely to have also contributed to this MIR emission.

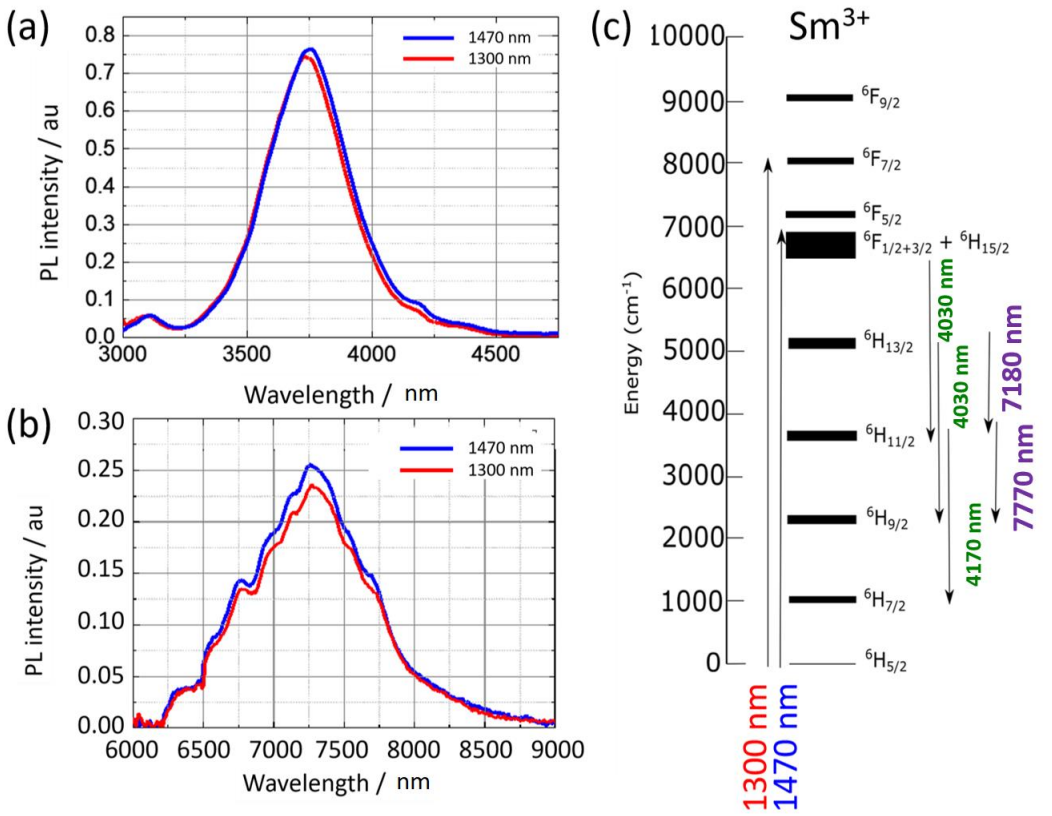


Figure 4.9 (a) and (b) Photoluminescence spectra of the 1000 ppmw Sm^{3+}-doped $Ge_{19.4}Sb_{9.7}Se_{67.9}Ga_3$ at. % unstructured glass fibre (F099RERC), pumped at 1470 nm wavelength with 300 mW (upper (blue) curve at peak wavelength, or pumped at 1300 nm wavelength with 350 mW to give: (a) PL between 3 and 4.5 μm and (b) PL between 6 and 9 μm. Fibre-end collection of the PL was applied, at the fibre end opposition to that pumped. PL was-centred at 3750 nm, and 7250 nm, in (a), and (b), respectively. (c) Energy level diagram of Sm^{3+}, indicating pump absorption transitions and emission transitions contributing to spectra in (a) and (b)[19].

This same sample (*i.e.*, the 1000 ppmw Sm^{3+}-doped $Ge_{19.4}Sb_{9.7}Se_{67.9}Ga_3$ at. % unstructured fibre F099RERC) was investigated for <3 µm PL, by end-pumping at 1470 nm / 300 mW. A MCT detector (operating: 2-6 µm) was used with the Ge lens pair (Figure 4.8) acting as a 2 µm long-pass filter. The measured spectrum was calibrated for system response.

Emission associated with Sm^{3+}: $^6H_{13/2} \rightarrow {}^6H_{7/2}$ centred at 2.59 µm (high branching ratio: 0.42) was expected to dominate the PL spectrum. Both $^6H_{11/2} \rightarrow {}^6H_{5/2}$ centred at 2.85 µm (high branching ratio: 0.56) and ($^6F_{1/2}$, $^6F_{3/2}$, $^6H_{15/2}$) $\rightarrow {}^6H_{9/2}$ centred at 2.65 µm (low branching ratio: 0.18) were considered to potentially contribute. From Figure 4.10, PL was observed from 2250-3200 nm, centred at 2.7 µm. This result partially confirms non-quenching of the transition $^6H_{11/2} \rightarrow {}^6H_{5/2}$ as PL was

observed at~ 2.8 µm. Near-IR PL emissions from 1.6 – 2.0 µm were reported by Starecki *et al.* when a 500 ppmw Sm^{3+} $Ga_5Ge_{20}Sb_{10}Se_{65}$ was pumped at 1.45 µm [113]. However, the germanium lenses incorporated into the optical rig (Figure 4.8) acted as 2 µm long-pass filters, preventing similar measurements with the 1000 ppmw Sm^{3+}-doped $Ge_{19.4}Sb_{9.7}Se_{67.9}Ga_3$ at. % fibre.

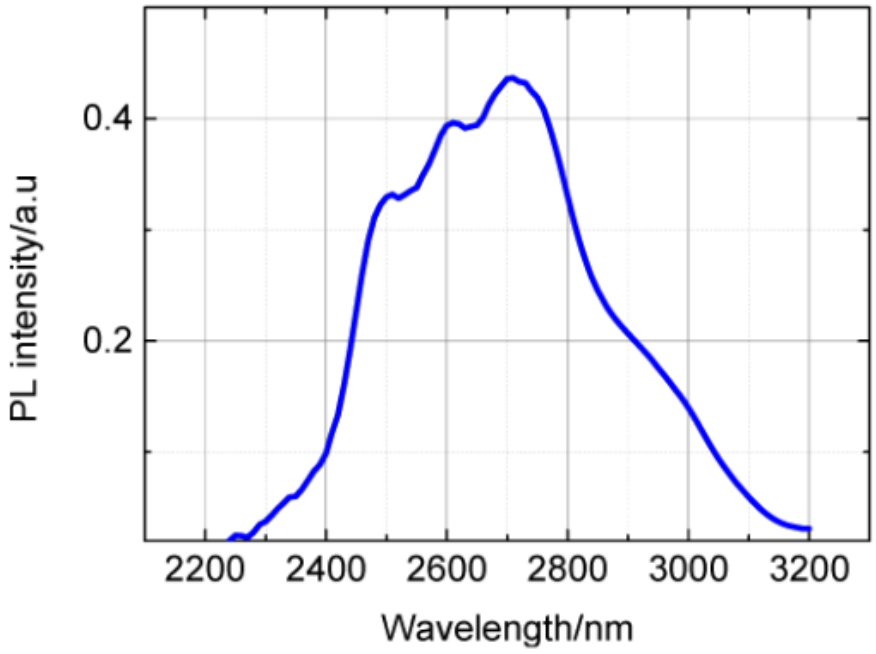


Figure 4.10 Photoluminescence spectrum of the 1000 ppmw Sm^{3+}doped $Ge_{19.4}Sb_{9.7}Se_{67.9}Ga_3$ at. % unstructured fibre when end pumped at 1470 nm wavelength with 300 mW power. Fibre end collection of the PL was applied, and the spectrum was corrected for system response[19].

4.2.3.2 PL lifetime measurements of 1000 ppmw Sm^{3+} doped $Ge_{19.4}Sb_{9.7}Se_{67.9}Ga_3$ at. % unstructured fibre

For the PL lifetime measurements, the fibre was end-pumped with modulated light from the pump laser at 1470 nm. A function generator (GW INSTEK GFG-3015) coupled to laser diode drivers (Thorlabs: LDC240C) was used to produce a square-wave signal, which modulated the laser diode, switching it on and off. The resultant periodic PL excitation from the fibre under the side emission set-up (Figure 4.11),

and close to the pumped fibre end, was then directed through the pair of Ge lenses and through the long-pass filter (cut-on at 3 µm or 6.15 µm) into the MCT detector. The MCT detector was used to measure the intensity decay of the fibre PL side-emission. The signal from the MCT photodetector was directed to an oscilloscope (PicoTech). To suppress noise, averaging over several thousand excitation processes was performed several times.

For lifetime measurement at nominally 3.75 µm wavelength, the 3 µm cut-on filter and MCT photodetector (Vigo System PVI-4TE-6, operation: 2-6 µm) were used. This detector and preamplifier together have a quoted bandwidth of 17 MHz (rise time 20 ns). For the lifetime measurement nominally at 7.25 µm wavelength, the 6.15 µm cut-on filter and second MCT detector (Vigo System PVI-4TE-8: operation: 3-9 µm) were used. The detector quoted bandwidth with preamplifier was 150 kHz, with a rise time of 2 µs.

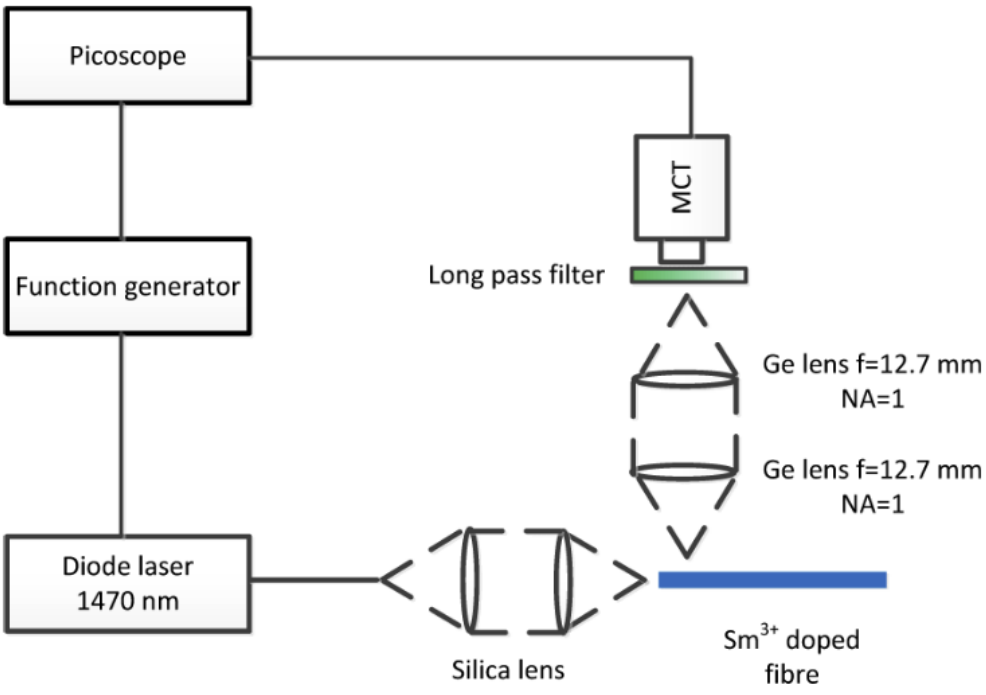


Figure 4.11 Fibre side-collection set-up for measurement of PL lifetimes from 1000 ppmw Sm^{3+}doped $Ge_{19.4}Sb_{9.7}Se_{67.9}Ga_3$ at. % unstructured fibre F099RERC. 75 mm length and 415 ±3 µm diameter. Lifetimes measured ca. 3.7 and 7.3 µm following pumping at 1.470 µm[19].

Figure 4.12 presents PL decay of the fibre using a MCT detector (PVI-4TE-5) and cut-on filter at 3.00 µm. PL was centred at 3.75 µm (Figure 4.9). As low pump power as possible was used to minimise sample heating. The decay was measured from the fibre-side. Measurements were repeated three times, with lifetimes of 0.100 ms, 0.102 ms and 0.101 ms being recorded.

A single exponential was applied to each of these three measurements, but it was not possible to achieve a perfect fit to the measured data. It was proposed in Crane *et al.* [19] that this PL lifetime was due to a combination of two transitions: $^6H_{13/2} \rightarrow {}^6H_{9/2}$ at ~3.7 µm (branching ratio 0.33) [113] and $^6H_{11/2} \rightarrow {}^6H_{7/2}$ at~ 4.1 µm (branching ratio 0.35)[113] (figure 4.9c); as each have similar branching ratios [113]. Emission from ($^6F_{1/2}$, $^6F_{3/2}$, $^6H_{15/2}$) → $^6H_{11/2}$ at ~ 4.03 µm (branching ratio 0.06)[113] may have additionally contributed, despite the low branching ratio.

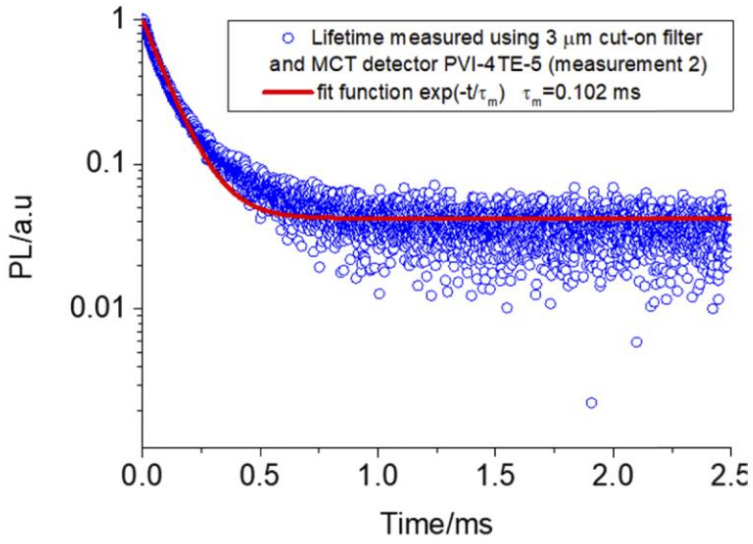


Figure 4.12 Photoluminescent lifetime of 1000 ppmw Sm^{3+} doped $Ge_{19.4}Sb_{9.7}Se_{67.9}Ga_3$ at. % unstructured glass fibre centred at 3.75 µm with cut-on filter at 3.00 µm and fibre-side collection. Typical measurement, 2nd of 3 measurements; to suppress noise, averaging over several thousand excitation processes per measurement was performed. Lifetimes measured at 0.101 ms, 0.102 ms, and 0.100 ms.

The lifetimes of the 3.75 µm photoluminescence in the undistilled 1000 ppmw Sm^{3+} doped $Ge_{19.4}Sb_{9.7}Se_{67.9}Ga_3$ at. % unstructured fibre presented in Figure 4.12 (mean: 0.101 ms, 101 µs) are longer than those reported for the same transition in alternative chalcogenide glass fibres. Starecki *et al.* measured a lifetime of 10 µs at 3.7 µm, in a distilled 500 ppmw Sm^{3+} $Ge_{20}Sb_{10}Se_{65}Ga_5$ in a fibre with high losses

of 7-18 dB/m between 7-8 µm wavelength [113]. Shiryaev *et al.* measured a lifetime of 60 µs at 3.7 µm in a distilled, high purity 700 ppmw Sm^{3+} doped $Ga_{2.2}Ge_{26.5}As_{14.6}Se_{56.7}$ bulk glass, with its corresponding fibre exhibiting losses of 0.5 dB/m at 5.7 µm[115].

Figure 4.13 presents the PL decay centred at 7.25 µm of the of the fibre using the MCT detector (PVI-4TE-8) and cut-on filter at 6.15 µm (see Fig. 4.9b). As low pump power as possible was used to minimise heating of the sample. The decay was measured from the fibre-side. The average calculated PL lifetime centred at 7.25 µm was in the range of 0.1 ms; measurements were repeated 3 times: yielding measured lifetimes of 0.0975 ms, 0.0971 ms and 0.104 ms. A single exponential fitting to the measured data was applied but was not a perfect fit. It was suggested that this is because there could be more than one transition contributing: $^6H_{13/2} \rightarrow {}^6H_{11/2}$ at around 7.18 µm (branching ratio 0.08) and $^6H_{11/2} \rightarrow {}^6H_{9/2}$ at around 7.77 µm (branching ratio 0.08)[113]; these two transitions have identical calculated branching ratios[113] and so likely both contribute to the photoluminescence centred between these two emissions. To the Author's knowledge, there are currently no other reported lifetime measurements at this 7.25 µm wavelength in Sm^{3+} doped chalcogenides.

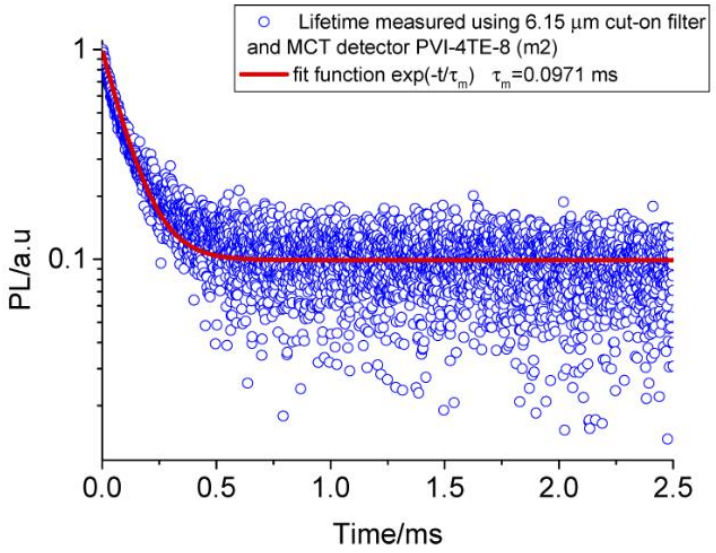


Figure 4.13 Photoluminescent lifetime of 1000 ppmw Sm^{3+} doped $Ge_{19.4}Sb_{9.7}Se_{67.9}Ga_3$ at. % unstructured fibre (F099RERC) centred at 7.25 µm with cut-on filter at 6.15 µm measurement (2nd of 3 measurements, to suppress noise, averaging over several thousand excitation processes per measurement was performed).

4.3 Dy^{3+} $Ge_{19.4}Sb_{9.7}Se_{67.9}Ga_3$ at. % unstructured fibre (F104RERC)

Following the success of the 1000 ppmw Sm^{3+} doped $Ge_{19.4}Sb_{9.7}Se_{67.9}Ga_3$ at. % unstructured glass fibre (F099RERC) that exhibited low fibre losses, good devitrification resistance, and facilitated longer wavelength rare earth radiative transitions than that seen in arsenic glasses, it was decided to attempt to dope the composition with another rare earth element. Dysprosium was chosen due to its potential PL emission around 6.2-6.5 µm [49,142] which coincides with the low optical loss region of the host glass composition ($Ge_{19.4}Sb_{9.7}Se_{67.9}Ga_3$ at. %) and potentially covered the surgically relevant wavelength of 6.45 µm (See Section 2.5) It was also a rare earth element that had been extensively researched in arsenic-based glasses by the Mid-IR Photonics Group at Nottingham[50,52,53,55,95,133,184] allowing comparisons to be made between the host glass compositions. Initial work began with a 1000 ppmw Dy foil doped glass preform (M236RERC, 1000 ppmw Dy^{3+} $Ge_{19.4}Sb_{9.7}Se_{67.9}Ga_3$ at. %) (fabrication details in Section 3.2). The resulting rod preform was successfully drawn to 30 m of 200 ± 10 µm diameter fibre and 5 sections of 1 m length cane with a diameter of 1000 ± 50 µm (Code: F102RERC). The 1000 ppmw Dy^{3+} fibre was of reasonable handleability compared to the 1000 ppmw Sm^{3+} $Ge_{19.4}Sb_{9.7}Se_{67.9}Ga_3$ at. % fibre. However, multiple fibre samples failed to transmit any measurable amount of mid-IR light when a fibre loss measurement was attempted. As the fibre drawing process proceeded without any issues like that detailed in Section 4.1.2 with the $Ge_{20}Sb_{10}Se_{65}Ga_5$ at. % fibre, and considering light was unable to be transmitted through samples < 200 mm in length, a DSC investigation (detailed in section 3.3.1) was carried out to assess if a potential phase separation had occurred (Figure 4.15). No abnormalities were observed, with the measured onset T_g (232 °C) matching that of the 1000 ppmw Sm^{3+} doped $Ge_{19.4}Sb_{9.7}Se_{67.9}Ga_3$ at. % glass (Figure 4.3).

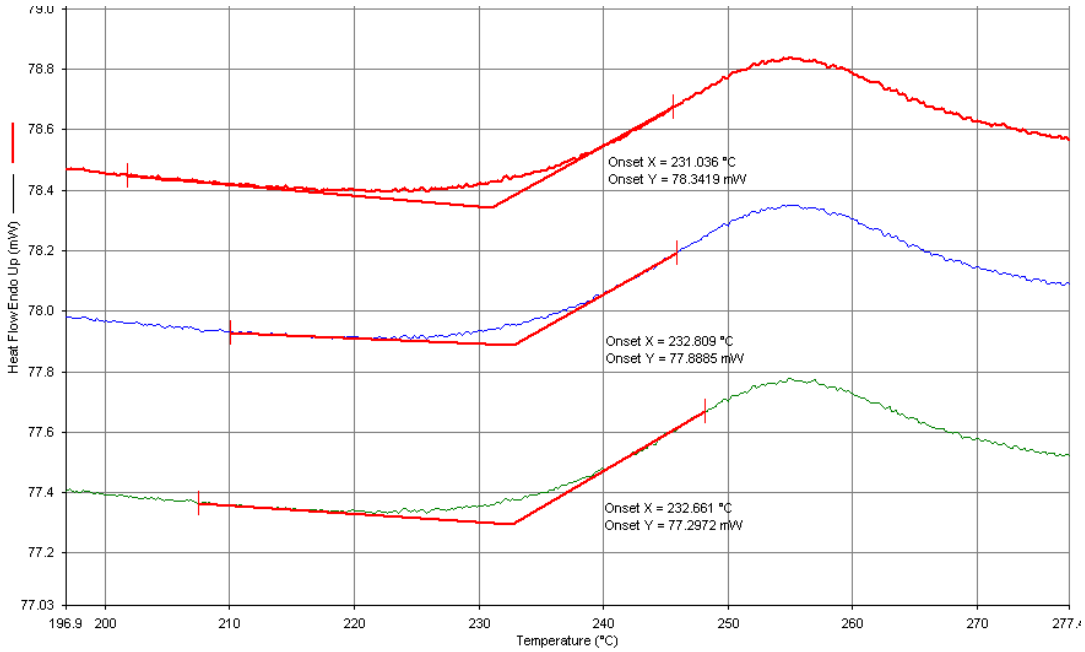


Figure 4.15 DSC cycles of a 12 mg sample of $Ge_{19.4}Sb_{9.7}Se_{67.9}Ga_3$ at. % doped with 1000 ppmw Dy^{3+}. Average T_g onset of 232.16 °C +0.640/-1.132 °C. Cycle 1 measurement excluded, Cycle 2 in green, Cycle 3 in blue, Cycle 4 in red. Sample was annealed at a T_g of 232 °C. Sample preparation and interpretation elaborated in section 3.3.1.

Due to the documented effects of rare earth doping on crystallisation behaviour in chalcogenide glasses [50–52,55,133], it was decided to fabricate an additional Dy^{3+} doped $Ge_{19.4}Sb_{9.7}Se_{67.9}Ga_3$ at. % rod preform, with a reduced doping concentration of 500 ppmw (M240RERC). This is the same doping concentration used in an arsenic-based fibre ($Ge_{16.5}As_{16}Se_{64.5}Ga_3$ at. %) that exhibited low losses of 1.16 dB/m at 6.56 µm without any distillation processes[53]. Dy^{3+} doping concentrations of 1000 ppmw have been achieved in $Ge_{20}Sb_{10}Se_{65}Ga_5$ at. % by Starecki *et al.* [25] fibres that had been subject to gettering and distillation processes to improve glass purity. A sample of this rod preform was removed for FTIR analysis (Section 4.3.1) and then was drawn to fibre (Section 4.3.2).

4.3.1 FtIR analysis of 500 ppmw Dy^{3+} doped bulk $Ge_{19.4}Sb_{9.7}Se_{67.9}Ga_3$ at. % glass.

A disc cut from the 500 ppmw Dy^{3+} doped $Ge_{19.4}Sb_{9.7}Se_{67.9}Ga_3$ at. % rod preform (M240RERC) was polished to a 1 µm finish (Section 3.3.7) and a NIR measurement was taken (Figure 4.16). In this case, a MIR measurement was forgone due to time constraints and the lack of Dy^{3+} electronic absorptions in the mid-IR. Figure 4.17, adapted from Shaw *et al.*[49] was used to label the

Dy^{3+}electronic absorption peaks. These labels agree with work from Starecki *et al.* [25] in a similar, $Ge_{20}Sb_{10}Se_{65}Ga_5$ at. % glass system, and work from Park *et al.* in a $Ge_{30}Ga_2Sb_8Se_{60}$ host glass[185]. The band at around 2.8 µm is attributed to both the O-H extrinsic impurity vibrational absorption as well as the electronic absorption Dy^{3+}: $^6H_{15/2} \rightarrow {}^6H_{13/2}$.

The peak at 1.7 µm was attributed to Dy^{3+}: $^6H_{15/2} \rightarrow {}^6H_{11/2}$. The peak at 1.3 µm was attributed to two closely spaced energy levels of Dy^{3+}: $^6H_{15/2} \rightarrow {}^6H_{9/2} + {}^6F_{11/2}$. The peak at 1.1 µm was also attributed to two closely spaced levels of Dy^{3+}: $^6H_{15/2} \rightarrow {}^6H_{7/2} + {}^6F_{9/2}$ (Figure 4.16).

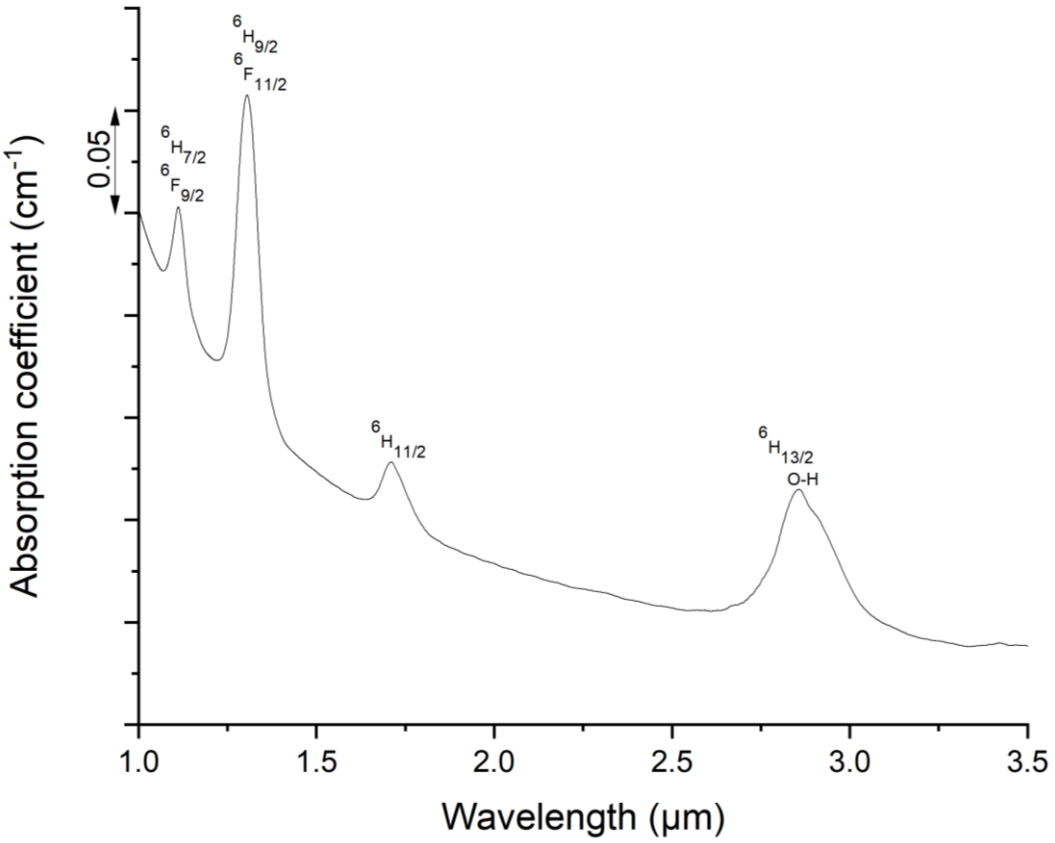


Figure 4.16 Absorption spectra of bulk 500 ppmw Dy^{3+}doped $Ge_{19.4}Sb_{9.7}Se_{67.9}Ga_3$ at. % glass (M240RERC) spanning 1 – 3.5 µm. Sample was polished to 1 µm finish. FTIR sample chamber was purged with dry air for 40 minutes before scanning to reduce effects of atmospheric O-H absorptions.

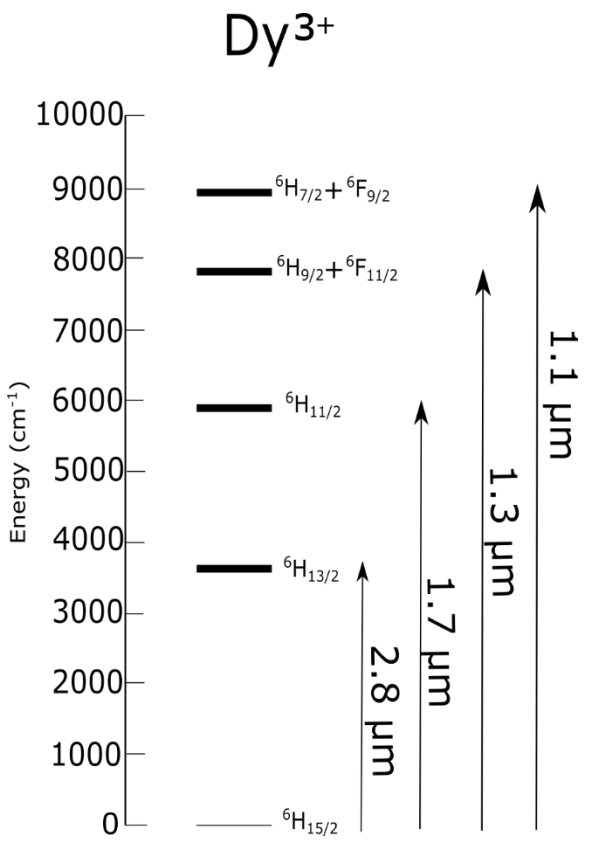


Figure 4.17 Dy^{3+} energy level diagram. Redrawn from [49].

4.3.2 Fibre drawing and fibre loss of 500 ppmw Dy^{3+} doped $Ge_{19.4}Sb_{9.7}Se_{67.9}Ga_3$ at. % unstructured fibre (F104RERC)

The remainder of the 500 ppmw Dy^{3+}-doped $Ge_{19.4}Sb_{9.7}Se_{67.9}Ga_3$ at. % rod preform (M240RERC) was then etched in ambient temperature propylamine for 90 hours under dust cover (Table 3.1 for sources and purity) before being rinsed in subsequent acetone, then isopropanol washes. The preform was then dried under vacuum at around 0.5-1 mbar in a glovebox antechamber for at least 90 minutes to prepare for fibre drawing. The fibre was drawn as detailed in Section 3.2.9. Around 30 m of 200 µm fibre was drawn, before the cane drawer was used to draw 6, 500 – 750 mm lengths of 1000 ± 50 µm cane. The fibre was given the identification code F104RERC.

Figure 4.18 shows the MIR optical loss for the 500 ppmw Dy^{3+} doped $Ge_{19.4}Sb_{9.7}Se_{67.9}Ga_3$ at. % unstructured fibre. The 4.4-4.9 µm region has been omitted due to strong absorptions introduced by the extrinsic impurity Se-H. The lowest loss in this fibre was around 3.2 dB/m at 6.63 µm. The measurement was

initiated with 3 m of fibre. As described in 4.2.2, a longer fibre sample was targeted as this provided a more accurate measurement, reflecting the quality of the glass system and fibre geometry[134]. This fibre loss was greater than that recorded in Section 4.2.2, of that reported in a 1000 ppmw Dy^{3+} doped $Ge_{20}Sb_{10}Se_{65}Ga_5$ at. % fibre fabricated by Starecki *et al.* (< 1dB/m lowest loss) [25], and of that reported in a 500 ppmw Dy^{3+} doped $Ge_{16.5}As_{16}Se_{64.5}Ga_3$[53] fabricated by Tang *et al.*

The Ge-O absorption band is substantially smaller than that observed in the 1000 ppmw Sm^{3+} foil doped $Ge_{19.4}Sb_{9.7}Se_{67.9}Ga_3$ at. % unstructured fibre (Figure 4.7) despite no difference in precursor purification and fibre fabrication method. This was proposed to be a product of the rare earth ion dopants. As rare earth foils (which do not undergo any prior purification aside a mechanical scratching of the surface with germanium pieces) were used for both glasses, it is possible that the different foils had different oxygen content. This is potentially due to different purification methods being used for different rare earth elements and subsequently different ppmw of oxide base impurities between elements[186,187]. This is further evidenced as the Ge-O peak is less prominent in the 500 ppmw Dy^{3+} fibre than the 1000 ppmw Sm^{3+} fibre, meaning less oxide impurities have been introduced. A counterpoint is that it may also partially reflect on the proclivity of rare earth elements to oxidise. It is possible that doped rare earth ions act to effectively getter oxide impurities in a glass during melting. If the oxygen is bonded to a rare earth ion, it will not present as a Ge-O absorption. Although, if this was entirely the case, it would be expected that the higher dopant concentration of 1000 ppmw Sm^{3+} $Ge_{19.4}Sb_{9.7}Se_{67.9}Ga_3$ at. % unstructured fibre (F099RERC) would lead to a smaller Ge-O band compared to the 500 ppmw Dy^{3+} doped $Ge_{19.4}Sb_{9.7}Se_{67.9}Ga_3$ at. % unstructured fibre (F104RERC), which is not the case presented here. With both the 500 ppmw Dy^{3+} doped $Ge_{19.4}Sb_{9.7}Se_{67.9}Ga_3$ at. % unstructured fibre and 1000 ppmw Sm^{3+} $Ge_{19.4}Sb_{9.7}Se_{67.9}Ga_3$ at. % unstructured fibre presented in this chapter undergoing identical fabrication procedures but producing fibres with differing background losses and impurity absorption peaks, it is likely that the dopant has a noticeable effect on fibre properties. This may be through the introduction of different levels of impurities or may be related to solubility/devitrification issues.

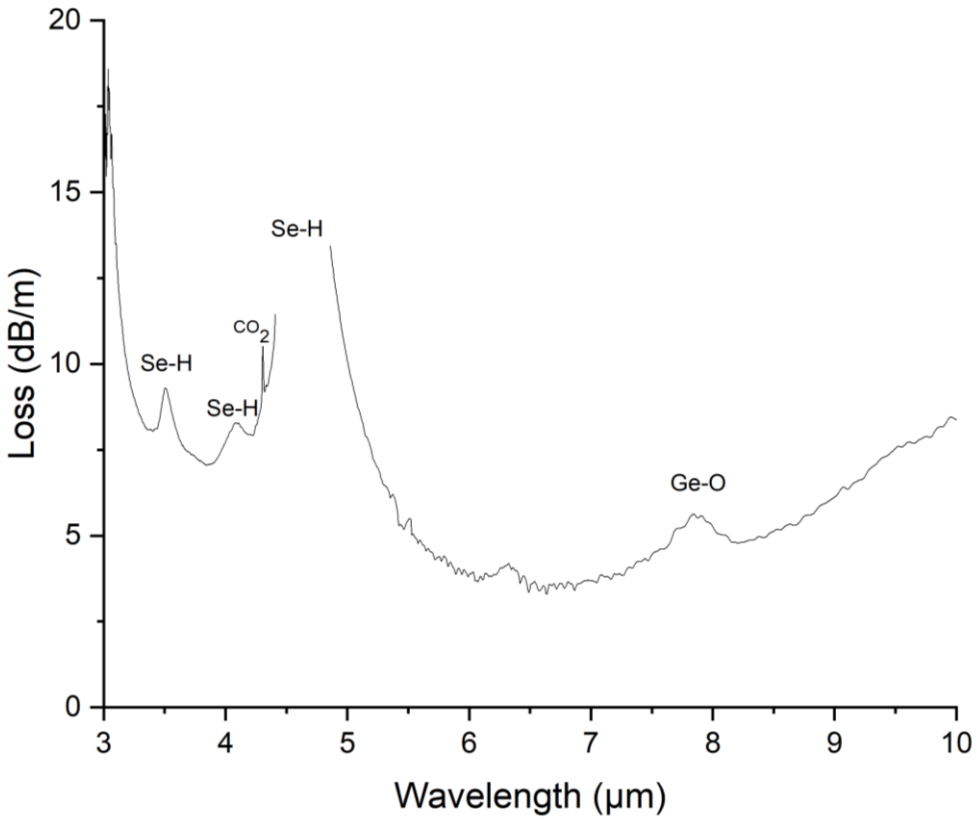


Figure 4.18 Mid-IR optical loss of 500 ppmw Dy^{3+} foil doped $Ge_{19.4}Sb_{9.7}Se_{67.9}Ga_3$ at. % unstructured fibre (F104RERC). Extrinsic impurity absorptions identified. Omission of data at 4.4-4.9 μm due to large extrinsic [H-Se-] absorption. Noise beyond 5 μm attributed to detector.

4.4 Summary of chapter 4.

Chapter 4 detailed the development of an antimony-based host glass system ($Ge_{19.4}Sb_{9.7}Se_{67.9}Ga_3$ at. %) which demonstrated good fibre drawing capability. This composition retained its fibre drawing capability when doped with up to 1000 ppmw Sm^{3+} in foil form. Below are key points of the chapter summarised:

- Undistilled $Ge_{20}Sb_{10}Se_{65}Ga_5$ at. % was not suitable for fibre drawing when doped with 1000 ppmw Sm^{3+} foil (M226RERC). Extensive crystallisation attributed to $GeSe_2$ was observed that prevented fibre drawing. Other groups utilising this composition report using distillation procedures to increase glass purity which may decrease the probability of heterogenous nucleation and subsequent crystallisation.

- Undistilled, undoped $Ge_{19.4}Sb_{9.7}Se_{67.9}Ga_3$ at. % (T_g 232 °C) (M235RC) was successfully drawn to low loss fibre (1.17 dB/m at 6.19 µm) (F101RC). The $Ge_{19.4}Sb_{9.7}Se_{67.9}Ga_3$ at. % composition was conceptually derived from the $Ge_{20}Sb_{10}Se_{70}$ glass documented in Parnell *et al.* [54].

- Undistilled, $Ge_{19.4}Sb_{9.7}Se_{67.9}Ga_3$ at. % retained its fibre drawing properties following doping with 1000 ppmw Sm^{3+} in foil form (M227RERC). A resulting fibre (F099RERC) with lowest losses of 2.15 db/m at 6.04 µm was fabricated[19].

- Photoluminescent emissions at 3.75 µm (photoluminescent lifetimes measured between 0.100 - 0.102 ms) and 7.25 µm (photoluminescent lifetimes measured between 0.0971 – 0.104 ms) were observed when pumping 1000 ppmw Sm^{3+} doped $Ge_{19.4}Sb_{9.7}Se_{67.9}Ga_3$ at. % fibre (F099RERC) at 1.3 µm and 1.47 µm[19].

- The 7.25 µm Sm^{3+} emission in 1000 ppmw Sm^{3+} doped $Ge_{19.4}Sb_{9.7}Se_{67.9}Ga_3$ at. % fibre (F099RERC) was the longest photoluminescence wavelength recorded by the Mid-IR Photonics Group, University of Nottingham, UK, and exceeding the 6 µm emission observed in GeAsSeGa and GeAsSeIn glasses doped with Pr^{3+} (Sakr *et al.*[86,94]).

- Doping an undistilled $Ge_{19.4}Sb_{9.7}Se_{67.9}Ga_3$ at. % preform with 1000 ppmw Dy^{3+} (M236RERC) yielded a poor optical quality fibre that was unable to be characterised (F102RERC). The dopant concentration was then reduced to 500 ppmw Dy^{3+} in a separate $Ge_{19.4}Sb_{9.7}Se_{67.9}Ga_3$ at. % preform (M240RERC) which was drawn to unstructured fibre (F104RERC) with lowest losses around 3.2 dB/m at 6.6 µm.

- It is proposed that doping was possible with 1000 ppmw Sm^{3+} but not 500 ppmw Dy^{3+} due to differences between the dopants. The current Author suggests this may be related to chemical purity of the rare earth dopant

sources or solubility/devitrification of the element in the glass. This may further explain the lowest losses of F104RERC (500 ppmw Dy^{3+} $Ge_{19.4}Sb_{9.7}Se_{67.9}Ga_3$ at. %) (3.2 dB/m at 6.6 µm) being higher than the lowest losses of F099RERC (1000 ppmw Sm^{3+} doped $Ge_{19.4}Sb_{9.7}Se_{67.9}Ga_3$ at. %) (2.15 db/m at 6.04 µm), despite the lower dopant concentration of 500 ppmw Dy^{3+} in F104RERC (compared to 1000 ppmw Sm^{3+} in F099RERC).

5. Development of antimony-based selenide chalcogenide cladding to clad antimony-based selenide rare earth ion doped core glass, aiming to make small-core fibre.

Chapter 4, Sections 4.2 and 4.3, presented the experimental work carried out during the Project to develop an unstructured, relatively low optical loss, core-glass fibre capable of being rare earth ion doped *i.e.* 1000 ppmw Sm^{3+}-doped $Ge_{19.4}Sb_{9.7}Se_{67.9}Ga_3$ at. % (Fibre code: F099RERC, lowest loss of 2.15 dB/m at 6.04 µm, Figure 4.7) and Dy^{3+}-doped $Ge_{19.4}Sb_{9.7}Se_{67.9}Ga_3$ at. % (Fibre code: F104RERC, lowest loss of 3.2 dB/m at 6.6 µm, Figure 4.18).

However, the overarching aim of the Project being the production of a chalcogenide glass, long-wavelength mid-IR fibre laser, for applications like new laser medical surgery, and for this a rare earth ion doped small-core, step-index fibre is essential. Thus, the next step in the development of long wavelength fibre lasers was to make a glass suitable to clad the dopable core glass presented in Chapter 4. Here in chapter 5, the process of identifying a new cladding glass, suitable for the $Ge_{19.4}Sb_{9.7}Se_{67.9}Ga_3$ at. % core glass is described. A series of glasses were fabricated and then characterised *via* differential scanning calorimetry (DSC) to assess the suitability of the composition's thermal characteristics to act as a cladding glass for $Ge_{19.4}Sb_{9.7}Se_{67.9}Ga_3$ at. %. Once compositions with suitable T_g values were identified, mid-IR VASE (Variable Angle Spectroscopic Ellipsometry) was used to assess the viability of the glasses optical properties to ensure a theoretical structured fibre would light guide in its core glass.

Section 5.1 begins with an explanation of the properties required for a composition to be used as a cladding glass for a predefined core composition. It then details the initial attempts to fabricate a small core fibre using a composition that was found to have insufficient devitrification resistance. Section 5.2 details the different glass compositions that were investigated as potential cladding glasses. Differential scanning calorimetry (DSC) was used to measure the T_g of novel prospective cladding compositions as a preliminary indicator of compatibility with the core. The refractive indices of these cladding glasses were then determined using mid-IR

ellipsometry with an in-house developed model and numerical aperture of potential fibres were calculated (see Section 5.3 and 5.4 below).

5.1 Requirements of cladding glass to be developed for core glass: rare earth ion doped $Ge_{19.4}Sb_{9.7}Se_{67.9}Ga_3$ at. %

The cladding glass for the core glass: rare earth ion doped $Ge_{19.4}Sb_{9.7}Se_{67.9}Ga_3$ at. % required certain material properties in order to be a suitable cladding for a small core fibre with potential for lasing. Firstly, the cladding glass required a closely matched glass transition temperature (T_g) to the already developed core glass, to try to avoid the introduction of any permanent stress in the preform and fibre during thermal processing to make them. In addition, the viscosity-temperature profile of the cladding glass was required to be closely matched to that of the core glass if it was to be a suitable candidate for fibre drawing; this is so that both glasses reach a fibre drawing viscosity ($>10^{4.5}$ Pa·s) of their supercooled melts at similar temperatures. If these are not closely matched, one glass may begin to draw while the second glass is at too high a viscosity to draw. Furthermore, the cladding glass and core glass thermal expansion coefficients (α) should be close, or at least $\alpha_{core} \geq \alpha_{cladding;}$ a larger α_{core} than $\alpha_{cladding}$ would mean that the cladding glass of the fibre and preform would tend to be in compression and hence the outer surface of preform or fibre held in compression and so 'thermally toughened' giving closure to Griffith flaws and a kind of protective armour to offset inadvertent mechanical damage, leading to higher fibre and preform Ultimate Fracture Stress (UFS). Finally, the core glass should have a larger refractive index than the cladding glass to be developed, to allow predetermined wavelengths of mid-IR light to waveguide in the core fibre and the refractive index dispersion of each glass be amenable to create suitable numerical aperture (NA) lasing fibre.

Previous work on step-index chalcogenide glass fibres in the University of Nottingham, UK, Mid-IR Photonics Group had primarily used low (1-3) at. %. additions of sulfur to compositions similar to the core glass to create a cladding with lower refractive index. This is a result of the smaller sulfur atom having electrons closer to the nucleus, than the larger selenium atom. This confers a lower polarisability as the volume of space taken up by the S electrons is smaller than that of Se electrons. It is this change in polarisability that is linked to the change in

refractive index[188]. As S and Se occupy the same structural niche in the glassy network, incorporating the two elements should provide a change in refractive index, while minimising changes to the glass matrix. Introducing sulfur to a composition could be as simple as a straight substitution of selenium for sulphur [189] or may involve alterations to each constituent element to accommodate the sulphur [94,110]. Research from others such as Wang *et al.* [190] also found success with introducing sulfur to a composition ($Ge_{15}Sb_{20}Se_{65-x}S_x$ (with x = 0, 16.25, 32.5, 48.75, and 65)) to decrease refractive index (RI), with increasing sulfur content leading to decreasing RI [190]. Whereas Zhang *et al.* altered germanium content to manipulate refractive index ($Ga_{(8-x)}Ge_xSb_{32}S_{60}$ (x= 0, 2, 4, 6, 8) with increasing germanium content in lieu of gallium leading to further decreases to RI [91].

5.1.1 Composition tailoring of the cladding glass for T_g matching to core glass $Ge_{19.4}Sb_{9.7}Se_{67.9}Ga_3$ at. %

During the designing of a new cladding composition, the first assessment of suitability was carried out with differential scanning calorimetry (DSC). A DSC measurement could be done comparatively quickly (relative to mid-IR ellipsometry) and would provide information on if the composition could be fibre drawn alongside the $Ge_{19.4}Sb_{9.7}Se_{67.9}Ga_3$ at. % core glass composition. If the T_g discrepancy was too high (see below paragraph), the composition could not be used as a cladding glass for $Ge_{19.4}Sb_{9.7}Se_{67.9}Ga_3$ at. %.

The initial target of this work was to closely match T_g 232 °C (± 10 °C) of the host core glass: $Ge_{19.4}Sb_{9.7}Se_{67.9}Ga_3$ at. % and any potential cladding compositions. As mentioned in Section 2.2, T_g is an isoviscous point in which the viscosity of the material is $10^{12.5}$ Pa·s. To fibre draw, these glasses must be heated until a viscosity $<10^{4.5}$ Pa·s is reached[191,192].

This target value of T_g (±10 °C) was derived from the work of Dr Harriet Parnell, (previously of the Mid-IR Photonics Group, University of Nottingham, UK), in which a $Ge_{20}Sb_{10}Se_{70}$ at. % core glass (Fibre code: F_HAP008, T_g 214 °C) was successfully fibre drawn with a $Ge_{20}Sb_{10}Se_{67}S_3$ at. % cladding glass (Fibre code: F_HAP004, T_g 224 °C)[193]. Using viscosity-temperature measurements, Parnell *et al.* [193] found that the $Ge_{20}Sb_{10}Se_{70}$ at. % core glass reached the fibre drawing

viscosity at 357.8 ±0.7 °C and the $Ge_{20}Sb_{10}Se_{67}S_3$ at. % cladding glass at 361.9 ±0.3 °C, a difference approximating 4 °C. As these glasses went on to be successfully co-extruded and subsequently successfully fibre drawn to a large core, step-index fibre (SIF), therefore the 10 °C Δ (224 °C – 214 °C) in T_g was proposed as a benchmark difference in T_g which would lead to extrusion-compatible (for co-extrusion) and fibre drawing-compatible core and cladding glasses for making SIFs. However, this approximation disregards the potential that changing compositional elements other than sulfur (e.g., germanium, antimony, or gallium) may have a different impact on the change in temperature-viscosity values.

Therefore, here, in this work, the DSC measured T_g of this exploratory cladding glass was very roughly assumed also to give an indication of the viscosity-temperature relationship of the core glass and the cladding glass, and these were assumed to have close extrusion and fibre drawing temperatures simply because they have close T_gs. If the T_g of a newly created cladding glass was outside this ±10 °C range, the composition was deemed unsuitable for use as a cladding glass with the $Ge_{19.4}Sb_{9.7}Se_{67.9}Ga_3$ at. % core. However, it must be noted that this is a gross oversimplification as it assumes that the 'fragility' of each supercooled liquid is the same, as follows.

The fragility of a glass melt is defined as the rate of change of viscosity with temperature and is a concept devised by Angell [194]. So, although T_g may be matched, it is not necessarily true that the extrusion and fibre-drawing viscosities will be matched in temperature, as ideally they should be, of the core and cladding glasses. Angell presents a universal plot of $\log_{10}$ (viscosity) *versus* reduced temperature (*i.e.* (T_g/K / T/K) on which all glass forming melts lie. As T_g is a universal viscosity point, all glasses are coincident at the reduced T_g (=1) [194] (Figure 5.1). In relation to chalcogenide-based glasses, Figure 5.2 shows a similar universal plot, comparing GeSI chalcohalide glasses with silica and ZBLAN[195].

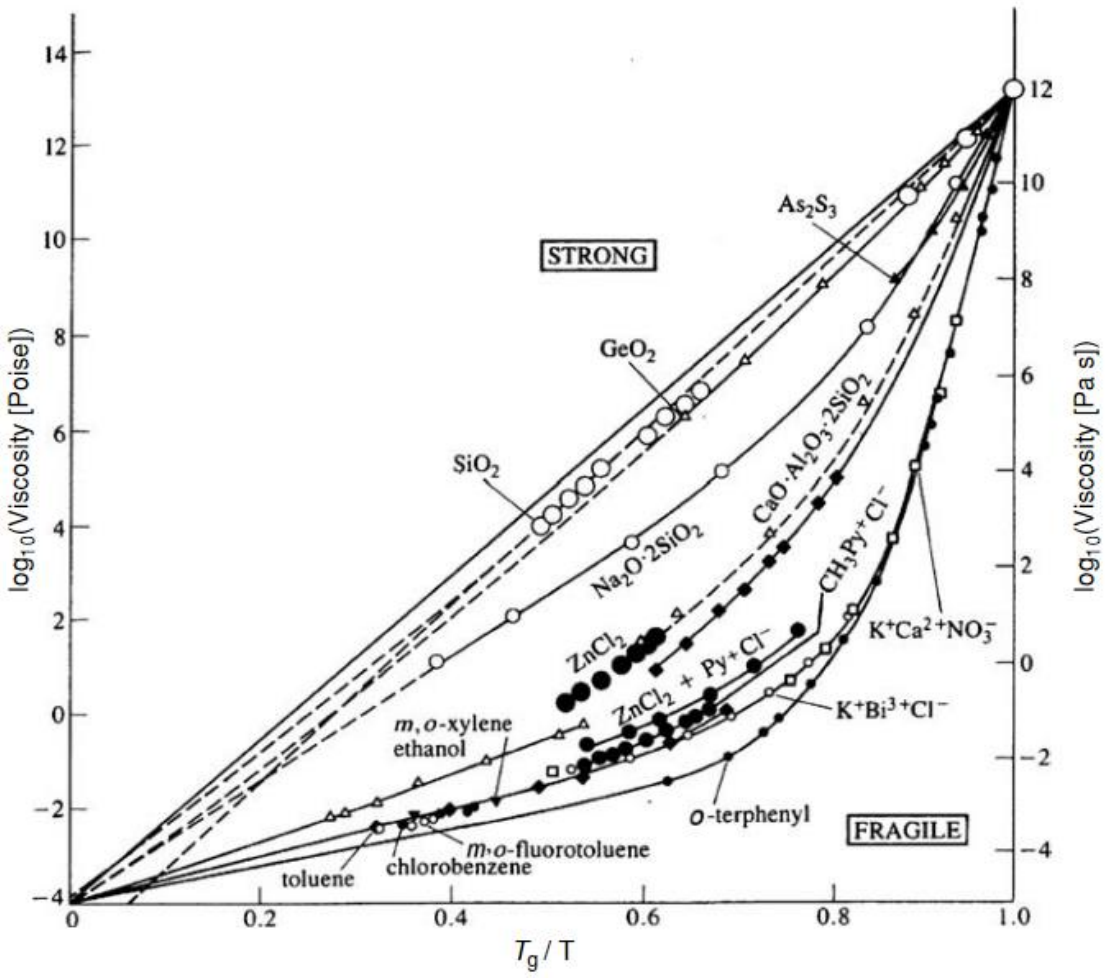


Figure 5.1 To illustrate the Angell concept of fragility: "Viscosities of a variety of glass-forming systems as a function of reduced reciprocal temperature (Kelvin)Tg/T, where T_g is defined as the temperature when the viscosity=10^{12} Pa s". Graph taken from [194]*, figure caption from* [72] .

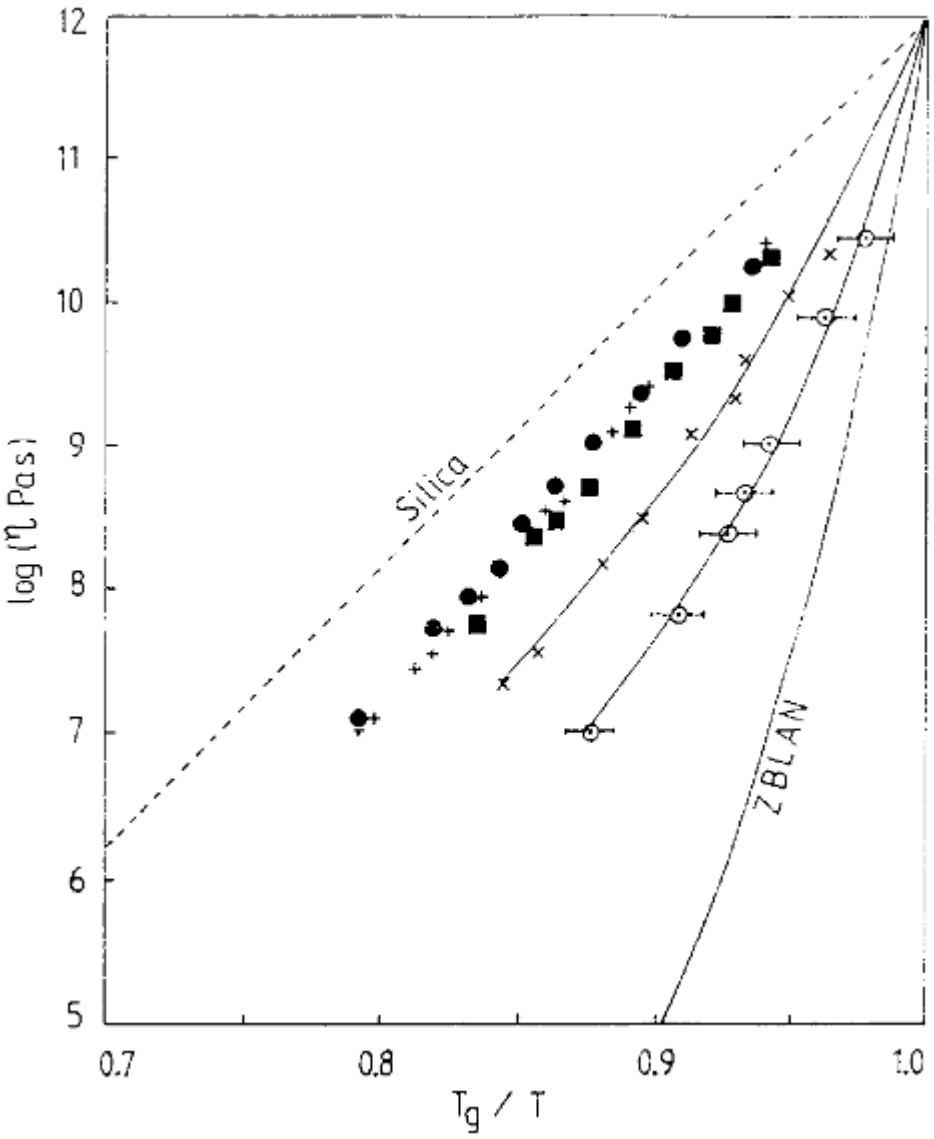


Figure 5.2 As Figure 5.1, the figure is illustrative of Angell's concept of fragility [194]. *Viscosities of a GeSI chalcohalide, silica, and ZBLAN glass-forming systems as a function of reduced reciprocal temperature (Kelvin)Tg/T, where T_g is defined as the temperature when the viscosity=10^{12} Pa s. Graph taken from* [195].

Figure 5.1 is described by Furniss and Seddon [72] as follows, "silica glass-forming liquid exhibits one extreme of behaviour, the plot being almost linear. As the temperature is raised above T_g, the silica liquid becomes more fluid; the atomic units which flow past one another under shear become smaller, but the mechanism of shear remains cleavage of silica bridging chemical bonds (≡Si-O-Si≡) of covalent character, successively increasingly broken in number as the temperature is increased. This accounts for the linearity (Arrhenian) of the silica plot. Silica is

described by Angell as a strong liquid, meaning a 3-dimensional, mutually supporting strongly covalently bonded liquid. In direct contrast, multicomponent fluorozirconate ionic liquids experience a catastrophic breakdown of the lattice just above T_g and consequent large fall in viscosity; they are termed fragile liquids. The multicomponent fluorozirconate glass lattice is composed of a variety of relatively weak chemical bonds and as the temperature is increased above T_g, stronger chemical bonds are successively broken under shear, accounting for the nonlinear $\log_{10}$ viscosity/ reduced temperature behaviour. It is worth pointing out that many of the novel inorganic compound glasses being developed relatively recently exhibit more fragile behaviour than silica, implying rigorous temperature control is thus a prerequisite for shaping operations." [72].

Considering the above arguments on glass fragility, initial work to produce a suitable cladding glass for the $Ge_{19.4}Sb_{9.7}Se_{67.9}Ga_3$ at. % core glass composition led to the design of a $Ge_{19.4}Sb_{9.7}Se_{65}Ga_3S_{2.9}$ at. % (Melt code designation: M237RC) cladding glass composition which failed to draw to fibre. The theory behind the composition design and fibre drawing process is elaborated upon in Section 5.1.2.1, below.

Following the failure to fibre draw $Ge_{19.4}Sb_{9.7}Se_{65}Ga_3S_{2.9}$ at. % (M237RC), a series of glasses was made based on the $Ge_{19.4}Sb_{9.7}Se_{67.9}Ga_3$ at. % core glass composition. The first three samples, (M262RC-M264RC, Table 5.1 for compositions) all included the addition of 1-2 at. % sulfur, substituting the S for the Se, while trying to reduce the gallium in the glass composition to 1-2 at. %, also by substituting the Ga for the Se. The series can be described as Series (i) $Ge_{19.4}Sb_{9.7}Ga_{1-2}Se_{67.9-(Ga+S)}S_{1-2}$ at %.

For the next series, Series (ii), the first two glasses (M265RC and M266RC, Table 5.1 for composition) followed a $Ge_{19.4}Sb_{9.7}Ga_{2-3}Se_{67.9-(Ga)}S_2$ at % formula. This had sulfur content fixed at 2 at. % and selenium substituted for gallium at 2-3 at. %. This design was to increase the cladding glass composition T_g using gallium following feedback from Series (i) as Series (i) glasses exhibited T_gs below the 232 ±10 °C T_g target to match the $Ge_{19.4}Sb_{9.7}Se_{67.9}Ga_3$ at. % core glass composition, as further elaborated through Section 5.2.2. A final attempt in Series (ii) was then made to remove sulfur and gallium entirely from the glass (M267RC, Table 5.1 for

composition) while also maintaining a close T_g to the $Ge_{19.4}Sb_{9.7}Se_{67.9}Ga_3$ at. % core composition (232 ±10 °C), again, further elaborated in Section 5.2.2.

5.1.2 Substitution of 3 at.% selenium with 3 at. % sulfur in the $Ge_{19.4}Sb_{9.7}Se_{67.9}Ga_3$ at. % core glass composition, to form a lower refractive index cladding glass with the composition: $Ge_{19.4}Sb_{9.7}Se_{65}Ga_3S_{2.9}$ at. %

5.1.2.1 Philosophy of Composition design and glass melting of $Ge_{19.4}Sb_{9.7}Se_{65}Ga_3S_{2.9}$ at. % (M237RC)

As stated in Section 4.1, the $Ge_{19.4}Sb_{9.7}Se_{67.9}Ga_3$ at. % RE ion dopable core composition was actually based on ideas enacted for a $Ge_{20}Sb_{10}Se_{70}$ at. % glass detailed in [54,183,193]; thus, from initial work on $Ge_{20}Sb_{10}Se_{70}$ at. % in [196], a successful step-index fibre with a numerical aperture (NA) of 0.26 over the 3-15 µm wavelength region was made with a $Ge_{20}Sb_{10}Se_{70}$ at. % core and a $Ge_{20}Sb_{10}Se_{67}S_3$ at. % cladding (3 at. % S for 3 at. % Se from core to cladding glass) as reported in Parnell *et al.* [189,193]. In the current work, here, the cladding for the core glass: $Ge_{19.4}Sb_{9.7}Se_{67.9}Ga_3$ at. % was also designed with a straight S for Se atomic substitution and glass melting for of the cladding glass: $Ge_{19.4}Sb_{9.7}\mathbf{Se_{65}}Ga_3\mathbf{S_{2.9}}$ at. % (Code M237RC) was trialled, as now follows.

Thus, a large boule (~70 g, 26.5/30 mm = ID/OD (internal diameter/outer diameter) mm ampoule) of the sulfur doped selenide chalcogenide glass of composition of $Ge_{19.4}Sb_{9.7}\mathbf{Se_{65}}Ga_3\mathbf{S_{2.9}}$ at. % (Code: M237RC) was melted for 12 hours at 900 °C as specified in Table 3.6. A large boule was made so the resulting glass could be extruded to a jacket cladding tube (extrusion details in Section 3.2.8) which could then be drawn cane-in-tube (cane of core glass: RE ion doped $Ge_{19.4}Sb_{9.7}Se_{67.9}Ga_3$ at. %) to a structured, step-index (SIF) fibre (fibre drawing details in Section 3.2.9). The design of this cladding composition aimed to mirror the 3 at. % S for Se substitution reported in [189,193] for the core /cladding $Ge_{20}Sb_{10}Se_{70}$ at. % / $Ge_{20}Sb_{10}Se_6S_3$ at. %. As this cladding glass was a new composition, an estimate of T_g was made for annealing. As discussed by Wang *et al.*[190] and Savage *et al.* [197],

substituting the atomically smaller, lower RAM sulfur for selenium was expected to increase the T_g. This can be explained because for the chalcogen Group of the Periodic Table, the smaller sulfur atom has bonding electrons closer to the nucleus, than the larger selenium atom, and so sulfur forms stronger bonding than selenium; a more strongly bonded network glass exhibits a higher T_g. Work from Parnell *et al.* [183,193] (previously of the Mid-IR Photonics Group, University of Nottingham, UK) found that a substitution of 3 at. % S for Se ($Ge_{20}Sb_{10}Se_{70}$ at. % to $Ge_{20}Sb_{10}Se_{67}S_3$ at. %) corresponded with a 10 °C increase in T_g, raising it from 214 °C to 224 °C. Therefore, as the new glass composition here: $Ge_{19.4}Sb_{9.7}Se_{65}Ga_3S_{2.9}$ at. % was close to that glass composition $Ge_{20}Sb_{10}Se_{67}S_3$ at. %, a T_g of 242 °C ($Ge_{19.4}Sb_{9.7}Se_{67.9}Ga_3$ at. % T_g 214 °C + 10 °C) was 'guestimated' for using, and the new cladding glass composition was annealed at 242 °C.

Following this annealing, of the 70 g cladding glass $Ge_{19.4}Sb_{9.7}Se_{65}Ga_3S_{2.9}$ at. % (M237RC), the ~ 50 mm long, 26.5 mm cross-sectional diameter, chalcogenide glass rod boule was removed from the silica glass melt ampoule and the top ~ 10 mm section, including the contraction cone, was removed using the low-speed saw and some of that glass was prepared for DSC (sample preparation was explained in Section 3.3.1), as discussed in the next section 5.1.2.2.

5.1.2.2 DSC for T_g of $Ge_{19.4}Sb_{9.7}Se_{65}Ga_3S_{2.9}$ at. % (M237RC)

The three DSC consecutive isochronal runs on the same sample returned an average T_g of 232.7 °C (Figure 5.3) therefore the same T_g of ~ 232 °C was found both for the newly made cladding glass ($Ge_{19.4}Sb_{9.7}Se_{65}Ga_3S_{2.9}$ at. %, Melt code: M237RC) as also found for the doped antimony core glass ($Ge_{19.4}Sb_{9.7}Se_{67.9}Ga_3$ at. %, Melt code: M240RERC) (compare Figures 4.3 and 5.3). However, this T_g result meant that the 'guestimated' annealing temperature for the cladding glass: $Ge_{19.4}Sb_{9.7}Se_{65}Ga_3S_{2.9}$ at. %, Melt code: M237RC at 242 °C had been too high by 10 °C and this may have led to unwanted nucleation occurring in this cladding glass boule during its annealing process.

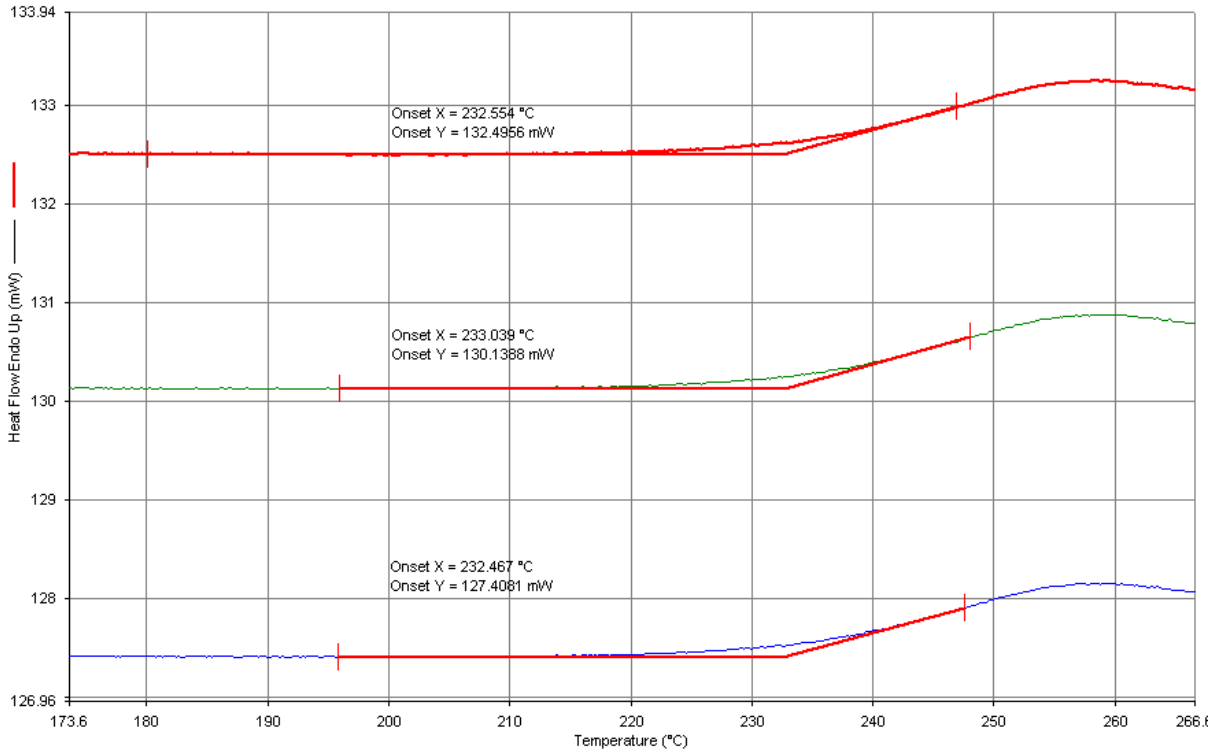


Figure 5.3 Three consecutive DSC cycles at 10 °C/min heating and cooling of a 9 mg sample of $Ge_{19.4}Sb_{9.7}Se_{65}Ga_3S_{2.9}$ at. % (M237RC) showing an average T_g onset of 232.686 °C +0.352/ -0.219 °C, rounded to 232.7 °C. Cycle 1 measurement excluded (due to the different sample thermal history of melt-cool and annealing at 'guestimated' annealing temperature), Cycle 2 blue, Cycle 3 in green, Cycle 4 in red. Sample was annealed at a provisional T_g of 242 °C due to no previous knowledge of T_g. Sample preparation and interpretation elaborated in section 3.3.1.

5.1.3.2 Extrusion of outer cladding tube: cladding glass: $Ge_{19.4}Sb_{9.7}Se_{65}Ga_3S_{2.9}$ at. % (M237RC) (to clad cane of core glass: $Ge_{19.4}Sb_{9.7}Se_{67.9}Ga_3$ at. % + 500 ppmw Dy foil (M240RERC)).

Although no refractive index data had been obtained for the cladding composition whose synthesis was discussed in the previous Section 5.1.3.1: $Ge_{19.4}Sb_{9.7}Se_{65}Ga_3S_{2.9}$ at. %, Melt code: M237RC, preparations were made to extrude the as-annealed boule to a cladding tube in preparation for cane-in-rod fibre drawing to make step index fibre of core/cladding = $Ge_{19.4}Sb_{9.7}Se_{67.9}Ga_3$ at. % + 500 ppmw Dy foil (M240RERC)/ $Ge_{19.4}Sb_{9.7}Se_{65}Ga_3S_{2.9}$ at. %, (M237RC). To extrude the cladding tube, the extrusion furnace was set to 320 °C (temperature values approximated to those used for $Ge_{20}Sb_{10}Se_{67}S_3$ at. % in [193]). Although the

top 10 mm including the contraction cone was removed with the low-speed saw, the boule was inserted into the extruded with this top portion facing up. This would mean the top half of the boule would be the last portion of glass to exit the extruder, which was deemed the safer situation, as at the contraction cone is anticipated to contain agglomerated impurities with lower density than the chalcogenide melt, which rise to the top of the melt during vertical melt refining (see Table 3.6 and Section 3.2.4). A starting load of 200 kg was ramped to 500 kg and the boule was extruded to a 130 mm length jacket tube with an OD of 9.84 mm and an ID of ≈ 1 mm. A dry nitrogen flow was introduced from the base of the extruder to minimise oxidative changes to the glass when heated above T_g. Further details of the extrusion process are in Section 3.2.8.

The bore of the jacket tube appeared to be concentric and had a straight tube geometry throughout the length of the tube, as judged by visually looking through the tube at ambient light coming through the bore. A UV (ultraviolet) curable resin was then applied to one end of the tube and was adhered to an aluminium preform holder (Figure 3.4) and left to cure under ambient temperature for 24 hours. Following application of the resin, the chalcogenide glass tube was stored under vacuum in a glovebox antechamber (0.5-1 mbar, 50-100 Pa). This aluminium holder had a ~ 8 mm bore, keeping both ends of the cladding tube open. The fibre drawing process would be terminated before the aluminium holder and resin moved too close to the fibre tower heating elements, so risk of contamination *via* volatilisation of aluminium or polymer, or its additives was deemed to be minimal.

5.1.3.3 Drawing of fibre from cane-in-tube (*i.e.* cane of core glass: $Ge_{19.4}Sb_{9.7}Se_{67.9}Ga_3$ at. % + 500 ppmw Dy foil (F104RERC, M240RERC) in tube of cladding glass: $Ge_{19.4}Sb_{9.7}Se_{65}Ga_3S_{2.9}$ at. % (M237RC)

As described in Section 4.3.2, a cane had been fabricated of M240RERC ($Ge_{19.4}Sb_{9.7}Se_{67.9}Ga_3$ at. % + 500 ppmw Dy foil) (Table 3.1 for sources and purity) with a nominal diameter of 950 µm (now termed F104RERC). This cane had been stored, for approximately one month, in the inert, dry nitrogen (BOC, 99.998%) atmosphere of a glovebox (MBraun 150B-G, ≤1 ppm H_2O and ≤1 ppm O_2) to minimise any oxidation effects that could have occured on the cane surface. The F104RERC cane was propylamine etched by full immersion in propylamine (Table

3.2 for sources and purity) for 24 hours at ambient temperature, under ambient atmosphere, under dust cover. The F104RERC cane was then washed in acetone and isopropanol (Table 3.2 for sources and purity) and dried under vacuum at around 0.5-1 mbar (50-100 Pa) in a glovebox antechamber (see above) for 30 minutes. This cane preparation of F104RERC (drawn from melt M240RERC) ($Ge_{19.4}Sb_{9.7}Se_{67.9}Ga_3$ at. % + 500 ppmw Dy foil) was performed in conjunction with the cladding glass extrusion. That is, as the M237RC cladding glass was being extruded, the cane of F104RERC was immersed in propylamine for etching. Thus, the 950 μm OD cane of F104RERC ($Ge_{19.4}Sb_{9.7}Se_{67.9}Ga_3$ at. % + 500 ppmw Dy foil, M240RERC) was then inserted through the bore of the aluminium holder (see previous Section 5.1.3.2 where installment of this holder around the tube was described) and into the ~ 1mm diameter orifice of the jacket tube (M237RC, $Ge_{19.4}Sb_{9.7}Se_{65}Ga_3S_{2.9}$ at. %) in preparation for fibre drawing. Full details on the fibre drawing procedure, including preform preparation and heating methods are detailed in Section 3.2.9.

As the rod-in-tube preform was heated to the fibre drawing temperature, on the fibre draw tower, a slight skin began to form on the outer surface of the jacket tube. The preform gob initially dropped, as expected, but the resulting fibre broke almost immediately. A second and third attempt were made by extending more of the preform into the hot zone of the draw tower, each time resulting in an extremely fragile fibre which was incapable of being drawn and wound onto a drum. At this point it was determined that the composition was unsuitable for fibre drawing and the fibre drawing was aborted. As explained in Section 4.1.2, the skin like effect that was hypothesised to be primarily attributed to $GeSe_2$. However, the skin-forming effects observed on the M237RC ($Ge_{19.4}Sb_{9.7}Se_{65}Ga_3S_{2.9}$ at. %) cladding tube during the attempted fibre draw appear to be much more severe, in the sense that the skin effects were more prevalent on the surface and led to breaking of the fibre during drawing, than that seen in Section 4.1.2, with the undistilled 1000 ppmw Sm^{3+} $Ge_{20}Sb_{10}Se_{65}Ga_5$ at. % preform (M226RERC). This skin effect leading to fibre failure was also documented by Parnell *et al.*[54] as shown in Figure 5.4(A,C,D) from [54] in a $Ge_{25}Sb_{10}Se_{65}$ composition of which the Authors hypothesised the aforementioned composition had poor thermal stability and poor devitrification resistance. Thus, to recap the discussion in Section 4.1.2, it is

proposed that the cladding tube composition of M237RC ($Ge_{19.4}Sb_{9.7}Se_{65}Ga_3S_{2.9}$ at. %) has poor devitrification resistance similar to what was seen in M226RERC ($Ge_{20}Sb_{10}Se_{65}Ga_5$ at. %, Section 4.1.2) and crystalline formations were nucleated and grew (Section 2.2.3 and 2.2.4) during the thermal working above T_g (232 °C) during the extrusion (320 °C) and then again during the subsequent fibre draw (T_g + ~150°C for fibre drawing viscosity ($10^{4.5}$ Pa·s) [54]) resulting in a cane-in-tube preform with poor fibre drawability.

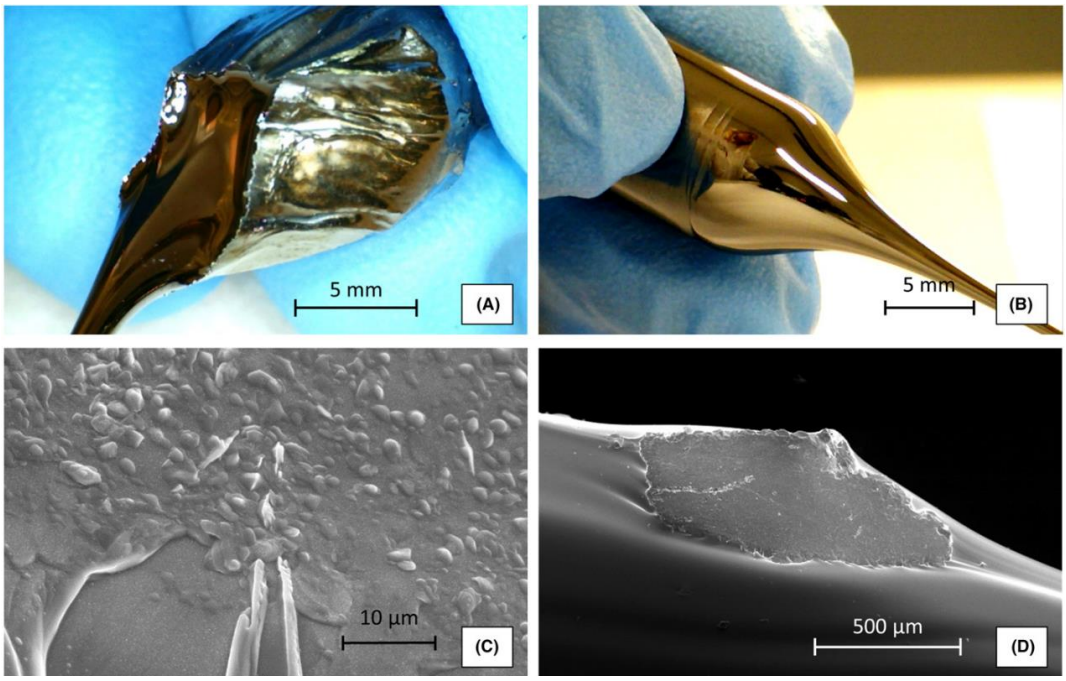


Figure 5.4 "A) stoichiometric $Ge_{25}Sb_{10}Se_{65}$at. % preform imaged after fibre-drawing; (B) non-stoichiometric $Ge_{20}Sb_{10}Se_{70}$at. % preform imaged after fibre-drawing; (C) and (D) SEM micrographs of sections of the "skin-like" layer which had detached from the bulk of the $Ge_{25}Sb_{10}Se_{65}$at. % preform onto the fibre". Caption and image from Parnell et al.[54].

5.2 Series (i) and Series (ii) of exploratory cladding glass compositions: Alterations to sulphur, selenium, germanium, and gallium content of $Ge_{19.4}Sb_{9.7}Se_{67.9}Ga_3$ at. % in designing a drawable cladding glass

From the previous Section 5.1.3.3, the poor-quality fibre drawing of the $Ge_{19.4}Sb_{9.7}Se_{65}Ga_3S_{2.9}$ at. % (M237RC) cladding tube was reminiscent of what was observed in the 1000 ppmw Sm^{3+} $Ge_{20}Sb_{10}Se_{65}Ga_5$ at. % (M226RERC) work detailed in Section 4.1.2. Both glasses had failed to fibre draw upon the formation of a surface skin-layer on the preform during the heating stage of fibre drawing that work from Parnell *et al.* suggests is crystalline[54].

Note also that previous work [55,133] had shown that gallium was the predominant element involved in devitrification of $Ge_{16.5}As_{(19-x)}$ $Ga_xSe_{64.5}$ at. % fibres and as-annealed bulk glass samples, through the development of modified, face centred cubic α-Ga_2Se_3 and α-Ge_2Se_3. X-ray diffractometry identified face centred cubic α-Ga_2Se_3 peaks in both powdered bulk and powdered fibre samples, with high resolution transmission electron microscopy (TEM) and energy dispersive X-ray spectroscopy (EDX) elemental analysis also corroborating the present of Ga_2Se_3 in fibre samples [55,133].

Therefore, compositions with decreased gallium content were next designed with the intention of decreasing the probability of unwanted crystallisation of the cladding glass during fibre drawing. This followed the same vein as work in Tang *et al.* in which no α-Ga_2Se_3 peaks were identified using X-ray diffraction (XRD) measurements following a decrease in gallium content from 10 at. % to 3 at. % following the composition formula $Ge_{16.5}As_{(19-x)}$ $Ga_xSe_{64.5}$ at. % [55,133]. With α-Ga_2Se_3 being the prominent crystal structure present in the bulk glasses produced by Tang *et al.*, it was hypothesised that by reducing Ga from 10 at. % to 3 at. % in the $Ge_{16.5}As_{(19-x)}$ $Ga_xSe_{64.5}$ at. % formula would lead to decreased devitrification. Glasses with the $Ge_{16.5}As_{16}Ga_3Se_{64.5}$ at. % composition exhibited no α-Ga_2Se_3 XRD peaks, although 20-150 nm sized crystals were identified in $Ge_{16.5}As_{16}Ga_3Se_{64.5}$ at. % doped with 3000 ppmw $DyCl_3$ [55,133].

The substitution of gallium for selenium in $Ga_xGe_{25}As_{15}Se_{60-x}$ (x = 0-5) compositions has been shown to increase the refractive index of the resulting fibres from 2.5164 at 2.0 µm in $Ge_{25}As_{15}Se_{60}$ to 2.585 at 2.0 µm in $Ga_5Ge_{25}As_{15}Se_{55}$ by Shiryaev *et al.* [172]. The authors then found that their 5 at. % Ga containing composition ($Ga_5Ge_{25}As_{15}Se_{55}$) crystallised during their DSC measurements, with them concluding it had poor crystallisation resistance.

5.2.1 Series (i) of exploratory cladding glasses: M262RC, M263RC, M264RC

5.2.1.1 Philosophy of design of compositions for Series (i)

Considering the factors described above, it was decided to decrease gallium content of the Series (i) cladding glass from M237RC, $Ge_{19.4}Sb_{9.7}Se_{65}Ga_3S_{2.9}$ at. % to 1-2 at. % to improve devitrification resistance, maintain 1-2 at. % sulfur content to increase T_g (which would be decreased upon reduction of gallium content) and lower refractive index, and selenium content was increased (in place of the decreased S and Ga) to make up the difference to further reduce refractive index and improve composition stability to crystallisation during fibre drawing as suggested in [54].

Again, the first set of glasses in of this series were designed around M237RC ($Ge_{19.4}Sb_{9.7}Se_{65}Ga_3S_{2.9}$ at. %). Series (i) focused on the reduction or removal of gallium from 3 at. % to 0 at. % Ga in M262RC ($Ge_{20}Sb_{10}Se_{68}S_2$) and to 1 at. % Ga in M263RC ($Ge_{19.4}Sb_{9.7}Se_{67.9}Ga_1S_2$), M264RC ($Ge_{19.4}Sb_{9.7}Se_{68.9}Ga_1S_1$) and a lowering of sulphur content from 2.9 at. % S to 2 at. % S in M262RC and M263RC, and 1 at. % S in M264RC. The composition of M262RC ($Ge_{20}Sb_{10}Se_{68}S_2$) was designed to be like the $Ge_{20}Sb_{10}Se_{67}S_3$ composition that was successfully drawn to step-index fibre [189,193]. These alterations to both the gallium and sulphur was predicted to lower T_g of the resulting glasses when compared to the failed M237RC ($Ge_{19.4}Sb_{9.7}Se_{65}Ga_3S_{2.9}$ at. %) composition[113,172], while keeping the refractive index values below that of the core glass (M240RERC, $Ge_{19.4}Sb_{9.7}Se_{67.9}Ga_3$ at. %)[189].

5.2.1.2 Fabrication of Series (i) exploratory cladding glasses

To avoid using a large amount of precursor material with every melt, the following series (both Series (i) and Series (ii)) of glasses were only produced in small masses (≈ 10 g) in which samples for DSC and ellipsometry could be taken. In a 10/14 mm ID/OD melting ampoule, this produced ~ 30 mm long glass rod including ~ 10 mm long contraction cone. The purification of materials (Table 3.1 for sources and purity) was performed as described in Section 3.2.2, and melting was performed as described in Section 3.2.4.

The development of the six glasses over two series (Series (i) and (ii)) with three glasses in each series, was due to practicality with the glass melting process. All precursors were heat treated as described in Section 3.2.2. As explained in Section 3.2.2.2, when selenium is used in glasses that are sulfur containing, the selenium is heat treated in a separate silica glass ampoule containment and removed from this ampoule using the low-speed saw, then the bulk selenium is broken into fragments which could then be batched into a second silica glass melt ampoule (10/14 ID/OD). This second silica glass ampoule would have been used during the sulfur heat treatment, and so contains the heat-treated sulfur in a suitable desired quantity, ready for the additional precursors.

A 30 g melt of selenium precursor, which had been heat-treated in the separate silica glass ampoule, was in fact only sufficient to make the first three glasses of the series, termed "Series (i)" consisting of $Ge_{20}Sb_{10}Se_{68}S_2$ at. % (M262RC), $Ge_{19.4}Sb_{9.7}Se_{67.9}Ga_1S_2$ at. % (M263RC), $Ge_{19.4}Sb_{9.7}Se_{68.9}Ga_1S_1$ at. % (M264RC). The facilities of the Mid-IR Photonics Group, University of Nottingham house two melting furnaces and two annealing furnaces. This allowed $Ge_{20}Sb_{10}Se_{68}S_2$ at. % (M262RC) and $Ge_{19.4}Sb_{9.7}Se_{67.9}Ga_1S_2$ at. % (M263RC) to be batched, sealed, and placed in the two melting furnaces (as described in Section 3.2) in tandem, with $Ge_{19.4}Sb_{9.7}Se_{68.9}Ga_1S_1$ at. % (M264RC) being batched and sealed the following day. M264RC was then melted, quenched, and annealed once the furnaces were vacant of the previous two melts. This aimed to minimise the time the heat-treated selenium was free standing in the glovebox. Although the atmosphere was dry and inert (< 0.1 ppm H_2O and < 0.1 ppm O_2), it was preferred that the selenium was batched and sealed as soon as possible to avoid contamination as much as possible

for instance 1 ppm hydride (from H_2O) will cause an optical loss of 1 dB/m in the finished fibre (Table 2.3 [132]). Using this method, it was possible to have all three samples of Series (i) exploratory cladding glass prepared within two weeks, from the silica ampoule containment cleaning steps (Section 3.2.1) through to the glass melt quenching annealing stage (Section 3.2.6). The annealing temperatures were predicted to be between 214 °C (T_g of $Ge_{20}Sb_{10}Se_{70}$ at. %) made by Parnell *et al.* [54,193] and 232 °C (T_g of $Ge_{19.4}Sb_{9.7}Se_{65}Ga_3S_{2.9}$ at. %) made here (Section 5.1.2, Figure 5.3). 222 °C was the calculated annealing temperature used for $Ge_{20}Sb_{10}Se_{68}S_2$ at. % (M262RC), $Ge_{19.4}Sb_{9.7}Se_{67.9}Ga_1S_2$ at. % (M263RC), and $Ge_{19.4}Sb_{9.7}Se_{68.9}Ga_1S_1$ at. % (M264RC).

Table 5.1 details the T_g measured for each member of the Series (i) glasses: $Ge_{19.4}Sb_{9.7}Ga_{1-2}Se_{67.9-(Ga+S)}S_{1-3}$ at. %, M262RC to M264RC, as well as their measured refractive indices (RI) at specific wavelengths (see Section 5.4).

To reiterate from Section 5.2.1.1, the measured T_g of new compositions was used as a "litmus test" for suitability as a cladding glass and so was the first characteristic measured for. It was not until a composition with a suitable T_g (M266RC and M267RC, Series (ii), Table 5.1) was identified, that any mid-IR ellipsometry (Section 5.4) was conducted.

5.2.1.3 T_g and refractive index (RI) values of Series (i) glasses M262-M264RC

Series (i) exploratory cladding glasses made in 10g melts with the calculated annealing temperature of 222 °C were then analysed *via* DSC to determine if any of the compositions measured a T_g within the aforementioned (Section 5.1.1) 232 °C ± 10 °C range in order to match the core glass, $Ge_{19.4}Sb_{9.7}Se_{67.9}Ga_3$ at. % (F104RERC, M240RERC). A small disc sample (~2.5 mm in thickness) was taken from the preform of each Series (i) glass, then polished and hot pressed (to ~1.5 mm in thickness) for ellipsometry, further elaboration on the process is in Section 3.3.5 and Section 5.3.2.

From Table 5.1 and Figure 5.5, M262RC ($Ge_{20}Sb_{10}Se_{68}S_2$ at. %) had a measured T_g of 217 °C which fell well within predictions as $Ge_{20}Sb_{10}Se_{67}S_3$ at. % and $Ge_{20}Sb_{10}Se_{70}$ at. % have their T_g at 232 °C and 214 °C degrees, respectively. The

calculated refractive index value (Section 5.3) of 2.5290 at 3.1 µm (data not shown here) in M262RC ($Ge_{20}Sb_{10}Se_{68}S_2$ at. %) is lower than what was observed in a $Ge_{20}Sb_{10}Se_{67}S_3$ at. % prism (2.5322 at 3.1 µm) measured by Fang *et al.* [189]. This was unexpected as it was predicted that increasing sulfur would correspond to a lower refractive index[94,109,189]. However, this discrepancy can likely be described by the differing experimental set ups used between the investigations. Work in Section 5.4 utilises variable angle spectroscopic ellipsometry on flat, polished, disc samples, whereas work in Fang *et al.* [189] uses modelled data taken from minimum deviation measurements on prisms.

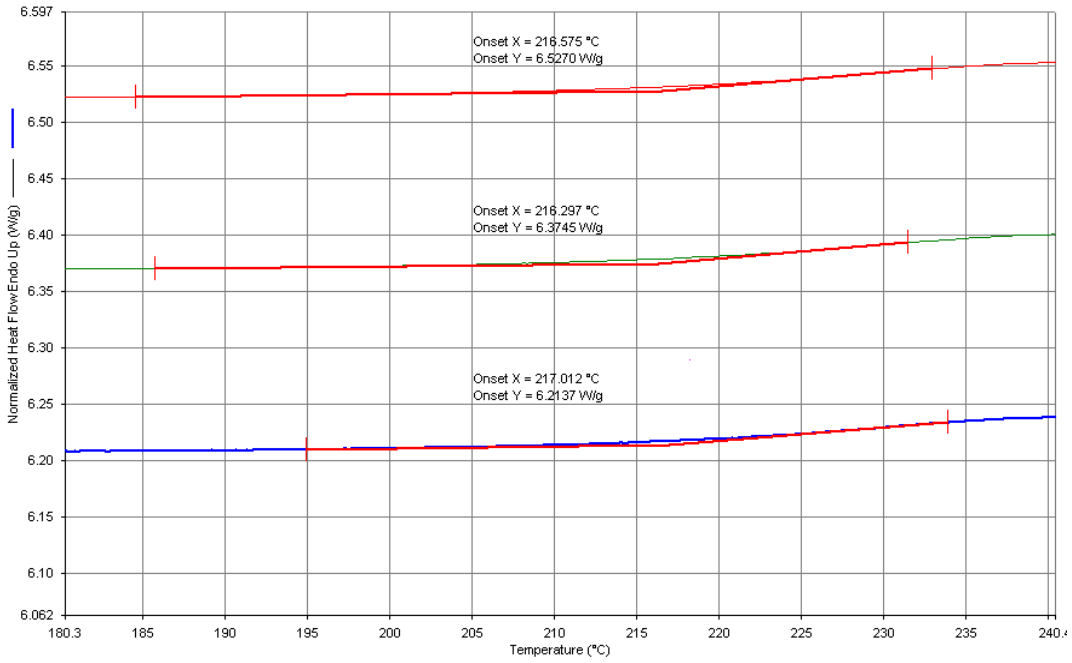


Figure 5.5 Three consecutive DSC cycles at 10 °C/min heating and cooling of a 7 mg sample of $Ge_{20}Sb_{10}Se_{68}S_2$ at. % (M262RC) showing an average T_g onset of 216.628 °C +0.332/ -0.331 °C, rounded to 217 °C. Cycle 1 measurement excluded (due to the different sample thermal history of melt-cool and annealing at 'guestimated' annealing temperature), Cycle 2 blue, Cycle 3 in green, Cycle 4 in red. Sample was annealed at a provisional T_g of 222 °C due to no previous knowledge of T_g. Sample preparation and interpretation elaborated in Section 3.3.1.

M263RC ($Ge_{19.4}Sb_{9.7}Se_{67.9}Ga_1S_2$ at. %) (Figure 5.6) and M264RC ($Ge_{19.4}Sb_{9.7}Se_{68.9}Ga_1S_1$ at. %) (Figure 5.7) measured at an unexpectedly low T_g of 209 °C and 210 °C, respectively, despite retaining 1 at. % gallium. This is likely explained by the at %. increase in the chalcogen content across both the

compositions in substitution from gallium. Gallium has been shown to cause drastic increases in T_g [90,172] due to its tetravalent bonding in the glasses[62] and an increase in the at. % of the weakly bonding, larger atomic mass selenium and small at. % of sulfur would both contribute to the lower T_g. Compared to M262RC ($Ge_{20}Sb_{10}Se_{68}S_2$ at. %), both M263RC ($Ge_{19.4}Sb_{9.7}Se_{67.9}Ga_1S_2$ at. %) and M264RC ($Ge_{19.4}Sb_{9.7}Se_{68.9}Ga_1S_1$ at. %) have higher refractive indices, as expected due to the increase in gallium content in substitution for Se [172]. The lower refractive index of M263RC when compared to M264RC was also expected due to the additional +1 at. % sulfur in place of selenium. From Table 5.1 and Figures 5.5, 5.6, and 5.7, no compositions from exploratory cladding glass Series (i) exhibited a suitable T_g to act as a cladding glass for M240RERC ($Ge_{19.4}Sb_{9.7}Se_{67.9}Ga_3$), as the T_g matching criteria of 232 °C (±10 °C) was not met. A second series of glasses, Series (ii) (Section 5.2.2), were designed with increased gallium or germanium content to raise the T_g to reach the preferred range of 232 °C (±10 °C).

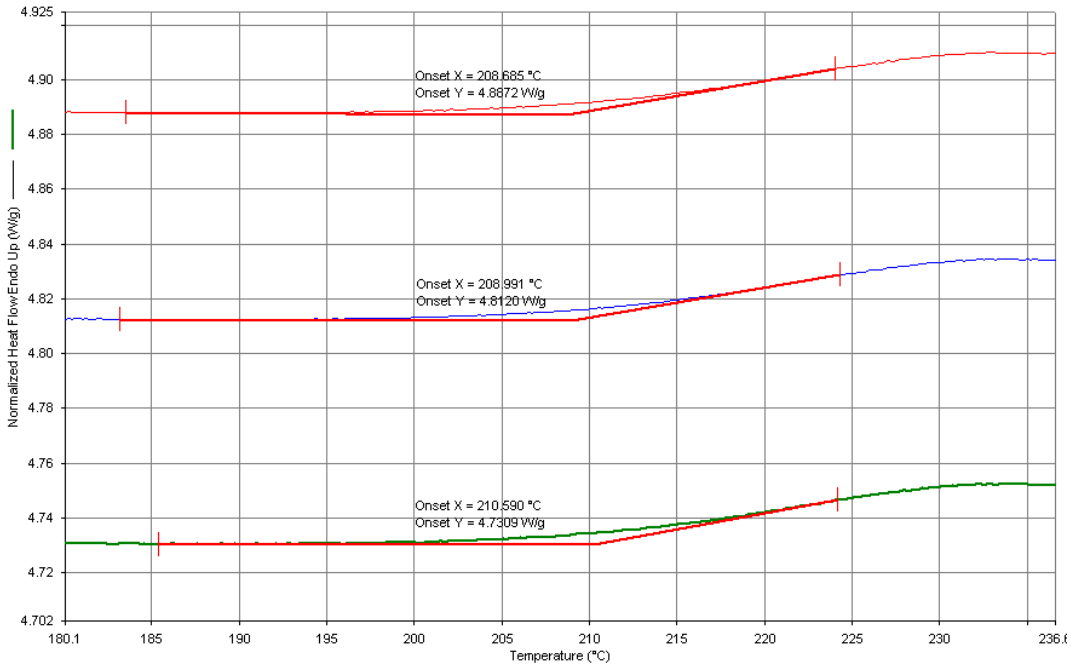


Figure 5.6 Three consecutive DSC cycles at 10 °C/min heating and cooling of a 11 mg sample of $Ge_{19.4}Sb_{9.7}Se_{67.9}Ga_1S_2$ at. % (M263RC) showing an average T_g onset of 209.442 °C +1.148/ -0.757 °C, rounded to 209 °C. Cycle 1 measurement excluded (due to the different sample thermal history of melt-cool and annealing at 'guestimated' annealing temperature), Cycle 2 green, Cycle 3 in blue, Cycle 4 in red. Sample was annealed at a provisional T_g of 222 °C due to no previous knowledge of T_g. Sample preparation and interpretation elaborated in Section 3.3.1.

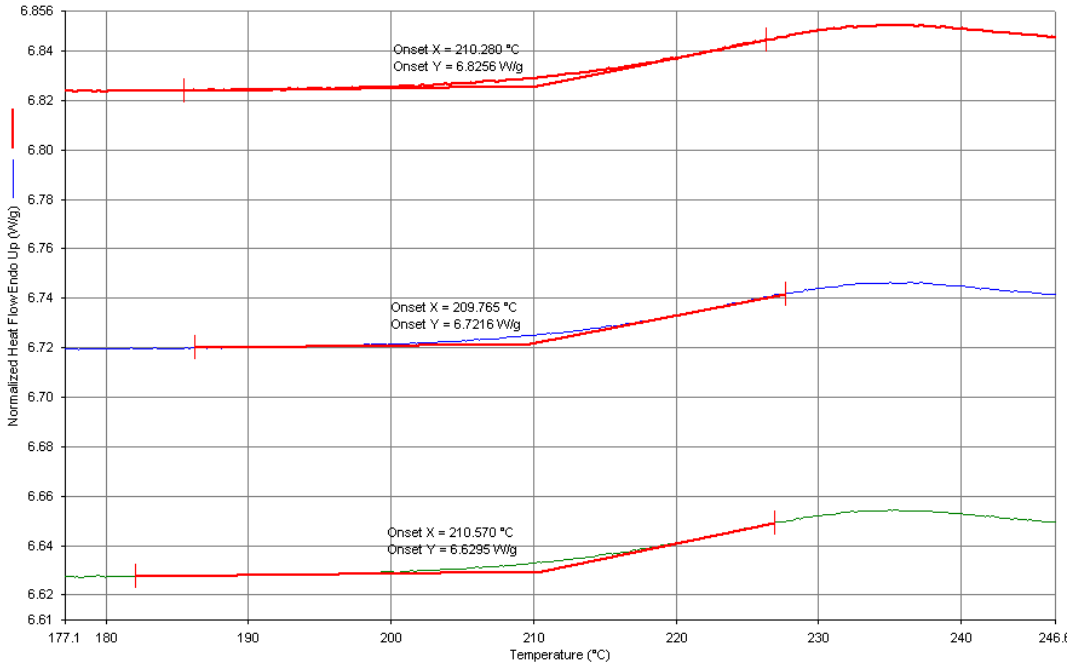


Figure 5.7 Three consecutive DSC cycles at 10 °C/min heating and cooling of a 10 mg sample of $Ge_{19.4}Sb_{9.7}Se_{68.9}Ga_1S_1$ at. % (M264RC) showing an average T_g onset of 210.205 °C +0.365 / -0.440 °C, rounded to 210 °C. Cycle 1 measurement excluded (due to the different sample thermal history of melt-cool and annealing at 'guestimated' annealing temperature), Cycle 2 green, Cycle 3 in blue, Cycle 4 in red. Sample was annealed at a provisional T_g of 222 °C due to no previous knowledge of T_g. Sample preparation and interpretation elaborated in Section 3.3.1.

5.2.2 Series (ii) of exploratory cladding glasses: M265RC, M266RC, M267RC

5.2.2.1 Philosophy of design of compositions for Series (ii)

Following the results of Series (i) exploratory cladding glasses, it became apparent that the next compositions, Series (ii), needed to be designed with a higher T_g in order to reach the desired 232 (± 10 °C) T_g of the core glass. The first two glasses of the series, M265RC and M266RC, were based on the M263RC composition ($Ge_{19.4}Sb_{9.7}Se_{67.9}Ga_1S_2$ at. %) but had incremental increases of 1 at. % gallium in substitution of selenium: M265RC; $Ge_{19.4}Sb_{9.7}Se_{66.9}Ga_2S_2$ at. %, M266RC; $Ge_{19.4}Sb_{9.7}Se_{65.9}Ga_3S_2$ at. %. The formula could be described as $Ge_{19.4}Sb_{9.7}Se_{(66.9-Ga)}Ga_{(1-2)}S_2$ at. %.

As hypothesised above in Section 5.1.2.1, the T_g of these compositions was expected to increase with an increasing at. % of Ga in lieu of Se. This hypothesis

was validated as increasing Ga at. % led to an increase in T_g from 210 °C in M263RC ($Ge_{19.4}Sb_{9.7}Se_{67.9}\mathbf{Ga_1}S_2$ at. %) to 220 °C for M265RC ($Ge_{19.4}Sb_{9.7}Se_{66.9}\mathbf{Ga_2}S_2$ at. %) and 229 °C for M266RC ($Ge_{19.4}Sb_{9.7}Se_{65.9}\mathbf{Ga_3}S_2$ at. %) (See Table 5.1).

Refractive index values of Series (ii) cladding glasses M265RC ($Ge_{19.4}Sb_{9.7}Se_{66.9}Ga_2S_2$ at. %) and M266RC ($Ge_{19.4}Sb_{9.7}Se_{65.9}Ga_3S_2$ at. %) were expected to be larger than that of the Series (i) of the exploratory cladding glass composition, M263RC ($Ge_{19.4}Sb_{9.7}Se_{67.9}Ga_1S_2$ at. %), as the sulfur content in each of these latter glasses (M265RC, M266RC) had been fixed at 2%, while the gallium content was increased to 2 and 3 at. %, respectively, at the expense of selenium content. This was anticipated due to work by Shiryaev *et al.* [172] which demonstrated that substituting gallium for selenium in $Ga_xGe_{25}As_{15}Se_{60-x}$ (x = 0-5) increased the refractive index (RI) of the resulting fibres with increasing Ga content from 2.5164 at 2.0 μm in $Ge_{25}As_{15}Se_{60}$ to 2.585 at 2.0 μm in $Ga_5Ge_{25}As_{15}Se_{55}$.

As explained in Section 4.1.2.1, the core glass M240RERC, $Ge_{19.4}Sb_{9.7}Se_{67.9}Ga_3$ at. %, (and subsequently, the Series (i) exploratory cladding glasses M262-M264RC, See Table 5.1 for composition) was designed around the $Ge_{20}Sb_{10}Se_{70}$ at. % composition detailed in [54,189,193] , notably now with the addition of gallium facilitated through the removal of Ge-Sb-Se congruently *i.e.*, in the 20:10:70 same ratio as that of the starting composition. M263RC ($Ge_{19.4}Sb_{9.7}Se_{67.9}Ga_1S_2$ at. %) retained this formula with the congruent reduction of Ge-Sb-Se in this ratio, with the S and the Ga then added. M265RC ($Ge_{19.4}Sb_{9.7}Se_{66.9}Ga_2S_2$ at. %) and M266RC ($Ge_{19.4}Sb_{9.7}Se_{65.9}Ga_3S_2$ at. %) however, deviated from this ratioed congruent removal of Ge:Sb:Se (= 20:10:70) as a system. Thus, for these two compositions: M265RC and M266RC, selenium was directly substituted for gallium starting from the M263RC ($Ge_{19.4}Sb_{9.7}Se_{67.9}Ga_1S_2$ at. %) composition by 1 at. % Se for 1 at. % Ga in M265RC ($Ge_{19.4}Sb_{9.7}Se_{66.9}Ga_2S_2$ at. %) and by 2 at. % Se for 2 at. % Ga in M266RC ($Ge_{19.4}Sb_{9.7}Se_{65.9}Ga_3S_2$ at. %).

These latter controlled compositional changes now resulted in two compositions in which the Ge:Sb:Se content is no longer in the 20:10:70 ratio that the dopable core glass, M240RERC $Ge_{19.4}Sb_{9.7}Se_{67.9}Ga_3$ at. %, and Series (i) exploratory cladding

glasses M263RC ($Ge_{19.4}Sb_{9.7}Se_{67.9}Ga_1S_2$ at. %) and M264RC ($Ge_{19.4}Sb_{9.7}Se_{68.9}Ga_1S_1$ at. %) are based off.

M267RC ($Ge_{21}Sb_{10}Se_{69}$ at. %) was designed with the goal of excluding gallium and sulphur from the cladding glass composition while also providing a suitable refractive index and T_g. With the removal of these two elements, sulfur and gallium, that are known to increase the glass transition temperature, as seen with Ga when substituted for selenium (Shiryaev *et al.* $Ga_xGe_{25}As_{15}Se_{60-x}$ (x = 0; 1; 2; 3; 4; 5[172]) and arsenic (Tang, $Ge_{16.5}As_{16}Ga_3Se6_{45}$ T_g = 239 °C; $Ge_{16.5}As_9Ga_{10}Se6_{45}$ T_g= 267 °C[31]) and with S when substituted for Se (Parnell, $Ge_{20}Sb_{10}Se_{70}$ T_g = 214 °C, $Ge_{20}Sb_{10}Se_{67}S_3$ T_g = 224 °C[193] and Wang *et al.* [190] ($Ge_{15}Sb_{20}Se_{65}$ T_g = 228.8 °C, $Ge_{15}Sb_{20}Se_{32.5}S_{32.5}$ $T_g \approx$ 238 °C) , the germanium content of M267RC ($Ge_{21}Sb_{10}Se_{69}$ at. %) was increased by 1 at. %, with a corresponding 1 at. % decrease of selenium (from the base Parnell *et al.* composition: $Ge_{20}Sb_{10}Se_{70}$[54]) to try and offset this potential decrease in T_g. This philosophy was further supported by Zhang *et al.* who reported germanium having similar effects to gallium on T_g increases in $Ga_{(8-x)}Ge_xSb_{32}S_{60}$ (x=0,2,4,6,8) glasses, while also providing a decrease in refractive index[91]. It was reported that substituting gallium for germanium led to a T_g increase of 2 °C between $Ga_{(8)}Ge_0Sb_{32}S_{60}$ (T_g 240 °C) and $Ga_0Ge_8Sb_{32}S_{60}$ (T_g 242 °C), while the RI at 10 µm wavelength drops from 2.643 in $Ga_{(8)}Ge_0Sb_{32}S_{60}$ to 2.579 in $Ga_0Ge_8Sb_{32}S_{60}$ [91].

5.2.2.2 Fabrication of Series (ii) exploratory cladding glasses

The fabrication of the Series (ii) glasses was conducted in a method like that described in Section 5.2.1.2 to make the Series (i) glasses. That is, small masses (≈ 10 g) were made in a 10/14 mm ID/OD melting ampoule from which samples for DSC and ellipsometry could be taken. Again, as before for Series (i), a 30 g melt of heat-treated selenium precursor prepared in a separate 10/14 mm ID/OD silica glass ampoule which was then divided for use in M265RC ($Ge_{19.4}Sb_{9.7}Se_{66.9}Ga_2S_2$ at. %), M266RC ($Ge_{19.4}Sb_{9.7}Se_{65.9}Ga_3S_2$ at. %), and M267RC ($Ge_{21}Sb_{10}Se_{69}$ at. %). As before for Series (i), the Series (ii) glasses here were also annealed at the calculated T_g of 222 °C.

As explained in Section 3.2.2, in experimentally carrying out the glass melting of sulfur-containing selenide glasses, the process requires that the selenium is heat treated in a separate silica glass ampoule containment which is then broken open, the selenium is then shattered by being broken up in an agate pestle and mortar inside the MBraun glovebox (< 1ppm H_2O and < 1ppm O_2) and batched into the sulfur purification/melting silica glass ampoule containment. This procedure is necessary because the sulfur sticks as a solid, intractable block after heating to purify it (see Section 3.2.2.2) whereas the selenium after purification in its ampoule containment is more tractable and can be removed to be combined with the sulfur and the rest of the melt components added. It should also be noted that this requires an additional large boule silica glass ampoule such as a 26.5/30 mm ID/OD ampoule to heat-treat the large mass of Se (to be shattered and batched into the 26.5/30 mm ID/OD sulfur purification/melt ampoule) that is required to make a cladding glass boule that is a suitable size for extrusion (>70 g), increasing time and monetary cost of glass fabrication.

It should also be noted that this procedure needed for glass compositions containing both S and Se, requiring both of these precursor elements having to be purified prior to glass melting, introduces the risk of small pieces of silica glass *i.e.*, silica glass shards (originating from breaking up the selenium purification silica glass ampoule containment) being introduced into the main chalcogenide glass melt. As the S and Se need to be heat treated in separate silica glass ampoules, it is unavoidable that one of the ampoules needs to be opened to extract the precursor (usually Se) for batching into the melt ampoule. These silica glass shard pieces can subsequently act as small scattering centres in the resulting fibre, or act as heterogenous nucleation sites for crystallisation during the glass making process (see Section 2.3.3.2). Therefore, removal of the sulfur from M267RC ($Ge_{21}Sb_{10}Se_{69}$ at. %) meant that this glass could be made in one ampoule, avoiding the above issues of having to extract Se and potentially introducing silica glass shards into the chalcogenide melt.

Gallium, as also explained in Section 3.2.2.5, although source able at 7n purity (see Table 3.1), as-sourced presents itself with a layer of what is assumed to be β Ga_2O_3 on its surface before batching despite storage in a screw top polyethylene bottle

stored inside the inert atmosphere of the MBraun glovebox (< 0.1 ppm H_2O, < 0.1 ppm O_2). Although, just prior to batching, this surface film is methodically mechanically removed from the surface, *via* serial transfers between weigh boats (Fisherbrand™ Polystyrene, 85mL) (see Section 3.2.2.5 for details), no further purification method is used during this work. That is viewed as not satisfactory but inevitable in the absence of a more sophisticated method of gallium purification. There is a high probability, therefore, gallium containing glasses have some of this oxide impurity incorporated into the chalcogenide melts, and ultimately, fibres. There is also the documented presence of modified, face centred cubic α-Ga_2Se_3 in gallium containing glasses[50,52,53]. Tang *et al.* found that powdered bulk 1000-3000 ppmw Dy^{3+} $Ge_{16.5}As_9Ga_{10}Se_{64.5}$ at. % exhibited XRD peaks for α-Ga_2Se_3 and later identified nanocrystal α-Ga_2Se_3 in 3000 ppmw Dy^{3+} $Ge_{16.5}As_{16}Ga_3Se_{64.5}$ at. % using TEM-EDX [50,52,53]. Therefore, by removing gallium, a potential oxide impurity (providing impurity absorption bands and potentially acting as a heterogenous nucleation point) source that has been shown to decrease devitrification resistance is avoided. In summary, this rationale shows the extreme advantage in having a cladding glass without gallium as in the Series (ii) exploratory cladding glass: M267RC ($Ge_{21}Sb_{10}Se_{69}$ at. %).

5.2.2.3 T_g and refractive index (RI) values of Series (ii) glasses (M265-M267RC)

Like Series (i), Series (ii) exploratory cladding glasses made in 10g melts with the calculated annealing temperature of 222 °C were then analysed *via* DSC to determine if any of the compositions measured a T_g within the aforementioned (Section 5.1.1) 232 °C ± 10 °C range in order to match the core glass, $Ge_{19.4}Sb_{9.7}Se_{67.9}Ga_3$ at. % (F104RERC, M240RERC). A small disc sample (~2.5 mm in thickness) was taken from the preform of each Series (ii) glass, then polished and hot pressed for ellipsometry, further elaboration on the process is in Section 3.3.5 and Section 5.3.2.

From Table 5.1 and Figure 5.8, M265RC ($Ge_{19.4}Sb_{9.7}Se_{66.9}Ga_2S_2$ at. %) had a measured T_g of 220 °C. As elaborated in Section 5.2.1.1, this was anticipated as M265RC had a 1 at. % Ga substitution for Se, when compared to M263RC ($Ge_{19.4}Sb_{9.7}Se_{67.9}Ga_1S_2$ at. %), a substitution which Shiryaev *et al.*[172] reported led to

an increase in T_g in a $Ga_xGe_{25}As_{15}Se_{60-x}$ glass series. The same work by Shiryaev *et al.*[172] in the same glass series reported that the substitution of the gallium for the selenium would increase RI of the glass with increasing gallium content. However, the reverse effect was observed here. M263RC ($Ge_{19.4}Sb_{9.7}$**$Se_{67.9}Ga_1$**S_2) measured a RI of 2.5423 at 2.8 µm, whereas M265RC ($Ge_{19.4}Sb_{9.7}$**$Se_{66.9}Ga_2$**S_2 at. %) measured a RI of 2.5218 at 2.8 µm (Values taken from Table 5.1). Here it is then suggested that the effects of gallium for selenium substitutions on RI are partially compositional dependent as the work from Shiryaev *et al.*[172] is arsenic-based, while here the compositions are antimony-based. It is also to be noted that Shiryaev *et al.*[172] only measured RI up to 2 µm, whereas work here only measured RI from 2 µm, limiting ability to compare further.

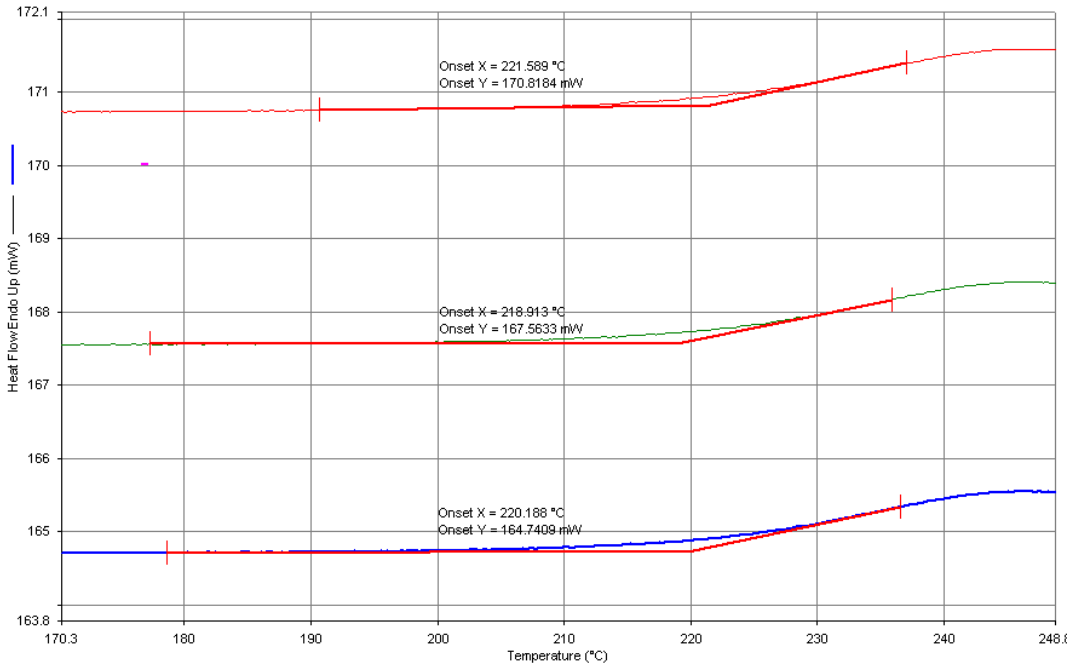


Figure 5.8 Three consecutive DSC cycles at 10 °C/min heating and cooling of a 10 mg sample of ($Ge_{19.4}Sb_{9.7}Se_{66.9}Ga_2S_2$ at. %) (M265RC) showing an average T_g onset of 220.23 °C +1.359 / -1.317 °C, rounded to 220 °C. Cycle 1 measurement excluded (due to the different sample thermal history of melt-cool and annealing at 'guestimated' annealing temperature), Cycle 2 blue, Cycle 3 in green, Cycle 4 in red. Sample was annealed at a provisional T_g of 222 °C due to no previous knowledge of T_g. Sample preparation and interpretation elaborated in Section 3.3.1.

M266RC ($Ge_{19.4}Sb_{9.7}$**$Se_{65.9}Ga_3$**S_2 at. %), as anticipated, exhibited an increase in T_g to 229 °C when compared to both M263RC ($Ge_{19.4}Sb_{9.7}$**$Se_{67.9}Ga_1$**S_2 at. %, T_g 209 °C) and M265RC ($Ge_{19.4}Sb_{9.7}$**$Se_{66.9}Ga_2$**S_2 at. %, T_g 220 °C) with its additional 1 at.

% gallium in substitute for 1 at. % selenium (from M263RC and M265RC). Figure 5.9 shows the DSC scans for the sample.

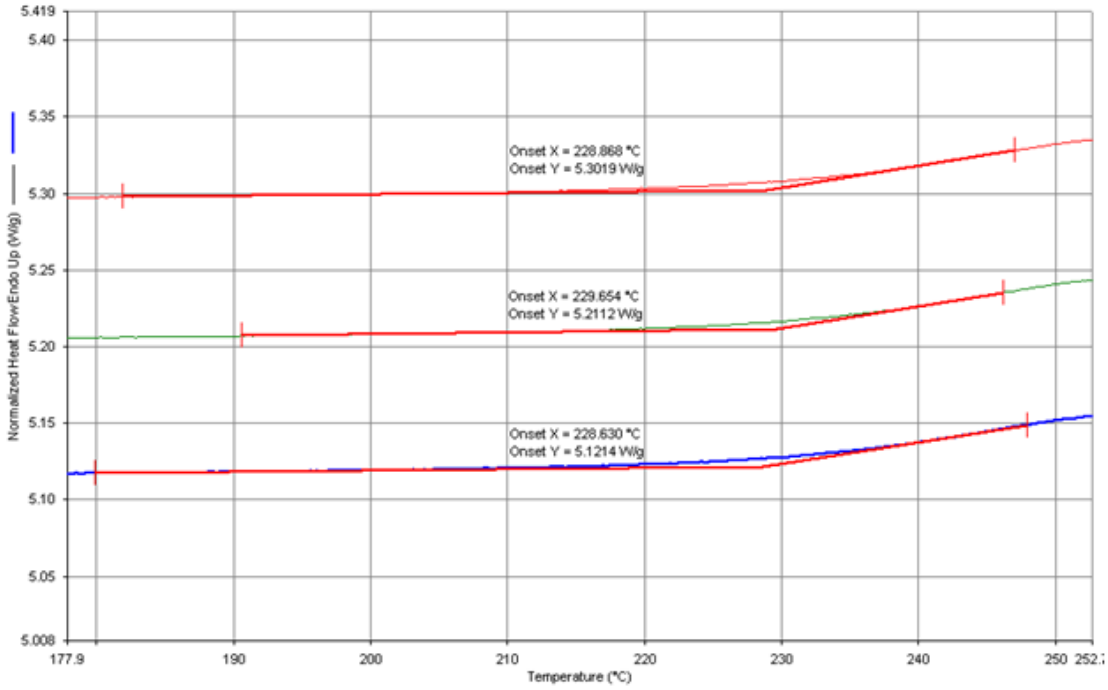


Figure 5.9 Three consecutive DSC cycles at 10 °C/min heating and cooling of a 10 mg sample of M266RC ($Ge_{19.4}Sb_{9.7}Se_{65.9}Ga_3S_2$ at. %) showing an average T_g onset of 229.05 °C +0.604 / -0.182 °C, rounded to 229 °C. Cycle 1 measurement excluded (due to the different sample thermal history of melt-cool and annealing at 'guestimated' annealing temperature), Cycle 2 blue, Cycle 3 in green, Cycle 4 in red. Sample was annealed at a provisional T_g of 222 °C due to no previous knowledge of T_g. Sample preparation and interpretation elaborated in Section 3.3.1.

Comparing the RI values of M266RC (2.5301 at 2.8 µm) with M265RC (2.5218 at 2.8 µm), the values begin to align with the observations of Shiryaev *et al.*[172] that increasing Ga substitution for Se leading to increasing RI. The divergence in M265RC and M266RC from the ratio of Ge:Sb:Se from 20:10:70 used in M263RC may explain why the refractive index (RI) value is lower than what was predicted from M263RC. Again, it was predicted that M265RC ($Ge_{19.4}Sb_{9.7}Se_{66.9}Ga_2S_2$ at. %) and M266RC ($Ge_{19.4}Sb_{9.7}Se_{65.9}Ga_3S_2$ at. %) would have similar or higher RI when compared to M263RC ($Ge_{19.4}Sb_{9.7}Se_{67.9}Ga_1S_2$ at. %). This is due to S being fixed at 2 at. %, and Se being removed to accommodate Ga (2 at. % Ga in M265RC and 3 at. % Ga in M266RC), which Shiryaev *et al.* [172] reported that this gallium for selenium substitution led to an increase in RI in a $Ga_xGe_{25}As_{15}Se_{60-x}$ (x = 0-5) series of glasses.

So, despite this change in host glass components' ratio, the RI values of both M265RC ($Ge_{19.4}Sb_{9.7}Se_{66.9}Ga_2S_2$ at. %) and M266RC ($Ge_{19.4}Sb_{9.7}Se_{65.9}Ga_3S_2$ at. %) both lent themselves to be used as a potential cladding: for instance, compared to a RI of 2.549 at 2.8 µm exhibited by the core glass (M240RERC, $Ge_{19.4}Sb_{9.7}Se_{67.9}Ga_3$ at. %), these two potential cladding glasses at the same wavelength of 2.8 µm, exhibited a RI of 2.5218 for M265RC and 2.5301 for M266RC (See Table 5.1 for details).

Based off the $Ge_{20}Sb_{10}Se_{70}$ at. % (T_g 214 °C) composition as reported by Parnell *et al.*[544], 1 at. % germanium was substituted for selenium in this base $Ge_{20}Sb_{10}Se_{70}$ at. % resulting in M267RC of the exploratory cladding glass Series (ii) having a composition of $Ge_{21}Sb_{10}Se_{69}$ at. % and a T_g of 227 °C (Figure 5.10 and Table 5.1). This was in line with predictions that an increase in Ge in lieu of Se would increase T_g (Parnell *et al.* [544] reporting $Ge_{20}Sb_{10}Se_{70}$ at. % (T_g 214 °C) to $Ge_{25}Sb_{10}Se_{65}$ at. % (T_g 314 °C).

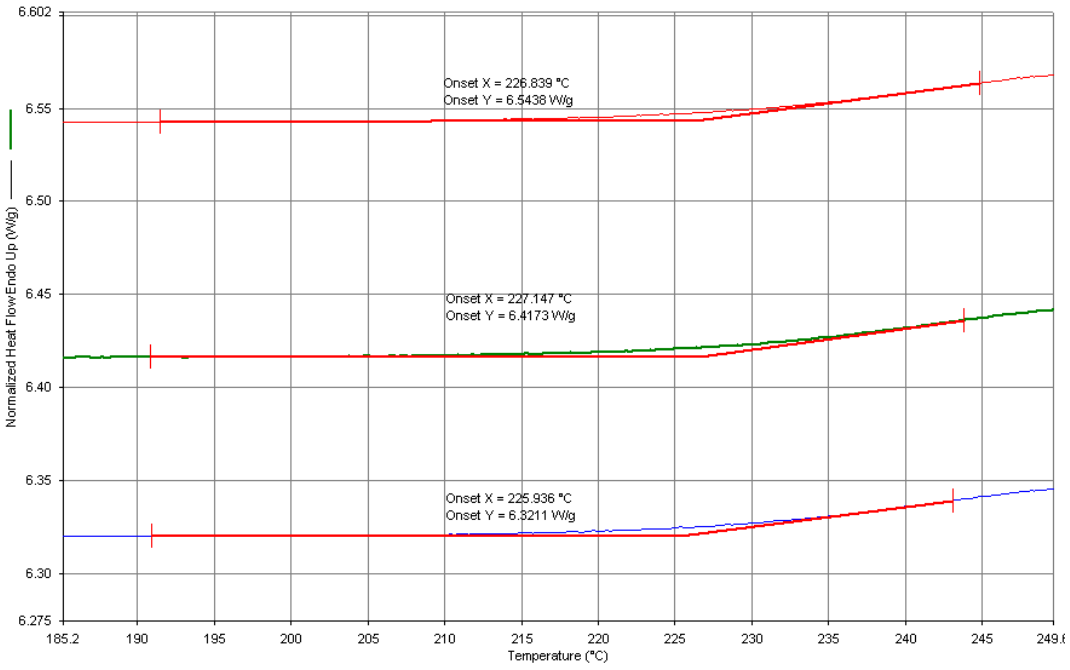


Figure 5.10 Three consecutive DSC cycles at 10 °C/min heating and cooling of a 10 mg sample of $Ge_{21}Sb_{10}Se_{69}$ at. % (M267RC) showing an average T_g onset of 226.64 °C +0.507 / -0.704 °C, rounded to 227 °C. Cycle 1 measurement excluded (due to the different sample thermal history of melt-cool and annealing at 'guestimated' annealing temperature), Cycle 2 blue, Cycle 3 in green, Cycle 4 in red. Sample was annealed at a provisional T_g of 222 °C due to no previous knowledge of T_g. Sample preparation and interpretation elaborated in Section 3.3.1.

Moreover, the refractive index values of this newly developed cladding glass, M267RC: $Ge_{21}Sb_{10}Se_{69}$ at. %, (2.5257 at 2.8 µm, Table 5.1) which was similar to that measured for Series (i) exploratory cladding glass M262RC: $Ge_{20}Sb_{10}Se_{68}S_2$ at. % (2.5266 at 2.8 µm, Table 5.1).

Importantly, this rationale above and all of the observations indicate that a 1 at. % substitution of Ge for Se provides comparable refractive index decrease to 2 at. % S for Se, while providing a comparatively larger increase to T_g. Compare the + 3 °C T_g increase from $Ge_{20}Sb_{10}Se_{70}$ at. %: T_g 214 °C to $Ge_{20}Sb_{10}Se_{68}\mathbf{S_2}$ at. % (M262RC): T_g 217 °C, RI at 2.8 µm = 2.5266 whereas there was a + 13 °C T_g increase from $\mathbf{Ge_{20}}Sb_{10}Se_{70}$ at. %: T_g 214 °C to $\mathbf{Ge_{21}}Sb_{10}Se_{69}$ at. % (M267RC): T_g 227 °C, RI at 2.8 µm = 2.5257).

The Series (ii) exploratory cladding glasses resulted in two compositions (M266RC: $Ge_{19.4}Sb_{9.7}Se_{65.9}Ga_3S_2$ at. % and M267RC: $Ge_{21}Sb_{10}Se_{69}$ at. %) with a measured T_g that fell within our desired range of T_g 232 °C (± 10 °C), the T_g of host core glass: $Ge_{19.4}Sb_{9.7}Se_{67.9}Ga_3$ at. % (M240RERC, Table 5.1) with both M266RC and M267RC glasses exhibiting refractive index values (2.5301 at 2.8 µm and 2.5257 at 2.8 µm, respectively, Table 5.1) that would provide suitable light guiding when used as a core glass for the rare earth ion dopable core $Ge_{19.4}Sb_{9.7}Se_{67.9}Ga_3$ at. % composition (M240RERC, Table 5.1) as in the fibres F099RERC (1000 ppmw Sm^{3+} $Ge_{19.4}Sb_{9.7}Se_{67.9}Ga_3$ at. %) and F104RERC (500 ppmw Dy^{3+} $Ge_{19.4}Sb_{9.7}Se_{67.9}Ga_3$ at. %).

Table 5.1 aggregates the data discussed through Section 5.1 and 5.2. Melt codes and their corresponding batched composition, alongside their measured EDX composition, to further validate composition, (Section 3.3.4 for details) are stated. The T_g of each cladding glass (M237RC, M262RC-M267RC) and the core glass (M240RERC) are given. The core glass, M240RERC ($Ge_{19.4}Sb_{9.7}Se_{67.9}Ga_3$ at. %), was doped with 500 ppmw Dy^{3+}, therefore RI values are also given for the aforementioned glasses at 2.8 µm and 4.3 µm, corresponding to the mid-IR radiative transitions Dy^{3+}: $^6H_{13/2} \rightarrow {}^6H_{15/2}$ and Dy^{3+}: $^6H_{11/2} \rightarrow {}^6H_{13/2}$ which exhibit emission peaks at approximately 2.8 µm and 4.3 µm, respectively (See Section 6.3.2.3).

Table 5.1 Prospective, exploratory cladding glass compositions (Series (i) and Series (ii)) with measured T_g and refractive indices at specified wavelengths. (Note that the T_g and RI results for Series (i) are discussed in Section 5.2.1 and the T_g and RI results for Series (ii) are discussed in Section 5.2.2 and how RI results were measured are discussed later in Section 5.3).

Melt code (Series i/ii)	**Batched composition/ at. %**	**EDX composition/ at. %**	**T_g /(°C)**	**RI @ 2.8 µm**	**RI @ 4.3 µm**
M237RC (no series)	$Ge_{19.4}Sb_{9.7}Ga_3Se_{65}S_{2.9}$	-	232	-	-
M262RC (i)	$Ge_{20}Sb_{10}Se_{68}S_2$	$Ge_{20.23}Sb_{10.43}Se_{67.54}S_{1.8}$	217	2.5266	2.5264
M263RC (i)	$Ge_{19.4}Sb_{9.7}Se_{67.9}Ga_1S_2$	$Ge_{19.96}Sb_{9.95}Se_{66.80}Ga_{1.15}S_{2.14}$	209	2.5423	2.5405
M264RC (i)	$Ge_{19.4}Sb_{9.7}Se_{68.9}Ga_1S_1$	$Ge_{20.17}Sb_{10.18}Se_{67.55}Ga_{1.12}S_{0.98}$	210	2.5615	2.5565
M265RC(ii)	$Ge_{19.4}Sb_{9.7}Se_{66.9}Ga_2S_2$	$Ge_{19.21}Sb_{10.43}Se_{66.15}Ga_{2.05}S_{2.16}$	220	2.5218	2.5185
M266RC(ii)	$Ge_{19.4}Sb_{9.7}Se_{65.9}Ga_3S_2$	$Ge_{19.43}Sb_{9.98}Se_{65.52}Ga_{3.07}S_{2.0}$	229	2.5301	2.5285
M267RC(ii)	$Ge_{21}Sb_{10}Se_{69}$	$Ge_{20.84}Sb_{10.38}Se_{68.78}$	227	2.5257	2.5229
M240RERC **(core glass)**	(500 ppmw Dy^{3+}) $Ge_{19.4}Sb_{9.7}Se_{67.9}Ga_3$	$Ge_{19.66}Sb_{10.62}Se_{66.45}Ga_{3.27}$	232	2.549	2.5422

Refractive index (RI) values taken from models fitted from 2 – 30 µm. Averaged over three measurement angles (55 °, 65 °, 75 °).

5.2.3 Summary of effects of varying S, Se, Ga, and Ge at. % content in the exploratory cladding glass series on T_g and RI, and how these dictates cladding glass choices for the core glass composition $Ge_{19.4}Sb_{9.7}Se_{67.9}Ga_3$ at. %

Here a final summary of the effects of composition changes on T_g and RI are discussed. Section 5.4 details an overall rationale for the final choice in cladding glass composition for the core glass $Ge_{19.4}Sb_{9.7}Se_{67.9}Ga_3$ at. %.

5.2.3.1 Summary of effects of compositional changes on T_g

In relation to T_g, changes of the exploratory cladding glasses with changing composition several trends are identified. Considering the 2 at. % substitution of S for Se from the Parnell composition $Ge_{20}Sb_{10}Se_{70}$ at. % [54,193] to $Ge_{20}Sb_{10}Se_{68}S_2$ at. %, an increase in T_g from 214 °C to 217 °C was observed. This trend of increasing T_g continues with 3 at. % S for Se where Parnell reports the T_g of $Ge_{20}Sb_{10}Se_{67}S_3$ at. %[193]. Further discussion of this trend is limited as all the Series (i) and (ii) exploratory cladding glasses were fixed with 2 at. % S, except for M264RC ($Ge_{19.4}Sb_{9.7}Se_{68.9}Ga_1S_1$ at. %), which was not further investigated due to its T_g being outside the desired range of T_g 232 °C (± 10 °C), the T_g of host core glass: $Ge_{19.4}Sb_{9.7}Se_{67.9}Ga_3$ at. % (M240RERC).

Substitution of gallium for selenium, while the remainder of the composition was fixed, was shown to increase T_g. This is seen between Series (i) M263RC ($Ge_{19.4}Sb_{9.7}Se_{67.9}Ga_1S_2$ at. %), Series (ii) M265RC ($Ge_{19.4}Sb_{9.7}Se_{66.9}Ga_2S_2$ at. %), and Series (ii) M266RC ($Ge_{19.4}Sb_{9.7}Se_{65.9}Ga_3S_2$ at. %), which corresponded to T_g of 209 °C, 220 °C, and 229 °C, respectively.

Substitution of germanium for selenium was also shown to increase T_g. Comparing the Parnell composition $Ge_{20}Sb_{10}Se_{70}$ at. % [54,193] with $Ge_{21}Sb_{10}Se_{69}$ at. % (M267RC) shows an increase of 13 °C from 214 °C to 227 °C (M267RC).

5.2.3.2 Summary of effects of compositional changes on RI

There is less of a general trend to be identified in the exploratory cladding glass series regarding refractive index changes following Ga at. % compositional substitutions for Se. Considering the Series (i) M263RC ($Ge_{19.4}Sb_{9.7}Se_{67.9}Ga_1S_2$ at.

%, RI at 2.8 µm: 2.5423), Series (ii) M265RC ($Ge_{19.4}Sb_{9.7}Se_{66.9}Ga_2S_2$ at. %, RI at 2.8 µm: 2.5218), and Series (ii) M266RC ($Ge_{19.4}Sb_{9.7}Se_{65.9}Ga_3S_2$ at. %, RI at 2.8 µm: 2.5301) series, which remained fixed in composition with increasing at. % substitutions of gallium for selenium. RI decreases between the 1 at. % Ga M263RC (RI at 2.8 µm: 2.5423) and 2 at. % Ga M265RC (RI at 2.8 µm: 2.5218), but then RI increases between the 2 at. % Ga M265RC and 3 at. % Ga M266RC (RI at 2.8 µm: 2.5301).

As previously elaborated in Section 5.2.2.3, it is suggested that a 1 at. % substitution of Ge for Se provides comparable refractive index decrease to 2 at. % S for Se. This is suggested through comparing $Ge_{20}Sb_{10}Se_{68}S_2$ at. % (M262RC) with RI at 2.8 µm = 2.5266 to $Ge_{21}Sb_{10}Se_{69}$ at. % (M267RC) with RI at 2.8 µm = 2.5257 using $Ge_{20}Sb_{10}Se_{70}$ at. % as a base reference composition.

Due to the lack of variation on sulfur content between the exploratory cladding glass series glasses, and lack of RI data at 2.8 or 4.3 µm for the $Ge_{20}Sb_{10}Se_{70}$ at. % composition, no conclusions are drawn regarding sulfur content and RI here.

5.3 Mid-IR ellipsometry to calculate refractive index values in chalcogenide bulk samples of potential cladding glasses (Table 5.1) to match core glass (*e.g.*, M240RERC ($Ge_{19.4}Sb_{9.7}Se_{67.9}Ga_3$ at. % + 500 ppmw Dy foil)

5.3.1 Introduction

From the rationale in Section 5.2.3 and results in Table 5.4, there are two cladding compositions M266RC ($Ge_{19.4}Sb_{9.7}Se_{65.9}Ga_3S_2$ at. %, T_g = 229 °C) and M267RC $Ge_{21}Sb_{10}Se_{69}$ at. % T_g = 227 °C) fitting the glass transition temperature criteria of T_g ± 10 °C of the core glass (*e.g.*, M240RERC ($Ge_{19.4}Sb_{9.7}Se_{67.9}Ga_3$ at. % + 500 ppmw Dy foil: Tg = 232 °C.

It was next necessary to determine if the refractive index of either of the potential cladding glasses (M266RC ($Ge_{19.4}Sb_{9.7}Se_{65.9}Ga_3S_2$ at. %) and M267RC ($Ge_{21}Sb_{10}Se_{69}$ at. %)) was suitable to act as a cladding glass in a step-index fibre in

terms of whether their refractive index was lower than that of the RE-doped core glass (*e.g.* M240RERC (F104RERC) ($Ge_{19.4}Sb_{9.7}Se_{67.9}Ga_3$ at. % + 500 ppmw Dy foil). The methodology of sample preparation and measurements is presented in the next Section 5.3.2.

5.3.2 Methodology of refractive index measurements and sample preparation

The rod preforms listed in Table 5.1 were the small-scale ~ 10 g as-melted glasses (see Section 5.2.1.2 and 5.2.2.2) that were annealed at the 'guestimated' annealing temperature of 222 °C because these Tgs were unknown until measured by means of DSC (as listed in Table 5.1). A small disc of glass (approximately 2.5 mm thickness) was cut from each of these preforms listed in Table 5.1 and both circular faces polished to a 1 µm finish, before being hot-pressed to approximately 1.5 mm to ensure flatness of the faces and that the opposite sides were parallel. Further details on sample preparation are in Section 3.3.5.

The refractive index (RI) dispersion measurements were taken using an IR-VASE (infrared – variable angle spectroscopic ellipsometry) (Woollam, USA) which utilised a Globar light source, which was used to measure transmission between wavelengths of 1.5-40 µm of the chalcogenide samples ~1.5 mm in thickness (the distance between the opposite parallel disc faces, thus the sample optical pathlength). Transmission measurements were used in initial attempts to model refractive indices from the resulting reflectance measurements by including Gaussian absorptions into the model at wavelengths associated with oxide and hydride impurities in the glass. Following these optical transmission measurements of the discs using the Globar light source, one side of the chalcogenide disc was roughened with a Dremel tool, to prevent internal specular reflections from the back face of the sample, and a reflectance measurement was taken. This reflectance measurement gave an output of two values, psi and delta, both functions are related to the ratio of Fresnel reflection coefficients for p- and s- polarised light that describe the change in polarisation of light when it interacts with a surface (see Section 3.3.5 for further explanation). By constructing a mathematical model, it is possible to accurately calculate desired optical characteristics such as refractive index (n) or absorption coefficients (k) from the measured values. Section 5.3.4

details the various models made using the General Oscillator Layer (GenOsc®) function in CompleteEase software (v 6.53 and v 5.10) which facilitated the inclusion of multiple oscillator functions into one complex model.

5.3.3 Transmittance measurements of bulk glass samples for use in refractive index ellipsometry models

In making and interpreting the ellipsometry measurements of the refractive index dispersion of samples of the chalcogenide glasses listed in Table 5.1, the aim was to create an ellipsometry model capable of fitting the measurements which was based on the real, measurable, physical characteristics of the chalcogenide glass composition itself. The intrinsic and extrinsic absorption bands of the glass would affect refractive index through the Kramers-Kronig relationship as the optical constants change[198]. Transmittance measurements for each of the disc samples, cut from the rod preforms listed in Table 5.1, that had been ground and polished to a 1 μm finish and then hot-pressed to ~1.5 mm to ensure that opposite disc faces were flat and parallel, were obtained first using the IR-VASE. For transmittance measurements, two cycles consisting of 10 scans at 8 cm^{-1} resolution were collected to obtain an averaged transmittance spectrum. This is because the roughening treatment with the Dremel tool would prevent any transmittance through a sample, and initial work aimed to use intrinsic and impurity absorptions observed in the transmittance measurements into the ellipsometry model. From the transmittance data (Figure 5.11) it was possible to identify the various impurity absorptions (e.g. Se-H at 4.55 μm) alongside the electronic absorptions characteristic of the 500 ppmw dysprosium dopant. The absorptions at around 12.7 μm and 17.6 μm, are identified as Ge-O and Sb-O, respectively in [182,199]. Due to the prevalence of these absorptions, initial ellipsometry models were developed using multiple Gaussian oscillators centred on each wavelength associated with impurity and electronic absorptions (see Section 5.3.2.1). The aim, as stated earlier, was to create an ellipsometry model which was based on the real, measurable, physical optical characteristics of the chalcogenide glass composition itself and hence potentially a predictive model for unknown chalcogenide glass compositions. It should be noted that, in Figure 5.11, the absorption band at 12.7 μm is substantially reduced in the

core glass composition M240RERC ($Ge_{19.4}Sb_{9.7}Se_{67.9}Ga_3$ at. % + 500 ppmw Dy foil) compared to the other (exploratory cladding) glasses (M237RC, M262RC-M267RC, Table 5.1 for compositions) present in Figure 5.11.

This much reduced Ge-O absorption band at 12.7 μm wavelength is thought to potentially be a result of the introduction of dysprosium into the glass melt as follows. Rare earth elements are extremely electropositive (ability to donate electrons in a chemical bond) and thus have a high affinity for oxygen [186,200] to react and form a rare earth oxide compound. The dysprosium therefore may have acted as an oxygen getter. So, in the thermodynamic equilibrium of the glass melting conditions, in competition with the other species present that may also react with adventitious oxygen (and *via* hydration and hydrolysis may also, or alternatively react with water) reducing the probability of ≡Ge-O, ≡Ga-O and -Se-O bonds forming in the glass and thus minimising the decrease in transmission at the fingerprint for Ge-O vibrational absorption.

It is to be noted that % transmittance was not calculated from the optical pathlengths. Therefore, the relative vertical values of % Transmission are not quantitative. Sample discs of core glass M240RERC ($Ge_{19.4}Sb_{9.7}Se_{67.9}Ga_3$ at. % + 500 ppmw Dy foil) and Series (ii) cladding glass M267RC ($Ge_{21}Sb_{10}Se_{69}$ at. %) were hot pressed to a thickness of 1.3 mm and 1.2 mm, respectively. The remaining compositions in Figures 5.11 and 5.12 were hot pressed to approximately 1.5 mm.

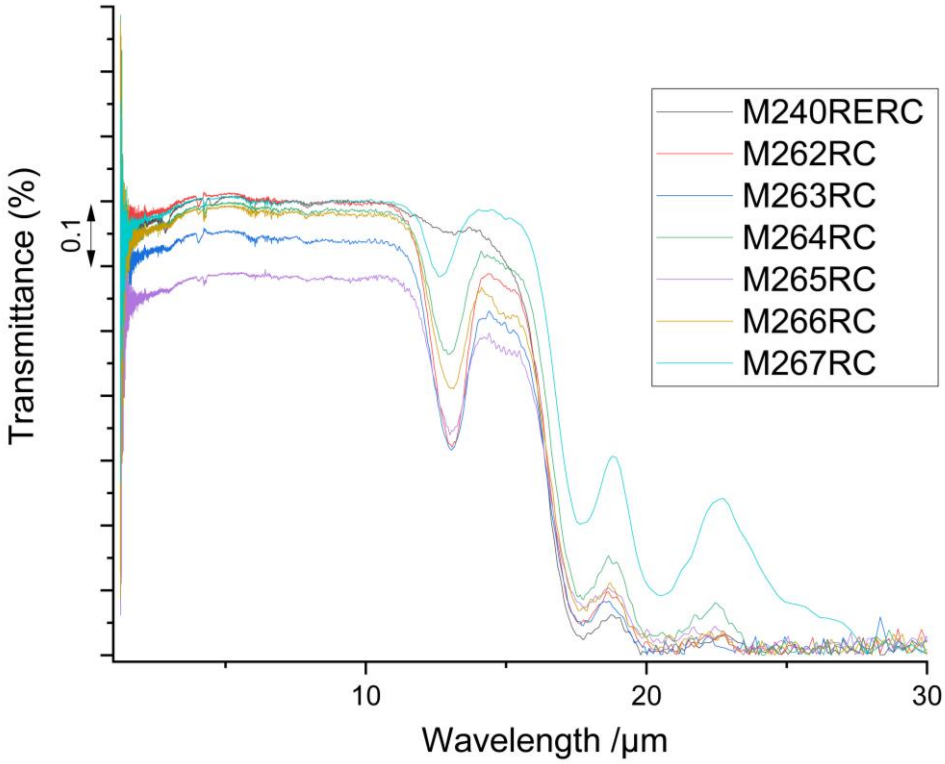


Figure 5.11 Transmittance spectra, as measured from the IR-VASE, from 1.5 μm to 30 μm for each glass composition detailed in Table 5.1. Samples were discs cut from the as-annealed preforms listed in Table 5.1. These preforms were annealed at the 'guestimated' T_g of 222 °C as DSC measurements were carried out after the melt-quench and annealing process. These disc samples had a thickness approximately 1.5 mm between faces with a 1 μm polish and had been subject to a hot-pressing treatment to ensure flatness and that opposite faces were parallel. The grey in colour plot corresponding to the dopable host core glass, M240RERC ($Ge_{19.4}Sb_{9.7}Se_{67.9}Ga_3$ at. % + 500 ppmw Dy foil), shows the previously mentioned reduction of the 12.7 μm Ge-O impurity absorption band. Two cycles consisting of 10 scans at 8 cm^{-1} resolution were collected to obtain an averaged transmittance spectrum. Note: % Transmission was not calculated from the optical pathlengths. Therefore, the relative vertical values of % Transmission are not quantitative. In any case the effect of background scattering loss due to imperfect grinding/polishing is present.

Figure 5.12 shows the same measurements as shown in Figure 5.11 but with the X-axis fixed between 2 – 10 μm wavelength. That is, it is the same set of data as Figure 5.11 but re-scaled to visually aid the following discussion on impurity absorption bands between 2-10 μm. The absorption at 4.0 μm seen in the exploratory cladding glasses Series (i) and (ii) M262RC-M266RC (See Table 5.1 for compositions) is attributed to S-H absorptions[201]. The absorption is smaller in M264RC ($Ge_{19.4}Sb_{9.7}Se_{68.9}Ga_1S_1$ at. %, Series (i)) due to the lower S content (1 at. %) and is absent from the sulfur free compositions M240RERC

($Ge_{19.4}Sb_{9.7}Se_{67.9}Ga_3$ at. % + 500 ppmw Dy foil, core glass) and M267RC ($Ge_{21}Sb_{10}Se_{69}$ at. %, Series (ii)). Despite the low sulfur content (1-2 at. %) there is a notable reduction in the prevalence of the Se-H absorption band at 4.55 µm (Table 2.3, Section 2.3.3.2) in Series (i) M262RC ($Ge_{20}Sb_{10}Se_{68}S_2$ at. %), Series (i) M263RC ($Ge_{19.4}Sb_{9.7}Se_{67.9}Ga_1S_2$ at. %), Series (i) M264RC ($Ge_{19.4}Sb_{9.7}Se_{68.9}Ga_1S_1$ at. %), Series (ii) M265RC ($Ge_{19.4}Sb_{9.7}Se_{66.9}Ga_2S_2$ at. %), and Series (ii) M266RC ($Ge_{19.4}Sb_{9.7}Se_{65.9}Ga_3S_2$ at. %), when compared to core glass M240RERC (($Ge_{19.4}Sb_{9.7}Se_{67.9}Ga_3$ at. % + 500 ppmw Dy foil) and M267RC ($Ge_{21}Sb_{10}Se_{69}$ at. %, Series (ii)). This reduction of the Se-H impurity absorption at 4.55 µm due to unwanted hydrogen impurities preferentially bonding to the atomically smaller, more electronegative sulphur over selenium. This preferential bonding is due to the -S-H bond being stronger than the equivalent -Se-H bond that is more thermodynamically stable and so forms preferentially over the -Se-H bond, for instance at the high temperatures encountered during glass melting when true thermodynamic equilibrium can be attained in a kinetically accessible timescale.

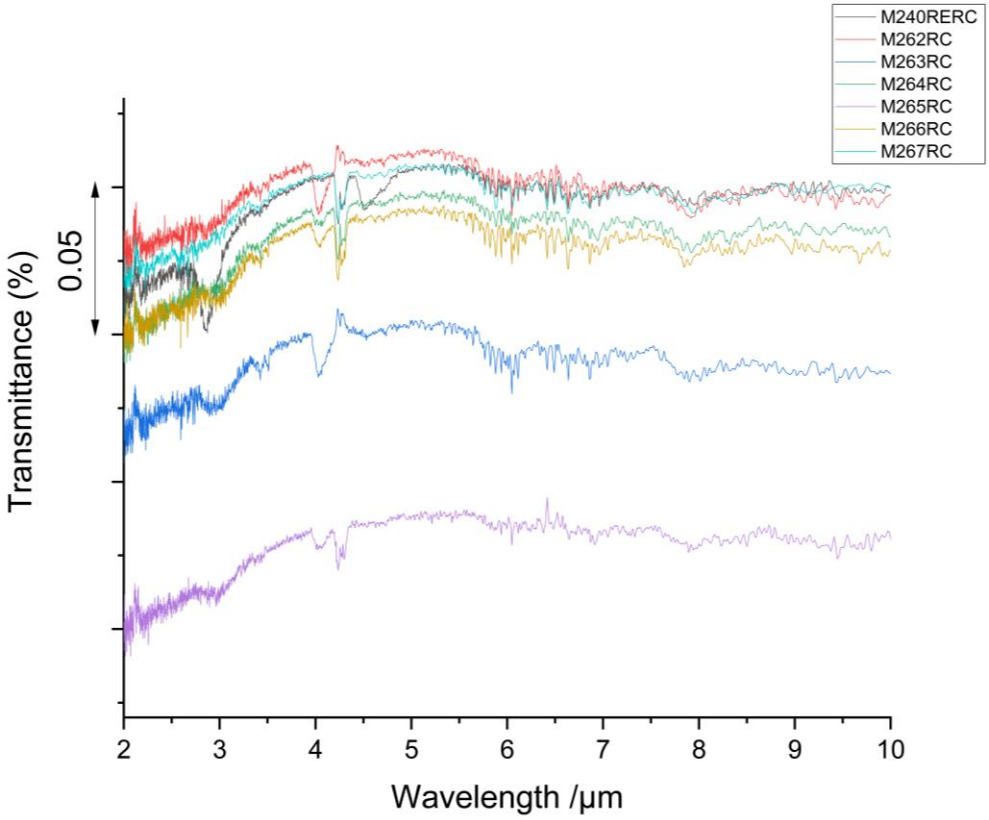


Figure 5.12 Transmittance spectra, as measured from the IR-VASE, from 2 μm to 10 μm wavelength for each glass composition detailed in Table 5.1. This is the same data presented in Figure 5.11 but re-scaled to better observe absorption peaks between 2-10 μm. Samples were discs cut from the as-annealed preforms listed in Table 5.1. These preforms were annealed at the 'guestimated' T_g of 222 °C as DSC measurements were carried out after the melt-quench and annealing process. These disc samples had a thickness approximately 1.5 mm between faces with a 1 μm polish and had been subject to a hot-pressing treatment to ensure flatness and that opposite faces were parallel. The grey in colour plot corresponding to the dopable host core glass, M240RERC ($Ge_{19.4}Sb_{9.7}Se_{67.9}Ga_3$ at. % + 500 ppmw Dy foil), shows the previously mentioned reduction of the 12.7 μm Ge-O impurity absorption band. Two cycles consisting of 10 scans at 8 cm^{-1} resolution were collected to obtain an averaged transmittance spectrum. Note: % Transmission was not calculated from the optical pathlengths. Therefore, the relative vertical values of % Transmission are not quantitative. In any case the effect of background scattering loss due to imperfect grinding/polishing is present.

5.3.4 Development of a GenOsc® Layer based model for refractive index determination

The companion software to the mid-IR VASE equipment, CompleteEase (Woollam, USA), was used to develop the models required to fit the measured ellipsometry data. All models were based off of a General Oscillator layer (GenOsc®). The General Oscillator Layer function models the dielectric function

of the bulk chalcogenide samples as calculated from the chosen oscillators (real and complex terms) and dispersion equations input into the model. In practical terms, it linearly combines the chosen oscillators (functions of wavelength) to explain the values taken from the spectroscopic measurement, psi (Ψ) and delta (Δ). To quantify how well the model fitted to the measured Ψ and Δ values, the CompleteEase software calculates a mean squared error (MSE) value. This value is based on the differences between measured data and modelled data over the entire wavelength range modelled. While a value of "1" is considered an ideal fit, the software developers (Woollam, USA) note that for models developed for thicker samples or samples with multiple layers, MSE values can exceed "10" and still be considered a well-fitting model. The models were developed with the intention to get the lowest MSE value with a minimal number of oscillations. If a new oscillator was added but did not provide a 10% reduction in MSE then it was not incorporated into the final model.

The spectroscopic ellipsometry measurement was taken after one surface of the 1 µm polished, hot pressed bulk glass sample had been roughened sufficiently using a Dremel rotary tool fitted with a diamond point wheel bit (unspecified diamond particle size and finish quality) as previously described in Section 3.3.5. As part of the VASE (Variable Angle Spectroscopic Ellipsometry) system, multiple angles of incident are used to create a complete measurement. For all glasses here subject to ellipsometry, 55 °, 65 °, and 75 ° angles were used, each angle was scanned for three cycles consisting of 20 scans each. Measurements were collected at a resolution of 4 cm^{-1}. Although the VASE measurement recorded between 1.5 – 40 µm, these mathematical models were applied over a 2 – 30 µm wavelength range for each glass. This is due to the high amount of noise < 2 µm and > 30 µm which would affect the fit of the model within this range. As seen in Figure 5.4, transmission is near zero beyond 25 µm and so it was not seen as necessary to model refractive index beyond 30 µm as there is no practical use for these compositions in a chalcogenide step-index fibre at these wavelengths. Below 2 µm it would be preferable to take a measurement with a near-IR ellipsometer.

5.3.4.1 Multiple Gaussian oscillator model

With the initial aim to fit the model to the absorptions measured from the transmission measurements, the $Ge_{19.4}Sb_{9.7}Se_{67.9}Ga_3$ at. % + 500 ppmw Dy foil doped core host glass, M240RERC, was the first sample modelled. The electronic absorptions of dysprosium were anticipated to add an additional degree of complexity to the model. It was proposed that if the multiple Gaussian model was suitable for the doped glass, it would also be suitable for the undoped cladding glass. Initial models for M240RERC ($Ge_{19.4}Sb_{9.7}Se_{67.9}Ga_3$ at. % + 500 ppmw Dy foil) had Gaussian oscillators placed at 2.8 µm (Dy $^6H_{13/2}$ and -OH), 4.6 µm (Se-H), 12.7 µm (Ge-O), and 17.6 µm (Sb-O). There are three fit parameters for each Gaussian included. Amp (no units) is amplitude, En (eV) is centre energy, and Br (eV) is broadening (See Table 5.2). The CompleteEase software can visualise the fit of the model in real time as the parameters are manually altered. Einf (E infinite) adds an offset which approximates effects of absorptions outside of measured wavelengths. Einf was not manually altered but modelled automatically by the CompleteEase software to find the best fit. With the addition of each Gaussian, the fit of the model became more erratic and changing the broadness and amplitude of the oscillators did not provide any reasonable improvement to the model fit. Reduction in the number of Gaussian oscillators also did not improve the fit of the model and so the concept of a multiple Gaussian model was retired.

5.3.4.2 Three oscillator model (2 Pole, 1 Gaussian)

Previous work from the Mid-IR photonics group at University of Nottingham, UK, from the PhD work of Dr Yuanrong Fang [202]had identified that a two-term Sellmeier model provided a superior fit to experimentally measured data and by assigning the Sellmeier coefficients used in the model to the shortwave electronic absorption edge, or, optical bandgap and vibrational band fundamental absorption, the model can then be considered an interpretation of the physical properties of the glass[202,203]. Therefore, the second model for core glass M240RERC, $Ge_{19.4}Sb_{9.7}Se_{67.9}Ga_3$ at. % + 500 ppmw Dy foil, was initially composed of two pole (Sellmeier) oscillators beginning at around 0.6 µm and 42 µm with the intention that the CompleteEase software would find the optimal wavelengths *via* its regression analysis. That is, 0.6 µm and 42 µm were chosen as very rough values

representing the shortwave electronic absorption edge and vibrational fundamental absorption edge of selenide-based chalcogenide glasses, respectively, and then the CompleteEase software was instructed to fine tune the Sellmeier parameters, including wavelength (centre energy, eV) to optimise the model fit. These values were chosen based on work by Dantanarayana *et al.* [203] studying Ge-As-Se glasses who, using a similar two-term Sellmeier model, used values below 0.7 µm and above 33 µm to represent the short (electronic) and long (vibrational) wavelength edge in their model, respectively[203]. As Sellmeier/pole oscillators have zero broadening, the fit parameters are amplitude (no units) and centre energy (eV). A best fit was achieved with the pole oscillators centred at 0.6 µm and 38.9 µm (see Table 5.2).

A Gaussian oscillator was then added at 20.7 µm to assess if this would improve the model fit. At 20.7 µm, the inclusion of the Gaussian oscillator slightly worsened the MSE value given. By manually shifting this Gaussian to the longer wavelengths, the MSE value began to improve until 33.15 µm (Table 5.2). At which point the MSE value began to decrease again. This improvement satisfied a proposed criteria by Dr Nikolaos Kalfagiannis, who was the point of contact for the IR-VASE use at the iSmart facility, Nottingham Trent University, UK, (where the IR-VASE used in this Project was housed) in which the addition of any oscillator should give at least a "$>10\%$ improvement to MSE" and so this Gaussian at 33.15 µm was incorporated into the model. This absorption can be attributed to polymeric Se-Se chains [204–206] which are expected to be prevalent in M240RERC, $Ge_{19.4}Sb_{9.7}Se_{67.9}Ga_3$ at. % with a Se at. % content at 67.9 %.

Einf, again, was automatically handled by CompleteEase. This three-oscillator model (2 Pole, 1 Gaussian) was then ran twice more with the same parameters to ensure consistency and that the regression analysis did not improve or worsen the MSE value given. The surface roughness function of the Gen-Osc layer was then applied. This uses a Bruggeman effective media approximation to model the optical constants of a homogenous, mixed layer as part void-part sample with a 50:50 distribution. The part void is given constants of $n = 1$, $k = 0$. It was intended that this layer would account for a lower refractive index, thin surface oxide layer that is assumed to be present on the surface of the glasses. The layer is

homogenous and not graded. This provided an improved MSE value and a visible improvement to the graphed model fit. The parameters in the final model are given in Table 5.2.

This three-oscillator model (2 Pole (Sellmeier), 1 Gaussian) was subsequently applied to the ellipsometry data for each glass measured that is: (Series (i) and (ii) exploratory cladding glasses, Section 5.2, Table 5.1 for compositions) and core glass M240RERC (Section 4.1.2.1, Table 5.1 for compositions). Consistent model fittings, as measured by MSE, were found for each glass sample (Table 5.2). The model parameters and MSE values for each sample are listed in Table 5.2. To reiterate what was stated above, the mean square error (MSE) value is based on the differences between measured data and modelled data over the entire wavelength range modelled. A value of "1" is considered an ideal fit but the software developers (Woollam, USA) note that for models developed for thicker samples or samples with multiple layers, MSE values can exceed "10" and still be considered a well-fitting model.For each sample, the oscillators centre energy (En) was manually set and locked to 0.6 µm for Pole 1, 40 µm for Pole 2, and 34 µm for Gaussian. The remaining parameters (amplitude and Einf) were fitted *via* CompleteEase regression analysis. The centre energy values were then also permitted to be fitted by the software regression analysis to further optimise the MSE value. Once a respectable MSE value had been achieved (between 2-6) with these three oscillators (two pole, one Gaussian), the surface roughness function was added to the model. The regression analysis was then ran a third time with all the aforementioned parameters to find the optimal surface roughness value. In every case, the addition of a surface roughness value improved the MSE value.

The refractive index values taken from these models were then compared to those of similar composition found in literature as an additional validity check[110,189]. Using a similar model, Fang *et al.* determined the refractive index (RI) value of $Ge_{20}Sb_{10}Se_{70}$ at. % at 5 µm as 2.544[189]. Using the model described in Table 5.2, the refractive index value of $Ge_{21}Sb_{10}Se_{69}$ at. % (M267RC) at 5 µm as 2.521. As anticipated due to Ge being added in lieu of the larger, more polarisable Se, the higher Ge content composition ($Ge_{21}Sb_{10}Se_{69}$ at. %) has a slightly lower RI than $Ge_{20}Sb_{10}Se_{70}$ at. % (1 at. % Ge for Se giving a 0.023 decrease).

Table 5.2 Parameters used in each "Three oscillator model" for exploratory cladding glasses (Section 5.2) and M240RERC core glass in CompleteEase v6.53 (Glass compositions detailed below) over the 2-30 µm wavelength range.

Glass code	Surf. rough. (nm)	Einf	Pole 1		Pole 2		Gaussian			MSE (2-30 µm)
			Amp (no units)	En (eV) (µm)	Amp (no units)	En (eV) (µm)	Amp (no units)	Br (eV)	En (eV) (µm)	
M240RERC $Ge_{19.4}Sb_{9.7}Se_{67.9}Ga_3$ at. % + 500 ppmw Dy foil **(core glass)**	7.92	5.691	3.2557	2.058 (0.602)	0.0085	0.0319 (38.865)	1.8587	0.0036	0.0374 (33.1497)	2.719
M262RC $Ge_{20}Sb_{10}Se_{68}S_2$ at. % **(Series i)**	12.23	6.246	0.6759	2.122 (0.5843)	0.0011	0.0283 (43.8092)	0.3035	0.0249	0.0363 (34.1543)	3.185
M263RC $Ge_{19.4}Sb_{9.7}Se_{67.9}Ga_1S_2$ at. % **(series i)**	5.52	6.303	0.7001	2.122 (0.5843)	0.0011	0.0283 (43.8092)	0.3315	0.0222	0.0363 (34.1543)	2.954
M264RC $Ge_{19.4}Sb_{9.7}Se_{68.9}Ga_1S_1$ at. % **Series (i)**	9.86	5.814	2.9061	2.040 (0.6077)	0.0007	0.0318 (38.9874)	2.0853	0.00398	0.0369 (33.5989)	3.448
M265RC $Ge_{19.4}Sb_{9.7}Se_{66.9}Ga_2S_2$ at. % **Series (ii)**	8.53	6.021	1.0579	1.695 (0.7314)	0.0007	0.0364 (34.0604)	0.3320	0.00732	0.0467 (26.5482)	4.447
M266RC $Ge_{19.4}Sb_{9.7}Se_{65.9}Ga_3S_2$ at. % **Series (ii)**	14.45	6.104	0.8624	1.697 (0.7306)	0.0009	0.0343 (36.1458)	0.3474	0.00706	0.0467 (26.5482)	2.080
M267RC $Ge_{21}Sb_{10}Se_{69}$ at. % **Series (ii)**	7.67	5.967	1.4525	1.916 (0.6471)	0.0009	0.0318 (38.9874)	0.9518	0.0052	0.0371 (33.4178)	2.444

En values given in eV (and µm). Models plotted over 2 – 30 µm wavelength range.

The resulting series of models had calculated MSE values between 2.080 and 4.447 (Table 5.2). This was below the quoted target of MSE values < 10 provided by the software manufacturer, dictated to the current author by Dr Nikolaos Kalfagiannis. As this Three oscillator model (two poles, one Gaussian) consistently provided good fittings to the 2-30 µm wavelength range measured data over the 7 different glass compositions detailed in Table 5.2 and used a similar framework to that described in Fang *et al.*[189,202] and Dantanarayana *et al.* [203] to provide a model based on the physical optical characteristics of the target glass, it was accepted as a usable model to determine refractive index for chalcogenide glass networks.

5.4 M266RC ($Ge_{19.4}Sb_{9.7}Se_{65.9}Ga_3S_2$ at. %) and M267RC ($Ge_{21}Sb_{10}Se_{69}$ at. %) as potential cladding glasses for small core, rare earth ion doped chalcogenide glass fibres whose core glass composition is similar to $Ge_{19.4}Sb_{9.7}Se_{67.9}Ga_3$ at. %

From the DSC data displayed in Table 5.1, M266RC ($Ge_{19.4}Sb_{9.7}Se_{65.9}Ga_3S_2$ at. %) and M267RC ($Ge_{21}Sb_{10}Se_{69}$ at. %) were the only compositions considered as potential claddings for the $Ge_{19.4}Sb_{9.7}Se_{67.9}Ga_3$ at. % host glass system (Such as 1000 ppmw Sm^{3+} $Ge_{19.4}Sb_{9.7}Se_{67.9}Ga_3$ at. % (F099RERC, M227RERC, Section 4.2), or 500 ppmw Dy^{3+} $Ge_{19.4}Sb_{9.7}Se_{67.9}Ga_3$ at. % (F104RERC, M240RERC, Section 4.3) as they were the only glasses that satisfied the criteria of having a T_g value of 232 °C ± 10 °C (the T_g for $Ge_{19.4}Sb_{9.7}Se_{67.9}Ga_3$ at. % (M227RERC, M240RERC). Using the refractive index values taken from the 3 oscillator models (Table 5.1 for RI values. Table 5.2 for model parameters), the numerical aperture of theoretical M266RC/M240RERC ($Ge_{19.4}Sb_{9.7}Se_{65.9}Ga_3S_2$ at. % / 500 ppmw Dy^{3+} $Ge_{19.4}Sb_{9.7}Se_{67.9}Ga_3$ at. %) and M267RC/M240RERC ($Ge_{21}Sb_{10}Se_{69}$ at. % / 500 ppmw Dy^{3+} $Ge_{19.4}Sb_{9.7}Se_{67.9}Ga_3$ at. %) step-index fibres could be calculated using Equation 5.1.

$$\sqrt{n_{core}^2 - n_{clad}^2} \qquad \text{Equation 5.1}$$

n = refractive index

Considering that the core glass, M240RERC ($Ge_{19.4}Sb_{9.7}Se_{67.9}Ga_3$ at. %), was doped with 500 ppmw Dy^{3+} it was of interest to calculate the numerical aperture at the dysprosium ion photoluminescence emission wavelengths 2.8 µm and 4.3 µm, corresponding to emissions from the $^6H_{13/2} \rightarrow {}^6H_{15/2}$ energy level and $^6H_{11/2} \rightarrow {}^6H_{13/2}$, respectively (see Figure 6.24).

Table 5.3 shows the calculated NA for both proposed fibres at these wavelengths (2.8 µm and 4.3 µm). M266RC/M240RERC ($Ge_{19.4}Sb_{9.7}Se_{65.9}Ga_3S_2$ at. % / 500 ppmw Dy^{3+} $Ge_{19.4}Sb_{9.7}Se_{67.9}Ga_3$ at. %) has a calculated NA lower at both 2.8 µm (NA= 0.3098) and 4.3 µm (NA= 0.3226) when compared to M267RC/M240RERC ($Ge_{21}Sb_{10}Se_{69}$ at. % / 500 ppmw Dy^{3+} $Ge_{19.4}Sb_{9.7}Se_{67.9}Ga_3$ at. %) at 2.8 µm (NA= 0.3438) and 4.3 µm (NA= 0.3638). To very roughly compare, previous work from the Mid-IR Photonics Group, University of Nottingham, UK, had used a GeAsSeGa at. % core/ $GeAsSe_{(-S)}GaS_3$ at. % cladding glass, to make small core rare earth doped fibres [110]. This resulted in a step-index fibre with an NA of ~0.4 across the 3.5-6 µm wavelength region [110].

Table 5.3 Calculated numerical aperture of potential structured fibres M266RC/M240RERC ($Ge_{19.4}Sb_{9.7}Se_{65.9}Ga_3S_2$ at. % / 500 ppmw Dy^{3+} $Ge_{19.4}Sb_{9.7}Se_{67.9}Ga_3$ at. %) and M267RC/M240RERC ($Ge_{21}Sb_{10}Se_{69}$ at. % / 500 ppmw Dy^{3+} $Ge_{19.4}Sb_{9.7}Se_{67.9}Ga_3$ at. %) at 2.8 µm and 4.3 µm wavelength.

	M266RC/M240RERC ($Ge_{19.4}Sb_{9.7}Se_{65.9}Ga_3S_2$ at. % / 500 ppmw Dy^{3+} $Ge_{19.4}Sb_{9.7}Se_{67.9}Ga_3$ at. %) numerical aperture	M267RC/M240RERC ($Ge_{21}Sb_{10}Se_{69}$ at. % / 500 ppmw Dy^{3+} $Ge_{19.4}Sb_{9.7}Se_{67.9}Ga_3$ at. %) numerical aperture
2.8 µm	0.3098	0.3438
4.3 µm	0.3226	0.3638

With the aim to optically pump an antimony-based dysprosium doped small core fibre at 2.8 µm, Equation 5.2 was used to calculated required NA values and core sizes to achieve single mode propagation.

$$r = \frac{2.405}{(k*NA)} \qquad \text{Equation 5.2}$$

r = radius of core NA = numerical aperture

k = cut off wavenumber (minimum wavelength that the fibre will still act single mode)

This gave target NA values of 0.19 to achieve single mode propagation of 2.8 µm light in a 10 µm core, and NA values of 0.13 to achieve single mode propagation of 2.8 µm light in a 15 µm core. The fibre fabrication detailed in Section 3.2.9 could be used to draw chalcogenide small core fibres with core diameters ranging from 5 – 30 µm, meaning that once the NA of the fibre is determined, a small core fibre with a suitable core size for the desired wavelength can then be drawn to match the criteria. With a lower core size limit of 5 µm using the fibre fabrication method in Section 3.2.9, an NA value of 0.25 at 2.8 µm is required, which is not met by either M266RC/M240RERC ($Ge_{19.4}Sb_{9.7}Se_{65.9}Ga_3S_2$ at. % / 500 ppmw Dy^{3+} $Ge_{19.4}Sb_{9.7}Se_{67.9}Ga_3$ at. %) or M267RC/M240RERC ($Ge_{21}Sb_{10}Se_{69}$ at. % / 500 ppmw Dy^{3+} $Ge_{19.4}Sb_{9.7}Se_{67.9}Ga_3$ at. %). These calculated NA requirements are also lower than the NA measured in the GeAsSeGa at. % core/ $GeAsSe_{(-S)}GaS_3$ at. % cladding glass small core fibre in Tang *et al.* [110] with an NA ~0.4 over 3.5-6 µm.

Despite neither M266RC/M240RERC ($Ge_{19.4}Sb_{9.7}Se_{65.9}Ga_3S_2$ at. % / 500 ppmw Dy^{3+} $Ge_{19.4}Sb_{9.7}Se_{67.9}Ga_3$ at. %) nor M267RC/M240RERC ($Ge_{21}Sb_{10}Se_{69}$ at. % / 500 ppmw Dy^{3+} $Ge_{19.4}Sb_{9.7}Se_{67.9}Ga_3$ at. %) being calculated to provide single-mode propagation of 2.8 µm light, both proposed fibres had calculated NA values that would provide sufficient core light guiding at the dysprosium emission wavelengths. With both M266RC ($Ge_{19.4}Sb_{9.7}Se_{65.9}Ga_3S_2$ at. %) and M267RC ($Ge_{21}Sb_{10}Se_{69}$ at. %) being considered functionally similar (both meet the T_g 232 °C (± 10 °C) of host core glass: $Ge_{19.4}Sb_{9.7}Se_{67.9}Ga_3$ at. % (M240RERC) and both provide core light guiding when used as cladding for $Ge_{19.4}Sb_{9.7}Se_{67.9}Ga_3$ at. %

(M240RERC), the decision of which glass to use as a cladding was decided as a matter of practicality.

As mentioned in Section 3.2.2.5 and Section 5.2.2.2, gallium did not undergo any prior purification beyond a mechanical physical transfer of Ga away from a thin film of what is assumed to be Ga_2O_3 on the surface of the Ga material stock. There is then the high probability that gallium containing glasses have some of this Ga_2O_3 impurity incorporated into the chalcogenide melts and thus included in fibres. The risk of oxide impurity introduction from Ga_2O_3 was avoided in M267RC ($Ge_{21}Sb_{10}Se_{69}$ at. %) as it is a gallium free composition. Section 4.1.2 details the potential of Ga to form an oxide-based skin layer on the surface of the glass during fibre drawing which is also prevented with its absence in M267RC ($Ge_{21}Sb_{10}Se_{69}$ at. %). Gallium has also been shown to devitrify with chalcogens in the form of crystalline α-Ga_2Se_3, which has been identified in arsenic-based glasses ($Ge_{16.5}As_{(19-x)}$ $Ga_xSe_{64.5}$ at. % formula) [55,133]. Additionally, the glass fabrication process is simpler with M267RC ($Ge_{21}Sb_{10}Se_{69}$ at. %) compared to M266RC ($Ge_{19.4}Sb_{9.7}Se_{65.9}Ga_3S_2$ at. %). As described in detail in Section 5.2.2.2, with M266RC, the selenium for sulfur containing selenide base melts needs to be prior purified in a separate silica ampoule (Section 3.2.2) which is then broken opened, and the selenium extracted. Opening the silica glass ampoule introduces the risk of small silica pieces in the forms of shards being present alongside the selenium, which is then mechanically broken down into smaller pieces with an agate (SiO_2) pestle and mortar before batching into a second silica glass ampoule containment that was used to heat-treat sulfur. When compared to the other exploratory cladding glasses (Table 5.1), M267RC ($Ge_{21}Sb_{10}Se_{69}$ at. %) fabrication, therefore, is a much "cleaner" and economical process in which only one ampoule is used as the selenium is purified in the melt ampoule and the germanium and antimony are batched in.

M266RC ($Ge_{19.4}Sb_{9.7}Se_{65.9}Ga_3S_2$ at. %) was also compositionally very similar to M237RC ($Ge_{19.4}Sb_{9.7}Se_{65}Ga_3S_{2.9}$ at. %), with M266RC having ~1 at. % less sulfur, and ~1 at. % more selenium. It was unlikely that this 1 at. % substitution would have a drastic effect on the fibre draw characteristics, so M266RC ($Ge_{19.4}Sb_{9.7}Se_{65.9}Ga_3S_2$ at. %) was deemed to have a high likelihood of failing to

fibre draw to a small core fibre (as did M237RC ($Ge_{19.4}Sb_{9.7}Se_{65}Ga_3S_{2.9}$ at. %) in Section 5.1.3.3).

For these reasons, M267RC ($Ge_{21}Sb_{10}Se_{69}$ at. %) was chosen as the prospective cladding glass for M240RERC (500 ppmw Dy^{3+} $Ge_{19.4}Sb_{9.7}Se_{67.9}Ga_3$ at. %). Figure 5.6 shows the refractive indices for both glasses over a 2-20 µm wavelength range as well as the corresponding numerical aperture (NA). The plotted lines show the model calculated values and the hollow circle markers are representative of the measured data over the three angles used (55, 65, 75 °) during spectroscopic ellipsometry.

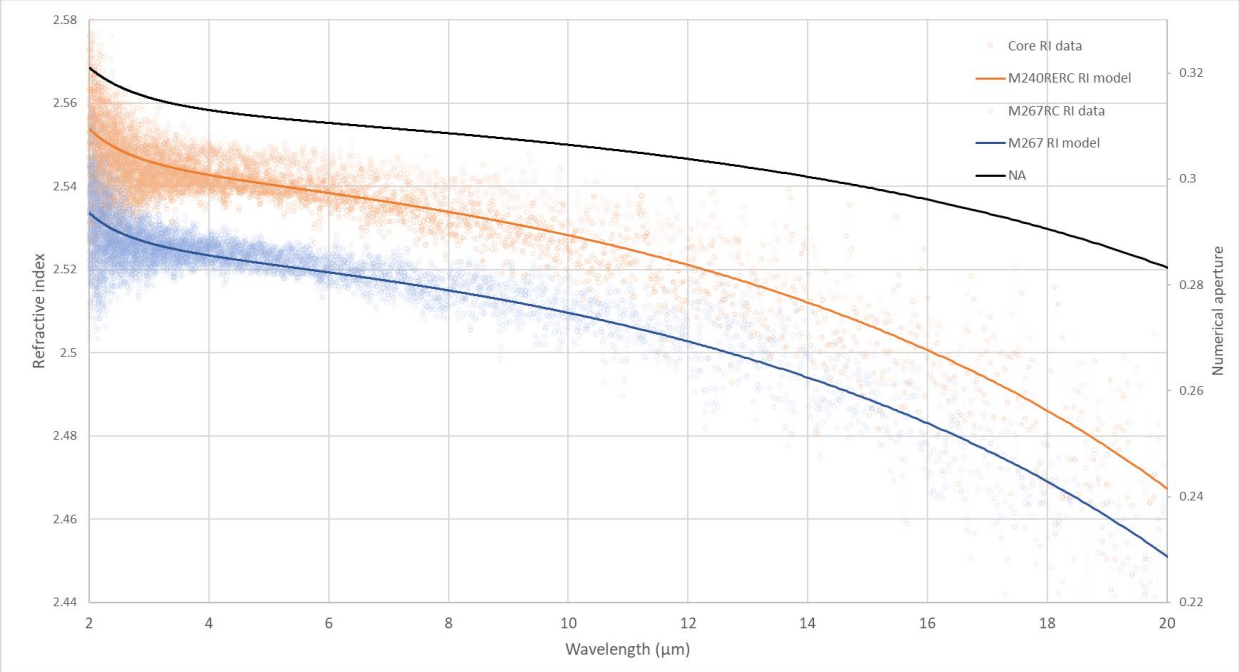


Figure 5.13 Refractive index data for the chosen core (M240RERC, 500 ppmw Dy^{3+} $Ge_{19.4}Sb_{9.7}Se_{67.9}Ga_3$ at. %) and cladding (M267RC, $Ge_{21}Sb_{10}Se_{69}$ at. %) glasses. Solid lines represent data collected from the three oscillator models for each composition. Hollow circles indicate measured data from the ellipsometry measurement. Grey line indicates numerical aperture over the wavelength range using Equation 5.1.

With M267RC ($Ge_{21}Sb_{10}Se_{69}$ at. %) being identified *via* DSC as having a suitable T_g and refractive index *via* variable angle spectroscopic ellipsometry to act as a cladding glass for M240RERC ($Ge_{19.4}Sb_{9.7}Se_{67.9}Ga_3$ at. %), it was decided to proceed with the melting and extrusion of a new $Ge_{21}Sb_{10}Se_{69}$ at. % cladding tube and attempt the fabrication of a core/clad ($Ge_{19.4}Sb_{9.7}Se_{67.9}Ga_3$ at. % / $Ge_{21}Sb_{10}Se_{69}$ at. %) antimony-based fibre (Chapter 6).

5.5 Summary of chapter 5

Chapter 5 detailed the development of a series of glasses with the aim of identifying a suitable cladding glass for the dopable $Ge_{19.4}Sb_{9.7}Se_{67.9}Ga_3$ at. % composition detailed in chapter 4 (Section 4.1, 4.2, and 4.3). Glasses were fabricated and then analysed *via* DSC and VASE to determine suitability. It was concluded that M267RC $Ge_{21}Sb_{10}Se_{69}$ at. % could act as a suitable cladding glass for M240RERC $Ge_{19.4}Sb_{9.7}Se_{67.9}Ga_3$ at. %.

- A $Ge_{19.4}Sb_{9.7}Se_{65}Ga_3S_{2.9}$ at. % (M237RC) cladding glass tube was extruded, and a rod-in-tube preform was assembled with a cane of 500 ppmw Dy^{3+} $Ge_{19.4}Sb_{9.7}Se_{67.9}Ga_3$ at. % (M240RERC). The M237RC cladding failed (shattered) during fibre drawing after the development of a surface-skin (attributed to the development of crystalline $GeSe_2$). It is suggested this skin layer was a product of poor devitrification resistance of M237RC. The design of M237RC followed the 3 at. % sulfur for selenium substitution method that was previously successful in GeAsSeGa/GeAsSeGaS glasses (Tang *et al*. [110])

- A series of exploratory cladding glasses (Table 5.1 for compositions) with varying S, Ga, and Ge content was fabricated. The preliminary aim of this series of glasses (divided into Series (i) and Series (ii) was to find a cladding glass composition that had a T_g to match that of the core host glass composition of M240RERC, $Ge_{19.4}Sb_{9.7}Se_{67.9}Ga_3$ at. %, of 232 °C with a ± 10 °C tolerance.

- The Series (i) glass M262RC ($Ge_{20}Sb_{10}Se_{68}S_2$ at. %, T_g 217 °C) T_g change was in line with predictions, as it was anticipated a decrease in S at. % would lead to a decrease in T_g compared to the Parnell composition ($Ge_{20}Sb_{10}Se_{67}$ at. %, T_g 224 °C)[193]. The other Series (i) glasses, M263RC ($Ge_{19.4}Sb_{9.7}Se_{67.9}Ga_1S_2$ at. %) and M264RC ($Ge_{19.4}Sb_{9.7}Se_{68.9}Ga_1S_1$ at. %), featuring the addition of 1 at. % gallium, was expected to raise the T_g comparative to the Parnell composition ($Ge_{20}Sb_{10}Se_{70}$, T_g 214 °C) [193], but

unexpectedly measured lowered T_g values of 209 °C and 210 °C, respectively.

- Series (ii) glasses M265RC ($Ge_{19.4}Sb_{9.7}Se_{66.9}Ga_2S_2$ at. %) and M266RC ($Ge_{19.4}Sb_{9.7}Se_{65.9}Ga_3S_2$ at. %), were based on Series (i) M263RC ($Ge_{19.4}Sb_{9.7}Se_{67.9}Ga_1S_2$ at. %, T_g 209 °C) with increasing Ga content in substitute for Se. This led to an expected rise in T_g from M263RC T_g 209 °C to 220 °C and 229 °C for M265RC and M266RC, respectively. M267RC ($Ge_{21}Sb_{10}Se_{69}$ at. %, T_g 227 °C) exhibited an anticipated T_g increase comparative to the Parnell composition ($Ge_{20}Sb_{10}Se_{70}$, T_g 214 °C) [193]. Series (ii) yielded two compositions which matched the T_g 232 ± 10 °C criteria of the core glass M240RERC: M266RC ($Ge_{19.4}Sb_{9.7}Se_{65.9}Ga_3S_2$ at. %) and M267RC ($Ge_{21}Sb_{10}Se_{69}$ at. %).

- All glasses from exploratory cladding glass series (i) and (ii) (Table 5.2) were investigated using VASE (Variable Angle Spectroscopic Ellipsometry). Transmission measurements were first taken, before the 1µm polished, hot-pressed samples were roughened (Section 5.3.4) and reflectance measurements were taken from all samples listed in Table 5.2.

- CompleteEase software utilising GenOsc® material layers was used to develop models to determine refractive index values from the measured reflectance data.

- Initial RI model designs involved the fitting of Gaussian oscillators to absorption peaks measured during transmission measurements. Fitting many iterations of this model design to M240RERC (500 ppmw Dy^{3+} $Ge_{19.4}Sb_{9.7}Se_{67.9}Ga_3$ at. %) ellipsometry data yielded bad fittings, and so the concept of fitting multiple Gaussian oscillators was retired.

- A three-oscillator model consisting of one Sellmeier centred close to the optical bandgap, one Sellmeier centred close to the vibrational band fundamental absorption, and a Gaussian oscillator assigned close to the

intrinsic Se-Se absorption was then trialled. A surface roughness function intended to represent any thin surface oxide layers on the samples was also incorporated into the three-oscillator model. This model provided a good fit to measured data for all exploratory cladding glasses (Series (i) and (ii), Table 5.2) investigated.

- All the exploratory cladding glasses (Table 5.2), with the exception of M264RC ($Ge_{19.4}Sb_{9.7}Se_{68.9}Ga_1S_1$ at. %), were modelled to have RI values below that of M240RERC ($Ge_{19.4}Sb_{9.7}Se_{67.9}Ga_3$ at. %) (Table 5.2 for values), indicating they could be used to sufficiently guide light in a M240RERC ($Ge_{19.4}Sb_{9.7}Se_{67.9}Ga_3$ at. %) core step-index fibre. M267RC ($Ge_{21}Sb_{10}Se_{69}$ at. %) was ultimately chosen as a cladding glass for M240RERC ($Ge_{19.4}Sb_{9.7}Se_{67.9}Ga_3$ at. %) due to it meeting the T_g 232 ± 10 °C criteria of the core glass M240RERC, its ease of fabrication, and its speculated increased devitrification resistance when compared to M266RC ($Ge_{19.4}Sb_{9.7}Se_{65.9}Ga_3S_2$ at. %).

6. Fabrication and characterisation of antimony-based, arsenic core /antimony cladding hybrid, and high purity arsenic-based, small-core, step index fibres resulting in: (i) 500 ppmw doped Dy^{3+} Sb fibre, (ii) 500 ppmw doped Ce^{3+} fibre, which exhibited the first recorded continuous wave chalcogenide fibre lasing beyond 5 μm wavelength, (iii) 500 ppmw doped Dy^{3+} As fibre, and (iv) 250 ppmw doped $DyCl_3$ fibre.

The following is an overview of the work to be presented in this Chapter 6 which was making a series of small-core, step index fibres; the section number where each part of the work can be found are given for convenience.

In Chapter 5, exploration of the cladding glass compositions was reported which had resulted in an antimony-based cladding glass (M267RC, $Ge_{21}Sb_{10}Se_{69}$ at. %) with refractive index dispersion (see Table 5.1 and Figure 5.13) and thermal properties (See Table 5.1 and Figure 5.9) compatible with the 500 ppmw Dy^{3+} doped antimony-based core glass M240RERC ($Ge_{19.4}Sb_{9.7}Se_{67.9}Ga_3$ at. %) whose development was described in Chapter 4, see in particular Section 4.3.

Based on the work reported in Chapters 4 and 5, a large cladding boule of the chosen cladding glass, $Ge_{21}Sb_{10}Se_{69}$ at. %, was produced (M287RC, note the updated code number as a new glass of this composition was made). This large undistilled boule (~90 g, 25.6 mm ID/ 30 mm OD silica containment ampoule) of M287RC was melted (as described Section 3.2.4, Table 3.6(ii)) and then annealed (Section 3.2.6) at the measured T_g of 227 °C. The contraction cone was cut from the as-annealed M287RC ($Ge_{21}Sb_{10}Se_{69}$ at. %) boule using a diamond saw blade, cleaned with acetone and isopropanol, and was then extruded between 310-320 °C with increasing force up to 500 kg to maintain an extrusion rate of 0.2 mm/min (Section 3.2.8 for details on glass boule preparation and extrusion procedure) to one large jacket tube (E093RC). The cladding glass extrudate, E093RC, was subsequently cleaved into two separate tubes of equal length (both still referred to as E093RC) Each of these two E093RC tubes were fabricated with the intention they would subsequently be used to form a small core fibre through a cane-in-tube fibre drawing method (see Section 3.2.9). The following two purposes are as follows.

Thus, Section 6.1 details the results of the first half of this cladding tube (E093RC, M287RC ($Ge_{21}Sb_{10}Se_{69}$ at. %) fibre drawn with a cane of F104RERC ($Ge_{19.4}Sb_{9.7}Se_{67.9}Ga_3$ at. % + 500 ppmw Dy foil, Section 4.3) to form what was, to the best of this Author's knowledge, the first rare earth ion doped antimony small core fibre made according to what was already reported in literature[18,25,193].

Section 6.2, in contrast, details the fabrication of an arsenic-based core, antimony-based cladding small core SIF fibre (F130RERC) using the second tube of E093RC (M287RC, $Ge_{21}Sb_{10}Se_{69}$ at. %) fibre drawn with a cane of F109REZQT(RCJN) ($Ge_{15}As_{21}Se_{63}Ga_1$ at. % + 500 ppmw Ce foil). This fibre (F130RERC, $Ge_{15}As_{21}Se_{63}Ga_1$ at. % + 500 ppmw Ce foil core/ $Ge_{21}Sb_{10}Se_{69}$ at. % clad) was then imaged under SEM by the current Author, and passed to Joel Nunes (PhD colleague, Mid-IR Photonics Group, University of Nottingham, UK) who recorded the first instance of CW mid-IR fibre lasing in a rare earth ion doped chalcogenide glass host (Section 6.2.3.3) [15].

Section 6.3 and Section 6.4 covers the fabrication and characterisation of distilled, high purity dysprosium doped glass systems. Section 6.3.3 describes the trialling and optimisation of a novel, all silica glass vessel-based distillation method for anhydrous $DyCl_3$ (rather than Dy foil), designed by the current Author, to produce large (mm scale), batch able crystals for a novel method of Dy^{3+} rare earth ion doping.

In Section 6.3.1, an ~80 g melt of $Ge_{15}As_{21}Se_{63}Ga_1$ at. % host glass (M283RERC), reported in Tang *et al.* [110] was first melted and annealed at 240 °C. The entirety of the melt was then distilled and then divided approximately in half (accounting for distillation and batching losses) to melt into two ~30 g preforms (Section 6.3.1).

One preform had been doped with 250 ppmw distilled $DyCl_3$ (as annealed rod: M286RERC, then fibre drawn to F126RERC cane and fibre), and a second doped with 500 ppmw Dy foil (as annealed rod: M285RERC, then fibre drawn to F125RERC cane and fibre). Each of these two fibres were drawn to unstructured fibre in order to be able to make a fibre loss measurement of the core host glass (Section 6.4.1). The two fibres (canes) were then also fibre drawn to small core fibre using the cane-in-tube method using a $Ge_{16.5}As_{16}Se_{61.5}Ga_3S_3$ at. % cladding glass (M284RC) that had been extruded (E092) to a jacket tube (Section 6.4.2).

The 500 ppmw Dy foil doped small core fibre (F127RERC, 500 ppmw Dy foil $Ge_{15}As_{21}Se_{63}Ga_1$ at. % core / $Ge_{16.5}As_{16}Se_{61.5}Ga_3S_3$ at. % cladding) and 250 ppmw distilled $DyCl_3$ small core fibre (F128RERC, 250 ppmw $DyCl_3$ $Ge_{15}As_{21}Se_{63}Ga_1$ at. % core / $Ge_{16.5}As_{16}Se_{61.5}Ga_3S_3$ at. % cladding) were structurally characterised using SEM (Section 6.4.2). Joel Nunes (PhD colleague, Mid-IR Photonics Group, University of Nottingham, UK) then supplied photoluminescence and lifetime measurements of both unstructured F125RERC alongside optical results from a novel set up that utilised powdered fibre samples (Section 6.4.3).

6.1 Antimony based; dysprosium (III) doped small core step-index fibre (500 ppmw Dy foil $Ge_{19.4}Sb_{9.7}Se_{67.9}Ga_3$ at. % / $Ge_{21}Sb_{10}Se_{69}$ at. %)

As stated above, the first fibre aimed for was a Dy^{3+}doped small-core SIF (step index fibre) using the core glass composition whose development is reported in Chapter 4 (see Section 4.3) of general, as batched glass composition: $Ge_{19.4}Sb_{9.7}Se_{67.9}Ga_3$ at. % and cladding glass of general, as batched glass composition: $Ge_{21}Sb_{10}Se_{69}$ at. % whose development is reported in Chapter 5 (see Section 5.2.2)

A large boule (~26.5 mm diameter, 60 mm length (after removal of contraction cone), nominally 80 g total weight) of said cladding glass: $Ge_{21}Sb_{10}Se_{69}$ at. % was produced and given the code M287RC. The sources and purities of the precursor chemicals used are detailed in Table 3.1. Pre-preparation of the silica glass containment ampoule is detailed in Section 3.2.1. The precursors were heat treated as described in Section 3.2.2. M287RC ($Ge_{21}Sb_{10}Se_{69}$ at. %) was not subject to distillation and was fabricated through the standard melt-quench method detailed in Section 3.2.4 and 3.2.6. The whole boule (M287RC, $Ge_{21}Sb_{10}Se_{69}$ at. %) was extruded at around 320 °C, with a ramping load of 200-500 Kg until completion of the extrusion to form one jacket tube (E093RC) with a length around 220 mm. The extrusion process was completed as normal (see Section 3.2.8) without issue. The extruded tube (E093RC, $Ge_{21}Sb_{10}Se_{69}$ at. %) had an OD of 10.22 mm, and an ID of 900 µm. Figure 6.1 shows the distal end (*i.e*, the first part of the glass to leave the extruder) of the extruded tube after removal from the extruder. On this distal end of the tube from the extruder, an unwanted rough surface pattern was observed by eye.

As this surface patterning was not wanted in the final fibre to be drawn, it was decided that this surfaced section would be used as the "gob" to initiate the fibre drawing method which would occlude this section of the cladding from the final fibre. This E093RC $Ge_{21}Sb_{10}Se_{69}$ at. % jacket tube was then scored with a diamond scribe and snapped to divide into two jacket tubes of roughly equal length (now referred to as E093RC-(i) and E093RC-(ii)). Both tubes were of comparable geometry, with both tubes being straight (as determined by light being observed through the ~900 µm boreholes from each end). E093RC-(i) was used here in Section 6.1, with the second tube, E093RC-(ii) used for the work reported in Section 6.2.



Figure 6.1 Rough section of extruded jacket tube E093RC (from M287RC, $Ge_{21}Sb_{10}Se_{69}$ at. %). This was the first portion of glass through the extruder, the glass boule was placed with the contraction cone end first. This section was not further investigated and was used to initiate the fibre drawing process.

An 850 µm diameter cane of F104RERC (M240RERC, $Ge_{19.4}Sb_{9.7}Se_{67.9}Ga_3$ at. % + 500 ppmw Dy foil, Section 4.3) was inserted into a 90 mm length E093RC-(i) ($Ge_{21}Sb_{10}Se_{69}$ at. %) jacket tube with an ID ≈ 1000 µm. Prior to the insertion, the F104RERC cane was etched *via* full submersion in propylamine, at room

temperature, ambient atmosphere, under dust cover, for 70 hours to remove/reduce any surface oxidation. The rod was then rinsed in acetone and isopropanol (Purity and source in Table 3.2) and dried from isopropanol under the vacuum of the MBraun glovebox antechamber (0.5-1 mbar (50- 100 Pa)). This rod-in-tube preform was successfully drawn to fibre (F129RERC, ($Ge_{19.4}Sb_{9.7}Se_{67.9}Ga_3$ at. % + 500 ppmw Dy foil core / $Ge_{21}Sb_{10}Se_{69}$ at. % cladding)) producing step index fibres with targeted core sizes of 10, 15, and 20 µm. The F129RERC fibre exhibited reasonable stability throughout the fibre drawing with outer diameter fluctuations between ± 15 µm. Around 10 meters of each fibre size was drawn. The SEM investigation of the fibres follows in Section 6.1.1.

6.1.1 SEM EDX characterisation of F129RERC ($Ge_{19.4}Sb_{9.7}Se_{67.9}Ga_3$ at. % + 500 ppmw Dy foil core / $Ge_{21}Sb_{10}Se_{69}$ at. % cladding) small core, antimony-based step-index fibre

From the fibre described previous in Section 6.1, a 10 mm section of F129RERC ($Ge_{19.4}Sb_{9.7}Se_{67.9}Ga_3$ at. % + 500 ppmw Dy foil core / $Ge_{21}Sb_{10}Se_{69}$ at. % cladding) was cleaved, mounted vertically onto an aluminium SEM stub, and coated with a (nominally) 10 nm carbon layer (thickness as calculated by the coater, Q150R ES, QuorumTech). A JEOL 6490LV was used to image the F129RERC fibre face. Details on sample preparation and equipment used are elaborated on in Section 3.3.3. Imaging with a secondary electron detector fitted inside the JEOL 6490 LV indicated that the cladding glass had drawn to a circular shape with a small hole (< 1 µm diameter) towards the centre (Figure 6.2A, small hole visible in Figure 6.2B).

To image the core and cladding glasses, a backscatter electron detector also fitted into the JEOL 6490LV was employed. Due to the close match of the core ($Ge_{19.4}Sb_{9.7}Se_{67.9}Ga_3$ at. %, M240RERC) and cladding ($Ge_{21}Sb_{10}Se_{69}$ at. %, M287RC) compositions, imaging of the interface between the two glasses with the backscatter detector was difficult (Figure 6.2B). The accelerating voltage of the tungsten filament was set to 25 kV (~2.5 x the x-ray emission line of Kα1 in gallium) to try to differentiate between the core/clad due to the lack of gallium in the cladding ($Ge_{19.4}Sb_{9.7}Se_{67.9}Ga_3$ at. % + 500 ppmw Dy foil/ $Ge_{21}Sb_{10}Se_{69}$ at. %).

However, the resulting backscatter detector image was not of desirable quality as it was still difficult to clearly image the two glasses (Figure 6.2B).

Backscatter electrons from a sample that are generated from the incident electrons of the source in the SEM are composition dependent, with the number of backscattered electrons increasing with the average atomic number of the specimen[207]. Leading to higher contrast/signal with higher mean atomic numbers[207]. As the both the core ($Ge_{19.4}Sb_{9.7}Se_{67.9}Ga_3$ at. %) and cladding ($Ge_{21}Sb_{10}Se_{69}$ at. %) compositions were conceptually based on the original $Ge_{20}Sb_{10}Se_{70}$ at. % glass detailed in Parnell and Parnell *et al.* [54,189,193], the mean average atomic number between the core and cladding was likely very similar, as follows. From the $Ge_{20}Sb_{10}Se_{70}$ at. % compositional ratio, the core glass M240RERC, $Ge_{19.4}Sb_{9.7}Se_{67.9}Ga_3$ at. %, has an addition of 3 at. % gallium (atomic number: 31) while retaining the $Ge_{20}Sb_{10}Se_{70}$ (20:10:70) ratio. The cladding glass M287RC, $Ge_{21}Sb_{10}Se_{69}$ at. %, also closely matched the $Ge_{20}Sb_{10}Se_{70}$ ratio with an additional 1 at. % germanium (atomic number: 32) in substitute from selenium (atomic number: 34). The closely matched core/cladding compositions, and the small difference in atomic numbers of gallium and germanium that were added to the core and cladding glass, respectively, did not lead to any significant change in mean atomic number between the two compositions. This made differentiation between the core and clad difficult with backscatter electron imaging.

The GeAsSeGa core /GeAsSeGaS clad step-index fibre in Tang *et al.*[110] used a 3 at. % substitution of S (atomic number: 16) for Se (atomic number: 34). This substitution by Tang *et al.* led to a decrease in mean atomic number of the sulfur containing cladding glass, which was observable with a backscatter electron detector. The higher mean atomic number of the sulfur free core glass would provide more signal, and thus appeared as a brighter spot in the centre of the fibre (as seen in Figure 4 of reference [110]).

The backscatter detector image in Figure 6.2B also shows the presence of a small hole, as indicated by a red arrow on the image. Although difficult to determine due to the poor contrast between the core and the cladding, the current Author suggests that this hole is present in the cladding glass and not interfering with the core/cladding interface. This suggestion is based on observations made by the

Author during the SEM investigation (not pictured in this work) and further evidenced by the observations of holes in the cladding in Figure 6.5 of F130RERC ($Ge_{19.4}Sb_{9.7}Se_{67.9}Ga_3$ at. % + 250 ppmw $DyCl_3$ / $Ge_{21}Sb_{10}Se_{69}$ at. %). Both F129RERC ($Ge_{19.4}Sb_{9.7}Se_{67.9}Ga_3$ at. % + 500 ppmw Dy foil/ $Ge_{21}Sb_{10}Se_{69}$ at. %) and F130RERC ($Ge_{19.4}Sb_{9.7}Se_{67.9}Ga_3$ at. % + 250 ppmw $DyCl_3$ / $Ge_{21}Sb_{10}Se_{69}$ at. %) used claddings from E093RC-(i) and E093RC-(ii), respectively, and so it is suggested that the E093RC extrusion process produced a cladding glass tube containing these holes, which were then observed in the resulting fibres.

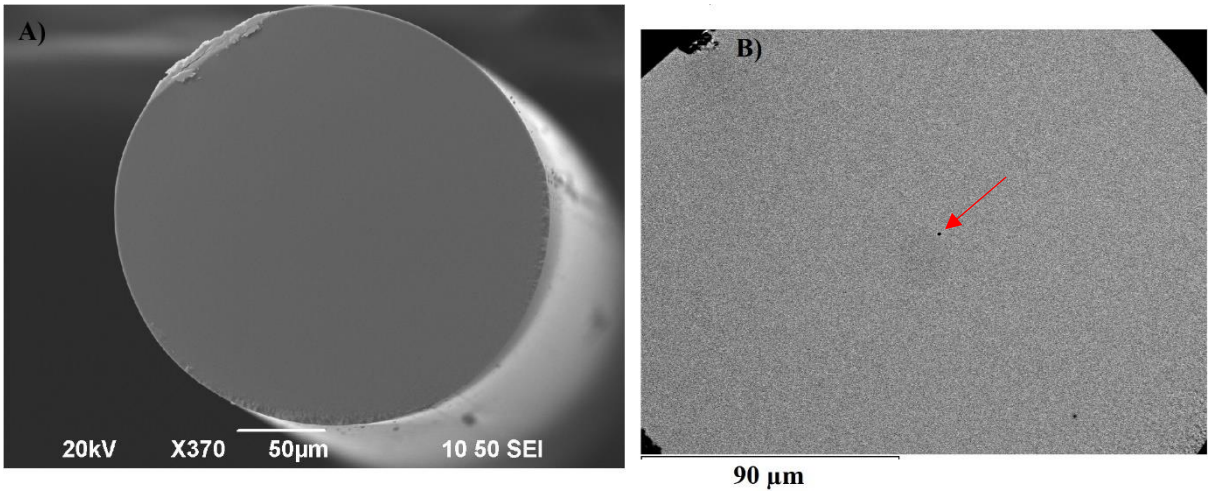


Figure 6.2 SEM micrographs of a nominally 250 µm OD, 20 µm core size sample of F129RERC ($Ge_{19.4}Sb_{9.7}Se_{67.9}Ga_3$ at. % + 500 ppmw Dy foil core glass / $Ge_{21}Sb_{10}Se_{69}$ at. % cladding glass). A) Secondary electron detector image showing good overall fibre shape. 20 Kv accelerating voltage, spot size of 50, 10 mm working distance. Small hole observed close to centre not visible on this image. B) Backscatter electron detector image. In B), note that the darker grey circle towards centre of image indicates the location of the core glass. The small black spot above this region (red arrow) is a small hole <1 µm in diameter that is suggested to be in the cladding.

With the accelerating voltage of the JEOL 6490LV tungsten filament electron source still set to 25 kV, the X-max 80 (Oxford instruments), the EDX detector, fitted inside the SEM was lowered ~ 20 mm away from the sample fibre face to create an elemental map of the fibre cross-section. The mapping process continually collected data for all elements simultaneously. The EDX software used a numerical scale of 1-6 indicating length of process times. As further described in Section 3.3.4, increasing process time would yield a more accurate elemental analysis, but drastically increase scan time. The process time was set to 3 (the upper limit of processing times generally used for elemental mapping). The elemental

mapping process was carried out for 70 minutes, being observed before deciding to manually end the scan. At the 70-minute mark, there was minimal change to the mapped data (as seen by the 'bleaching' of Se and Sb in Figure 6.3) and so the scan was ended.

Figure 6.3 shows the resulting mapped results for each constituent element (Ge, Sb, Se, Ga), excluding dysprosium, as dysprosium was added in quantities (500 ppmw Dy foil) which were too small to be imaged (< 1 at. % for this configuration of a JEOL 6490 LV and X-MAX 80 EDX detector). Again, due to the similarities in composition between the two glasses constituting the core and cladding of F129RERC ($Ge_{19.4}Sb_{9.7}Se_{67.9}Ga_3$ at. % + 500 ppmw Dy foil/ $Ge_{21}Sb_{10}Se_{69}$ at. %), differentiation by elemental mapping proved difficult.

On the other hand, from Figure 6.3, the presence of gallium can be seen in the core of this F129RERC SIF in the bottom right quadrant but with the low gallium at. % (3 at. %) in the core glass ($Ge_{19.4}Sb_{9.7}Se_{67.9}Ga_3$ at. % + 500 ppmw Dy foil), compared to 0 at. % in the cladding glass ($Ge_{21}Sb_{10}Se_{69}$ at. %), the elemental mapping does not provide a high enough quality image to accurately define the core/cladding interface nor core dimensions.

Resolution of the core shape may be possible with higher process times (that is, higher using a higher number on the scale used by the EDX software) and substantially longer scan times. A point and scan EDX method (Section 3.3.3) in which small areas (region size is "drawn" by the user or dependent on spot size of the beam selected in the SEM) was used to get a quantitative elemental analysis of the core and cladding glass. Thus, taking the mean average of three-point scans for both the core and cladding glasses measured the glass compositions as $Ge_{20.2}Sb_{10.95}Se_{66.15}Ga_{2.7}$ in the core (from $Ge_{19.4}Sb_{9.7}Se_{67.9}Ga_3$ at. % + 500 ppmw Dy foil as batched), and $Ge_{21.74}Sb_{11.30}Se_{66.96}$ in the cladding (from $Ge_{21}Sb_{10}Se_{69}$ at. % as batched). Discrepancies between the nominal batched composition and the EDX measured composition are likely the product of the overlapping X-ray emission bands of selenium, gallium, and germanium making accurate identification problematic for the INCA (Oxford instruments, UK) software that controls the EDX detector.

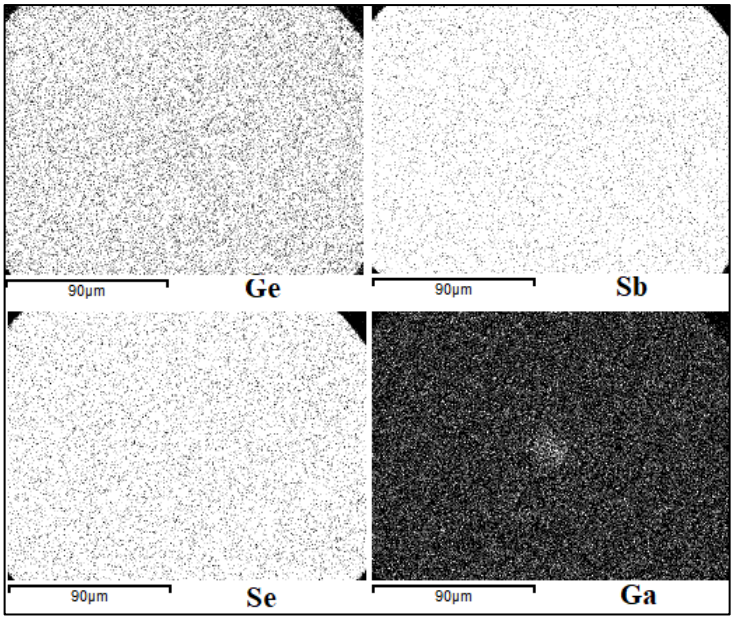


Figure 6.3 EDX elemental mapping of F129RERC ($Ge_{19.4}Sb_{9.7}Se_{67.9}Ga_3$ at. % + 500 ppmw Dy foil core glass / $Ge_{21}Sb_{10}Se_{69}$ at. % cladding glass). Due to the closely matched Ge, Sb, and Se at. % between the core and cladding compositions, differentiation was not possible as shown by the invisible core in the Ge, Sb, and Se mapping here. Core position is defined in the Ga map, but the lack of resolution in the Ga map (due to there only being 3 at. % Ga in the core glass and 0 at. % Ga in the cladding glass and hence only a small difference in gallium content) hinders the ability to make any conclusions on the precise core shape from the Ga map.

Despite the difficulty of the structural characterisation of the F129RERC fibre geometry, the extrusion of the cladding glass (M287RC, $Ge_{21}Sb_{10}Se_{69}$ at. %) and the subsequent fibre drawing of F129RERC ($Ge_{19.4}Sb_{9.7}Se_{67.9}Ga_3$ at. % + 500 ppmw Dy foil/ $Ge_{21}Sb_{10}Se_{69}$ at. %) nonetheless successfully resulted in an antimony-based small-core, rare earth ion doped fibre. Both the core $Ge_{19.4}Sb_{9.7}Se_{67.9}Ga_3$ at. % (development of composition detailed in Chapter 4) and the cladding $Ge_{21}Sb_{10}Se_{69}$ at. % (development of composition detailed in Chapter 5) compositions developed during this work were tailored to have matched thermal and optical properties (see Table 5.1, Section 5.2.3), and apparently sufficient devitrification resistance to tolerate the additional thermal working of extrusion and fibre drawing, as evidenced by the successful fabrication of the fibre and by the above SEM (EDX) investigation.

As previously mentioned, to the best of this Author's knowledge, this was the first rare earth ion doped antimony small core fibre ever made according to what was already reported in literature [18,25,193].

The next, Section 6.2, describes fabrication of a very different fibre. Thus, instead of fabrication of a Dy^{3+}-doped Sb-based glass core in an Sb-based cladding glass as in the current Section 6.1, Section 6.2 describes fabrication of a Ce^{3+}-doped As-based glass core in an Sb-based cladding glass.

6.2 Mid-IR fibre lasing in a 500 ppmw cerium (III) doped arsenic-based core glass (F109REZQT(RCJN), $Ge_{15}As_{21}Se_{63}Ga_1$ at. % + 500 ppmw Ce^{3+} doped) and antimony-based cladding glass (M287RC, $Ge_{21}Sb_{10}Se_{69}$ at. %, E093RC) drawn to a small-core, step index fibre (F130RERC) in a laser cavity

This Section 6.2 describes mid-infrared fibre lasing in a 500 ppmw cerium (III) doped arsenic-based core glass and antimony-based cladding glass to fabricate a small-core, step index fibre in a laser cavity. The reasoning for switching to the Ce^{3+} doped As-based fibre is elaborated in the below paragraph.

An additional cladding glass jacket tube (M287RC, $Ge_{21}Sb_{10}Se_{69}$ at. % E093RC-(ii)) was produced as a backup in case of material failure during the fibre drawing for the F129RERC ($Ge_{19.4}Sb_{9.7}Se_{67.9}Ga_3$ at. % + 500 ppmw Dy foil core/ $Ge_{21}Sb_{10}Se_{69}$ at. % cladding) as mentioned in Section 6.1. Due to the success of the dysprosium doped antimony core (Section 4.3)/antimony cladding (Section 5.2.3) small-core SIF F129RERC's drawing (Section 6.1), a second rod-in-tube preform was produced and drawn to fibre (F130RERC, $Ge_{15}As_{21}Se_{63}Ga_1$ at. % + 500 ppmw Ce^{3+} doped core / $Ge_{21}Sb_{10}Se_{69}$ at. % cladding) in an analogous way to the method used for F129RERC (Section 6.1). With no other rare earth ion doped antimony-based canes readily available in storage, it was decided to use a 500 ppmw cerium foil doped arsenic-based chalcogenide cane with a composition of $Ge_{15}As_{21}Se_{63}Ga_1$ (F109REZQT(RCJN)) as a substitute for an antimony-based cane in a SIF fibre. (F109REZQT(RCJN)) was drawn from the as-annealed preform: M259REZQT. A bulk sample of the M259REZQT as-annealed preform was later used for mid-IR ellipsometry to calculate the NA of F130RERC as further described in Section 6.2.2. The Ce^{3+} doped F109REZQT(RCJN) was chosen as, when pumping at 4.15 µm, due to the electronic structure of Ce^{3+}, excited state absorption is avoided and

there is a small quantum defect with expected emissions at around 5.14 µm (see Section 6.2.3, Figure 6.7A+B).

Although an arsenic-based core glass rod in antimony-based cladding extruded tube fibre drawing to step-index fibre had not been attempted previously in the Mid-IR Photonics Group, these core ($Ge_{15}As_{21}Se_{63}Ga_1$ at. %, F109REZQT(RCJN)) and cladding ($Ge_{21}Sb_{10}Se_{69}$ at. %, M287RC, E093RC-(ii)) glasses had similar T_g values (240 °C and 227 °C, respectively) but it was not known if the viscosity-temperature relationship between this core and cladding glass would be similar enough to facilitate drawing.

A F109REZQT(RCJN) ($Ge_{15}As_{21}Se_{63}Ga_1$ at. % + 500 ppmw Ce^{3+}) cane that was previously stored in the inert atmosphere of a glovebox (< 1 ppmw O_2 and H_2O) for around 17 months with a diameter of 500 µm was selected as the cane sample to be drawn rod-in-tube to step-index fibre. This was etched for 72 hours in ambient temperature propylamine, at ambient atmosphere, under dust cover, with the cane fully submersed. This cane of F109REZQT(RCJN) was then cleaned with acetone, then isopropanol (Table 3.2 for sources and purity), before being dried from the isopropanol under the vacuum of a MBraun glovebox antechamber. This etched cane was inserted into a 60 mm long cladding tube (E093RC-(ii), $Ge_{21}Sb_{10}Se_{69}$ at. %, M287RC) and fibre drawn on the modified Heathway fibre draw tower located in a class 10,000 cleanroom facility (see Section 3.2.9 for details).

Small-core step-index fibre was successfully drawn to have three nominal outer diameters, which necessarily controls to inner diameter of the core. 340 µm OD (outer diameter) with a 20 µm core diameter, 225 µm OD with a 15 µm core diameter, and 170 µm OD with a 10 µm core diameter, of total length around 40 meters. The fibre was given the identification code F130RERC ($Ge_{15}As_{21}Se_{63}Ga_1$ at. % + 500 ppmw Ce^{3+} doped core / $Ge_{21}Sb_{10}Se_{69}$ at. % cladding).

The next Section, 6.2.1, describes the SEM EDX imaging and analysis of the F130RERC fibre cross-section.

6.2.1 SEM EDX characterisation of F130RERC ($Ge_{15}As_{21}Se_{63}Ga_1$ at. % + 500 ppmw Ce^{3+} doped core / $Ge_{21}Sb_{10}Se_{69}$ at. % cladding)

Three fibre samples (i)-(iii) of F130RERC ($Ge_{15}As_{21}Se_{63}Ga_1$ at. % + 500 ppmw Ce^{3+} doped core / $Ge_{21}Sb_{10}Se_{69}$ at. % cladding), of nominal 15 µm core diameter and 225 µm OD, were cleaved orthogonally on the automated Vytran cleaver (see Section 3.3.6 for cleaving details), mounted vertically onto an aluminium SEM stub, and coated with a (nominally) 10 nm carbon layer (thickness as calculated by the coater, Q150R ES, QuorumTech) and the samples were imaged in cross-section using a JEOL 6490LV SEM. Further details on sample preparation and equipment are in Section 3.3.3.

Figure 6.4A is an image taken of fibre sample (i) with a secondary electron detector. The cladding shape of fibre sample (i) is circular, and the fibre end face appeared free from any holes or other defects larger than an estimated ~0.1 µm (based on the scale seen in Figure 6.4B). The F130RERC fibre sample (i) measured 249 µm ± 5 µm OD with a core diameter of 13.5 µm (as measured both horizontally and vertically, see Figure 6.4B top-right inset). Due to the As-based core and Sb-based cladding compositional difference, the contrast of the core/cladding interface can just about be seen without the use of the backscatter detector in Figure 6.4A. Moreover, Figure 6.4B was taken with a backscatter electron detector to highlight further the compositional differences to better image the interface. As the arsenic atomic number is 33 and the antimony atomic number is 51, the average atomic number of the arsenic-based core was lower than that of the antimony-based cladding. Due to this, in Figure 6.4B, the As-based core glass presents a darker shade than the Sb-based cladding composition as the As-based composition produced lower signal for detection than the antimony-based glass cladding[207].

From Figure 6.4B, like the outer perimeter of the cladding, the core of F130RERC fibre sample (i) is symmetrical, circular, and concentric (centre of core ~125 ± 5 µm from fibre perimeter).

By comparison, although sample (i) of F130RERC ($Ge_{15}As_{21}Se_{63}Ga_1$ at. % + 500 ppmw Ce^{3+} doped core / $Ge_{21}Sb_{10}Se_{69}$ at. % cladding) was taken from a section of comparably high-quality fibre (as judged by good fibre morphology, free from

observable defects seen in SEM), fibre samples (ii) and (iii) of F130RERC displayed multiple defects during SEM imaging (Figure 6.5). The outer cladding of fibre sample (ii) (Figure 6.5A) was slightly misshapen into an oval shape and two small holes were identified towards the centre of the cladding, but away from the core/cladding interface (as seen in the inset of Figure 6.5A). Figure 6.5A is a secondary electron image of the cross-sectional fibre face of F130RERC fibre sample (ii), with the inset of Figure 6.5A being an image taken using a backscatter detector to highlight the locations of the holes in the cladding (further highlighted with red arrows).

Figure 6.5B, a secondary electron detector image, shows that sample (iii) of F130RERC had a good core/cladding morphology but a large hole (~5.2 µm diameter) was present at the core/cladding interface with a smaller hole <1 µm diameter (indicated by red arrow) also at the interface. This gap defect at the interface is suggested to be the result of the cladding glass tube failing to fully collapse around the rod (cane) during the fibre drawing stage (see Section 3.2.9). Although a vacuum is applied to the preform during the fibre drawing, variations in topography or composition of both the outer diameter of the cane and the inner diameter of the cladding tube can potentially lead to regions of fibre in which this core-hole-cladding interface is produced.

Following the observation of these holes within the cladding glass and at the core/cladding interface, it was decided that any fibre piece to be used in optical experiments would have its cleaved fibre face thoroughly examined using visible light microscopy to minimise the chances of using a fibre sample with defects at the core/cladding interface which could interfere with light guiding in the core of the glass.

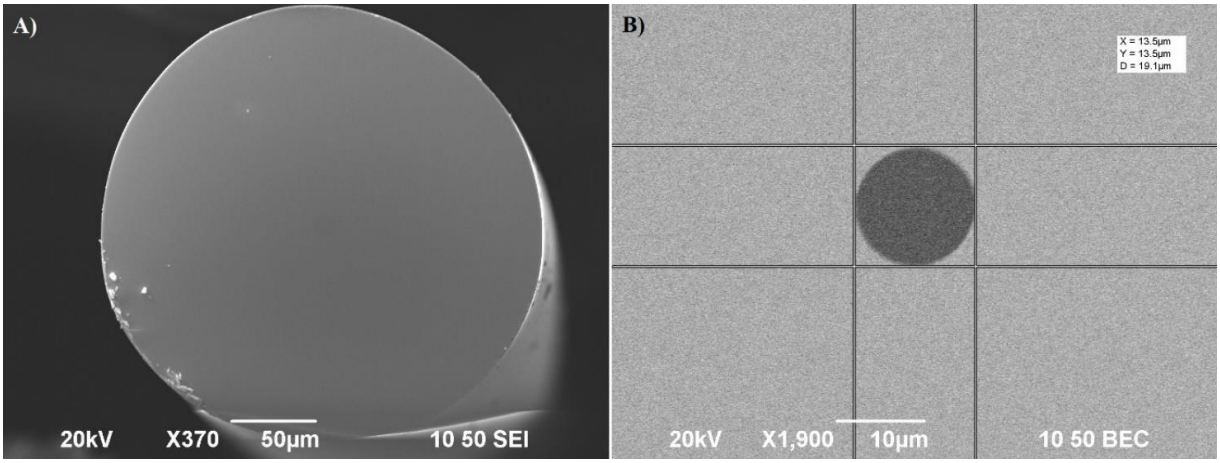


Figure 6.4 SEM micrograph of sample (i) of F130RERC ($Ge_{15}As_{21}Se_{63}Ga_1$ at. % + 500 ppmw Ce^{3+} doped core / $Ge_{21}Sb_{10}Se_{69}$ at. % cladding) 10 mm working distance, spot size of 50, 20 kV accelerating voltage. A) Secondary electron image of entire fibre end face. Faint darker circle in centre is the core glass. B) Backscattered electron image showing core/cladding interface. Grid lines added to measure core size of 13.5 µm in both horizontal and vertical lines.

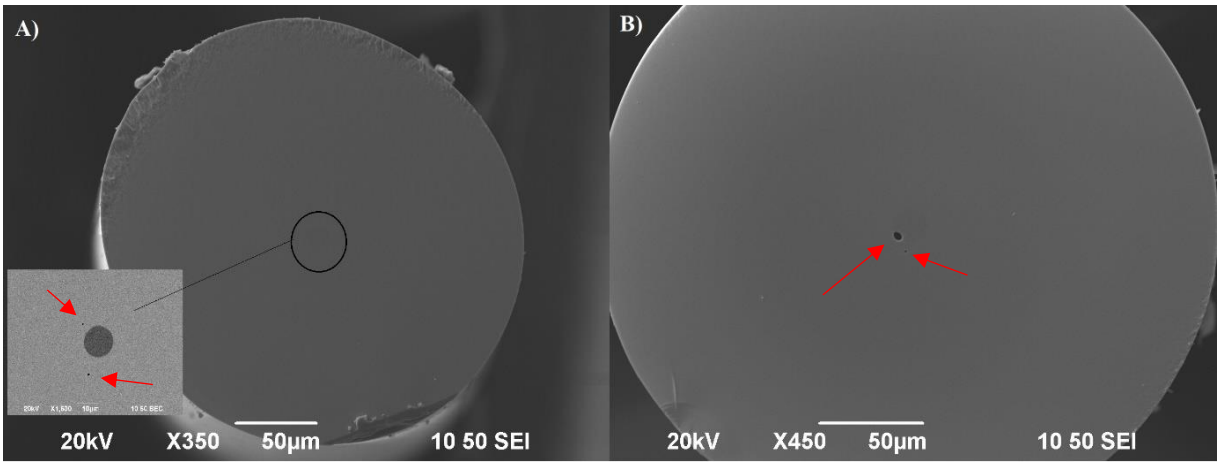


Figure 6.5 SEM micrographs taken of sample (ii) and sample (iii) of F130RERC ($Ge_{15}As_{21}Se_{63}Ga_1$ at. % + 500 ppmw Ce^{3+} doped core / $Ge_{21}Sb_{10}Se_{69}$ at. % cladding). A) Sample (ii) with the visibly oval cladding shape. Inset is a backscatter electron detector image which highlights two holes present in the cladding (red arrows indicate location). B) Sample (iii) with a large hole (~5.2 µm diameter) at the core/cladding interface and a smaller hole <1 µm also at the core/cladding/ interface (red arrows indicate location).

Although the SEM investigation of F130RERC ($Ge_{15}As_{21}Se_{63}Ga_1$ at. % + 500 ppmw Ce^{3+} doped core / $Ge_{21}Sb_{10}Se_{69}$ at. % cladding) determined there were large defects in the form of holes in the cladding glass and at the core/cladding interface (as seen in F130RERC fibre samples (i) and (ii)), the SEM investigation also

indicated that there were defect free regions of fibre (as seen in F130RERC fibre sample (i)). The As-based core glass ($Ge_{15}As_{21}Se_{63}Ga_1$ at. %) and the Sb-based cladding glass ($Ge_{21}Sb_{10}Se_{69}$ at. %) had readily fibre drawn with no observable difficulties during fibre drawing such as surface skin formation (as reported in Section 5.1.3.3).

The following Section, Section 6.2.2, details the development of a mid-IR ellipsometry model for a bulk sample of the Ce^{3+} doped core host glass (M259REZQT, $Ge_{15}As_{21}Se_{63}Ga_1$ at. % + 500 ppmw Ce^{3+}) which was then used to calculate the numerical aperture of F130RERC ($Ge_{15}As_{21}Se_{63}Ga_1$ at. % + 500 ppmw Ce^{3+} doped core / $Ge_{21}Sb_{10}Se_{69}$ at. % cladding).

6.2.2 Calculating numerical aperture using mid-IR ellipsometry models of the glasses comprising F130RERC ($Ge_{15}As_{21}Se_{63}Ga_1$ at. % + 500 ppmw Ce^{3+} doped core (M259REZQT) / $Ge_{21}Sb_{10}Se_{69}$ at. % cladding (M287RC))

As mentioned in Section 6.2, the unstructured cane that was used to form the core glass of SIF F130RERC was assigned the fibre code F109REZQT(RCJN). This fibre was drawn from an as-annealed preform with the melt code M259REZQT ($Ge_{15}As_{21}Se_{63}Ga_1$ at. % + 500 ppmw Ce^{3+}). A variable angle spectroscopy ellipsometry (VASE) bulk disc sample from the preform used to draw unstructured fibre and cane (F109REZQT(RCJN)), M259REZQT ($Ge_{15}As_{21}Se_{63}Ga_1$ at. % + 500 ppmw Ce foil), this ellipsometry sample was prepared as described in Section 3.3.5. An ellipsometry model for M259REZQT was then designed and numerical aperture of F130RERC was calculated using results from the VASE measurements of the M267RC cladding glass ($Ge_{21}Sb_{10}Se_{69}$ at. %) (see Section 5.3.4, Table 5.1, and Table 5.2) as the composition was identical to that of M287RC ($Ge_{21}Sb_{10}Se_{69}$ at. %).

An IR-VASE ellipsometer (Mark II, Woollam) was used to take ellipsometry measurements at 55 °, 65 °, and 75 °. Each angle was scanned for three cycles consisting of 20 scans each. Measurements were collected at a resolution of 2 cm^{-1}. The three oscillator (2 pole, 1 Gaussian) method of data modelling, as described in

Section 5.3.4.2, was again used to create a suitable model. These models were applied over a 2-30 µm wavelength range.

The parameters used for the modelling of the As-based core glass, M259REZQT ($Ge_{15}As_{21}Se_{63}Ga_1$ at. % + 500 ppmw Ce foil), and the Sb-based cladding glass, M267RC ($Ge_{21}Sb_{10}Se_{69}$ at. %), used in F130RERC are detailed in Table 6.1. Again, although M287RC ($Ge_{21}Sb_{10}Se_{69}$ at. %) was used as the cladding in F130RERC, M267RC ($Ge_{21}Sb_{10}Se_{69}$ at. %) has an identical as-batched composition and so data acquired in Table 5.1, Section 5.2.3 on M267RC was used for F130RERC in Table 6.1. The models for the core M259REZQT and cladding M267RERC glasses followed the same "three-oscillators" model, comprising of one Sellmeier (pole) oscillator centred in the electronic absorption edge, a second Sellmeier (pole) oscillator centred in the vibrational absorption edge, and a Gaussian centred around 30-40 µm. The "three-oscillators" model is further described in Section 5.3.4.2.

From Table 6.1, the key take-away is the MSE (mean square error) values, used to indicate the quality of the fit of the model to the measured data, indicating that the three-oscillator model developed for antimony-based glasses (developed in Section 5.3.4.2) was also suitable to the model RI of the arsenic-based $Ge_{15}As_{21}Se_{63}Ga_1$ at. % + 500 ppmw Ce foil composition (MSE: 3.264). To repeat, values closer to "1" indicates a better fitting of modelled to measured data, and values of 2-6 were earlier (Section 5.3.4.2) deemed to provide an acceptable fit for the measurements in this project. The three-oscillator model for the As-based M259REZQT ($Ge_{15}As_{21}Se_{63}Ga_1$ at. % + 500 ppmw Ce foil) provided an MSE value (3.264) which fit this criteria.

Table 6.1 The 'three oscillators' model parameters used for both the As-based core (M259REZQT, $Ge_{15}As_{21}Se_{63}Ga_1$ at. % + 500 ppmw Ce foil) and Sb-based cladding glasses (M267RC, $Ge_{21}Sb_{10}Se_{69}$ at. %) of F130RERC over the 2-30 µm wavelength range.

Glass code	Surf. Rough. (nm)	Einf	Pole 1		Pole 2		Gaussian			MSE (2-30 µm)
			Amp (no units)	En (eV) (µm)	Amp (no units)	En (eV) (µm)	Amp (no units)	Br (eV)	En (eV) (µm)	
M259REZQT	7.87	6.461	0.4727	1.785 (0.6946)	0.001083	0.0320 (38.7450)	0.219481	0.2302	0.0314 (39.4604)	3.264
M267RC	7.67	5.967	1.4525	1.916 (0.6471)	0.0009	0.0318 (38.9874)	0.9518	0.0052	0.0371 (33.4178)	2.444

Figure 6.6 shows the modelled and measured refractive index dispersion data for both the As-based core glass ($Ge_{15}As_{21}Se_{63}Ga_1$ at. % + 500 ppmw Ce foil, M259REZQT) and Sb-based cladding glass ($Ge_{21}Sb_{10}Se_{69}$ at. %, M267RC) glasses of the small-core step-index fibre F130RERC over a 2-12 µm wavelength range. The plotted lines indicate the modelled data for the corresponding glasses and the hollow circle plots indicate measured data from the glasses over the multiple scans. The refractive index of the core glass, M259RERC ($Ge_{15}As_{21}Se_{63}Ga_1$ at. % + 500 ppmw Ce foil), at 2 µm was modelled to be 2.5737 with RI declining across the wavelength range investigated to 2.5490 at 12 µm. The cladding glass, M267RC ($Ge_{21}Sb_{10}Se_{69}$ at. %), exhibited a similar decline with a RI at 2µm (2.5306) dropping to 2.5027 at 12 µm. This wavelength range was capped at 12 µm as the NA values beyond this wavelength were out of the scope of this project, and by restricting the wavelength range modelled, a better fitting model (MSE value closer to 1) could be applied. The numerical aperture of the fibre over this range is also displayed *via* the red dotted plot with a scale on the right-side Y-axis of Figure 6.6. Over the 2-12 µm wavelength range, NA values between 0.46 and 0.485 were calculated.

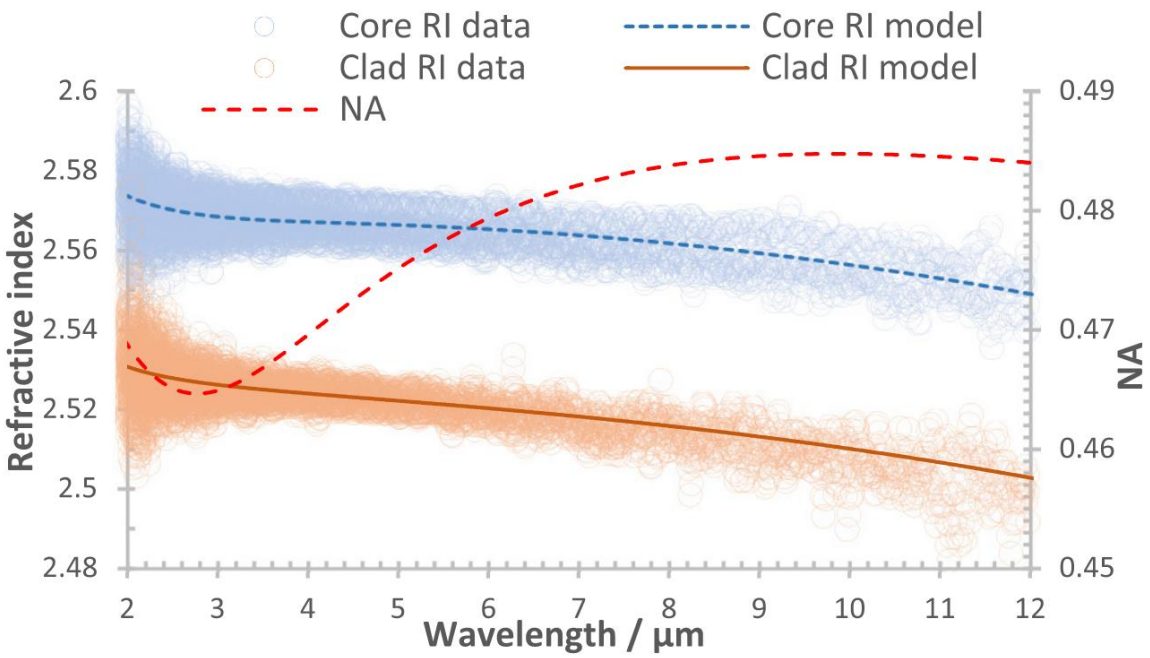


Figure 6.6 Measured and modelled refractive index data for the chosen core (M259REZQT, $Ge_{15}As_{21}Se_{63}Ga_1$ at. % + 500 ppmw Ce foil) and cladding (M267RC, $Ge_{21}Sb_{10}Se_{69}$ at. %) glasses. Line plots represent data collected from the three oscillator models for each composition. Hollow circle plots indicate measured data from the ellipsometry measurement. Red dotted line shows calculated NA of the fibre over the wavelength region.

Table 6.2 has the calculated numerical aperture values (Equation 5.1) of F130RERC using RI data for the As-based core (M259REZQT, $Ge_{15}As_{21}Se_{63}Ga_1$ at. % + 500 ppmw Ce foil) and Sb-based cladding (M267RC, $Ge_{21}Sb_{10}Se_{69}$ at. %) glasses at wavelengths relevant to the Ce^{3+} pumping scheme used (NA: 0.4704 at 4.15 µm) in photoluminescent and lasing experiments and measured output lasing wavelengths (e.g., NA: 0.4757 at 5.128 µm) (see Section 6.2.3.3 for pumping scheme and lasing results).

Table 6.2 Refractive index (RI) values and numerical aperture for the core and cladding glasses of F130RERC at input pumping and output lasing wavelengths (see Section 6.2.3.3).

Wavelength (μm)	Core RI M259REZQT(RCJN)	Clad RI M267RC	Numerical aperture (F130RERC)
4.151248	2.5675	2.5230	0.4704
5.128495	2.5663	2.5218	0.4757
5.169401	2.5663	2.5217	0.4759
5.279948	2.5661	2.5215	0.4764

6.2.3 Mid-IR FtIR, photoluminescence, photoluminescence lifetimes, and fibre loss in unstructured F109REZQT(RCJN) ($Ge_{15}As_{21}Se_{63}Ga_1$ at. % + 500 ppmw Ce^{3+}) and fibre lasing in small core step-index fibre F130RERC ($Ge_{15}As_{21}Se_{63}Ga_1$ at. % + 500 ppmw Ce^{3+} doped core/ $Ge_{21}Sb_{10}Se_{69}$ at. % (M287RC) cladding)

The following section covers various optical characterisation investigations into bulk as-annealed M259REZQT ($Ge_{15}As_{21}Se_{63}Ga_1$ at. % + 500 ppmw Ce^{3+}), unstructured fibre F109REZQT(RCJN)$Ge_{15}As_{21}Se_{63}Ga_1$ at. %, and small-core SIF F130RERC as follows.

A FtIR bulk sample of the core glass (M259REZQT, $Ge_{15}As_{21}Se_{63}Ga_1$ at. % + 500 ppmw Ce^{3+}) used in the F130RERC ($Ge_{15}As_{21}Se_{63}Ga_1$ at. % + 500 ppmw Ce^{3+} doped core / $Ge_{21}Sb_{10}Se_{69}$ at. % cladding) step-index fibre was prepared and investigated for mid-IR absorptions, allowing a suitable pump scheme using a 4.15 μm quantum cascade laser (QCL) (Pranalytica) to be devised (Section 6.2.3.1). This pumping scheme (Figure 6.7B for Ce^{3+} energy level) avoided excited state absorption and a low quantum defect with predicted emissions. Fibre optical loss and photoluminescence measurements were then taken using an unstructured fibre sample of the core glass used in the small core, SIF, F130RERC, F109REZQT(RCJN) ($Ge_{15}As_{21}Se_{63}Ga_1$ at. % + 500 ppmw Ce^{3+}) (see Section 6.2.3.2). A laser cavity for F130RERC ($Ge_{15}As_{21}Se_{63}Ga_1$ at. % + 500 ppmw Ce^{3+} doped core / $Ge_{21}Sb_{10}Se_{69}$ at. % cladding) was then designed by Joel Nunes (PhD

colleague, Mid-IR photonics group, University of Nottingham) and the fibre was pumped with varying powers at 4.15 µm. Three laser peaks were identified at 5.13 µm, 5.17 µm, and 5.28 µm (Section 6.2.3.3). The results of this lasing experiment are published in Nunes *et al.* [15].

6.2.3.1 FtIR characterisation of as-annealed, bulk M259REZQT ($Ge_{15}As_{21}Se_{63}Ga_1$ at. % + 500 ppmw Ce^{3+})

A bulk disc sample (~3 mm) was cut from the preform (M259REZQT, $Ge_{15}As_{21}Se_{63}Ga_1$ at. % + 500 ppmw Ce^{3+}) that was drawn to unstructured F109REZQT(RCJN) (and subsequently into F130RERC) and polished to a 1 µm finish (as described in Section 3.3.7) and 2.45 mm thickness. A Bruker IFS 66/S fitted with a Globar light source, calcium fluoride beam splitter, and DTGS detector was used to measure absorption between 3-10 µm (further details in Section 3.3.7).

From Figure 6.7A, the absorption band attributed to Ce^{3+}: $^2F_{5/2} \rightarrow {}^2F_{7/2}$ was measured, centred at 4.63 µm (2160 cm^{-1}) and covering the 3.5–6 µm (1660-2900 cm^{-1}) wavelength range. As the optical pathlength was purged to remove CO_2, the additional peak at around 4.2 µm is attributed to Se-H impurity absorptions present in the glass (Table 2.3, Section 2.3.3.2 from [132]). Figure 6.7B compares the measured absorption spectrum to the energy level diagram of Ce^{3+}, showing the agreement of the distance between that of the ground state to excited state is 4.54 µm (2200 cm^{-1})[208], and identified 4.15 µm as a suitable pumping wavelength for Ce^{3+} [15].

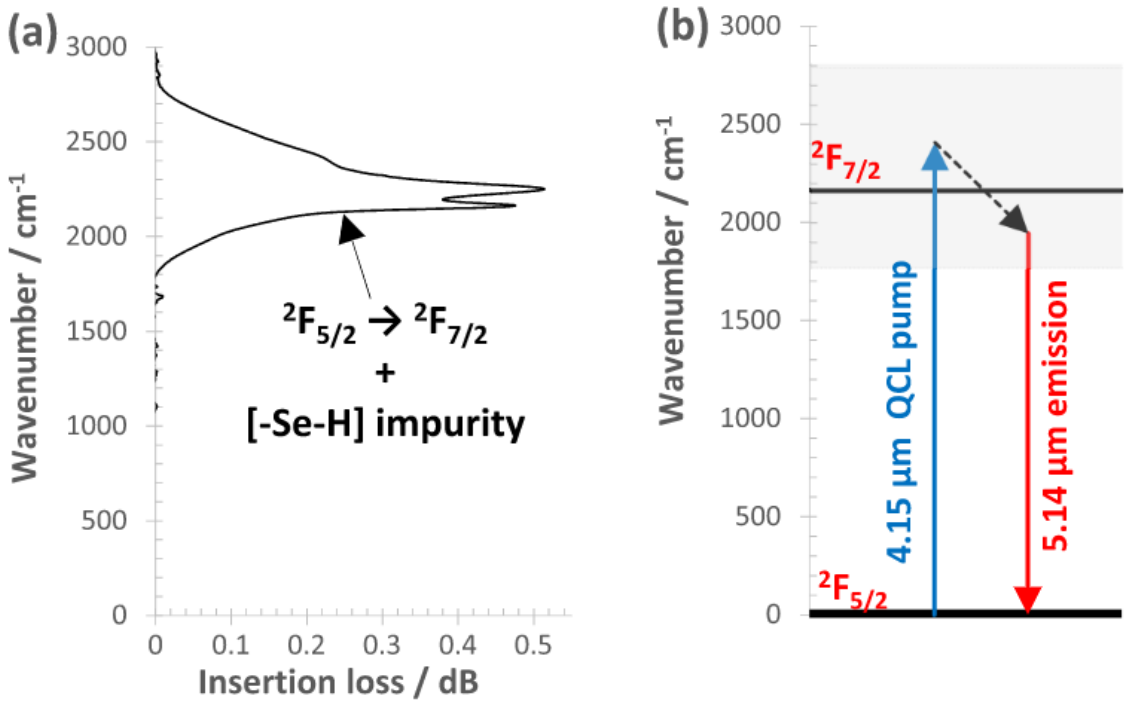


Figure 6.7 A) Mid-IR absorption spectrum of 500 ppmw Ce foil doped $Ge_{15}As_{21}Se_{63}Ga_1$ at. % (M259REZQT). Sample was 2.45 mm thickness, polished to 1 µm finish. FTIR sample chamber was purged with dry air for 40 minutes before scanning to reduce effects of atmospheric O-H and CO_2 absorptions. B) Ce^{3+}electronic energy level diagram with the 4.15µm QCL (quantum cascade laser) pump source and expected 5.14µm emission.

6.2.3.2 Fibre optical loss, photoluminescence (PL), and PL lifetime of unstructured fibre F109REZQT(RCJN) ($Ge_{15}As_{21}Se_{63}Ga_1$ at. % + 500 ppmw Ce^{3+})

(i) Fibre optical loss measurement of unstructured fibre F109REZQT(RCJN) ($Ge_{15}As_{21}Se_{63}Ga_1$ at. % + 500 ppmw Ce^{3+})

The fibre optical loss measurement was carried out using the cut-back method, with the initial fibre length of 2.75 m of the undistilled, unstructured F109REZQT(RCJN) ($Ge_{15}As_{21}Se_{63}Ga_1$ at. % + 500 ppmw Ce^{3+}), of fibre OD: 246 ± 8 µm (described in Section 3.3.6). The fibre length was cut back to a final length of 470 mm, with 1157 mm being removed for the "group 2 cutback". F109REZQT(RCJN) was drawn from an as-annealed preform of M259REZQT. As described in Section 3.3.9, the starting length of the fibre was determined by using a separate test piece of the same fibre (300 mm) and measuring the intensity of the transmitted light. This measured intensity was then used to approximate the

maximum length of fibre that could be used, with the aim to use the longest fibre length at which signal could still be detected.

The lowest loss recorded for unstructured F109REZQT(RCJN) ($Ge_{15}As_{21}Se_{63}Ga_1$ at. % + 500 ppmw Ce^{3+}) across the 6.6-7.1 µm wavelength range was 2.16 dB/m (Figure 6.8). This is comparable to the lowest losses of 2.0 dB/m at 6.77 µm recorded in a fibre with an identical composition, $Ge_{15}As_{21}Se_{63}Ga_1$, doped with 500 ppmw Pr^{3+} with the host glass distilled with oxygen and hydrogen getters to further remove impurities (Tang *et al.*) [110]. However, F109ZQT(RCJN) ($Ge_{15}As_{21}Se_{63}Ga_1$ at. % + 500 ppmw Ce^{3+}) optical loss was greater than that recorded in an undistilled $Ge_{16.5}As_{16}Se_{64.5}Ga_3$ fibre doped with 500 ppmw $DyCl_3$ which measured lowest losses of 1.16 db/m at 6.56 µm (Tang *et al.*) [55].

From Figure 6.8, the unstructured F109REZQT(RCJN) ($Ge_{15}As_{21}Se_{63}Ga_1$ at. % + 500 ppmw Ce^{3+}) exhibited bands at 2.8 µm and 7.8-8.0 µm are attributed to O-H [209] and ≡Ge-O/=As-O [210,211] impurity vibrational absorptions, respectively (also see Table 2.3). The partially truncated band spanning from 3.4-6 µm is attributed to both the Ce^{3+} electronic absorption ($^2F_{5/2} \rightarrow {}^2F_{7/2}$) (see Figure 6.7) and the -Se-H impurity vibrational absorption.

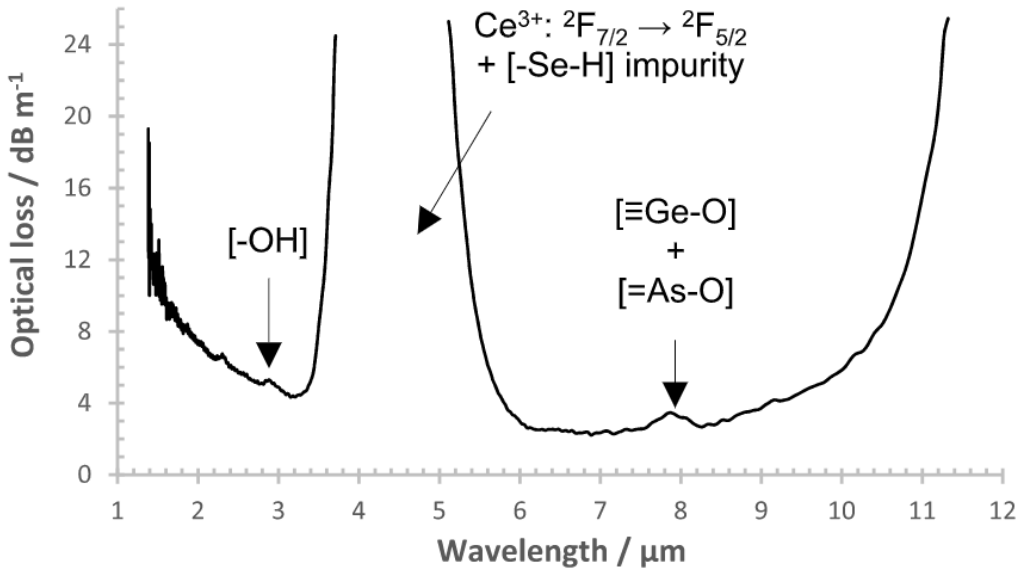


Figure 6.8 Fibre optical loss spectra for unstructured fibre F109REZQT(RCJN) ($Ge_{15}As_{21}Se_{63}Ga_1$ at. % + 500 ppmw Ce^{3+}). Bands are labelled as extrinsic impurity absorptions and Ce^{3+} electronic absorptions (Figure 6.7). Lowest optical loss of 2.16 dB/m was across 6.6-7.1 µm. Measurement carried out on 2.75 m length of fibre with OD of 246 ± 8 µm.

(ii) Photoluminescence (PL) and PL lifetimes of unstructured fibre F109REZQT(RCJN) ($Ge_{15}As_{21}Se_{63}Ga_1$ at. % + 500 ppmw Ce^{3+})

Figure 6.9A shows a schematic diagram of the optical set up used to record mid-IR photoluminescence (PL) and PL lifetime measurements from F109REZQT(RCJN) ($Ge_{15}As_{21}Se_{63}Ga_1$ at. % + 500 ppmw Ce^{3+}). A 4.15 µm continuous wave (CW) quantum cascade laser (QCL) (Pranalytica High Power Laser System, Pranalytica) operating at 100 mW of output power was used to pump a 93.4 mm length, 220 µm outer diameter F109REZQT(RCJN) fibre sample. The 4.15 µm QCL pump laser was focused onto the launch face of the F109REZQT(RCJN) sample using an aspheric lens (Thorlabs, 390028-E, f = 5.95 mm). The Ce^{3+} photoluminescence (and unabsorbed pump light) was collected from the opposing end face of the fibre and collimated with a germanium lens (Edmund Optics #89-607, f = 12.5 mm) and directed towards a calcium fluoride lens (CaF_2) (Thorlabs, LA5370, f = 40 mm) which focused the light into the monochromator. As the pump source overlaid the cerium (III) emission wavelengths, measurements were taken with a 4.203 µm long wave pass filter when measuring emission wavelengths >4.4 µm and no filter was used for emission wavelengths < 3.9 µm.

Figure 6.9B shows the measured emission spectrum with a broad emission band covering the 3.4 – 5.8 µm wavelength range, with a peak centred around 4.6 µm. The broad emission wavelength was entirely attributed to varying Stark levels of the first excited state to ground state transition $^2F_{7/2} \rightarrow {}^2F_{5/2}$ energy levels [36]. The intensity of the secondary peak around 5.2 µm was attributed to be a product of reabsorption along the sample length. For the PL lifetime measurements, F109REZQT(RCJN) ($Ge_{15}As_{21}Se_{63}Ga_1$ at. % + 500 ppmw Ce^{3+}) was end-pumped with modulated light with a 50% duty cycle from the 4.15 µm pump laser. The resultant periodic PL excitation from the opposing cleaved end of the F109REZQT(RCJN) was then collimated with a germanium lens (Edmund Optics #89-607, f = 12.5 mm) and directed towards a calcium fluoride lens (CaF_2) (Thorlabs, LA5370, f = 40 mm) and focused onto a detector (PVI-4TE, Vigo Systems). The signal from the MCT photodetector was directed to an oscilloscope (PicoTech). To suppress noise, averaging over several thousand excitation processes was performed several times. Lifetimes of 3.6 ms were recorded at 3.8

μm, 4.6 μm, and 5.2 μm, notably longer than that of Ce^{3+} $^3F_{7/2}$ previously reported in literature (1.33 ms) by Churbanov *et al.* in a $Ge_{20}Sb_{10}Se_{65}Ga_5$ bulk glass [114].

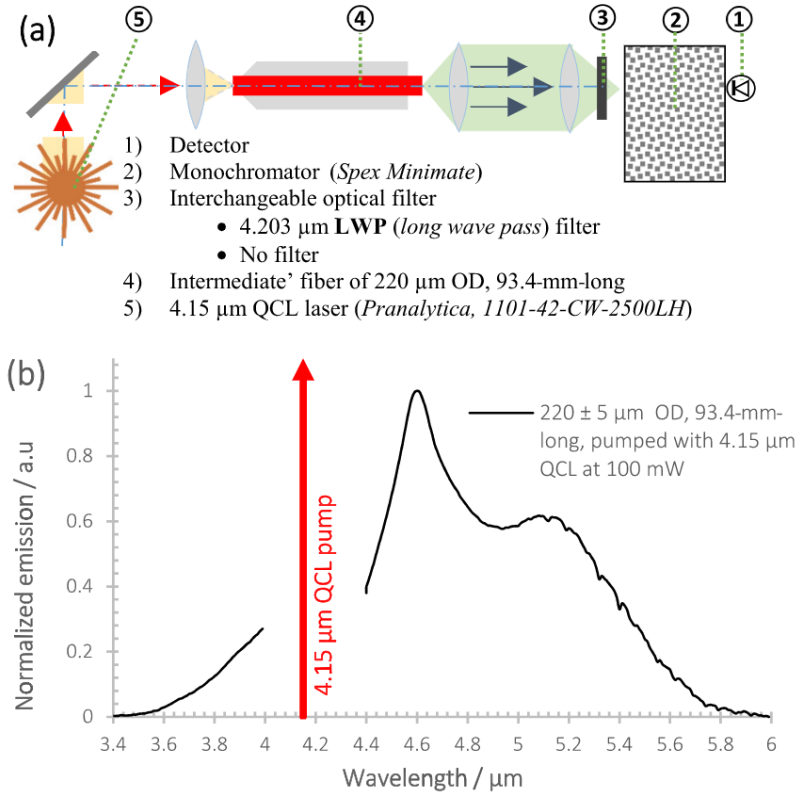


Figure 6.9 A) Schematic diagram of optical set up used for photoluminescent measurements of F109REZQT(RCJN). B) Measured emission spectra of unstructured F109REZQT(RCJN) ($Ge_{15}As_{21}Se_{63}Ga_1$ at. % + 500 ppmw Ce^{3+}) covering the 3.4-6.0 μm region. Taken from [15].

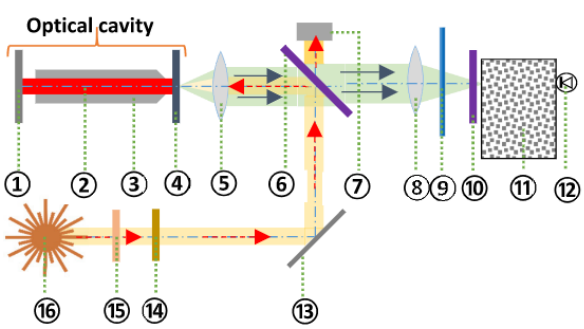
6.2.3.3 Mid-IR fibre lasing at 5.13, 5.17, and 5.28 μm in small-core step-index fibre: F130RERC ($Ge_{15}As_{21}Se_{63}Ga_1$ at. % + 500 ppmw Ce^{3+} doped core / $Ge_{21}Sb_{10}Se_{69}$ at. % cladding)

This section details the design of a laser cavity for F130RERC ($Ge_{15}As_{21}Se_{63}Ga_1$ at. % + 500 ppmw Ce^{3+} doped core / $Ge_{21}Sb_{10}Se_{69}$ at. % cladding) and the subsequent lasing emissions observed when optically pumping F130RERC at 4.15 μm within said cavity.

The optical laser cavity was set up as in Figure 6.10, as follows. A 64 mm length, 180 μm OD, 9 μm core diameter fibre length of F130RERC ($Ge_{15}As_{21}Se_{63}Ga_1$ at. % + 500 ppmw Ce^{3+} doped core / $Ge_{21}Sb_{10}Se_{69}$ at. % cladding) was cleaved

orthogonally at both ends using a Vytran cleaver (cleave methods detailed in Section 3.3.6) and fitted into the optical cavity. Sources of equipment are noted in Figure 6.10. The fibre was fixed onto a stainless-steel V-groove using a UV-curable polymer resin and coated with an indium-gallium-tin eutectic (4N, Alfa Aesar, melting point 10.7 °C as per Alfa Aesar) to act as a cladding mode stripper and facilitate heat dissipation. To complete the optical cavity, the input fibre end face was butt-coupled to a 4.421 µm short wave pass filter (SWP) of 87 % reflectivity and 0.2 % transmission at the lasing wavelengths (~5.1 µm). The distal fibre end face was butt-coupled to a planar gold mirror of 95.8 % reflectivity.

The 4.15 µm QCL pump laser, operated as a continuous wave (CW), was passed through a polariser and quarter wave plate to prevent back reflections and unpolarised Ce^{3+} emissions from interfering with the pump source. A 4.203 µm long wave pass (LWP) filter was used as a dichroic mirror to reflect the 4.15 µm pump source to the fibre whilst allowing the output emission from F130RERC to pass through. Based on the SWP and the F130RERC core diameter and NA, focusing the pump source through the 4.421 µm SWP filter and into the 9 µm diameter core gave a predicted coupling efficiency of around ~19 % [15]. Just preceding the monochromator (Spex Minimate) and detector (PVI 4TE, Thorlabs), a 4.630 µm LWP filter was placed to prevent the 4.15 µm pump from damaging the detector. The monochromator-detector set up allowed measurements with a spectral resolution of around 15 nm of the Ce^{3+} output emission. Due to the poor transmission characteristics of the 4.421 µm SWP filter (#4 in Figure 6.10, 0.2 % transmission at lasing wavelengths 5.1-5.3 µm), the output power of F130RERC ($Ge_{15}As_{21}Se_{63}Ga_1$ at. % + 500 ppmw Ce^{3+} doped core / $Ge_{21}Sb_{10}Se_{69}$ at. % cladding) could not be accurately measured using the thermal power meter (S302C, Thorlabs) and so was deemed to be sub-100 µW [15].



1) Gold mirror (*Thorlabs, ME1-M01*), $R_{@5.14\,\mu m}$ = 95.8 %
2) 9 µm core, 190 µm OD, 64-mm-long filter, coated with InGaSn alloy
3) Stainless steel V-groove fiber holder
4) 4.421 µm SWP (*short wave pass*) filter (*Northumbria Optical Coatings Ltd (**NOC**), SWP-17220-1-1-17*), $R_{@5.14\,\mu m}$ = 87 %, $T_{@5.14\mu m}$ = 0.2 %
5) Bi-convex CaF_2 (*calcium fluoride*) lens, f = 15 mm (*Thorlabs, LB5766-E*)
6) 4.203 µm LWP (*long wave pass*) filter (*NOC, SLWP-4203-001138*)
7) Thermal power meter (*Thorlabs, C-Series S302C*)
8) CaF_2 lens, f = 50 mm (*Thorlabs, LA5763*)
9) Mechanical chopper (*Bentham Instruments*)
10) 4.630 µm LWP filter (*NOC, SLWP-4630-000434*)
11) Monochromator (*Spex Minimate*) with a 0.25 mm entrance and exit slits, equipped with diffraction grating blazed at 6 µm with a spectral resolution of ~15 nm. Interior purged with dry, atmosphere
12) Mercury cadmium telluride detector (*Vigo Systems, PVI-4TE-6*)
13) Gold mirror (*Thorlabs, ME1-M01*)
14) One-fourth wave plate (*Thorlabs, WPLQ05M-4000*)
15) Polarizer (*Thorlabs, LPMIR050-MP2*)
16) 4.15 µm QCL laser (*Pranalytica, 1101-42-CW-2500LH*) operated in either CW or electronically modulated

Figure 6.10 Schematic diagram of the optical set up with which the mid-IR fibre lasing was measured in small-core step-index fibre F130RERC ($Ge_{15}As_{21}Se_{63}Ga_1$ at. % + 500 ppmw Ce^{3+} doped core / $Ge_{21}Sb_{10}Se_{69}$ at. % cladding). Description of the role of each component listed in above paragraph, Taken from Nunes et al. [15].

Figure 6.11 shows the measured cavity emission intensity, over a range of increasing CW 4.15 µm pump powers, from the cavity which comprised the small-core, step-index fibre: F130RERC ($Ge_{15}As_{21}Se_{63}Ga_1$ at. % + 500 ppmw Ce^{3+} doped core / $Ge_{21}Sb_{10}Se_{69}$ at. % cladding), with an abutted dichroic mirror at each end (see Figure 6.10).

The lasing threshold was at 40 mW of CW input power with observed continuous wave lasing peaks at 5.13 µm (peak A), 5.17 µm (peak B), and 5.28 µm (peak C). Increasing the pump power led to a red shift of peaks A, B, and to a lesser extent, C (as beyond 211 mW, this peak was lost). Peak B intensity was maximised at 424 mW and experienced a slight decrease in intensity when pump power was increased to 616 mW. Peak A intensity continuously increased, almost linearly, with increasing pump power. The 4.15 µm pump source was then electronically modulated with a 50 % duty cycle to measure cavity "fall time" which was found to be 2.5 µs at 5.127 µm[15]. Figure 6.12 plots the calculated areas under the three peaks as pumping power increases. From Figure 6.12, although area under each of the peaks B and C begin to decrease in intensity, above a pump power of 86 mW, the area under peaks A and "the total area under A, B, and C" increases nearly linearly with increasing pump power indicating total output emission remains linear.

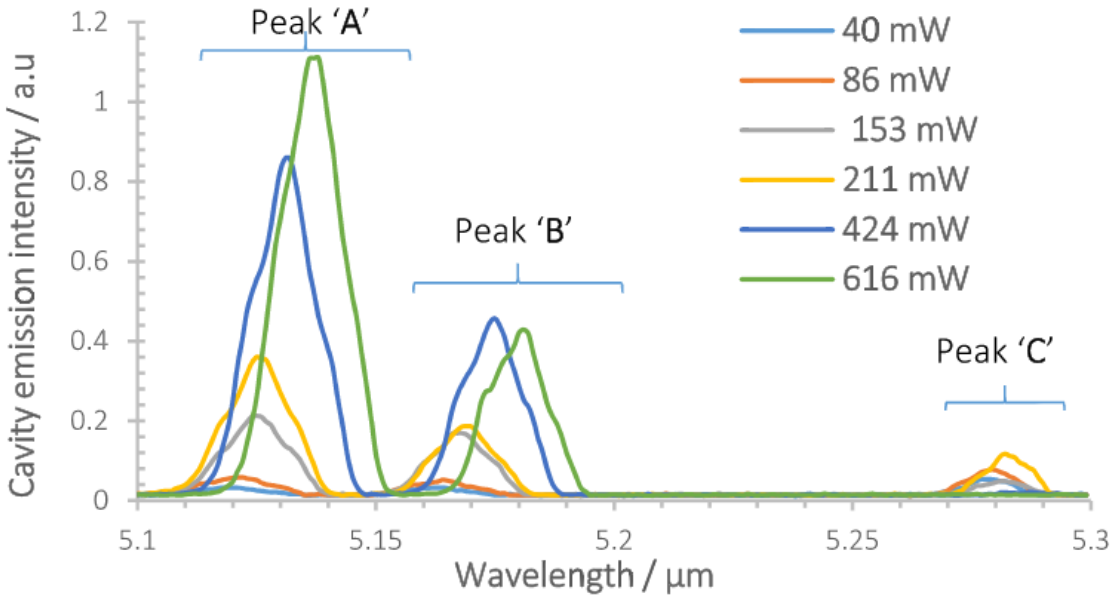


Figure 6.11 F130RERC ($Ge_{15}As_{21}Se_{63}Ga_1$ at. % + 500 ppmw Ce^{3+} doped core / $Ge_{21}Sb_{10}Se_{69}$ at. % cladding) lasing emission intensity with varying 4.15 µm QCL pump powers. Increasing pump power intensity leads to a near linear increase in output power of peak 'A' as well as slightly red shifting the peak emission. Peak 'B' emission intensity peaks at 424 mW, with output intensity dropping at 616 mW but also continues to red shift. Peak 'C' emission intensity peaks at 211 mW, with a red shift observed between 86 and 211 mw input power.

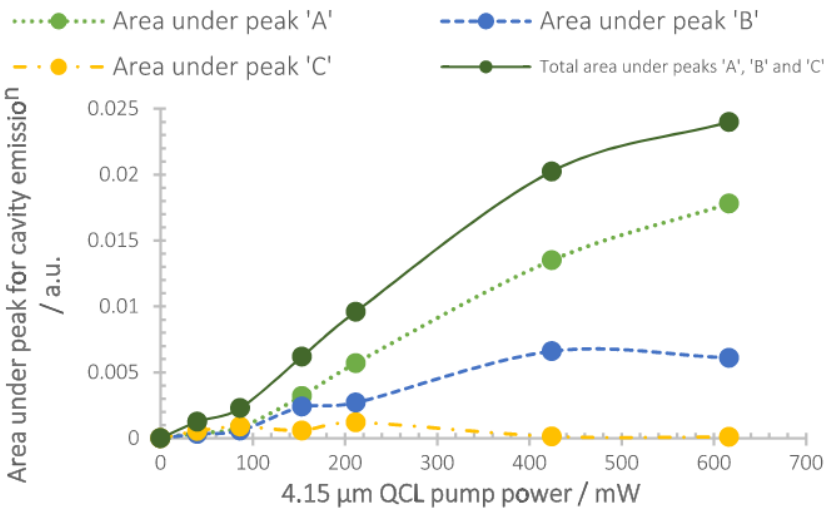


Figure 6.12 Areas of the F130RERC ($Ge_{15}As_{21}Se_{63}Ga_1$ at. % + 500 ppmw Ce^{3+} doped core / $Ge_{21}Sb_{10}Se_{69}$ at. % cladding) emission peaks (Figure 6.11) with increasing 4.15 µm QCL pump powers used to measure lasing action. Total area increases almost linearly with increasing pump power, largely due to the Area under peak 'A' increasing.

The multiple lasing wavelengths, observed in Figure 6.11, may be attributed to multiple Stark levels in both the ground state ($^2F_{5/2}$) and excited state ($^2F_{7/2}$) of Ce^{3+} [212]. Thus, crystal field and spin-orbital interactions have been proposed to split $^2F_{5/2}$ into three energy levels and $^2F_{7/2}$ into four [15,213,214]. Oddly, the ground state of Ce^{3+} ions has been inferred to have a thermally populated first excited Stark level which is apparently populated at ambient temperatures in Ce^{3+} doped garnet crystals[213]. Low temperature mid-IR absorption measurements of these Ce^{3+} doped garnets found there was large splitting of $^2F_{7/2}$ up to 4000 cm^{-1} (2.5 µm)[214]. Theoretical crystal field analysis of Ce^{3+} with 4f–4f intra-shell transitions has shown Ce^{3+} ions spectrally extending to ~3700 cm^{-1} due to the large splitting of the $^2F_{7/2}$ excited state [213].

In 2021, Fjodorow *et al.* [125] measured a similar lasing in a 12 mm diameter, 24 mm length, $Ge_{20}Sb_{10}Se_{65}Ga_5$ chalcogenide glass rod doped with $3\times10^{19}cm^{-3}$ Ce^{3+} with a noisy CW output of peak intensity of 35 mJ of 5.2 µm output lasing [125]. The resulting 5.2 µm emission, with a spikey output intensity, was recorded after pumping with a homemade Fe:ZnSe pump laser emitting 250 µs pulses with a maximum pulse energy of 500 mJ at 4.1 µm.

In a similar timeframe, 2021, coinciding with the measurement of Ce^{3+}doped chalcogenide fibre lasing in the work reported in this thesis of F130RERC ($Ge_{15}As_{21}Se_{63}Ga_1$ at. % + 500 ppmw Ce^{3+} doped core / $Ge_{21}Sb_{10}Se_{69}$ at. % cladding) at ~5.2 µm, Shiryaev *et al.* [56] observed lasing at 5.38 µm in a 1050 ppmw Tb^{3+} doped core $Ga_{3.2}Ge_{24.9}As_{15.3}Se_{56.6}$ / $Ge_{18}As_{22}S_{60}$ cladding fibre (NA ~1) when pumped at 1.98 µm. It is to be noted that, the mid-IR chalcogenide fibre lasing reported in both Section 6.2.3.3 [15] and Shiryaev *et al.* [56] were the first reports of mid-IR fibre lasing in rare earth doped chalcogenide glass fibres. The core glass was distilled with oxygen and hydrogen getters, then a double crucible method was used to form fibre of core diameter of 18 µm and an OD of 400 µm [56]. A 20 µm thick "F42 fluoroplastic coating" was used to coat the fibre [56]. Lasing was observed from a 20 cm length of fibre. Despite the distillation in the presence of getters, the minimum fibre losses were higher (3dB/m at 7.1 µm) in 1050 ppmw Tb^{3+} doped core $Ga_{3.2}Ge_{24.9}As_{15.3}Se_{56.6}$ [56] than the 2.16 dB/m at 6.6-7.1 µm recorded in the core glass used here in the current Author's work in F130RERC ($Ge_{15}As_{21}Se_{63}Ga_1$ at. % + 500 ppmw Ce^{3+} doped core / $Ge_{21}Sb_{10}Se_{69}$ at. % cladding) (Section 6.2.3.2)[15].

The terbium used by Shiryaev *et al.* [56] was purified through a chemical vapour transport method, however the reasoning for increased losses (3dB/m at 7.1 µm) compared to F130RERC (2.16 dB/m at 6.6-7.1 µm) can be speculated. Like what was previously discussed in Section 4.3.2, one suggestion is that the losses may have been a product of the increased dopant concentration (1050 ppmw Tb^{3+} in [56] compared to 500 ppmw in F130RERC [15]) bringing higher concentrations of extrinsic impurities into the host glass due to the tendency of rare earths to oxidise. A second suggestion is potential differences in purification methods being used for different rare earth elements (in this case, Tb and Dy) and subsequently different ppmw of oxide base impurities between elements[186,187]. The inclusion of these oxide-based impurities could then potentially adversely affect solubility/devitrification resistance of the host glass and lead to higher losses.

Returning now to discussion of the fibre lasing achieved here at beyond 5 µm wavelength in the 500 ppmw Ce^{3+} doped small-core, step-index fibre F130RERC ($Ge_{15}As_{21}Se_{63}Ga_1$ at. % + 500 ppmw Ce^{3+} doped core / $Ge_{21}Sb_{10}Se_{69}$ at. % cladding), the output power of Ce^{3+} lasing in F130RERC was suggested to be < 100 µW when pumped at 616 mW of 4.15 µm; this power 'guestimate' was purely on what would have been detectable at the power meter and yet the power meter did not register the laser output. Similarly, output power of Tb^{3+} lasing was suggested by Shiryaev *et al.* [56] to be <10 µW when pumped with 2 W of 1.98 µm[56]. It is suggested for our work that the Ce^{3+} doped fibre laser cavity could be improved in terms of the goal of for tapping off more of the laser power for its numerical measurement by: (i) retaining the gold mirror at the opposite end of the cavity from that pumped, but (ii) changing the dichroic mirror at the opposite end of the fibre to <87% reflection of the lasing wavelength rather than the ~ 87% used here. With such a new mirror, then it should be possible to register the laser power at the power meter and hence calculate the true output power of the fibre laser for increasing pump power.

Returning now to the Tb^{3+} doped fibre from Shiryaev *et al.* [56], it is important to point out the rather large difference in T_g values of 41 °C reported for their Tb^{3+} doped core glass ($Ga_{3.2}Ge_{24.9}As_{15.3}Se_{56.6}$) and cladding glass ($Ge_{18}As_{22}S_{60}$), was substantially larger than the "± 10 °C" target described in Section 5.3 for our work in making thermally matched core and cladding glasses for rare earth ion doping of

the core and drawing to small-core, step index fibre. Although is it to be noted that the core of Shiryaev *et al.* [56] was selenide based and the cladding was sulfur based, and that Shiryaev *et al.* [56] did not carry out preform-drawing but drew the core/cladding fibre from the melt using the double -crucible process. The double-crucible fibre drawing process tends to take place at ~ $10^{3.5}$ Pa s (private communication from Prof AB Seddon, University of Nottingham, UK, who was informed by Professor Mikhail Churbanov of the Russian Academy of Sciences, High Purity Institute, Nizhny Novgorod). Thus, in fact, the viscosity-temperature curves may have been a suitable match using the double-crucible method to fabricate the fibre in Shiryaev *et al* [56]. Results of mid-IR chalcogenide fibre lasing in both Section 6.2.3.3 [15] and Shiryaev *et al.* [56] were the first reports of mid-IR fibre lasing in rare earth doped chalcogenide glass fibres.

In terms of function as a surgical laser/biologically relevant light source, the wavelengths measured from F130RERC ($Ge_{15}As_{21}Se_{63}Ga_1$ at. % + 500 ppmw Ce^{3+} doped core / $Ge_{21}Sb_{10}Se_{69}$ at. % cladding) are of little function due to lack of relevant absorptions. Nitric oxide, a gaseous cell signalling molecule, absorbs at around 5.2 μm [46]. However, the molecule has a physiological lifetime of around 2 ms and is present in concentrations between 100 pM and 5 nM [215,216], making it an unattractive competitor to the 6.1 μm and 6.45 μm target wavelengths covering overlapping water and protein absorption bands.

The next section, Section 6.3, describes the fabrication process of a distilled As-based core glass ($Ge_{15}As_{21}Se_{63}Ga_1$ at. %) that was divided to two preforms doped independently with $DyCl_3$ and Dy foil. A novel, all silica glass vessel-based distillation method for anhydrous $DyCl_3$ under open vacuum is also described.

6.3 Fabrication of Dy^{3+} doped $Ge_{15}As_{21}Se_{63}Ga_1$ at. % glass preform *via* distillation of core glass material and its doping with Dy foil and $DyCl_3$ following a novel, all silica glass vessel-based distillation method for anhydrous $DyCl_3$

The work reported in this, and the following Section, was in pursuit of fibre lasing in a dysprosium (III) doped small-core step-index chalcogenide fibre, potentially targeting the surgically relevant 6.1 μm emission [8,141] (as discussed in Section 2.4). Emission close to this could come from the Dy^{3+} excited state to ground state $^6F_{11/2} \longrightarrow {}^6H_{11/2}$ energy levels [142].

An ~80 g $Ge_{15}As_{21}Se_{63}Ga_1$ at. % core glass (M283RERC) was melted. This melt was then distilled with hydrogen and oxygen getters (D047RERC) (see Section 3.2.5). An updated design to the previous silica glass distillation rigs was used (Section 3.2.5 and appendix 1 for technical drawing, description of rig, and its advantages). The distilled host glass was then remelted. This remelt was then divided into two and the gallium (which is unable to be distilled in elemental form at temperatures used in the silica glass vessel) was then added. One melt being batched with 3N dysprosium foil (Table 3.1) (M285RERC, $Ge_{15}As_{21}Se_{63}Ga_1$ at. % + 500 ppmw Dy foil), and the second melt batched with 3N dysprosium (III) chloride (Table 3.1) (M286RERC, $Ge_{15}As_{21}Se_{63}Ga_1$ at. % + 250 ppmw $DyCl_3$). Moreover, this latter $DyCl_3$ was subjected to its own distillation procedure in which no getter was present to hopefully separate $DyCl_3$ from more refractory oxide or metal impurites.

For further context, but more fully elaborated in Section 6.4, these two core glasses (M285RERC $Ge_{15}As_{21}Se_{63}Ga_1$ at. % + 500 ppmw Dy foil and M286RERC $Ge_{15}As_{21}Se_{63}Ga_1$ at. % + 250 ppmw $DyCl_3$) were drawn to an unstructured intermediate fibre and cane (M285RERC drawn to F125RERC, M286RERC drawn to F126RERC). Next, two small-core step-index fibres using a $Ge_{16.5}As_{16}Se_{61.5}Ga_3S_3$ at. % cladding glass (M284RC, E092RC) were produced as follows. The 500 ppmw Dy foil cane F125RERC + E092RC(i) jacket tube was fibre drawn to F127RERC ($Ge_{15}As_{21}Se_{63}Ga_1$ at. % + 500 ppmw Dy foil core/ $Ge_{16.5}As_{16}Se_{61.5}Ga_3S_3$ at. % cladding). The 250 ppmw $DyCl_3$ cane F126RERC +

E092RC-(ii) was fibre drawn to $Dycl_3$ F128RERC ($Ge_{15}As_{21}Se_{63}Ga_1$ at. % + 250 ppmw $DyCl_3$ core/ $Ge_{16.5}As_{16}Se_{61.5}Ga_3S_3$ at. % cladding).

The following is an overview of the distillation process of a $Ge_{15}As_{21}Se_{63}Ga_1$ at. % host core glass (Section 6.3.1) that was to be melted into two separate preforms containing either Dy foil dopant or $DyCl_3$ dopant. Section 6.3.2 describes unsuccessful attempts to distil $DyCl_3$ in a closed vacuum silica glass vessel system with Section 6.3.3 describing a successful attempt to distil $DyCl_3$ in an open vacuum silica glass vessel system.

6.3.1 Distillation of $Ge_{15}As_{21}Se_{63}Ga_1$ at. % host glass (M283REC, D047RERC)

An ~80 g glass boule of $Ge_{15}As_{21}Se_{63}$ at. % (Ga_1 was excluded until post distillation) was melted with 1000 ppmw $TeCl_4$ (see table 3.1) as described in Section 3.2.4. The given melt code for this glass was M283RERC. This melted boule was quenched, annealed (Section 3.2.6), broken in the MBraun glovebox (<0.1 ppm H_2O and < 0.1 ppm O_2) using an agate mortar and pestle, and the broken pieces batched into a newly designed silica glass distillation rig (Custom design, fabricated by Multi-lab, UK). 700 ppmw aluminium (in wire form, see Table 3.1) was cut to an appropriate weight (0.0416 g Al wire for a 59.4906 g distillation) also batched into the charge chamber of the rig (see Figure 3.2, Appendix 1).

This was the first instance of using the updated silica glass distillation rigs (Figure 3.2), the design differences between the old and new designs of rigs are discussed in detail in Section 3.2.5.

Once M283RERC ($Ge_{15}As_{21}Se_{63}$ at. % + 1000 ppmw $TeCl_4$ + 700 ppmw Al) had been batched and sealed into the silica glass distillation ampoule (as described in Section 3.2.5), an initial bakeout was carried out in the charge chamber in order to encourage the outgassing of HCl. This HCl was a by-product of $TeCl_4$ hydrogen gettering previously applied. Next, the glass was distilled in an open vacuum system (*i.e.* the silica glass rig was connected at the opposite end to the charge end by connection to the turbo-pump capable of achieving 10^{-3}-10^{-4} Pa pressure inside the rig (see section 3.2.5) by heating between 650-700 °C (Section 3.2.5, Table 3.7 for further details). Following the distillation, the silica glass distillation rig was sealed off, under vacuum, at the 100 mm 10/14 link tube and the 160 mm 10/14 exit

tube (see Figure 3.2, Appendix 1), to form a separated silica glass ampoule and the distillate was homogenised in a rocking furnace for 2 hours at 850 °C. The homogenised distillate melt was air quenched and annealed at 240 °C for an hour, then allowed to cool to room temperature. This final glass was given the code D047RERC ($Ge_{15}As_{21}Se_{63}$ at. %).

6.3.2 Closed vacuum distillation of anhydrous dysprosium (III) chloride (D043RC)

The initial attempt to distil anhydrous $DyCl_3$ (Table 3.1 for sources and purity) was carried out in a closed vacuum system (D043RC), as follows. A GE214A 10 mm ID/14 mm OD silica ampoule (Multi-Lab, UK) was heated with an oxy-propane torch around its perimeter, 100 mm from the closed base of the ampoule. Once sufficiently heated to an appropriate softness, with the heated silica emitting a faint orange/white coloured glow, the tube was bent to a 40 ° angle and gently annealed with the oxypropane torch (Figure 6.13). The inclusion of this bend meant that batching the $DyCl_3$ directly into the charge end of the tube was no longer feasible. Batching issues were further exacerbated by static attraction of the ultra-dry powdered $DyCl_3$ to the interior wall of the silica ampoule. So, a work-around was devised as follows.

Silica glass tubing of a 5 mm ID/ 7 mm OD (Multi-Lab, UK) was also glass worked, with the oxy-propane torch, to form 20 mm length delivery ampoules, that were closed at one end. The smaller delivery ampoules were then air and vacuum baked in a 10 mm ID/ 14 mm OD silica ampoule as described in Section 3.2.1. The $DyCl_3$ (approx. 0.5 g per 5 mm/ 7 mm ID/OD ampoule) was then batched into one of these smaller delivery ampoules which could then be carefully guided and dropped through the open end of the bent 10/14 mm ID/OD distillation ampoules (see Figure 6.13). This facilitated an easy delivery of the $DyCl_3$ to the charge section of the rig while ensuring no material was ‘lost’ through static electrical interaction induced adherences with other sections of the bent ampoule rig during batching, while allowing the $DyCl_3$ to distil out of the open end of the 5 mm/ 7 mm ID/OD tube. Only one 5 mm/ 7 mm delivery ampoule with 0.5 g $DyCl_3$ was used in a GE214A 10 mm ID/14 mm OD bent tube silica distillation ampoule. This bent tube ampoule was then placed under vacuum and, when interior pressures reached 10^{-3} Pa, it was sealed using an oxy-propane torch.

Type K Thermocouples (Nickel-Chromium / Nickel-Alumel, RS components) were next wired to four sections of the ampoule (Figure 6.13). From Figure 6.13, the two thermocouples labelled “Charge 1” and “Charge 2” were used to monitor the temperature at the initial batched location of the $DyCl_3$. The thermocouple labelled “Link”, monitored the temperature at the bend in the distillation tube. Lastly, the thermocouple labelled “Collection” monitored temperature at a section of the ampoule that was outside of the clamshell furnace where it was anticipated material could condense.

The charge section of the ampoule was then placed into a clamshell furnace (Carbolite, UK) with the sealed collection end held outside the furnace using a laboratory clamp. Furnace wool (SuperWool, Morgan thermal ceramics) was then packed around the ampoule to further insulate the charge chamber inside the furnace.

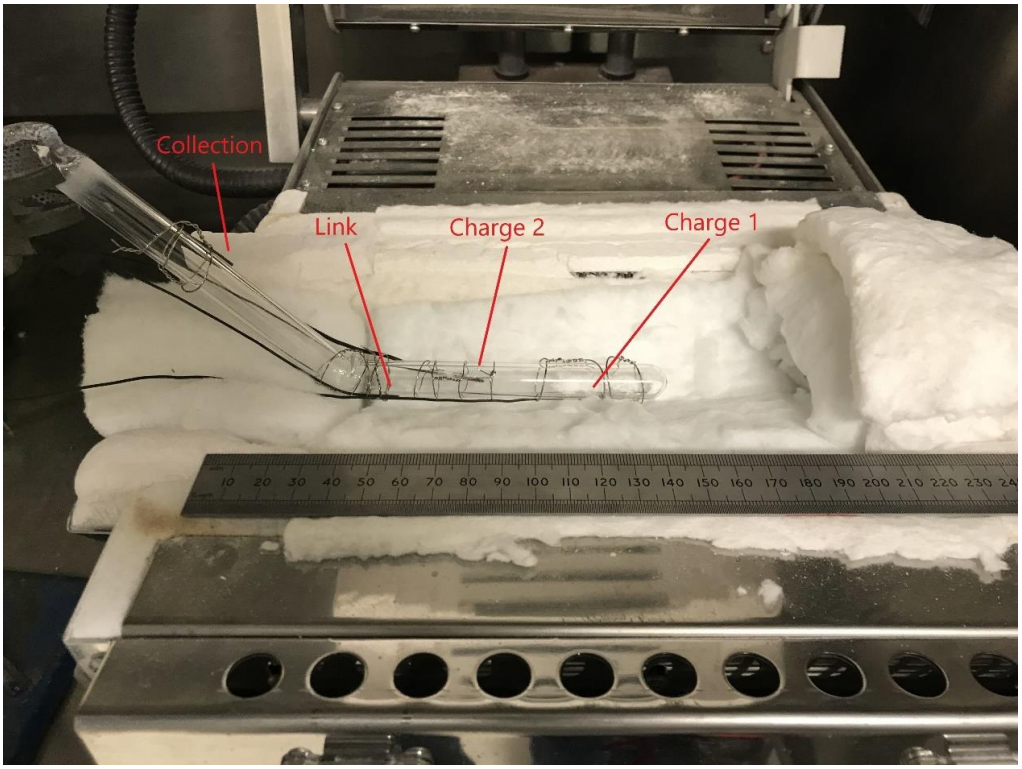


Figure 6.13 The operational set up for the closed vacuum system $DyCl_3$ distillation (Code: D043RC) within the bent silica glass tube holding the charge sealed under vacuum). Thermocouple positions on the silica ampoule and their assigned names annotated. “Charge 1” and “Charge 2” were used to monitor the temperature at the initial batched location of the $DyCl_3$. “Link”, monitored the temperature at the bend in the distillation tube. “Collection” monitored temperature at a section of the ampoule where it was anticipated material could condense ~0.5 g of $DyCl_3$ was used in this batch attempt.

The furnace was then set to step change from room temperature to 450 °C, then ramp at 50 °C/ hour to 850 °C. The ampoule was periodically visually checked at the condensate end emerging from the furnace roughly every hour above 500 °C to observe the status of the distillation process. In literature, $DyCl_3$ was shown to distil from a tantalum crucible at a rate of 1 g/min at 850 °C at a pressure of 10^{-4} Pa [186]. The charge chamber was held approximately isothermally between 800-835 °C for 90 minutes; it is important to note that further temperature increases were not feasible with the set up used as here (see Figure 6.13) as, despite the furnace insulation wool packing the distillation chamber in the furnace, the collection chamber was being subject to increasingly high temperatures through radiant heat from the interior of the furnace. After 90 minutes, with no observable material movement to the collection chamber, the process was stopped, and the ampoule was cooled to room temperature. Figure 6.14 shows the measured temperature profiles throughout the closed distillation process.

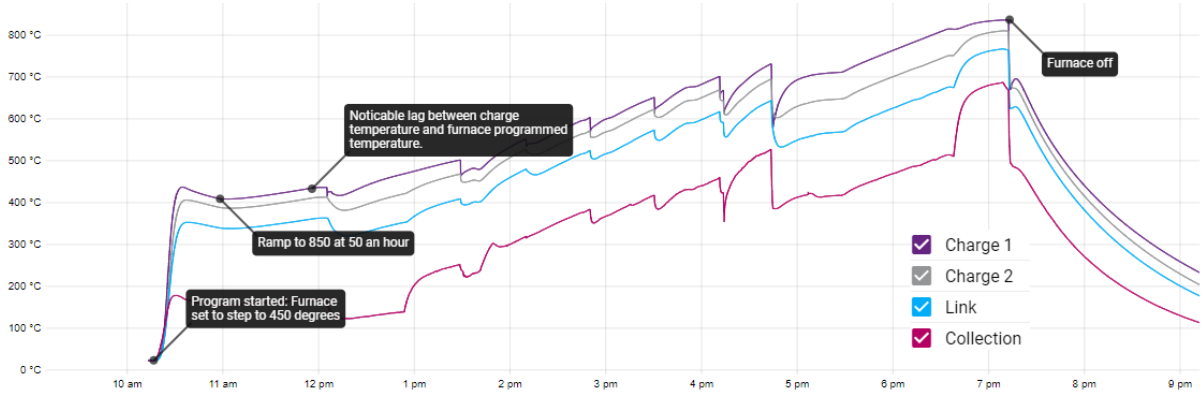


Figure 6.14 Monitoring of D043RC closed $DyCl_3$ distillation process. Temperature profiles of each section of the ampoule measured by the external thermocouples in the charge chamber, link tube (bend), and collection chamber shown in Fig. 6.13. The periodic dips in temperature were the result of temporarily displacing insulating blanket to observe the distillation process.

Upon inspection of the ampoule after the aborted $DyCl_3$ closed distillation, it was noted that the $DyCl_3$ had melted from a white powder form and resolidified in a colourless, translucent, crystalline appearing form in the charge portion of the ampoule (Figure 6.15A). Given the melting temperature of $DyCl_3$ (647 °C) and the temperature measured in Charge 1 and 2 being above 647 °C for ~3 hours, this melting and then freezing of $DyCl_3$ was anticipated. Small black deposits (<1 mm in diameter) were noted on the collection side of the bend linking the two sections of the ampoule (Figure 6.15B). It is possible that this was the result of partial

heating of $DyCl_3$ particulates that adhered to the side of the ampoule during batching. It could also be the result of a more volatile contaminant that did manage to distil away from the $DyCl_3$ bulk and through the ampoule, but this was not Dy metal itself as this melts under ambient atmosphere at 1412 °C[217]. No elemental analysis was conducted to determine the content of these black deposits, however, $DyCl_2$ is described to be a glossy black colour in appearance which may indicate a reduction of $DyCl_3$ had occurred [218].

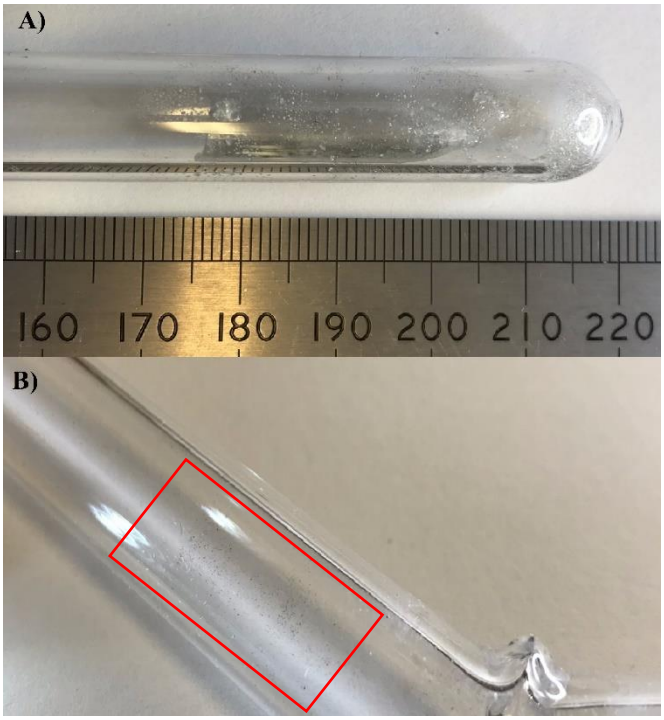


Figure 6.15 Observations after the closed distillation of $DyCl_3$ (D043RC) A) colourless, crystalline in appearance $DyCl_3$ remaining in the charge chamber following the attempted distillation. B) Dark deposits on the collection side of the bend linking the charge-collection chambers (highlighted by red rectangle). No substantial $DyCl_3$ movement nor distillation was observed.

With the closed vacuum distillation of $DyCl_3$ unsuccessful, it was decided to repeat the process using an open vacuum system (D044RC).

6.3.3 Open vacuum distillation of anhydrous dysprosium (III) chloride (D044RC)

Following the lack of results with the closed vacuum distillation, an open, drawing vacuum distillation was attempted. Thus, a second bent tube (10 mm ID/14 mm OD, GE214A, Multi-Lab) and 5 mm/7 mm ID/OD open one end delivery ampoule were prepared as described in Section 6.3.2. Again, approximately 0.5 g of $DyCl_3$

(Table 3.1 for source and purity) was batched into the 5 mm/ 7 mm ID/OD ampoule, which was subsequently gently dropped into the charge end of the main 10 mm/ 14 mm ID/OD bent tube silica glass distillation ampoule. Note that all batching was done in the dry nitrogen atmosphere of a MBraun glovebox (< 0.1 ppm H_2O, < 0.1 ppm O_2). This distillation ampoule was fitted to a Saunders' valve inside the MBraun glovebox, then brought out from the glovebox and attached to the vacuum pump system (Figure 6.16). External thermocouples were fixed in an identical fashion to that seen in Figure 6.13. The ampoule was then wrapped in insulating blanket (SuperWool, Morgan Thermal Ceramics) and placed into a 28 mm ID tube resistance furnace (constructed in-house). The use of this tube furnace meant that the $DyCl_3$ charge chamber could be more efficiently insulated, and the furnace provide a more stable, localised heating to the sample when compared to the clamshell furnaced used during the previous closed distillation (Section 6.3.2). This improvement, however, was at the expense of no longer being able to easily observe the distillation process as the tight packing of the furnace wool and thermocouples hindered furnace mobility. Figure 6.16 shows the set up used.



Figure 6.16 Experimental set up for the open vacuum system $DyCl_3$ distillation. Thermocouple positioning identical to that in Figure 6.13.

The ampoule was again pumped down to 10^{-3} Pa using a diffusion pump, with a liquid nitrogen cooled cold trap between the pump and the bent tube silica distillation rig to protect this pump, and the heating schedule was started as follows.

The furnace was heated to 500 °C at 250 °C/ hour and then held for 15 minutes at 500 °C to stabilise readings between the furnace controller thermocouple readout and the external thermocouple readout. Figure 6.17 shows the external thermocouple temperature profiles throughout the process. At this stage, some furnace blanket was rearranged, causing the decrease in temperature at 3:00 pm seen in Fig. 6.17. The furnace was then programmed to a maximum temperature of 900 °C at 250 °C/ hour ramp rate, with the sample being above the 850 °C proposed distillation temperature for 30 minutes. Comparing Figure 6.14 and Figure 6.17, this open distillation method using the tube furnace was superior in context of temperature control of the marked thermocouple zones allowing a much more stable heating profile with less radiant heat increasing the temperature of the (ideally cool) collection tube, with the added potential to reach higher maximum temperatures, as follows.

From Figure 6.14, the closed distillation shows that when the maximum temperature of the charge chamber was reached (835 °C), the collection chamber was around 690 °C. Ideally, this chamber would be at a temperature lower than the melting temperature of $DyCl_3$ (647 °C) to encourage condensing of the $DyCl_3$ to a solid form, away from the charge chamber. Thus, monitoring of the open distillation as seen in Figure 6.16 indicates that the open distillation (as opposed to closed, as seen in Figure 6.14) was able to reach higher a maximum temperature in the charge chamber (870 °C) while keeping the collection chamber at a far lower temperature of ~50 °C. This temperature gradient between the charge and distillation chambers of around 820 °C was expected to aid in the $DyCl_3$ distillation process.

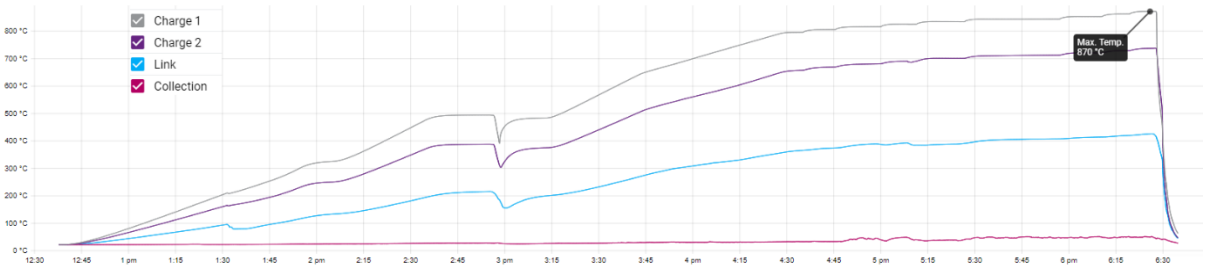


Figure 6.17 Monitoring of the $DyCl_3$ open distillation process (D044RC) Temperature profiles of each section of the ampoule measured by external thermocouples. Thermocouple placement on ampoules was identical to what was shown in Fig. 6.13.

Following this 0.5-hour heat treatment >850 °C, the furnace and insulating blanket were removed to observe any $DyCl_3$ material movement. The bulk of the material was observed towards the link bend (Figure 6.18A) with some remnants still being present in and around the 5 mm/ 7 mm ID/OD delivery ampoule which was still sitting in the charge section of the bent silica glass tube distillation ampoule (charge chamber not imaged in Figure 6.18A). The distilled material, assumed still to be $DyCl_3$, was observed visually to be present in two morphologies.

Around 70 mm beyond the delivery ampoule, having moved towards the collection chamber but still before the linking bend, lay a deposited layer of colourless, crystalline appearing deposits, some as large as that had 2 mm formed (Figure 6.18B). Whereas, further along the main silica glass distillation ampoule towards the relatively cooler link bend and in the link bend, the condensed material was in the form of a fine powder layer (Figure 6.18A). It was proposed that the higher temperatures in the region 70 mm above the delivery ampoule in close proximity to "Charge 2" which was the position of one of the external thermocouples was more conducive to crystal growth when compared to the cooler temperatures closer to the link tube/bend region (the position of the "link" external thermocouple).

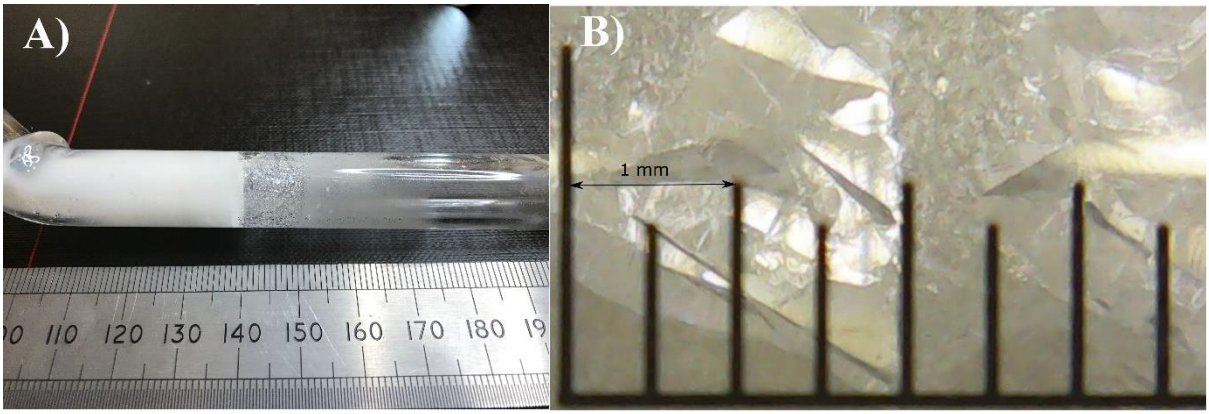


Figure 6.18 Observations after the open distillation process of $DyCl_3$ A) From the photographic image, the two morphologies of distilled $DyCl_3$ observed were as follows: from 100-140 mm on rule: collected material was in the form of a fine white powder; from 140-150 mm on rule: colourless crystal deposits. From 100-140 mm on rule: collected material was in the form of a fine white powder. From 140-150 mm on rule: Colourless crystal deposits. B) Close up photographic image taken of the crystalline deposit present between 140-150 mm on ruler as shown, 70 mm from base of charge chamber.

Considering the 5 mm/ 7 mm ID/OD delivery tube and the base of the charge chamber had observably less $DyCl_3$ post-heat treatment and a substantial amount of material assumed to be $DyCl_3$ was present towards the linking bend tube as described above, the distillation method was deemed a success. However, this was purely a conclusion drawn on visual observations of material movement, and at this stage no conclusions could be made regarding material composition or purity. That is, it could not be assessed visually if the colourless crystal deposits were $DyCl_3$, if remaining deposits in the charge chamber were more refractory contaminants, or even if the $DyCl_3$ was still in anhydrous form.

The D044RC distillation ampoule was taken back into the dry nitrogen atmosphere of a MBraun glovebox (< 0.1 ppm H_2O, < 0.1 ppm O_2). Due to the poor annealing of the bent portion of the 10 mm/ 14 mm ID/OD bent tube silica glass distillation ampoule, the ampoule could easily be snapped into two pieces along this bend. Stainless-steel tweezers were used for the removal of the some of the larger colourless crystals, at the 140-150 mm region in Figure 6.18A, and set aside for batching into the doped glass, M286RERC $Ge_{15}As_{21}Se_{63}Ga_1$ at. % + 250 ppmw $DyCl_3$ (further details in Section 6.4). The ampoule was then broken *via* percussion at this 140-150 mm region, and a portion of the broken silica glass ampoule with the crystal-like structures deposited on the interior surface was set aside for SEM-EDX analysis. This was done to preserve the morphology of the crystal-like structures on the silica glass for SEM analysis.

A second break in the bent tube silica glass distillation ampoule was made *via* percussion at the site of the 5 mm/ 7 mm ID/OD delivery tube at base of the charge chamber (not displayed in Figure 6.18), where a grey-white coloured deposit was present outside of the delivery tube, on the interior side of the distillation ampoule. As before, a portion of the broken silica glass ampoule with the grey-white deposited on the interior surface (to retain the deposit morphology) was set aside for SEM-EDX analysis.

These sections of broken silica glass tubing containing: (i) the grey-white coloured deposit and (ii) the suspected distilled dysprosium chloride colourless crystals were placed onto an aluminium SEM stub and coated with a nominally 10 nm layer of carbon (thickness as calculated by the coater, Q150R ES, QuorumTech). The

samples were then imaged using SEM (JEOL 6490LV, See Section 3.3.3). Due to the hygroscopic nature of $DyCl_3$, any time spent in atmosphere was minimised.

As seen in Figure 6.19, a SEM micrograph of the (i) grey-white deposit that was present at the base of the charge chamber, the deposit was present in three different morphologies. The first morphology, as indicated by the red box labelled "1" was present in a relatively flat form on the silica glass. A second form, as indicated by the red box labelled "2" was present in a dendritic morphology. The third form, as indicated by the red box labelled "3" appeared to be formed of multiple smaller features of various shapes and sizes, conferring a "roughness" to the region.

Three SEM-EDX area elemental composition scans (see Section 3.3.4) were conducted over each region of differing morphology, as indicated by the three labelled red boxes. This was to investigate if there was a meaningful difference in composition between morphologies. The mean averaged elemental composition results of the three scans for each region shown in Figure 6.19 are displayed as "regions 1, 2, and 3", respectively, in Table 6.3.

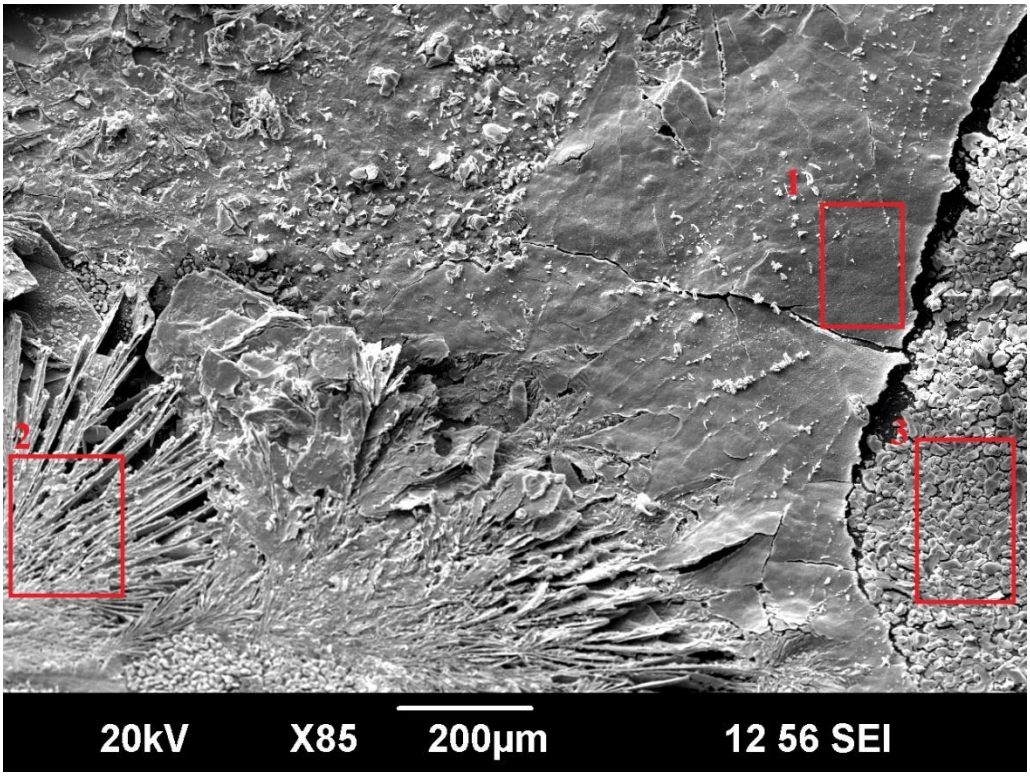


Figure 6.19 Observations after the open distillation of $DyCl_3$ (D044RC). SEM image of the remnant, undistilled, (i) grey-white material present at the base of the silica glass charge chamber on the interior of the distillation ampoule, outside the delivery ampoule. Material was retained on the

silica glass substrate for the SEM in order to maintain morphology. Red squares highlight the three scanned regions: labelled here as 1, 2, and 3. The elemental analysis results of these three regions is shown in Table 6.3.

From Table 6.3 and Figure 6.20, three main contaminants aluminium, zinc, and ytterbium were identified as present in each region studied *i.e.*, the three regions labelled 1-3 in Figure 6.19. $DyCl_3$ has been shown to interact with silica ampoules at high temperatures (96 hours at 930 °C), leading to chemical corrosion of the silica glass substrate as found by Tang *et al.* [52] in which $DyCl_3$ was heated in an otherwise empty silica glass ampoule, under vacuum. Although the length of time of the open $DyCl_3$ distillation process was a substantially shorter time than reported in Tang *et al.* [52] of 96 hours, the presence of silica glass corrosion, potentially leading to silica glass contaminants alongside these $DyCl_3$ deposits could not be ruled out. However, as the SEM-EDX elemental analysis was performed on samples still present on the silica ampoule distillation rig, detection of released/ corroded silica on the $DyCl_3$ was unreliable as X-ray emissions from the underlying silica ampoule would also have likely been detected.

Between the different three different morphologies seen in regions 1, 2, and 3 in the SEM micrograph of the (i) grey-white deposit at the base of the distillation ampoule (Figure 6.19), dysprosium and chlorine content varied. Between the "flat" region 1 and the "dendritic" region 2, dysprosium and chlorine content were comparable with region 1 scans showing slightly higher dysprosium at 48.497 at. % compared to 45.147 at. % in the region 2 scans. Chlorine in region 1 measured at 49.630 at. % with region 2 measuring slightly higher chlorine at 53.213 at. %. However, region 3, with the variable shaped, rough surface morphology, measured Dy at 27.837 at. % and Cl at 70.820 at. %.

It is to be noted that that expected atomic % ratio of pure $DyCl_3$ (at. % is what is presented in this current work) is 25 at. % Dy to 75 at. % Cl_3 whereas, if weight % was investigated, a ratio of 60.4 wt. % Dy to 39.6 % Cl_3 would indicate pure $DyCl_3$. Thus, region 3 was measured to have Dy and Cl at. % close to the expected ratio (Dy 25: Cl 75), whereas regions 1 and 2 have a ratio closer to 50:50. It is possible that during the distillation, $DyCl_3$ maybe have been reduced to $DyCl_2$, with potentially HCl being produced with other contaminants in the material. This reduction may have continued to produce small amounts of elemental Dy (which

may explain the grey colouring of the sample) and 3HCl. It is suggested that regions 1 and 2 were comprised of a mix of $DyCl_3$, $DyCl_2$, and Dy, which the area SEM-EDX scan averaged out to these ~50:50 ratios.

Figure 6.20 shows the X-ray emission spectrum of an SEM-EDX area scan of region 1 of the (i) grey-white deposit from the residual material at the base of the silica glass open distillation ampoule, as labelled in Figure 6.19, to aid the following argument. It is possible that although aluminium (Al) (0.567 at. %) and ytterbium (Yb) (0.823 at. %) were seemingly detected using SEM-EDX of region 1, that Al and Yb are not actually present in the sample, but that instead this was due to the emission lines of dysprosium closely overlapping those of Yb and Al and so were mistakenly suggested by the software used as different elements. Additionally, as zinc has no overlapping peaks it can more confidently be concluded that this contaminant is indeed present.

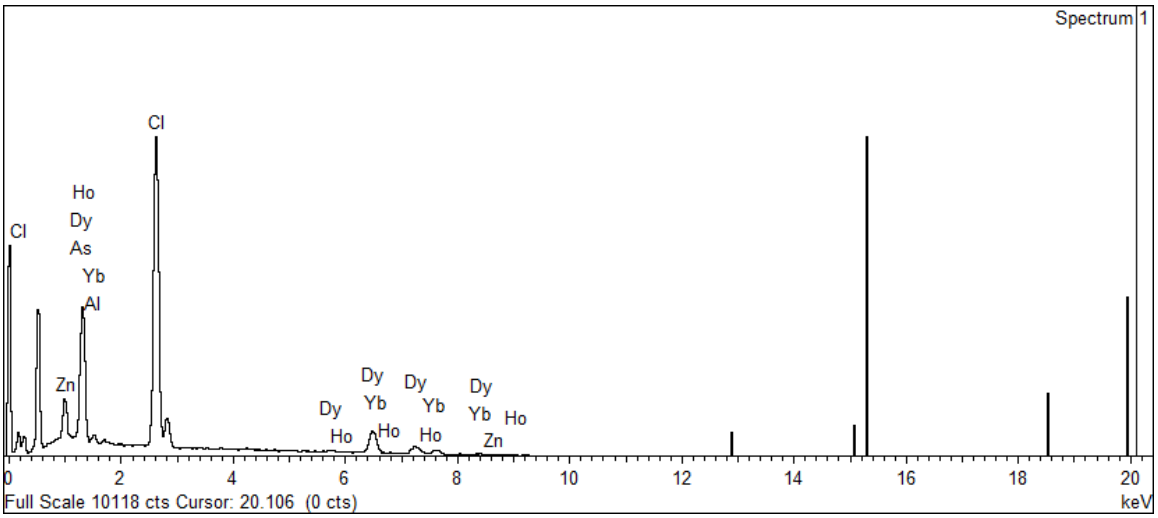


Figure 6.20 Observations after the open distillation of $DyCl_3$. X-ray emission spectrum of region 1 of the (i) grey-white deposit material present at the base of the silica glass charge chamber on the interior of the distillation ampoule, outside the delivery ampoule as shown in Figure 6.19. The annotated elements are automatically proposed by the SEM-EDX software (INCA, Oxford instruments) in response to measured X-ray emissions. Elements suggested by this programme may not necessarily be detected by the SEM-EDX scan, this explains the lack of As and Ho in Table 6.3.

Table 6.3 SEM-EDX elemental analysis of (i) grey-white material present at the base of the silica glass charge chamber (Figure 6.19) and (ii) distilled colourless crystals (Figure 6.21) after the open distillation of $DyCl_3$. All values given as atomic %.

SEM-EDX area scans on Fig. 6.19, sample (i)					
Region	Dy/ at. %	Cl/ at. %	Zn/ at. %	Al/ at. %	Yb/ at. %
1	48.497	49.630	0.483	0.567	0.823
2	45.147	53.213	0.550	0.277	0.813
3	27.837	70.820	0.273	0.540	0.590
SEM-EDX area scans on Fig. 6.21, sample (ii)					
1	40.75	58.46	0.11	0.40	0.28
2	24.54	74.29	0.28	0.38	0.5

A second set of SEM-EDX scans were carried out on a section of the distilled, colourless crystalline material that had condensed close to the link bend, 70 mm from the base of the charge chamber, between 140-150 mm on the ruler in Figure 6.18A. Figure 6.21 shows the SEM image of the (ii) colourless crystalline sample with two red marks on the image itself. The marks indicate the location of the two "point and ID" SEM-EDX scans (see Section 3.3.4), the results of which are reported in Table 6.3. Although precautions had been taken to minimise $DyCl_3$ sample exposure to atmosphere during transit from the Mid-Infrared Photonics Group's laboratories to the different nmRC Building where the carbon coater and SEM equipment. It was observed that the colourless crystalline deposits began to degrade during the imaging process. The (ii) crystalline sample was removed from the MBraun glovebox (< 0.1 ppm H_2O, < 0.1 ppm O_2) and spent ~5 minutes in ambient atmosphere in travel to the carbon coater, which operates under vacuum, before spending another ~3 minutes in ambient atmosphere before being transferred to the vacuum chamber of the SEM.

The (ii) translucent crystalline deposit began to transition into a powder form which split/crack the larger crystals (~500 µm in size) apart, thus exposing layers of material that had not been carbon coated. Charging was observed during the

imaging of these samples, as evidenced by the horizontal lines present across the image as seen in Figure 6.21.

The two "point and ID" SEM-EDX scans of the (ii) colourless crystalline deposit measured similar compositions were observed to that which was present in the (i) grey-white charge chamber material of the silica glass distillation ampoule, including the detection of the same contaminant materials (Al, Yb, Zn, all <0.5 at. % in (ii)). Point and ID scan "1" of the (ii) colourless deposit found Dy 40.75 at. % and Cl 58.46 at. %. This was comparable to the at. % seen in regions 1 and 2 of (i) grey-white charge chamber material (see above and Table 6.3). Point and ID scan "2" of the (ii) colourless deposit found Dy 24.54 at. % and Cl 74.29 at. %. This was comparable to the at. % seen in region 3 of (i) grey-white charge chamber material (see above and Table 6.3), and was closer to the expected "pure $DyCl_3$" ratio of Dy 25: Cl 75 at. %.

The contaminant materials (Al, Yb, Zn) in the distilled (ii) colourless crystalline deposit were present in notably lower concentrations than sample (i) grey-white material deposit. To compare between region SEM-EDX area scan 1 of (i) grey-white material and region 1 point and ID scan of (ii) colourless crystalline deposit, Al was present in at. % of 0.567 and 0.4, respectively. Yb was present in at. % of 0.823 and 0.28, respectively. Zn was present in at. % of 0.483 and 0.11, respectively.

These two point and ID SEM-EDX scans on the (ii) colourless crystalline deposit confirmed the presence of dysprosium in the distillate material, with lower Al, Yb, and Zn impurity content when compared to undistilled charge. Although it must be noted that the (optically active) dysprosium content apparently varies between at least ~24 at. % to ~41 at. % in different crystals.

It is therefore suggested that, until further replicability and optimisation studies are conducted, future batching of distilled dysprosium chloride crystals, such as those imaged of (ii) colourless crystalline deposits (Figure 6.21), into a chalcogenide glass melt would be carried out under the assumption that the compound is $DyCl_3$. However, it must be noted that there is potential to have a higher "actual" amount of Dy^{3+} in these crystals as evidenced by a higher ratio of Dy at. % to Cl at. % (e.g.

scan 1 of sample (ii) (Table 6.3) with Dy 40.75 at. % and Cl 58.46 at. %) than the expected "pure $DyCl_3$" ratio of Dy 25: Cl 75 at. %.

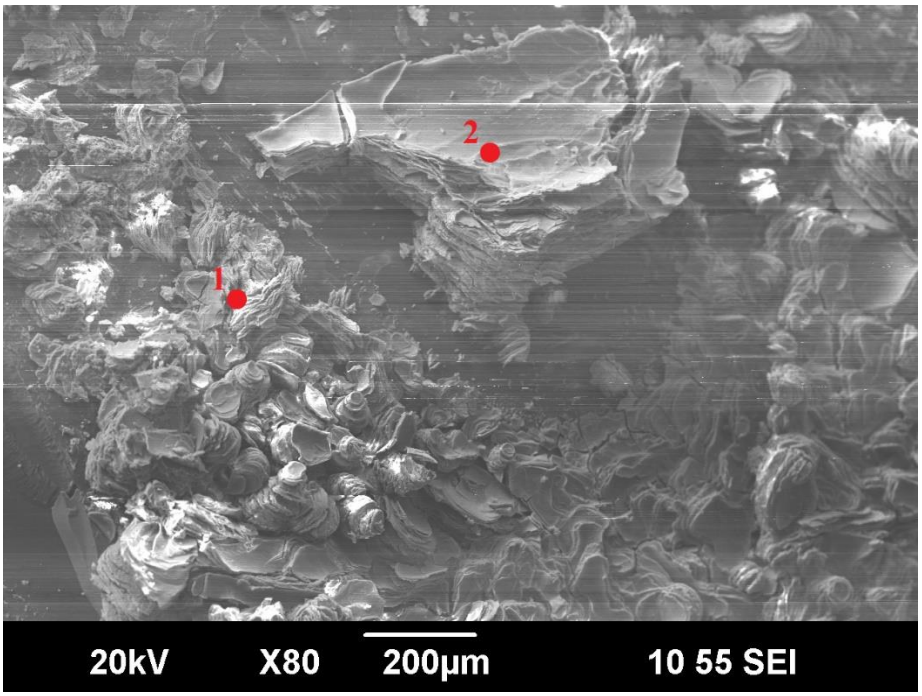


Figure 6.21 SEM image of distilled, colourless crystals from the region shown in Figure 6.18A and B present outside the charge chamber, 70 mm from base of the distillation ampoule.

Following the relative success of the open tube distillation of $DyCl_3$, and distillation of a $Ge_{15}As_{21}Se_{63}Ga_1$ at. % host glass (M283RERC, D046RERC) two dysprosium doped fibres were produced as elaborated in, the next section, Section 6.4. One fibre was doped with 500 ppmw Dy foil (F125RERC), and the second fibre doped with 250 ppmw of the newly distilled $DyCl_3$ (F126RERC). These fibres are characterised and then drawn to small-core, step-index fibres (F127RERC and F128RERC, respectively).

6.4 Fabrication and characterisation of 500 ppmw Dy foil (M285RERC) and 250 ppmw distilled $DyCl_3$ (M286RERC) doped $Ge_{15}As_{21}Se_{63}Ga_1$ at. % unstructured (F125RERC, F126RERC, respectively) and step-index fibres (F127RERC, F128RERC, respectively) with the cladding glass $Ge_{16.5}As_{16}Se_{61.5}Ga_1S_3$ (M284RC, E092RC)

As briefly described in Section 6.3, the distilled $Ge_{15}As_{21}Se_{63}Ga_1$ at. % rare earth ion dopable, host, core glass (M283RERC, D046RERC) was split into two batches. One melt was doped with 500 ppmw Dy foil (M285RERC, $Ge_{15}As_{21}Se_{63}Ga_1$ at. % + 500 ppmw Dy foil) (see Section 3.2.7) in which the Dy foil surface was thoroughly mechanically exfoliated using germanium pieces (Table 3.1 for purity and source). The second melt was doped with 250 ppmw open vacuum distilled dysprosium chloride (Section 6.3.3) (M286RERC, $Ge_{15}As_{21}Se_{63}Ga_1$ at. % + 250 ppmw $DyCl_3$). It is important to note the lowered doping concentration of dysprosium chloride (250 ppmw $DyCl_3$ compared to 500 ppmw Dy foil) was chosen as it had been shown a strong proclivity to cause devitrification in a selenide based $Ge_{16.5}As_{16}Ga_3Se_{64.5}$ chalcogenide glass during the glass melting process by Tang *et al.* [52]. It is also to note that although 250 ppmw $DyCl_3$ was added, this corresponds to an actual ~**150** ppmw Dy^{3+} concentration due to the ~60:40 ratio of the mass of Dy to Cl_3. However, throughout this work, the term "250 ppmw $DyCl_3$" is used. These two glasses were remelted at 850 °C for 2 hours before being quenched, then annealed (see Section 3.2.7) at T_g (240 °C).

Both of the rod preforms, as-annealed, were propylamine (Table 3.2 for source and purity) etched *via* full submersion at ambient temperature and atmosphere, under dust cover for 96 hours before being cleaned with acetone and isopropanol (Table 3.2 for chemical purities and sources) and dried between 0.5-1 Pa in the vacuum chamber of the MBraun glovebox. The preforms were then drawn to both fibre and cane. The fibre was produced for the purpose of performing a cut-back, wide-band optical loss measurement (small core fibre cannot be interrogated for optical loss wideband due to not at present having a sideband mid-IR light source available which is capable of being able to focus enough photons into a small-core fibre). These unstructured intermediate fibres (F125RERC, $Ge_{15}As_{21}Se_{63}Ga_1$ at. % + 500

ppmw Dy foil and F126RERC, $Ge_{15}As_{21}Se_{63}Ga_1$ at. % + 250 ppmw $DyCl_3$) were also investigated for photoluminescence, and photoluminescent lifetime characteristics. A novel set up designed and operated by Joel Nunes (PhD colleague, Mid-IR Photonics Group, University of Nottingham, UK) used also powdered F125RERC fibre samples to measure photoluminescence and photoluminescent lifetimes.

Following this, an extruded jacket tube composed of $Ge_{16.5}As_{16}Se_{61.5}Ga_1S_3$ at. % (M284RC, E092RC) was fabricated and cleaved to two tubes, E092RC-(i) and E092RC-(ii), like the method described earlier in Sections 6.1 and 6.2. These two E092RC tubes were then used to make a rod-in-tube preform for F125RERC $Ge_{15}As_{21}Se_{63}Ga_1$ at. % + 500 ppmw Dy foil and F126RERC $Ge_{15}As_{21}Se_{63}Ga_1$ at. % + 250 ppmw $DyCl_3$ (see Section 3.2.9).

Two small-core step-index fibres using the $Ge_{16.5}As_{16}Se_{61.5}Ga_3S_3$ at. % cladding glass (M284RC, E092RC) were produced as follows:

The 500 ppmw Dy foil cane F125RERC + E092RC-(i) jacket tube was fibre drawn to F127RERC ($Ge_{15}As_{21}Se_{63}Ga_1$ at. % + 500 ppmw Dy foil core/ $Ge_{16.5}As_{16}Se_{61.5}Ga_3S_3$ at. % cladding).

The 250 ppmw $DyCl_3$ cane F126RERC + E092RC-(ii) was fibre drawn to $Dycl_3$ F128RERC ($Ge_{15}As_{21}Se_{63}Ga_1$ at. % + 250 ppmw $DyCl_3$ core/ $Ge_{16.5}As_{16}Se_{61.5}Ga_3S_3$ at. % cladding).

The step-index fibres (F127RERC and F128RERC) were then characterised using SEM to image the core/clad interface.

Section 6.4.1 covers the fibre loss measurements of F125RERC ($Ge_{15}As_{21}Se_{63}Ga_1$ at. % + 500 ppmw Dy foil) and F126RERC ($Ge_{15}As_{21}Se_{63}Ga_1$ at. % + 250 ppmw $DyCl_3$). Section 6.4.2 covers the fibre drawing of F127RERC ($Ge_{15}As_{21}Se_{63}Ga_1$ at. % + 500 ppmw Dy foil core/ $Ge_{16.5}As_{16}Se_{61.5}Ga_3S_3$ at. % cladding) and F128RERC ($Ge_{15}As_{21}Se_{63}Ga_1$ at. % + 250 ppmw $DyCl_3$ core/ $Ge_{16.5}As_{16}Se_{61.5}Ga_3S_3$ at. % cladding). Section 6.4.3 covers photoluminescence (PL) and PL lifetime measurements of F125RERC ($Ge_{15}As_{21}Se_{63}Ga_1$ at. % + 500 ppmw Dy foil) and FtIR absorption measurement using a bulk sample of its parent preform M285RERC ($Ge_{15}As_{21}Se_{63}Ga_1$ at. % + 500 ppmw Dy foil).

6.4.1 Fibre loss of unstructured, distilled, dysprosium doped fibres (F125RERC ($Ge_{15}As_{21}Se_{63}Ga_1$ at. % + 500 ppmw Dy foil) and F126RERC ($Ge_{15}As_{21}Se_{63}Ga_1$ at. % + 250 ppmw open-distilled $DyCl_3$))

The 500 ppmw dysprosium foil and 250 ppmw dysprosium chloride doped fibres were drawn as unstructured fibres and cane and assigned the fibre codes F125RERC ($Ge_{15}As_{21}Se_{63}Ga_1$ at. % + 500 ppmw Dy foil) and F126RERC ($Ge_{15}As_{21}Se_{63}Ga_1$ at. % + 250 ppmw $DyCl_3$), respectively. Two fibre loss measurements were carried out on each fibre, as follows. The first was a broadband mid-IR fibre loss measurement using a Globar© light source, KBr beam splitter, and a DTGS detector (see Section 3.3.6). The second was a narrow-band near-infrared measurement only using a tungsten light source, CaF_2 beamsplitter, InSb and InGaAs detectors. Further details are in Section 3.3.6.

Figure 6.22 shows the fibre loss spectra of the two fibres, with data from both the mid-IR and near-IR fibre loss measurements. F125RERC ($Ge_{15}As_{21}Se_{63}Ga_1$ at. % + 500 ppmw Dy foil) exhibited comparatively lower losses with the lowest loss of 2.07 dB/m at 6.13 µm, while F126RERC ($Ge_{15}As_{21}Se_{63}Ga_1$ at. % + 250 ppmw $DyCl_3$) demonstrating its lowest loss of 4.86 dB/m at 6.085 µm. However, additionally F126RERC ($Ge_{15}As_{21}Se_{63}Ga_1$ at. % + 250 ppmw $DyCl_3$) exhibited high losses in the near-IR, sub-3 µm wavelength range; This is indicative of the presence of scattering centres along the fibre length studied. The well documented tendency of $DyCl_3$ to encourage devitrification is the likely cause of these scattering centres even in low concentrations[50–53]. For instance, Tang *et al.* [52] identified strong near-IR scattering during an FtIR investigation of an undistilled 1000 ppmw $DyCl_3$ doped $Ge_{16.5}As_9Ga_{10}Se_{64.5}$.

Despite these extra near-IR scattering centres manifested in the near-IR wavelength region (see Figure 6.22), of the unstructured F126RERC ($Ge_{15}As_{21}Se_{63}Ga_1$ at. % + 250 ppmw $DyCl_3$), the absorption band centred around 2.8 µm (corresponding to -OH [132]and Dy^{3+}: $^6H_{15/2}$ ground state → $^6H_{13/2}$ absorption (see Figure 6.24B)) exhibited a lower loss when compared to F125RERC ($Ge_{15}As_{21}Se_{63}Ga_1$ at. % + 500 ppmw Dy foil). This is likely due to a lower amount of dopant being included in F126RERC (**150** ppmw Dy^{3+} from the **250** ppmw open-distilled **$DyCl_3$** as opposed to 500 ppm Dy^{3+} in F125RERC) but may also be due, in part, to the dysprosium chloride distillation process further removing oxide and hydride impurities from the

batched material. Furthermore, there is also the possibility of [Cl^-] from the $DyCl_3$ reacting with [-H] unwanted impurity in the glass to form HCl, which is already a gas at ambient temperature and pressure, thus reducing H content free to form the -OH vibrational absorption as follows, in this case to form the gallium-dysprosium complex referred to in Section 2.3.1 and equation 6.1:

$$DyCl_3 + \text{-Se-Ga(-Se-H)-Se-} \rightarrow HCl\uparrow + \text{Se-Ga(-Se-)-Se-Dy-Cl} \qquad \text{Equation 6.1}$$

It could be also speculated that oxide impurities may also be sequestered by dysprosium driven by free energy considerations to form Dy_2O_3, as the formation of dysprosium oxide will have been free energy driven as compared to the formation of dysprosium selenide, due to the greater stability of the dysprosium oxide chemical bond. Moreover, as dysprosium is the most electropositive (electron attracting) species in the melt, compared to the 'p' block elements such as Ge, Ga, As, Sb, Se, the Dy^{3+} would have gettered unwanted oxygen contamination in the glass melt where reaction rates are high and so kinetics would not have held up the free-energy driven processes. Any dysprosium oxide formation could lead to the manifestation of Dy_2O_3 particulate scattering centres causing high losses in the near-IR as Dy_2O_3 particulates would precipitate from the glass melt and remain as suspended nano- or micro- particles in the quenched and annealed glass. These speculations are evidenced by the presence of Dy_2O_3 found by *via* XRD analysis of undistilled bulk glass by Tang et al.[50] in a 2000 ppmw $DyCl_3$ containing $Ge_{16.5}As_{16}Ga_3Se_{64.5}$ at. % glass.

The Se-H peak centred around 4.5 µm, (at 4.55 µm according to Yadav *et al.* [132], see Table 2.3, Section 2.3.3.2) is often very large (typically ~40 dB/m) and broad in undistilled chalcogenide fibres. However, as seen in Figure 6.22, the -Se-H band is well defined in the F125RERC ($Ge_{15}As_{21}Se_{63}Ga_1$ at. % + 500 ppmw Dy foil) spectrum. This is indicative of an effective distillation of the parent host glass, M283RERC ($Ge_{15}As_{21}Se_{63}Ga_1$ at. %), that was distilled for M285RERC and F125RERC ($Ge_{15}As_{21}Se_{63}Ga_1$ at. % + 500 ppmw Dy foil) using the newly designed silica glass distillation rig (Section 3.2.5 and 6.3.1). F125RERC exhibits the lowest optical loss demonstrated to date by the Mid-Infrared Photonics Group for a RE ion

doped fibre at the 4.51 µm -Se-H absorption at 9.65 dB/m; this lowest loss -Se-H band is a significant breakthrough.

In contrast, as seen in Figure 6.22, the 4.5 µm -Se-H vibrational absorption band of the unstructured F126RERC ($Ge_{15}As_{21}Se_{63}Ga_1$ at. % + 250 ppmw $DyCl_3$) was so large and broad that not enough photons were able to get through to the mid-IR detectors (see Section 3.3.6 for detectors used) in the optical circuit and so these data have omitted from the spectrum in Figure 6.22.

In conclusion, even with the open distillation of dysprosium chloride under vacuum, its efficacy as a dopant was hindered by the strong scattering losses in the near-IR (<3 µm wavelength) introduced to the fibre F126RERC ($Ge_{15}As_{21}Se_{63}Ga_1$ at. % + 250 ppmw $DyCl_3$) (see Figure 6.22).

If these scattering inclusions seen in Figure 6.22 for F126RERC ($Ge_{15}As_{21}Se_{63}Ga_1$ at. % + 250 ppmw $DyCl_3$) were a product of nucleation of small selenide based crystals, then this effect could be mitigated by increasing the rate of cooling during the quenching of the bulk glass or through a more rapid fibre drawing process to minimise the time the glass spends above T_g to minimise probability of formation of this type of scattering inclusions. However, if the scattering inclusions were due to Dy^{3+} in the $DyCl_3$ dopant gettering of contamination oxide, followed by precipitation of oxide particulates in the melt which would have remained in the quenched glass, then the oxide formation would have taken place during the glass melting itself and the quench rate will have had little effect on the oxide formation and near-IR scattering loss. In this latter case, the quenching rate could certainly not have been manipulated to eradicate such dysprosium oxide scattering centres.

By comparison, the undistilled 500 ppmw Dy^{3+} foil doped $Ge_{19.4}Sb_{9.7}Se_{67.9}Ga_3$ at. % (F104RERC) reported in Section 4.3.2 (Figure 4.17) measured lowest losses of 3.2 dB/m at 6.63 µm, and like F126RERC ($Ge_{15}As_{21}Se_{63}Ga_1$ at. % + 250 ppmw $DyCl_3$), had such a large [-Se-H] vibrational absorption band that this could not successfully be resolved (Figure 4.18, Section 4.3.2) with the broadband, Globar© blackbody mid-IR source and InSb/MCT detector used in the fibre loss measurement rig described in Section 3.2.9. Although, as stated above, it is not anticipated that the 4.5 µm -Se-H absorption band can be resolved in an undistilled fibre with the fibre loss rig described in Section 3.2.9.

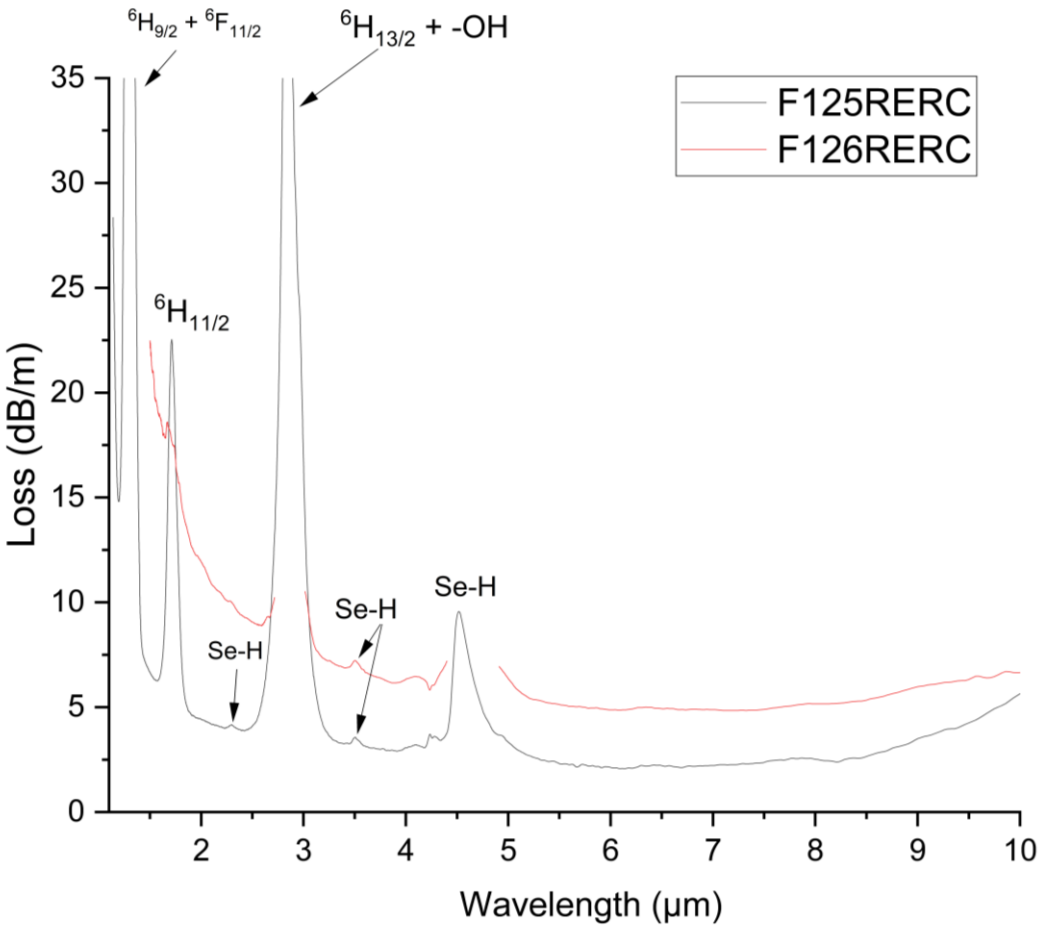


Figure 6.22 Fibre loss spectra of both unstructured fibres F125RERC ($Ge_{15}As_{21}Se_{63}Ga_1$ at. % + 500 ppmw Dy foil) and F126RERC ($Ge_{15}As_{21}Se_{63}Ga_1$ at. % + 250 ppmw $DyCl_3$). Impurity vibrational and rare earth ion electronic absorptions are labelled. Total spectra are composites of both the near-IR and mid-IR optical loss measurements (see Section 3.2.9 for procedure).

The following section details the fabrication of a $Ge_{16.5}As_{16}Se_{61.5}Ga_3S_3$ at. % cladding glass (M284RC, E092RC) that was extruded to a cladding jacket tube. This jacket tube was divided into two and used to make two small-core, step-index fibres using cane of F125RERC ($Ge_{15}As_{21}Se_{63}Ga_1$ at. % + 500 ppmw Dy foil) and F126RERC ($Ge_{15}As_{21}Se_{63}Ga_1$ at. % + 250 ppmw $DyCl_3$) to make F127RERC ($Ge_{15}As_{21}Se_{63}Ga_1$ at. % + 500 ppmw Dy foil core / $Ge_{16.5}$ As_{16} $Se_{61.5}$ Ga_3S_3 at. %) and F128RERC ($Ge_{15}As_{21}Se_{63}Ga_1$ at. % + 250 ppmw distilled $DyCl_3$ core / $Ge_{16.5}$ As_{16} $Se_{61.5}$ Ga_3S_3 at. %), respectively. These two new fibres were investigated *via* SEM.

6.4.2 Fibre drawing and SEM characterisation of distilled small-core step-index fibres: F127RERC ($Ge_{15}As_{21}Se_{63}Ga_1$ at. % + 500 ppmw Dy foil core / $Ge_{16.5}As_{16}Se_{61.5}Ga_3S_3$ at. % cladding) and F128RERC ($Ge_{15}As_{21}Se_{63}Ga_1$ at. % + 250 ppmw distilled $DyCl_3$ core / $Ge_{16.5}As_{16}Se_{61.5}Ga_3S_3$ at. % cladding)

This section will describe the fibre drawing and SEM analysis and imaging characterisation of the distilled core glass, small-core, step-index fibres F127RERC ($Ge_{15}As_{21}Se_{63}Ga_1$ at. % + 500 ppmw Dy foil core / $Ge_{16.5}As_{16}Se_{61.5}Ga_3S_3$ at. % cladding) and F128RERC ($Ge_{15}As_{21}Se_{63}Ga_1$ at. % + 250 ppmw distilled $DyCl_3$ core / $Ge_{16.5}As_{16}Se_{61.5}Ga_3S_3$ at. % cladding).

An undistilled $Ge_{16.5}As_{16}Se_{61.5}Ga_3S_3$ at. % cladding glass (M284RC, E092RC) was extruded to a jacket tube 200 mm in length. This was then divided (*i.e.* scored with a diamond scribe or glass cutter and snapped) into two cladding glass tubes ~ 100 mm each in length. The cladding tubes had a nominal internal diameter (ID) around 1000 µm and a nominal outer diameter (OD) around 10 mm.

The as-annealed rod unstructured preforms of the gettered and distilled M285RERC ($Ge_{15}As_{21}Se_{63}Ga_1$ at. % + 500 ppmw Dy foil) and gettered and distilled M286RERC ($Ge_{15}As_{21}Se_{63}Ga_1$ at. % + 250 ppmw open distilled $DyCl_3$) whose fabrication was described in Section 6.3, were drawn to cane of both F125RERC and F126RERC, respectively. Note that the cane-drawing was done at the same time as the drawing of the unstructured fibres, and from the same preform. The 800 µm diameter cane drawn from each of F125RERC and F126RERC were propylamine etched for around 16 hours, these canes were fully immersed, at room temperature, under dust cover, in ambient atmosphere before being cleaned with isopropanol and dried in the MBraun glovebox antechamber. See Table 3.2 for sources and purities of the chemicals used.

Each 800 µm cane of F125RERC and F126RERC was next fitted separately into one of the two cladding tubes E092RC-(i) and E092RC-(ii) ($Ge_{16.5}As_{16}Se_{61.5}Ga_3S_3$ at. %). Each of these two rod-in-tube preforms was then drawn to each of four nominal target sizes. 100 µm OD/ 10 µm diameter core; 150 µm OD/ 15 µm diameter core; 200 µm OD/ 20 µm diameter core; 300 µm OD/ 30 µm diameter core. Around 67 m in total of small-core, distilled core glass step-index fibre

F127RERC ($Ge_{15}As_{21}Se_{63}Ga_1$ at. % + 500 ppmw Dy foil core / $Ge_{16.5}As_{16}Se_{61.5}Ga_3S_3$ at. %) and 58 m in total of small-core, distilled core glass step-index fibre F128RERC ($Ge_{15}As_{21}Se_{63}Ga_1$ at. % + 250 ppmw open distilled $DyCl_3$ core / $Ge_{16.5}As_{16}Se_{61.5}Ga_3S_3$ at. %) was drawn.

Samples of the nominal 200 µm OD/ 20 µm diameter core fibres of F127RERC and 128RERC were then taken for SEM to image the geometry: core shape and core/clad interface. To achieve the SEM imaging as before, 10 mm fibre sections of F127RERC and F128RERC were cleaved (using the Vytran cleaver, Section 3.3.6), mounted vertically onto an aluminium SEM stub, and coated with a (nominally) 10 nm carbon layer (thickness as calculated by the coater, Q150R ES, QuorumTech) to avoid charging effects inside the electron microscope. A JEOL 6490LV was used to image the fibre faces. Details on sample preparation and equipment used are elaborated on in Section 3.3.3.

The small-core, step-index fibre imaging results are shown in Figure 6.23A. Figure 6.23A is an image taken of F127RERC ($Ge_{15}As_{21}Se_{63}Ga_1$ at. % + 500 ppmw Dy foil core / $Ge_{16.5}As_{16}Se_{61.5}Ga_3S_3$ at. %) using a backscatter detector. From Figure 6.23A, the core is circular, and concentric with the cladding, but the sample studied had two defects, confirmed as holes using a more topography sensitive secondary electron detector (image not presented here), exactly at the interface between the two glasses (black circles at the core boundaries). Figure 6.23B is a backscatter image of F128RERC ($Ge_{15}As_{21}Se_{63}Ga_1$ at. % + 250 ppmw open distilled $DyCl_3$ core / $Ge_{16.5}As_{16}Se_{61.5}Ga_3S_3$ at. %). Again, from Figure 6.23B, the core is circular

and concentric, but no defects, nor potentially gaps or holes were observed at the core/cladding glass interfaces in the all the samples imaged.

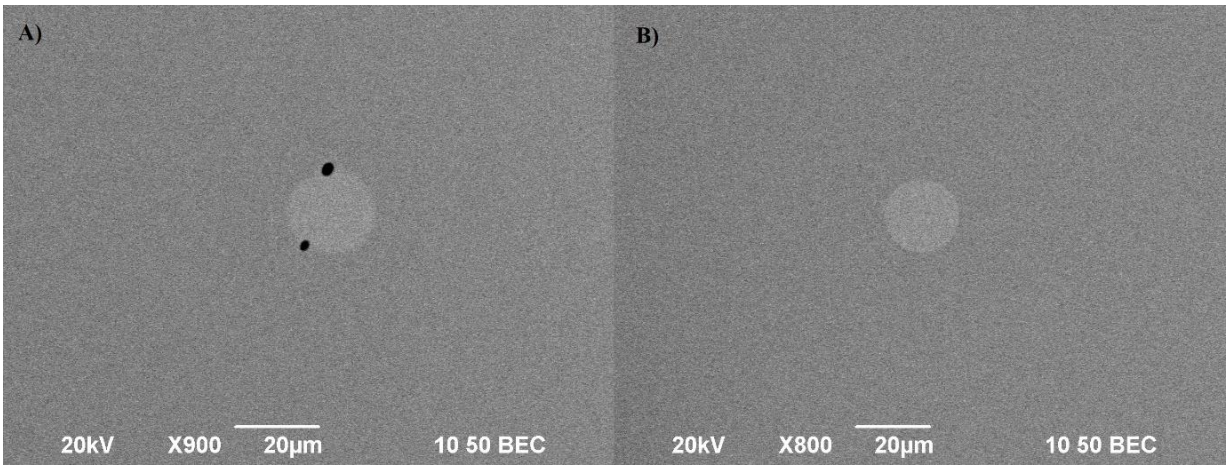


Figure 6.23 Backscatter electron SEM image taken of: A) F127RERC ($Ge_{15}As_{21}Se_{63}Ga_1$ at. % + 500 ppmw Dy foil core / $Ge_{16.5}As_{16}Se_{61.5}Ga_3S_3$ at. % cladding) and B) F128RERC ($Ge_{15}As_{21}Se_{63}Ga_1$ at. % + 250 ppmw open distilled $DyCl_3$ core / $Ge_{16.5}As_{16}Se_{61.5}Ga_3S_3$ at. % cladding). Prior to SEM imaging, the fibres had been coated with a 10 nm carbon layer to avoid charging effects. From these images, both cores were concentric with the cladding and had maintained a circular shape.

The following section, Section 6.4.3, returns to F125RERC ($Ge_{15}As_{21}Se_{63}Ga_1$ at. % + 500 ppmw Dy foil) and its parent preform, M285RERC. This bulk glass and fibre were chosen for characterisation due to its remarkably low optical fibre losses, as described in Section 6.4.1. Bulk sample M285RERC is investigated *via* FtIR to measure Dy^{3+} absorptions then PL and PL lifetime measurements of unstructured fibre, and crushed fibre F125RERC samples are made.

6.4.3 Absorption measurements of M285RERC ($Ge_{15}As_{21}Se_{63}Ga_1$ at. % + 500 ppmw Dy foil) and photoluminescence, and PL lifetime measurements of unstructured F125RERC ($Ge_{15}As_{21}Se_{63}Ga_1$ at. % + 500 ppmw Dy foil)

6.4.3.1 FtiR absorption measurement of bulk M285RERC ($Ge_{15}As_{21}Se_{63}Ga_1$ at. % + 500 ppmw Dy foil)

This section presents the near-IR and mid-IR absorption spectrum of M285RERC ($Ge_{15}As_{21}Se_{63}Ga_1$ at. % + 500 ppmw Dy foil), as measured by FtIR analysis. M285RERC was the parent bulk preform that was subsequently drawn to F125RERC ($Ge_{15}As_{21}Se_{63}Ga_1$ at. % + 500 ppmw Dy foil).

A bulk disc of M285RERC ($Ge_{15}As_{21}Se_{63}Ga_1$ at. % + 500 ppmw Dy foil) of thickness 2.875 mm was polished to a 1 µm finish (see Section 3.3.7). Near- and mid-IR FtIR measurements were taken as described in Section 3.3.7 to a resolution of 4 cm^{-1}. Figure 6.24A shows the measured absorption bands exhibited by the 2.875 mm thick bulk sample, and the vibrational (-Se-H and -OH at 2217 cm^{-1} and 3498 cm^{-1}, respectively) and Dy^{3+} electronic absorptions (all other labelled bands) they are attributed to. Note that the baseline host glass absorptions have been removed. Figure 6.24B shows the electronic energy level diagram for Dy^{3+} plotted (to scale, energy wise) next to the measured data from Figure 6.24A showing the potential for the exhibited spectral absorption bands. The energy levels in Figure 6.24B, plotted using the measured spectrum data in Figure 6.24A, were shown to agree with work by Starecki *et al.*[25] in a 1000 ppmw Dy^{3+} doped $Ga_5Ge_{20}Sb_{10}Se_{65}$ glass (also see Figure 4.17).

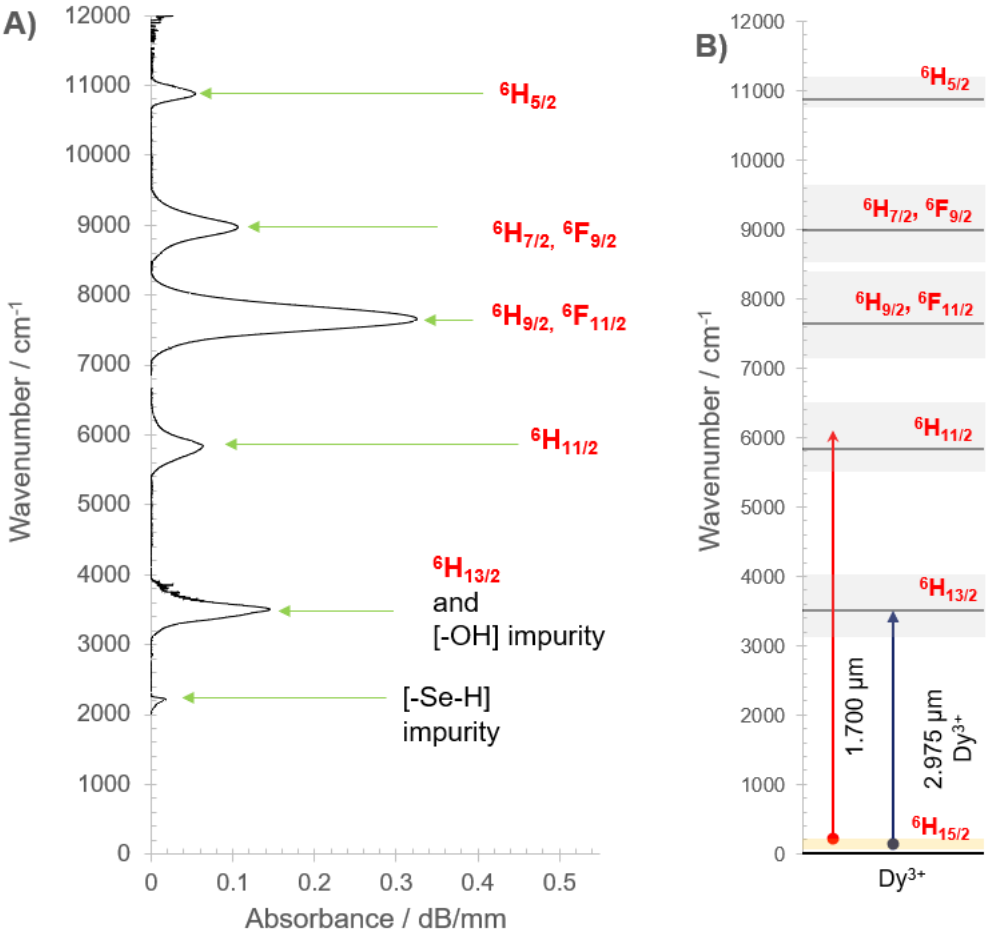


Figure 6.24 A) Measured absorption spectrum from bulk, 2.85 mm thickness polished sample of M285RERC ($Ge_{15}As_{21}Se_{63}Ga_1$ at. % + 500 ppmw Dy foil) with the host glass baseline removed. B) Dy^{3+} energy level diagram plotted to scale energy wise.

6.4.3.2 Photoluminescence (PL) and PL lifetimes of fibre samples of unstructured F125RERC ($Ge_{15}As_{21}Se_{63}Ga_1$ at. % + 500 ppmw Dy foil)

This section presents the PL emission spectrum and PL lifetimes exhibited by unstructured, distilled F125RERC ($Ge_{15}As_{21}Se_{63}Ga_1$ at. % + 500 ppmw Dy foil) in fibre form. F125RER was chosen for characterisation due to its remarkably low optical fibre losses, as described in Section 6.4.1

The 83.34 mm length of unstructured, distilled F125RERC ($Ge_{15}As_{21}Se_{63}Ga_1$ at. % + 500 ppmw Dy foil) of diameter 186 µm was cleaved both ends (using a Vytran cleaver, details in Section 3.3.6) and incorporated into the photoluminescence detection rig shown in Figure 6.25. A fibre coupled 1.7 µm pump source (QPC Lasers Inc., BrightLase®) was collimated and directed to a Black Diamond

($Ge_{28}Sb_{12}Se_{60}$) aspheric lens (390028-E, Thorlabs, f = 5.95 mm) which was used to focus the pump source onto the cleaved input face of the fibre.

The Dy^{3+} output emissions and any unabsorbed pump light from the opposing end face to the input end were modulated with a mechanical chopper (operating at 8 Hz) before being passed through two identical CaF_2 lenses (LA5370, Thorlabs, f = 40 mm) to first collect and then collimate the output, and finally focus the light through a long wave pass (LWP) filter (Northumbria Optical Coatings) and into the monochromator (TMc300, Bentham) for detection on a upon exiting the monochromator. Grating 2 (Figure 6.25) of the monochromator was used in each fibre measurement taken which spans the wavelength range 2.4 – 8.0 µm. Photoluminescent (PL) intensity measurements were then collected using a MCT (mercury-cadmium-telluride) detector (PVI-4TE-6, Vigo Systems).

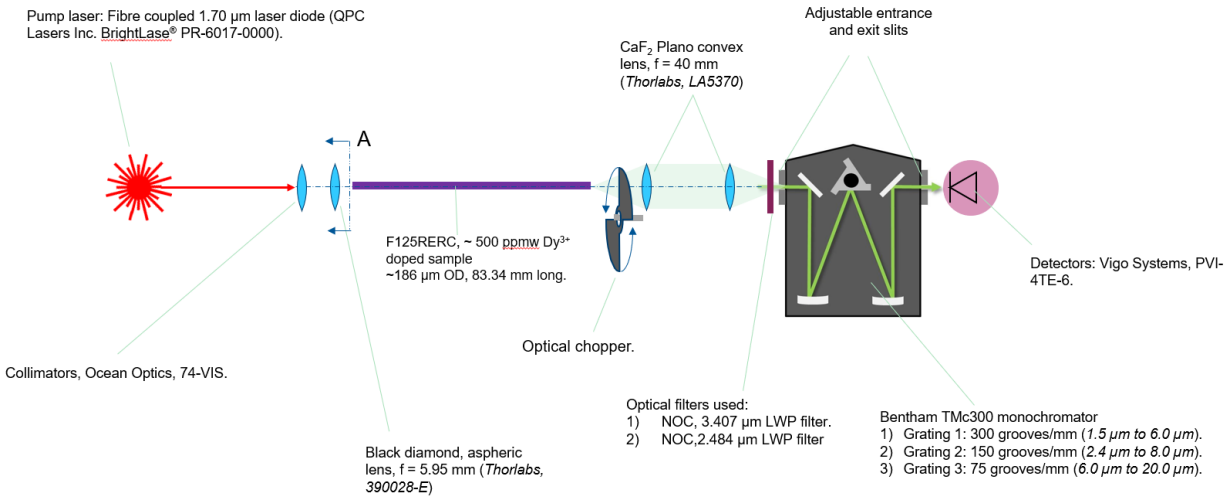


*Figure 6.25 Optical set up used to measure Dy^{3+} photoluminescence emitted at the opposing end face to the launch, pump input face of unstructured fibre F125RERC ($Ge_{15}As_{21}Se_{63}Ga_1$ at. % + 500 ppmw Dy foil). "**A**" denotes the region where pump power measurements were recorded.*

The first PL measurement incorporated a 2.484 µm LWP (long wave pass) preceding the monochromator to investigate the wavelength region of emission between 2.6 - 5.1 µm (Figure 6.27), and to exclude any unabsorbed pump light from entering the monochromator. Figure 6.27 shows measured emission data from unstructured F125RERC fibre sample ($Ge_{15}As_{21}Se_{63}Ga_1$ at. % + 500 ppmw Dy foil)

when pumped at increasing powers at 1.7 µm. The scanning range was 2.6-5.1 µm with a 2.484 µm LWP filter used in circuit (see Figure 6.25). In Figure 6.27A, measured intensity of the two Dy^{3+} radiative transitions at 2.975 µm (Dy^{3+}: $^6H_{13/2} \rightarrow {}^6H_{15/2}$) and 4.375 µm ($Dy^{3+}$: $^6H_{11/2} \rightarrow {}^6H_{13/2}$) with increasing pump powers is shown (Figure 6.26 for Dy^{3+} energy level diagram. In Figure 6.27B, the normalised emission data for the spectra measured with different pump powers indicates that the same PL line shape is exhibited at increasing pump power. In Figure 6.27C, a linear increase of the measured emission intensity of both of the two Dy^{3+} radiative transitions at 2.975 ($^6H_{13/2} \rightarrow {}^6H_{15/2}$) and 4.375 µm ($^6H_{11/2} \rightarrow {}^6H_{13/2}$) with increasing pump power is shown.

From Figure 6.26 and Figure 6.27, the Dy^{3+}: $^6H_{13/2} \rightarrow {}^6H_{15/2}$ emission transition provided photoluminescence over the 2.7 – 3.4 µm region with the peak intensity centred at 2.975 µm. The Dy^{3+}: $^6H_{11/2} \rightarrow {}^6H_{13/2}$ transition provided photoluminescence over the 3.8 – 5.1 µm range with the peak centred around 4.375 µm (Fig. 6.27A). The emission intensities scaled linearly with increasing pump power (Figure 6.27C). As the optical set up was an open tabletop system, absorption of atmospheric CO_2 can be observed at ~4.25 µm. Figure 6.27B shows the normalised PL spectra of the Dy^{3+} dopant ion in fibre F125REC, demonstrating the similarities of emissions between the scans at the pump powers used. That is, by increasing the input 1.7 µm pump power, there are no changes to the emission band profile in the form of band broadening or sharpening, nor are there any blue- or red-shifts of the emission bands.

Comparing the work of Starecki *et al.*[25], in a 1000 ppmw Dy^{3+} doped antimony-based selenide unstructured fibre of composition: $Ge_{20}Sb_{10}Se_{65}Ga_5$, the Dy^{3+}: $^6H_{11/2} \rightarrow {}^6H_{13/2}$ emission transition branching ratio (β), was calculated (using Judd-Ofelt analysis) at 13 % [25]. The subsequent transition from $^6H_{13/2}$ to the ground state: Dy^{3+}: $^6H_{13/2} \rightarrow {}^6H_{15/2}$ emission branching ratio is calculated by Starecki *et al.* [25] as 100 %. Despite the large differences in branching ratio between the Dy^{3+}: $^6H_{11/2} \rightarrow {}^6H_{13/2}$ (β:13 %, 4.375 µm emission) and Dy^{3+}: $^6H_{13/2} \rightarrow {}^6H_{15/2}$ (β: 100 %, 2.975 µm emission), there is a marked discrepancy in emission intensity between the 4.375 µm (4.55 a.u. at 285 mW 1.7 µm pump) and 2.975 µm (0.65 a.u. at 285 mW 1.7 µm pump) emissions. This discrepancy in emission intensity may be a result of the measurements not being corrected for system response. The Dy^{3+}: $^6H_{13/2} \rightarrow {}^6H_{15/2}$

(β: 100 %, 2.975 µm emission) may also be affected by the -OH impurity absorption at 2.9 µm (see Table 2.3 [132]) and ground state Dy^{3+}: $^{+}$: $^{6}H_{13/2} \rightarrow {}^{6}H_{15/2}$ reabsorption of the emitted 2.975 µm light (see also Figure 6.26).

.

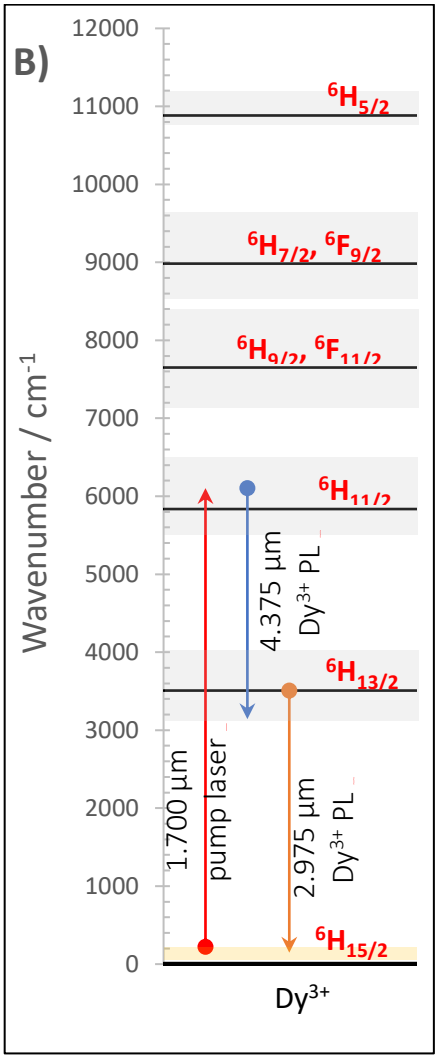


Figure 6.26 Electronic energy level diagram for Dy^{3+} showing measured PL emissions from Dy^{3+} doped unstructured F125RERC ($Ge_{15}As_{21}Se_{63}Ga_1$ at. % + 500 ppmw Dy foil) (see Figure 6.27) when optically energised using a 1.7 µm wavelength pump laser.

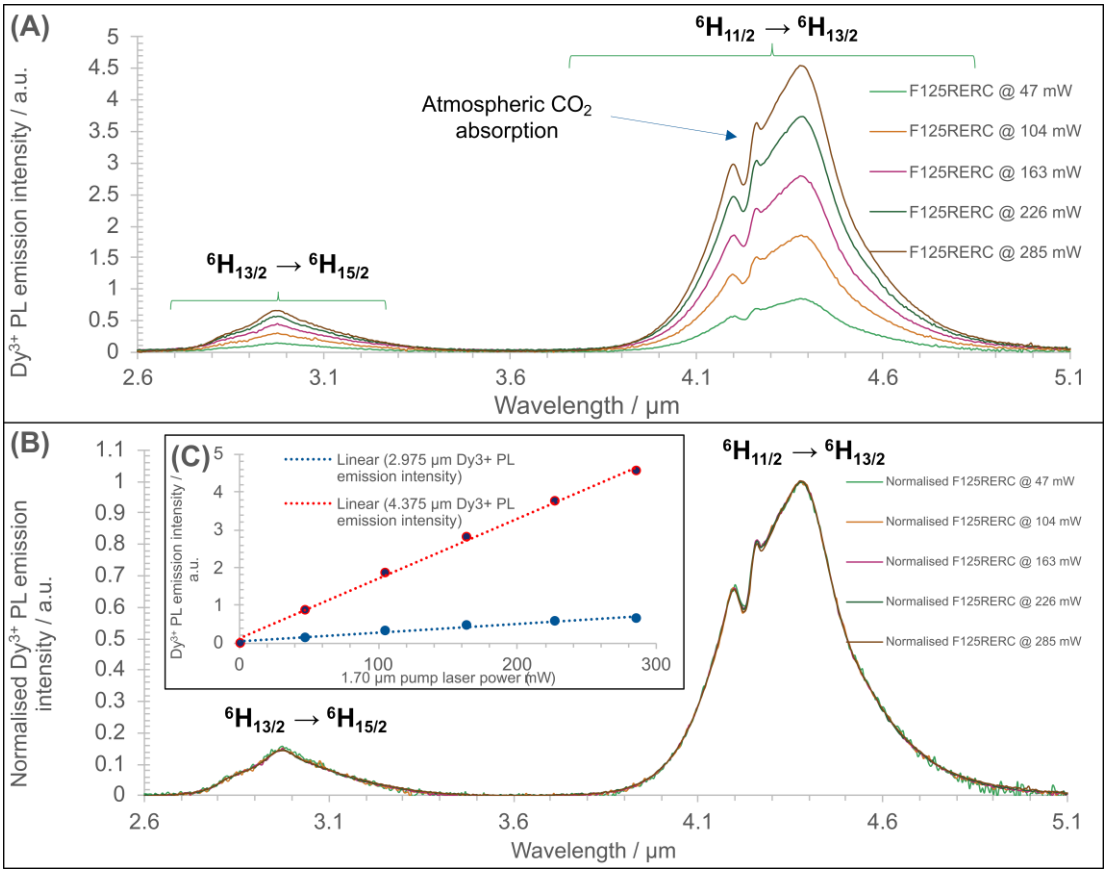


Figure 6.27. Measured emission data from unstructured F125RERC fibre sample ($Ge_{15}As_{21}Se_{63}Ga_1$ at. % + 500 ppmw Dy foil) when pumped at increasing powers at 1.7 μm. Scan range was 2.6-5.1 μm with a 2.484 μm LWP filter used in circuit (see Figure 6.25). (A) Measured intensity of the two Dy^{3+} radiative transitions at 2.975 μm (Dy^{3+}: $^6H_{13/2} \rightarrow {}^6H_{15/2}$) and 4.375 μm ($Dy^{3+}$: $^6H_{11/2} \rightarrow {}^6H_{13/2}$) with increasing pump powers (Figure 6.26 for Dy^{3+} energy level diagram. (B) Normalised emission data for the spectra measured with different pump powers showing that the same PL line shape is exhibited at increasing pump power. (C) Linear increase of the measured emission intensity of both of the two Dy^{3+} radiative transitions at 2.975 ($^6H_{13/2} \rightarrow {}^6H_{15/2}$) and 4.375 μm ($^6H_{11/2} \rightarrow {}^6H_{13/2}$) with increasing pump power.

For the next experiment, the 1.7 μm pump laser was retained, but the 2.484 LWP filter was replaced with a 3.407 μm LWP and scanning ranges were altered to 3.6 – 6.0 μm. Again, the same 83.34 mm length of distilled, unstructured F125RERC ($Ge_{15}As_{21}Se_{63}Ga_1$ at. % + 500 ppmw Dy foil) of diameter 186 μm (cleaved both ends with a Vytran cleaver (see Section 3.3.6)) sample was kept in the optical rig.

Figure 6.28A shows the measured emissions when pumped with 47 mW and 104 mW of CW at 1.7 μm wavelength into the $^6H_{15/2} \rightarrow {}^6H_{11/2}$ ground state absorption band of Dy^{3+}. Again, the $^6H_{11/2} \rightarrow {}^6H_{13/2}$ transition emitted over the 3.8 – 5.0 μm range with the peak centred around 4.375 μm. As anticipated from the M285RERC

($Ge_{15}As_{21}Se_{63}Ga_1$ at. % + 500 ppmw Dy foil) FtIR absorption work (Section 6.4.3.1), the Dy^{3+} energy level diagram (Figure 6.26), and the previous results shown in Figure 6.27, no emissions were observed beyond 5 µm. Figure 6.27B (inset) shows the normalised peaks overlaid, proving the line-shape remained constant with increasing pump power up to 104 mW.

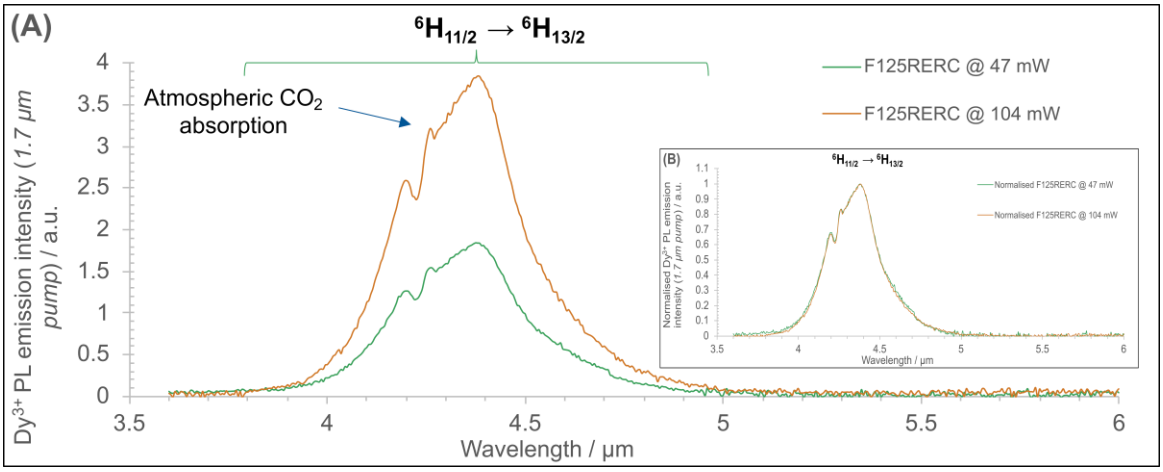


Figure 6.28 Measured emission data from unstructured fibre F125RERC ($Ge_{15}As_{21}Se_{63}Ga_1$ at. % + 500 ppmw Dy foil) when pumped at 47 mW and 104 mW at 1.7 µm wavelength CW. The scan range of the monochromator grating was 3.6-6 µm and a 3.407 µm LWP filter was used (see Figure 6.25). (A) Measured intensity of the Dy^{3+}: $^6H_{11/2} \rightarrow {}^6H_{13/2}$ transition at two pump powers, 47 mW and 104 mW. (B) Normalised emission data at both pump powers: 47 mW and 104 mW.

While retaining the same 83.34 mm length of distilled, unstructured F125RERC ($Ge_{15}As_{21}Se_{63}Ga_1$ at. % + 500 ppmw Dy foil) of diameter 186 µm (cleaved both ends with a Vytran cleaver (see Section 3.3.6)) sample in the optical rig, the 3.407 µm LWP was exchanged back for the 2.484 µm LWP filter.

The detector was then connected to an oscilloscope (PicoTech) and the mechanical chopper was set to RMS (Root Mean Square) modulate the Dy^{3+} emissions at 8 Hz. and the samples were pumped with 276 mW at 1.7 µm wavelength. The Dy^{3+}: $^6H_{13/2} \rightarrow {}^6H_{15/2}$ radiative emission of 2.98 µm (see Figure 6.26) was best fitted to a single exponential decay of a radiative lifetime: τ_{rad} = 5.21 ms (Figure 6.29A). The Dy^{3+}: $^6H_{11/2} \rightarrow {}^6H_{13/2}$ emission of 4.399 µm (Figure 6.26) was also fitted to single exponential decay with a τ_{rad} = 1.75 ms (Figure 6.29B). Both lifetimes were longer than those measured in by Starecki et al. [25] in a 1000 ppmw Dy^{3+} doped $Ge_{20}Sb_{10}Se_{65}Ga_5$ fibre sample with Dy^{3+}: $^6H_{13/2} \rightarrow {}^6H_{15/2}$, τ_{rad} = 3.3 ms, Dy^{3+}: $^6H_{11/2} \rightarrow {}^6H_{13/2}$, τ_{rad} = 1.46 ms compared to 5.21 ms and 1.75 ms measured by the current

Author. It is suggested that the increased Dy^{3+} PL lifetimes in fibre F125RERC ($Ge_{15}As_{21}Se_{63}Ga_1$ at. % + 500 ppmw Dy foil) samples are a result of the distilled F125RERC having fewer oxide and hydride impurities than the glass reported on by Starecki *et al.* [25] resulting in a lower overall phonon energy host glass system.

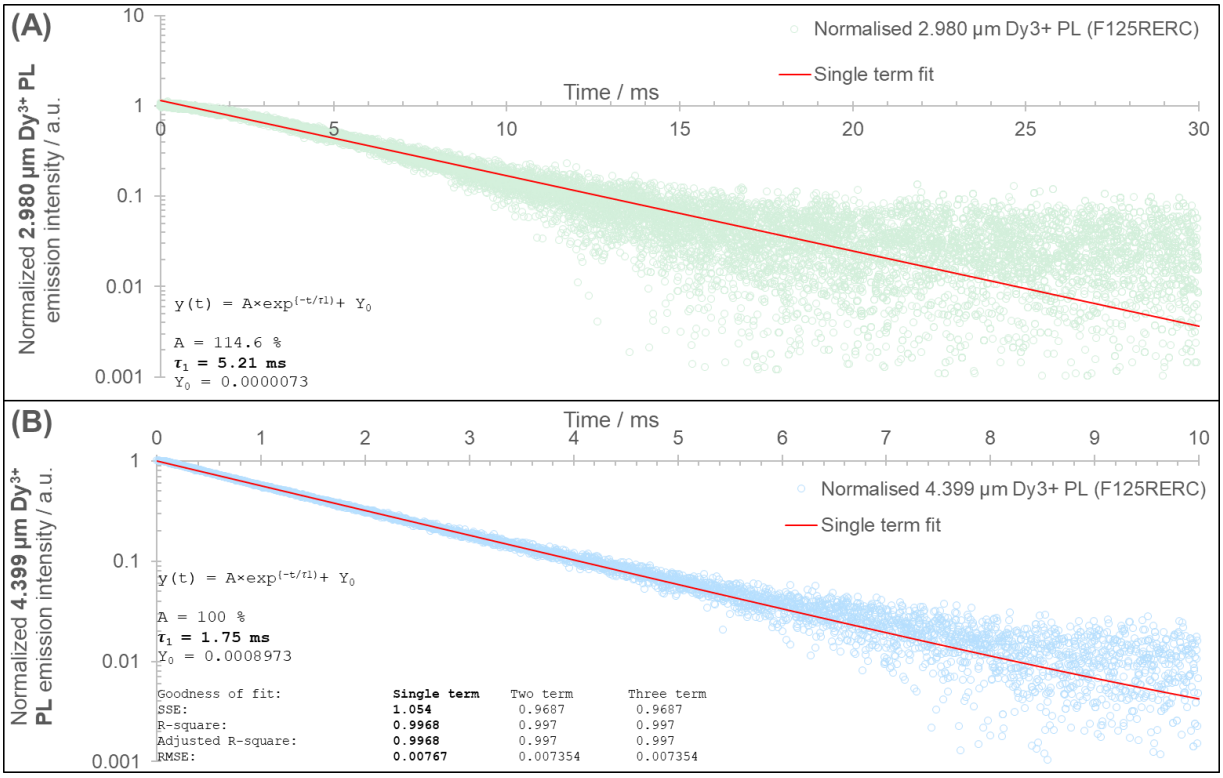


Figure 6.29 Photoluminescent lifetimes of Dy^{3+} emissions emitted from unstructured fibre F125RERC ($Ge_{15}As_{21}Se_{63}Ga_1$ at. % + 500 ppmw Dy foil) (A) Dy^{3+}: $^6H_{13/2} \rightarrow {}^6H_{15/2}$ at 2.980 µm and (B) Dy^{3+}: $^6H_{11/2} \rightarrow {}^6H_{13/2}$ at 4.399 µm. 276 mW CW pump power at 1.7 µm wavelength was used throughout.

6.4.3.3 Photoluminescence (PL) and PL lifetimes of powdered samples of unstructured F125RERC ($Ge_{15}As_{21}Se_{63}Ga_1$ at. % + 500 ppmw Dy foil)

This section presents the PL emission spectrum and PL lifetimes exhibited by a powdered sample of unstructured, distilled F125RERC ($Ge_{15}As_{21}Se_{63}Ga_1$ at. % + 500 ppmw Dy foil). Two CaF_2 windows were used to sandwich the powder sample into a sample holder which was then inserted into the optical rig. The aim of this powdered fibre holder was to potentially reduce the effects of reabsorption along the sample length when measuring photoluminescence and lifetimes.

The F125RERC fibre sample was removed from the optical pathlength and replaced, in a similar position in the optical pathlength, with a powder sample holder; the rest of the optical rig remained as described above in Section 6.4.3.2 and Figure 6.25, as seen in Figure 6.30. The holder sealed together two CaF_2 windows with chalcogenide granules (129 ± 47 µm) sandwiched between. This chalcogenide powder was ground in the dry nitrogen environment of the MBraun glovebox (<0.1 ppm H_2O and < 0.1 ppm O_2) to minimise the formation of oxide layers on the granules. The powder sample holder also facilitated the use higher pump powers (532 – 1330 mW in powder versus 47-104 mW in fibre (see Section 6.4.3.2) without incurring damage to the sample.

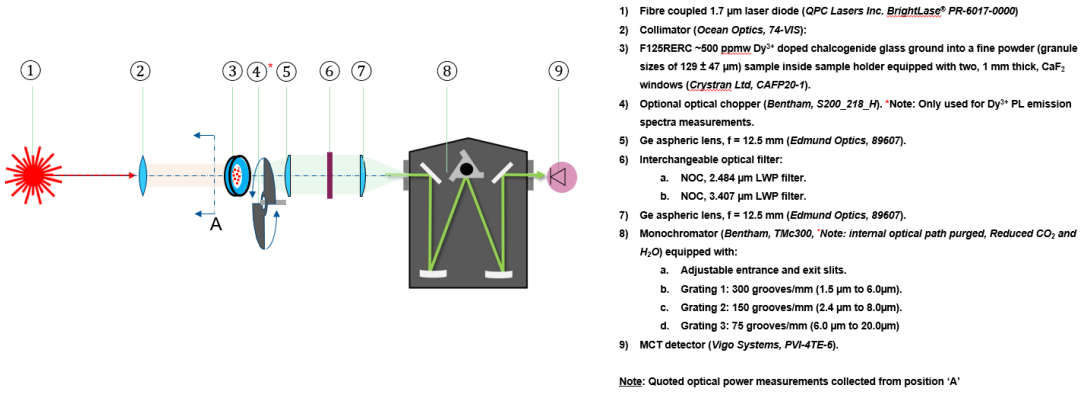


Figure 6.30 Optical set up used to measure Dy^{3+} photoluminescence emitted from the opposing CaF_2 window of a sample holder containing a powdered sample of unstructured fibre F125RERC ($Ge_{15}As_{21}Se_{63}Ga_1$ at. % + 500 ppmw Dy foil).

The first measurement with the powdered F125RERC ($Ge_{15}As_{21}Se_{63}Ga_1$ at. % + 500 ppmw Dy foil) holder used the 2.484 µm LWP and scans were conducted across the 2.6 - 5.1 µm region (Figure 6.31). The Dy^{3+}: $^6H_{13/2} \rightarrow {}^6H_{15/2}$ transition provided photoluminescence over the 2.7 – 3.4 µm region with the peak intensity centred at 2.975 µm. The Dy^{3+}: $^6H_{11/2} \rightarrow {}^6H_{13/2}$ transition provided photoluminescence over the 3.8 – 5.1 µm range with the peak centred around 4.375 µm (Figure 6.31A). Again, as observed in the F125RERC unstructured fibre samples (Figure 6.27A), the emission intensity scaled roughly linearly with increasing 1.7 µm pump power. Figure 6.31B shows the normalised spectra measured at different pump powers showing the line shape remained consistent

between 525 mW and 1330 mW of 1.7 µm wavelength pump power. This was also seen with the unstructured fibre F125RERC sample in Figure 6.27B.

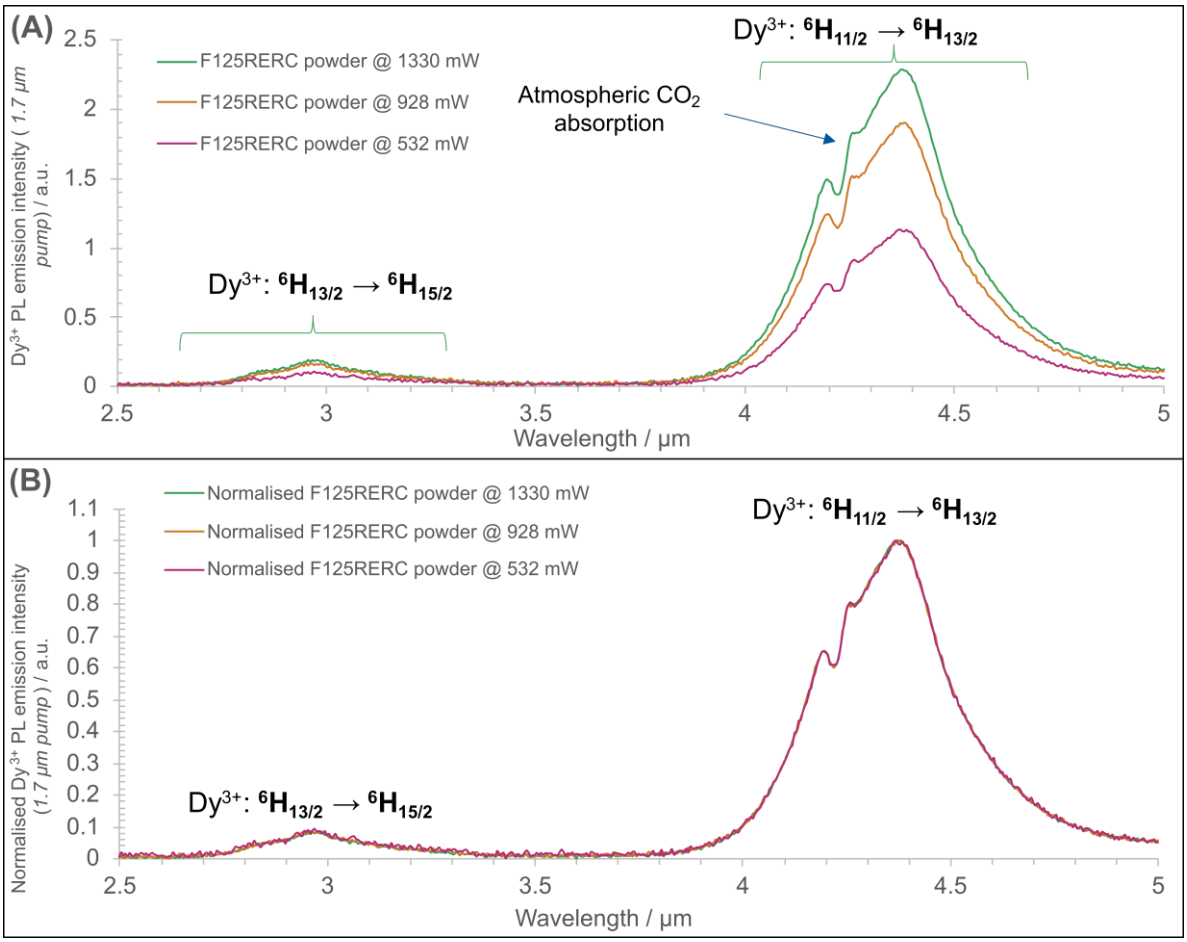


Figure 6.31 Measured emission data from powdered samples of F125RERC ($Ge_{15}As_{21}Se_{63}Ga_1$ at. % + 500 ppmw Dy foil) when pumped at increasing powers at 1.7 µm wavelength CW. The scan range of the monochromator was 2.5-5 µm and a 2.484 µm LWP filter was used (Figure 6.30 for optical set up). (A) Measured intensity of the Dy^{3+} radiative transitions centred at 2.975 (Dy^{3+}: $^6H_{13/2} \rightarrow {}^6H_{15/2}$) and 4.375 µm ($Dy^{3+}$: $^6H_{11/2} \rightarrow {}^6H_{13/2}$). (B) Normalised emission data for the spectra measured with different pump powers showing the same line shape is exhibited at increasing pump powers.

The 2.484 LWP filter was then replaced with a 3.407 µm LWP but scanning ranges were altered to 3.6 – 6.5 µm. Figure 6.32A shows the measured emissions when pumped with increasing powers of 1.7 µm CW from 532 mW to 1330 mW. The Dy^{3+}:$^6H_{11/2} \rightarrow {}^6H_{13/2}$ transition emitted over the 3.8 – 5.1 µm range with the peak centred around 4.375 µm. As before, from the Dy^{3+} energy level diagram (Figure 6.26), and the previous results shown in Figure 6.27, no emissions were anticipated to be observed beyond 5 µm. However, the monochromator scan was set to go to

6.5 µm. This scan was extended to this 6.5 µm range purely to investigate if anything, at all, could be detected (*i.e*, perhaps an unreported reabsorption and subsequent emission). Due to the increased pump powers used for the powder sample compared to the fibre sample, (up to 1330 mW) blackbody radiation was observed >5 µm, labelled in Figure 6.32A. Figure 6.32B shows the normalised peaks overlaid, again showing the same line shape is exhibited at increasing pump powers.

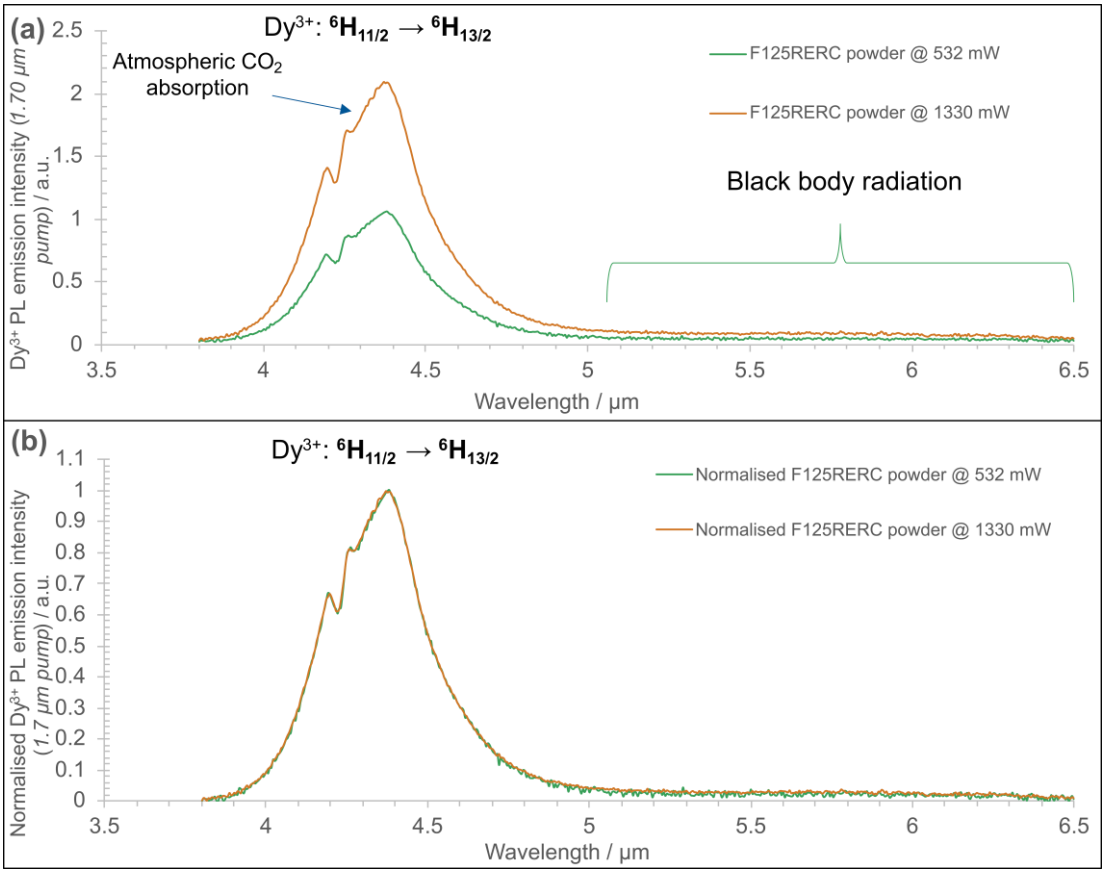


Figure 6.32 Measured emission data from powdered fibre F125RERC ($Ge_{15}As_{21}Se_{63}Ga_1$ at. % + 500 ppmw Dy foil) when pumped at 532 mW and 1330 mW at 1.7 µm wavelength CW. The scan range of the monochromator grating was 3.8-6.5 µm and a 3.407 µm LWP filter was used (see Figure 6.30). (A) Measured intensity of the Dy^{3+}: $^6H_{11/2} \rightarrow {}^6H_{13/2}$ transition at two pump powers, 532 mW and 1330 mW. (B) Normalised emission data at both pump powers: 532 mW and 1330 mW.

The detector was again connected to an oscilloscope (PicoTech), the mechanical chopper set to RMS modulate at 8 Hz, and the 3.407 µm LWP was exchanged for

the 2.484 µm LWP. The samples were pumped with 1330 mW at 1.7 µm wavelength and lifetime measurements were taken. Figure 6.33 A and B show the Dy^{3+}: $^6H_{13/2} \rightarrow {}^6H_{15/2}$ transition fitted to single exponential decay of radiative lifetime: $\tau_{rad} \approx 5.15$ and 5.12 ms at 2.855 and 2.955 µm respectively. Figure 6.33 C, D, and E show the Dy^{3+}: $^6H_{11/2} \rightarrow {}^6H_{13/2}$ transition fitted to single exponential decay with $\tau_{rad} \approx 1.67$ ms at 4.12 µm, 1.71 ms at 4.375 µm, and 1.78 ms at 4.76 µm. These values agree with the fibre sample measurements taken in Section 6.4.3.2 from F125RERC fibre samples of lifetimes: $^6H_{13/2} \rightarrow {}^6H_{15/2}$, τ_{rad} = 5.21 ms. $^6H_{11/2} \rightarrow {}^6H_{13/2}$, τ_{rad} = 1.75 ms). The F125RERC powdered sample lifetimes remained longer, as explained in Section 6.4.3.2, than those reported in similar Dy^{3+} doped chalcogenide glasses in literature from Starecki *et at.* in 1000 ppmw Dy^{3+} doped $Ge_{20}Sb_{10}Se_{65}Ga_5$ fibre samples ($^6H_{13/2} \rightarrow {}^6H_{15/2}$, τ_{rad} = 3.3 ms. $^6H_{11/2} \rightarrow {}^6H_{13/2}$, τ_{rad} = 1.46 ms)) [25].

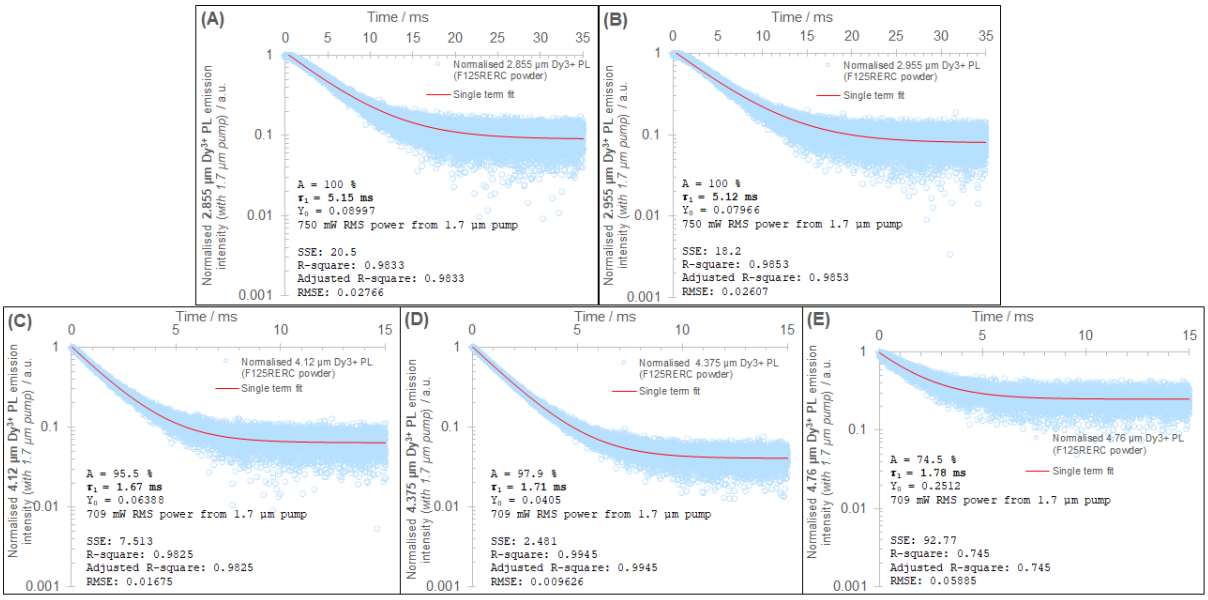


Figure 6.33 Photoluminescent lifetimes of Dy^{3+} emissions emitted from powdered fibre F125RERC ($Ge_{15}As_{21}Se_{63}Ga_1$ at. % + 500 ppmw Dy foil) (A) Dy^{3+}: $^6H_{13/2} \rightarrow {}^6H_{15/2}$ at 2.855 µm, (B) Dy^{3+}: $^6H_{13/2} \rightarrow {}^6H_{15/2}$ at 2.955 µm. (C) Dy^{3+}: $^6H_{11/2} \rightarrow {}^6H_{13/2}$ at 4.12 µm (D) Dy^{3+}: $^6H_{11/2} \rightarrow {}^6H_{13/2}$ at 4.375 µm, and (E) Dy^{3+}: $^6H_{11/2} \rightarrow {}^6H_{13/2}$ at 4.76 µm. 1330 mW CW pump power at 1.7 µm wavelength was used throughout.

6.5 Summary of chapter 6

Chapter 6 detailed the fabrication and characterisation of an antimony-based, dysprosium doped, small core, step-index fibre (F129RERC ($Ge_{19.4}Sb_{9.7}Se_{67.9}Ga_3$ at. % + 500 ppmw Dy foil core / $Ge_{21}Sb_{10}Se_{69}$ at. % cladding)). A cerium doped arsenic-based core glass was rod-in-tube fibre drawn to a small core fibre with an antimony-based cladding glass (F130RERC, $Ge_{15}As_{21}Se_{63}Ga_1$ at. % + 500 ppmw Ce^{3+} doped core / $Ge_{21}Sb_{10}Se_{69}$ at. % cladding). F130RERC was one of the first instances of mid-IR lasing in chalcogenide fibre. A silica ampoule-based method of distilling dysprosium chloride was designed and successful. An arsenic-based glass was distilled in the presence of getters and divided into two. One sample was doped with dysprosium foil (M285RERC ($Ge_{15}As_{21}Se_{63}Ga_1$ at. % + 500 ppmw Dy foil) and the second was doped with this distilled dysprosium chloride ($Ge_{15}As_{21}Se_{63}Ga_1$ at. % + 250 ppmw $DyCl_3$). These were then successfully drawn to unstructured fibre (F125RERC: $Ge_{15}As_{21}Se_{63}Ga_1$ at. % + 500 ppmw Dy foil, and F126RERC: $Ge_{15}As_{21}Se_{63}Ga_1$ at. % + 250 ppmw $DyCl_3$) and cane. These canes were then drawn to two separate small core, step-index fibres: F127RERC ($Ge_{15}As_{21}Se_{63}Ga_1$ at. % + 500 ppmw Dy foil core / $Ge_{16.5}As_{16}Se_{61.5}Ga_3S_3$ at. % cladding) and F128RERC ($Ge_{15}As_{21}Se_{63}Ga_1$ at. % + 250 ppmw distilled $DyCl_3$ core / $Ge_{16.5}As_{16}Se_{61.5}Ga_3S_3$ at. % cladding).

- F129RERC ($Ge_{19.4}Sb_{9.7}Se_{67.9}Ga_3$ at. % + 500 ppmw Dy foil/ $Ge_{21}Sb_{10}Se_{69}$ at. %) was successfully fibre drawn to (to the current Author's knowledge) the first rare earth doped, small-core, step-index antimony-based fibre.

- F130RERC ($Ge_{15}As_{21}Se_{63}Ga_1$ at. % + 500 ppmw Ce^{3+} doped core / $Ge_{21}Sb_{10}Se_{69}$ at. % cladding), a hybrid of an arsenic-based core and antimony-based cladding was successfully fibre drawn.

- F130RERC ($Ge_{15}As_{21}Se_{63}Ga_1$ at. % + 500 ppmw Ce^{3+} doped core / $Ge_{21}Sb_{10}Se_{69}$ at. % cladding), (NA ~0.47) exhibited mid-IR fibre lasing at 5.13 µm, 5.17 µm and 5.28 µm when pumped at 4.15 µm. One of the first recorded instances of rare earth ion doped chalcogenide mid-IR fibre lasing.

- F130RERC ($Ge_{15}As_{21}Se_{63}Ga_1$ at. % + 500 ppmw Ce^{3+} doped core / $Ge_{21}Sb_{10}Se_{69}$ at. % cladding) fibre lasing tended towards increased output power at 5.13 µm with increased input power. This was to the detriment of lasing output power at 5.17 µm and 5.28 µm.

- These lasing wavelengths have no biological significance.

- Anhydrous $DyCl_3$ powder was distilled between 800-870 °C in a GE214A silica ampoule that was modified *via* hot working to form a bend. The resultant crystalline appearing distillate was measured have lower Al, Yb, and Zn impurities than undistilled $DyCl_3$ was batched into a distilled $Ge_{15}As_{21}Se_{63}Ga_1$ at. % host glass (M286RERC, F126RERC).

- A $Ge_{15}As_{21}Se_{63}Ga_1$ at. % host glass was distilled in the presence of Al (oxygen getter) and $TeCl_4$ (hydrogen getter). This distillate was divided into two and batched with 250 ppmw distilled $DyCl_3$ in one portion (M286RERC, F126RERC), and 500 ppmw of mechanically exfoliated (using germanium) dysprosium foil (M285RERC, F125RERC) in the other.

- F125RERC ($Ge_{15}As_{21}Se_{63}Ga_1$ at. % + 500 ppmw Dy foil) and F126RERC ($Ge_{15}As_{21}Se_{63}Ga_1$ at. % + 250 ppmw $DyCl_3$) were then drawn to small core, step-index fibres (F127RERC and F128RERC, respectively, see above summary for compositions) and characterised *via* SEM.

- Dysprosium (III) photoluminescent emissions and lifetimes at 3.0 µm (τ_{rad} = 5.21 ms) and 4.399 (τ_{rad} = 1.75 ms) in F125RERC were recorded in fibre samples. These lifetimes are longer than those previously measured in Dy^{3+} doped glasses (Starecki *et al.* [25]) which the current Author suggests is related to the high purity of the distilled F125RERC ($Ge_{15}As_{21}Se_{63}Ga_1$ at. % + 500 ppmw Dy foil).

7. Antireflective moth eye nanoimprinting on chalcogenide bulk glasses fibre end faces.

Throughout the work detailed in this thesis, and across available literature, optical experiments using chalcogenide glasses are primarily conducted with free space optics. The high refractive index of the chalcogenide glasses versus air leads to significant losses due to Fresnel reflection (Equation 7.1 and 7.2). For a fibre with a refractive index of 2.4, at 2 μm wavelength, up to 17% of light can be lost at each interface[219]. Commonly used methods to reduce end-face reflection involve coating fibre ends with thin films of materials that have a refractive index of that between air and the fibre[220]. These can be further designed to exploit thin film interference to constructively interfere incoming light at specific wavelengths, thus improving transmission. However, the chemical and thermal properties of chalcogenide glass fibres do not lend themselves well to thin film coating processes as there are few optically compatible materials that can be used at the lower processing temperatures chalcogenide requires. Thin films that have been successfully deposited have proven to have poor laser damage threshold, making them practically unsuitable[221,222]. Lord Rayleigh proposed that an object with a continuously changing refractive index from air to the bulk i.e., going from 100% porosity to 0% porosity (similar to the 50:50 surface roughness function for ellipsometry modelling, described in Section 5.3.2.2) will demonstrate no reflection [223].

$$r_s = \frac{n_1 \cos\theta_1 - n_2 \cos\theta_2}{n_1 \cos\theta_1 + n_2 \cos\theta_2} \qquad \text{Equation 7.1}$$

$$r_p = \frac{n_1 \cos\theta_2 - n_2 \cos\theta_1}{n_1 \cos\theta_2 + n_2 \cos\theta_1} \qquad \text{Equation 7.2}$$

r_s = reflection for -S polarized light r_p = reflection for -P polarized light.

n_1 and n_2 = refractive index of the two substrates. θ_1 and θ_2 = propagation angles from normal.

Antireflecting (AR) topological nano- and micro-structures that can be imprinted on the chalcogenide glass fibre end face, usually through a hot embossing technique, have been developed and characterised by several research groups[221,224,225]. The hot embossing process involves taking the chalcogenide glass above its T_g, at which point the material can be considered a highly viscous supercooled liquid (see Section 2.2.2, Figure 2.6 for further details). This viscous supercooled liquid is

then pressed into the nano- or micro-structure mould to confer its shape to the glass surface. The glass is then removed from the mould and cooled back below T_g, at this point the glass is again considered a solid, but the mould pattern is now "frozen in" to the glass surface. The design of the in-house made hot embossing/pressing rig used at the Mid-Infrared Photonics Group, University of Nottingham, UK, is developed throughout Sections 7.1- 7.3.

These aim to replicate the gradual change in refractive index from air to the fibre end face as proposed by Lord Rayleigh[223]. These periodic antireflective microstructures, also named "moth eye", patterns were extensively modelled using various methods such as EMT (effective medium theory), FEM (finite element method), RCWA (rigorous coupled wave analysis), and FDTD (Finite-difference time-domain) to determine the patterns that provided optimal increases in transmission over a broadband wavelength range[224,225]. These "moth eye" AR patterns have been named as such, due to their structural biomimicry of the antireflective structures, present on the corneal surface of the order of insects, Lepidoptera (butterflies and moths)[226].

These AR patterns have been modelled using a variety of shapes such as sinusoidal, ellipsoidal, pyramidal, truncated cones, and conical. These shapes may either protrude from the surface of the fibre face (termed: positive feature) or may be imprinted into the surface of the fibre face (termed: negative feature). The periodic spacing between these features as well as the feature heights determine the wavelength range and peak wavelength at which these patterns confer an AR surface. Current literature on these moth eye structures, covering both modelling studies and optical measurements of hot embossed chalcogenide glasses for near- and mid-IR AR is discussed as follows.

Weiblen *et al.* concluded that a repeating, hexagonally packed, negative, half ellipsoid structure performed best in the model but may be difficult to transfer to a fibre tip [224]. Lotz *et al.* [225] modelled a similar hexagonally packed, ellipsoid structure but truncated the tip of each individual protrusion (Figure 7.1). Contrary to the comments regarding structure shape in Weiblen *et al.*[224], this aimed to recreate the type of structure that commonly resulted from their pressing experiments[225]. Simulations from Petersen *et al.* [227] have shown that this truncation

of structure tip seen during production leads to a reduced efficacy of the antireflection properties, blue shifts the wavelength at which peak Δ increase in transmission occurs and decreases the broadband range at which transmission is increased[227].

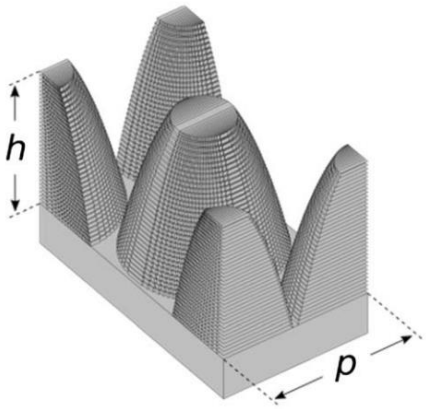


Figure 7.1 RCWA model showing the truncated ellipsoidal structure modelled in Lotz et al. "h" denotes height of the structure. "p" denotes pitch. [225].

The height and width of the individual features as well as the pitch between them were also varied during optimization. By varying these values, the wavelength which undergoes peak increase in transmission can be controlled. By increasing the height and pitch, the wavelength range which undergoes increase in transmission is increased to become more broadband [225].

Sanghera *et al.* [219] proposed that to reduce reflection losses, the height of the features should be greater than λ/2 and to reduce diffraction effects, the pitch should be λ/2n. "n" being the refractive index of the material [219]. However, no experimental or modelled data in literature has been shown to follow either rule.

As seen in Lotz *et al.*, a pitch of 900 nm and a height of 815 nm led to a peak increase in transmission of 12% at 3.3 µm with a +11% Δ in transmission across 2.8-4.1 µm. By increasing pitch to 1200 nm and height to 1550 nm, peak +Δ in transmission was shifted to 7.8 µm with +12% Δ over 6.8-8.7 µm [225].

Weiblen *et al.* using RCWA found that, over a 2-5 µm wavelength range, increasing feature height led to increased transmission but increasing pitch size decreased transmission [224]. Changing the feature tip width, feature base width, and periodicity, provided the biggest changes to transmission between 1-5 µm with patterns with narrow tips, wide bases, and large heights providing optimal

transmission [224]. Experimental results have shown agreement with Weiblen in which increased feature depth led to a more broadband antireflection [228]. This is likely due to structures of this morphology providing a more gradual gradient of refractive index between air and the sample. This agrees with effective medium theory (EMT) in which the effective refractive index for subwavelength surface features at a particular cross section is dependent on the ratio of each medium present [229].

Another factor in mould design is whether the pattern imprinted is either positive or negative. A positive mould consists of a surface with protrusions coming out of the flat surface, this embosses holes or wells into the fibre face. A negative mould has the wells going from the surface and into the bulk of the mould. In this case, the heated glass flows into the individual wells to form the antireflection pattern. Sanghera *et al.* [219] compared the effects of two similar sized positive and negative moulds on As_2S_3 glass. A positive mould (pitch 800 nm, height 900-1000 nm) was measured to have a maximum transmission of 94.5% [219]. A negative mould (pitch 800 nm, height 800 nm) was measured to have a maximum transmission of 97.5% [219]. Comparatively, the unmodified control face had a maximum transmission of 83% [219].

Other work has also found that optimal mould topography is based on the feature shape. Half ellipsoids were found to be most effective with a negative fibre pattern (imparted with a positive mould) whereas pyramidal shapes in a positive fibre pattern (negative mould) were modelled to have the best increase in transmission [224].

With the chalcogenide glasses detailed in this thesis having documented high refractive index values (>2.5) (Section 5.3.2.2) and higher pump powers correlating to higher output chalcogenide lasing powers (Section 6.2.3.3), the prospect of reducing Fresnel reflection with embossed moth eye structures was attractive. The work detailed in this chapter is the result of multiple MSc and M.Eng student projects in which a supervisory role was played by the current Author, as well as conducting further experimentation independently. Section 7.1 details the modelling of a near-IR moth eye pattern designed for 1.5 µm and bulk glass embossing of this initial moth eye design. Section 7.2 details initial

experimentation of pressing the moth eye design into chalcogenide glass fibre faces. Section 7.3 details the optimization of the fibre moth eye rig to include an automated feedback-controlled system monitoring temperature and force distributed on the fibre tip.

7.1 Antireflective patterning for 1.5 μm and bulk sample embossing.

The aim of this initial work was to develop an antireflective topological patterning for making a mould to achieve antireflection in the end of chalcogenide selenide-based glass optical fibres. Initially the wavelength of anti-reflection was selected to be 1.5 μm in order to ensure efficient 1.5 μm pump laser delivery into a chalcogenide glass fibre containing a Bragg-grating defined rare earth ion doped cavity for long wavelength mid-infrared fibre lasing.

The following is an overview of the research reported in the following sub-sections of Section 7.1. This initial work was conducted with the help of MSc student Sam Shea. FDTD (finite-difference time-domain) modelling was employed by him to calculate the anti-reflectance values for various feature morphologies as pitch/height values to find optimal spacings for the pattern, as covered in Section 7.1.1. A FDTD model was then constructed by Sam Shea for the design of the mould to for achieving a theoretical optimal anti-reflectance value.

The mould making process was then empirically optimised in School of Physics and Astronomy by Dr Chris Mellor and Dr Richard Cousins. They commented that the theoretically optimal mould feature size was small, to achieve for the 1.5 μm wavelength AR, and it was difficult to get the correct feature depth. A silicon mould/shim (terms used interchangeably in this chapter) was produced by Dr Richard Cousins and Dr Chris Mellor from the School of Physics at the University of Nottingham using electron beam lithography (EBL) and dry plasma etching. The design parameters and fabrication process are described in Section 7.1.2.

Section 7.1.3 describes the method of hot embossing/pressing chalcogenide bulk glass discs with the fabricated, as-received mould. Section 7.1.4 details a reflectometry experiment, aiming to quantify the efficacy of the pressing technique

and measure any potential AR effects on the transferred pattern. In Section 7.1.5, These chalcogenide discs were then investigated with scanning electron microscopy to observe the imprinted features. An antimony-based composition, $Ge_{20}Sb_{10}Se_{70}$ at. %, was used for the bulk pressings due to the ease of manufacture, its resistance to devitrification, and its known refractive index dispersion[189].

7.1.1 FDTD modelling for 1.55 µm anti-reflectance on $Ge_{10}Sb_{20}Se_{70}$ at. % bulk glass

Previous literature on chalcogenide glass moth eye antireflective patterns had focused on increasing optical fibre transmission in the mid-IR[219,225,230]. With the overarching aim of the PhD project being mid-IR fibre lasing, it was decided to design an antireflective pattern for 1.55 µm in the near-IR to increase input power into a fibre. This targeted a pumping wavelength for praseodymium (III) emissions which provided an output of 3.5-5.5 µm[110]. Using the commercial modelling software: Lumerical FDTD (Ansys/Lumerical, Canada), three morphologies (Cones, cylinders, and paraboloids) were modelled, each in a hexagonally close packed formation. This hexagonally packed formation was chosen as it is biomimetic of what is seen in moths[220,231]. Using the parameter sweeping function of the software, variables such as height, width, pitch, and wavelength of incident light could be modified across a simulation. To avoid excessive modelling timescales, it was decided to limit the parameter sweep to two variables in one model. The target parameters for these initial models were feature height and pitch. A third value, termed "fill factor" or density, describes the percentage of a surface which has the moth eye pattern imparted on it. In models shown here, the diameter: pitch value, the ratio of the maximum feature diameter compared to the pitch was used as a simplification of fill factor to decrease modelling times. It is to be noted that these models are to be compared to a flat chalcogenide surface free from any anti-reflectance patterning. Equation 7.1 shows a simplified (non-polarisation dependent) Fresnel equation for reflection (R) from normal incidence light [232].

$$R = \frac{(n_1 - n_2)}{(n_1 + n_2)}$$ Equation 7.1

n_1 = launch medium refractive index n_2 = incidence medium refractive index

Considering an interface of air (n = 1) to $Ge_{20}Sb_{10}Se_{70}$ at. % (n = 2.58 at 1.55 µm), reflectance would be around 0.195, or 19.5%. Therefore, any value found to be lower than this was deemed antireflecting. Lumerical models output contour plots in which reflectivity values of the chosen variable are represented over a colour gradient of blue (20% reflection, no effect) to yellow (0% reflection) over a wavelength range of 1-5 µm.

7.1.1.1 Diameter over pitch optimisation for conical geometries.

To determine the optimal density of the microstructures on the mould surface, a diameter over pitch parameter was used. It was calculated as the ratio of the maximum feature diameter to minimum lateral separation between individual features. Simply put, the closer the ratio is to 1, the more densely populated the fibre face with nanostructures. It was expected that increasing the density of the features would yield the best anti-reflection [230]. However, in conversation with our mould manufacturers (Dr Chris Mellor and Dr Richard Cousins, School of Physics and Astronomy, University of Nottingham, UK), it was explained that a maximum diameter:pitch (d:p) value of 0.9 was achievable. This was due to the need for some dead space (10-100 nm) between individual features for successful mould fabrication. Figure 7.2 shows a contour plot of reflectance values with an increase in diameter:pitch values from 0.1 to 0.9 over a 1 – 5 µm wavelength range. The model was designed as a repeating close hexagonally packed, conical pattern with feature heights fixed at 1.5 µm and pitch at 2.0 µm. This height, pitch, and shape was set as an approximation of what could feasibly be fabricated by our mould suppliers. Across the wavelength range tested, an increase in microstructure density towards a d:p value of 0.9 led to a decrease in reflectance. In the 2-5 µm range, reflectance values as low as 0.02 (2%) were modelled with a d:p value of 0.9. The efficacy was reduced in the 1-2 µm region (6% reflectance at 0.9 d:p) in all d:p values modelled.

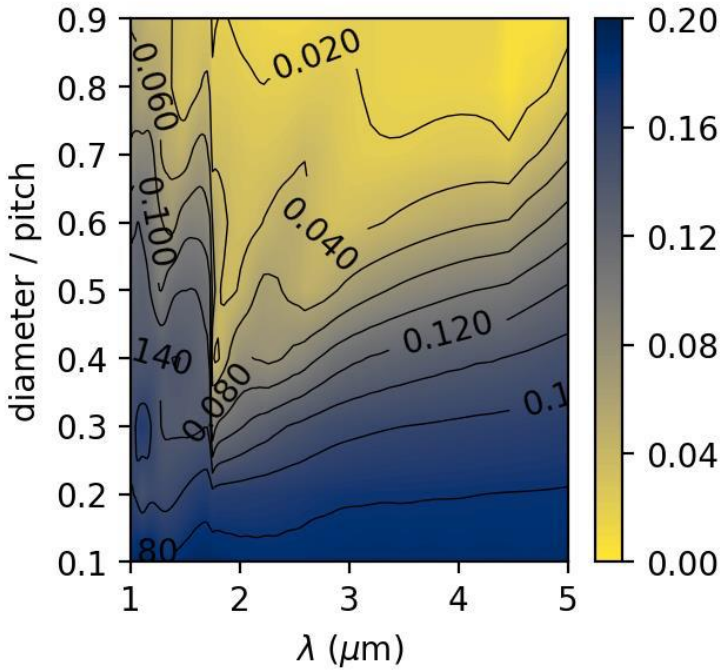


Figure 7.2 Contour plot of the effects of changing d:p value on reflectance across a 1-5 µm wavelength range. Model based on the patterning of a chalcogenide glass with a NA of ~2.58 at 1.55 µm with hexagonally close packed cones with height 1.5 µm, pitch 2 µm. General trend of increasing d:p ratio leading to decreased reflectance from 2-5 µm.

7.1.1.2 Height and pitch optimisation for conical, cylindrical, and paraboloid geometries.

Using a diameter:pitch value fixed at 0.9, the previously determined optimum value, further models were developed to find optimal feature height, pitch, and shape. Feature heights were modelled from 0.6 µm to 1.6 µm in 0.1 µm increments. 1.6 µm was specified as a limitation to which the mould suppliers could not reliably create features beyond this depth. Pitch values were modelled from 0.2 µm to 3 µm in 0.2 µm increments. Although simulations were conducted for each of these parameter increments mentioned, only the best performing geometries are shown here for clarity. The three geometries modelled were conical, paraboloid, and cylindrical.

Figure 7.3 shows the reflectance of conical features with a fixed height of 1.6 µm over a range of pitch values. Optimal antireflection over the 1-5 µm wavelength range was seen with pitch values between 0.5 µm to 2 µm. Within these pitch

values, reflectance was at around 2% with some wavelength ranges exhibiting 1% reflectance. A pitch value of 1.3 µm would demonstrate 1% reflectance over the 2-4.5 µm wavelength range.

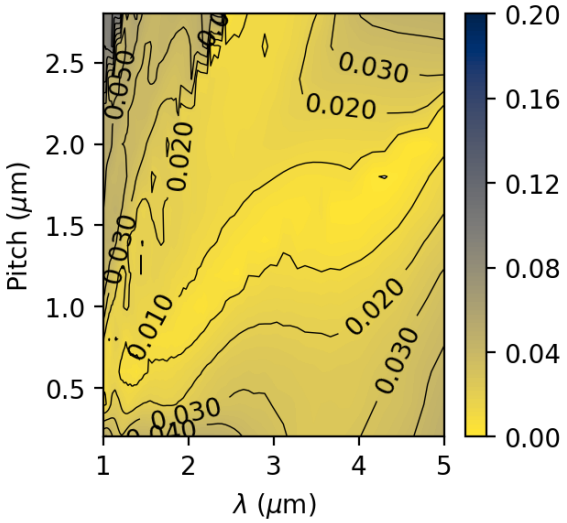


Figure 7.3 Contour reflectance plot of conical hexagonally closed packed features with a fixed height of 1.6 µm and a d:p ratio of 0.9. The effects of pitch were modelled over a 2-5 µm wavelength range. Model based on the patterning of a chalcogenide glass with a NA of ~2.58 at 1.55 µm.

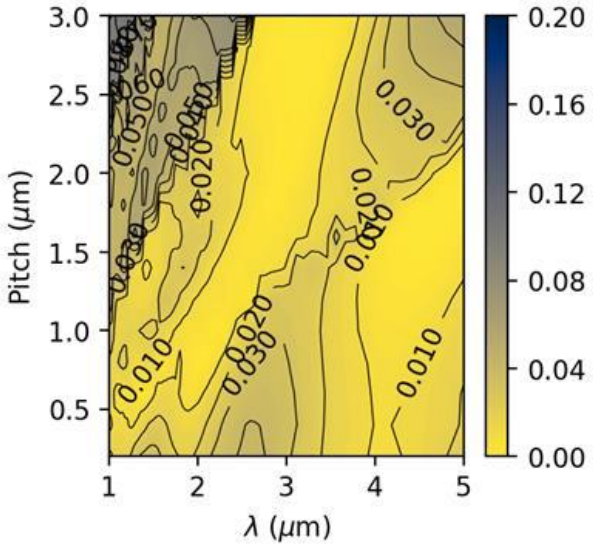


Figure 7.4 Contour reflectance plot of paraboloidal, hexagonally closed packed features with a fixed height of 1.2 µm and a d:p ratio of 0.9. The effects of pitch were modelled over a 2-5 µm wavelength range. Model based on the patterning of a chalcogenide glass with a NA of ~2.58 at 1.55 µm.

Paraboloidal features with a height of 1.2 µm, a d:p value of 0.9, and a pitch of 1.2 µm were found to provide the strongest antireflective effects (Figure 7.4) of the geometries modelled. This design was modelled to show reflectance of 0.01-0.02 (1-2%) across a wavelength range of 1-2.5 µm and 3.5-5 µm. A small band between 2.5-3.5 µm showed slightly increased reflection of 3%.

Lastly, a pitch model for cylindrical features was developed using a fixed height value of 1.4 µm and a d:p value of 0.9 (Figure 7.5A). Reflectance values compared to the paraboloid and conical models are markedly higher with an optimal reflectance value of 4% in the 3-4 µm region at 0.5-1 µm pitch and a small band between 2-2.3 µm with a reflectance of 8%. Considering the poor performance of this particular pattern, a second model was developed in which the d:p value was decreased to 0.5 (Figure 7.5B).

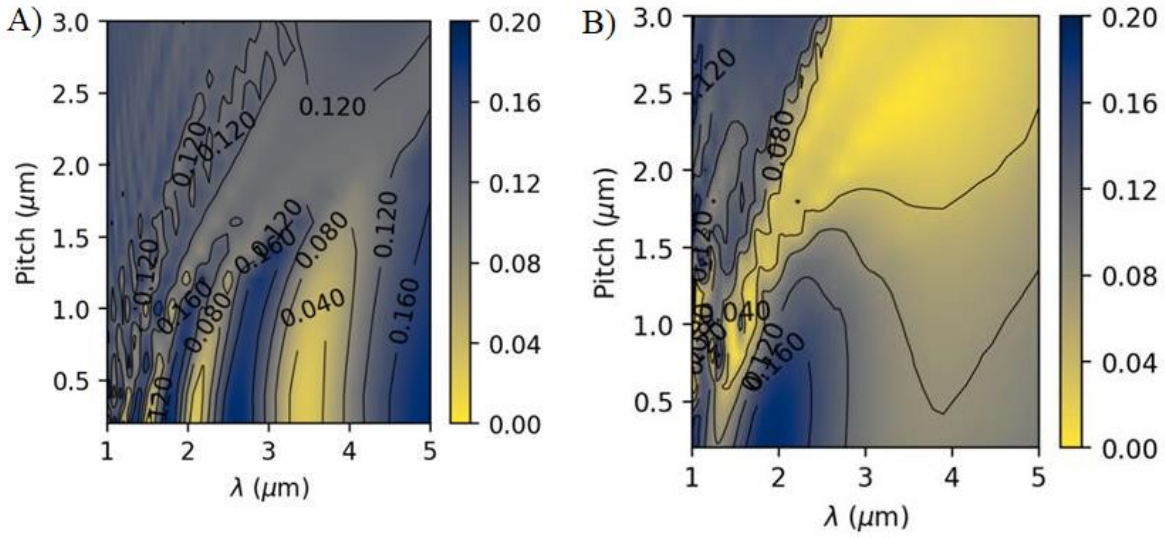


Figure 7.5 Contour reflectance plots showing the effect of pitch on reflectance over a 1-5 µm wavelength range. A) cylindrical structures with a height of 1.4 µm and a d:p ratio of 0.9. B) cylindrical structures with a height of 1.4 µm and a d:p ratio of 0.5. Model based on the patterning of a chalcogenide glass with a NA of ~2.58 at 1.55 µm.

By decreasing the d:p ratio to reduce the feature density, effectively "thinning out" the pattern, a stronger antireflective response was seen in the model. Peak antireflection was still less effective than the paraboloids and cones (4% reflectance on cylinders vs 1%) but there was a broadband improvement over the 2-5 µm wavelength range for pitches >1.8 µm. Unlike the conical and paraboloid structures which provide a gradual increase in refractive index as the cross-section ratio of air

to glass increases further into the feature depth (as explained in EMT)[219,220], it can be explained that the high d:p value for the cylindrical geometries mimicked a secondary flat surface sitting on top of the fibre face. By decreasing the d:p value and subsequently spacing the features out, there was likely more of a gradient of interface for the incident light to reflect between individual features leading to multiple chances for internal reflections[220].

7.1.2 Fabrication process of produced silicon mould "1550NM".

The mould/shim (terms used interchangeably in this chapter) was produced by Dr Richard Cousins and Dr Chris Mellor from the School of Physics at the University of Nottingham. This mould was assigned the code "1550NM", standing for the peak modelled AR wavelength of 1550 nm, with NM standing for "negative mould". A silicon wafer was coated with 500 nm SiO_2 (to potentially act as a non-stick surface for chalcogenides) and then a 500 nm PMMA (polymethylmethacrylate) resist. This was subject to electron beam lithography (EBL) to pattern the resist and the wafer was then dry plasma etched. This produced a negative mould (features below the mould surface, think "female topology") with hexagonal close-packed paraboloidal pattern with a pitch of 600 nm and 550 nm initial hole diameter. The intention is the supercooled chalcogenide glass would flow into the wells of this mould, and thus have chalcogenide glass protrusions on the fibre end face or bulk surface (think, "male topology"). Three variants were produced in which these holes tapered to a final diameter of 120 nm, 160 nm, or 210 nm. Final depth measurements of these holes could not be taken from the patterned wafer but was assumed to be around 1.5 µm on the advice of Dr Cousins.

7.1.3 Hot pressing of moth eye patterns onto $Ge_{20}Sb_{10}Se_{70}$ at. % (M182HAP) bulk samples.

The glass sample preparation was identical to that detailed in Section 3.3.5 with the hot-pressing method used for this moth eye bulk sample work being slightly modified in which the use of the ultra-flat tungsten carbide discs was forgone and instead a smaller tungsten carbide anvil was used (compared with what is described in Section 3.3.5). The intention behind the change of this optical flat to a smaller

anvil was that it would be easier to ensure that weight distribution of the mould was centred on the glass sample, and being of smaller mass and thermal inertia, take less time to reach the target temperature, and be less likely to be strongly adhered to the tungsten carbide surface upon completion due to a decrease surface contact area between the smaller anvil and the silicon mould 1550NM. The bulk glass $Ge_{20}Sb_{10}Se_{70}$ at. % (M182HAP) samples (≈ ⌀ 10 mm, ≈ 3 mm thickness, 1 µm polish) were sandwiched between a silicon shim/mould (1550NM A-F, Figure 7.6) with the desired pattern on the base of the sandwich, under the glass disc, and a smaller tungsten carbide anvil resting on top of the glass disc.

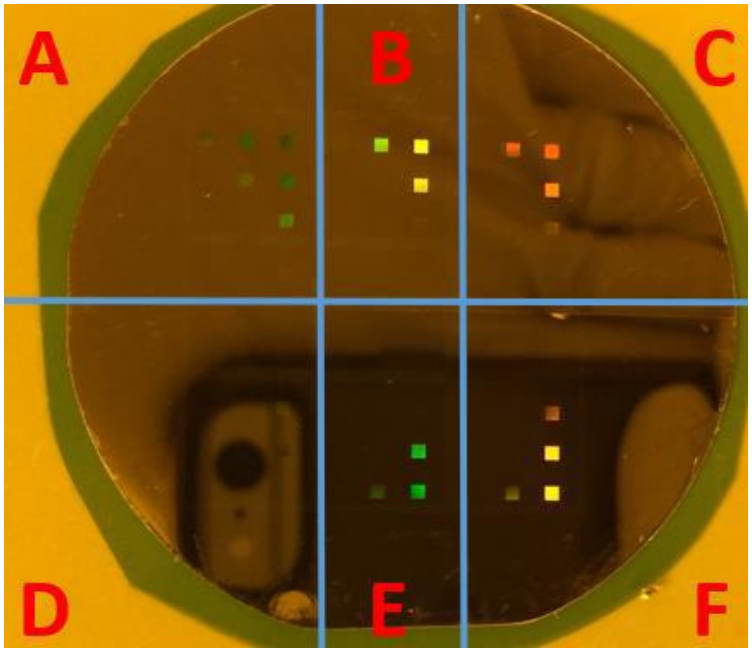


Figure 7.6 The silicon wafer 1550NM (5 inch diameter) with the moth eye patterns etched on. This wafer was then segmented as indicated by the blue lines and alphabetically labelled sections. The smaller squares are diffraction patterns imparted by the moth eye pattern.

With a chalcogenide glass disc sample $Ge_{20}Sb_{10}Se_{70}$ at. % (M182HAP) set between the anvil and the silicon shim, the vacuum chamber was pumped down to a pressure of 10^{-3} Pa. A low pressure was employed to try and mitigate any potential oxidative effects that were likely to occur at the temperatures used[225] and it was also theorised that chalcogenide supercooled melt infiltration of the negative mould (1550NM) would be increased if each well on the mould were evacuated of atmosphere. The aluminium hot plates (as described in Section 3.3.5) were heated to 200 °C at a ramp rate of 200 °C/ hour and the temperature was then held for 18 minutes to equilibrate with the sample, shim, and anvil. The sample was then

heated at a ramp rate of 100 °C/ hour above T_g to values between 242-255 °C. This was 28-41 °C above the T_g of the $Ge_{20}Sb_{10}Se_{70}$ at. % (M182HAP) bulk glass. This temperature was then held for 10 minutes to again allow for equilibration before the pressing procedure was initiated. Pressing was carried out with forces between 30-50 N depending on the press. This force was continued until the bulk sample had compressed between 200 – 500 µm. Following pressing, samples were cooled to T_g (214 °C) and then left to anneal at T_g for 2 hours. Samples were then allowed to cool to room temperature overnight. Table 7.1 details the individual pressings carried out by MSc project student, Sam Shea, and the parameters used. The pressings were carried out in two batches. The prefix "ME" meaning "Moth Eye" was added to each number press. ME001- ME004 were carried out in batch one. After poor anti-reflectance results were observed (Section 7.1.4) with these samples, the pressing parameters were altered with decreased temperatures (255 °C to 242 °C) and greatly increased pressing times in sample codes ME005 and ME006 ($Ge_{20}Sb_{10}Se_{70}$ at. % (M182HAP)). Press temp. is the target temperature set on the hotplates which are in contact with the silicon mould and the tungsten carbide anvil. Force is the applied force as the two hot plates are brought closer to each other, with the silicon mould- $Ge_{20}Sb_{10}Se_{70}$ at. % disc- tungsten carbide anvil sandwich in between. Distance pressed is how far the hot plates travel during the pressing schedule. For example, a pressing distance of 500 µm would reduce the thickness of the chalcogenide sample by 500 µm. Time pressed is the total time taken to reach the target distances pressed, in ME005 and ME006, additional time was added once the distance pressed metric was reached, with the intention to allow glass to further flow into the mould.

Table 7.1 Pressing codes and parameters used for bulk chalcogenide samples: $Ge_{20}Sb_{10}Se_{70}$ at. % (M182HAP) using Mould: 1550NM

Press code	Press temp. /(°C)	Force/ (N)	Distance pressed/ (μm)	Time pressed/ (min)
ME001	255	32-37	250	58
ME002	255	30-36	200	27
ME003	255	40-45	200	8.5
ME004	255	42-47	200	6
ME005	242	25-34	200	102
ME006	242	27-35	500	262

Removal of the chalcogenide bulk samples from the shim-glass-anvil configuration proved difficult post-pressing with the chalcogenide glass $Ge_{20}Sb_{10}Se_{70}$ at. % (M182HAP) strongly adhered to both the silicon shim and the tungsten carbide anvil. Removal of the silicon shim was feasible with a short submersion period (< 30 minutes, fully submerged) in acetone (Table 3.2 for source and purity), but strong mechanical force was the only feasible method to remove the samples from the tungsten carbide anvil. This led to visible degradation of the back surface of the chalcogenide glass samples. Optical visible light diffraction effects, as seen on the silicon shims (Figure 7.6), were observed on each chalcogenide sample pressed, indicating there was some degree of pattern transfer regardless of parameters used (Figure 7.7).

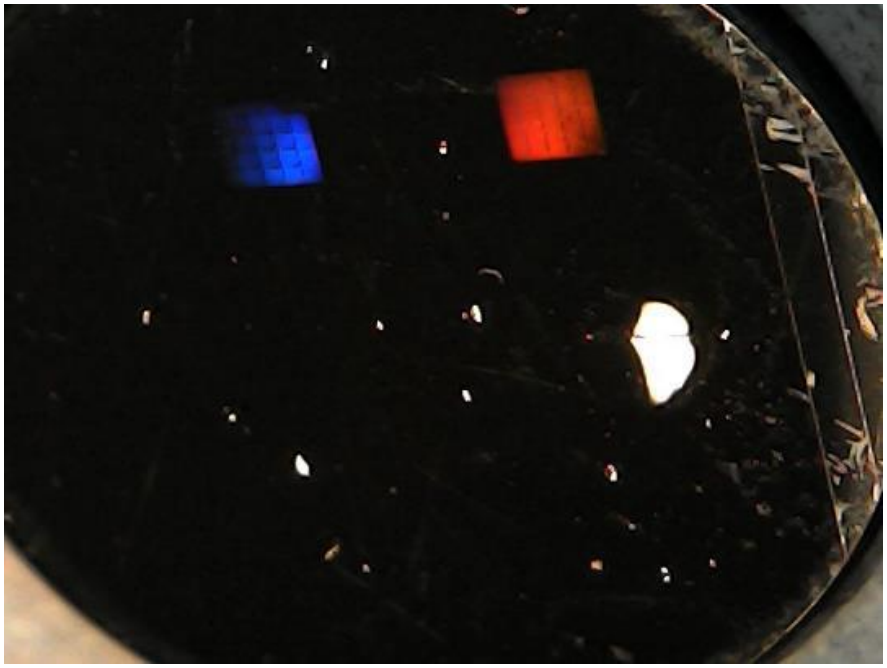


Figure 7.7 Diffraction effects (manifested as visible light colouration) indicating patterning seen on ME006 ($Ge_{20}Sb_{10}Se_{70}$ at. % M182HAP) post pressing at 242 °C, 27 – 35 N of force for 262 minutes, leading to a 500 µm distance pressed of the chalcogenide glass.

7.1.4 1.55 µm reflectometry of pressed bulk glass $Ge_{20}Sb_{10}Se_{70}$ at. % (M182HAP) samples.

As visible light diffraction effects were observable on the surface of the chalcogenide glass bulk (Figure 7.7), it was therefore assumed that some pattern transfer had occurred through chalcogenide glass $Ge_{20}Sb_{10}Se_{70}$ at. % (M182HAP) inflow into the negative silcon mould (1550NM). To determine if the moulded patterns on the chalcogenide glass samples exhibited anti-reflectance, a reflectometry rig was designed to test the samples, as follows.

A 1.55 µm diode laser (Keysight 81989A, Agilent) outputting 16.8 mW power was directed through a 500 µm diameter aperture and onto the pressed samples ($Ge_{20}Sb_{10}Se_{70}$ at. %, M182HAP) (see pressing procedure in Section 7.1.3) mounted onto an adjustable, rotating stage (see Figure 7.8). This rotating stage was positioned at a 2 ° angle of incidence to the laser to allow reflections to be directed to a power meter (PM122, Thorlabs) and avoid measurements of any higher order reflections (that is, internal reflections from the posterior of the sample). The optical set up is shown in Figure 7.8 as drawn by MSc student Sam Shea. Measurements were taken from imprinted sections of the sample (as indicated by

diffraction effects) and pattern-free, polished sections to allow for a comparison. Table 7.2 shows the reflectance results for both the polished surface and the moth-eye patterned surface. Note that the Reflectance Δ (%) column only considers the rounded measured value, not the standard deviation.

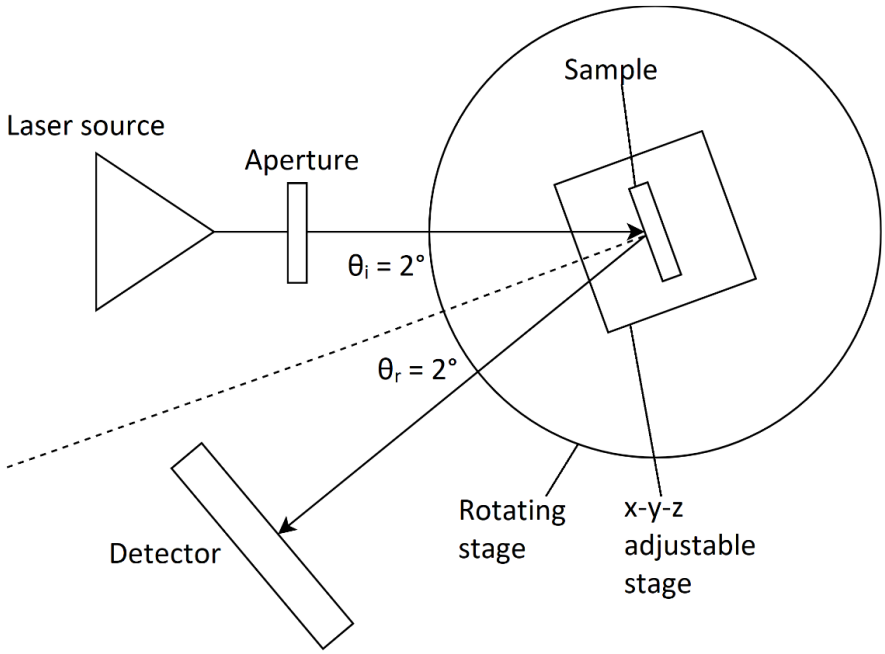


Figure 7.8 Schematic showing the 2 ° reflectometry set up for pressed samples. Beam path length: 500 mm (source to aperture); 700 mm (source to sample); 1000 mm (source to detector). Drawn by MSc student Sam Shea.

Table 7.2 Reflected powers of both polished and moth-eye patterned surfaces on bulk glass $Ge_{20}Sb_{10}Se_{70}$ at. % (M182HAP).

Press code	Reflected power (Polished)		Reflected power (moth eye)		Δ Reflectance
	Measured/ (mW)	%	Measured/ (mW)	%	(%)
ME001	3.04±0.02	18.1±0.14	2.98±0.08	17.7±0.45	-0.4
ME002	4.42±0.38	26.3±2.28	4.29±0.44	25.5±2.60	-0.8
ME003	3.71±0.16	22.1±0.93	3.54±0.09	21.1±0.55	-1.0
ME004	3.32±0.11	19.8±0.63	3.50±0.38	20.8±2.25	+1.0
ME005	3.73±0.35	22.2±2.05	3.38±0.09	20.1±0.55	-2.1
ME006	3.71±0.11	22.1±0.68	3.00±0.18	17.9±1.05	-4.2

Reflectance Δ (%) column only considers the rounded measured value, not the standard deviation.

The initial batch of samples (ME001-ME004, bulk glass discs $Ge_{20}Sb_{10}Se_{70}$ at. % (M182HAP)) demonstrated minimal changes to reflectance values between polished surfaces of the sample and anticipated moth eye patterned surfaces of the same sample. ME001 (Δ -0.4 %), ME002 (Δ -0.8 %), and ME003 (Δ -1 %) all measured a small % of antireflection, with ME004 (Δ 1 %) exhibiting an increase in reflection. Both the polished and patterned measurements falling within the calculated standard deviation of each other (ranging from 0.14 % in ME001 to 2.28 % in ME002, see Table 7.2), making it impossible to draw any conclusions on efficacy of the patterning.

The second batch (ME005 and ME006, bulk glass discs $Ge_{20}Sb_{10}Se_{70}$ at. % (M182HAP)) was subject to longer pressing times with the intention of allowing more time for the supercooled glass melt to flow into the narrow wells of the negative mould and the temperature was subsequently reduced (from 255 °C in ME001-004 to 242 °C in ME005 and ME006) to try and mitigate the risk of devitrification. To recall discussion in Section 2.2.3 and 2.2.4, the atomically disordered structure of glass is frozen in when the glass is below T_g, above T_g however, there is potential for the atoms to rearrange into a crystal structure, as is thermodynamically favourable. Therefore, any time period in which a

chalcogenide glass is above its T_g should be minimised. Also recall from Section 2.2.2 and Figure 2.6, and Section 2.2.4, Figure 2.8, that this crystallisation rate is thus time and temperature dependent, with higher temperatures (above T_g but below T_m) increasing nucleation and growth rate. Hence, the lowered pressing temperatures if pressing times were increased. In the case of ME006, bulk glass discs $Ge_{20}Sb_{10}Se_{70}$ at. % (M182HAP), the distance pressed (*i.e.*, how far the hot plates moved during the pressing procedure) (see Table 7.1) was also substantially increased to 500 µm from 200-250 µm in previous pressings (ME001-ME005). Despite these parameter changes between ME001-ME004 and ME005-ME006 of decrease temperature (242 °C from 255 °C, respectively) and increase pressing time (from 6-58 minutes to 102-262 minutes, respectively), measured reflectance values (ME005, 20.1±0.55 % and ME006, 17.9±1.05 %) were still markedly below the values predicted by the modelling of hexagonally close packed paraboloid features of 1-2 % power reflected at 1.55 µm (see Figure 7.4). Although comparing polished sections to moth eye patterned sections of ME005 and ME006 showed a Δ reflection of -2.1 % and -4.2%, respectively (Table 7.2), suggesting there was some pattern transfer that conferred a small degree of AR.

These measured reflectance values of ME002-ME005 were also greater than what was calculated to be maximum reflectance from the Fresnel equations from the refractive index dispersion measurement of $Ge_{20}Sb_{10}Se_{70}$ at. % [189] (M182HAP) (19.4%, equation 7.1) although this is suggested to be a result of the experimental set up itself and not a material-based issue. That is, there remained potential for higher order reflections from the back, interior surface of the chalcogenide bulk glass sample to be reflected out onto the detector, despite the 2 ° angle of incidence of the 1.55 µm source to the chalcogenide glass bulk sample, increasing the power reflected to the detector.

To compare with Lotz *et al.* [225,233], who demonstrated successful nanoimprinting of As_2Se_3 windows, found a $\Delta T \geq 10$ % (ΔT = change in transmission) increase in transmission when pressing in bulk samples[225,233]. Although note, Lotz *et al.* [225,233] measured transmission when comparing to the reflectance measurements in the current work presented here.

7.1.5 SEM imaging of hot-pressed bulk samples $Ge_{20}Sb_{10}Se_{70}$ at. % (M182HAP)

With the measured results (17.7-25.5 %, see Table 7.2) differing so greatly from those modelled (1-2 %, see Figure 7.4), it was proposed that there was still an issue with the pressing process and therefore the pattern being imparted during the processing was not true to the pattern of the mould. SEM imaging in a JEOL 6490LV fitted with a secondary electron detector was employed to view the features on the bulk sample surfaces (Section 3.3.3 for more details). Discs were mounted onto an aluminium SEM stub and coated with a (nominally) 10 nm carbon layer (thickness as calculated by the coater, Q150R ES, QuorumTech) to avoid charging effects. ME003 $Ge_{20}Sb_{10}Se_{70}$ at. % (M182HAP) was the first bulk glass sample analysed as it was shown to provide the best reflectance performance out of the initial batch pressings.

Figure 7.9 shows the structures in the glass sample with a magnification bar of 10 μm. It is clear the pattern had begun to imprint into the chalcogenide surface and the close hexagonal packing of the features can be seen. The larger box shapes are a result of stitching errors introduced during the lithography process. As it would be too time consuming to design the negative mould pattern for the entire 1mm x 1mm area, a smaller section is designed and repeated near each other until the desired mould size is achieved. These stitching errors are the result of overlapping features between two boxes. The vertical scratch coming from the base of the image was likely introduced during the sample removal process. The tungsten anvil placed on the back side of the sample during pressing strongly adhered to the chalcogenide glass bulk sample after the pressing and made its removal difficult. Strong mechanical hand force was applied through a metal file acting as a lever at the point of contact to remove the finished, patterned chalcogenide bulk glass sample from the anvil.

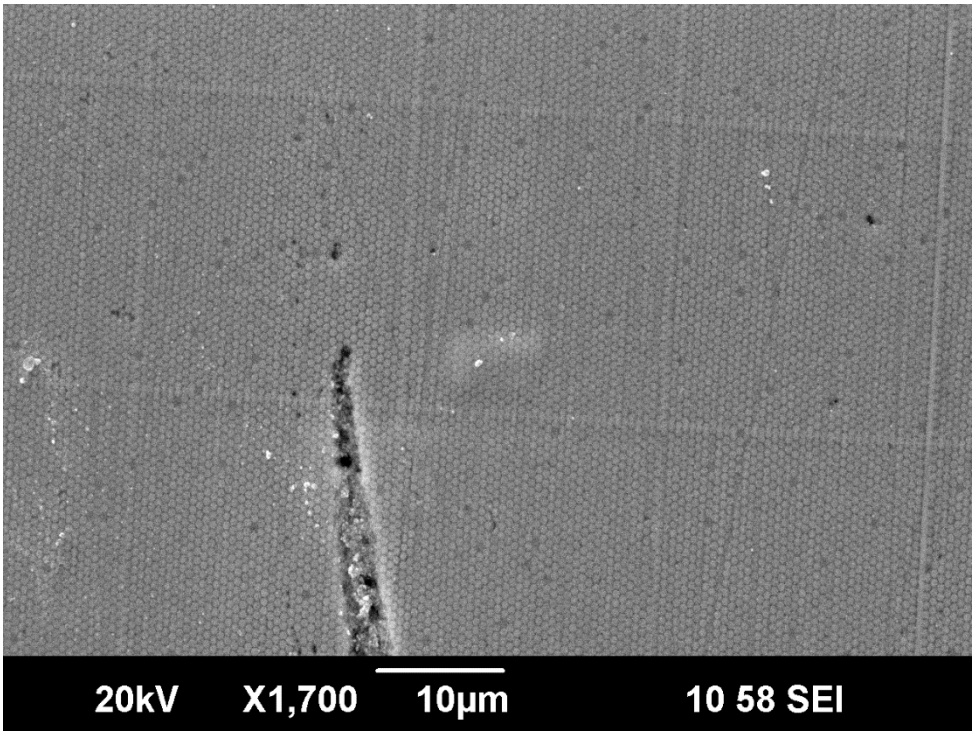


Figure 7.9 Bulk glass pressing results using 1550NM on ME003. Secondary electron image of ME003 $Ge_{20}Sb_{10}Se_{70}$ at. % bulk glass sample (M182HAP). The scale bar is 10 µm Note the stitching pattern inherent to the silicon mould has transferred to the chalcogenide glass bulk sample, imparting a grid pattern on the surface of the chalcogenide glass.

Figure 7.10 shows a SEM image of a small section of the same sample, ME003 bulk glass sample of $Ge_{20}Sb_{10}Se_{70}$ at. % (M182HAP), at a higher magnification compared to Figure 7.9, with a magnification bar of 1 µm. The sample stage was tilted at 16 ° relative to the detector to image any mould-pressed protruding features on the sample surface. At these magnifications, it was difficult to achieve high quality micrographs due to the use of a tungsten filament electron source (as opposed to a field emission gun (FEG)) in the SEM. This was because at the time of investigation, a FEG containing SEM was not available. In Figure 6.10, the red circle highlights what appears to be the beginnings of feature formation on the chalcogenide glass surface, with orange circle point at what appears to be the tip of a conical shape, but this is a highly localised result with the surrounding features failing to display such a shape.

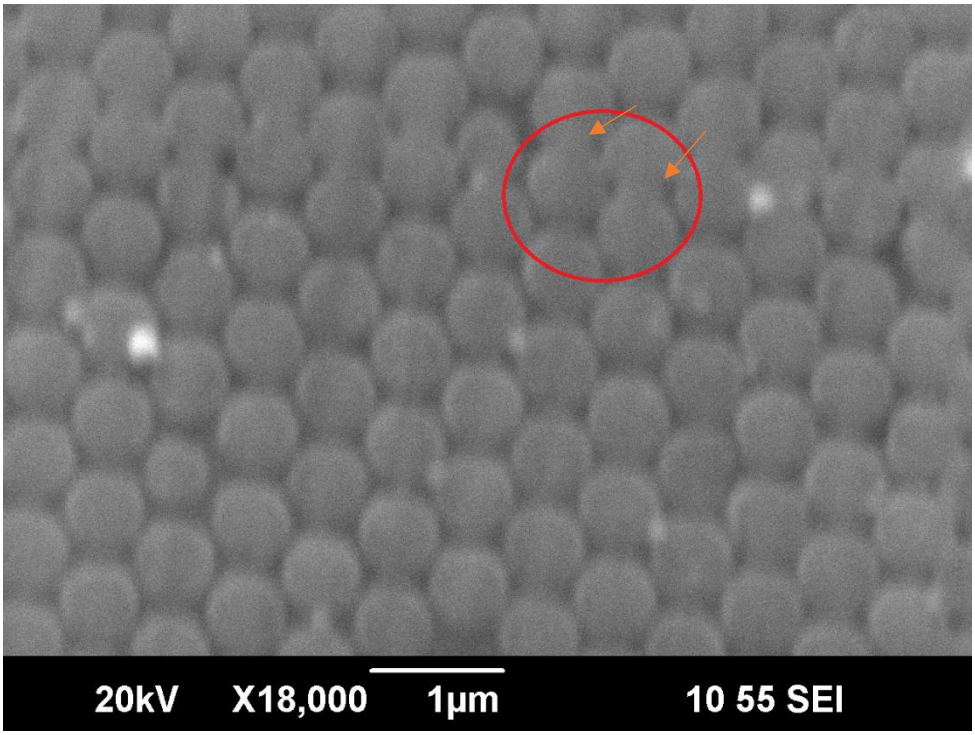


Figure 7.10 Bulk glass pressing results using 1550NM on ME003. Secondary electron micrograph of glass sample ME003 $Ge_{20}Sb_{10}Se_{70}$ at. % (M182HAP). The magnification bar is 1 µm. The sample stage was tilted 16 ° relative to the detector to attempt to image feature height. Within the red circle identifies small conical protrusions indicating local mould infiltration. Orange arrows point to tip of conical structure.

A second bulk chalcogenide glass sample, ME005 $Ge_{20}Sb_{10}Se_{70}$ at. % (M182HAP), from the second batch using revised parameters (see Table 7.1), was also imaged; from Figure 7.11 (like Figure 7.10, had a scale bar of 1 µm), the pressing of ME005 shows a slight improvement to feature shape compared to ME003 (compared Figures 7.11 and Fgure 7.10, respectively). Figure 7.11 shows that the mould pressed features in ME005 have adopted more of an egg-like shape indicating that the increased press time (8.5 minutes for ME003 compared to 262 minutes for ME005) had allowed the supercooled chalcogenide glass to infiltrate further into the mould.

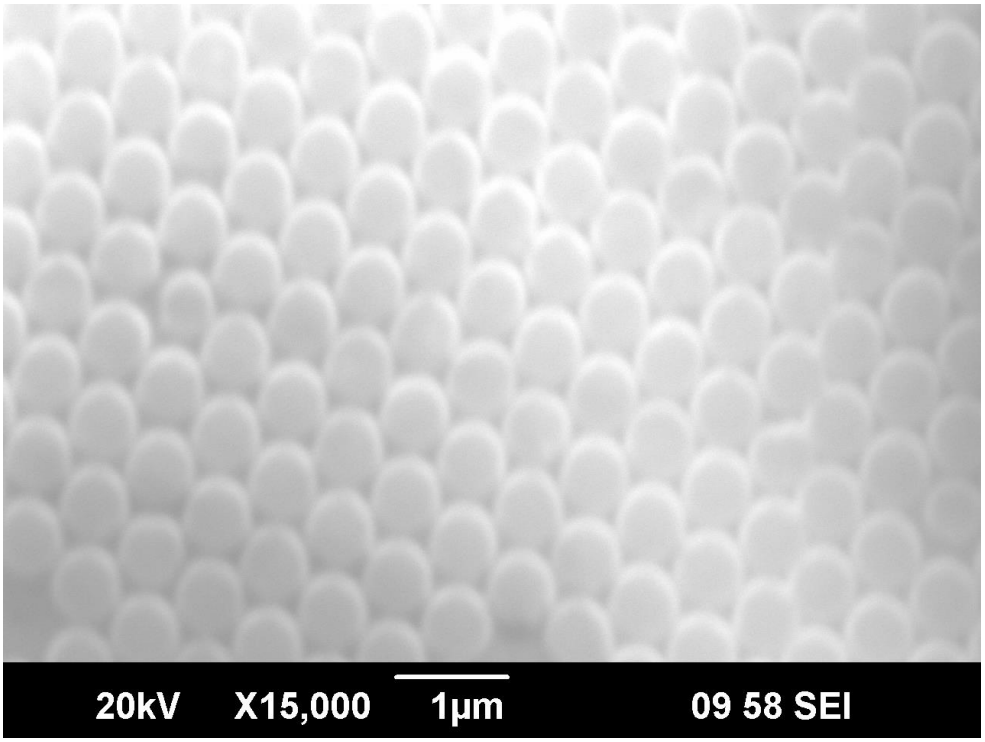


Figure 7.11 Bulk glass pressing results using 1550NM on ME005. Secondary electron image of ME005 $Ge_{20}Sb_{10}Se_{70}$ at. % (M182HAP). Note a magnification bar of 1 µm. The sample stage tilted 16 ° relative to the detector in attempt to image feature height and profile.

From Figures 7.9 – 7.11 it is apparent that there are the beginnings of feature transfer from the negative patterned mould to the chalcogenide bulk glass samples, but that the mould topology was poorly replicated. This is likely the result of the experimental pressing set up used to imprint the samples not being optimally adjusted. By having the bulk samples free standing in the hot press equipment between the shim and anvil, the glass supercooled melt was allowed to flow laterally outwards as the axial force was applied. Due to the larger starting surface area of the bulk glass sample relative to the to mould (⌀ 10 mm sample pressing onto 1 mm x 1 mm square, the size of the mould patterning) and the small wells of the mould potentially creating a surface tension effect. So increasing the temperature of the pressing, and hence decreasing the glass viscosity, may have a greater effect of increasing the rate of lateral flow as opposed to increasing glass melt infiltration into the mould. Likewise, increasing the force used during the pressing during press ME006 did lead to slightly better reflectance results but the resulting disc was a notably different shape in comparison to other samples and partially fractured upon removal.

Lotz *et al.* incorporated aluminium rings around their chalcogenide windows to contain this lateral flow of glass and direct the glass into their moulds[225]. It was concluded that the pressing set up used here was inadequate without some form of constraining band to hold the supercooled glass melt. As the end goal was to produce antireflective structures for fibre faces, it was decided to not make any modifications to the bulk sample hot pressing set up and instead move to fibre tip pressing.

7.2 Imprinting of anti-reflective moth eye structures onto unstructured $Ge_{19.4}Sb_{9.7}Se_{67.9}Ga_3$ at. % (F101RC) fibre end faces.

The second stage of this work was conducted with the help of MSc student Sijie He and the following is an overview of the work undertaken. To hot press the moth-eye pattern onto an unstructured fibre end face, a new pressing rig was designed (Figure 7.12). A fibre sample was loaded into a stainless-steel V-groove attached to a force sensor and manually driven into the heated mould. Various temperature parameters were tested while force values were fixed. Samples were imaged using SEM and reflectance measurements were taken to gauge efficacy of pattern transfer. The composition of interest was changed from $Ge_{20}Sb_{10}Se_{70}$ at. % (M182HAP) to $Ge_{19.4}Sb_{9.7}Se_{67.9}Ga_3$ at. % (F101RC) as this latter composition is suitable for rare earth ion doping and was planned to be used as a host composition for ions that could suitably be pumped at 1.55 μm.

Section 7.2.1 covers the design process of the hot-pressing rig for chalcogenide fibre end faces. Section 7.2.2 details the manually controlled hot-pressing procedure, the parameters that were deemed optimal, and the moth eye shims that were tested (see A-F in Figure 7.6). Section 7.2.3 covers the SEM investigation of the moth eye hot-pressed unstructured chalcogenide fibre end faces.

7.2.1 Design of a hot-pressing rig for chalcogenide fibres.

The silicon shim, 1550NM (Section 7.1.2), was placed on a hot plate fitted with induction heating coils (made in-house) and powered through a PID (proportional-integral-differential) controller (Eurotherm). A K-type thermocouple (RS components) was inserted through the underside of the hotplate just below the

surface which provided feedback to the controller. This hotplate was mounted on top of two translational stages (facilitating movement in the x and y axis) and two additional tilt stages to accommodate for any angles to the fibre tip post-cleave (cleaving performed using a Vytran automated cleaver, see Section 3.3.6). A V-groove fitted with a force sensor (FSC102, Thorlabs) was mounted onto another translational stage and secured above the shim. This sensor was then connected to a strain gauge reader (KSG101, Thorlabs) to give an immediate readout of applied forces.

By limiting the fibre travel to only the Z-axis, it allowed the position of the fibre and shim to be aligned when the system was "cold", so the fibre only needed to be translated up and down during the hot press. Figure 7.12 shows a photo of the system with each component labelled. The silicon shims used were the same used in Section 7.1, see shims A-F Figure 7.6. A visible light USB camera were fixed to the sides of the hot plate for easy and accurate alignment of the hot plate with the fibre end face. The heat shield was rotated in between the force sensor and hot plate and only moved into the position seen in figure 7.12 when pressing was about to commence. This aimed to reduce any adverse effects of the heat on the force sensor. A dry air flow was directed just above the surface of the silicon shim to minimise the radiant heat from the hot plate reaching the force sensor. It also aimed to locally lower the humidity of the pressing region to minimise the effects of ambient H_2O on the chalcogenide glass fibre when heated in atmosphere. This dry air flow was used as it was readily available in the laboratory of the Mid-Infrared Photonics Group, University of Nottingham, UK, but ideally a dry inert gas supply would be used to additionally minimise the presence of atmospheric oxygen.

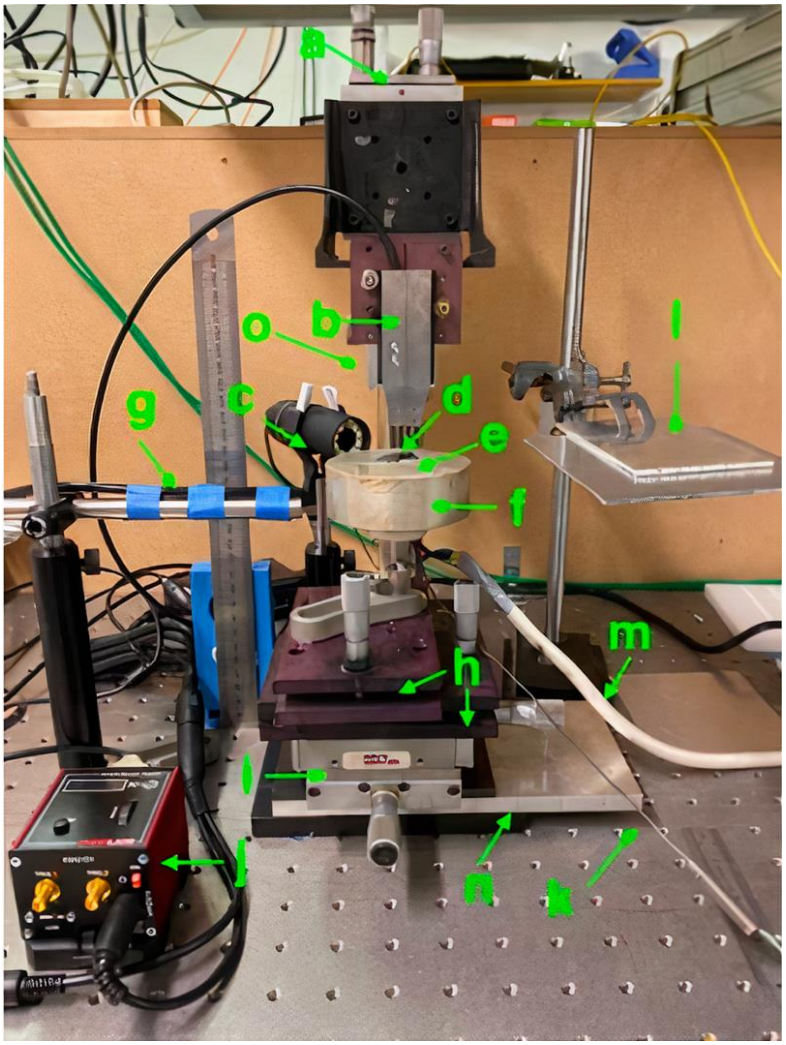


Figure 7.12 Photograph of the fibre end face hot-pressing rig, components labelled as follows: (a) Z- axis translational stage. (b) Force sensor with V-groove. (c) Camera. (d) Silicon shim. (e) Silica slide (f)Aluminium hot plate. (g) Dry air source. (h) Tilt stages. (i) Translation stage. (j) Strain gauge reader. (k) Hot plate thermocouple. (l) Aluminium heat shield. (m) Hot plate power cable. (n) Adapter plate to fit to optical table. (o) Mounting stage for force sensor.

Following the assembly of the rig in Figure 7.12, $Ge_{19.4}Sb_{9.7}Se_{67.9}Ga_3$ at. % (F101RC) fibre samples were hot-pressed using different 1550NM shims (see Figure 7.6 A-F) to determine an optimal pressing scheme for moth eye pattern transfer.

7.2.2 Manually controlled hot-pressing of $Ge_{19.4}Sb_{9.7}Se_{67.9}Ga_3$ at. % (F101RC) fibres.

This section covers the various pressing parameters that were trialled to determine optimal moth eye pattern transfer during the hot-pressing of F101RC $Ge_{19.4}Sb_{9.7}Se_{67.9}Ga_3$ at. % using the fibre hot-pressing rig developed in Section 7.2.1. Differing 1550NM shims (see A-F in Figure 7.6) were used to investigate potential differences in feature height between the shims.

$Ge_{19.4}Sb_{9.7}Se_{67.9}Ga_3$ at. % fibre samples (F101RC) of nominal diameter of 230 µm (+/- 10 µm) were used for each pressing on the fibre pressing rig. Samples were cleaved (Vytran cleaver, see Section 3.3.6) and only selected for use if the cleave angle was visibly close to 0 °. Although tilt stages were incorporated into the rig to account of angled cleaves, it proved easier to re-cleave a sample with a large angle instead of adjusting for each fibre.

For each pressing, the force sensor was removed from the rig for ease of access when mounting the sample. The fibre was slotted into the force sensor V-groove with a 1 mm overhang on the pressing end. This fibre was secured using Kapton tape and magnets to ensure the fibre did not slide through the groove once force was applied. The force sensor V-groove was then reattached to the Z-axis translation stage above the hot plate. The desired silicon shim mould of 1550NM was then placed onto the hot plate and the force sensor was slowly lowered down. Adjustments could then be made to the position of the silicon shim mould using the X and Y translation stages that the hot plate was fixed to. This ensured that the desired mould pattern aligned with the fibre tip. A visible light USB camera (see (c) in Figure 7.12) focused on the hot plate surface allowed a fine tuning of alignment of the fibre tip and hot plate (Figure 7.13).

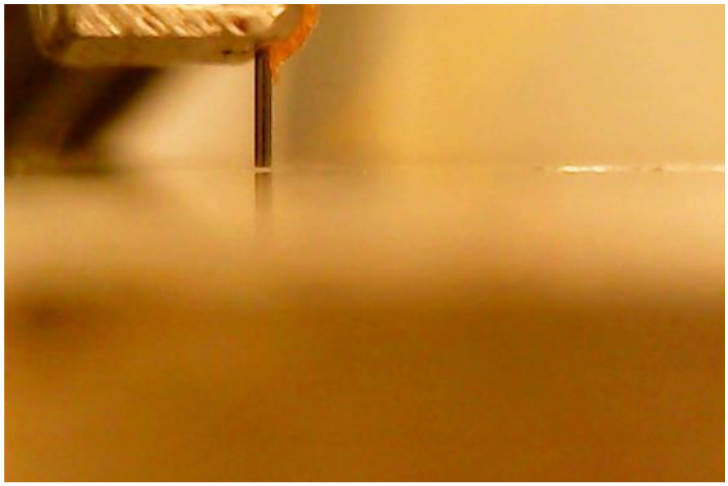


Figure 7.13 F101RC $Ge_{19.4}Sb_{9.7}Se_{67.9}Ga_3$ at. % fibre, secured in a stainless-steel V-groove in the hot-pressing rig (see Figure 7.12). Photograph showing a demonstration on the use of cameras to align a fibre tip with hot plate. It was desired to avoid any relative angle of the fibre face to the hot plate as this would have impaired fibre imprinting.

Once the mould pattern on the shim and the fibre were aligned, the force sensor and fibre were retracted back to the starting position and the heating schedule for the hot plate was started. In the literature, As_2Se_3 fibre pressings were conducted at around T_g +50 °C [234]. The T_g of the $Ge_{19.4}Sb_{9.7}Se_{67.9}Ga_3$ at. % (F101RC) was measured at 237 °C (see Figure 4.2, Section 4.1.2.1) and so samples were taken to either 270 °C, 280 °C, 285 °C, or 300 °C in preliminary pressing tests (data not presented here). Figure 7.14 shows visible micrographs, with scalebar of 100 µm, taken through optical microscopy (Vickers M17 with GXoptical detection camera GXCAM-5), in reflection, to observe the side profiles of hot-pressed fibres. At each pressing between the temperatures 270 – 285 °C a characteristic "elephant's foot" pattern was observed, demonstrating an increase in surface area at the fibre end face.

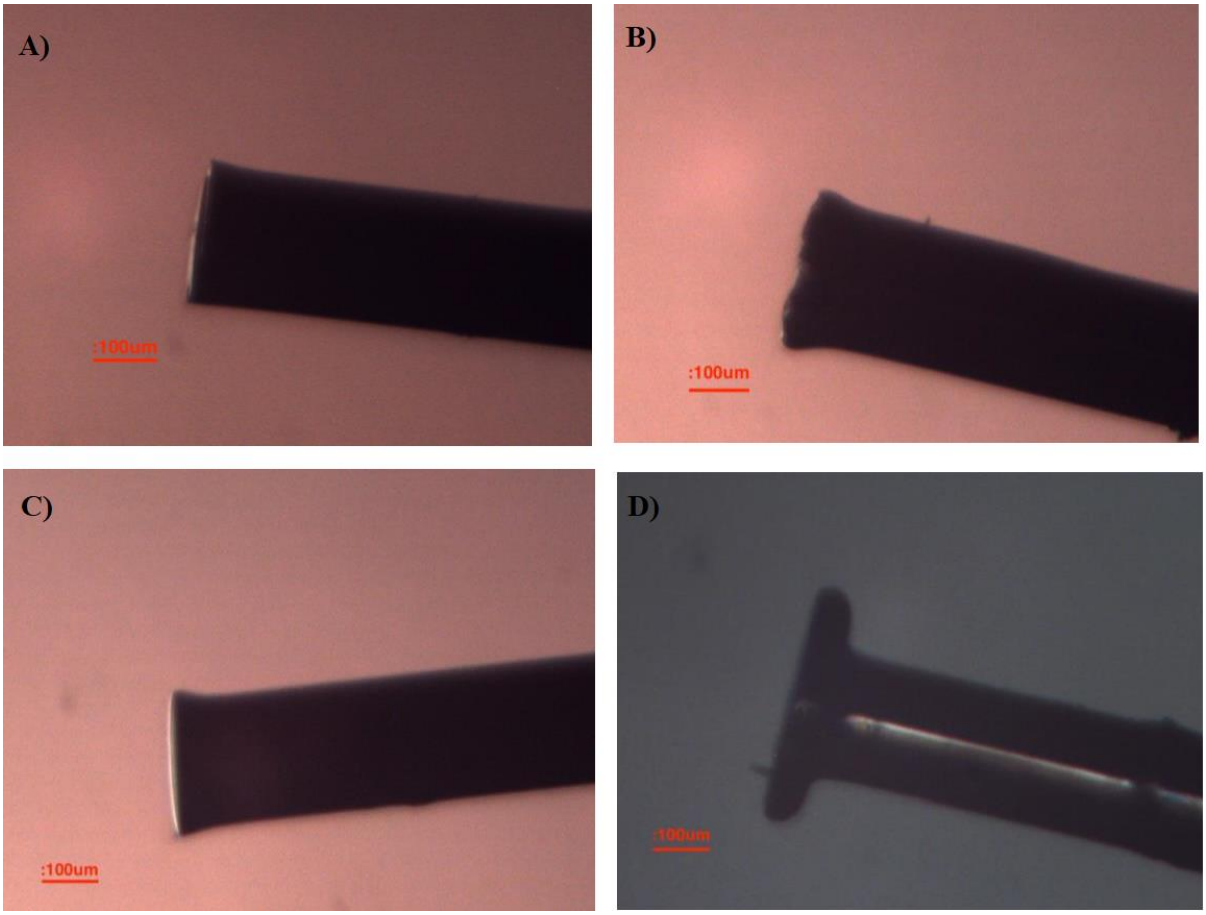


Figure 7.14 Fibre end face pressing results using 1550NM(e) (see Figure 7.6) F101RC unstructured fibres $Ge_{19.4}Sb_{9.7}Se_{67.9}Ga_3$ at. % pressed at A) 270 °C B) 280 °C C) 285 °C D) 300 °C. All pressings were done at 1.75 N for 10 seconds. Reflection images taken from a visible light camera (GXoptical detection camera GXCAM-5) mounted to light microscope (Vickers M17), scale bar of 100 µm.

Pressing at 300 °C led to the formation of a "disc" like shape at the fibre end. This was compared to the phenomenon seen with the bulk sample discs in which the samples that exhibited large amounts of lateral flow demonstrated poor pattern transfer. From these preliminary tests it was decided that 285 °C for F101RC $Ge_{19.4}Sb_{9.7}Se_{67.9}Ga_3$ at. % with a T_g of 237 °C, so T_g +48 °C was the optimum pressing temperature and was subsequently used for each pressing. This was a similar difference to fibre end hot-pressing temperatures used by Sanghera *et al.*[219] who hot pressed As_2S_3 (T_g 201 °C [235]) fibres between 220-240 °C, giving a difference of T_g +19-39 °C.

A force of 1 N was found by Lotz [234] to provide suitable pattern transfer to 170 µm diameter As_2Se_3 fibre at 225 °C [234]. As the unstructured $Ge_{19.4}Sb_{9.7}Se_{67.9}Ga_3$ at. % fibre (F101RC) in the work performed by the current Author had a larger diameter of 230 µm, a greater force would need to be applied to provide comparable results. Using equation 7.4, it was determined that 1.75 N would provide similar effects to the fibre tip.

$$P = \frac{F}{A} \qquad \text{Equation 7.4}$$

P = Pressure F = Force A = surface area of contact point

Upon reaching the target temperature at the silicon mould, the Z-axis stage (Figure 7.12a) was translated down, by hand, until the strain gauge read at value of 1.75 N applied force. It was found that once the 1.75 N of force was applied to the fibre tip onto the hot plate, the force readout on the strain gauge reader would decrease over time. This was due to the fibre tip beginning to spread out across the surface of the mould as the supercooled glass melt (now above its T_g) flows laterally. Therefore, in relation to equation 7.4, A is increasing, and so total pressure is decreasing. To counteract this, the force was gradually, manually increased during the pressing to maintain a constant force of 1.75 N. Pressings were done with a 10 second press time, followed by a 10 second period with no additional force applied. This "rest" phase aimed to further facilitate glass infiltration into the hot mould while minimising an increase in surface area due to the applied force. The fibre was then slowly lifted away from contact with the mould and then rapidly retracted away from the hot plate to the loading position. Preliminary pressings were carried out to determine the optimal pressing temperature.

Nine pressings were carried out, labelled MEF01-MEF09 (the prefix MEF meaning "moth eye fibre") (see Table 7.3). The moulds used for each pressing were changed each time (with some repeats, see Table 7.3 for poor quality pressings) but the pressing parameters being fixed as follows: 285 °C pressing temperature with 1.75 N force applied and maintained for 10 seconds, followed by 10 seconds in which the fibre end face was still on the mould, but the 1.75 N force was not maintained. Table 7.3 shows which shim (A-F in Figure 7.6), and which mould

pattern on the shim (note that there were between 2-6 of the 1 mm x 1 mm mould patterns per A-F shim in Figure 7.6) was used for each pressing. E.g., the fourth pattern on shim D is here termed "D(4)".

Table 7.3 Pressing codes and shim (and mould pattern) used for F101RC $Ge_{19.4}Sb_{9.7}Se_{67.9}Ga_3$ at. % unstructured fibre chalcogenide samples.

Press code	MEF 01	MEF 02	MEF 03	MEF 04	MEF 05	MEF 06	MEF 07	MEF 08	MEF 09
Shim (pattern no.)	D(4)	D(4)	D(2)	C(1)	C(2)	C(2)	A(1)	A(2)	A(3)

The following section, Section 7.2.3, details the light microscopy and SEM investigation following the pressing of samples MEF01-MEF09, from unstructured F101RC $Ge_{19.4}Sb_{9.7}Se_{67.9}Ga_3$ at. % fibres.

7.2.3 SEM and light microscopy imaging of imprinted fibre samples.

Following the pressing of samples MEF01-MEF09, the pressed F101RC $Ge_{19.4}Sb_{9.7}Se_{67.9}Ga_3$ at. % fibres were imaged under visible light microscopy. Fibre end faces that exhibited interesting features were then taken for SEM imaging.

Upon completion of the pressing process (see Section 7.2.2), the fibre samples were removed from the force sensor V-groove and the faces were imaged under visible light microscopy (Vickers M17 with GXoptical detection camera GXCAM-5) in reflection. Although the features could not be properly observed at the magnifications available, it provided an indication as to whether a pressing was successful. All fibre samples were of unstructured F101RC $Ge_{19.4}Sb_{9.7}Se_{67.9}Ga_3$ at. %. Figure 7.15 shows MEF03 observed at x10 and x100 magnification, nominal at point of use of microscope. As seen in Figure 7.15A, using x10 magnification (nominal), the moth eye pattern has been (partially) imprinted across the entire fibre face. At x100 magnification (nominal, Figure 7.15B), individual <1 μm "dotted" microstructures can be seen in the close packed hexagonal pattern, as well as the

stitching errors present on the mould. The brighter spots were sections of the mould which had no wells and so the fibre face remained flat.

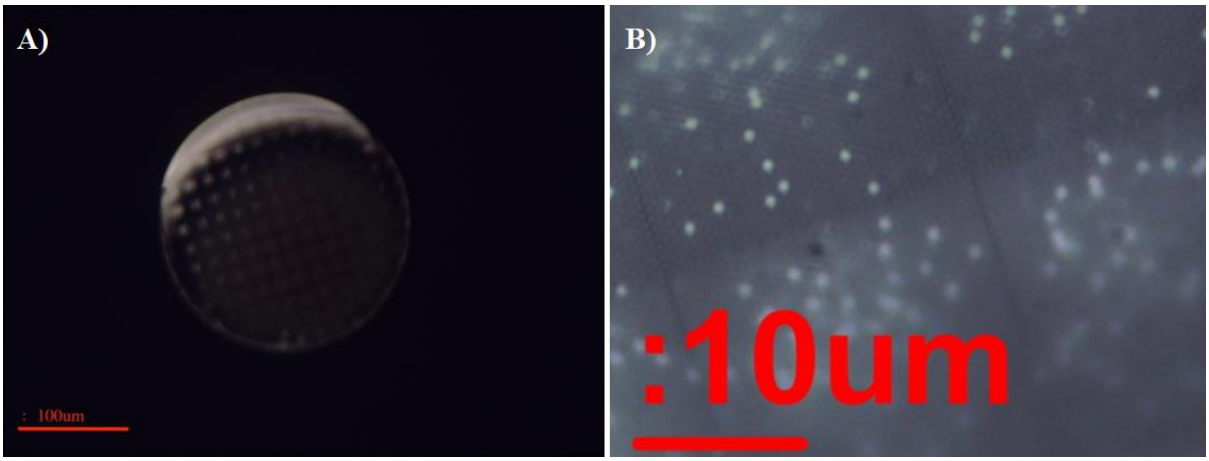


Figure 7.15 Fibre end face pressing results of MEF03. Reflection light microscopy images of unstructured fibre F101RC ($Ge_{19.4}Sb_{9.7}Se_{67.9}Ga_3$ at. %) (Vickers M17 with GXoptical detection camera GXCAM-5). Pressed at 285 °C with 1.75 N for 10 seconds, followed by a 10 second relaxation period. A) Showing the entire fibre tip with a 100 µm scale bar. B) Showing where individual microstructures become apparent with a 10 µm scale bar.

Unstructured fibre F101RC ($Ge_{19.4}Sb_{9.7}Se_{67.9}Ga_3$ at. %): MEF03 was then taken for SEM imaging to analyse further the fibre tip. A JEOL 7100F equipped with a field emission gun (FEG) electron source and secondary electron detector was used to achieve the high resolutions required to image the features. For fibre imaging, fibres were mounted vertically onto an aluminium SEM stub and coated with a (nominally) 10 nm carbon layer (thickness as calculated by the coater, Q150R ES, QuorumTech) to avoid charging effects. Figure 7.16A is a top-down view of the moth-eye structures. Without imaging the samples at an angle to get a side profile view, it was not possible to assess feature height or geometry. However, it was apparent that shaping of the supercooled glass melt had taken place to a further extent than what was seen with the bulk samples in Section 7.1. Figure 7.16B shows the stitching patterns seen previously (see Figure 7.9 and Figure 7.15) as well as regions of the mould without any wells.

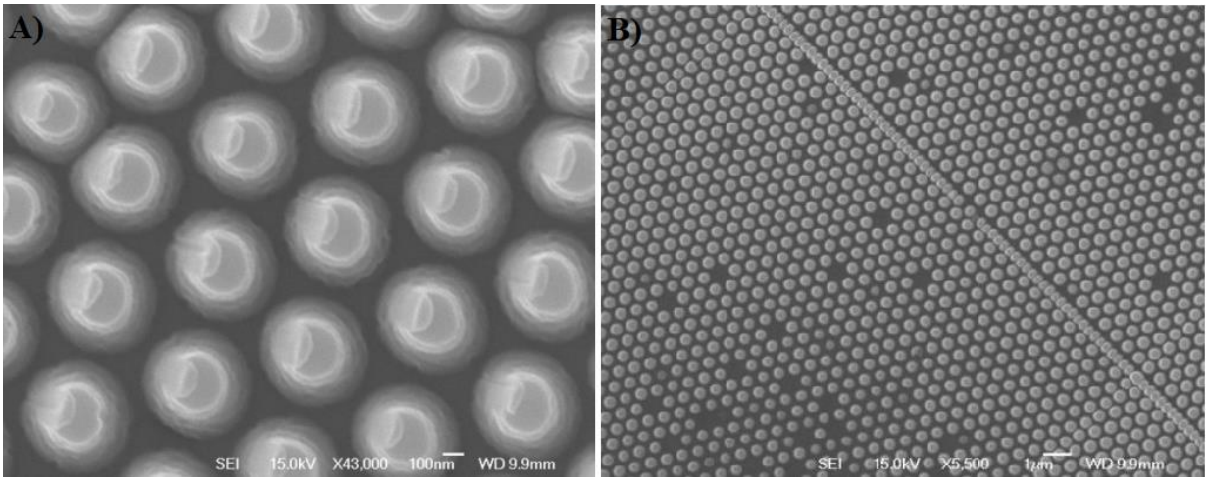


Figure 7.16 Fibre end face pressing results of MEF03. SEM micrographs of F101RC ($Ge_{19.4}Sb_{9.7}Se_{67.9}Ga_3$ at. %) MEF03 taken with JEOL 7100F. A) Top down view of individual features with scalebar of 100 nm. B) A section of the fibre tip showing missing features and stitching patterns with a scalebar of 1 µm.

During the pressing of unstructured fibre F101RC ($Ge_{19.4}Sb_{9.7}Se_{67.9}Ga_3$ at. %): MEF04, a large portion of the fibre face remained on the mould surface resulting in a large void on the tip (Figure 7.17A). It was proposed that there was a bubble or other defect close to the surface of the face which led to material failure during the pressing. Small sections of glass around the void were pulled from the surface ≈ 90 ° perpendicular to the fibre tip. This allowed an imaging of the features from a side-on profile (Figure 7.17B). From Figure 7.17B, although the angle is uncertain and a true value of feature height could not be taken, a rough estimate of feature height was estimated to be around 500 nm. This is still substantially shorter than the 1.5 µm height value given by the mould manufacturer.

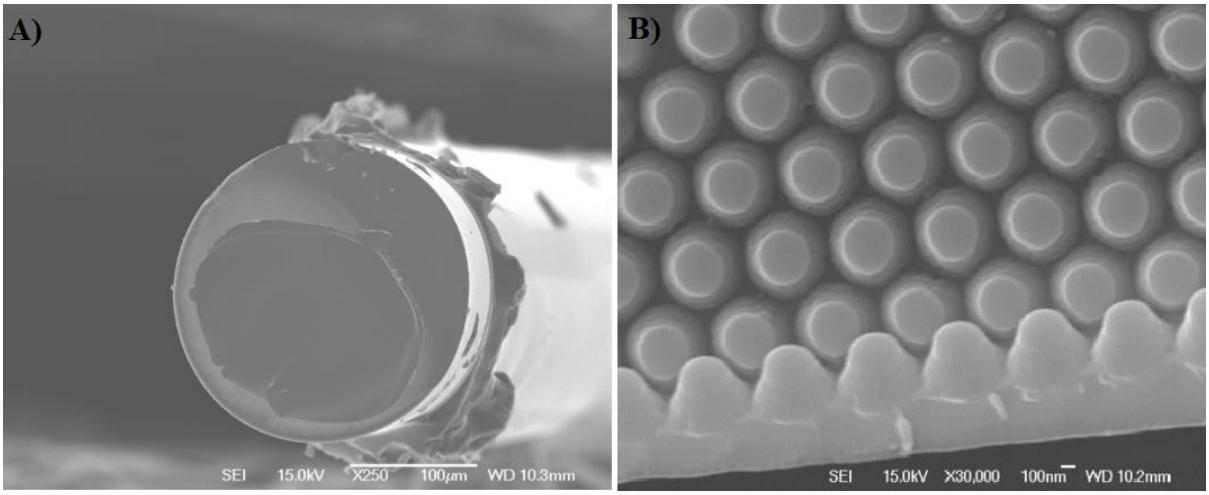


Figure 7.17 Fibre end face pressing results of MEF04. SEM micrographs of unstructured F101RC ($Ge_{19.4}Sb_{9.7}Se_{67.9}Ga_3$ at. %) MEF04 taken with JEOL 7100F. A) Macro-view of fibre face showing the large void introduced during pressing. Scale bar 100 µm. B) Close up view of the damaged perimeter around the void. Scale bar 100 nm. The angle of the glass provides a side on view of the features. Feature heights were estimated to be around ~500 nm.

Unstructured fibre F101RC ($Ge_{19.4}Sb_{9.7}Se_{67.9}Ga_3$ at. %): MEF05 was also selected for SEM imaging as it displayed a reasonable degree of pattern imprinting under light microscopy and the presence of a defect towards the edge of the end face (highlighted red circle in Figure 7.18A). This defect was likely the product of particulate matter present on either the mould or fibre surface at the time of pressing. This mould appeared to have a quadrant with a high number of defects in which the lithography process failed to form the desired wells. This is presented as the groupings of bright circular regions in Figure 7.18 (showing the end face at x10 (A) and x100 (B) (nominal, at microscope) magnification). For this sample, SEM imaging was carried out with a JEOL 6490LV fitted with a tungsten electron source and a secondary electron detector. This microscope was not capable of achieving the high resolutions reached with the JEOL 7100F that was previously used resulting in the images being taken at a lower magnification.

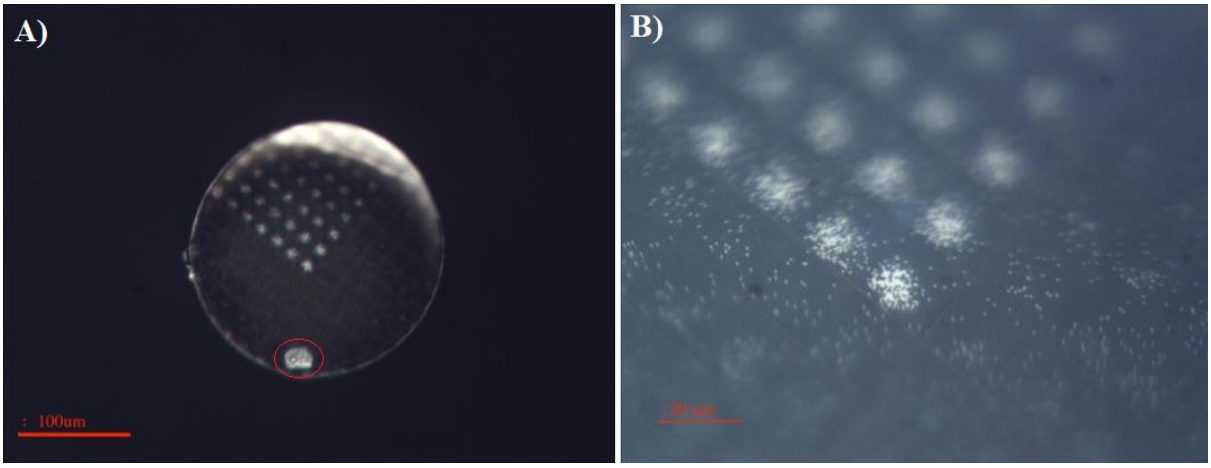


Figure 7.18 Fibre end face pressing results of MEF05. Reflection light microscopy images of unstructured fibre F101RC ($Ge_{19.4}Sb_{9.7}Se_{67.9}Ga_3$ at. %) (Vickers M17 with GXoptical detection camera GXCAM-5). A) Macro-view of fibre face with a scale bar of 100 µm. Red circle indicating damaged region of fibre tip that was not successfully imprinted. It was assumed surface debris on either the fibre or mould interfered with the pressing process. B) Light (white) regions indicative of regions of the silicon shim that was not patterned during the mould fabrication process, scale bar 20 µm.

Figure 7.19A shows an overview of the fibre end face. The quadrant division of the patterned regions is outlined by stitching errors crossing along the centre of the fibre. By comparing figure 7.18A and 7.19A, it is confirmed that the brighter regions seen under light microscopy are the result of a flat fibre surface. This is either the product of inadequate pressing procedures or a poor-quality region of the mould. As the remainder of the fibre face was successfully imprinted, it was proposed this was likely due to the (lack of) mould pattern. Figure 7.19B was taken with the sample mounted horizontally and then tilted 5 ° away from the detector. This aimed to get a better side view profile than mounting the fibres vertically and then changing the angle relative to the detector. The result of this is a side profile view taken at the point of the defect circled in Figure 7.18A. From Figure 7.19B, at a 5 ° angle, the resulting height of these features is around 320 nm.

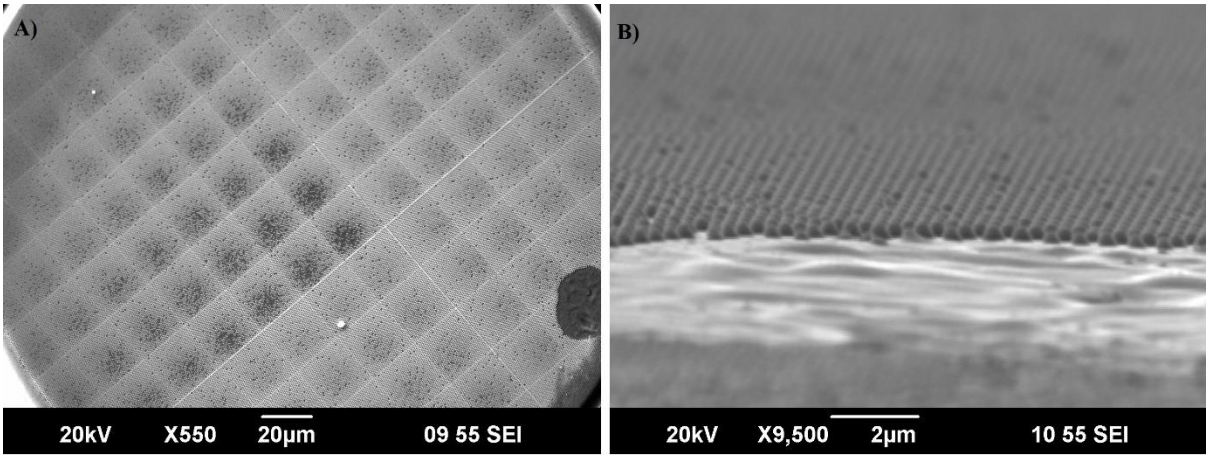


Figure 7.19 Fibre end face pressing results of MEF05. SEM micrographs of unstructured F101RC ($Ge_{19.4}Sb_{9.7}Se_{67.9}Ga_3$ at. %) MEF05 taken with JEOL 7100F. A) an overview of the fibre end face. Scale bar of 20 µm. Darker regions here are presented as the lighter "spots" in Figure 7.18. B) Sample mounted horizontally and tilted 5 ° away from the detector. This allowed a view of the feature height from the defect region. Scale bar of 2 µm.

With this fibre pressing set up, imprinting efficacy was markedly improved when compared to the bulk sample pressings. Individual features could be identified at the fibre surface, but these were still below the modelled optimum height determined in Section 7.1.

As each pressing (MEF01-MEF09) of unstructured F101RC ($Ge_{19.4}Sb_{9.7}Se_{67.9}Ga_3$ at. %) was carried out with different moulds but similar parameters, it was decided that subsequent pressings (Section 7.3) would be carried out with varying parameters. Maintaining a constant force on the fibre tip was a frequently difficult issue as application of the force was carried out by the operator manually (decreasing the height of the vertical translation stage the force sensor and strain gauge reader were attached to). This meant that pressing forces would frequently fluctuate during and between presses based on operator skill. The effects of the varying pressing forces were likely minimised by the fixed temperature values chosen. At 285 °C, lateral flow of the fibre tip was minimised as the glass supercooled melt viscosity would remain relatively high, so brief pressure fluctuations would not have drastic effects. However, this likely also hampered chalcogenide infiltration of the mould. The observed features had height values between 20-33% of the expected total height of the mould (300 nm and 500 nm features, 1500 nm proposed mould depth). By increasing the temperature, thus lowering viscosity, and increasing flow into the mould, and increasing the dwell

time following pressing, allowing more time for the viscous glass to flow into the mould, imprinting of the fibre could potentially be improved while minimising lateral flow.

The following section details the redesign of the fibre hot-pressing rig designed in Section 7.2.1 to include an motorised linear translation stage to automate the pressing forces on the fibre end face. Various pressing parameters such as temperature and force were trialled, before fibres were characterised using microscopy.

7.3 An automated, feedback loop controlled stage for optimised imprinting onto chalcogenide fibre faces.

One of the predominant issues with the fibre pressing set up described in the previous Section 7.2 was replicability. Although it was intended that pressing temperature and force were fixed, the varying forces applied during each manual, individual press, as well as between different fibre samples made it difficult to draw comparisons between the different moulds used. By newly substituting the manually controlled Z-axis translation stage with a motorised linear translation stage (LTS300, ThorLabs), applied force could be controlled and maintained electronically. With the pressing forces being consistently moderated, modification of pressing times and temperatures could be made to find the optimal pressing parameters. This work was done in collaboration with MSc student Sook Ten. Although based at University of Nottingham, Malaysia campus, Sook contributed the code controlling the translation stage and was able to operate the equipment remotely from 5000 km using Microsoft Teams software.

Section 7.3.1 details the redesign of the fibre hot-pressing rig to incorporate an automated, motorised linear translation stage, which was coded to maintain a predefined pressing force from the fibre tip onto a mould pattern. In Section 7.3.2, selected samples from these pressings are investigated using visible light microscopy and SEM.

7.3.1 Incorporation and automated control of the linear translation stage to the imprinting rig.

Within this section, the assembly of an automated, motorised, fibre hot-pressing rig is detailed. The feedback control loop coded by Dr David Furniss and MSc Student Sook Ten that automated this rig is also explained.

The linear translation stage (LTS) (LTS300, Thorlabs) was vertically mounted using a Z-axis bracket fitted to an optical breadboard plate for stability. Two additional right-angle brackets were fitted to the motorised stepper unit which allowed the fibre to traverse along the Z-axis with an accuracy of ± 5 μm of the set position. With a total height of 300 mm of stage travel, the force sensor could be moved to the distal end of the translation stage and not be adversely affected by the radiant heat from the hot plate. This also allowed easier removal and mounting of samples without the need to remove the force sensor resulting in a higher output of fibre pressings than previously possible. With heating of the force sensor no longer an issue, the aluminium heat shields were removed from the rig. The hot plate and its mountings were left identical to that seen in Figure 7.12.

A photograph of the pressing set up with the LTS is shown in Figure 7.20. The LTS could be controlled either using the physical buttons (as seen towards the top of Figure 7.20) or through the Python compatible software, Kinesis (Thorlabs).

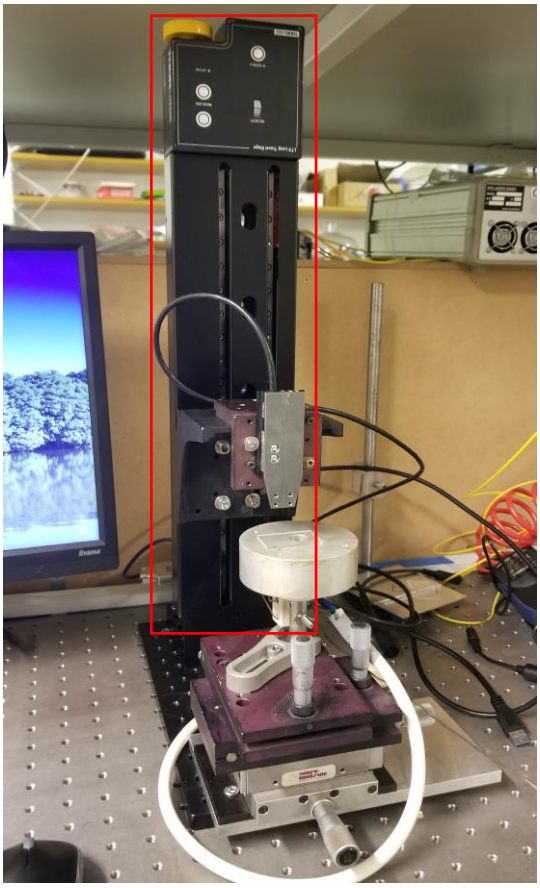


Figure 7.20 Photograph of the modified fibre hot-pressing rig used to emboss moth eye patterns onto chalcogenide fibre end faces, with the v-groove force sensor attached to the newly fitted, electronically controlled, linear translation stage (highlighted with red rectangle). For scale, the total length of the LTS300 (Thorlabs) is 500 mm.

The Kinesis software (Thorlabs) was compatible with both the LTS and the strain gauge reader. Both pieces of hardware could be controlled through individual software modules specific to the equipment. The strain gauge reader module allowed the equipment to be zeroed electronically and produce read outs in real time. The LTS module allowed the stage to be homed or moved to specific locations. It was through the additional Python code that interactions between these two pieces of hardware were coordinated. A graphical user interface (GUI) was developed using QT designer (QT company, Finland) to include the Thorlabs Kinesis modules alongside additional widgets such as a graphing interface which took inputs from both pieces of hardware (Strain gauge and LTS) to plot fibre position (a function of how far the translation stage has travelled) and applied force (N) over the pressing period. The basic feedback loop of the code is described in Figure 7.21.

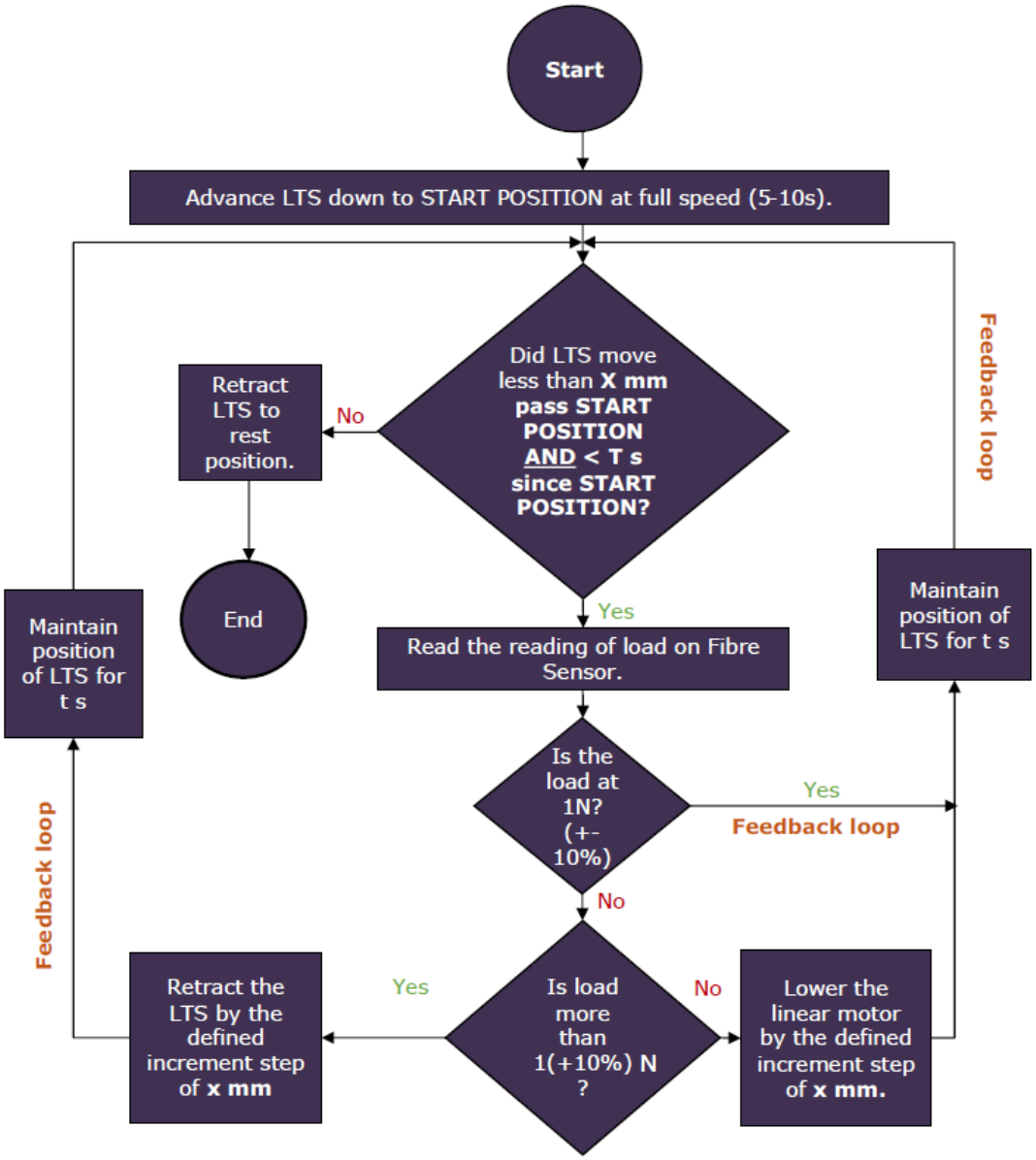


Figure 7.21 Flow chart describing the function and feedback loop of the Python™ code to control the LTS incorporated into the fibre hot-pressing rig. The system brings the fibre sample to a predefined point before slowly stepping towards the hot plate until force is measured by the strain gauge reader. Produced by MSc student Sook Ten.

The pressing process begins with LTS bringing the force sensor mounted fibre rapidly (0.5 cm per second) from the load position to a preset datum situated < 1 mm away from the heated silicon mould. From here the fibre is slowly advanced at a predefined increment step rate (e.g., 0.004 mm steps) until the force sensor records a load. The fibre continues to advance until the target load is reached. A percentage based dead band value was used to define a tolerance of force values between which no additional LTS movement would occur. This was to avoid a

constant back and forth stepping of the LTS when minor fluctuations in pressure occurred. The step was maintained for a predefined loop time (e.g., 0.03 seconds) after which the programme would recheck the applied force. If the force applied had moved out of the target set point (± dead band set %) then the stage would retract or advance an increment step appropriately to maintain the force value. This looping would continue until the defined press time had been reached.

An additional safety feature included in the GUI (graphical user interface) was "Press down max". If the LTS advanced passed a certain distance, the downward movement of the LTS would cease and the LTS would return to the load position, thus ending the process. This meant that if the fibre tip failed under load, the stage would not advance to the point where the force sensor itself was being pressed into the hot plate. The GUI also allowed for easy modifications to these pressing parameters as seen in Figure 7.22.

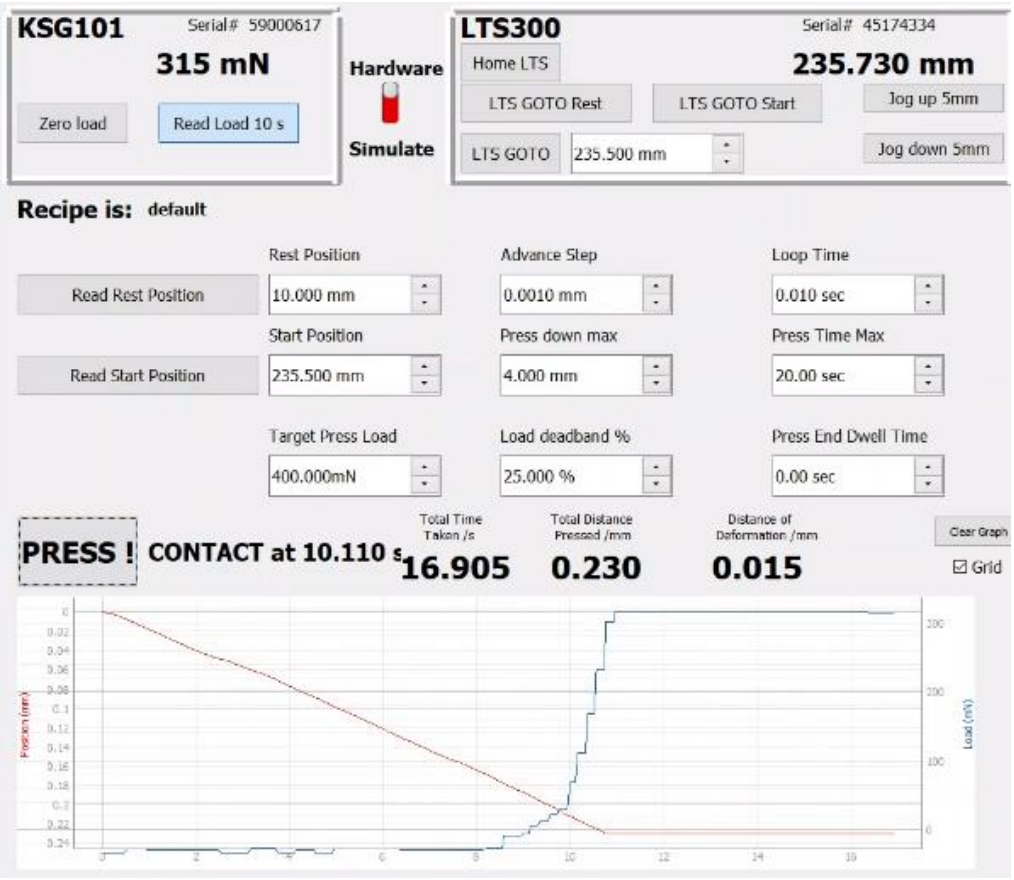


Figure 7.22 Screenshot of the GUI (graphical user interface) used to control the LTS (linear translation stage) with feedback from the force sensor and strain gauge reader. Image taken during a press, applied load and sensor position plotted graphically. Various parameters displayed in spinner boxes.

Following the incorporation of the motorised, feedback loop controlled, LTS, the following section, Section 7.3.2, details a series of pressings using the newly automated moth eye hot-pressing rig while varying temperature and pressing time. These hot-pressed fibres were then investigated using visible light microscopy and SEM.

7.3.2 Effects of varying pressing parameters of the automated, feedback loop-controlled fibre hot-pressing rig as seen through microscope characterisation of pressed $Ge_{15}As_{22}Se_{63}$ at. % (F124CODF) unstructured fibres.

This section details the series of moth eye fibre end face hot-pressings, using the newly designed, automatic feedback loop controlled hot-pressing rig, that were carried out on $Ge_{15}As_{22}Se_{63}$ at. % (F124CODF) unstructured fibres. Temperature and pressing time parameters were changed, and hot-pressed fibres were imaged under visible light microscopy and SEM to determine pressing efficacy.

Three experimental sessions were conducted in collaboration with Dr David Furniss (Mid-IR Photonics group, University of Nottingham,) in which we (Dr Furniss and the current Author) were physically present alongside the moth eye rig. MSc student Sook Ten (located in Malaysia) was present *via* Microsoft teams directly linked to the computer that controlled the rig. This allowed cleaving of the fibres, assessing the pre-press fibre face quality, mounting of the fibre, and assessing the fibre post-pressing with optical microscopy to be conducted at University of Nottingham, Nottingham campus, UK, while Sook Ten could control the pressing procedures from Malaysia.

For each session, an unstructured $Ge_{15}As_{22}Se_{63}$ at. % (F124CODF) fibre was used for pressing. $Ge_{15}As_{22}Se_{63}$ at. % had optical properties (refractive index of 2.5546 at 3.1 μm) like that which the modelling results in Section 7.1 were based on ($Ge_{10}Sb_{20}Se_{70}$ at. %, refractive index of 2.5466 at 3.1 μm [189]), had a similar T_g value (240 °C) to the previous fibre from Section 7.2 (232 °C for $Ge_{19.4}Sb_{9.7}Se_{67.9}Ga_3$ at. %, F101RC), had a similar diameter (210 μm (± 30 μm) of F124CODF, to 230 μm (± 10 μm) of F101RC (thus required pressing force is similar), and was readily available in the laboratory, as the previous stock of unstructured F101RC $Ge_{19.4}Sb_{9.7}Se_{67.9}Ga_3$ at. % had been used.

The first two experimental laboratory sessions were used to investigate what the optimal parameters for fibre imprinting were in order to ensure that the pressing movement was steady, and the loop was adequately responding to feed back. These parameters are noted under Table 7.3. During these initial two sessions, it was also found that with this set up, fibres were prone to failure when applying loads beyond 400 mN. The third session consisted of 8 pressings of $Ge_{15}As_{22}Se_{63}$ at. % (F124CODF) unstructured fibres (AMEF001-AMEF008) with variations to applied load, temperature, and press time. The 1550NM(c) shim was used for each pressing of this series, although different mould patterns on this shim were trialled (note the multiple 1mm x 1mm patterns on Figure 7.6). The suffix "AMEF" used as an identifier meaning "Automated Moth Eye Fibre". The parameters used for each pressing of unstructured 210 µm (± 30 µm) diameter F124CODF $Ge_{15}As_{22}Se_{63}$ at. % to AMEF001-008 are in Table 7.3.

Post-pressing, the fibre tip was imaged with visible light microscopy (Vickers M17 with GXoptical detection camera GXCAM-5) from a top-down view, in reflection, to observe the imprinted features and then mounted horizontally to image the characteristic elephant's foot shape, at the fibre end face, to get a further indication of lateral flow of the supercooled glass melt at the fibre tip. From these microscopy images, two samples (AMEF002 and AMEF007) were identified as the potential "best presses" despite debris interfering with the pressing in both cases (see Figure 7.23A, B and Figure 7.23C, D, respectively). At x10 magnification, nominally at the microscope, the moth eye patterning on these samples, particularly the stitching errors, were clearly visible and this was taken as a sign of good press quality as the patterning on the mould had replicated on the fibre tip.

From the side profile (see Figure 7.23A and C), the elephant's foot material distribution on AMEF002 and AMEF007 (F124CODF, $Ge_{15}As_{22}Se_{63}$ at. %) was visually prominent but not excessive, compared to, for example, Figure 7.14D in Section 7.2.2 in which the fibre end face was pressed to a disc-like shape. This prominent, but not drastic material distribution as seen in AMEF002 and AMEF007 was considered an indicator of press parameter efficacy as it demonstrated temperature and force values were sufficient for supercooled glass melt shaping, without causing excess lateral flow at the tip.

Table 7.4 Pressing parameters used for AMEF001-AMEF008 (unstructured 210 µm (± 30 µm) diameter F124CODF fibre, $Ge_{15}As_{22}Se_{63}$ at. %) Values of parameters under this Table were fixed for each press.

Press code	AMEF001	AMEF002	AMEF003	AMEF004	AMEF005	AMEF006	AMEF007	AMEF008
Load /(mN)	400	400	400	300	300	400	400	400
Temperature /(°C)	310	310	305	305	300	300	300	290
Press time /(s)	15	15	15	25	25	25	25	35

Advance Step= 0.002 mm, Press Down Max= 4 mm, Load Deadband= 18 %, Loop Time= 0.01 s, Press End Dwell Time= 1.00 s.

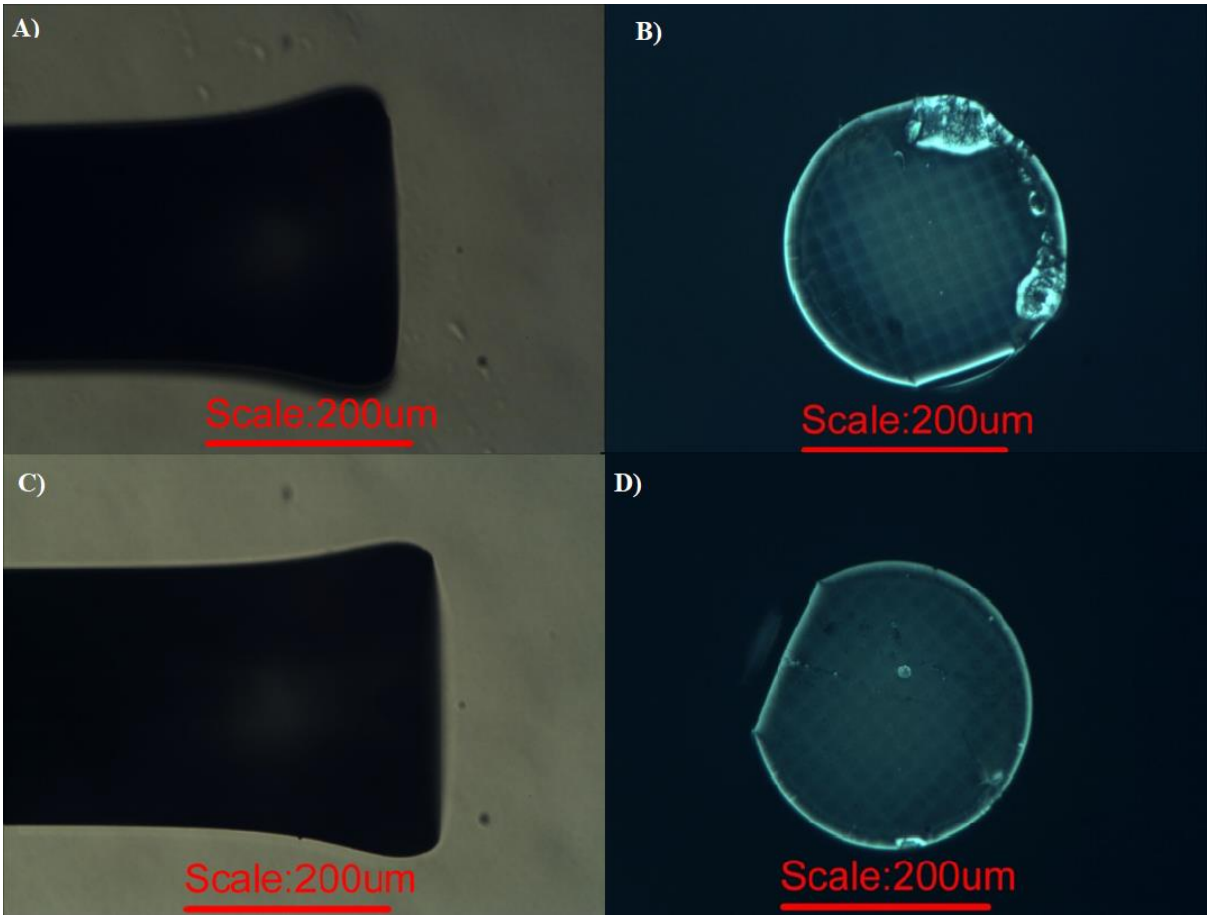


Figure 7.23 Fibre end face pressing results of unstructured 210 µm (± 30 µm) diameter F124CODF fibre, $Ge_{15}As_{22}Se_{63}$ at. %. Optical micrograps taken in the visible light in reflection of AMEF002 (A and B) and AMEF007 (C and D) in both a vertical and horizontal mounting. Scale bar of 200 µm used for each image. Stitching errors of the silicon mould are clearly visible on both vertical images indicating pattern imprinting.

Unstructured F124CODF fibre, $Ge_{15}As_{22}Se_{63}$ at. % hot-pressed samples: AMEF002 and AMEF007 were mounted vertically against an aluminium block, as described in Section 3.3.3, and a 2 nm thick iridium coating (thickness calculated by the coater, Q150R ES, QuorumTech). Iridium was used as a coating due to its fine grain size (1-2 nm compared to 5-10 nm for gold) and high secondary electron yield (the electrons used to image topography). This coating and a JEOL 7100F was used by Dr Richard Cousins to obtain high resolution images of the imprinted structures. Figure 7.24 shows high magnification images of features from both AMEF002 (A) and AMEF007 (B). AMEF002, despite its higher pressing temperature (310 °C for AMEF002, compared to 300 °C for AMEF007), exhibited feature heights shorter than that seen in AMEF007 (349 nm compared to 516 and 434 nm). These heights are comparable to what was observed on the manually

pressed fibres as reported in Section 7.2.3 (~500 nm height). The pressing time for AMEF007, however, was 66% longer than that of AMEF002 (25 seconds compared to 15 seconds). At the temperatures used for these pressings (310 °C for AMEF002, compared to 300 °C for AMEF007), it is likely that the extra 10 °C only provided a marginal decrease in viscosity of the supercooled glass melt and so increase the pressing time beneficially produced a much more pronounced effect on mould infiltration.

In figure 7.24B, the central features of AMEF007 appear to taper to a much finer tip than what was seen in other presses (Figure 7.24A for AMEF002 and Figure 7.19B for MEF05 in Section 7.2.3). It is possible that with this particular mould pattern on the 1550NM(c) shim, feature depth was shallower than what was predicted by the mould manufacturer (1.5 µm feature depth, see Section 7.1.2) and the supercooled glass melt in this pressing was getting close to total infiltration of the mould. To recall from Section 7.1.2, the mould patterns produced had holes that tapered to a final diameter of 120 nm, 160 nm, or 210 nm, but the manufacturer did not specify the final diameter individual patterns taper to. In the case of Figure 7.24B, the individual feature annotated with a height of 434 nm has an approximate tip width of ~225 nm.

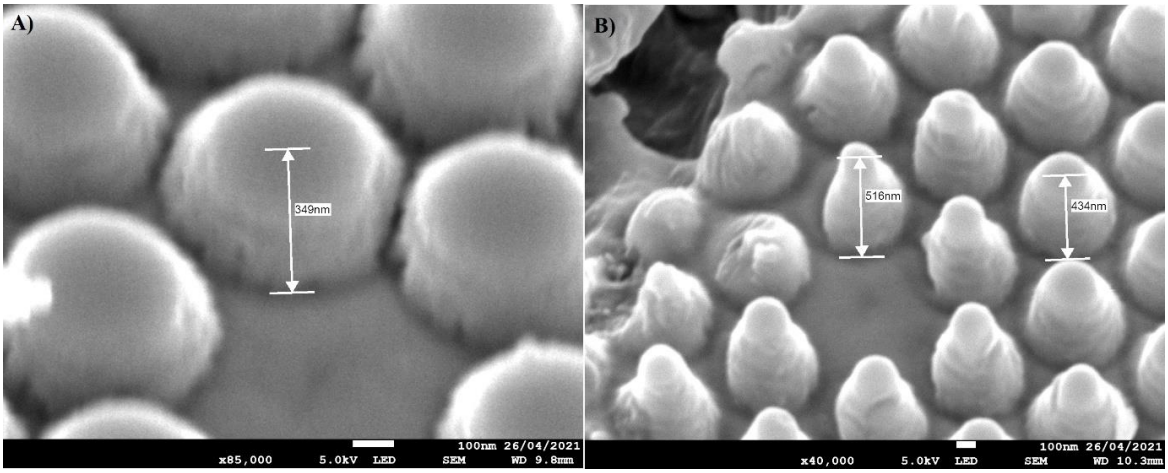


Figure 7.24 Fibre end face pressing results of unstructured 210 µm (± 30 µm) diameter F124CODF fibre, $Ge_{15}As_{22}Se_{63}$ at. %. SEM micrograph of A) AMEF002 with a scale bar of 100 nm and B) AMEF007 also with a scale bar of 100 nm. Iridium coated samples in JEOL 7100F. Parameters used for individual presses in Table 7.3. Measured feature heights of individual features are annotated.

From Figure 7.24A and B, the features measured in unstructured fibre F124CODF $Ge_{15}As_{22}Se_{63}$ at. % samples: AMEF002 and AMEF007 are smaller in height (maximum feature height of 516 nm recorded in this work) when compared to those reported in literature, as follows. Lotz *et al*. [225] hot-pressed fibre end faces with truncated, ellipsoidal, hexagonally packed moth eye features with a feature height of 1550 ± 25 nm and pitch of 900 nm which provided + $\Delta T \geq 12$ % over the 6.8–8.7 μm region on hot pressed fibre tips [225]. Lotz *et al.* [225] also found that a reduction to 815 ± 15 nm height, 900 nm pitch provided a similar increase in % of light transmitted, but at a shorter wavelength range (+ $\Delta T \geq 11$ % over 2.8–4.1 μm) [225]. In another report from Lotz *et al.* [233], hexagonally packed "secant ogive" moth eye features were measured at a maximum height of 2093 nm on a bulk As_2Se_3 window (approximately four times the height of the 516 nm maximum feature height reported in this current work). This 2093 nm in height feature provided a + $\Delta T \geq$ 11.93 % over the 3.3–12 μm region [233]. Due to time constraints, no reflectance or transmission measurements were made on samples AMEF001-008 (F124CODF fibre, $Ge_{15}As_{22}Se_{63}$ at. %).

At this stage, no conclusions could be made on the efficacy of the moulds designed. Further work is needed to attempt to optimise the mould pressing parameters to achieve better patterning on the fibre tip. These pressing parameters then need to be validated through either transmission or reflectance measurements. However, the standardisation of pressings facilitated by the automated hot pressing rig is a step forward to achieving consistent antireflective patterning on chalcogenide fibres.

7.4 Summary of Chapter 7

Chapter 7 details the development and optimisation of a hot nanoimprinting rig capable of embossing chalcogenide bulk glasses and fibres with a pattern that was modelled to be antireflective in the near-infrared (1.55 μm) region. Patterning of bulk glasses was not successful with the hot pressing set up used. A nanoimprinting rig designed for fibre samples controlled through an automated feedback loop of applied force provided the best results in terms of pattern transfer to a fibre face.

- FDTD (Finite-Difference Time-Domain) modelling of conical moth eye features found optimal antireflection (2 % reflectance) over a 1-5 μm wavelength with a diameter:pitch ratio of 0.9, height of 1.6 μm, and pitch between 0.5 – 1.5 μm.

- FDTD modelling of paraboloid moth eye features found optimal antireflection (1-2 % reflectance) over 1-2.5 μm and 3.5-5 μm μm wavelength with a diameter:pitch ratio of 0.9, height and pitch of 1.2 μm. This was the best antireflection performance modelled in this work, with this structure model exhibiting lowest reflectance.

- FDTD modelling of cylindrical moth eye features found optimal antireflection (8 % reflectance) over a 3 - 5 μm wavelength with a diameter:pitch ratio of 0.5, height of 1.4 μm, and pitch between 2 – 3 μm.

- A silicon wafer was subject to EBL (electron beam lithography) and dry plasma etching to produce a mould with hexagonal close-packed paraboloidal patterns with pitches of 600 nm and 550 nm initial hole diameters. Three variants were produced in which these holes tapered to a final diameter of 120 nm, 160 nm, or 210 nm. Depth was assumed to be around 1.5 μm.

- Hot pressing of bulk chalcogenide samples (M182HAP, $Ge_{20}Sb_{10}Se_{70}$ at. %) with the silicon moulds/shims proved unsuccessful. The pressing mechanism encouraged lateral flow of the supercooled glass melt movement, as opposed to axial flow into the wells in the mould.

- A manually controlled, fibre face hot embossing rig was designed. Pattern transfer, as imaged *via* SEM, was improved when compared to the bulk glass pressings. Feature heights of around ~500 nm were measured on fibre faces of unstructured F101RC ($Ge_{19.4}Sb_{9.7}Se_{67.9}Ga_3$ at. %)

- To improve replicability of hot pressing of fibres, an automated, feedback loop-controlled fibre pressing rig was designed. This successfully maintained pre-set applied force values *via* the use of a computer controlled LTS (linear translation stage) to F124CODF unstructured fibre ($Ge_{15}As_{22}Se_{63}$ at. %). Pattern transfer was comparable to the manually controlled system showing measured features with heights between 349 nm and 516 nm, with more pressing experiments needed to determine reliability.

8. Conclusions and future work

Conclusions drawn from the work presented in chapters 4-7 are discussed in section 8.1. Overall conclusions from the work are discussed in Section 8.2. Further avenues of research that could be investigated as a follow up to this work are discussed in section 8.3.

8.1 Conclusions

8.1.1 Chapter 4 - Development of a novel antimony-based chalcogenide glass host composition with Sm^{3+} and Dy^{3+} doping

- Chapter 4 details the development of the $Ge_{19.4}Sb_{9.7}Se_{67.9}Ga_3$ at. % host glass composition which can be fibre drawn after rare earth doping up to 1000 ppmw. This was developed after a failure to draw a 1000 ppmw Sm^{3+} doped $Ge_{20}Sb_{10}Se_{65}Ga_5$ at. % fibre (M226RERC).
- The poor drawability of $Ge_{20}Sb_{10}Se_{65}Ga_5$ at. % fibre (M226RERC) was paralleled with the poor drawability of $Ge_{25}Sb_{10}Se_{65}$ at. % documented in Parnell *et al.* [54]. This was proposed to be a result of the formation of monoclinic $GeSe_2$ due to the high Ge(+Ga) content in both compositions.
- An undoped preform of $Ge_{19.4}Sb_{9.7}Se_{67.9}Ga_3$ at. % (M235RC) (DSC T_g measured at 232 ±1 °C) was successfully fibre drawn exhibiting its lowest optical losses of 1.17 dB/m at 6.19 µm (F101RERC).
- A 1000 ppmw Sm^{3+} doped $Ge_{19.4}Sb_{9.7}Se_{67.9}Ga_3$ at. % preform was produced (M227RERC). A bulk glass sample piece with 2.74 mm thickness was polished to a 1 µm finish and analysed using FTIR. The electronic absorptions of Sm^{3+} were labelled in good agreement with those previously reported in literature in similar host glasses (Figure 4.5).
- The remainder of the 1000 ppmw Sm^{3+} doped $Ge_{19.4}Sb_{9.7}Se_{67.9}Ga_3$ at. % preform was propylamine etched and then successfully fibre drawn (F099RERC) with no observable skin effects that were present on the 1000 ppmw Sm^{3+} doped $Ge_{20}Sb_{10}Se_{65}Ga_5$ at. % fibre. The resulting fibre F099RERC exhibited lowest losses of 2.15 dB/m at 6.04 µm.

- 1000 ppmw Sm^{3+} doped $Ge_{19.4}Sb_{9.7}Se_{67.9}Ga_3$ at. % (F099RERC) fibre mid-IR photoluminescence when excited with 350 mW of 1.3 µm or 300 mW of 1.47 µm pump sources was measured. Both pump schemes observed an emission centred around 3.75 µm, spanning 3.25-4.5 µm, which was attributed to the $^6H_{13/2} \rightarrow {}^6H_{9/2}$ radiative transition. Both pump schemes also observed an emission centred around 7.25 µm, spanning 6-9 µm, which was attributed to the $^6H_{13/2} \rightarrow {}^6H_{11/2}$ and $^6H_{11/2} \rightarrow {}^6H_{9/2}$ radiative transitions.
- Using a 1.47 µm pump source to excite 1000 ppmw Sm^{3+} doped $Ge_{19.4}Sb_{9.7}Se_{67.9}Ga_3$ at. % fibre (F099RERC), photoluminescent lifetimes of the emission centred at 3.75 µm were measured at an average of 0.101 ms. Lifetimes of the emission centred at 7.25 µm provided a rounded average of 0.1 ms.
- 1000 ppmw Sm^{3+} doped $Ge_{19.4}Sb_{9.7}Se_{67.9}Ga_3$ at. % (F099RERC) fibre near-infrared photoluminescence when excited with 300 mW of 1.47 µm pump sources was also measured. An emission centred around 2.7 µm, spanning 2.25-3.2 µm, was attributed to Sm^{3+}: $^6H_{13/2} \rightarrow {}^6H_{7/2}$, $^6H_{11/2} \rightarrow {}^6H_{5/2}$, ($^6F_{1/2}$, $^6F_{3/2}$, $^6H_{15/2}$) $\rightarrow {}^6H_{9/2}$.
- A 1000 ppmw Dy^{3+} doped $Ge_{19.4}Sb_{9.7}Se_{67.9}Ga_3$ at. % preform (M236RERC) was fabricated and drawn to fibre (F102RERC), this fibre failed to transmit sufficient mid-IR light to perform a fibre loss measurement.
- A 500 ppmw Dy^{3+} doped $Ge_{19.4}Sb_{9.7}Se_{67.9}Ga_3$ at. % preform (M240RERC) was fabricated and drawn to fibre (F104RERC), the lowest optical loss in this fibre was measured around 3.2 dB/m at 6.63 µm.

8.1.2 Chapter 5 - Development of antimony-based selenide chalcogenide cladding glass for rare earth ion doped, small-core fibre.

- Chapter 5 focuses on the development of a suitable cladding glass for the $Ge_{19.4}Sb_{9.7}Se_{67.9}Ga_3$ at. % host glass developed in Chapter 4 with the aim to produce a small core, step-index fibre.
- A $Ge_{19.4}Sb_{9.7}Se_{65}Ga_3S_{2.9}$ at. % cladding glass (M237RC) was designed based on the selenium-for-sulfur substitution that had seen success in previous work in arsenic based cladding compositions from the Mid-IR Photonics Group, University of Nottingham. Although the T_g value of this

new cladding composition matched that of the host glass designed in Chapter 4 (T_g of ~ 232 °C), this new cladding glass was not suitable for fibre drawing.

- A series of glasses with the compositions $Ge_{19.4}Sb_{9.7}Ga_{1-2}Se_{67.9-(Ga+S)}S_{1-3}$ at. % were fabricated (see Table 5.1 for compositions and codes). An additional composition not following this formula, $Ge_{21}Sb_{10}Se_{69}$ at. % (M267RC), was also made. The six glasses in this series were characterised *via* DSC, SEM-EDX, mid-IR VASE. Out of this series of glasses only two compositions, from series (ii), $Ge_{21}Sb_{10}Se_{69}$ at. % (M267RC) and $Ge_{19.4}Sb_{9.7}Se_{65.9}Ga_3S_2$ at. % (M266RC), had a suitable T_g match of 232 ± 10 °C with the core $Ge_{19.4}Sb_{9.7}Se_{67.9}Ga_3$ at. % (M240RERC).
- The Series (i) glass M262RC ($Ge_{20}Sb_{10}Se_{68}S_2$ at. %, T_g 217 °C) T_g change was in line with predictions, as it was anticipated a decrease in S at. % would lead to a decrease in T_g compared to the Parnell composition ($Ge_{20}Sb_{10}Se_{67}$ at. %, T_g 224 °C)[193]. The other Series (i) glasses, M263RC ($Ge_{19.4}Sb_{9.7}Se_{67.9}Ga_1S_2$ at. %) and M264RC ($Ge_{19.4}Sb_{9.7}Se_{68.9}Ga_1S_1$ at. %), featuring the addition of 1 at. % gallium, was expected to raise the T_g comparative to the Parnell composition ($Ge_{20}Sb_{10}Se_{70}$, T_g 214 °C) [193], but unexpectedly measured lowered T_g values of 209 °C and 210 °C, respectively.
- Series (ii) glasses M265RC ($Ge_{19.4}Sb_{9.7}Se_{66.9}Ga_2S_2$ at. %) and M266RC ($Ge_{19.4}Sb_{9.7}Se_{65.9}Ga_3S_2$ at. %), were based on Series (i) M263RC ($Ge_{19.4}Sb_{9.7}Se_{67.9}Ga_1S_2$ at. %, T_g 209 °C) with increasing Ga content in substitute for Se. This led to an expected rise in T_g from M263RC T_g 209 °C to 220 °C and 229 °C for M265RC and M266RC, respectively. M267RC ($Ge_{21}Sb_{10}Se_{69}$ at. %, T_g 227 °C) exhibited an anticipated T_g increase comparative to the Parnell composition ($Ge_{20}Sb_{10}Se_{70}$, T_g 214 °C) [193].
- All glasses from exploratory cladding glass series (i) and (ii) (Table 5.2) were investigated using VASE (Variable Angle Spectroscopic Ellipsometry). Transmission measurements were first taken, before the 1µm polished, hot-pressed samples were roughened (Section 5.3.4) and reflectance measurements were taken from all samples listed in Table 5.2.

- Ellipsometry models were developed to fit the measured ellipsometry data using CompleteEase (Woollam, USA), the companion software for the IR-VASE. A GenOsc® layer was used as the basis for each model.
- Initial RI model designs involved the fitting of Gaussian oscillators to absorption peaks measured during transmission measurements. Fitting many iterations of this model design to M240RERC (500 ppmw Dy^{3+} $Ge_{19.4}Sb_{9.7}Se_{67.9}Ga_3$ at. %) ellipsometry data yielded bad fittings, and so the concept of fitting multiple Gaussian oscillators was retired.
- A three-oscillator model consisting of one Sellmeier centred close to the optical bandgap, one Sellmeier centred close to the vibrational band fundamental absorption, and a Gaussian oscillator assigned close to the intrinsic Se-Se absorption was then trialled. A surface roughness function intended to represent any thin surface oxide layers on the samples was also incorporated into the three-oscillator model. This model provided a good fit to measured data for all exploratory cladding glasses (Series (i) and (ii), Table 5.2) investigated.
- All the exploratory cladding glasses (Table 5.2), with the exception of M264RC ($Ge_{19.4}Sb_{9.7}Se_{68.9}Ga_1S_1$ at. %), were modelled to have RI values below that of M240RERC ($Ge_{19.4}Sb_{9.7}Se_{67.9}Ga_3$ at. %) (Table 5.2 for values), indicating they could be used to sufficiently guide light in a M240RERC ($Ge_{19.4}Sb_{9.7}Se_{67.9}Ga_3$ at. %) core step-index fibre. M267RC ($Ge_{21}Sb_{10}Se_{69}$ at. %) was ultimately chosen as a cladding glass for M240RERC ($Ge_{19.4}Sb_{9.7}Se_{67.9}Ga_3$ at. %) due to it meeting the T_g 232 ± 10 °C criteria of the core glass M240RERC, its ease of fabrication, and its speculated increased devitrification resistance when compared to M266RC ($Ge_{19.4}Sb_{9.7}Se_{65.9}Ga_3S_2$ at. %).
- Further regarding $Ge_{21}Sb_{10}Se_{69}$ at. % (M267RC), The omission of gallium removed a potential source of oxide impurities and corresponding crystal structures (α-Ga_2Se_3) from the composition. This composition also avoided the need to purify, extract, and batch selenium into a separate ampoule containing heat treated sulfur.

8.1.3 Chapter 6 - Fabrication and characterisation of antimony-based, arsenic core /antimony cladding hybrid, and high purity arsenic-based step index fibres resulting in the first recorded chalcogenide fibre lasing.

- Chapter 6 covers the fabrication and characterisation of four fibres. The first (F129RERC) is a dysprosium doped, antimony based small core fibre made with the antimony core ($Ge_{19.4}Sb_{9.7}Se_{67.9}Ga_3$ at. %) and cladding ($Ge_{21}Sb_{10}Se_{69}$ at. %) composition developed in chapters 4 and 5, respectively. The second (F130RERC), a $Ge_{15}As_{21}Se_{63}Ga_1$ at. % + 500 ppmw Ce^{3+} doped core/ $Ge_{21}Sb_{10}Se_{69}$ at. % cladding fibre was one of the first demonstrations of mid-IR fibre lasing in a chalcogenide glass. The third and fourth (F127RERC, F128RERC), $Ge_{15}As_{21}Se_{63}Ga_1$ at. % core glasses doped with either 500 ppmw Dy foil or 250 ppmw distilled $DyCl_3$ was then clad with $Ge_{16.5}As_{16}Se_{61.5}Ga_3S_3$ at. %.
- SEM-EDX characterisation of F129RERC was difficult due to the closely matched average atomic mass of the two glasses. No photoluminescence study was performed.
- F130RERC (500 ppmw Ce^{3+} doped, undistilled core with lowest losses of 2.16 dB/m at 6.6-7.1 µm) was optically pumped at 4.15 µm (NA: 0.4704), three laser peaks at 5.12 µm (NA: 0.4757), 5.17 µm (NA: 0.4759), and 5.28 (NA: 0.4764) were observed. Power output was below the sensitivity limit of available power meters 100 µW. Cavity fall time was found to be 2.5 µs at 5.127 µm.
- With increasing pump power into F130RERC, total area under peak increased nearly linearly with power. The 5.13 µm emission peak continued to increase at higher pump powers with the 5.17 and 5.28 µm peak decreasing.
- The emissions were attributed to Ce^{3+}: $^2F_{7/2} \rightarrow {}^2F_{5/2}$. The various emissions between one radiative transition were attributed to Stark splitting in both energy levels.
- A novel, silica vessel open distillation of anhydrous $DyCl_3$ was successfully carried out. Subjecting $DyCl_3$ to 850 °C for 0.5 hours at 10^{-3} Pa yielded two forms of distilled $DyCl_3$. Large colourless crystals and a fine colourless powder which condensed at different sections of the distillation rig. These

distilled large colourless crystals were shown to have lower levels of Al, Yb, and Zn contaminant levels when compared to undistilled $DyCl_3$: Al from 0.567 at. % undistilled to 0.4 at. % distilled. Yb from 0.823 at. % undistilled to 0.28 at. % distilled. Zn from 0.483 at. % undistilled to 0.11 at. % distilled.

- A $Ge_{15}As_{21}Se_{63}Ga_1$ at. % host glass was distilled in the presence of Al (oxygen getter) and $TeCl_4$ (hydrogen getter). This distillate was divided into two and batched with 250 ppmw distilled $DyCl_3$ in one portion (M286RERC, F126RERC), and 500 ppmw of mechanically exfoliated (using germanium) dysprosium foil (M285RERC, F125RERC) in the other.
- F125RERC ($Ge_{15}As_{21}Se_{63}Ga_1$ at. % + 500 ppmw Dy foil) and F126RERC ($Ge_{15}As_{21}Se_{63}Ga_1$ at. % + 250 ppmw $DyCl_3$) were then drawn to small core, step-index fibres (F127RERC and F128RERC, respectively, with a cladding of E092RC ($Ge_{16.5}As_{16}Se_{61.5}Ga_1S_3$ at. %) and characterised *via* SEM.
- F125RERC (Distilled $Ge_{15}As_{21}Se_{63}Ga_1$ at. % + 500 ppmw Dy foil) measured its lowest loss of 2.07 dB/m at 6.13 µm. F126RERC (Distilled $Ge_{15}As_{21}Se_{63}Ga_1$ at. % + 250 ppmw distilled $DyCl_3$) measured its lowest loss of 4.86 dB/m at 6.085 µm.
- F125RERC (Distilled $Ge_{15}As_{21}Se_{63}Ga_1$ at. % + 500 ppmw Dy foil) Dy^{3+} photoluminescence was investigated in both fibre and powdered sample form utilising a novel powder sample holder. A 1.7 µm pump laser was used to observe the Dy^{3+}: $^6H_{13/2} \rightarrow {}^6H_{15/2}$ emission which emitted over the 2.7-3.4 µm region and Dy^{3+}:$^6H_{11/2} \rightarrow {}^6H_{13/2}$ which emitted over the 3.8-5.1 µm region. There were no notable discrepancies between sample form.
- Photoluminescent lifetimes between the two F125RERC sample forms (fibre and powder) also had negligible differences with $^6H_{13/2} \rightarrow {}^6H_{15/2}$, τ_{rad} = 5.21 ms. $^6H_{11/2} \rightarrow {}^6H_{13/2}$, τ_{rad} = 1.75 ms in F125RERC fibre form and $^6H_{13/2} \rightarrow {}^6H_{15/2}$, τ_{rad} = 5.15 ms. $^6H_{11/2} \rightarrow {}^6H_{13/2}$, τ_{rad} = 1.71 ms in F125RERC powder form.

8.1.4 Chapter 7 - Antireflective moth eye nanoimprinting on chalcogenide fibre faces.

- Chapter 7 describes the development of an infrared antireflective "moth eye" pattern mould and the subsequent trials to determine the optimal parameters to hot emboss this pattern onto a chalcogenide fibre face.
- FDTD (Finite-Difference Time-Domain) modelling was used to determine an optimal antireflective moth eye structure operating at 1.55 µm, a prospective pump wavelength for Pr^{3+} doped fibres. Close hexagonally packed conical, paraboloidal, and cylindrical geometries were modelled at a range of different heights, pitches, and fill factors (diameter:pitch ratio).
- Paraboloidal features with a height of 1.2 µm, a d:p value of 0.9, and a pitch of 1.2 µm were found to provide the strongest antireflective effects over the 1-5 µm wavelength range. Silicon moulds with a hexagonal close-packed paraboloidal pattern with a pitch of 600 nm and 550 nm initial hole diameter which tapered to either a 120 nm, 160 nm, or 210 nm final diameter with a depth ~1.5 µm were produced.
- Attempts to imprint this structure onto bulk glass samples $Ge_{20}Sb_{10}Se_{70}$ at. % (M182HAP) yielded poor results. Upon application of force the bulk glass discs began to disperse across the mould with minimal glass infiltration into the mould.
- A fibre face hot pressing rig was designed in which manual application of force to a fibre tip *via* a translation stage was monitored using a v-groove force sensor. The silicon mould was situated on top of a hot plate set to the desired pressing temperature and the fibre face F101RC ($Ge_{19.4}Sb_{9.7}Se_{67.9}Ga_3$ at. %) was brought down to the heated mould. This method yielded better pressings than the bulk sample in terms of mould replication on the fibre tip, as validated with SEM, but there was a noted difficulty with maintaining the correct amount of force throughout the pressing procedure.
- An automated, feedback loop controlled hot pressing rig for fibre faces was then designed. This utilised a computer-controlled translation stage which would lower or raise the fibre, F124CODF ($Ge_{15}As_{22}Se_{63}$ at. %), based on real time feedback from the v-groove force sensor. This eliminated pressing force discrepancies introduced by operator ability and aimed to improve reproducibility.

- A range of pressing times and temperatures were then investigated in search of optimal pressing parameters to replicate the mould pattern onto the fibre face.

8.2 Overall conclusions of the work

As stated in the introduction (Section 1), the overall aim of this Project was to develop new rare earth ion doped chalcogenide glass compositions capable of facilitating mid-IR fibre lasing, with the intention to develop a laser light source emitting at biologically relevant (protein and water absorption) wavelengths such as 6.1 µm or 6.45 µm [8,26]. This was an ambitious aim in the absence of any previous reporting of mid-IR wavelength fibre lasing in rare earth ion doped chalcogenide glasses.

A novel antimony-based, rare earth ion dopable chalcogenide core glass composition was designed ($Ge_{19.4}Sb_{9.7}Se_{67.9}Ga_3$ at. %) as a lower phonon energy, cytocompatible alternative to arsenic-based fibres. This core glass composition could be doped with up to 1000 ppmw Sm^{3+} and could be drawn to low optical loss fibre (2.15 dB/m at 6.04 µm, F099RERC) using the fibre drawing set up used by the Mid-Infrared Photonics Group, University of Nottingham, UK, without requiring distillation. This antimony-based core glass exhibited photoluminescence (PL) emissions out to 9 µm, beating the previous long wavelength PL record of 6 µm recorded by the Mid-Infrared Photonics Group in a Pr^{3+} doped arsenic-based fibre (Sakr *et al.* [86,94]). This novel composition ($Ge_{19.4}Sb_{9.7}Se_{67.9}Ga_3$ at. %) was also successfully doped with 500 ppmw Dy^{3+} and also drawn to low loss fibre 3.2 dB/m at 6.63 µm (F104RERC).

In pursuit of mid-IR chalcogenide fibre lasing, a suitable cladding glass for the newly developed core glass ($Ge_{19.4}Sb_{9.7}Se_{67.9}Ga_3$ at. %) composition was required in order to make a small-core, step-index fibre. A series of glasses were fabricated and characterised using DSC (differential scanning calorimetry) and mid-IR VASE (variable angle scanning ellipsometry). During this mid-IR VASE characterisation, a "three-oscillator" model (Section 5.3.4.2) was developed to fit the results of the spectroscopic ellipsometry measurements. This "three-oscillator" model could

successfully be translated to fit both antimony- and arsenic-based glass compositions. Through this investigation, an antimony-based cladding glass with suitable optical and thermal properties to match those of the novel core glass, $Ge_{19.4}Sb_{9.7}Se_{67.9}Ga_3$ at. %, was identified ($Ge_{21}Sb_{10}Se_{69}$ at. %, M267RC and M287RC). This $Ge_{21}Sb_{10}Se_{69}$ at. % cladding was successfully drawn to small-core, step-index fibre with both an antimony-based core glass (F129RERC, $Ge_{19.4}Sb_{9.7}Se_{67.9}Ga_3$ at. % + 500 ppmw Dy foil core / $Ge_{21}Sb_{10}Se_{69}$ at. % cladding) and an arsenic-based core glass (F130RERC, $Ge_{15}As_{21}Se_{63}Ga_1$ at. % + 500 ppmw Ce^{3+} doped core / $Ge_{21}Sb_{10}Se_{69}$ at. % cladding).

Investigations conducted on these above mentioned novel chalcogenide glass fibre compositions designed during this Project, led to the first recorded instance of CW mid-IR fibre lasing, with emissions measured at 5.13 µm, 5.17 µm, and 5.28 µm from a rare earth ion (Ce^{3+}) doped chalcogenide glass host (Section 6.2.3.3) F130RERC ($Ge_{15}As_{21}Se_{63}Ga_1$ at. % + 500 ppmw Ce^{3+} doped core / $Ge_{21}Sb_{10}Se_{69}$ at. % cladding) [15].

Additionally, a biomimetic, antireflective (AR) moth eye pattern was iteratively designed, and an automated hot-pressing rig was assembled to hot-emboss the antireflective pattern to a supercooled glass melt fibre end face. Optimal pressing parameters were investigated with continually improved pattern transfer observed throughout the investigation.

8.3 Future work

The realisation of mid-IR chalcogenide fibre lasing in Ce^{3+} doped fibre was an important step forward to the continuing development of rare earth doped fibres as a source of mid-IR light. Developments in host glass compositions, such as with the antimony glasses, have recorded longer wavelength photoluminescent emissions than what has previously been seen in arsenic glasses, but further progress needs to be made on two fronts: Increasing lasing output power, and accessing additional wavelengths such as the surgically relevant wavelengths 6.1 µm or 6.45 µm.

8.3.1 Further investigations of doped core glasses.

Most of the rare earth doped compositions investigated by the Mid-IR Photonics group, University of Nottingham, UK, incorporate gallium as the rare earth ion solubilising agent. Gallium does not undergo any thermal or chemical pre-purification and has an observable skin layer, assumed to be gallium oxide (β Ga_2O_3) on its surface with precautions taken to mechanically omit this layer from any batched material. Oxide based extrinsic impurity bands, such as Ge-O at ~8 μm, are commonly muted in optical loss spectra of rare earth ion doped chalcogenide glasses when compared to chalcogenide glasses that are absent of rare earth doping. Considering these muted absorption bands, alongside the identification of rare earth oxides in doped arsenic-based glasses (Tang *et al.* [53,133], it can be speculated that rare earth ion dopants are gettering oxide impurities introduced into the chalcogenide glass during glass melting. At best, this is putting a proportion of the population of rare earth ions into a higher phonon energy environment which is not conducive to facilitating mid-IR radiative transitions, and at worse leading to the formation of crystal structures. Gallium oxide removal using equipment available to the Mid-IR Photonics Group, Nottingham, UK, remains difficult with currently only one suitable reported gallium purification method involving the distillation of gallium iodide [22]. If purification of Ga remains problematic, it may serve better to switch to an alternative solubilising agent.

Sakr *et al.* compared Pr^{3+} doped glasses with gallium alongside Pr^{3+} doped glasses with the higher atomic mass rare earth solubiliser, indium (In). Despite indium also lacking a suitable oxide removal procedure, they reported superior photoluminescence in the indium containing samples and attributed this to the lower average phonon energy environment provided by the indium, compared to gallium [86]. They noted that In containing glasses required a lower doping concentration < 1000 ppmw to avoid crystallisation. The development of a GeSbSeIn glass may prove to provide stronger photoluminescence out towards the longer emission wavelengths such as the 7.25 μm emission measured in the Sm^{3+} doped GeAsSeGa fibre (Section 4.2). Due to the inclination for antimony-based glasses to crystallise, which is likely to be further exacerbated by the inclusion of indium, it is proposed to begin with 1 at. % indium and 250 – 500 ppmw of rare earth dopant. An initial composition design would follow the same (20:10:70) ratio detailed in Section 4.1 with a suggested composition of $Ge_{19.8}Sb_{9.9}Se_{69.3}In_1$.

In a similar vein, doping of an arsenic-based fibre with 1000 ppmw Sm foil and following the same pumping scheme described in Section 4.2 (1.3 µm and 1.47 µm) would provide an insight into whether an arsenic-based fibre can facilitate radiative transitions at wavelengths longer than 6 µm (the current longest wavelength rare earth radiative emission recorded from As-based fibre, Sakr *et al.* [86,94]).

Work from Velmuzhov *et al.* detailed the alloying of gallium with rare earth foil by baking the two elements at 700 °C under 10^{-3} Pa open vacuum [236]. This was said to produce an exothermic reaction leading to the release of hydride impurities present in the rare earth. A replication of this method would allow a comparative study between a Ge scratched rare earth foil doped glass and a glass doped with gallium alloyed foil to determine efficacy. Both doped glasses should come from a large single initial melt to avoid batch-to-batch variation.

Differing baseline losses and impurity absorption peaks are observed in optical fibre loss graphs doped with different rare earth ions, despite identical precursor purification methods being followed. Fabricating a large boule chalcogenide glass that is then divided, doped and remelted with separate rare earth foil dopants, drawn to fibre, and optical loss measured may help to identify trends between solubility/purity issues with commercially available rare earth foil sources.

Photoluminescence of Dy^{3+} in the antimony-based small core fibre has not yet been investigated. Pumping at 1.1 and 1.3 µm could potentially provide longer wavelength radiative emissions than what has previously been measured in arsenic-based Dy^{3+} doped glasses by the Mid-IR Photonics group, University of Nottingham, UK. This suggestion is based on work from Starecki *et al.* [25] who measure the first recorded instance of 7.2 µm emissions from Dy^{3+} in chalcogenide glass fibres [25]. It is suggested the Dy^{3+}: $^6F_{11/2} \rightarrow {}^6H_{11/2}$ (5.4-6.2 µm) [142] (see Section 2.4.1) transition is targeted.

The distillation of $DyCl_3$ yielded two different morphologies of distilled product. A comparison study in which both morphologies are doped into identical compositions would identify if one were superior to the other. As it appears the morphology is temperature dependent, with the large translucent crystals forming at higher temperatures than the powder form, the experimental design can then be modified to increase yield of the superior form.

8.3.2 Further investigations of cladding glasses.

With the development of a gallium- and sulfur-free antimony-based cladding glass, it would be a step forward to design also a gallium- and sulfur-free arsenic-based cladding glass. Although the antimony-based cladding performed well in terms of compatible thermal-processing with both arsenic and antimony-based doped core glasses, identifying more suitable cladding glasses allows additional tailoring to desired small core fibre properties such as numerical aperture for different investigations/studies/applications. That is, the more suitable cladding glasses that are designed and characterised, the easier it becomes to mix-and-match core and cladding glasses to achieve a wider range of step-index fibres with differing optical properties.

Currently, core chalcogenide glass compositions generally remain static due to gallium and rare earth elements increasing the crystallisation risk. Arsenic-based glasses are found to be more forgiving than their antimony-based counterparts regarding devitrification during fibre fabrication and thus As-based glasses appear to be a more suitable route to developing a larger library of cladding compositions (and subsequently fibres with different properties).

Two methods are proposed here for developing new As-based chalcogenide cladding glasses. For existing cladding glasses, returning the sulfur content to the selenium at. %, and distribution of the Ga content across the composition could provide a suitable starting point. For example, $Ge_{16.5}As_{16}Se_{61.5}Ga_3S_3$ at. % could be modified to $Ge_{18}As_{17}Se_{65}$ at. % that is, 3 at. % S removed and added as 3 at.% Se, with the 3 at. % Ga divided between 1.5 at. % increase in Ge (to increase T_g and reduce RI), 1 at. % As (to increase T_g) and 0.5 % Se (for devitrification resistance). Further alterations to Ge or As can be made iteratively to reach a desired refractive index and T_g accordingly. The second method would be to remove gallium from a core glass composition and substitute it with germanium. For example, $Ge_{15}As_{21}Se_{63}Ga_1$ at. % to $Ge_{16}As_{21}Se_{63}$ at. %. Both examples are an oversimplification as the design process is not as cut-and-dry as described but each characterised composition provides valuable information on this potentially iterative process. This can be used to build a database of atomic percent changes

and their corresponding effects on T_g, refractive index, and devitrification resistance in glasses.

8.3.3 Further improvements to moth eye antireflection nanoimprinting.

The initial mould design was focused on optimising antireflection in the near-IR (1.55 μm) to improve rare earth ion pumping efficiency. Due to the wavelength dependent relationship between antireflection properties and feature size and pitch, this required a densely populated mould with small features. This mould was also produced as a negative, that is, chalcogenide glass had to flow into the mould. This combination of many small, close packed features on a negative mould was proposed to hinder the pressing process due to various surface tension effects.

A moth eye mould design operating in the mid-IR would require larger features, with further spacing between features. This would hopefully reduce some of these surface tension effects and provide a more forgiving hot-pressing process on the fibre tip allowing better pattern replication. Additionally, the mould can be designed as a positive. In this case, the heated mould has protrusions which press into the fibre tip to impress the pattern. With this, any surface tension effects are expected to be avoided.

Lotz *at al.* indicated that hot nanoimprinting of their mould onto a chalcogenide window led to the accelerated formation of an oxide layer on the surface of the chalcogenide [225]. Relocating the hot-pressing rig to a vacuum chamber or the inert environment of a glove box may provide a way to mitigate this oxidation effect.

Reflectance results were only conducted onto poorly pressed bulk chalcogenide glass samples. To get a practical measure of the efficacy of the nanoimprinting parameters used on fibre, a rig needs to be designed to measure either reflectance or transmission of pressed fibre samples.

9. References

1 BSI ISO. *20473:2007 Optics and photonics — Spectral bands*. British Standards Institution (BSI); 2015.

2 Starecki F, Charpentier F, Doualan JL, Quetel L, Michel K, Chahal R, Troles J, Bureau B, Braud A, Camy P, Moizan V, Nazabal V. Mid-IR optical sensor for CO_2 detection based on fluorescence absorbance of Dy^{3+}:$Ga_5Ge_{20}Sb_{10}S_{65}$ fibers. *Sens Actuators B Chem* 2015;**207**:518–25. https://doi.org/10.1016/j.snb.2014.10.011.

3 Guo B, Wang Y, Peng C, Zhang HL, Luo GP, Le HQ, Gmachl C, Sivco DL, Peabody ML, Cho AY. Laser-based mid-infrared reflectance imaging of biological tissues. *Opt Express* 2004;**12**:208. https://doi.org/10.1364/OPEX.12.000208.

4 Selvaraj R, Vasa NJ, Nagendra SMS, Mizaikoff B. Advances in mid-infrared spectroscopy-based sensing techniques for exhaled breath diagnostics. *Molecules* 2020. https://doi.org/10.3390/molecules25092227.

5 Mabwa D, Gajjar K, Furniss D, Schiemer R, Crane R, Fallaize C, Martin-Hirsch PL, Martin FL, Kypraios T, Seddon AB, Phang S. Mid-infrared spectral classification of endometrial cancer compared to benign controls in serum or plasma samples. *Analyst* 2021. https://doi.org/10.1039/d1an00833a.

6 Edwards G, Logan R, Copeland M, Reinisch L, Davidson J, Johnson B, Maciunas R, Mendenhall M, Ossoff R, Tribble J, Werkhaven J, O'Day D. Tissue ablation by a free-electron laser tuned to the amide II band. *Nature* 1994;**371**:416–9. https://doi.org/10.1038/371416a0.

7 Seddon AB. Mid-Infrared Molecular Sensing. *Springer Handbook of Glass*, vol. 47. 2019. p. 1585–632.

8 Serebryakov VA, Boĭko É v., Petrishchev NN, Yan a. v. Medical applications of mid-IR lasers Problems and prospects. *Journal of Optical Technology* 2010;**77**:6. https://doi.org/10.1364/JOT.77.000006.

9 Mackanos M a., Simanovskii DM, Schriver KE, Hutson MM, Contag CH, Kozub J a., Jansen ED. Pulse-Duration-Dependent Mid-Infrared Laser Ablation for Biological Applications. *IEEE Journal of Selected Topics in Quantum Electronics* 2012;**18**:1514–22. https://doi.org/10.1109/JSTQE.2012.2188501.

10 Yao Y, Hoffman AJ, Gmachl CF. Mid-infrared quantum cascade lasers. *Nat Photonics* 2012:432–9. https://doi.org/10.1038/nphoton.2012.143.

11 Waynant RW, Ilev IK, Gannot I. Mid-infrared laser applications in medicine and biology. *The Royal Society* 2001:635–44.

12 Cui S, Chahal R, Boussard-Plédel C, Nazabal V, Doualan JL, Troles J, Lucas J, Bureau B. From selenium- to tellurium-based glass optical fibers for infrared spectroscopies. *Molecules* 2013;**18**:5373–88. https://doi.org/10.3390/molecules18055373.

13 Lucas P, Wilhelm AA, Videa M, Boussard-Plédel C, Bureau B. Chemical stability of chalcogenide infrared glass fibers. *Corros Sci* 2008;**50**:2047–52. https://doi.org/10.1016/j.corsci.2008.04.020.

14 Jackson SD. Towards high-power mid-infrared emission from a fibre laser. *Nat Photonics* 2012;**6**:423–31. https://doi.org/10.1038/nphoton.2012.149.

15 Nunes J, Sojka L, Crane R, Furniss D, Mabwa D, Xiao B, Benson T, Farries M, Kalfagiannis N, Barney E, Phang S, Seddon A, Sujecki S, Tang Z. Room temperature mid-infrared fiber lasing beyond 5 μm in chalcogenide glass small-core fiber. *Opt Lett* 2021;**46**:3504–7. https://doi.org/10.1364/ol.430891.

16 Churbanov MF, Denker BI, Galagan BI, Koltashev V v., Plotnichenko VG, Snopatin GE, Sukhanov M v., Sverchkov SE, Velmuzhov AP. Laser potential of Pr3+ doped chalcogenide glass in 5-6 μm spectral range. *J Non Cryst Solids* 2021;**559**:. https://doi.org/10.1016/j.jnoncrysol.2020.120592.

17 Churbanov MF, Denker BI, Galagan BI, Koltashev V v., Plotnichenko VG, Sukhanov M v., Sverchkov SE, Velmuzhov AP. First demonstration of ~ 5 μm laser action in terbium-doped selenide glass. *Appl Phys B* 2020;**126**:. https://doi.org/10.1007/s00340-020-07473-w.

18 Denker BI, Galagan BI, Koltashev VV, Plotnichenko VG, Snopatin GE, Sukhanov MV, Sverchkov SE, Velmuzhov AP. Continuous Tb-doped fiber laser emitting at ~5.25 μm. *Opt Laser Technol* 2022;**154**:108355. https://doi.org/10.1016/j.optlastec.2022.108355.

19 Crane R, Seddon A, Sojka L, Furniss D, Nunes J, Barney E, Farries M, Benson T, Sujecki S. Experimental photoluminescence and lifetimes at wavelengths including beyond 7 microns in Sm^3+-doped selenide-chalcogenide glass fibers. *Opt Express* 2020;**28**:12373–84. https://doi.org/10.1364/oe.383033.

20 Shiryaev VS, Karaksina E v., Kotereva T v., Churbanov MF, Velmuzhov AP, Nezhdanov A v. Special pure Pr(3+) doped Ga 3 Ge 31 As 18 Se 48 glass for active mid-IR optics. *J Lumin* 2019;**209**:225–31. https://doi.org/10.1016/j.jlumin.2019.01.060.

21 Chahal R, Starecki F, Doualan J-L, Němec P, Trapananti A, Prestipino C, Tricot G, Boussard-Pledel C, Michel K, Braud A, Camy P, Adam

J-L, Bureau B, Nazabal V. Nd $^{3+}$:Ga-Ge-Sb-S glasses and fibers for luminescence in mid-IR: synthesis, structural characterization and rare earth spectroscopy. *Opt Mater Express* 2018;**8**:1650. https://doi.org/10.1364/OME.8.001650.

22 Karaksina E v., Shiryaev VS, Kotereva T v., Churbanov MF. Preparation of high-purity Pr^{3+} doped Ge-Ga-Sb-Se glasses with intensive middle infrared luminescence. *J Lumin* 2016;**170**:37–41. https://doi.org/10.1016/j.jlumin.2015.10.015.

23 Sojka L, Tang Z, Furniss D, Sakr H, Fang Y, Beres-Pawlik E, Benson TM, Seddon AB, Sujecki S. Mid-infrared emission in Tb^{3+}-doped selenide glass fiber. *J Opt Soc Am B* 2017;**34**:70–9. https://doi.org/10.1364/JOSAB.34.000A70b.

24 Nunes JJ, Crane RW, Tang Z, Sójka Ł, Kalfagiannis N, Furniss D, Farries MC, Benson TM, Sujecki S, Seddon AB. Mid-infrared photoluminescence in Ce^{3+} doped selenide-chalcogenide glass and fiber 2022.

25 Starecki F, Louvet G, Ari J, Braud A, Doualan JL, Chahal R, Hafienne I, Boussard-Plédel C, Nazabal V, Camy P. Dy^{3+} doped GaGeSbSe fiber long-wave infrared emission. *J Lumin* 2020;**218**:3–8. https://doi.org/10.1016/j.jlumin.2019.116853.

26 Edwards GS, Hutson MS, Hauger S, Kozub JA, Shen J-H, Shieh C, Topadze K, Joos K. Comparison of OPO and Mark-III FEL for Tissue Ablation at 6.45 Mm.

27 Mabwa D, Kubiena T, Parnell H, Su R, Furniss D, Tang Z, Leach R, Benson TM, Scotchford CA, Seddon AB. Evaluating the cytotoxicity of Ge-Sb-Se chalcogenide glass optical fibres on 3T3 mouse fibroblasts. *RSC Adv* 2021;**11**:8682–93. https://doi.org/10.1039/d0ra00353k.

28 Patil UA, Dhami LD. Overview of lasers. *Indian J Plast Surg* 2008;**41**:S101–13.

29 Einstein A. The Quantum Theory of Radiation. *Physikalische Zeitschrift XVIII* 1917.

30 Wilson J, Hawkes JFB. *Optoelectronics: An Introduction*. Prentice-Hall International; 1983.

31 Tang Z. *Rare earth ion doped selenide-based chalcogenide glasses and fibres towards mid-infrared lasers*. University of Nottingham; 2012; 2012.

32 Kimura M. *Fiber Lasers: Research, Technology and Applications*. New York: Nova Science; 2009.

33 Paschotta R. *Encyclopedia of Laser Physics and Technology*. 1st ed. Zurich: John Wiley and Sons; 2008.

34 Daniel JMO, Simakov N, Tokurakawa M, Ibsen M, Clarkson WA. Ultra-short wavelength operation of a thulium fibre laser in the 1660–1750 nm wavelength band. *Opt Express* 2015;**23**:18269. https://doi.org/10.1364/OE.23.018269.

35 Seddon AB, Tang Z, Furniss D, Sujecki S, Benson TM. Progress in rare-earth-doped mid-infrared fiber lasers. *Opt Express* 2010;**18**:26704. https://doi.org/10.1364/OE.18.026704.

36 Sanghera JS, Shaw LB, Aggarwal ID. Chalcogenide glass-fiber-based mid-IR sources and applications. *IEEE Journal on Selected Topics in Quantum Electronics* 2009;**15**:114–9. https://doi.org/10.1109/JSTQE.2008.2010245.

37 Agrawal G. Applications of Nonlinear Fiber Optics (Second Edition). *Applications of Nonlinear Fiber Optics (Second Edition)*. Burlington: Academic Press; 2008. p. 179–244.

38 Eggleton BJ, Madden S, Luther-Davies B, Choi D-Y, Wang R, Baker NJ, Rode A. Integrated shadow mask for sampled Bragg gratings in chalcogenide (As_2S_3) planar waveguides. *Opt Express* 2007;**15**:7708. https://doi.org/10.1364/oe.15.007708.

39 Asobe M, Ohara T, Yokohama I, Kaino T. Fabrication of Bragg grating in chalcogenide glass fibre using the transverse holographic method. *Electron Lett* 2002;**32**:1611. https://doi.org/10.1049/el:19961046.

40 Ahmad R, Rochette M. Photosensitivity at 1550 nm and Bragg grating inscription in As_2Se_3 chalcogenide microwires. *Appl Phys Lett* 2011;**99**:061109. https://doi.org/10.1063/1.3625942.

41 Bernier M, Asatryan KE, Vallée R, Plotnichenko VG, Galstian TM, Vasil'ev SA, Medvedkov OI, Gnusin PI, Dianov EM. Second-order Bragg gratings in single-mode chalcogenide fibres. *Quantum Elec (Woodbury)* 2011;**41**:465–8. https://doi.org/10.1070/qe2011v041n05abeh014521.

42 Brawley GA, Ta'eed VG, Bolger JA, Sanghera JS, Aggarwal I, Eggleton BJ. Strong photoinduced Bragg gratings in arsenic selenide optical fibre using transverse holographic method. *Electron Lett* 2008;**44**:846. https://doi.org/10.1049/el:20080784.

43 Bernier M, El-Amraoui M, Couillard JF, Messaddeq Y, Vallée R. Writing of Bragg gratings through the polymer jacket of low-loss As_2S_3fibers using femtosecond pulses at 800 nm. *Opt Lett* 2012;**37**:3900. https://doi.org/10.1364/OL.37.003900.

44 Ghatak A, Thyagarajan K. Optical Waveguides and Fibers. *Fundamentals of Photonics*. 1000 20th Street, Bellingham, WA 98227-0010 USA: SPIE; 2000. p. 249–92.

45 Zlatanov N. *Introduction to Fiber Optics Theory*. 2017.

46 Hemati T, Weng B. The Mid-Infrared Photonic Crystals for Gas Sensing Applications. *Photonic Crystals - A Glimpse of the Current Research Trends*. IntechOpen; 2019.

47 Petersen CR, Møller U, Kubat I, Zhou B, Dupont S, Ramsay J, Benson T, Sujecki S, Abdel-Moneim N, Tang Z, Furniss D, Seddon A, Bang O. Mid-infrared supercontinuum covering the 1.4-13.3 μm molecular fingerprint region using ultra-high NA chalcogenide step-index fibre. *Nat Photonics* 2014;**8**:830–4. https://doi.org/10.1038/nphoton.2014.213.

48 Maes F, Fortin V, Poulain S, Poulain M, Carrée J-Y, Bernier M, Vallée R. Room-temperature fiber laser at 3.92 μm. *Optica* 2018;**5**:761. https://doi.org/10.1364/OPTICA.5.000761.

49 Shaw LB, Cole B, Thielen PA, Sanghera JS, Aggarwal ID. Mid-wave IR and long-wave IR laser potential of rare-earth doped chalcogenide glass fiber. *IEEE J Quantum Electron* 2001;**37**:1127–37. https://doi.org/10.1109/3.945317.

50 Tang Z, Neate NC, Furniss D, Sujecki S, Benson TM, Seddon AB. Crystallization behavior of Dy^{3+}-doped selenide glasses. *J Non Cryst Solids* 2011;**357**:2453–62. https://doi.org/10.1016/j.jnoncrysol.2010.11.065.

51 Cheng Y, Tang Z, Neate NC, Furniss D, Benson TM, Seddon AB. The influence of dysprosium addition on the crystallization behavior of a chalcogenide selenide glass close to the fiber drawing temperature. *Journal of the American Ceramic Society* 2012;**95**:3834–41. https://doi.org/10.1111/jace.12014.

52 Tang Z, Furniss D, Neate NC, Barney E, Benson TM, Seddon AB. Dy $^{3+}$ -Doped Selenide Chalcogenide Glasses: Influence of Dy $^{3+}$ Dopant-Additive and Containment. *Journal of the American Ceramic Society* 2016;**99**:2283–91. https://doi.org/10.1111/jace.14218.

53 Tang Z, Furniss D, Fay M, Neate NC, Sujeeki S, Benson TM, Seddon AB. Crystallization and Optical Loss Studies of Dy 3+ -Doped, Low Ga Content, Selenide Chalcogenide Bulk Glasses and Optical Fibers. *Processing, Properties, and Applications of Glass and Optical Materials*. The American Ceramic Society; 2012. p. 193–9.

54 Parnell H, Furniss D, Tang Z, Neate NC, Benson TM, Seddon AB. Compositional dependence of crystallization in Ge–Sb–Se glasses

relevant to optical fiber making. *Journal of the American Ceramic Society* 2018;**101**:208–19. https://doi.org/10.1111/jace.15212.

55 Tang Z, Furniss D, Fay M, Neate NC, Sujeeki S, Benson TM, Seddon AB. Crystallization and Optical Loss Studies of Dy^{3+}-Doped, Low Ga Content, Selenide Chalcogenide Bulk Glasses and Optical Fibers. *Processing, Properties, and Applications of Glass and Optical Materials*. Hoboken; 2012.

56 Shiryaev VS, Sukhanov M v., Velmuzhov AP, Karaksina E v., Kotereva T v., Snopatin GE, Denker BI, Galagan BI, Sverchkov SE, Koltashev V v., Plotnichenko VG. Core-clad terbium doped chalcogenide glass fiber with laser action at 5.38 μm. *J Non Cryst Solids* 2021;**567**:. https://doi.org/10.1016/j.jnoncrysol.2021.120939.

57 Schweizer T, Samson BNN, Moore RCC, Hewak DWW, Payne DNN. Rare-earth doped chalcogenide glass fibre laser. *Electron Lett* 1997;**33**:414–6.

58 Rao KJ. *Structural Chemistry of Glasses*. Oxford: Elsevier Science; 2002.

59 Levesque L, Robaczewski A. Very accurate temperature control of bones by a CO_2 laser for medical applications. *Appl Opt, AO* 2017;**56**:3923–8. https://doi.org/10.1364/AO.56.003923.

60 Kaplan M, Hazelbaker AK, Vitruk P. Infant Frenectomy with 10,600 nm Dental CO_2 Laser. *WAGD Newsletter* 2015:10–2.

61 Poulain M. Halide glasses. *J Non Cryst Solids* 1983;**56**:1–14. https://doi.org/10.1016/0022-3093(83)90439-8.

62 Eggleton BJ, Luther-Davies B, Richardson K. Chalcogenide photonics. *Nat Photonics* 2011;**5**:141–8. https://doi.org/10.1038/nphoton.2011.309.

63 Walsh BM, Barnes NP. Lanthanide Glass Spectroscopy and Fiber Lasers. In: Hussain N, Santos J, editors. *Physics and chemistry of rare-earth ion doped glasses*. Zurich: Trans Tech Publications LTD; 2008. p. 3–44.

64 Snopatin GE, Shiryaev VS, Plotnichenko VG, Dianov EM, Churbanov MF. High-purity chalcogenide glasses for fiber optics. *Inorganic Materials* 2009;**45**:1439–60. https://doi.org/10.1016/0022-3093(94)00688-1.

65 Lucas J. Infrared glasses. *Curr Opin Solid State Mater Sci* 1999;**4**:181–7. https://doi.org/10.1016/S1359-0286(99)00007-8.

66 Lucas J, Troles J, Zhang XH, Boussard-Pledel C, Poulain M, Bureau B. Glasses to see beyond visible. *Comptes Rendus Chimie* 2018;**21**:916–22. https://doi.org/10.1016/j.crci.2018.02.010.

67 Dong L, Samson B. *Fiber Lasers: Basics, Technology, and Applications*. Boca Raton: CRC Press; 2016.

68 Julien C, Barnier S, Massot M, Chbani N, Cai X, Loireau-Lozac'h AM, Guittard M. Raman and infrared spectroscopic studies of GeGaAg sulphide glasses. *Materials Science and Engineering B* 1994;**22**:191–200. https://doi.org/10.1016/0921-5107(94)90243-7.

69 Weszka J. Raman scattering in In_2Se_3 and $InSe_2$ amorphous films. *J Non Cryst Solids* 2000;**265**:98–104. https://doi.org/10.1016/S0022-3093(99)00710-3.

70 Uemura O, Hayasaka N, Tokairin S, Usuki T. Local atomic arrangement in Ge-Te and Ge-S-Te glasses. *J Non Cryst Solids* 1996;**205–207**:189–93. https://doi.org/10.1016/S0022-3093(96)00376-6.

71 Shelby JE. *Introduction to Glass Science and Technology*. 2nd ed. Cambridge; 2005.

72 Furniss D, Seddon AB. Thermal Analysis of Inorganic Compound Glasses and Glass-Ceramics. *Principles and Applications of Thermal Analysis*. 2008. p. 410–48.

73 Zachariasen WH. The atomic arrangement in glass. *J Am Chem Soc* 1932;**54**:3841–51. https://doi.org/10.1021/ja01349a006.

74 Mcnaught AD, Wilkinson A. Glass transition. *IUPAC Compendium of Chemical Terminology (the 'Gold Book')* 1997.

75 Gao S, Simon SL. Measurement of the limiting fictive temperature over five decades of cooling and heating rates. *Thermochim Acta* 2015;**603**:123–7. https://doi.org/10.1016/j.tca.2014.08.019.

76 Badrinarayanan P, Zheng W, Li Q, Simon SL. The glass transition temperature versus the fictive temperature. *J Non Cryst Solids* 2007;**353**:2603–12. https://doi.org/10.1016/j.jnoncrysol.2007.04.025.

77 Gao S, Simon SL. Measurement of the limiting fictive temperature over five decades of cooling and heating rates. *Thermochim Acta* 2015;**603**:123–7. https://doi.org/10.1016/j.tca.2014.08.019.

78 Volmer M. Kinetik der Phasenbildung. *Angewandte Chemie* 1939;**52**:503–4. https://doi.org/10.1002/ange.19390523006.

79 Holland W, Beall GH. *Glass Ceramic Technology*. 2nd ed. Hoboken: Wiley; 2012.

80 Boldyreva E, Dera P. High-Pressure Crystallography: From Fundamental Phenomena to Technological Applications. Dordrecht: Springer Netherlands; 2010. p. 503–5.

81 McMillan PW. *Glass-Ceramics*. 2nd ed. University of Michigan: Academic Press; 1964.

82 Sroor FMA, Edelmann FT. Lanthanides: Tetravalent Inorganic. *Encyclopedia of Inorganic and Bioinorganic Chemistry*. John Wiley & Sons, Ltd; 2012.

83 Bettencourt-Dias A. The Electronic Structure of the Lanthanides. In: Atwood DA, editor. *The Rare Earth Elements: Fundamentals and Applications*. Chicester: Wiley; 2013.

84 Atwood DA. The Rare Earth Elements - A Special Group of Metals. *The Rare Earth Elements: Fundamentals and Applications*. Singapore: Wiley; 2013.

85 Tao G, Guo H, Feng L, Lu M, Wei W, Peng B. Formation and properties of a novel heavy-metal chalcogenide glass doped with a high dysprosium concentration. *Journal of the American Ceramic Society* 2009;**92**:2226–9. https://doi.org/10.1111/j.1551-2916.2009.03205.x.

86 Sakr H, Furniss D, Tang Z, Sojka L, Moneim NA, Barney E, Sujecki S, Benson TM, Seddon AB. Superior photoluminescence (PL) of Pr^{3+}-In, compared to Pr^{3+}-Ga, selenide-chalcogenide bulk glasses and PL of optically-clad fiber. *Opt Express* 2014;**22**:21236. https://doi.org/10.1364/OE.22.021236.

87 Aitken BG, Ponader CW, Quimby RS. Clustering of rare earths in GeAs sulfide glass. *Comptes Rendus Chimie* 2002;**5**:865–72. https://doi.org/10.1016/S1631-0748(02)01458-3.

88 Ainslie BJ. A Review of the Fabrication and Properties of Erbium-Doped Fibers for Optical Amplifiers. *Journal of Lightwave Technology* 1991;**9**:220–7. https://doi.org/10.1109/50.65880.

89 Abdellaoui N, Starecki F, Boussard-Pledel C, Shpotyuk Y, Doualan J-L, Braud A, Baudet E, Nemec P, Cheviré F, Dussauze M, Bureau B, Camy P, Nazabal V. Tb 3+ doped Ga_5 Ge_{20} Sb_{10} Se_{65-x} Te_x (x = 0-37.5) chalcogenide glasses and fibers for MWIR and LWIR emissions. *Opt Mater Express* 2018;**8**:2887. https://doi.org/10.1364/OME.8.002887.

90 Starecki F, Abdellaoui N, Braud A, Doualan J-L, Boussard-Plédel C, Bureau B, Camy P, Nazabal V. 8 μm luminescence from a Tb^{3+}GaGeSbSe fiber. *Opt Lett* 2018;**43**:7–10. https://doi.org/10.1364/OL.43.001211.

91 Zhang M, Yang Z, Li L, Wang Y, Qiu J, Yang A, Tao H, Tang D. The effects of germanium addition on properties of Ga-Sb-S chalcogenide glasses. *J Non Cryst Solids* 2016;**452**:114–8. https://doi.org/10.1016/j.jnoncrysol.2016.08.023.

92 Charpentier F, Starecki F, Doualan JL, Jóvári P, Camy P, Troles J, Belin S, Bureau B, Nazabal V. Mid-IR luminescence of $Dy^{3+}$and Pr^{3+}doped $Ga_5Ge_{20}Sb_{10}S(Se)_{65}$ bulk glasses and fibers. *Mater Lett* 2013;**101**:21–4. https://doi.org/10.1016/j.matlet.2013.03.062.

93 Tanaka K. *Structural phase transitions in chalcogenide glasses*. vol. 39. 1989.

94 Sakr H, Tang Z, Furniss D, Sojka L, Sujecki S, Benson TM, Seddon AB. Promising emission behavior in Pr3+/In selenide-chalcogenide-glass small-core step index fiber (SIF). *Opt Mater (Amst)* 2017;**67**:98–107. https://doi.org/10.1016/j.optmat.2017.03.034.

95 Sójka Ł, Tang Z, Zhu H, Bereś-Pawlik El, Furniss D, Seddon ABB, Benson TMM, Sujecki S. Study of mid-infrared laser action in chalcogenide rare earth doped glass with Dy^{3+}, $Pr^{3+}$and Tb^{3+}. *Opt Mater Express* 2012;**2**:1632–40. https://doi.org/10.1364/OME.2.001632.

96 Ichikawa M, Ishikawa YI, Wakasugi T, Kadono K. Mid-infrared emissions from Ho^{3+}in Ga_2S_3-GeS_2-Sb_2S_3 glass. *J Lumin* 2012;**132**:784–8. https://doi.org/10.1016/j.jlumin.2011.11.007.

97 Zhang M, Yang A, Peng Y, Zhang B, Ren H, Guo W, Yang Y, Zhai C, Wang Y, Yang Z, Tang D. Dy-doped Ga-Sb-S chalcogenide glasses for mid-infrared lasers. *Mater Res Bull* 2015;**70**:55–9. https://doi.org/10.1016/j.materresbull.2015.04.019.

98 Pelé AL, Braud A, Doualan JL, Chahal R, Nazabal V, Boussard-Plédel C, Bureau B, Moncorgé R, Camy P. Wavelength conversion in Er^{3+} doped chalcogenide fibers for optical gas sensors. *Opt Express* 2015;**23**:4163. https://doi.org/10.1364/OE.23.004163.

99 Pelé AL, Braud A, Doualan JL, Starecki F, Nazabal V, Chahal R, Boussard-Plédel C, Bureau B, Moncorgé R, Camy P. Dy^{3+}doped GeGaSbS fluorescent fiber at 4.4 μm for optical gas sensing: Comparison of simulation and experiment. *Opt Mater (Amst)* 2016;**61**:37–44. https://doi.org/10.1016/j.optmat.2016.04.016.

100 Starecki F, Morais S, Chahal R, Boussard-Plédel C, Bureau B, Palencia F, Lecoutre C, Garrabos Y, Marre S, Nazabal V. IR emitting Dy^{3+}doped chalcogenide fibers for in situ CO_2 monitoring in high pressure microsystems. *International Journal of Greenhouse Gas Control* 2016;**55**:36–41. https://doi.org/10.1016/j.ijggc.2016.10.015.

101 Chahal R, Starecki F, Boussard-Plédel C, Doualan JL, Michel K, Brilland L, Braud A, Camy P, Bureau B, Nazabal V. Fiber evanescent wave spectroscopy based on IR fluorescent chalcogenide fibers. *Sens Actuators B Chem* 2016;**229**:209–16. https://doi.org/10.1016/j.snb.2016.01.091.

102 Yang A, Zhang M, Li L, Wang Y, Zhang B, Yang Z, Tang D. Ga-Sb-S Chalcogenide Glasses for Mid-Infrared Applications. *Journal of the American Ceramic Society* 2016;**99**:12–5. https://doi.org/10.1111/jace.14025.

103 Yang A, Qiu J, Zhang M, Ren H, Zhai C, Qi S, Zhang B, Tang D, Yang Z. Mid-infrared luminescence of Dy^{3+} ions in modified Ga-Sb-S chalcogenide glasses and fibers. *J Alloys Compd* 2017;**695**:1237–42. https://doi.org/10.1016/j.jallcom.2016.10.251.

104 Ari J, Starecki F, Boussard-Plédel C, Ledemi Y, Messaddeq Y, Doualan J-L, Braud A, Bureau B, Nazabal V. Co-doped Dy^{3+} and Pr^{3+} Ga_5 Ge_{20} Sb_{10} S_{65} fibers for mid-infrared broad emission. *Opt Lett* 2018;**43**:2893. https://doi.org/10.1364/OL.43.002893.

105 Xiao X, Xu Y, Guo H, Wang P, Cui X, Lu M, Wang Y, Peng B. Theoretical Modeling of 4.3 μm Mid-Infrared Lasing in Dy^{3+}-Doped Chalcogenide Fiber Lasers. *IEEE Photonics J* 2018;**10**:. https://doi.org/10.1109/JPHOT.2018.2803155.

106 Sukhanov M v., Velmuzhov AP, Kotereva T v., Skripachev I v., Churbanov MF. New approach for preparation of high-purity sulfide-germanium glasses doped with praseodymium. *Opt Mater Express* 2019;**9**:3204. https://doi.org/10.1364/OME.9.003204.

107 Xiao X, Xu Y, Cui J, Liu X, Cui X, Wang X, Dai S, Guo H. Structured active fiber fabrication and characterization of a chemically high-purified Dy^{3+} -doped chalcogenide glass. *Journal of the American Ceramic Society* 2020;**103**:2432–42. https://doi.org/10.1111/jace.16921.

108 Sójka L, Tang Z, Furniss D, Sakr H, Oladeji A, Bereś-Pawlik E, Dantanarayana H, Faber E, Seddon AB, Benson TM, Sujecki S. Broadband, mid-infrared emission from Pr^{3+} doped GeAsGaSe chalcogenide fiber, optically clad. *Opt Mater (Amst)* 2014;**36**:1076–82. https://doi.org/10.1016/j.optmat.2014.01.038.

109 Furniss D, Sakr H, Tang Z, Sojka L, Sujecki S, Barney E, Benson TM, Seddon AB. Development of praseodymium-doped, selenide chalcogenide glass, step-index fibre towards mid-infrared fibre lasers. *International Conference on Transparent Optical Networks* 2014:3–6. https://doi.org/10.1109/ICTON.2014.6876432.

110 Tang Z, Furniss D, Fay M, Sakr H, Sójka L, Neate N, Weston N, Sujecki S, Benson TM, Seddon AB. Mid-infrared photoluminescence in small-core fiber of praseodymium-ion doped selenide-based chalcogenide glass. *Opt Mater Express* 2015;**5**:870. https://doi.org/10.1364/OME.5.000870.

111 Sojka L, Tang Z, Sakr H, Furniss D, Benson TM, Seddon AB, Barney E, Beres-Pawlik E, Sujecki S. Spectroscopy of mid-infrared (4.8μm)

photoluminescence in Tb3+ doped chalcogenide glass and fibre. *International Conference on Transparent Optical Networks* 2015:7–9. https://doi.org/10.1109/ICTON.2015.7193669.

112 Karaksina E v., Shiryaev VS, Churbanov MF, Anashkina EA, Kotereva T v., Snopatin GE. Core-clad Pr^{3+}-doped Ga(In)-Ge-As-Se-(I) glass fibers: Preparation, investigation, simulation of laser characteristics. *Opt Mater (Amst)* 2017;**72**:654–60. https://doi.org/10.1016/j.optmat.2017.07.012.

113 Starecki F, Braud A, Abdellaoui N, Boussard-plédel C, Bureau B, Nazabal V. 7 to 8 μm emission from Sm^{3+} doped selenide fibers. *Opt Express* 2018;**26**:26462–9. https://doi.org/10.1364/OE.26.026462.

114 Churbanov MF, Denker BI, Galagan BI, Koltashev V v., Plotnichenko VG, Sukhanov M v., Sverchkov SE, Velmuzhov AP. Cascade sensitization of mid-infrared Ce3+ luminescence by Dy3+ ions in selenide glass. *J Lumin* 2021;**231**:. https://doi.org/10.1016/j.jlumin.2020.117809.

115 Shiryaev VS, Sukhanov MV, Velmuzhov AP, Karaksina EV, Kotereva TV, Snopatin GE, Blagin RD, Denker BI, Galagan BI, Koltashev VV, Plotnichenko VG, Sverchkov SE. Preparation of high purity Sm3+-doped Ga-Ge-As-Se glass and low-loss fiber. *J Lumin* 2022;**242**:118552. https://doi.org/10.1016/j.jlumin.2021.118552.

116 Shpotyuk Y, Boussard-Pledel C, Nazabal V, Chahal R, Ari J, Pavlyk B, Cebulski J, Doualan JL, Bureau B. Ga-modified As_2Se_3-Te glasses for active applications in IR photonics. *Opt Mater (Amst)* 2015;**46**:228–32. https://doi.org/10.1016/j.optmat.2015.04.024.

117 Meng W, Xu Y, Guo H, Lu C, Hou C, Lu M, Wang P, Li W, Peng B, Lu Y, Wei W. Investigation of mid-IR luminescence properties and energy transfer in Dy^{3+}-doped and Dy^{3+}, Tm^{3+}-codoped chalcohalide glasses. *Opt Mater (Amst)* 2013;**35**:1499–503. https://doi.org/10.1016/j.optmat.2013.03.007.

118 Lu C, Guo H, Xu Y, Hou C, Lu M, He X, Wang P, Li W, Peng B. Mid-infrared emissions of Pr^{3+}-doped GeS_2-Ga_2S_3-CdI_2chalcohalide glasses. *Mater Res Bull* 2014;**60**:391–6. https://doi.org/10.1016/j.materresbull.2014.09.003.

119 Guo H, Xu Y, Chen H, He X, Cui X, Wang P, Lu M, Li W, Hou C, Peng B. Near- and mid-infrared emissions of Dy^{3+}doped and Dy^{3+}/Tm^{3+} co-doped lead cesium iodide modified chalcohalide glasses. *J Lumin* 2014;**148**:10–7. https://doi.org/10.1016/j.jlumin.2013.11.011.

120 Karaksina E v., Shiryaev VS, Kotereva T v., Velmuzhov AP, Ketkova LA, Snopatin GE. Preparation of high-purity Pr^{3+}doped Ge-As-Se-In-I

glasses for active mid-infrared optics. *J Lumin* 2016;**177**:275–9. https://doi.org/10.1016/j.jlumin.2016.05.005.

121 Wang Z, Guo H, Xiao X, Xu Y, Cui X, Lu M, Peng B, Yang A, Yang Z, Gu S. Synthesis and spectroscopy of high concentration dysprosium doped GeS_2-Ga_2S_3-CdI_2 chalcohalide glasses and fiber fabrication. *J Alloys Compd* 2017;**692**:1010–7. https://doi.org/10.1016/j.jallcom.2016.09.085.

122 Shiryaev VS, Karaksina E v., Kotereva T v., Churbanov MF, Velmuzhov AP, Sukhanov M v., Ketkova LA, Zernova NS, Plotnichenko VG, Koltashev V v. Preparation and investigation of Pr^{3+}-doped Ge–Sb–Se–In–I glasses as promising material for active mid-infrared optics. *J Lumin* 2017;**183**:129–34. https://doi.org/10.1016/j.jlumin.2016.11.032.

123 Guo Q, Xu Y, Guo H, Xiao X, Lin C, Cui X, Wang P, Gao F, Lu M, Peng B. Effect of iodine (I_2) on structural, thermal and optical properties of Ge-Sb-S chalcohalide host glasses and ones doped with Dy. *J Non Cryst Solids* 2017;**464**:81–8. https://doi.org/10.1016/j.jnoncrysol.2017.03.024.

124 Li M, Xu Y, Jia X, Yang L, Long N, Liu Z, Dai S. Mid-infrared emission properties of Pr^{3+} -doped Ge–Sb–Se–Ga–I chalcogenide glasses. *Opt Mater Express* 2018;**8**:1076–82. https://doi.org/10.1016/j.jlumin.2013.11.021.

125 Fjodorow P, Frolov MP, Leonov SO, Denker BI, Galagan BI, Sverchkov SE, Koltashev V v., Plotnichenko VG, Sukhanov M v., Velmuzhov AP. Mid-infrared laser performance of Ce 3+ -doped selenide glass . *Opt Express* 2021;**29**:27674. https://doi.org/10.1364/oe.433828.

126 Sanghera J, Gibson D. Optical properties of chalcogenide glasses and fibers. *Chalcogenide Glasses*. Cambridge: Woodhead; 2014. p. 113–38.

127 Wood DL, Tauc J. Weak absorption tails in amorphous semiconductors. *Phys Rev B* 1972;**5**:3144–51. https://doi.org/10.1103/PhysRevB.5.3144.

128 Urbach F. The long-wavelength edge of photographic sensitivity and of the electronic Absorption of Solids. *Physical Review* 1953;**92**:1324. https://doi.org/10.1103/PhysRev.92.1324.

129 Seddon AB, Sojka L, Shen M, Tang ZQ, Furniss D, Barney E, Sakr H, Jayasuriya D, Parnell H, Butterworth J, Crane RW, Nunes JJ, Mabwa DP, Farries M, Phang S, *et al.* Breaking through the wavelength barrier: The state-of-play on rare-earth ion, mid-infrared fiber lasers for the 4–10 μm wavelength region. *Mid-Infrared Fiber Photonics*. Elsevier; 2022. p. 401–502.

130 Kanamori T, Terunuma Y, Takahashi S, Miyashita T. Chalcogenide Glass Fibers for Mid-Infrared Transmission. *Journal of Lightwave Technology* 1984;**2**:607–13. https://doi.org/10.1109/JLT.1984.1073657.

131 Sanghera JS, Shaw LB, Aggarwal ID. Applications of chalcogenide glass optical fibers. *Journal of Optoelectronics and Advanced Materials* 2001;**3**:627–40. https://doi.org/10.1016/S1631-0748(02)01450-9.

132 Yadav A, Kang M, Goncalves C, Blanco C, Sharma R, Richardson K. Impact of raw material surface oxide removal on dual band infrared optical properties of As 2 Se 3 chalcogenide glass . *Opt Mater Express* 2020;**10**:2274. https://doi.org/10.1364/ome.400071.

133 Tang Z, Furniss D, Fay M, Neate NC, Cheng Y, Barney E, Sojka L, Sujecki S, Benson TM, Seddon AB. First identification of rare-earth oxide nucleation in chalcogenide glasses and implications for fabrication of mid-infrared active fibers. *Journal of the American Ceramic Society* 2014;**97**:432–41. https://doi.org/10.1111/jace.12732.

134 Tang Z, Shiryaev VS, Furniss D, Sojka L, Sujecki S, Benson TM, Seddon AB, Churbanov MF. Low loss Ge-As-Se chalcogenide glass fiber, fabricated using extruded preform, for mid-infrared photonics. *Opt Mater Express* 2015;**5**:1722. https://doi.org/10.1364/OME.5.001722.

135 Lezal D, Pedlíková J, Zavadil J, Kostka P, Poulain M. Preparation and characterization of sulfide, selenide and telluride glasses. *J Non Cryst Solids* 2003;**326–327**:47–52. https://doi.org/10.1016/S0022-3093(03)00375-2.

136 Kim WH, Nguyen VQ, Shaw LB, Busse LE, Florea C, Gibson DJ, Gattass RR, Bayya SS, Kung FH, Chin GD, Miklos RE, Aggarwal ID, Sanghera JS. Recent progress in chalcogenide fiber technology at NRL. *J Non Cryst Solids* 2016;**431**:8–15. https://doi.org/10.1016/j.jnoncrysol.2015.03.028.

137 Garcia-Lopez AC, Garcia-Rubio LH. Rayleigh-Debye-Gans as a model for continuous monitoring of biological particles: Part II, development of a hybrid model. *Opt Express* 2008;**16**:4671. https://doi.org/10.1364/OE.16.004671.

138 Fabbie P, Kundel L, Vitruk P. Tonue-Tie Functional release. *Laserfocus* 2016:13–8.

139 Stern J. Lasers in Spine Surgery: A Review. *SpineLine* 2009:17–23.

140 Fantarella D, Kotlow L. The 9.3-µm CO_2 Dental Laser: Technical Development and Early Clinical Experiences. *Journal of Laser Dentistry J Laser Dent* 2014;**2222**:10–27.

141 Kozub JA, Shen J-H, Joos KM, Prasad R, Shane Hutson M. Efficacy and predictability of soft tissue ablation using a prototype Raman-shifted alexandrite laser. *J Biomed Opt* 2015;**20**:105004. https://doi.org/10.1117/1.JBO.20.10.105004.

142 Walsh BM, Lee HR, Barnes NP. Mid infrared lasers for remote sensing applications. *J Lumin* 2016;**169**:400–5. https://doi.org/10.1016/j.jlumin.2015.03.004.

143 Jean B, Bende T. Mid-IR Laser Applications in Medicine. *Solid-State Mid-Infrared Laser Sources* 2003;**546**:511–46. https://doi.org/10.1007/3-540-36491-9_12.

144 *IEC 60825-1 Safety of laser products – Part 1: Equipment classification, requirements and user's guide*. IEC; 2001.

145 Chin JH, Okazaki M, Hu ZW, Miller JW, Hoffman BB. Activation of heat shock protein (hsp)70 and proto-oncogene expression by α1adrenergic agonists in rat aorta with age. *Journal of Clinical Investigation* 1996;**97**:2316–23. https://doi.org/10.1172/JCI118674.

146 Katzir A. *Lasers and Optical Fibers in Medicine*. San Diego: Academic Press; 1993.

147 Yadav RK. Definitions in laser technology. *J Cutan Aesthet Surg* 2009;**2**:45–6. https://doi.org/10.4103/0974-2077.53103.

148 Choi B, Welch AJ. Analysis of thermal relaxation during laser irradiation of tissue. *Lasers Surg Med* 2001;**29**:351–9. https://doi.org/10.1002/lsm.1128.

149 Kim B, Kim DY. Enhanced tissue ablation efficiency with a mid-infrared nonlinear frequency conversion laser system and tissue interaction monitoring using optical coherence tomography. *Sensors (Switzerland)* 2016;**16**:. https://doi.org/10.3390/s16050598.

150 Rossi F, Matteini P, Ratto F, Menabuoni L, Lenzetti I, Pini R. Laser Tissue Welding In Ophthalmic Surgery. *J Biophotonics* 2008;**1**:331–42. https://doi.org/10.1002/jbio.200810028.

151 Matteini P, Rossi F, Menabuoni L, Pini R. Microscopic characterization of collagen modifications induced by low-temperature diode-laser welding of corneal tissue. *Lasers Surg Med* 2007;**39**:597–604. https://doi.org/10.1002/lsm.20532.

152 Pavone FS. *Laser Imaging and Manipulation in Cell Biology*. Wiley-VCH; 2010.

153 Revell CK, Jensen OE, Shearer T, Lu Y, Holmes DF, Kadler KE. Collagen fibril assembly: New approaches to unanswered questions. *Matrix Biol Plus* 2021;**12**:. https://doi.org/10.1016/j.mbplus.2021.100079.

154 Rossi F, Matteini P, Ratto F, Menabuoni L, Lenzetti I, Pini R. Laser Tissue Welding In Ophthalmic Surgery. *J Biophotonics* 2008;**1**:331–42. https://doi.org/10.1002/jbio.200810028.

155 Bass LS, Treat MR. *Laser Tissue Welding: A Comprehensive Review of Current and Future Clinical Applications*. vol. 12315349. 1995.

156 Menovsky T, Beek JF, van Gemert MJC. Laser tissue welding of dura mater and peripheral nerves: A scanning electron microscopy study. *Lasers Surg Med* 1996;**19**:152–8. https://doi.org/10.1002/(SICI)1096-9101(1996)19:2<152::AID-LSM5>3.0.CO;2-R.

157 Stewart RB, Bass LS, Thompson JK, Nikoi ND, Becker G, Kung RTV. Improved microvessel repair: Laser welding with an anti-thrombotic solder. *Lasers Surg Med* 2002;**31**:36–40. https://doi.org/10.1002/lsm.10071.

158 Oskoui P, Stadler I, Lanzafame RJ. A preliminary study of laser tissue soldering as arterial wall reinforcement in an acute experimental aneurysm model. *Lasers Surg Med* 2003;**32**:346–8. https://doi.org/10.1002/lsm.10173.

159 Huang HC, Walker CR, Nanda A, Rege K. Laser welding of ruptured intestinal tissue using plasmonic polypeptide nanocomposite solders. *ACS Nano* 2013;**7**:2988–98. https://doi.org/10.1021/nn303202k.

160 Lauto A, Mawad D, Foster LJR. Adhesive biomaterials for tissue reconstruction. *Journal of Chemical Technology & Biotechnology* 2008;**83**:464–72. https://doi.org/10.1002/jctb.1771.

161 Bilici T, Tabakoğlu Ö, Kalaycioğlu H, Kurt A, Sennaroglu A, Gülsoy M. Low-Power Skin Welding by Thulium (Tm:YAP) Laser at 1980-Nm.

162 Rossi F, Pini R, Menabuoni L. Experimental and model analysis on the temperature dynamics during diode laser welding of the cornea. *J Biomed Opt* 2007;**12**:014031. https://doi.org/10.1117/1.2437156.

163 Yaws CL. *Vapor Pressure - Inorganic Compounds*. Second Edi. Elsevier Inc.; 1997.

164 Thomson GWm. The Antoine Equation for Vapor-pressure Data. *Chem Rev* 1946;**38**:1–39. https://doi.org/10.1021/cr60119a001.

165 Yaws CL. *Physical Properties - Inorganic Compounds*. Second Edi. Elsevier Inc.; 1997.

166 Sostman HE. Melting point of gallium as a temperature calibration standard. *Review of Scientific Instruments* 1977;**48**:127–30. https://doi.org/10.1063/1.1134992.

167 Zinkevich M, Aldinger F. Thermodynamic Assessment of the Gallium-Oxygen System. *Journal of the American Ceramic Society* 2004;**87**:683–91. https://doi.org/10.1111/j.1551-2916.2004.00683.x.

168 Vivek P Dwivedi. *The effect of liquid gallium on plastics.* MSc, Faculty of New Jersey Institute of Technology; 1995; 1995.

169 Greber JF. Gallium and Gallium Compounds. *Ullmann's Encyclopedia of Industrial Chemistry*. Wiley-VCH Verlag GmbH & Co. KGaA; 2000.

170 Kubaschewski O, Kubaschewski O, Alcock CB. *Metallurgical Thermochemistry*. Pergamon Press; 1967.

171 Furniss D, Seddon AB. Towards monomode proportioned fibreoptic preforms by extrusion. *J Non Cryst Solids* 1999;**256–257**:232–6. https://doi.org/10.1016/S0022-3093(99)00463-9.

172 Shiryaev VS, Karaksina E v., Churbanov MF, Kotereva T v., Stepanov BS, Ketkova LA, Evdokimov II, Koltashev V v., Plotnichenko VG, Filatov AI, Antonov IN. Special pure germanium-rich Ga-Ge-As-Se glasses for active mid-IR fiber optics. *Mater Res Bull* 2018;**107**:430–7. https://doi.org/10.1016/j.materresbull.2018.08.009.

173 Shiryaev VS, Karaksina E v., Velmuzhov AP, Sukhanov M v., Kotereva T v., Plekhovich AD, Churbanov MF, Filatov AI. Preparation and investigation of GaxGe25As15Se60-x (x = 1 ÷ 5) glasses. *Opt Mater (Amst)* 2017;**67**:38–43. https://doi.org/10.1016/j.optmat.2017.03.024.

174 Bletskan DI, Chepur D v, Mitrovtskii IM, Polazhinets N v, Potorii M v. Electrical and photoelectric properties of layered crystals of GeSe2 obtained by various methods 1985.

175 Petkov V, Qadir D, Shastri SD. Rapid structure determination of disordered materials: Study of GeSe 2 glass. *Solid State Commun* 2004;**129**:239–43. https://doi.org/10.1016/j.ssc.2003.10.007.

176 Aleksandrovich E v., Minaev VS, Timoshenkov SP. Structural relaxation of glassy GeSe2 during isothermal annealing below and above Tg. *Technical Physics* 2015;**60**:510–4. https://doi.org/10.1134/S1063784215040039.

177 Cui S, Boussard-Plédel C, Lucas J, Bureau B. Te-based glass fiber for far-infrared biochemical sensing up to 16 μm. *Opt Express* 2014;**22**:21253. https://doi.org/10.1364/OE.22.021253.

178 Tang G, Yang Z, Luo L, Chen W. Optical properties and local structure of Dy3+-doped chalcogenide and chalcohalide glasses. *Journal of Rare Earths* 2008;**26**:889–94. https://doi.org/10.1016/S1002-0721(09)60027-2.

179 Němec P, Oswald J, Frumar M, Němecova B. Optical propertie of germanium-gallium-selenium glasses doped by samarium. *Opt Mater* 2006;**28**:225–30.

180 Lezal D. *CHALCOGENIDE GLASSES-SURVEY AND PROGRESS*. vol. 5. 2003.

181 Moynihan CT, Macedo PB, Maklad MS, Mohr RK, Howard RE. Intrinsic and impurity infrared absorption in As2Se3 glass. *J Non Cryst Solids* 1975;**17**:369–85. https://doi.org/https://doi.org/10.1016/0022-3093(75)90127-1.

182 Savage JA, Webber PJ, Pitt AM. The potential of Ge-As-Se-Te glasses as 3–5 μm and 8–12 μm infrared optical materials. *Infrared Phys* 1980;**20**:313–20. https://doi.org/https://doi.org/10.1016/0020-0891(80)90045-7.

183 Fang Y, Furniss D, Jayasuriya D, Parnell H, Tang Z, Seddon AB, Benson TM. Determining the continuous thermo-optic coefficients of chalcogenide glass thin films in the MIR region using FTIR transmission spectra. *Opt Express* 2019;**27**:22275. https://doi.org/10.1364/oe.27.022275.

184 Sujecki S, Sójka L, Bereś-Pawlik E, Tang Z, Furniss D, Seddon AB, Benson TM. Modelling of a simple Dy 3+ doped chalcogenide glass fibre laser for mid-infrared light generation. *Opt Quantum Electron* 2010;**42**:69–79. https://doi.org/10.1007/s11082-010-9421-z.

185 Park BJ, Seo HS, Ahn J tae, Choi YG, Heo J, Chung WJ. Dy^{3+} doped Ge-Ga-Sb-Se glasses and optical fibers for the mid-IR gain media. *Journal of the Ceramic Society of Japan* 2008;**116**:1087–91. https://doi.org/10.1016/j.jnoncrysol.2005.07.008.

186 Krishnamurthy N, Gupta CK. *Extractive Metallurgy of Rare Earths*. 1st ed. Boca Raton: CRC Press; 2005.

187 Zhang Z, Jia Q, Liao W. *Progress in the Separation Processes for Rare Earth Resources*. vol. 48. 1st ed. Elsevier B.V.; 2015.

188 Anslyn E v, Dougherty DA, Dougherty E v, Books US. *Modern Physical Organic Chemistry*. University Science Books; 2006.

189 Fang Y, Furniss D, Jayasuriya D, Parnell H, Crane R, Tang ZQ, Barney E, Canedy CL, Kim CS, Kim M, Merritt CD, Bewley WW, Vurgaftman I, Meyer JR, Seddon AB, *et al.* Determining small refractive index contrast in chalcogenide-glass pairs at mid-infrared wavelengths. *Opt Mater Express* 2019;**9**:2022. https://doi.org/10.1364/OME.9.002022.

190 Wang R, Xu Q, Liu H, Sheng Y, Yang X. Structure and physical properties of Ge15Sb20Se65-xSx glasses. *Journal of the American Ceramic Society* 2018;**101**:201–7. https://doi.org/10.1111/jace.15206.

191 Rawson H. *Properties and Applications of Glass*. Elsevier Scientific Publishing Company; 1980.

192 Shelby JE. *Introduction to Glass Science and Technology*. 2nd ed. Cambridge; 2005.

193 Parnell H. *Towards a Ge-Sb-Se/S hyperspectral imaging probe for early cancer diagnosis*. University of Nottingham; 2018; 2018.

194 Angell CA. *STRUCTURAL INSTABILITY AND RELAXATION IN LIQUID AND GLASSY PHASES NEAR THE FRAGILE LIQUID LIMIT*. vol. 102. 1988.

195 Seddon AB, Hemingway MA. *Thermal characterisation of infrared-transmitting Ge-S-I glasses*. vol. 161. 1993.

196 Jessica Butterworth. *Mid-infrared transmitting Ge-Sb-Se chalcogenide glass fibres: for potential use in medical diagnostics*. PhD dissertation, University of Nottingham; 2017; 2017.

197 Savage SD, Miller CA, Furniss D, Seddon AB. Extrusion of chalcogenide glass preforms and drawing to multimode optical fibers. *J Non Cryst Solids* 2008;**354**:3418–27. https://doi.org/10.1016/j.jnoncrysol.2008.01.032.

198 van Nijnatten PA. *Determination of the optical constants of glass in the infrared using Kramers Kronig Analysis*. 1996.

199 Pamukchieva V, Todorova K, Mocioiu OC, Zaharescu M, Szekeres A, Gartner M. IR studies of impurities in chalcogenide glasses and thin films of the Ge-Sb-S-Te system. *J Phys Conf Ser* 2012;**356**:. https://doi.org/10.1088/1742-6596/356/1/012047.

200 Okabe TH, Zheng C, Taninouchi Y ki. Thermodynamic Considerations of Direct Oxygen Removal from Titanium by Utilizing the Deoxidation Capability of Rare Earth Metals. *Metallurgical and Materials Transactions B: Process Metallurgy and Materials Processing Science* 2018;**49**:1056–66. https://doi.org/10.1007/s11663-018-1172-4.

201 Sanghera J, Aggarwal ID. Development of chalcogenide fibers at NRL. *J Non Cryst Solids* 1997;**213**:.

202 Fang Y. *Assessing the optical properties of chalcogenide glasses and fibres: towards the development of new light sources.* PhD, University of Nottingham; 2019; 2019.

203 Dantanarayana HG, Abdel-Moneim N, Tang Z, Sojka L, Sujecki S, Furniss D, Seddon AB, Kubat I, Bang O, Benson TM. Refractive index dispersion of chalcogenide glasses for ultra-high numerical-aperture fiber for mid-infrared supercontinuum generation. *Opt Mater Express* 2014;**4**:1444. https://doi.org/10.1364/ome.4.001444.

204 Shiryaev VS, Filatov AI, Karaksina E v., Nezhdanov A v. Structural peculiarities of Ge-rich Ga-Ge-Sb-Se chalcogenide glasses. *J Solid State Chem* 2021;**303**:122454. https://doi.org/10.1016/j.jssc.2021.122454.

205 Jiang C, Cheng C, Zhu Q, Wang X, Nie Q, Dai S, Tao G, Zhu M, Liao F, Zhang P, Shen X, Xu T, Zhang P, Liu Z, Zhang X. Fabrication and characterization of Ge–Sb–Se–I glasses and fibers. *Appl Phys A Mater Sci Process* 2015;**120**:127–35. https://doi.org/10.1007/s00339-015-9179-z.

206 Olivier M, Tchahame JC, Němec P, Chauvet M, Besse V, Cassagne C, Boudebs G, Renversez G, Boidin R, Baudet E, Nazabal V. Structure, nonlinear properties, and photosensitivity of (GeSe_2)_100-x(Sb_2Se_3)_x glasses. *Opt Mater Express* 2014;**4**:525. https://doi.org/10.1364/ome.4.000525.

207 Robinson VNE. Imaging with backscattered electrons in a scanning electron microscope. *Scanning* 1980;**3**:15–26. https://doi.org/https://doi.org/10.1002/sca.4950030103.

208 Dieke GH, Crosswhite HM. *The Spectra of the Doubly and Triply Ionized Rare Earths*. 1963.

209 Moynihan C, Macedo P, Maklad M, Mohr R, Howard R. *INTRINSIC AND IMPURITY INFRARED ABSORPTION IN As2Se 3 GLASS*. vol. 17. 1975.

210 Nishii J, Yamashita T, Yamagishi T. *Oxide impurity absorptions in Ge-Se-Te glass fibres*. vol. 24. 1989.

211 Borisevich VG, Voitsekhovsky V v, Scripachev I v, Plotnichenko VG, Churbanov MF. Investigation of the influence of extrinsic hydrogen on the optical properties of chalcogenide glasses in the system As-Se. *Vysokochist Vesch* 1991;**1**:65.

212 Weber MJ. Optical spectra of Ce^{3+} and Ce^{3+}-sensitized fluorescence in YAlO3. *J Appl Phys* 1973;**44**:3205–8. https://doi.org/10.1063/1.1662735.

213 Przybylińska H, Ma CG, Brik MG, Kamińska A, Szczepkowski J, Sybilski P, Wittlin A, Berkowski M, Jastrzębski W, Suchocki A. Evidence of multicenter structure of cerium ions in gadolinium gallium garnet crystals studied by infrared absorption spectroscopy. *Phys Rev B Condens Matter Mater Phys* 2013;**87**:. https://doi.org/10.1103/PhysRevB.87.045114.

214 Przybylińska H, Ma CG, Brik MG, Kamińska A, Sybilski P, Wittlin A, Berkowski M, Zorenko Y, Gorbenko V, Wrzesinski H, Suchocki A. Electronic structure of Ce3+ multicenters in yttrium aluminum garnets. *Appl Phys Lett* 2013;**102**:. https://doi.org/10.1063/1.4812190.

215 Hall CN, Garthwaite J. What is the real physiological NO concentration in vivo? *Nitric Oxide* 2009:92–103. https://doi.org/10.1016/j.niox.2009.07.002.

216 Thomas DD, Liu X, Kantrow SP, Lancaster JR. *The biological lifetime of nitric oxide: Implications for the perivascular dynamics of NO and O 2*. vol. 98. 2001.

217 The Editors of Encyclopaedia Britannica. *Dysprosium*. Encylopaedia Britannica. 2022.

218 Macintyre JE. *Dictionary of Inorganic Compounds*. Taylor & Francis; 1992.

219 Sanghera J, Florea C, Busse L, Shaw B, Miklos F, Aggarwal I. Reduced Fresnel losses in chalcogenide fibers by using anti-reflective surface structures on fiber end faces. *Opt Express* 2010;**18**:26760. https://doi.org/10.1364/OE.18.026760.

220 Raut HK, Ganesh VA, Nair AS, Ramakrishna S. Anti-reflective coatings: A critical, in-depth review. *Energy Environ Sci* 2011;**4**:3779–804. https://doi.org/10.1039/c1ee01297e.

221 MacLeod BD, Hobbs DS, Sabatino III E. Moldable AR microstructures for improved laser transmission and damage resistance in CIRCM fiber optic beam delivery systems. *Window and Dome Technologies and Materials XII* 2011;**8016**:80160Q. https://doi.org/10.1117/12.883281.

222 Joseph Weiblen R, Florea CM, Busse LE, Brandon Shaw L, Menyuk CR, Aggarwal ID, Sanghera JS. Irradiance enhancement and increased laser damage threshold in As_2S_3 moth-eye antireflective structures. *Opt Lett* 2015;**40**:4799. https://doi.org/10.1364/ol.40.004799.

223 Rayleigh, Lord. On Reflection of Vibrations at the Confines of two Media between which the Transition is Gradual. *Proceedings of the London Mathematical Society* 1879;**s1-11**:51–6. https://doi.org/10.1112/plms/s1-11.1.51.

224 Weiblen RJ, Menyuk CR, Busse LE, Shaw LB, Sanghera JS, Aggarwal ID. Optimized moth-eye anti-reflective structures for As_2S_3 chalcogenide optical fibers. *Opt Express* 2016;**24**:10172. https://doi.org/10.1364/OE.24.010172.

225 Lotz MR, Petersen CR, Markos C, Bang O, Jakobsen MH, Taboryski R. Direct nanoimprinting of moth-eye structures in chalcogenide glass for broadband antireflection in the mid-infrared. *Optica* 2018;**5**:557–63. https://doi.org/10.1364/OPTICA.5.000557.

226 Bernhard CG, Miller WH. A Corneal Nipple Pattern in Insect Compound Eyes. *Acta Physiol Scand* 1962;**56**:385–6. https://doi.org/10.1111/j.1748-1716.1962.tb02515.x.

227 Petersen CR, Lotz MB, Markos C, Woyessa G, Furniss D, Seddon AB, Taboryski RJ, Bang O. Thermo-mechanical dynamics of nanoimprinting anti-reflective structures onto small-core mid-IR chalcogenide fibers [Invited]. *Chinese Optics Letters* 2021;**19**:030603. https://doi.org/10.3788/col202119.030603.

228 Florea C, Sanghera J, Busse L, Shaw B, Aggarwal I. Improved laser damage threshold for chalcogenide glasses through surface microstructuring. *Photonic and Phononic Properties of Engineered Nanostructures* 2011;**7946**:794610. https://doi.org/10.1117/12.877292.

229 Lalanne P, Lemercier-lalanne D. On the effective medium theory of subwavelength periodic structures. *J Mod Opt* 1996;**43**:2063–85. https://doi.org/10.1080/09500349608232871.

230 Weiblen RJ, Menyuk CR, Busse LE, Shaw LB, Sanghera JS, Aggarwal ID, Eiblen RJW, Lorea CMF. Irradiance enhancement and increased laser damage threshold in As 2 S 3 moth-eye antireflective structures 2016;**40**:12545–50. https://doi.org/10.1364/OE.24.010172.

231 Brunner R, Deparnay A, Helgert M, Burkhardt M, Lohmüller T, Spatz J. Product Piracy from nature: Biomimetic Microstructures and Interfaces for High-Performance Optics. *Proceedings of SPIE - The International Society for Optical Engineering* 2008;**7057**:. https://doi.org/10.1117/12.795939.

232 Paschotta R. Fresnel equations. *Encyclopedia of Laser Physics and Technology* 2008. https://doi.org/ISBN 978-3-527-40828-3.

233 Lotz M, Needham J, Jakobsen MH, Taboryski R. Nanoimprinting reflow modified moth-eye structures in chalcogenide glass for enhanced broadband antireflection in the mid-infrared. *Opt Lett* 2019;**44**:4383. https://doi.org/10.1364/ol.44.004383.

234 Mikkel Berri Lotz. *Nanoimprinted antireflective surface nanostructures for optical applications in the mid-infrared*. Copenhagen: DTU ; 2019; 2019.

235 Skripachev I v., El-Amraoui M, Messaddeq Y, Santagneli SH. Study of the glass transition temperature of as-s glasses for the fabrication of chalcogenide optical fibers. *Int J Appl Glass Sci* 2013;**4**:256–65. https://doi.org/10.1111/ijag.12020.

236 Velmuzhov AP, Sukhanov M v., Plotnichenko VG, Plekhovich AD, Shiryaev VS, Churbanov MF. Preparation of REE-doped Ge-based chalcogenide glasses with low hydrogen impurity content. *J Non Cryst Solids* 2019;**525**:119669. https://doi.org/10.1016/j.jnoncrysol.2019.119669.

Appendix 1 – Redesigned distillation rig.

